ADVANCED CEMENTITIOUS COMPOSITE DEVELOPMENT FOR RESILIENT AND SUSTAINABLE INFRASTRUCTURE

by

Ravi Ranade

A dissertation submitted in partial fulfillment
of the requirements for the degree of
Doctor of Philosophy
(Civil Engineering)
in The University of Michigan
2014

Doctoral Committee:

Professor Victor C. Li, Chair
Professor Gregory A. Keoleian
Associate Professor Jerome P. Lynch
Assistant Professor Jeffrey T. Scruggs

To my parents and teachers,
who have always shown me the right path.

Acknowledgements

First and foremost, I would like to sincerely thank my advisor, Dr. Victor Li. He has been a great mentor for me, academically and otherwise. His guidance and support throughout my doctoral research were indispensable for completing this dissertation, for which I am forever indebted. I am grateful to my committee members Dr. Gregory Keoleian, Dr. Jerome Lynch, and Dr. Jeffrey Scruggs for their valuable inputs and suggestions in the fields of Industrial Ecology, Structural Engineering, and Infrastructure Systems; all of which have shaped this research and enabled me to adopt holistic systems thinking in materials design.

I acknowledge the US Army Corps of Engineers – Engineer Research and Development (ERDC) Center for funding a major part of this research via contract #W912HZ-08-C-0056. The engineers at ERDC, specifically William Heard, Todd Rushing, and Jason Roth, have been close collaborators in this research. Helpful discussions with Tom Slawson, Tony Cummins, Ed O'Neil, James Davis, Brett Williams, and Jedadiah Burroughs are gratefully acknowledged. I am grateful to Professor Klaas van-Bruegel and his research group (particularly Dr. Ye Guang) for hosting me at TU Delft, where I learned the skills of micro-analysis of concrete.

I am grateful to our lab technicians: Bob Spence, Bob Fischer, Jan Pantolin, and Rick Burch, who have facilitated uninterrupted laboratory work which was vital for the timely progress of this research. I would also like to thank the administrative staff of the Civil and

Engineering Department: Jessica Taylor, Kimberly Simmons, Nancy Osugi, Matt Blank, Sherry Brueger, and Patricia Brainard for providing assistance in fellowship/grant applications and other financial matters.

I am thankful to my colleagues and friends at the ACE-MRL lab. Most importantly, I would like to thank Michael Stults, as almost half of the research presented in this dissertation was conducted with his collaboration. Qian (Maple) Zhang provided crucial assistance in the construction of the drop-weight impact test setup, and in performing the experiments, for which I am truly grateful. I would also like to express my gratitude for the senior group members, particularly, Mo Li, En-hua Yang, and Estela Garcez for teaching the art of making ECC and training on the lab equipment. Insightful interactions with Xiaoyan Huang, Emily Herbert, Aaron Sakulich, and Matthew Fadden are also appreciated.

Finally, from the bottom of my heart, I would like to thank my family and close friends, whose constant love and support gave me the courage and patience needed to undertake this seemingly daunting task. Even from thousands of miles away in India, I strongly felt the love and warmth of my parents, Pramod and Madhuri Ranade, to whom I dedicate this dissertation. I would like to thank Siddhartha Nadukuru and Kalyan Nadella for being the greatest roommates and friends. I am thankful for the love and affection received from the Mikelonis family (Anne, Gretchen, and David) and from the Sapre family (Pallavi, Kishor, Aakash, and Miheer) that made me feel at home in Michigan!

Table of Contents

Dedication ii

Acknowledgements iii

List of Tables xi

List of Figures xiii

Abstract xx

PART I: INTRODUCTION 1

CHAPTER 1: INTRODUCTION 1

1.1 Background and Motivation 1

1.2 Research Objectives 6

1.3 Material Design Approach 7

1.4 Dissertation Organization 9

PART II: MATERIAL DEVELOPMENT 14

CHAPTER 2: REVIEW OF MECHANICALLY HIGH-PERFORMING CONCRETES 14

2.1 Introduction 14

2.2 Historical Development of High Strength Concrete (HSC) 16

2.3 Principles of Design for High Compressive Strength 21

2.4 Historical Development of High Ductility Concretes 24

2.5 Principles of Design for High Tensile Ductility 27

2.6 Conclusions: Contrasting Design Philosophies of HSC and ECC 31

CHAPTER 3: MECHANICAL CHARACTERIZATION OF COR-TUF 38

3.1 Introduction 38

3.2 Materials and Mix Proportions 39

3.3 Composite Mechanical Response 41
3.3.1 Specimens 41
3.3.2 COR-TUF 7-4-2 Curing Procedure 43
3.3.3 Experimental Setup 44
3.3.4 Results and Discussion 47
3.4 Micro-scale Experimental Investigation 52
3.4.1 Specimens 52
3.4.2 Experimental Setup 54
3.4.3 Results and Discussion 55
3.5 Micro-scale Analytical Investigation 64
3.5.1 Mathematical Model 64
3.5.2 Comparison with Experimental Results 70
3.6 Single-crack Behavior of COR-TUF 71
3.7 Summary and Conclusions 75

CHAPTER 4: DEVELOPMENT OF HIGH STRENGTH-HIGH DUCTILITY CONCRETE (HSHDC) 79
4.1 Introduction 79
4.2 Design Objective and Approach 80
4.3 Materials and Mix Proportions 81
4.4 Specimens and Experimental Setup 87
4.5 Experimental Results and Discussion 88
4.6 Summary and Conclusions 96

CHAPTER 5: COMPOSITE PROPERTIES OF HIGH STRENGTH-HIGH DUCTILITY CONCRETE 99
5.1 Introduction 99
5.2 Experimental Investigation 100
5.2.1 Materials and Mix Proportions 100
5.2.2 HSHDC Mixing Procedure 101
5.2.3 Specimens 107
5.2.4 HSHDC Curing Procedure 107

5.2.5 Experimental Setup 108
5.3 Results and Discussion 111
5.3.1 Fresh Properties and Density 111
5.3.2 Direct Tension Behavior 113
5.3.3 Uniaxial Compression Behavior 117
5.3.4 Indirect Tension Behavior 120
5.3.5 Flexural Behavior 121
5.3.6 Multiple Cracking 123
5.4 Summary and Conclusions 125

CHAPTER 6: MICROSTRUCTURE AND MICROMECHANICS OF HIGH STRENGTH-HIGH DUCTILITY CONCRETE 129
6.1 Introduction 129
6.2 Microstructure of HSHDC 131
6.3 Largest Flaw Size Distribution 139
6.3.1 Relevance 139
6.3.2 Observation Method 139
6.3.3 Observations 140
6.4 Fiber Distribution 142
6.4.1 Relevance and Observation Quantities 142
6.4.2 Observation Method 144
6.4.3 Observations 147
6.5 Experimental Investigation of the Micromechanical Behavior of HSHDC 151
6.5.1 Specimens 151
6.5.2 Experimental Setup and Procedure 154
6.5.3 Single-fiber Pullout Test Results 155
6.5.4 Deduction of Fiber/Matrix Interfacial Bond Properties for Aligned Fibers 161
6.5.5 Deduction of the Snubbing Coefficient (f) for Inclined Fibers ($\phi > 0°$) 163
6.5.6 Proposed Inclination-dependent Hardening Mechanism 165
6.5.7 Single-crack Test Results 170

6.6 Analytical Investigation of the Micromechanical Behavior of HSHDC 171
6.6.1 Comparison with Observed Single-crack Behavior of Notched Coupons 172
6.6.2 Implications for Multiple Cracking 173
6.6.3 Comparison with Direct Tension Test Results of HSHDC Dogbones 176
6.7 Summary and Conclusions 178

PART III: MATERIAL AND STRUCTURAL RESILIENCE 183

CHAPTER 7: RATE EFFECTS IN HIGH STRENGTH-HIGH DUCTILITY CONCRETE 183

7.1 Introduction 183
7.2 Review of Rate effects in Concrete, ECC, and COR-TUF 184
7.2.1 Concrete 184
7.2.2 ECC 189
7.2.3 COR-TUF 192
7.3 Experimental Investigation 193
7.4 Experimental Results and Discussion 196
7.4.1 Composite Response 196
7.4.2 Micro-scale Behavior 202
7.5 Scale-linking Analysis 208
7.6 Conclusions 212

CHAPTER 8: BEHAVIOR OF HSHDC SLABS UNDER IMPACT AND BLAST LOADS 216

8.1 Introduction 216
8.2 Experimental Investigation through Drop-weight Tests 218
8.2.1 Specimens 218
8.2.2 Experimental Setup and Procedure 219
8.2.3 Results and Discussion 222
8.3 Finite Element Analysis of the Drop-Weight Tests 234
8.3.1 Introduction 234
8.3.2 Geometry and Meshing 237
8.3.3 Material Model for Slab Elements 240

8.3.4 Material Model for Impact Head and Base Support 261
8.3.5 Loading, Boundary Conditions, and Contacts 261
8.3.6 Results of the FE Analysis 263
8.3.7 Layered Slabs 277
8.4 FE Simulation of HSHDC Slabs under Air-blasts 282
8.4.1 Introduction to Blast Loads 282
8.4.2 Blast Load Cases and Simulation in LS-Dyna 285
8.4.3 Results and Discussion 288
8.5 Conclusions 297

PART IV: INFRASTRUCTURE SUSTAINABILITY AND INTEGRATION WITH RESILIENCE 302

CHAPTER 9: DEVELOPMENT OF GREEN, DURABLE HSHDC AND IMPACTS ON INFRASTRUCTURE SUSTAINABILITY 302

9.1 Introduction 302
9.2 Development of Green HSHDC 307
9.2.1 Experimental Investigation 307
9.2.2 Results and Discussion 310
9.3 Development of Durable HSHDC 313
9.3.1 Plasma Treatment Approach 314
9.3.2 Coupling Agent Approach 324
9.4 Environmental Life Cycle Assessment of an HSHDC Infrastructure Application 331
9.4.1 Introduction to Life Cycle Assessment (LCA) and Bridge Deck Model 332
9.4.2 Model Parameters 337
9.4.3 Results of LCA and Discussion 342
9.5 Conclusions 346

CHAPTER 10: NEW FRAMEWORK FOR ASSESSING THE IMPACT OF MATERIALS ON INFRASTRUCTURE RESILIENCE AND SUSTAINABILITY SIMULTANEOUSLY 354

10.1 Introduction 354
10.2 Resilience and Sustainability Metrics 357

10.3 Proposed Framework 363
10.4 Example Structural Application 366
10.5 Discussion of M-ϕ and F-Δ curves 375
10.6 Conclusions 378

PART V: SYNTHESIS 381
CHAPTER 11: CONCLUDING REMARKS **381**
11.1 Research Overview 381
11.2 Scientific Contributions and Research Impact 389
11.3 Recommendations for Future Research 394

List of Tables

Table 1.1: Eco-properties of Concrete 4

Table 3.1: Mix Proportions of COR-TUF (by weight) 39
Table 3.2: Geometry and Mechanical/Physical Properties of the Steel Fiber 39
Table 3.3: Summary of uniaxial tension properties of COR-TUF specimens 50
Table 3.4: Compressive strengths of COR-TUF cubes 51
Table 3.5: Mathematical equations for modeling hooked steel fiber pullout 65
Table 3.6: Fiber/matrix interaction properties of hooked steel fibers in COR-TUF matrix 69

Table 4.1: Mixture proportions 82
Table 4.2: Average mechanical properties 89

Table 5.1: Mix proportions of HSHDC 100
Table 5.2: Geometry and mechanical/physical properties of the PE Fiber 100
Table 5.3: Uniaxial compressive strengths of HSHDC cubes 119
Table 5.4: Summary of properties of HSHDC 126

Table 6.1: Summary of single-fiber pullout test results 160
Table 6.2: σ-δ analysis results 176
Table 6.3: Summary of micro-scale properties of HSHDC 180

Table 7.1: Summary of properties of HSHDC dogbone specimens under direct tension 197

Table 8.1: Experimental parameters of the drop-weight tests. 222
Table 8.2: Loading surfaces input parameter determination for HSHDC 252
Table 8.3: Loading surfaces input parameters for COR-TUF 253
Table 8.4: Other input parameters for HSHDC and COR-TUF 254

Table 8.5: Input parameters for MAT_003 material model 261
Table 8.6: Input parameters for contact definition in LS-Dyna 263
Table 8.7: Comparison of FE analysis with experimental results of the first impact 266
Table 8.8: Optimization analysis 281
Table 8.9: Input parameters for the LOAD-BLAST keyword 287

Table 9.1: Carbon and energy intensities of ingredients of various concretes 304
Table 9.2: Mix proportions of cement and its substitute in green HSHDCs (by weight) 308
Table 9.3: Chemical and physical analysis of the class F fly ash 309
Table 9.4: Mechanical and environmental performance of Green HSHDCs 312
Table 9.5: Interfacial bond properties observed in the first series of single fiber pullout specimens 319
Table 9.6: Influence of heat curing on the interfacial bond properties 322
Table 9.7: Mechanical performance of durable HSHDCs – plasma approach 323
Table 9.8: Mechanical performance of durable HSHDCs – coupling agent approach 328
Table 9.9: Influence of silane coupling agents on the interfacial bond properties 329
Table 9.10: Service life estimation of HSHDC link-slabs 340

Table 10.1: Life-cycle environmental and economic cost calculations 374

List of Figures

Figure 1.1: Performance Driven Design Approach (PDDA) applied to cementitious materials 8

Figure 2.1: (a) Typical tensile stress-strain curve and crack width-strain curve of ECC
(b) Saturated multiple cracking in ECC 27
Figure 2.2: Conceptual bridging stress - crack opening (σ-δ) relation 29

Figure 3.1: Dogbone specimen geometry for tensile testing of HPFRCC 42
Figure 3.2: Coupon specimen geometry for tensile testing of COR-TUF 42
Figure 3.3: Large dogbone specimen geometry for tensile testing of COR-TUF 43
Figure 3.4: Direct uniaxial tension test setup for COR-TUF coupons 45
Figure 3.5: Direct uniaxial tension test setup for large dogbones of COR-TUF 46
Figure 3.6: Three-point bending test setup for matrix fracture toughness determination 47
Figure 3.7: Uniaxial tension response of COR-TUF coupons 48
Figure 3.8: Uniaxial tension response of COR-TUF large dogbones 48
Figure 3.9: Pronounced matrix spalling evident in large dogbone breaks 51
Figure 3.10: Geometry of Dramix ZP 305 fiber showing hook dimensions 53
Figure 3.11: Single fiber pullout geometry for steel fibers embedded in COR-TUF matrix 54
Figure 3.12: (a) Sketch of the Single Fiber Pullout Test Setup (b) Picture of actual specimen test setup for a specimen with embedment length $\approx L_f/2 = 15$ mm 54
Figure 3.13: Experimentally determined single fiber pullout curves of hooked fibers with varying embedment lengths (L_e) 57
Figure 3.14: Schematic representation of the five pullout stages of hooked steel fibers 58
Figure 3.15: Meaning of symbols used in Figure 3.14 using Stage 3 as a representative figure 58
Figure 3.16: Various of stages of hooked steel fiber pullout of specimen #3 in Figure 3.13(a) with $L_e = L_f/2$ 61

Figure 3.17: Zoomed view of Figure 3.16 resolving Stages 1 and 2 61
Figure 3.18: Experimentally determined single fiber pullout curves of straight fibers (without hooks) with varying embedment lengths (L_e) 63
Figure 3.19: Observed Stage 2 displacements in SFP-H specimens 67
Figure 3.20: Plot of observed P_{peak} vs. L_e of SFP-H specimens for determining τ_0 and P_2 68
Figure 3.21: Comparison of experimental and analytical curves for the pullout of a hooked steel fiber embedded with length of 15 mm ($L_f/2$) in COR-TUF matrix 70
Figure 3.22: Schematic depiction of a crack opening 71
Figure 3.23: Computed single-crack (σ-δ) behavior of COR-TUF 73

Figure 4.1: Direct tension test setup for dogbone specimens 88
Figure 4.2: Representative tensile stress-strain curves 95
Figure 4.3: Comparison Chart 95

Figure 5.1: HSHDC Mixing Procedure 101
Figure 5.2: Various stages of HSHDC mixing 102
Figure 5.3: Uniaxial tension and compression test setups 110
Figure 5.4: Flexure test setup for 4″x4″x14″ beams 111
Figure 5.5: Flow curves of HSHDC and ECC matrixes 112
Figure 5.6: Direct tension behavior of HSHDC dogbone specimens 114
Figure 5.7: Pre-first crack direct tension test results of four dogbones (#1-4) 116
Figure 5.8: Uniaxial compression behavior of HSHDC 2″ cube specimens 118
Figure 5.9: Comparison of tensile-to-compressive strength ratios of various concretes 120
Figure 5.10: Indirect tension behavior of HSHDC (Ø4″ x 8″) split-cylinders 121
Figure 5.11: Flexural behavior of HSHDC 4″ x 4″ x 14″ beams 122
Figure 5.12: Crack patterns at failure in HSHDC specimens 124

Figure 6.1: Micromechanical Investigation Procedure 131
Figure 6.2: SEM micrographs of the HSHDC ingredients 134
Figure 6.3: Energy-dispersive spectra of HSHDC ingredients 135
Figure 6.4: SEM micrographs of HSHDC sections 136
Figure 6.5: Energy-spectra at points A and B 138

Figure 6.6: EDS analysis of segment AB 138
Figure 6.7: An HSHDC dogbone specimen cross-section 140
Figure 6.8: Distribution of largest flaw size across 80 HSHDC dogbone specimen cross-sections 141
Figure 6.9: Fluorescence imaging of HSHDC specimen cross-sections 145
Figure 6.10: Observed and best-fit fiber orientation distributions 148
Figure 6.11: Observed and theoretical fiber numbers 150
Figure 6.12: Single-fiber pullout test: (a) Casting of specimens (b) One specimen (c) Test setup 153
Figure 6.13: Single-crack specimen geometry and test setup 154
Figure 6.14: Representative experimental single-fiber pullout curves 157
Figure 6.15: Complete single fiber pullout test curves for aligned fibers ($\phi = 0°$) with varying embedment lengths (L_e) 158
Figure 6.16: Complete single fiber pullout test curves for various fiber inclination angles (ϕ) and embedment lengths (L_e) 159
Figure 6.17: Deduction of interfacial bond (τ_0 and G_d) 162
Figure 6.18: Deduction of snubbing coefficient (f) 164
Figure 6.19: Observed and modeled single fiber pullout behavior of specimen number 43 166
Figure 6.20: Deduction of $\mu.\varphi$ for specimen number 43 166
Figure 6.21: Deduction of inclination hardening parameter (μ) 167
Figure 6.22: Schematic depiction of inclination-dependent hardening mechanism 169
Figure 6.23: SEM generated micrographs of the embedded ends of the pulled out fibers 169
Figure 6.24: Measured and computed (using ECC and HSHDC models) crack bridging relations of HSHDC rectangular coupons 171
Figure 6.25: Computed σ-δ curves at $V_f = 2\%$ for various orientation distributions 174
Figure 6.26: Computed σ-δ curves for HSHDC dogbones at various fiber volume fractions 177

Figure 7.1: Effect of strain rate on tensile strength of concrete 185
Figure 7.2: Effect of strain rates on compressive strength of concrete 185
Figure 7.3: Rate dependence of M45-ECC (a) uniaxial tensile stress-strain response (b) ultimate tensile strain capacity 189

Figure 7.4: Rate dependence of interfacial parameters of ECC 190
Figure 7.5: Uniaxial tensile stress-strain curves of rate tailored ECC using hybrid fibers 191
Figure 7.6: Direct tension test setup with lost motion assembly 195
Figure 7.7: Direct tension response of HSHDC dogbones at various strain rates 196
Figure 7.8: Rate effects on first crack strength and ultimate tensile strength of dogbone specimens 199
Figure 7.9: Rate effects on tensile strain capacity and average residual crack width of dogbone specimens 200
Figure 7.10: Correlation between tensile strain capacity and $PSH_{strength}$ 201
Figure 7.11: Rate effects on fiber/matrix interfacial bond properties 203
Figure 7.12: Rate effects on fiber/matrix interaction properties 204
Figure 7.13: Rate effects on fiber properties 205
Figure 7.14: Rate effect on matrix fracture toughness 206
Figure 7.15: Measure of variation in fiber/matrix interaction properties determination 207
Figure 7.16: Rate effects on the computed fiber-bridging (σ-δ) behavior of HSHDC 208
Figure 7.17: Comparison of experimentally determined rate effects on composite tensile properties with analytically predicted results 210
Figure 7.18: Comparison of observed rate effects in first crack strength of composite specimens and matrix fracture toughness 211

Figure 8.1: Geometry of the slabs used in drop-weight tests 218
Figure 8.2: (a) Drop-weight impact test setup (b) Instrumentation [zoomed view of the dashed circle in (a)] (c) Specimen Holder 220
Figure 8.3: Observed contact force-time history of the first impact on HSHDC slab H4.60-1 225
Figure 8.4: Observed average acceleration-time history of the drop-weight assembly during the first impact on HSHDC slab H4.60-1 225
Figure 8.5: Derived velocity-time history of the drop-weight assembly during the first impact on HSHDC slab H4.60-1 226
Figure 8.6: Derived displacement-time history of the drop-weight assembly during the first impact on HSHDC slab H4.60-1 226
Figure 8.7: Comparison of HSHDC and COR-TUF slabs under multiple impacts 229

Figure 8.8: Damage condition of the COR-TUF slab C3.25-1 after impact #19 with 3″ head 231
Figure 8.9: Damage condition of the HSHDC slab H3.25-1 after impact #20 with 3″ head 231
Figure 8.10: Damage condition of the COR-TUF slab #1 after impact #15 233
Figure 8.11: Damage condition of the HSHDC slab #1 after impact #20 233
Figure 8.12: FE model of the drop-weight test 239
Figure 8.13: Mesh convergence study with impact velocity of 4.60 m/s 239
Figure 8.14: Stress-invariants ξ, r, θ and concrete's failure surface used in LS-Dyna material model MAT_072R3 243
Figure 8.15: Schematic representation of the fixed loading surface locations 247
Figure 8.16: η-λ relation for HSHDC used in MAT_072R3 model 250
Figure 8.17: Rate effects model ('load curve' in LS-dyna) for material strength 256
Figure 8.18: Uniaxial tensile behavior of a single HSHDC element in LS-Dyna 258
Figure 8.19: Uniaxial compressive behavior of a single HSHDC element in LS-Dyna 259
Figure 8.20: Comparison of HSHDC and COR-TUF single element behaviors 260
Figure 8.21: Boundary conditions of the slab-impact problem 262
Figure 8.22: Comparison of FE analysis with experimentally determined force-time history of an HSHDC slab hit by 16 kg drop-weight at 4.6 m/s 265
Figure 8.23: Locations of selected displacements for querying FE stress and strain profiles 267
Figure 8.24: Hydrostatic pressure distribution at the centroidal section of the slab 271
Figure 8.25(b): Maximum principal (tensile) strain distribution at the bottom face of the slab 273
Figure 8.26(b): Minimum principal (compressive) stress distribution at the top face of the slab 275
Figure 8.27: Relative distance between the centroidal nodes of the impact head and the slab 276
Figure 8.28: One of the layered configurations of the slab 278
Figure 8.29: Displacement-time histories of layered slab 279
Figure 8.30: Performance-cost tradeoff of safe slab configurations 281
Figure 8.31: Typical blast pressure-time variation 283
Figure 8.32: Geometry of the FE simulation of blast loads of HSHDC and COR-TUF slabs 286
Figure 8.33: Average blast pressure and slab displacement in response to a 0.5 kg TNT charge placed at 0.91 m 289
Figure 8.34: Normal stress at time points A to F (Figure 8.33) on the blast face of the slab 290

Figure 8.35: Maximum principal (tensile) strain on the back face of the slab 291
Figure 8.36: Comparison of HSHDC and COR-TUF slabs' responses to W=0.5 kg detonation at 0.91 m 292
Figure 8.37: Response of HSHDC slab under varying charge weights placed at 0.91 m 293
Figure 8.38: Influence of varying the charge weight on the maximum mid-point displacement of the HSHDC slab 294
Figure 8.39: Response of HSHDC slab under varying standoff distance of 0.5 kg TNT charge 295
Figure 8.40: Influence of varying the standoff distance on the maximum mid-point displacement of the HSHDC slab 295
Figure 8.41: Variation of slab displacement with the scaled distance 296

Figure 9.1: Carbon-MSI of various concretes 303
Figure 9.2: Energy-MSI of various concretes 304
Figure 9.3: Environmental versus mechanical performance of green HSHDCs 313
Figure 9.4: General structure of a silane coupling agent (SCA) 325
Figure 9.5: Tensile performance of durable HSHDC: D-V-1.0% 328
Figure 9.6: Crack width versus mechanical performance of durable HSHDCs 330
Figure 9.7: Bridge deck system definition 334
Figure 9.8: Life cycle of a bridge deck 336
Figure 9.9: Lepech's post-depassivation service life estimation model 341
Figure 9.10: Maintenance schedules of bridge decks with conventional expansion joints and HSHDC link-slabs 342
Figure 9.11: CO_2 emissions over 90 years' service life of the bridge deck 343
Figure 9.12: Primary energy consumption over 90 years' service life of the bridge deck 344

Figure 10.1: Resilience Triangle 358
Figure 10.2: Resilience Loss (R_L) and Resilience Index (R) 358
Figure 10.3: PEER methodology for performance-based earthquake engineering 360
Figure 10.4: Qualitative variation of damage with overload and tensile strain capacity of concrete 362
Figure 10.5: Column example (a) Elevation: support conditions and loading (b) Cross-section: reinforcement detailing 367

Figure 10.6: M-ϕ and F-Δ relations for the column designed with Concrete 1 368
Figure 10.7: M-ϕ relations for the columns designed with various concrete materials 369
Figure 10.8: F-Δ relations for the columns designed with various concrete materials 370
Figure 10.9: M-ϕ relations for the columns designed to meet the resilience criterion 371
Figure 10.10: F-Δ relations for the columns designed to meet the resilience criterion 372

Abstract

Concrete is the most used engineering material on this planet and has supported the prosperous growth of civilizations for the last five centuries as the main construction material (besides steel); however, its brittleness and negative environmental impact have limited the resilience and sustainability of the concrete infrastructure (buildings, roads, bridges, dams, power plants, etc.). With rapidly increasing global demand for infrastructure development and repair against a backdrop of climate change, terrorism, and tightening budgets, there is a growing need to overcome these limitations of the concrete infrastructure. This doctoral research attempts to address this challenge by systematically developing and investigating a new class of concrete at multiple length-scales through the application of micromechanics, structural analysis, life cycle assessment, and multi-scale modeling techniques.

The new class of concrete, named High Strength-High Ductility Concrete (HSHDC), developed in this research possesses unprecedented combination of ultra-high compressive strength (> 150 MPa) and tensile ductility (> 3%) in one material, along with durability (tight crack widths) and environmental greenness (of material as well as structural life-cycle). While each of these properties has been individually infused in concrete in the past, their integration has not been possible due to starkly contrasting design philosophies employed in their development. A systematic integrated approach that preserves the essential conditions for achieving ultra-high compressive strength (such as dense particle packing), and simultaneously optimizes the

fiber/matrix interaction to satisfy the necessary micromechanics conditions of tensile strain hardening is used in this research to achieve HSHDC with unparalleled combination of compressive strength and tensile ductility.

The resilience of HSHDC was examined at multiple length scales in this doctoral research. While the micro-scale and composite-scale experiments provided insights into the influence of high strain rates (up to 10/s) on the material's mechanical performance, drop-weight impact tests and 3D rate-dependent finite element simulation of blast loads revealed the behavior of HSHDC slabs under extreme loading conditions.

Versions of HSHDC for specifically enhancing its environmental sustainability, while maintaining and improving resilience, were developed in this research as well. Post-industrial recycled materials were used to substitute up to 25% cement (by weight), while maintaining the mechanical properties of HSHDC. A novel use of silane coupling agents and plasma treatment of fibers aimed at enhancing the fiber/matrix interfacial bond in HSHDC to achieve tighter crack widths (close to 100 μm) and greater durability was demonstrated in this research. The influence of using these greener and more durable versions of HSHDC on the environmental performance of bridge decks was evaluated using life cycle assessment.

With the above activities, this doctoral research has opened a new avenue for material research and development, which, instead of trading-off strength for ductility/durability (and vice-versa), achieves both the objectives simultaneously, which is expected to significantly enhance the resilience and sustainability of the 21st century infrastructure.

PART I: INTRODUCTION

CHAPTER 1: INTRODUCTION

1.1 Background and Motivation

The demand for infrastructure development and maintenance has grown exponentially in the first decade of the 21st century and this trend is expected to continue in the near future. A healthy infrastructure consisting of building transportation, water, power, emergency facilities, and telecommunication systems is necessary for sustaining a modern day society. In fast-developing economies, huge investments in building new infrastructure are being made to support their rapid economic growth. For example, China and India invested about 9% and 5% of their GDP, respectively, in the last two decades on infrastructure development.[1,2,3] In the developed economies, the existing infrastructure is in dire need for maintenance and repair. For instance, the current state of US infrastructure is graded "D+" by ASCE (American Society of Civil Engineers).[4] It is estimated that an investment of roughly $3.6 trillion is needed by the year 2020 for a substantial improvement of the US infrastructure. Increasing the quantity of infrastructure globally while improving its quality to satisfy the extremely high demand for infrastructure development and maintenance will be a major challenge for engineers in the coming decades.

The quality of the current infrastructure development in terms of its resilience and sustainability is not satisfactory. The lack of resilience of the current infrastructure has been proven multiple times in the past decade in the face of natural disasters and manmade attacks. Most recent example is the Typhoon Haiyan (Yolanda) in November, 2013, which decimated the infrastructure in several major cities of the Philippines and killed thousands of people. Another recent example at home is the series of devastating tornados striking central and southern US in 2012, which killed tens of people and destroyed infrastructure worth millions of dollars. At the same time, the huge burdens on the natural environment, economy, and society associated with material production and repeated maintenance of infrastructure systems have been highlighted. All the existing construction materials have large carbon footprint and energy intensity. An urgent task faced by the research community is the development of a new generation of construction materials that supports infrastructure resilience and sustainability simultaneously.

Concrete is the most commonly used construction material in the existing infrastructure. It is a versatile material with broad structural applications. It uses widely available and abundant ingredient materials for its production. Unlike steel, concrete is relatively inexpensive, moldable, and also durable as far as corrosion is concerned. As a result, concrete is the most used engineering material in the world – the global annual consumption of concrete is about 12 billion metric tons.[5] Due to the extensive use of concrete in infrastructure, the quality of concrete significantly affects the health of civil infrastructure worldwide.

Despite the remarkable properties of concrete, concrete infrastructure lacks resilience and durability due to its intrinsic brittle nature. Concrete has a fracture toughness of 0.1 to 1 MPa$\sqrt{m}$[6]

and is, therefore, one of the most brittle engineering materials in use. The brittleness of concrete causes large cracks under service loads with mm-size crack openings even when reinforced with steel rebars. This behavior adversely affects the durability of concrete structures. The brittle behavior of concrete also leads to catastrophic structural failure in the face of extreme natural and manmade loads thus degrading the resilience of infrastructure. Therefore, overcoming the brittleness of concrete should be the design objective for achieving infrastructure resilience and durability.

The use of concrete in large quantities is environmentally unsustainable, despite the abundance of the major raw ingredients. The production of concrete causes deterioration of the natural environment through utilization of tremendous amounts of energy, emission of greenhouse gases and wastes, and large scale scarring of natural land. Some of the important environmental impact indicators of concrete are given in Table 1.1. The component of concrete responsible for the majority of the environmental impact is cement. It typically constitutes about 10-20% (depending on strength) of concrete volume. Cement production in the US is 10 times energy intensive as compared to the average GDP. According to the Cement Sustainability Initiative (WBSCD),[7] the production of 1 metric ton cement requires about 4.8 GJ of energy and generates about 0.85 metric ton CO_2 in the most efficient cement plants. Cement production accounted for roughly 7% (2.4 billion metric tons[8]) of the global anthropogenic greenhouse gas emissions (34 billion metric tons[9]) in 2009. Besides greenhouse gases, cement production is also responsible for significant amounts of SO_x, NO_x, particulate matter, and other pollutants.[10] Thus, for reducing the impacts of infrastructure on the natural environment, not only the quality of concrete should be improved (in terms of overcoming its brittleness) but its dependence on

cement and other energy and carbon intensive materials over its lifetime (including its initial construction and repair events) should also be decreased simultaneously.

Table 1.1: Eco-properties of Concrete (Source: Ashby[5])

Property	**Typical Range**
Embodied energy (primary production)	1 – 1.3 MJ/kg
CO_2 footprint (primary production)	0.13 – 0.15 kg/kg
Water usage	1.7 – 5.1 liter/kg
Eco-indicator	3.6 – 4 milli-points/kg

Over the last three decades, significant advances have been made toward improvement of concrete's mechanical properties (both strength and ductility) and environmental performance. Modern high strength concretes such as Very-High/Ultra-High Strength Concrete (VHSC/UHPC), Reactive Powder Concrete (RPC), Macro Defect Free cement (MDF), concrete Densified with Small Particles (DSP), and Ductal (a commercial UHPC) have compressive strengths in excess of 100 MPa (up to 800 MPa with temperature and pressure curing).[11] These materials have been used in some of the tallest structures in the world built during the last decade as they allow size efficient structural elements to maximize usable space.[12] Similar progress has been made towards improving the ductility of concrete. The strain capacity of the current generation high ductility concretes, such as Engineered Cementitious Composites (ECC), Strain Hardening Cementitious Composites (SHCC), and some High Performance Fiber Reinforced Cement Composites (HPFRCC), has been substantially improved to about 2-6% (similar to ductile metals). Such high ductility materials have been successfully used in structures in seismically active regions for preventing catastrophic collapse. For improving concrete's environmental performance, researchers all over the world have investigated a variety of

recycled materials, such as fly ash, silica fume, slag, VCAS, Poraver, recycled aggregates, reused concrete, etc. These recycled materials have been shown to not only reduce the energy intensity and carbon footprint of concrete at the material production stage but also during the entire life cycle of concrete structures by improving their durability. Thus, with the existing knowledge, concrete can be designed for either high strength or high ductility or high greenness.

Despite the advances in concrete's strength, ductility, and greenness, these developments have been so far decoupled from each other. The high strength concretes typically have an extremely brittle matrix.[13,14] Although most of the tensile stress is carried by the steel reinforcement,[15] certain ductility of concrete is required for the integrity of reinforced concrete structural members under multi-directional dynamic loads.[16] Such loads are common during extreme natural and manmade events such as earthquakes, tornados, hurricanes, and blasts. The brittleness of high strength concrete is, therefore, compensated by the addition of short fibers; however, it results in a tension softening response characterized by decreasing load carrying capacity with increasing strain after the first crack formation. On the other hand, the compressive strength of high ductility concretes is typically less than 70 MPa which, although quite high, is 2-3 times lesser than that of the aforementioned high strength concretes. Furthermore, the high strength and high ductility concretes utilize more cement and highly processed materials per unit volume. This makes these high mechanically performing concretes two to three times more carbon and energy intensive and up to 1-2 orders of magnitude costlier than normal concrete per unit volume. At the same time, there has been only limited success in achieving mechanically superior concretes with recycled materials. A new concrete with all these three qualities of high strength, high ductility, and high greenness is, therefore, required for building a resilient and

sustainable infrastructure of the 21st century, which is the motivation behind this doctoral research.

1.2 Research Objectives

The goal of this doctoral research is to develop a new class of advanced cementitious materials with unprecedented combination of ultra-high compressive strength and tensile ductility, while simultaneously minimizing their environmental impact. The underlying scientific quest is to understand the behavior of these novel materials at multiple length scales through a micromechanics-based approach thus advancing the knowledge frontiers of high performance concretes and their interactions with the built and natural environments.

Specific research objectives to achieve the aforementioned goal are:

(a) To identify the challenges for integrating high compressive strength and tensile ductility in a single concrete by reviewing previously developed high strength and high ductility concretes and comparing their design philosophies.

(b) To elucidate the reasons behind lack of tensile ductility in an Ultra-High Performance Concrete (UHPC) using micromechanical analysis.

(c) To develop a High Strength-High Ductility Concrete (HSHDC) with the target combination of compressive strength and tensile ductility by overcoming these challenges.

(d) To investigate the mechanical and rheological properties of HSHDC.

(e) To investigate the microstructure and micro-scale fiber/matrix interaction of HSHDC.

(f) To determine the strain-rate effects on the tensile behavior of HSHDC at various length-scales.

(g) To investigate the resilience of HSHDC slabs under extreme loads, i.e. impacts and blasts, experimentally as well as analytically.

(h) To minimize the carbon footprint and energy intensity of HSHDC by incorporating recycled material alternatives, and at the same time, enhance the long-term durability and environmental sustainability of HSHDC through crack width reduction by fiber/matrix interface modification, and to compare the implications of using HSHDC versus ECC and other conventional materials on the environmental sustainability of an infrastructure application (link-slabs).

(i) To develop a novel framework for evaluating the implications of adopting advanced materials on the resilience and sustainability of infrastructure simultaneously.

As explained in the thesis outline below, each of these broad objectives motivates one chapter in this thesis.

1.3 Material Design Approach

The design of advanced cementitious materials in this research is largely based on the Performance Driven Design Approach (PDDA)[17,18] shown in Figure 1.1. At the heart of this framework are the micromechanics based analytical and numerical modeling tools developed at UM by Li and his fellow researchers.[19,20,21,22,23,24] This theoretical framework is supplemented by experimental determination and verification of material behavior at multiple length-scales. The PDDA combined with the Performance Based Design Concept (PBDC)[25,26] for structural design

forming the Integrated Structures and Materials Design Framework (ISMD)[27] has been successfully implemented over the last decade to design a class of ultra-ductile materials, Engineered Cementitious Composites (ECC), for a variety of structural applications.

Composite material properties related to cementitious materials (Figure 1.1), such as strength, ductility, crack width, transport properties, etc. are determined by the desired structural and environmental performance of infrastructure at higher length scales. Towards smaller length scales, composite properties are dependent on the microstructure and the complex interaction of various phases (fiber, aggregate, cement paste, and interfaces). Hence, the material microstructure can be optimally tailored to achieve target composite properties, which are determined by the required structural and environmental performance.

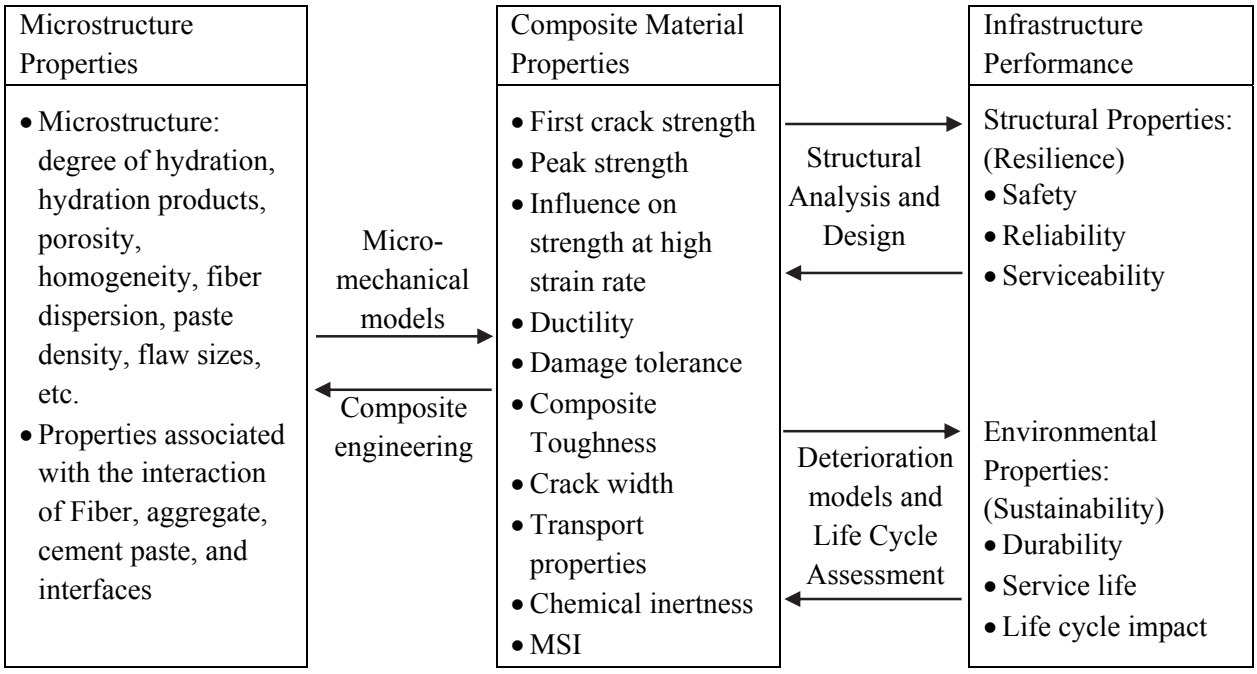

Figure 1.1: Performance Driven Design Approach (PDDA) applied to cementitious materials (after Li[17])

1.4 Dissertation Organization

This dissertation is organized into five parts containing a total of eleven chapters. The first part of this dissertation contains only the introductory chapter, where the background and motivation behind the documented research are presented. This is followed by nine specific research objectives, which motivate Chapters 2-10 in this dissertation. While the details of the research approach and tasks carried out for achieving each of these objectives are included in the respective chapters, the underlying material design approach is presented in the first chapter.

Part II of this dissertation is comprised of five chapters related to the material development of the High Strength-High Ductility Concrete (HSHDC), which combines ultra-high compressive strength with tensile ductility. In Chapter 2 (the first chapter of Part II), a review and historical development of concretes with high compressive strengths and high tensile ductility is presented to summarize the mechanical properties and the design principles of these concretes. A micromechanics-based investigation of a UHPC to determine the fundamental reasons behind its lack of tensile ductility is presented in Chapter 3. Based on the ideas developed in Chapters 2 and 3, the development of HSHDC utilizing the principles of micromechanics is reported in Chapter 4. The composite properties of HSHDC and its performance under flexure and split-tension loads, along with its rheological properties and density, are reported in Chapter 5. Micro-scale investigation of fiber/matrix interactions in HSHDC that result in the unique composite performance is detailed in Chapter 6.

In Part III of this dissertation, the material and structural resilience of HSHDC and its slabs are examined. In Chapter 7, the strain rate effects on the tensile behavior of HSHDC are investigated at composite scale (through uniaxial tension tests) and at micro-length scale (through single fiber pullout tests). The influence of the micro-length scale rate effects on the composite behavior is also discussed through scale-linking modeling in this chapter. The experimental results of drop weight impact tests on HSHDC and COR-TUF (a UHPC) thin slabs are included in Chapter 8. The simulation of these drop weight experiments using non-linear rate-dependent 3D finite element method is also presented in Chapter 8. This model is intended to provide insights into the material and structural behaviors at high strain rates and to guide future design of structural members made with HSHDC.

In Part IV of this dissertation, the focus shifts from resilience towards sustainability aspects of HSHDC and its potential infrastructure applications; nevertheless, adequate resilience and mechanical performance of HSHDC are maintained. In Chapter 9, the development of Green HSHDC by incorporating recycled matrix materials is documented. Also included in this chapter are the details of fiber/matrix interfacial bond enhancements, through plasma treatment of fibers and use of coupling agents, to reduce crack widths in HSHDC for improving long term durability. Furthermore, the life cycle assessments of bridge decks containing link-slabs made with these HSHDCs and their comparison with ECC link-slab and conventional expansion joint are also included in Chapter 9. In Chapter 10, a novel framework for evaluating the impacts of material properties on infrastructure resilience and sustainability, simultaneously, is presented. Treating resilience as constraint and minimizing the environmental and economic costs, the

application of this framework for evaluating the performance of various materials in a simple structural application is demonstrated.

Part V of this dissertation contains only one chapter synthesizing the knowledge generated in this dissertation. Chapter 11 summarizes the scientific contributions of this doctoral research and its broader impacts on infrastructure resilience and sustainability. In addition, recommendations for future research on further investigating HSHDC and similar advanced materials and their potential infrastructure applications are included in Chapter 11.

References

1. Bhattacharyay, B. (2010) "Estimating Demand for Infrastructure in Energy, Transport, Telecommunications, Water and Sanitation in Asia and the Pacific: 2010-2020" *ADBI Working Paper 248.* Tokyo, Japan: Asian Development Bank Institute, pp. 3-24.

2. ULI & E&Y (2012) "Global Update" In *Infrastructure 2012: Spotlight on Leadership*. Washington DC: Urban Land Institute, pp. 9-22.

3. MGI (2013) "Exhibit 2" In *Infrastructure Productivity: How to Save $1 trillion a year*, McKinsey Global Institute: McKinsey Infrastructure Practice, pp. 12.

4. ASCE (2013) "2013 Report Card for America's Infrastructure" Washington DC: American Society of Civil Engineers.

5. Ashby, M. F. (2009) "Resource Consumption" In *Materials and the Environment: Eco-Informed Material Choice.* Burlington, MA: Butterworth-Heinemann, pp. 17-19.

6. Bazant, Z. P. & Planas, J. (1998) "Variability of Apparent Fracture Toughness for Concrete." In *Fracture and Size Effect in Concrete and Other Quasibrittle Materials*, Washington DC: CRC Press, pp. 101-103.

7. WBCSD (2008) "Performance Data" In *Cement Industry Energy and CO_2 Performance*, Geneva, Switzerland: World Business Council for Sustainable Development, pp. 14-33.

8. USGS (2010) "Cement" In *Mineral commodity summaries*, Washington DC: US Geological Survey, pp. 38-39.

9. Quere, C. L., et al. (2009) "Trends in the sources and sinks of carbon dioxide" *Nature Geoscience,* 2, 831-836.

10. Worrell, E., Price, L. M., Hendriks, C. & Meida, L. O. (2001) "Carbon Dioxide Emissions from the Global Cement Industry" *Annual Review of Energy and the Environment*, 26, 303-329.

11. Richard, P. & Cheyrezy, M. (1994) "Reactive Powder Concretes with High Ductility and 200-800 MPa Compressive Strength." In *Concrete Technology: Past, Present, and Future, SP-144*, P. K. Mehta (Ed.), Farmington Hills, MI: American Concrete Institute, pp. 507-518.

12. PCA (2013) *Concrete Technology*: *CTT Newsletter Timeline*. Accessed June 1, 2013, at Portland Cement Association Website: http://www.cement.org/tech/ctt_timeline.asp

13. Gettu, R., Bazant, Z. P. & Karr, M. E. (1990) "Fracture Properties and Brittleness of High-Strength Concrete" *ACI Materials Journal,* 87(6), 608-618.

14. Bazant, Z. P. & Planas, J. (1998) "Estimation of the Equivalent LEFM Crack Extension" In *Fracture and Size Effect in Concrete and Other Quasibrittle Materials*, Washington DC: CRC Press, pp. 109-110.

15. ACI Committee 318 (2008) "Design Strength" In *Building Code Requirements for Structural Concrete (ACI 318-08) and Commentary*, Farmington Hills, MI: American Concrete Institute, pp. 117-118.

16. Williamson, E. B., et al. (2010) "Literature Review" In *Blast-Resistant Highway Bridges: Design and Detailing Guidelines - NCHRP Report 645*, Washington DC: Transportation Research Board, National Academy of Sciences, pp. 8-24.

17. Li, V. C. (1992) "Performance Driven Design of Fiber Reinforced Cementitious Composites," In Proc. of *4th RILEM International Symposium on Fiber Reinforced Concrete*, R. N. Swamy (Ed.). Sheffield, UK: E & FN Spon, pp. 12-30.

18. Li, V. C. (1993) "From Micromechanics to Structural Engineering – The Design of Cementitious Composites for Civil Engineering," *JSCE Journal of Structural Mechanics and Earthquake Engineering*, 10(2), 37-48.

19. Li, V. C., Wang, Y. & Backer S. (1990) "Effect of Inclining Angle, Bundling and Surface Treatment on Synthetic Fibre Pull-Out from a Cement Matrix," *Composites*, 21(2), 132-140.

20. Li, V. C., Wang, Y. & Backer, S. (1991). "A Micro Mechanical Model of Tension Softening and Bridging Toughening of Short Random Fiber Reinforced Brittle Matrix Composites," *Journal of Mechanics and Physics of Solids*, 39(5), 607-625.

21. Li, V.C. & Leung, C.K.Y. (1992) "Steady State and Multiple Cracking of Short Random Fiber Composites." *ASCE Journal of Engineering Mechanics*, 118(11), 2246-2264.

22. Lin, Z., Kanda, T. & Li, V. C. (1999) "On Interface Property Characterization and Performance of Fiber Reinforced Cementitious Composites" *RILEM Journal of Concrete Science and Engineering*, 1, 173-84.

23. Li, V. C., Wang, S. & Wu, C. (2001) "Tensile Strain-Hardening Behavior of PVA-ECC" *ACI Materials Journal*, 98(6), 483-492.

24. Li, V. C., Wu, C., Wang, S., Ogawa, A. & Saito, T. (2002) "Interface Tailoring for Strain-Hardening PVA-ECC" *ACI Materials Journal*, 99(2), 463-472.

25. Chandler, A. M. & Lam, N. T. (2001) "Performance-based design in earthquake engineering: a multidisciplinary review," *Engineering Structures*, 23, 1525-1543.

26. FEMA (1997) "Introduction" In *NEHRP Guidelines for the Seismic Rehabilitation of Buildings (FEMA Publication 273)*, Washington DC: Federal Emergency Management Agency, pp. 1.1-17.

27. Li, V. C. (2007) "Integrated structures and materials design" *RILEM Journal of Materials and Structures, 40*(4), 387-396.

PART II: MATERIAL DEVELOPMENT

CHAPTER 2: REVIEW OF MECHANICALLY HIGH-PERFORMING CONCRETES

2.1 Introduction

The majority of research efforts to enhance the mechanical performance of concrete over the last sixty years have pursued the objective of achieving high compressive strength. The reason behind the historical emphasis on compressive strength is the economic merit of enhanced strength-to-weight ratio (along with higher stiffness and abrasion resistance) enabling the construction of larger structures such as multistoried buildings with more usable space or bridges with longer unsupported spans.[1] Additionally, most structural designs consider the strength and strain capacity of concrete in tension as negligible,[2] with conventional steel reinforcement responsible for efficiently carrying the tensile loads in structural members. Another perceived benefit of using high strength concretes is high durability due to dense particle packing and, as a result, improved transport properties of un-cracked concrete.[1] Thus, the historical pursuit of high compressive strength in concrete is justified by high strength-to-weight ratio and favorable transport properties (in un-cracked state) of high strength concrete (HSC).

In spite of the desirable properties of HSC, there are critical limitations due to the lack of damage tolerance in this material. HSC is more prone to cracking (with unlimited crack widths) under service loads than normal strength concrete due to higher brittleness.[3] This inevitable cracking of HSC under service loads significantly deteriorates its transport properties and durability.[4] Furthermore, most catastrophic collapses of concrete structures, under extreme loads such as earthquakes, hurricanes, impacts, and blasts, have occurred due to the weakness of concrete in tension, and not compression.[5,6,7,8] The steel reinforcement used in these structures, to carry the tensile load, is rendered ineffective in such extreme events due to loss of concrete confinement caused by load reversals and high displacement demands. Thus, only increasing the compressive strength of concrete is inadequate in providing required resilience and durability in concrete structures, and the need for improving the tensile ductility is recognized.

In the last two decades, independent of HSC research, there has been a growing interest towards achieving high tensile ductility for overcoming the brittleness of concrete. Recently, the high ductility concretes have been implemented in a number of structural applications where durability and large displacements are of primary concern.[9,10,11] In such applications, high ductility concretes capable of self-controlling the crack widths prevent the transport properties from significantly degrading after cracking, unlike HSC and normal concrete.[12] This enhances the life-cycle performance of the structure in terms of substantially reduced maintenance costs and environmental impacts.[13] Utilizing their tensile ductility to facilitate large energy dissipation, high ductility concretes have been used to redesign seismically resistant structures in Japan saving substantial costs.[14] Although high ductility concretes overcome the limitation of

brittleness, these concretes do not possess the high strength-to-weight ratio and associated benefits of HSC.

The objective of this chapter is to identify the challenges for integrating high compressive strength and tensile ductility in a single concrete by reviewing previously developed high strength and high ductility concretes and comparing their design philosophies. In this chapter, brief historical developments of some of the notable high strength and high ductility concretes are presented followed by the fundamental principles of designs of both concretes and their comparison.

2.2 Historical Development of High Strength Concrete (HSC)

Over the years, the definition of "high" (or "above average") strength concrete has been often revised, and even today, it is rather a notion subject to personal interpretation depending on the structural application and geographical region. ACI Committee 363[15] on HSC recognizes this fact, but recommends a minimum compressive strength of about 55 MPa (8000 psi) for an HSC. Nevertheless, since the invention of Portland cement in the early 19th century, there has been a steady trend of gradual increase in concrete strength up to late 1950s, when 35 MPa concrete was considered high strength.[15]

Starting in 1960s, the compressive strength of concrete achievable in laboratories and field applications in the US increased more rapidly to fulfill the construction needs of high-rises

in cities like Chicago and the vast bridge infrastructure of the National Highway System. A concrete compressive strength of 41 MPa was specified in 1960 by the Washington State Highway Department for constructing the thinnest prestressed concrete girders in the US at that time.[16] Concrete with compressive strength of 55 MPa was used in the precast piles at the Port of Seattle in early 1960s.[16]

The use of chemical admixtures such as water reducers in Japan (by Hattori[17]) and Germany (by Aignesberger[18]) in 1960s and 70s further contributed to the rise in compressive strengths of concrete. Chemical admixtures were introduced in the US in mid-1970s, and the Water Tower Place in Chicago became the world's tallest concrete building in 1974 utilizing 62 MPa concrete.[19] Concurrently, structures (mainly bridge girders) with concrete strength up to 90 MPa were constructed in Japan in 1970s by the National Railway.[20]

In the late 1970s and early 1980s, European researchers led by Hans Henrik Bache pioneered some of the world's highest strength concretes of that period. In his work at Aalborg Portland of Denmark, Bache combined the advances in chemical admixture technology with the concept of dense particle packing using ultra-fine particles to produce DSP (Densified with Small Particles) concretes with compressive strengths greater than 100 MPa.[21,22]

Another concrete developed in the same period as DSP concrete was Slurry Infiltrated Fiber Concrete (SIFCON), first introduced in 1979 by Lankard & Lease[23], and remains a subject of investigation to this date for various applications. SIFCON can be regarded as the first attempt to achieve high compressive strength (100-120 MPa) and tensile ductility (1-2%) in one

concrete. However, the practical use of this composite has been limited by high cost and weight due to high fiber content (up to 20% of total composite volume) and anisotropic behavior resulting in weak planes due to constrained randomness of fiber distribution.

The next technology to greatly enhance concrete strengths was autoclaving at high temperatures and pressures, assisted by the growing number and size of precast plants. By the late 1980s, several researchers worldwide were involved in developing the next generation of HSC by integrating autoclaving with chemical admixtures and dense particle packing. The term "Very High Strength Concrete (VHSC)" began to appear in literature in the 1980s to distinguish this class of concretes from previous HSCs. Double & Wise of CEMCOM Corporation (Lanham, MD) received a patent[24] for a "cementitious composite containing metal fiber" in 1988, with compressive strengths of 100-150 MPa. This composite was composed of American Petroleum Institute (API) class H cement, silica fume, a super-plasticizer, steel fibers (volume fraction of 5-20%), and either steel or ceramic aggregates. These mixes were cured for 4 hours after casting in a 90% humidity environment, then at 60°C in a lime-water solution for 4 hours, left to air dry for 5 days, then oven cured at high temperature of 150-350°C. Though the original intent was to use such material for vacuum molding, the resulting concept proved to be foundational for HSC in structural applications.

Building upon the above work by Double & Wise, researchers Richard & Cheyrezy at Bouygues in France (later acquired by Lafarge Corporation) developed a material in 1993 known as Reactive Powder Concrete (RPC)[25], which would later be marketed as Ductal®. In its initial form, RPC was produced with designations of RPC200 and RPC800, where the number indicates

the compressive strength of the material in MPa. RPC800 was a mixture very similar to that produced by Double & Wise, with the addition of confining pressure applied to the freshly poured mixture in order to reduce material porosity as far as possible, and very high heat (250 – 400 °C) applied to the demolded material. The RPC200 was a similar material with the exception that the steel aggregate and pressure setting were omitted. Due to their extremely high compressive strengths (consistently greater than 150 MPa) and very low permeability in the uncracked state, RPCs were called Ultra-High Performance Concretes (UHPC) in late 1990s (and even today) to distinguish from HSC and VHSC developed earlier. The first application of a commercial UHPC (Ductal) was the Shawnessy Light Rail Transit Station in Canada completed in 2004.[26]

The main objective of RPC development, in addition to high compressive strength, was the addition of a softening branch to the load-deflection curve of a structural element in flexure. Through the addition of this softening behavior, this new material was able to improve upon the energy dissipation normally found in structural concretes.[27] This was made possible by the inclusion of metal fibers, which served to hinder the ability of a crack to propagate/open in the brittle matrix. Though this concept was not new (much work had been done previously on SIFCON with much higher volume of fibers), it was one of the first mixtures to use metal fibers in more miscible volume fractions, on the order of 3-5%.[27] Several other studies ensued following the introduction of this material as its applications became more varied, including: patents on impact/shock/projectile resistance,[28] mixtures including inorganic microfibers (carbon, wollastonite, calcite, etc.) that are capable of being premixed,[29] fire resistance,[30] and finally mixtures produced at ready-mix plants in mixer trucks.[31]

The last (and the most recently developed) HSC discussed in this history is COR-TUF™. Using the principles underlying the development of RPC, researchers Neeley & Walley at the Waterways Experiment Station (now known as Engineer Research and Development Center [ERDC]) of the US Army Corps of Engineers in Vicksburg, MS, developed their first version of UHPC, called COR-TUF, in 1995 with compressive strength approaching 200 MPa.[32,33]

Since its first version, COR-TUF has been the subject of extensive study and permutation mainly at ERDC by O'Neil and others in order to further improve the compressive strength and enhance the toughness of COR-TUF in flexure. As documented in his PhD thesis,[34] O'Neil reduced the amount of sand and crushed quartz (silica flour) by about 70%, increased the amount of silica fume by about 60%, and decreased the water/cement ratio by about 20% to 0.22 from the mix design of Neely & Walley. These modifications were made in efforts to further increase the mix's particle packing density, as well as reduce the amount of hydrated binder. Furthermore, O'Neil evaluated different cements (and super-plasticizers) on their effect on strength and fresh properties of concrete, and replaced ASTM Type V used by Neeley & Walley with API Class H cement. O'Neil also investigated the effect of various curing regimes, the necessity of each constituent in the composite material, the addition of wollastonite microfibers, and the inclusion of microspheres. The fracture toughness of the material, with and without steel fibers, and with microspheres was also evaluated. Through these efforts, O'Neil was able to improve the compressive strength and flexural toughness of COR-TUF; however, tensile ductility still remained elusive. This version of COR-TUF developed by O'Neil in 2006 (later modified slightly by researchers at ERDC to accommodate the changes in commercially available raw material ingredients) is the starting point of the material development in this doctoral research.

2.3 Principles of Design for High Compressive Strength

Following the discussion in Section 2.2, the fundamental principles behind the design of high strength concretes (COR-TUF in particular) are summarized below.

(a) *Dense particle packing*

The compressive strength of concrete usually increases with its particle packing density. Denser particle packing (1) reduces the mean size of the capillary pores, and (2) may reduce water requirements (with spherical fine particles such as silica fume or fly ash) for achieving target workability.[35] Both effects increase the fracture toughness (K_{Ic}) of the hydrated cement paste, thereby increasing the compressive strength by resisting wing crack propagation from defect sites. This dense particle packing philosophy represents the prevailing material selection paradigm found in nearly every high and ultra-high performance concrete, wherein materials are selected based upon homogeneity as well as their size, utilizing order-of-magnitude difference in sizes to optimize geometric packing.

(b) *Minimization of the number and size of flaws*

Flaws in concrete are weak zones (nm-mm sizes) such as entrained or entrapped air voids, capillary pores, and weak interfaces between distinct phases (e.g. aggregate and hydrated cement paste) of this largely inhomogeneous and complex composite material. Under an applied load, stress concentrations develop around these flaws initiating micro-cracks, which grow into macro-cracks (if allowed to open unrestrained) and can cause failure at stresses lower than that needed to fail a flawless material. As complete elimination of flaws is unachievable in concrete,

minimization of their size and number is targeted to maximize compressive strength;[36] this is achieved by various methods including rheology control (to minimize air voids), reduction in size of aggregates (to decrease the perimeter of the individual weak aggregate/cement interface), lowering w/c ratio (to reduce porosity), and high pressure application.

(c) *Microstructure enhancements*

The compressive strength of concrete can be increased by enhancing the quality of microstructure in terms of calcium-silicate-hydrate (CSH) formation and microstructure densification. There are three methods commonly used to achieve microstructure enhancement in high strength concretes:

(i) Maximizing amorphous silica content through the use of mineral admixtures, such as fly ash and silica fume, consumes the free water and weak hydration products such as calcium hydroxide (CH) to produce stronger CSH and denser microstructure.[37]

(ii) Using coarse grained low calcium aluminate cements such as oil well (API Class H) cement reduces the water demand and the un-hydrated cement particles act as strong aggregates with dense interface.[34] Coarse grained cements also allow longer mixing times typically required for very high strength concretes as the water reducers take time to slowly coat the cement particles.

(iii) Heat and pressure treatment at a proper age (typically 4-7 days after casting) significantly accelerates the formation of hydration products, as well as favorably converts the amorphous CSH into stronger crystalline tobermorite (at temperatures greater than 100°C) of equal density in the presence of an amorphous silica source (such as silica fume). Heat and pressure treatment in the absence of a silica source

converts amorphous CSH into crystalline α-CSH of higher density, which increases the porosity and may lead to strength degradation.[38]

(d) *Toughness enhancements*

Due to its high brittleness,[39] HSC as such cannot be used in structural applications, and typically short fibers are added to enhance the fracture toughness of HSC. Although the addition of fibers enhances the composite's fracture toughness, fiber-reinforced HSCs do not possess tensile ductility and exhibit a post-peak softening behavior (quasi-brittle response) under direct tension (discussed in Chapter 3).

In view of the above discussion, it is important to note the distinction between improving fracture toughness of a concrete versus imparting tensile ductility to it. Fracture toughness enhancements lead to higher energy dissipation at the crack tip by preventing the crack from propagating, thus requiring larger force and energy to drive the crack. Fiber addition in HSC discussed above is an example of fracture toughness enhancement, where the fibers delay and stabilize the propagation of the crack. On the other hand, imparting tensile ductility to a concrete enables it to undergo inelastic deformation by allowing distributed micro-cracking in the matrix volume, suppressing the fracture failure mode. Thus, while all ductile concretes are inherently tough, all tough concretes are not necessarily ductile. The historical development of ductile concrete and its design principles are discussed in the following sections.

2.4 Historical Development of High Ductility Concretes

Compared to HSC, the history of high ductility concretes is relatively short. Although the initial systematic efforts for achieving tensile ductility in brittle materials (not specifically concrete) using continuous fibers date back to 1973 when Aveston & Kelly[40] first proposed the underlying theory of multiple fracture of fibrous composites, the development of high ductility concretes did not begin in earnest until the 1990s. Between 1973 and 1990, seminal contributions were made by Hillerborg (1976),[41] Morton & Groves (1976),[42] Naaman et al. (1970s),[43,44,45] Marshal & Cox (1988),[46] Wang, Li & Backer (1988),[47,48] and Krenchel & Stang (1989)[49] in understanding the key mechanisms of fiber/matrix interactions and steady-state crack propagation in fiber reinforced composites, which proved to be instrumental in the development of high ductility concretes.

In early 1990s, Li and his fellow researchers at the Massachusetts Institute of Technology and later at the University of Michigan developed a micromechanics-based multi-scale framework[50,51,52,53,54] for achieving high tensile ductility in concrete, and, as a direct application of this framework, pioneered the first high ductility concrete reinforced with short discontinuous fibers at low fiber volume – Engineered Cementitious Composites (ECC). The first version of ECC[54] developed in 1993 contained short Polyethylene (PE) fibers along with a carefully tailored cementitious matrix. However, due to cost considerations, PE fibers were replaced by high performance PVA fibers[55,56] near the late 1990s with extensive tailoring of the matrix and, particularly, fiber/matrix interface. Along with the PE and PVA fibers, other fibers such as Polypropylene, natural fibers[57] (wood and vegetable fibers), steel fibers[58] (hybridized with

polymer fibers), and carbon nanotubes[59] have been investigated with their respective matrixes for use in various ECCs and their applications.

Since 1998, ECC containing Poly-Vinyl Alcohol (PVA) fibers (or PVA-ECC) has been extensively investigated at University of Michigan and has also attracted the attention of numerous researchers around the world for a variety of practical applications.[9,10,11,13] Similar high ductility concretes are known as Strain Hardening Cementitious Composites (SHCC)[60,61] in Europe/Asia or Multiple Fine Cracking Fiber Reinforced Cementitious Composites[62] in Japan or ductile High Performance Fiber Reinforced Cementitious Composites[63] (HPFRCC)[i] in US/Europe. The "Strain Hardening Cementitious Composites" and "Multiple Fine Cracking Fiber Reinforced Cementitious Composites" are more descriptive terms, while the term "ECC" emphasizes the underlying micromechanics design basis of this class of material.

Recently, a few notable investigations have been conducted on combining high compressive strength and high tensile ductility in one concrete with limited success. The development of Ultra High Performance-Strain Hardening Cementitious Composites (UHP-SHCC) was reported in Kamal et al.[64] The best performing UHP-SHCC has an average compressive strength of 96 MPa (14 ksi) at 14 days, only half that of COR-TUF, and tensile ductility of 3.3% at 14 days after casting (longer age data are not reported in this reference[64]). The development of another such material, Ultra High Performance-Fiber Reinforced Concrete (UHP-FRC), is presented in Wille et al.[65] UHP-FRC has 28 days compressive strength of about 200 MPa (29 ksi) and tensile ductility of 0.6% which is at least 5 times less than ECC. None of

[i] It should be noted than certain UHPCs (e.g. Ductal) are also sometimes referred as HPFRCC but these concretes are at least an order of magnitude less ductile than ECC and other high ductility concretes mentioned above.

these composite materials truly combine the compressive strength of COR-TUF and tensile ductility of ECC in one material.

The last decade also saw the development of other ductile concretes using continuous fibers/fabric including Textile Reinforced Concrete (TRC)[66] at Universities of Aachen and Dresden in Germany, and pultruded continuous fiber reinforced concrete[67] at Arizona State University. TRCs contain multi-axial fabrics (made of glass fiber, carbon, or aramid) reinforcing the cementitious matrix, allowing thin-structured concrete elements with potentially high tensile strength and ductility. Unlike ECC and other high ductility concretes which contain randomly distributed fibers, TRC are anisotropic materials, especially under tension, with preferred loading directions along the perpendicular axes of the constituent fabrics. Another distinction between TRC and ECC is that while the fiber/matrix interfacial bond plays a significant role in the stress transfer between fibers and matrix in ECC, the chief mechanism of stress transfer in TRC is through anchoring effects at junction points of the orthogonal yarns. The geometry of the fabric (mesh size) is more important in TRC. While TRC is particularly suitable for thin manufacture structural elements, other high ductility concretes such as ECC can be adopted in precast elements or cast-in-place construction. ECC has also been extruded and shotcreted for applications in making pipes and repairing dams/tunnel lining. There is a growing community of researchers interested in TRC due to its remarkable properties; however, the focus of this doctoral research is on ductile concretes with short discontinuous fibers such as ECC, and its design principles are discussed in the next section.

2.5 Principles of Design for High Tensile Ductility

High tensile ductility of ECC and other high ductility concretes is a result of the formation of multiple fine cracks (Figure 2.1). These cracks are bridged by randomly distributed short fibers such that the composite integrity is maintained with increasing load carrying capacity. There are two necessary micromechanics-based conditions[52,54] that facilitate the steady state multiple cracking, which are discussed below.

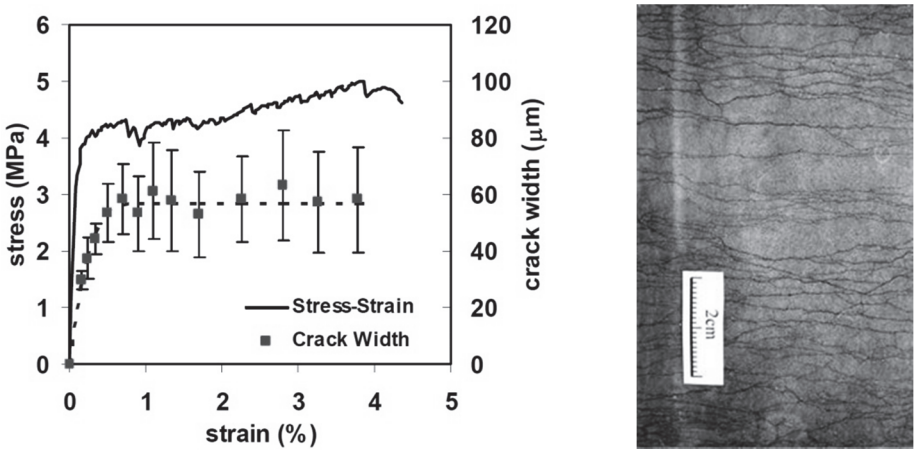

(a) (b)

Figure 2.1: (a) Typical tensile stress-strain curve and crack width-strain curve of ECC[68] (b) Saturated multiple cracking in ECC
(Source: Yang et al.[68])

The first necessary condition is called the strength criterion or crack initiation criterion (Eq. 2.1). This condition requires that the matrix cracks initiate at stresses lower than the bridging capacity of the least bridged crack [min(σ_0) in Eq. 2.1]. Crack initiation stress for the first crack (σ_{fc} in Eq. 2.1) (and subsequent cracks) can be computed from Irwin's fracture criterion[69] and the bridging capacity (σ_0) can be determined from the crack bridging behavior (σ-δ relation) shown in Figure 2.2. All micro-cracks in a multiple cracking composite have different σ_0 due to inhomogeneity of fiber dispersion (discussed in Section 6.4), and therefore, the

minimum of these bridging capacities [min(σ_0)] is critical for determining the upper bound for σ_{fc} in Eq. 2.1. The crack initiation criterion thus ensures the stability of crack bridging.

$$\sigma_{ss} = \sigma_{fc} \leq \min(\sigma_o) \tag{2.1}$$

The second necessary condition is called the energy criterion or crack propagation criterion (Eq. 2.2). This condition is based on the path independent J-integral formulation of the steady-state crack propagation problem in composites by Marshal and Cox.[46] In essence, the energy criterion requires that the total available crack driving energy (J_b' in Eq. 2.2) should be greater than the resistance of the composite to crack propagation (J_{tip} in Eq. 2.2). J_b' or complementary energy of crack bridging can be determined from the σ-δ relation (Figure 2.2). It can be interpreted as net energy available from external work done to the body less the energy absorbed by fibers from zero to steady state crack opening δ_0 during steady state crack propagation. J_{tip} can be approximated to G_m (fracture energy of the matrix) in case of brittle matrix composites such as ECC or other mortars. G_m is estimated from matrix fracture toughness (K_m) and modulus (E_m) as K_m^2/E_m. The crack propagation criterion ensures the flat crack formation (instead of oval-shaped Griffith cracks).

$$G_m \approx J_{tip} \leq J_b' = \sigma_0\delta_0 - \int_0^{\delta_0} \sigma(\delta)\, d\delta \tag{2.2}$$

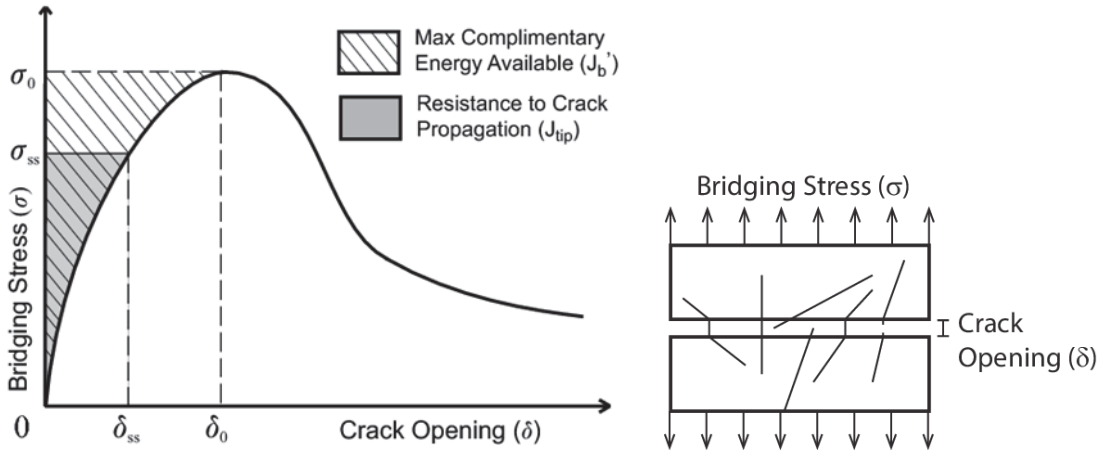

Figure 2.2: Conceptual bridging stress - crack opening (σ-δ) relation

The crack bridging behavior (σ-δ relation) can be either determined experimentally, from tension tests on notched specimens (forcing only one crack formation),[70] or analytically, from single fiber pullout behavior.[68] The pullout behavior of a single fiber is determined through single fiber pullout tests discussed below.

Single fiber pullout tests are used to characterize the interfacial bond properties of a single fiber embedded inside a cementitious matrix.[71] Using the tunnel crack propagation theory of fiber debonding/pullout, analytical expressions have been derived which model the single fiber pullout test results based on the interfacial bond properties, along with fiber and matrix properties. The interfacial bond properties typically determined from the single fiber pullout tests results are frictional bond (τ_0), chemical bond (G_d), and slip hardening coefficient (β).[72] In ECC, these interfacial bond properties are engineered specifically to satisfy the conditions (Eqs. 2.1 and 2.2) necessary for multiple steady-state cracking. An example of such interfacial tailoring is the deliberate oil coating of PVA fibers in ECC.[56] Thus, the interfacial bond properties obtained

from the single fiber pullout tests enable the micromechanical tailoring to achieve the desired composite macro-properties.

The interfacial properties determined from the single fiber pullout tests are used to predict the composite behavior at higher length scale using scale-linking model.[51] The bridging stress-crack opening relation (σ-δ) relation is predicted from the fiber, matrix, and interfacial properties using a statistical scale-linking model which accounts for the random orientations and embedment lengths of the fibers bridging a crack. The fiber orientation distribution is either assumed (2D uniform or 3D uniform) or measured using fluorescence microscope and digital image processing.[73] The composite stress-strain (σ-ε) curve is computed based on σ-δ relation with the knowledge of flaw size distribution.[74] Flaw size distribution determines the shape of the σ-ε curve. Fiber and flaw size distributions are dependent on material processing. The stress-strain relation is further used in analytical or finite element models along with structural shapes to compute structural response. This structural response is matched with the structural performance requirements, iteratively. Thus, the design for tensile ductility is based on scientific understanding of material behavior at various length scales, which is supported by empirical determination of interfacial properties and verification of composite behavior.

2.6 Conclusions: Contrasting Design Philosophies of HSC and ECC

In the design of HSCs, high compressive strength is the primary design objective and fibers are considered as add-on ingredients to impart toughness to the material with only secondary considerations to the micro-scale fiber/matrix interactions. On the other hand, in the design of ECC, these interactions are central for achieving ultra-high tensile ductility (up to 6%). In fact, the word "Engineered" in ECC is used to emphasize the micromechanics-based engineered nature of their design. Based on the discussions in previous sections, the following contrasts in design principles of HSC and ECC are noted.

(a) *Flaw size*

One of the central HSC design principles (Section 2.3) is to minimize the flaw size in the cementitious matrix. In contrast, the design principle of ECC is to control the flaw size within an optimum range in order to trigger multiple cracks and, therefore, impart tensile ductility. In fact, deliberate addition of flaws is one of the methods used in the past to enhance the tensile ductility of ECC.[75] Thus, for designing a concrete integrating high compressive strength and tensile ductility at the same time, it should be ensured that the bridging capacity is sufficiently large to avoid the violation of the strength criterion (Eq. 2.1) due to small sized flaws.

(b) *Matrix Fracture toughness*

The fracture toughness (K_m) of HSC matrix is higher (2-3 times) than that of ECC (note the distinction between matrix fracture toughness and composite toughness, the latter being higher for ECC than HSC). This is a direct result of the HSC design approaches of increasing the

density of particle packing and using coarser (and tightly bound) cement particles. Higher K_m is counterproductive for satisfying both the necessary conditions of multiple cracking (Eqs. 2.1and 2.2), as it increases both σ_{ci} as well as J_{tip}. As a result, higher bridging capacity (σ_0) and complementary energy (J_b') are needed to counter the increase in K_m and satisfy these conditions in a high strength composite.

(c) *Water content*

ECC and other high ductility concretes have extremely flowable matrixes, with rheology similar to that of self-consolidating concretes, to allow homogenous dispersion of fibers (particularly hydrophilic fibers such as PVA fibers) essential for tensile ductility. In spite of the relatively large dosage of water reducing admixtures, HSC matrixes (particularly that of COR-TUF and similar concretes with compressive strengths in excess of 150 MPa) are extremely viscous due to low w/c ratios, targeted for achieving low porosity and high compressive strength. Homogenous dispersion of fibers in matrixes with low w/c ratio is, therefore, a steep challenge.

The above dissimilarities in design principles of HSC and ECC point towards a fundamental difference in their underlying design philosophies. An HSC is designed to *prevent the damage* (in form of cracks) and remain elastic under service loads, while the fibers are engaged only near and past the ultimate limit state. The material's stress capacity continuously degrades after the onset of damage in HSC. On the other hand, ECC is designed to *manage the damage* by allowing controlled micro-cracking and efficient utilization of fibers even under service loads, if needed. The material's stress capacity increases with incremental damage in ECC. Such damage tolerance built into the design of ECC distinguishes it from HSC.

Reference

1. Caldarone, M. A. (2009) "Applications" In *High-Strength Concrete: A Practical Guide*, Taylor & Francis: New York, NY, pp.15-19.

2. ACI (2008) "Design Assumptions: 10.2.5" In *Building Code Requirements for Structural Concrete (ACI 318-08) and Commentary*, Farmington Hills, MI: American Concrete Institute, pp.130.

3. Gettu, R., Bazant, Z. P. & Karr, M. E. (1990) "Fracture Properties and Brittleness of High-Strength Concrete" *ACI Materials Journal,* 87(6), 608-618.

4. Aldea, C. –M., Shah, S. P. & Karr, A. (1999) "Permeability of Cracked Concrete" *Materials and Structures*, 32(5), 370-376.

5. Moehle, J. P. & Mahin, S. A. (1991) "Observations on the Behavior of Reinforced Concrete Buildings During Earthquakes" In *Special Publication SP-127*, Ghosh S. K. (Ed.), Farmington Hills, MI: American Concrete Institute.

6. Sheikh, S. A., Shah, D. V. & Khoury, S. S. (1994) "Confinement of High-Strength Concrete Columns" *ACI Structural Journal*, 91(1), 100-111.

7. Hadi, M. N. & Zhao, H. (2011) "Experimental study of high-strength concrete columns confined with different types of mesh under eccentric and concentric loads" *Journal of Materials in Civil Engineering*, 23 (6), 823-832.

8. Whittle, R. (2013) "Problems and Failures due to Inadequate Understanding of Materials' Properties" In *Failures in Concrete Structures: Case Studies in Reinforced and Prestressed Concrete*, Boca Raton, FL: CRC Press, pp. 57-68.

9. Fischer, G. & Li, V. C. (2002) "Influence of Matrix Ductility on the Tension-Stiffening Behavior of Steel Reinforced Engineered Cementitious Composites (ECC)" *ACI Structural Journal, 99*(1), 104-111.

10. Fukuyama, H., Matsuzaki, Y., Nakano, K. & Sato, Y. (1999) "Structural performance of beam elements with PVA-ECC" In *Proceedings of High Performance Fiber Reinforced Cement Composites - 3 (HPFRCC 3)*, Reinhardt, H. W. & Naaman A. (Eds.), Chapman & Hall, pp. 531-542.

11. Li, M. & Li, V. C. (2009) "Influence of Material Ductility on the Performance of Concrete Repair" *ACI Materials Journal*, 106(5), 419-428.

12. Lepech, M. D. & Li, V. C. (2009) "Water Permeability of Engineered Cementitious Composites" *Cement and Concrete Composites*, 31(10) 744-753, 2009.

13. Lepech, M. D. & Li, V. C. (2009) "Application of ECC for Bridge Deck Link Slabs" *Materials and Structures*, 42(9), 1185-1195.

14. Maruta, M., Kanda, T., Nagai, S. & Yamamoto, Y. (2005) "New High-rise RC Structure Using Pre-cast ECC Coupling Beam" *JCI Concrete Journal*, 43(11), 18-26.

15. ACI Committee 363 (2010) "Definition of High-Strength Concrete" In *State-of-the-Art Report on High-Strength Concrete*, Farmington Hills, MI: American Concrete Institute, pp. 3.

16. Caldarone, M. A. (2009) “Historical Background” In *High-Strength Concrete: A Practical Guide*, Taylor & Francis: New York, NY, pp.12-14.

17. Hattori, K. (1979) “Experience with MIGHTY Superplasticizer in Japan” In *ACI SP-62*, Malhotra, V. M. (Ed.), Farmington Hills, MI: American Concrete Institute, pp. 37-66.

18. Aignesberger, A. & Kern, A. (1981) “Use of Melamine-Based Superplasticizer as a Water Reducer” In *ACI SP-68*, Malhotra, V. M. (Ed.), Farmington Hills, MI: American Concrete Institute, pp. 61-80.

19. Aitcin, P. C. & Laplante, P. (1992) “The Development of High Performance Concrete in North America” In *High Performance Concrete: From Material to Structure*, Malier, Y. (Ed.), London, UK: E & FN Spon, pp. 414-415.

20. Kawai, T. (2005) “State-of-the-Art Report on High-Strength Concrete in Japan” In *Proceedings of JSCE-VIFCEA Joint Seminar on Concrete Engineering*, Tokyo, Japan: JSCE, pp. 87-107.

21. Bache, H. H. (1981) “Densified Cement/Ultrafine Particle-based Materials” In *Proceedings of 2nd International Conference on Superplasticizers in Concrete*, Ottawa, Canada, 10-12 June, 1981.

22. Bache, H.H. (1988) “The New Strong Cements: Their Use in Structures” *Physics in Technology*, 19, 43-50.

23. Lankard, D. R. & Lease, D. H. (1982) “Highly Reinforced Precast Monolithic Refractories” *Bulletin of American Ceramic Society*, 61(7), 728-732.

24. Double, D. D. & Wise, S. (1988) “Cementitious composite material containing metal fibers” US Patent #4,780,141.

25. Richard, P. & Cheyrezy, M. (1995) “Composition of Reactive Powder Concretes” *Cement and Concrete Research*, 25(7), 1501-1511.

26. Perry, V. H. & Zakariasen, D. (2004) “First Use of Ultra-High Performance Concrete for an Innovative Train Station Canopy” *Concrete Technology Today*, 25(2), 1-2.

27. Richard, P., Cheyrezy, M. & Roux, N. (1996) “Metal Fiber Concrete Compositions for Molding Concrete Elements, Elements Obtained and Curing Process” US Patent #5,503,670.

28. Clauvad, B., Cochet, G., Gnagne, C. & Targe, J. (2000) “Composite Concrete” US Patent #6,080,234.

29. Cheyrezy, M., Dugat, J., Clavaud, B., Orange, G. & Frouin, L. (2002) “Metal fibre concrete, cementitious matrix and premixes for preparing matrix and concrete” US Patent #6,478,867.

30. Orange, G., Prat, E., Casanova, P. & Behloul, M. (2005) “Fire-resistant high performance concrete composition” US Patent # U6,881,256 B2.

31. Casanova, P., Chong, H. & Clavaud, B. (2005) “Highly resistant and ductile fiber concrete” US Patent #6,887,309.

32. Neeley, B.D. & Walley, D.M. (1995) “Very High-Strength Concrete” *The Military Engineer*, 87(572), 36-37.

33. Cargile, J. D., O'Neil, E. F. & Neeley, B. D. (2002). "Very High-Strength Concretes for use in blast and penetration resistant structures." *AMPTIAC Quarterly,* 6(4), 61-66.

34. O'Neil, E. F. (2008) "On Engineering the Microstructure of HPCs to Improve Strength, Rheology, and Frangibility" PhD Dissertation, Evanston, IL: Northwestern University.

35. Mindess, S., Young, J. F. & Darwin, D. (2003) "Pozzolanic Materials: Physical Characteristics" In *Concrete (2nd Ed.)*, Upper Saddle River, NJ: Prentice Hall, pp. 100.

36. Birchall, J. D., Howard, A. J. & Kendall, K. (1981) "Flexural Strength and Porosity of Cements" *Nature*, 289, 388-390.

37. Mindess, S., Young, J. F. & Darwin, D. (2003) "Effects on Properties of Fresh and Hardened Concrete: Microstructure" In *Concrete (2nd Ed.)*, Upper Saddle River, NJ: Prentice Hall, pp. 108.

38. Mindess, S., Young, J. F. & Darwin, D. (2003) "Curing at Elevated Temperatures" In *Concrete (2nd Ed.)*, Upper Saddle River, NJ: Prentice Hall, pp. 295-301.

39. Bazant, Z. P. & Planas, J. (1998) "Brittleness of High Strength Concrete" In *Fracture and Size Effect in Concrete and Other Quasibrittle Materials*, New York, NY: CRC Press, pp. 323.

40. Aveston, J. & Kelly, A. (1973) "Theory of multiple fracture of fibrous composites" *Journal of Material Science*, 8, 352-362.

41. Hillerborg, A., Modeer, M. & Petersson, P. E. (1976) "Analysis of Crack Formation and Crack Growth in Concrete by Means of Fracture Mechanics and Finite Elements" *Cement and Concrete Research*, 6, 773-782.

42. Morton, J. & Groves, G. W. (1976) "The Effect of Metal Wires on the Fracture of a Brittle-Matrix Composite" *Journal of Material Science*, 11, 617-622.

43. Naaman, A.E., Argon, A. & Moavenzadeh, F. (1973) "A Fracture Model for Fiber Reinforced Cementitious Materials" *Cement and Concrete Research*, 3(4), 397-411.

44. Naaman, A.E., F. Moavenzadeh & F.J. McGarry (1974) "Probabilistic Analysis of Fiber Reinforced Concrete" *Journal of Engineering Mechanics*, 100(2), 397-413.

45. Naaman, A. E. & Shah, S. P. (1976) "Pull-Out Mechanism in Steel Fiber-Reinforced Concrete" *Journal of the Structural Division*, 102(8), 1537-1548.

46. Marshall, D., & Cox, B. N. (1988) "A J-integral Method for Calculating Steady-state Matrix Cracking Stress in Composites" *Mechanics of Materials*, 7, 127-133.

47. Wang, Y., Li, V.C. & Backer, S. (1988) "Modeling of Fiber Pull-out from a Cement matrix" International Journal of Cement Composites and Lightweight Concrete, (10)3, 143-149.

48. Wang, Y., Li, V.C & Backer, S. (1988) "Analysis of Synthetic Fiber Pull-Out from a Cement Matrix" Materials Research Society Symposia V.114: Bonding in Cementitious Composites, Mindess S. & Shah, S. P. (Eds.), pp. 159-166.

49. Krenchel, H. & Stang, H. (1989) "Stable Microcracking in Cementitious Materials" In *Proceedings of Brittle Matrix Composites 2*, Brandt, A.M. & Marshall, J.H. (Eds.), Springer Publications, pp. 20-33.

50. Li, V. C., Wang, Y. & Backer S. (1990) "Effect of Inclining Angle, Bundling and Surface Treatment on Synthetic Fibre Pull-Out from a Cement Matrix," *Composites*, 21(2), 132-140.

51. Li, V. C., Wang, Y. & Backer, S. (1991). "A Micro Mechanical Model of Tension Softening and Bridging Toughening of Short Random Fiber Reinforced Brittle Matrix Composites," *Journal of Mechanics and Physics of Solids*, 39(5), 607-625.

52. Li, V. C. & Leung, C. K. Y. (1992) "Steady State and Multiple Cracking of Short Random Fiber Composites." *ASCE Journal of Engineering Mechanics*, 118(11), 2246-2264.

53. Li, V. C. (1992) "Performance Driven Design of Fiber Reinforced Cementitious Composites," In Proc. of *4th RILEM International Symposium on Fiber Reinforced Concrete*, R. N. Swamy (Ed.). Sheffield, UK: E & FN Spon, pp. 12-30.

54. Li, V. C. (1993) "From Micromechanics to Structural Engineering – The Design of Cementitious Composites for Civil Engineering," *JSCE Journal of Structural Mechanics and Earthquake Engineering*, 10(2), 37-48.

55. Li, V. C., Wang, S. & Wu, C. (2001) "Tensile Strain-Hardening Behavior of PVA-ECC" *ACI Materials Journal*, 98(6), 483-492.

56. Li, V. C., Wu, C., Wang, S., Ogawa, A. & Saito, T. (2002) "Interface Tailoring for Strain-Hardening PVA-ECC" *ACI Materials Journal*, 99(2), 463-472.

57. Sierra-Beltran, M. G. & Schlangen, E. (2008) "Development of Ductile Cementitious Materials with Wood Fibers" In *Proceedings of 11th International Inorganic-Bonded Fiber Composites Conference*, Madrid, Spain, pp. 11-18.

58. Maalej, M., Quek, S. T. & Zhang, J. (2005) "Behavior of Hybrid-Fiber Engineered Cementitious Composites Subjected to Dynamic Tensile Loading and Projectile Impact" *Journal of Materials in Civil Engineering*, 17(2), 143-152.

59. Hoheneder, J. A. (2012) "Smart Carbon Nanotube/fiber and PVA Fiber-Reinforced Composites for Stress Sensing and Chloride Ion Detection" MSE Dissertation, Milwaukee, WI: University of Wisconsin.

60. RILEM TC 208-HFC (2013) "Strain Hardening Cement Composites: Structural Design and Performance" Rokugo, K. & Kanda, T. (Eds.), RILEM State-of-the-art Report, Vol. 6.

61. RILEM (2011) "Durability of Strain-Hardening Fiber-Reinforced Cement-Based Composites (SHCC)" Wittman, F. & Van Zijl, G. (Eds.), RILEM State-of-the-art Report, Vol. 4.

62. JSCE (2008) "Recommendations for Design and Construction of High Performance Fiber Reinforced Cement Composites with Multiple Fine Cracks." Tokyo, Japan: JSCE.

63. Naaman, A.E. & Reinhardt, H.W. (2003) "Setting the stage: toward performance-based classification of FRC composites" In *Proceedings of High Performance Fiber Reinforced Cement Composites-4 (HPFRCC-4)*, Naaman A. E. & Reinhardt, H.W. (Eds.), Bagneux, France: RILEM Publications S.A.R.L, pp. 1-4.

64. Kamal, A., Kuneida, M., Ueda, N. & Nakamura, H. (2009) "Evaluation of Crack Elongation Performance of UHP-SHCC as a Surface Repair Material" Tanabe et al. (Eds.) In Proc. of *Creep,*

Shrinkage, and Durability Mechanics of Concrete and Concrete Structures, London, UK: Taylor and Francis group, pp. 519-525.

65. Wille, K., Kim, D. J. & Naaman, A. E. (2010) "Strain-Hardening UHP-FRC with Low Fiber Contents" *Materials and Structures*, 44(3), 583-598.

66. RILEM TC-201 (2006) "Introduction" *Textile Reinforced Concrete: State-of-the-art Report*, Brameshuber, W. (Ed.), Bagneux, France: RILEM Publications S.A.R.L., pp. 1-10.

67. Mobasher, B. & Peled, A. (2006) "Distributed Cracking and Stiffness Degradation in Fabric-Cement Composites" *Materials and Structures*, 39, 317-331.

68. Yang, E. H., Wang, S., Yang, Y. & Li, V. C. (2008) "Fiber-bridging constitutive law of Engineered Cementitious Composites" *JCI J. of Advanced Concrete Technology*, 6(1), 1-13.

69. Irwin, G. R. (1957) "Analysis of stresses and strains near the end of a crack traversing a plate" *Journal of Applied Mechanics*, 24, 361-364.

70. Paegle, I. & Fischer, G. (2011) "Evaluation of Standardized Test Methods to Characterize Fiber Reinforced Cement Composites." Filho et al. (Eds.) In *Proceedings of SHCC-2*, Rio de Janeiro, Brazil, pp. 9-16

71. Katz, A. & Li, V. C. (1996) "A Special Technique for Determining the Bond Strength of Carbon Fibers in Cement Matrix by Pullout Test" *Journal of Materials Science Letters*, 15, 1821-23.

72. Lin, Z., Kanda, T. & Li, V. C. (1999) "On Interface Property Characterization and Performance of Fiber Reinforced Cementitious Composites" *Concrete Science and Engineering*, 1, 173-84.

73. Lee, B. Y., Kim, J. K., Kim, J. S. & Kim, Y. Y. (2009) "Quantitative Evaluation Technique of Polyvinyl Alcohol (PVA) Fiber Dispersion in Engineered Cementitious Composites" *Cement and Concrete Composites*, 31(6), 408-17.

74. Ranade, R., Stults, M.D., Lee, B. Y. & Li, V. C. "Effects of Fiber Dispersion and Flaw Size Distribution on the Composite Properties of PVA-ECC" In *Proceedings of High Performance Fiber Reinforced Cement Composites-6 (HPFRCC6)*, Parra-Montesinos, G.J., Reinhardt, H.W. & Naaman, A.E. (Eds.), Ann Arbor, MI, pp. 106-113.

75. Wang, S. & Li, V. C. (2004) "Tailoring of Pre-existing Flaws in ECC Matrix for Saturated Strain Hardening" In *Proceedings of FRAMCOS-5*, Li et al. (Eds.), Vail, CO, pp. 1005-1012.

CHAPTER 3: MECHANICAL CHARACTERIZATION OF COR-TUF

3.1 Introduction

As described in Chapter 2, COR-TUF[1] is a UHPC developed at ERDC, and its matrix has been optimized for achieving compressive strengths greater than 200 MPa following the principles of HSC design. Therefore, in this doctoral research, which aims at integrating high compressive strength and tensile ductility in one material, COR-TUF logically serves as one of the key starting points of investigation and material development.

The objectives of the research reported in this chapter are (i) to determine the uniaxial tension behavior of COR-TUF, and (ii) to elucidate the reason behind its lack of tensile ductility through micromechanics-based investigation. The uniaxial tension and compression responses are the fundamental properties that (along with the shear behavior) dictate the material performance under a variety of load combinations. While COR-TUF has been previously tested under flexure, indirect tension, impact, and blasts, there is no data in the literature regarding its behavior under uniaxial tension. This research aims to fill this gap. Furthermore, a detailed micro-scale investigation of COR-TUF is performed to acquire insights into the material behavior at this scale, which is used to explain the uniaxial tension behavior of the composite. The micro-scale behavior of COR-TUF, investigated in this chapter, is used to guide the

development of the material integrating high compressive strength and tensile ductility in the ensuing chapters.

3.2 Materials and Mix Proportions

The mix proportions of COR-TUF used in this research and the properties of the hooked steel fibers are given in Table 3.1 and Table 3.2, respectively. Similar to other high performance concretes, it consists of cementitious materials, fine aggregates, fibers, water, and HRWRA.

Table 3.1: Mix Proportions of COR-TUF (by weight)

Cement (LaFarge Class H)	Silica Fume (Elkem ES 900W)	Silica Sand (US Silica F 55)	Silica Flour (US Silica Sil-co-sil75)	Water[a] (Tap - warm)	Fibers (Dramix® ZP 305 Steel)	HRWRA (WR Grace ADVA 170[b])
1	0.389	0.967	0.277	0.208	0.31	0.00855

[a] Use warm tap water (27-37°C) at Ann Arbor, MI

[b] Replaced in equal weight proportion by ADVA 190 since 2011, when WR Grace Co. discontinued the production of ADVA 170.

Table 3.2: Geometry and Mechanical/Physical Properties of the Steel Fiber[2]

Diameter	Length	Volume Fraction	Nominal Strength	Young's Modulus	Specific Gravity	Melting Temp.
0.55 mm	30 mm	3.6%	1300 MPa	210 GPa	7.8	1500 °C

While the mix proportions are similar to O'Neil's mix,[1] the current mix constituents have been slightly modified. Instead of the chert sand used as aggregate by O'Neil, foundry sand F55 was used in this research as shown in Table 3.1 (as was the practice at ERDC[3] between 2008-

12).[i] Additionally, the dosage of High Range Water Reducing Admixture (HRWRA) was lowered from 0.03 used by O'Neil to 0.00855 used in this research (recommended by ERDC[3]). Furthermore, it was found that there is a difference in the water quality (most likely water hardness) and temperature between ERDC at Vicksburg, MS, and UM at Ann Arbor, MI, which causes an increase in fresh mixture stiffness as well as set retardation. To counteract this behavior, especially the set retardation, it was determined that hot water should be used. As such, all mixes made at UM use tap water heated to 27-37°C. There were no observable effects on the mechanical behavior (of COR-TUF produced at UM versus that produced by O'Neil at ERDC) resulting from these modifications in sand, HRWRA dosage, and water temperature.

The cementitious materials used in COR-TUF matrix are Class H cement and silica fume. Class H cement (also called "oil-well cement") is characterized by low calcium aluminate content and coarse particle size (mean diameter is 30-80 μm and Blaine fineness is 200-260 m^2/kg). Compared to other chemically similar cements of finer size, the larger particle size in Class H cement exerts lower water demand, which results in a denser and less porous microstructure. Silica fume is used as a highly reactive supplementary cementitious material to promote the formation of secondary hydration products, thereby maximizing the calcium silicate hydrate (CSH) content. A polycarboxylate-based HRWRA is used to maintain flowability and rheology of the mix at the very low water-cementitious material ratio (w/cm) of 0.15 used in COR-TUF. The cementitious materials in COR-TUF are selected to reduce the water demand, increase the formation of CSH, and promote homogeneity of the mix, all of which contribute to the high compressive strength performance.

[i] US Silica Co. has discontinued the production of F55 sand in 2012, and it is replaced by F60 sand (slightly finer grain size than F50) in the current (post 2012) mixes.

The aggregates or fillers used in COR-TUF matrix are primarily fine silica sand and ground silica supplemented by unreacted silica fume particles. Fine silica sand with a mean diameter of about 270 μm (maximum aggregate size of 600 μm) is used. Using such a small aggregate size reduces the size of the weak interfacial perimeter. Smaller aggregate also reduces the fracture toughness of the matrix (due to reduced aggregate interlock) for crack initiation and fracture work during steady state crack propagation (due to reduced tortuosity of crack path), both of which are desirable effects for composite ductility according to micromechanics. Fine particles of silica fume (0.1-1 μm) and ground silica (5-100 μm) increase the density of the matrix and interface by filling the larger voids. Thus, the aggregates or fillers in the COR-TUF matrix are intended to increase particle packing density, strengthen the aggregate-cement paste interface, and reduce matrix fracture toughness.

3.3 Composite Mechanical Response

3.3.1 Specimens

There are a number of specimen geometries used by researchers worldwide to perform direct uniaxial tension tests, and no particular geometry is treated as a standard. Due to growing interest in high ductility concretes, the Japan Society of Civil Engineers (JSCE)[4] has recommended the use of planar dogbone-shaped specimens (geometry shown in Figure 3.1) for tensile testing of such materials. However, the cross-section at the gauge region of these specimens is only 0.5″ x 1.2″, which severely limits the orientation of steel fibers (which have

length of 1.2″) if COR-TUF is cast in these specimen molds. Such artificial unidirectional orientation fails to capture the true material behavior with randomly distributed fibers. To accommodate the long steel fibers used in COR-TUF, planar coupon specimens with cross-section of 0.5″ x 3″ (Figure 3.2) and large dogbone specimens with gauge cross-section of 3″ x 3″ (Figure 3.3) were used in this part of the research to determine the performance of COR-TUF under direct uniaxial tension.

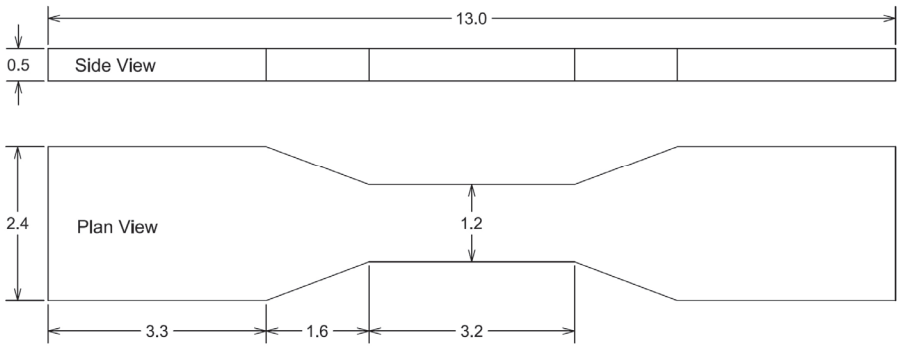

Figure 3.1: Dogbone specimen geometry for tensile testing of HPFRCC[4] (Not used for COR-TUF)
(All dimensions in inches)

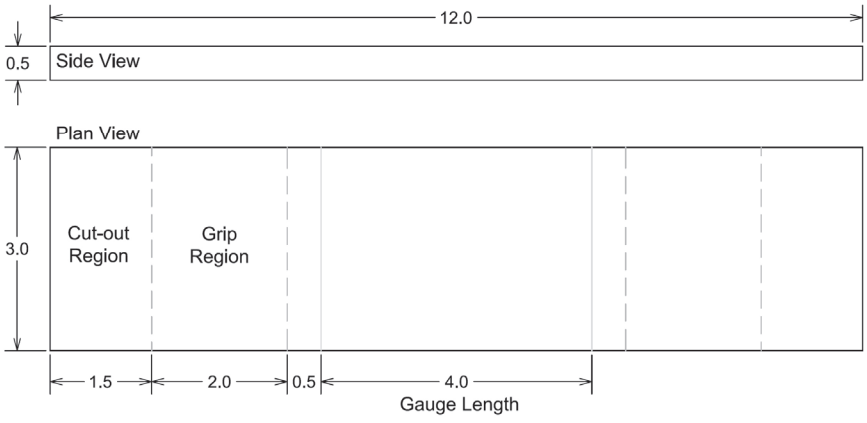

Figure 3.2: Coupon specimen geometry for tensile testing of COR-TUF
(All dimensions in inches)

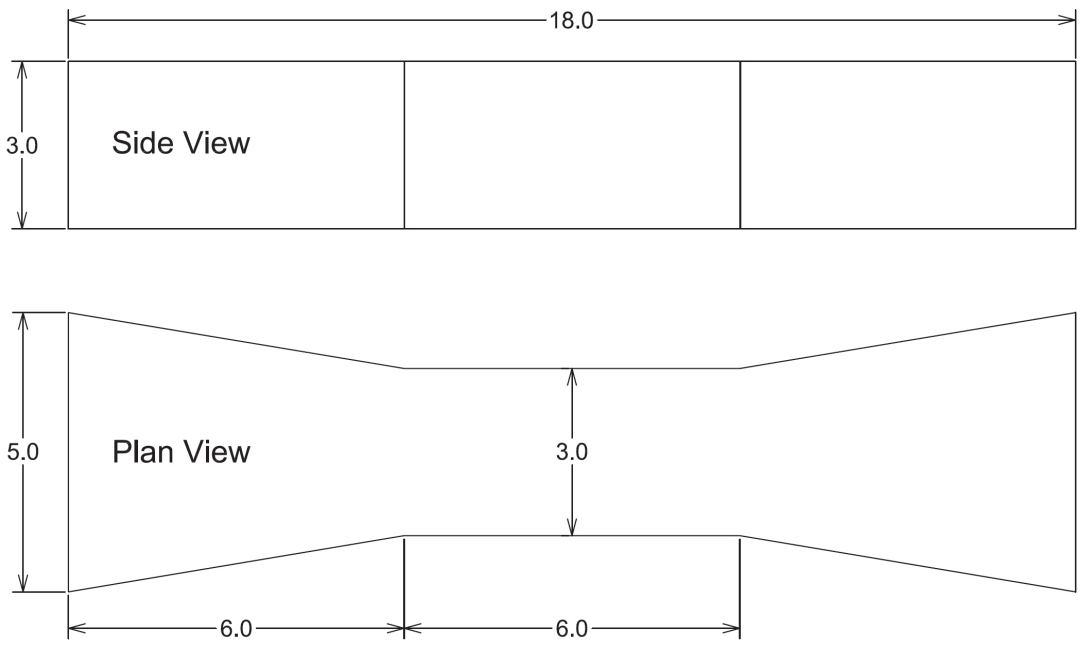

Figure 3.3: Large dogbone specimen geometry for tensile testing of COR-TUF
(All dimensions in inches)

In addition to the above specimens for tension tests, cube specimens of COR-TUF and beam specimens of its matrix (without fibers) were prepared for measuring the compressive strength of COR-TUF and the fracture toughness of its matrix, respectively. Two cube sizes with lengths 2″ and 3″ were used to ascertain the influence, if any, of the specimen size on the compressive strength of COR-TUF. Beams of size 12″x3″x1.5″ were cast for the experimental determination of fracture toughness of COR-TUF matrix.

3.3.2 COR-TUF 7-4-2 Curing Procedure

Elevated temperature curing, similar to that used by O'Neil[5] at ERDC, was adopted for accelerating the curing of COR-TUF specimens. The COR-TUF mix in its fresh plastic state was

poured at the middle of all tensile specimen molds placed on a vibration table. Under moderate vibration for about 3 minutes, the material slowly flowed towards the gripping ends. The 2 inch and 3 inch cubes were filled in two and three layers, respectively, of approximately 1 inch each. Each layer was tapped 25 times before filling the next layer on top. After complete filling, all the molds were sealed by plastic sheets and cured for 1 day at room temperature. Subsequently, the hardened specimens were removed from the molds and kept in a water tank for curing at room temperature (23±3°C) for 7 days. This was followed by elevated temperature curing for 4 days in water at 90°C and for 2 days in air at 90°C. The purpose of the elevated temperature curing was mainly to accelerate the primary and secondary hydration reactions so that COR-TUF attains close to its maximum compressive strength in 13 days (7-4-2) after demolding, instead of 90 days of curing at ambient temperature. The temperatures below 100°C are generally not enough to initiate significant morphological changes to the microstructure[6] of hydration products of oil well cement with low calcium aluminate contents. All COR-TUF specimens were tested at 15 days after casting.

3.3.3 Experimental Setup

The COR-TUF coupon specimens were tested under quasi-static uniaxial tension loading. After cutting off the end regions (Figure 3.2) of the coupons (to eliminate the rough ends), aluminum plates were glued to the grip region (Figure 3.2) of the coupons to achieve smooth gripping surfaces, thereby minimizing the stress concentrations. The coupons were gripped on these faces in a fixed-fixed type of end constraints. The tensile tests were conducted at a displacement rate of 0.5 mm/min using a displacement controlled closed loop test system with a maximum load capacity of 100 kN. The strain in all the coupons was computed from the average

of extensions of the specimen measured by two ultra-precision LVDTs mounted parallel to the two side edges of the coupon specimen (Figure 3.4).

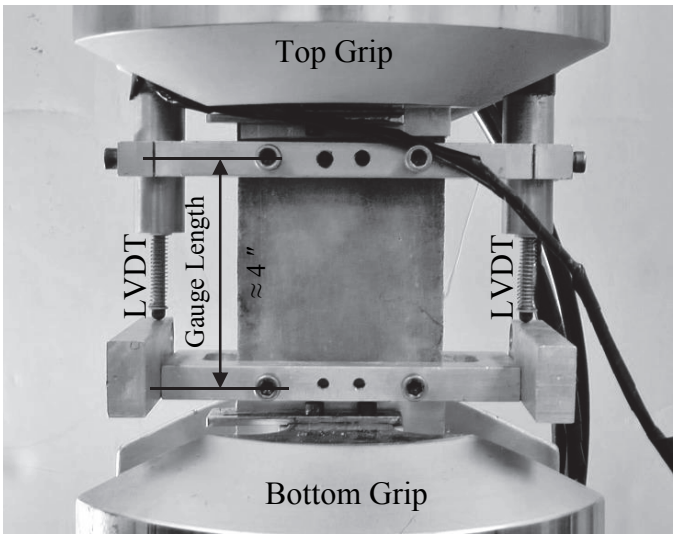

Figure 3.4: Direct uniaxial tension test setup for COR-TUF coupons

The large dogbone specimens of COR-TUF were tested using the same displacement rate as that used for coupons, along with two LVDTs (second LVDT at the back of the specimen), as shown in Figure 3.5. These dogbones were gripped on the sides at their wedge-shaped edges, instead of the planar gripping used for the coupons.

The test setup used in this study for cube compression tests on COR-TUF is similar to that recommended in ASTM C109.[7] A closed loop displacement controlled compression testing machine with maximum load capacity of 2200 kN was used to load the cubes. The compressive displacement rate applied on the cubes was 30 μm/min, which translates into 1300 N/s for 2 inch cubes assuming an elastic modulus of 50 GPa for COR-TUF. This loading rates fall within the recommended range of 900-1800 N/s in ASTM C109.[7] A faster displacement rate of 45 μm/min

was used for 3 inch cubes to maintain the stress rate of about 0.5 MPa/s, same as that used for 51 mm cubes.

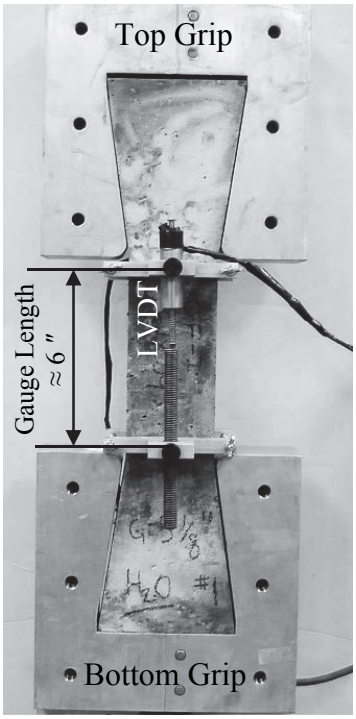

Figure 3.5: Direct uniaxial tension test setup for large dogbones of COR-TUF

The beam specimens of COR-TUF matrix were notched and tested using the procedure specified in ASTM E399.[8] Although the ASTM E399 standard was established for the determination of fracture toughness of metals, it has been shown to be valid for brittle mortar materials, where the fracture process zone is small so that the Linear Elastic Fracture Mechanics (LEFM) assumptions hold good.[9,10] After curing, the COR-TUF matrix beams were notched with notch depth/beam depth ratio of 0.4, as specified in ASTM E399. The notched beams were tested using three-point bending test setup shown in Figure 3.6. The compressive displacement at mid-point of the beam was applied at the rate of 1 μm/s. The fracture toughness was determined from the peak load at which the specimen fractures in accordance with ASTM E399.

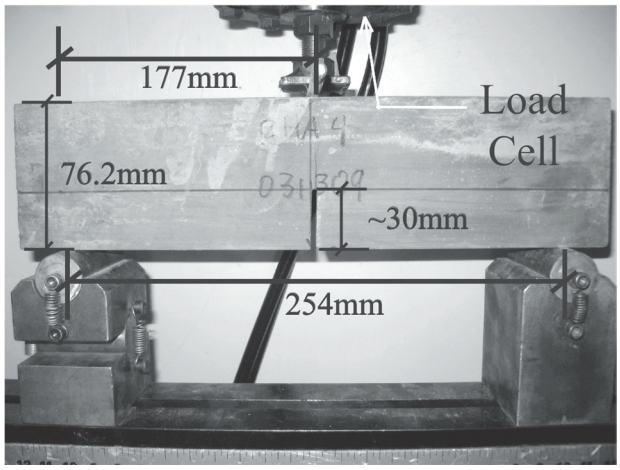

Figure 3.6: Three-point bending test setup for matrix fracture toughness determination

3.3.4 Results and Discussion

The uniaxial tensile responses of COR-TUF coupons and large dogbones are shown in Figure 3.7 and Figure 3.8, respectively. COR-TUF exhibits a quasi-brittle tensile behavior typical of fiber reinforced concretes (FRC). As a COR-TUF specimen is deformed under direct tension, average tensile stress in the specimen increases almost linear-elastically from zero. Simultaneously, local stress concentrations are created within the material microstructure near pre-existing flaws (Section 2.3). This leads to the initiation of a crack in COR-TUF matrix, typically at the largest flaw, causing a decrease in the pre-peak slope of the tensile stress-strain curve. The material behavior at this point changes to non-linear inelastic. The tensile stress increases further (but only slightly) to overcome the resistance to crack propagation offered by the steel fibers in COR-TUF. Due to the slight increase in tensile stress, a few more (only one to three) cracks initiate, signified by a few load drops and rise in the tensile stress-strain curves after the first crack. Meanwhile, the first crack continues to open, and as soon as the (oval-shaped) crack mouth opening displacement (CMOD) reaches a critical value, failure localizes at

this crack causing monotonic reduction of tensile stress thereon. Thus, in spite of relatively high volume of fibers (volume fraction of 3.6%), COR-TUF exhibits a tension-softening behavior.

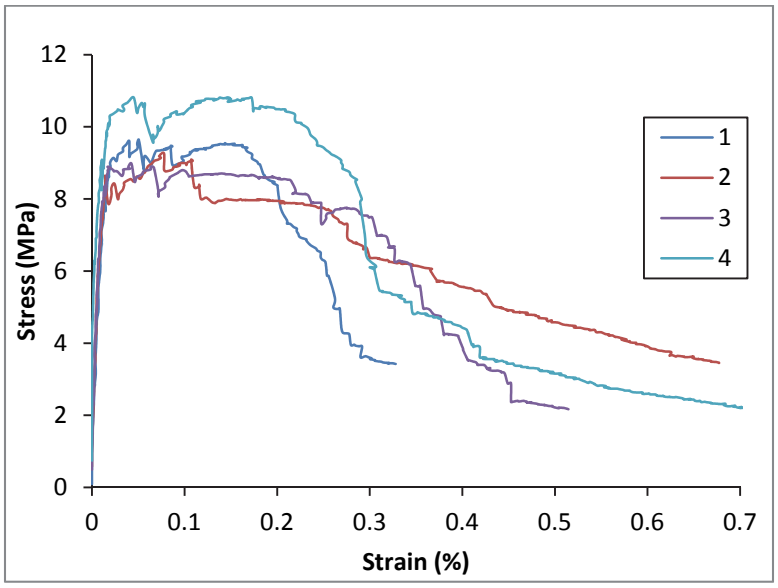

Figure 3.7: Uniaxial tension response of COR-TUF coupons

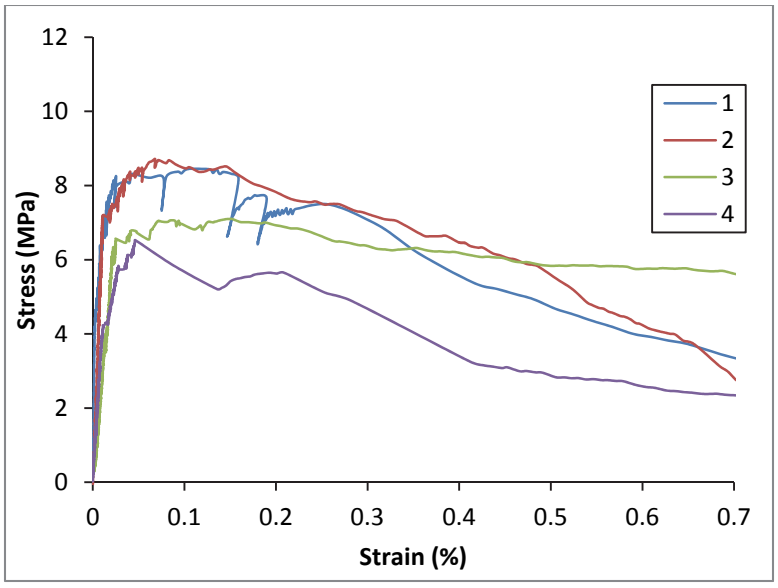

Figure 3.8: Uniaxial tension response of COR-TUF large dogbones

A summary of properties deduced from the tensile stress-strain curves of COR-TUF is shown in Table 3.3. Average initiation stress (σ_{ci}) of the first crack in COR-TUF coupons is 8.8 MPa, while the average ultimate tensile strength (σ_{ult}) is 9.3 MPa. Although σ_{ult} is higher than σ_{ci}, the difference is insufficient to trigger multiple cracks. As a result, the average tensile strain capacity (ε_{ult}), determined as the tensile strain corresponding to σ_{ult}, of COR-TUF coupons is only 0.07%. Such tensile ductility is similar to that of Ductal observed by Chanvillard & Riguad.[11] The coefficient of variation (COV) for ε_{tu} of COR-TUF coupons is high (≈ 75% of the average strain capacity), which indicates lack of homogeneity of material properties among the COR-TUF coupons. Similarly, the large dogbones of COR-TUF also exhibit a low average tensile strain capacity of 0.09% with a large variability. Due to a more three-dimensional distribution of fibers in large dogbones compared to coupons, the average σ_{ult} of large dogbones is about 10% lower than that of coupons, which is explained by the theoretical reduction in bridging efficiency from 0.64 to 0.50 when the fiber orientation distribution is changed from 2D to 3D.[12] Overall, both types of COR-TUF specimens exhibit a lack of tensile ductility with a strain-softening behavior, along with large variability in tensile properties, and the effect of increased randomness of fiber distribution in the depth dimension is reflected in the lower tensile stress capacity of large dogbones compared to coupons.

In the process of conducting the uniaxial tension tests on COR-TUF specimens, severe matrix spalling was observed (Figure 3.9) prior to the engagement of the steel fibers (as the exposed fiber end hooks were not deformed), resulting in a probable decrease in strain capacity and possibly ultimate strength. This spalling may have been caused by the interaction between a relatively stiff fiber and the extremely brittle matrix in which it is embedded.[13] As a crack opens

across an inclined fiber, the fiber exposed by the crack tends to align itself with the axis of loading. In the process of this straightening, the fiber imposes a stress on the matrix proportional to the transverse stiffness of the fiber. The transverse stiffness of the steel fibers used in COR-TUF is high, resulting in a tendency to spall the matrix around an inclined fiber prior to any appreciable contribution that fiber may have made to the bridging capacity of that crack. Further, due to the close proximity of the fibers to each other in the matrix, this effect is magnified even more, where less inclined fibers are prevented from engagement as well. Excessive matrix spalling due to high transverse stiffness of the steel fibers and extreme brittleness of the COR-TUF matrix significantly reduces the fiber bridging efficiency.

Table 3.3: Summary of uniaxial tension properties of COR-TUF specimens

Specimen Number	Crack Initiation Stress	Ultimate Tensile Strength	Tensile Strain Capacity
	σ_{ci} (MPa)	σ_{ult} (MPa)	ε_{ult} (%)
Coupons (Figure 3.7)			
1	9.0	9.6	0.05
2	8.3	9.3	0.08
3	8.9	9.0	0.04
4	8.8	10.8	0.14
Average	8.8	9.3	0.07
COV	3.6%	8.7%	58.1%
Large Dogbones (Figure 3.8)			
1	7.3	8.5	0.11
2	6.8	8.6	0.07
3	6.0	7.1	0.15
4	5.5	6.5	0.05
Average	6.4	7.6	0.09
COV	12.6%	13.7%	49.7%

Figure 3.9: Pronounced matrix spalling evident in large dogbone breaks

The compressive strengths of the 2 inch and 3 inch cubes are summarized in Table 3.4. The average compressive strength of the 2 inch cubes (201 MPa) is slightly (about 4%) higher than that of the 3 inch cubes (193 MPa). However, the strength variability (COV) of 3 inch cubes (2.03%) is slightly lower than that of 2 inch cubes (3.65%). This is expected as the local effect of a flaw or a weakness becomes less dominant as the specimen size increases.[14] Thus, the cube size influences the COR-TUF compressive strength and its variability, but by a small amount only.

Table 3.4: Compressive strengths of COR-TUF cubes

Specimen Number	2" cubes	3" cubes
	f_c' (MPa)	f_c' (MPa)
1	201	200
2	208	193
3	198	190
4	190	193
5	198	189
6	210	195
Average	201	193
COV	3.65%	2.03%

The average fracture toughness (K_m) of four notched COR-TUF matrix beams computed using ASTM E399 procedure was 1.17 MPa√m with a coefficient of variation of 2.5%. These results correspond well with those obtained by O'Neil[15] using other methods (1.10 MPa√m). Thus, COR-TUF matrix has a fracture toughness nearly 2-3 times that of typical ECC matrices.[16]

3.4 Micro-scale Experimental Investigation

3.4.1 Specimens

In order to investigate the micro-scale fiber-matrix interactions, single-fiber pullout (SFP) specimens with both hooked (called SFP-H specimens hereon) and straight fibers (called SFP-S specimens hereon) embedded inside the COR-TUF matrix were used in this study. Fiber pullout tests, which measure the force (versus displacement relative to matrix face) required to pull out a single fiber embedded in a matrix under uniaxial tension, are commonly used to investigate fiber-matrix bond behavior. As mentioned in Section 3.2, COR-TUF utilizes Dramix ZP 305 steel fibers (Figure 3.10) with hooks at both ends to provide anchorage inside the cementitious matrix. The hooked fiber pullout behavior using SFP-H specimens, therefore, capture the effects of frictional bond throughout the embedded fiber length plus the anchorage effects of these hooked ends. In order to decouple these two phenomena, SFP-S specimens (with hooks cut off) were used which only capture the effect of frictional bond of the fiber with the matrix. Straight fibers were obtained by cutting the hooked ends of the steel fibers used in COR-TUF. Care was taken to not produce an end button caused by the cutting process. Using the experimental results

of these two types of SFP specimens, fiber/matrix bond properties and anchorage effects of hooked ends are quantified in Section 3.5 through micromechanics-based analytical investigation.

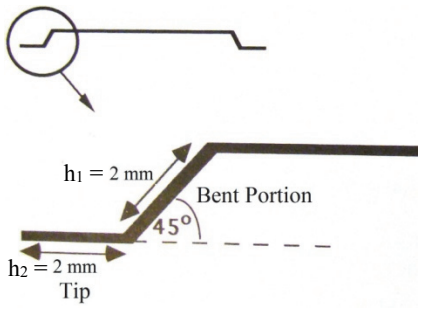

Figure 3.10: Geometry of Dramix ZP 305 fiber showing hook dimensions

Thirty SFP-H (with hooks) specimens were prepared for five embedment lengths (L_e): 5, 6, 7.5, 10, and 15 mm (including one entire hook), which respectively correspond to $L_f/6$, $L_f/5$, $L_f/4$, $L_f/3$, and $L_f/2$ (L_f is the length of the steel fiber equal to 30 mm). In addition, a limited number of SFP-S (with hooks cut off) specimens (three specimens per embedment length) were prepared for each of the three embedment lengths: 7.5, 10, and 15 mm. All the SFP specimens were prepared by simply planting the fiber in the fresh COR-TUF matrix and using moderate vibration. The geometry of the SFP specimens is shown in Figure 3.11. All SFP specimens were cured following the COR-TUF 7-4-2 curing procedure detailed in Section 3.3.2.

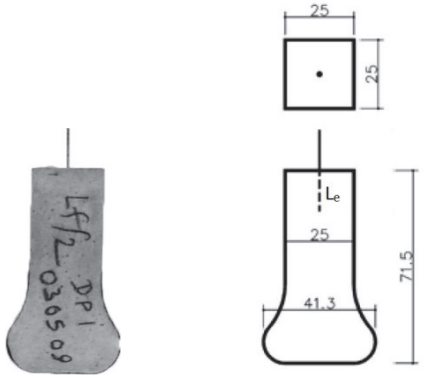

Figure 3.11: Single fiber pullout geometry for steel fibers embedded in COR-TUF matrix (All dimensions in mm)

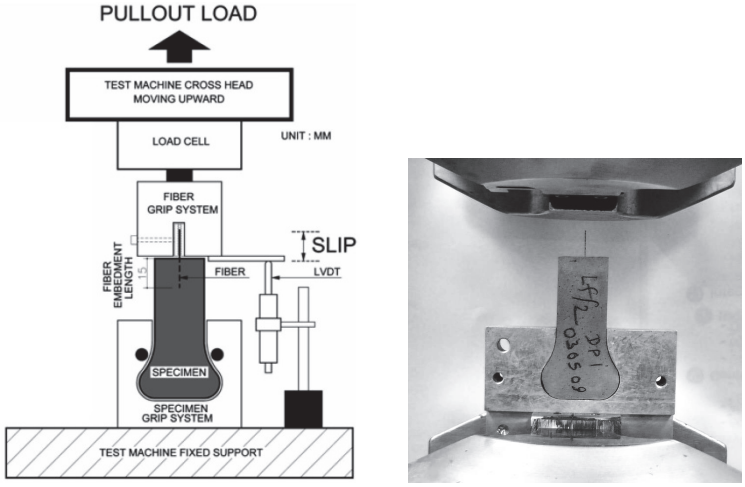

(a) (b)

Figure 3.12: (a) Sketch of the Single Fiber Pullout Test Setup (after Kim, et al[17]) (b) Picture of actual specimen test setup for a specimen with embedment length ≈ $L_f/2$ = 15 mm

3.4.2 Experimental Setup

The experimental setup (after Kim et al[17]) used for conducting the SFP tests on COR-TUF specimens is shown in Figure 3.12. These tests were conducted at two tensile displacement rates of 5 μm/s for the first 300 μm displacement and 10 μm/s thereafter (to limit experiment duration) using displacement controlled closed loop test system. A precision load cell with range

of ±1 kN was added in series with test setup to measure the pullout load. The displacement of the fiber relative to the matrix face was measured using a precision LVDT (Figure 3.12) with range of ±10 mm.

3.4.3 Results and Discussion

3.4.3.1 *Hooked fiber pullout*

The pullout force (P) versus relative displacement (u) curves (henceforth referred as P-u curves) of all the SFP-H specimens are shown below in Figure 3.13.

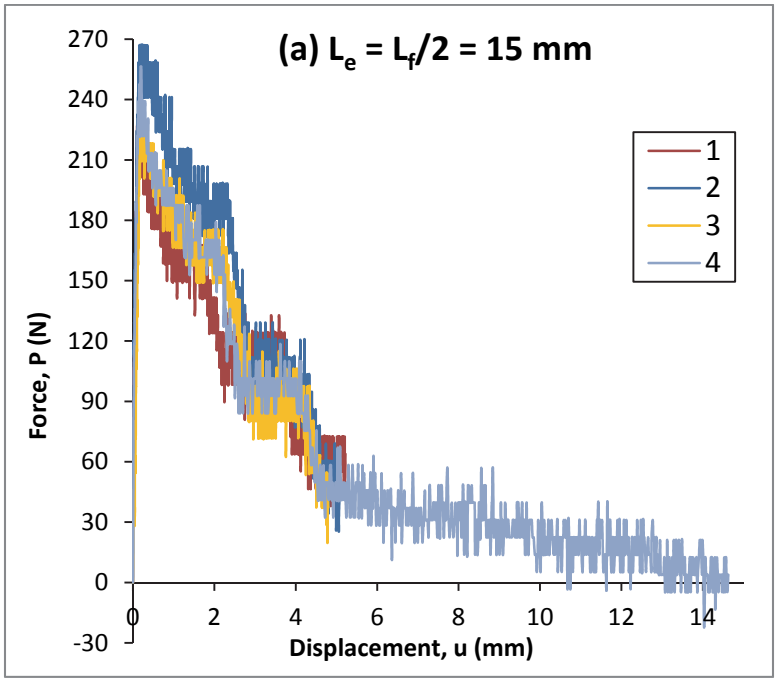

Figure 3.13: Experimentally determined single fiber pullout curves of hooked fibers with varying embedment lengths (L_e)

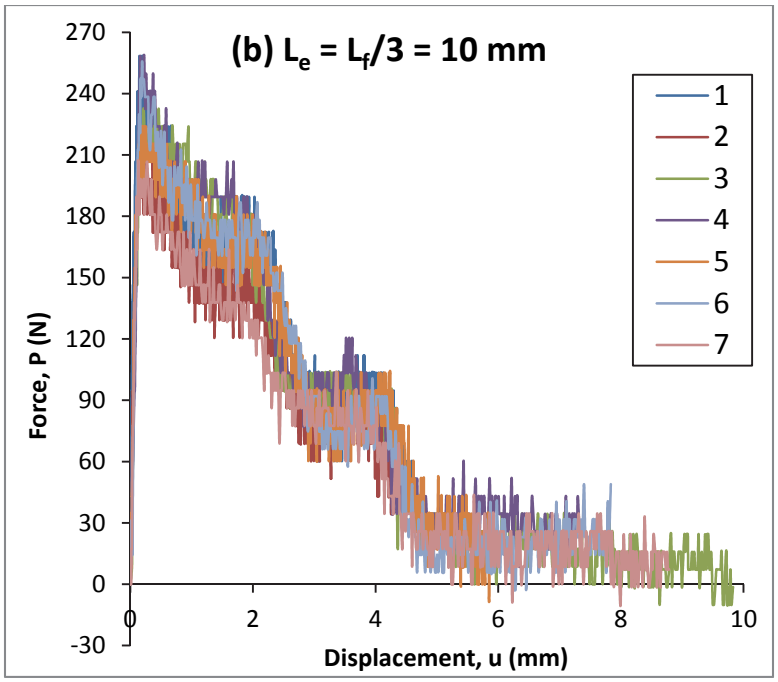

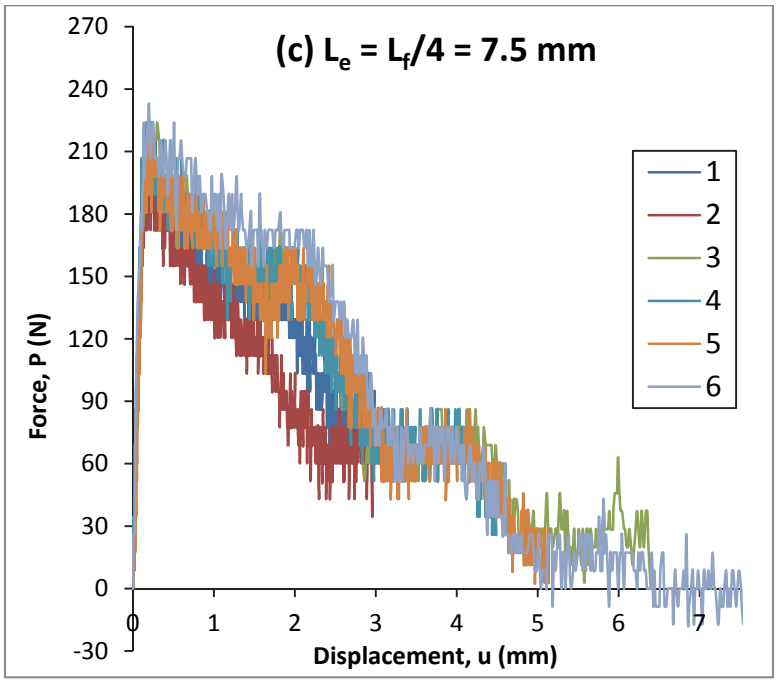

Figure 3.13: Experimentally determined single fiber pullout curves of hooked fibers with varying embedment lengths (L_e)

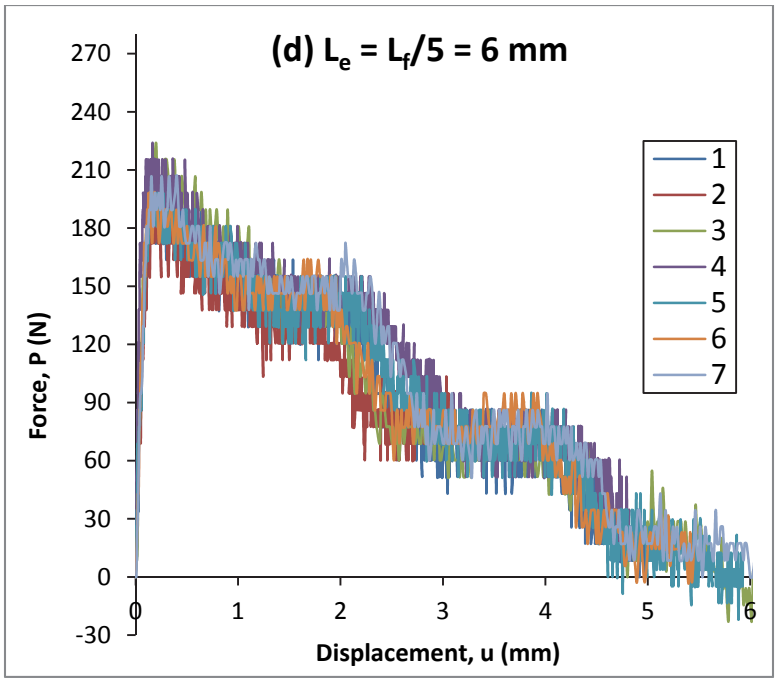

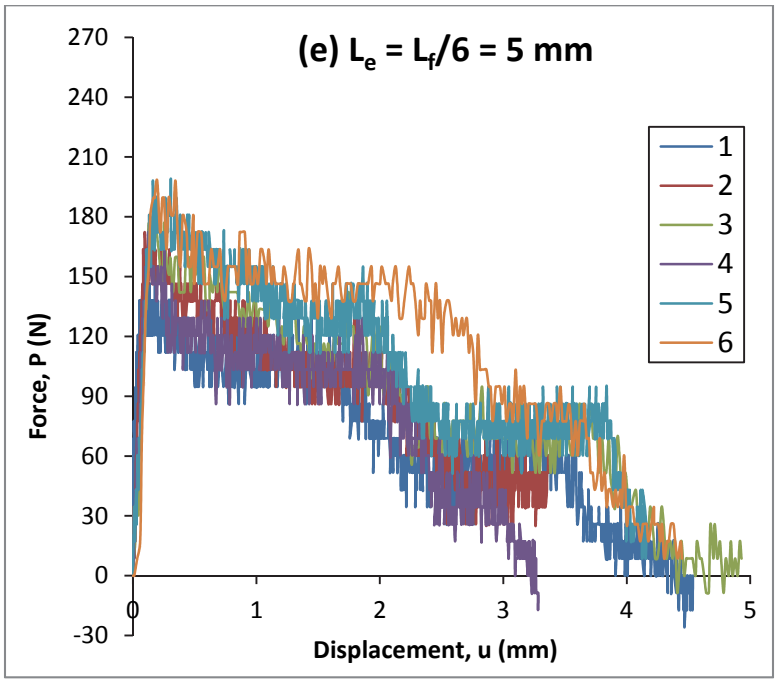

Figure 3.13: Experimentally determined single fiber pullout curves of hooked fibers with varying embedment lengths (L_e)

All the above P-u curves of SFP-H specimens can be divided into five distinct stages of fiber pullout,[18,19,20,21,22,23] which are explained here using Figure 3.14 (plus Figure 3.15) and the P-u curve (Figure 3.16 and Figure 3.17) of a representative specimen with embedment length, $L_e = L_f/2$.

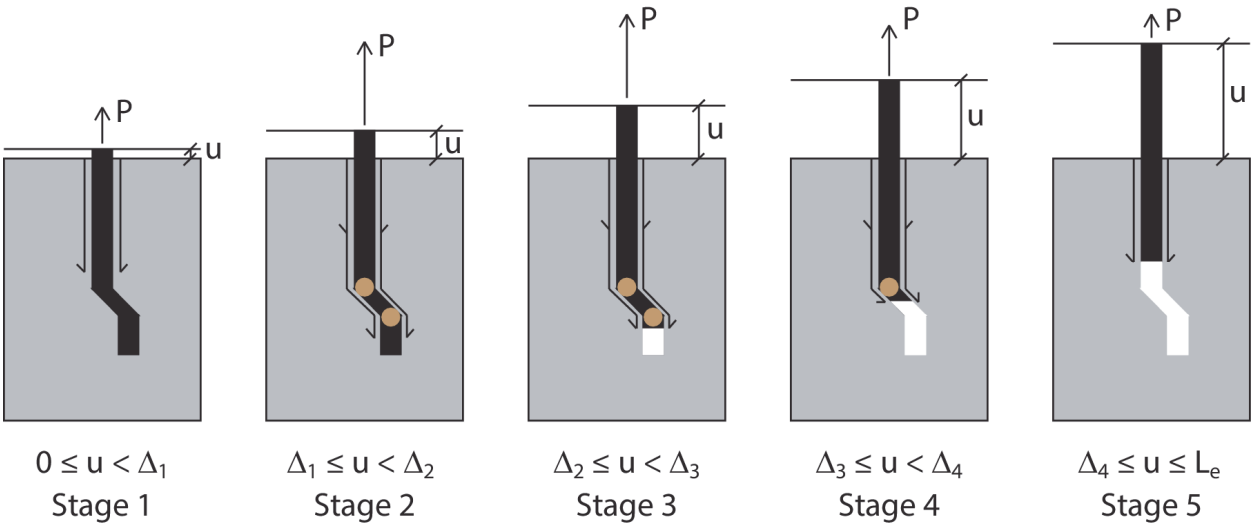

Figure 3.14: Schematic representation of the five pullout stages of hooked steel fibers

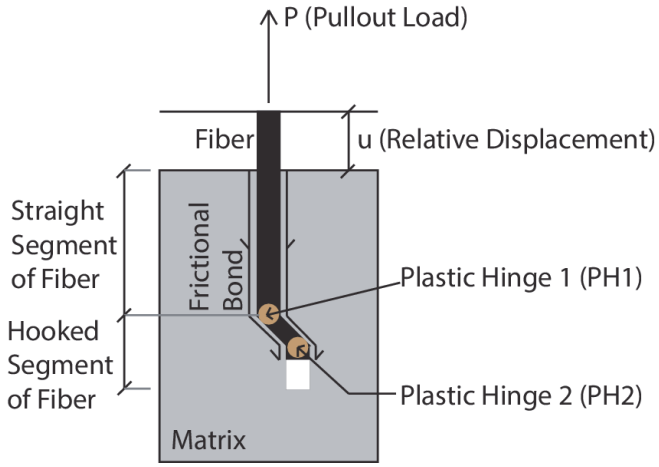

Figure 3.15: Meaning of symbols used in Figure 3.14 using Stage 3 as a representative figure

Stage 1: As the uniaxial tensile displacement is applied to pull the embedded segment of the fiber out of the matrix, a debond zone begins to propagate at the fiber/matrix interface starting at the matrix face (the point where the fiber enters the matrix). The steel fiber does not form any significant chemical bond with the matrix. As a result, a very small displacement ($u = \Delta_1$), corresponding to the elastic stretching of the straight segment of the fiber (shown in Figure 3.15) against the frictional stress, is caused at the end of Stage 1. In spite of such small displacement, considerable pullout resistance is generated due to high elastic modulus (≈ 210 GPa) and large cross-sectional area (diameter of 550 μm) of the steel fiber. The end of this stage is shown as a solid green line marked at $u = \Delta_1$ in Figure 3.17 (which focuses on the first two stages).

Stage 2: At the start of this stage, the debond zone begins to spread in the hooked segment of the fiber (Figure 3.15). However, even small displacement (needed for debonding) through the first bent region of the hook requires the formation of a plastic hinge (PH1 in Figure 3.15). This plastic deformation of steel fiber requires significant additional pullout force but causes reduction in the slope of the pullout curve (Figure 3.17) due to the yielding of steel.[18] As the debond zone progresses towards the second bent region of the hook and attempts to cross it, another plastic hinge is created (PH2 in Figure 3.15). Eventually, the debond zone reaches the embedded end of the fiber after the formation of the two plastic hinges; the pullout load (P) peaks at the end of Stage 2 and the corresponding displacement, u, is Δ_2.

Stage 3: The entire embedded segment of the fiber begins to pullout in this stage (Figure 3.14). As a result, the pullout load decreases due to reduction in the embedded length of the fiber and slip softening of the matrix tunnel around the fiber[24] (in contrast with slip hardening commonly

observed in polymer fiber pullout). There is additional softening at the plastic hinge regions due to the sharp bend geometry of the hook, which together with the slip softening in the straight segment of the fiber causes a concave up (and monotonically reducing) shape of the P-u curve after achieving peak load. During Stage 3, both plastic hinges as shown in Figure 3.14 are active in addition to the frictional bond at fiber/matrix interface. By the end of Stage 3, the embedded end of the fiber is about to pass through the plastic hinge PH2, when u is Δ_3, which is approximately equal to Δ_2 + 2 mm (length of the straight portion of the hook tip - Figure 3.10).

Stage 4: The start of this stage is marked by the gradual deactivation of the plastic hinge PH2 as the embedded end of the steel fiber passes through the corresponding bent region causing a drop in the pullout load (in addition to the softening mechanisms described in Stage 3) over a displacement approximately equal to the fiber diameter (d_f), as shown in Figure 3.16. The other plastic hinge PH1 and the frictional bond (Figure 3.14) remain the two mechanisms of force transfer between the fiber and matrix beyond $u = \Delta_3 + d_f$. By the end of Stage 4, the embedded end of the fiber is about to pass through the plastic hinge PH1, when u is Δ_4, which is approximately equal to Δ_3 + 2 mm (length of the inclined portion of the hook tip - Figure 3.10).

Stage 5: Similar to Stage 4, the start of Stage 5 is marked by the gradual deactivation of the plastic hinge PH1 over a displacement almost equal to d_f. Beyond $u = \Delta_4 + d_f$, the frictional bond is the only remaining mechanism of force transfer between the fiber and matrix, and, as will be shown below, the pullout curve of the hooked fiber almost coincides with that of a straight fiber (without hooked end) of equal embedment length. The pullout force gradually decreases to zero when the displacement, $u \approx L_e + \Delta_1$.

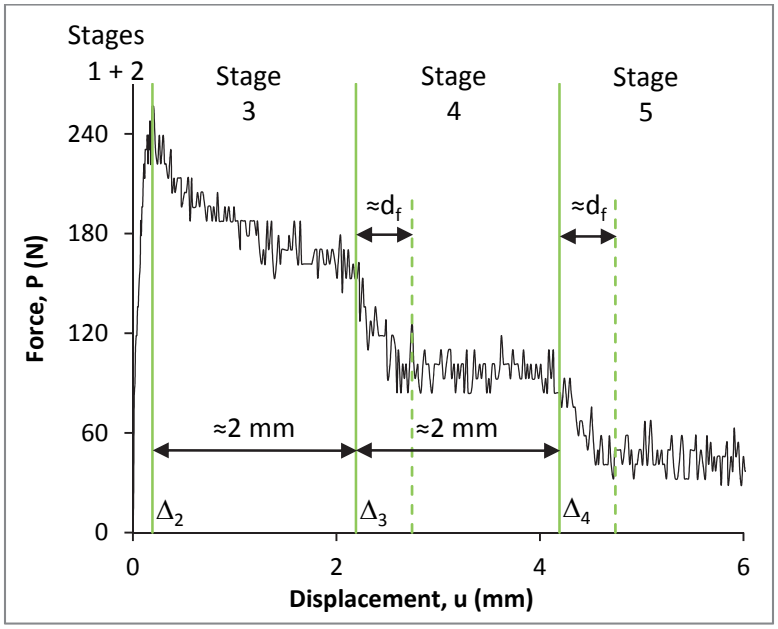

Figure 3.16: Various of stages of hooked steel fiber pullout of specimen #3 in Figure 3.13(a) with $L_e = L_f/2$

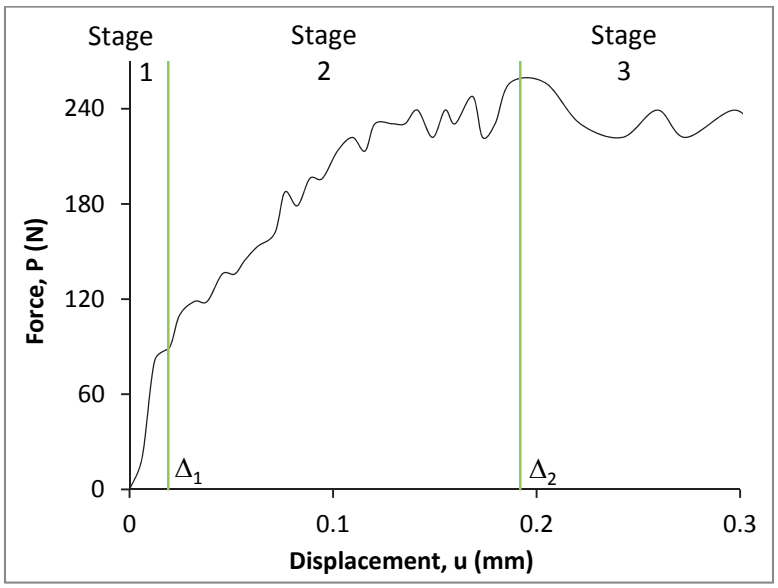

Figure 3.17: Zoomed view of Figure 3.16 resolving Stages 1 and 2

3.4.3.2 *Straight fiber pullout*

The experimentally determined P-u curves of the SFP-S specimens with straight fibers of three different embedment lengths are shown in Figure 3.18. Due to the absence of hooked end, the pullout of straight steel fibers, similar to polymer fibers, has only two stages: debonding and pullout. Similar to Stage 1 of the hooked steel fiber pullout, the pullout load on the straight fiber initially increases with relative displacement, u, as the debond zone propagates from the matrix face towards the embedded end of the straight fiber. After complete debonding of the fiber, the entire fiber gradually pulls out of the matrix with only frictional bond acting on the fiber/matrix interface modified by the second order slip softening, which is observable as initial concave up followed by convex up curvatures of the monotonically decreasing P-u curves. There is no sudden drop in load after complete debonding (after peak load), which indicates the absence of chemical bond. The fiber pullout load gradually reduces to zero as displacement (u) approaches embedment length (L_e).

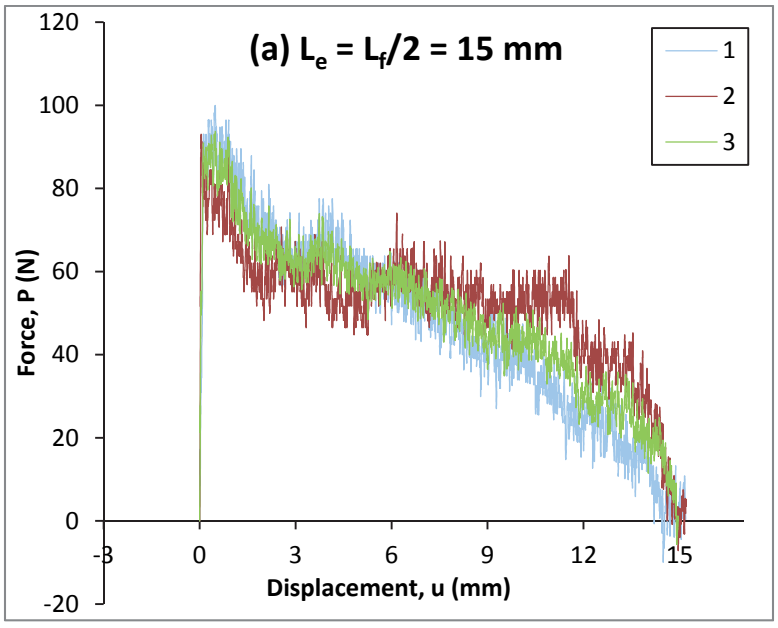

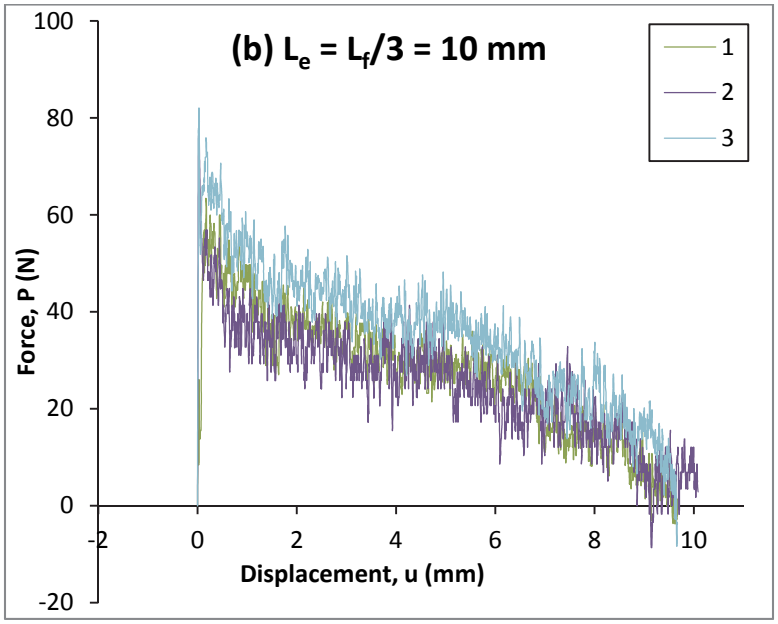

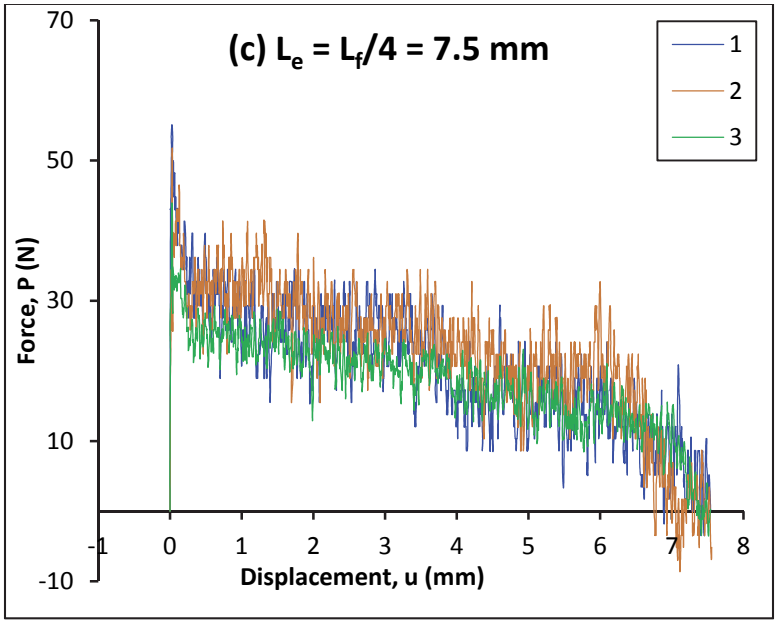

Figure 3.18: Experimentally determined single fiber pullout curves of straight fibers (without hooks) with varying embedment lengths (L_e)

3.5 Micro-scale Analytical Investigation

Based on the physical description of the fiber pullout behavior (of both hooked and straight steel fibers) in the last section, a mathematical analysis is presented in this section that leads to the determination of micro-scale fiber/matrix interaction properties. A mathematical model is presented here, which describes the observed fiber pullout behavior in terms of the fiber/matrix interaction properties. This model is a combination of polymer fiber pullout model[12] and mechanical anchorage model for hooked steel fibers.[18] Using this model and the observed data, the average fiber/matrix interaction properties are deduced, which are used in the next section to model the single-crack behavior of COR-TUF.

3.5.1 Mathematical Model

The mathematical expressions used to model each stage (stages are presented in Section 3.4.3.1) of the pullout of hooked steel fiber are shown in Table 3.5. The contributions from debond/pullout ($F_{d/p}$) and plastic hinge (F_{ph}) mechanisms (described above) are distinctly shown in this table. The total pullout load at any displacement, u, is the sum of these two contributions. Assumptions and the meaning of symbols used in these mathematical expressions are discussed below.

Debonding of only the straight part of the hooked fiber occurs in Stage 1, and therefore, L_e – 4 mm (4 mm is the total hook length) is used for computing the threshold displacement Δ_1. The chemical bond (G_d) and ratio of volume weighted moduli (η) are both assumed zero. In the

expression for debonding load in Stage 1, E_f and d_f are the fiber's elastic modulus and diameter, respectively, and τ_0 is the fiber/matrix interfacial frictional bond.

Table 3.5: Mathematical equations for modeling hooked steel fiber pullout

Stage	Displac-ement, u	Debond/Pullout Contribution ($F_{d/p}$)	Plastic Hinge Contribution (F_{ph})	Remarks
1	$[0,\Delta_1]$	$\pi\sqrt{\frac{\tau_0 E_f d_f^{\,3}}{2}u}$	0	$\Delta_1 = \frac{2\tau_0\left(L_e - 4\ mm\right)^2}{E_f d_f}$ for $L_e > 4$ mm; $\Delta_1 = 0$ for $L_e \le 4$ mm
2	$[\Delta_1,\Delta_2]$	$\pi\sqrt{\frac{\tau_0 E_f d_f^{\,3}}{2}}\times\ldots$ $\ldots\left(\sqrt{\Delta_1}+\sqrt{k\left(u-\Delta_1\right)}\right)$	$P_2\times\left[2\left(\frac{u-\Delta_1}{\Delta_2-\Delta_1}\right)\ldots\right.$ $\left.\ldots-\left(\frac{u-\Delta_1}{\Delta_2-\Delta_1}\right)^2\right]$	$\Delta_2 = \Delta_1 + 172\ \mu m$ for $L_e > 4$ mm; $\Delta_2 = 172.L_e/4$ for 2 mm $< L_e \le 4$ mm & use P_1 instead of P_2 for F_{ph} in all stages; $F_{ph} = 0$ for $L_e \le 2$ mm in all stages
3	$[\Delta_2,\Delta_3]$	$\pi\tau_0 d_f (L_e - u + \Delta_2)\times$ $\left[1+\frac{\beta_1(u-\Delta_2)}{d_f}\ldots\right.$ $\left.\ldots+\frac{\beta_2(u-\Delta_2)^2}{d_f^2}\right]$	$F_3 = P_2\times\left[1+c_1\left(\frac{u-\Delta_2}{h_1+h_2}\right)\ldots\right.$ $\left.\ldots+c_2\left(\frac{u-\Delta_2}{h_1+h_2}\right)^2\right]$	$\Delta_3 = \Delta_2 + 2\ mm$
4	$[\Delta_3,\Delta_3+d_f]$	Ditto	$F_3\left(\Delta_3\right) -$ $\frac{u-\Delta_3}{d_f}\left[F_3\left(\Delta_3\right)-F_4\left(\Delta_4\right)\right]$	$F_3\left(\Delta_3\right) = F_3(at\ u=\Delta_3)$ $F_4\left(\Delta_4\right) = F_4(at\ u=\Delta_3)$
	$[\Delta_3+d_f,\Delta_4]$	Ditto	$F_4 = P_1\times\left[1+c_1\left(\frac{u-\Delta_2}{h_1+h_2}\right)\ldots\right.$ $\left.\ldots+c_2\left(\frac{u-\Delta_2}{h_1+h_2}\right)^2\right]$	$\Delta_4 = \Delta_3 + 2\ mm$
5	$[\Delta_4,\Delta_4+d_f]$	Ditto	$F_4\left(\Delta_4\right)-\frac{u-\Delta_4}{d_f}F_4\left(\Delta_4\right)$	
	$[\Delta_4+d_f,L_e+\Delta_2]$	Ditto	0	

The debonding of the fiber continues in Stage 2 in the hook region of the fiber, and, in addition, the formation of two plastic hinges occurs. It is mathematically difficult to differentiate the individual contributions from fiber debonding and plastic hinge formation as u increases from Δ_1 to Δ_2. As a result, a method of curve-fitting the observed fiber-pullout curves is used in this stage.[18] A parabolic increase in the force contribution from plastic hinge formation (F_{ph}) is assumed, which increases from 0 at Δ_1 to P_2 at Δ_2. The calculation of Δ_2 and P_2 is explained in the next two paragraphs. A small fraction, k (constant), of total displacement, u, is assumed to be contributed by the debonding of the hook. The value of k is computed by solving Eq. 3.1, which ensures the continuity of the debond/pullout contribution ($F_{d/p}$) at the end of Stage 2, when peak pullout load is achieved and $u = \Delta_2$.

$$\pi\sqrt{\frac{\tau_0 E_f d_f^{\,3}}{2}}\left(\sqrt{\Delta_1}+\sqrt{k.\left(\Delta_2-\Delta_1\right)}\right)=\pi d_f \tau_0 L_e \tag{3.1}$$

The total displacement of Stage 2 ($\Delta_2 - \Delta_1$) is assumed to be independent of L_e. The evidence for this is shown in Figure 3.19, which plots the Stage 2 displacement ($\Delta_2 - \Delta_1$) against L_e. There is no observable correlation between $\Delta_2 - \Delta_1$ and L_e in this figure, and therefore, an average value of $\Delta_2 - \Delta_1 = 172$ μm is assumed for all $L_e > 4$ mm ($\Delta_2 - \Delta_1$ is scaled down linearly with L_e for $L_e \leq 4$ mm).

P_2 is the hook pullout capacity, when both plastic hinges are just activated (with no slip yet), and is also assumed to be independent of the fiber embedment length (for $L_e > 4$ mm). Looking from the perspective of the hook, all the pullout force due to debonding of straight part is already transferred to the matrix regardless of the embedment length. Hence, the additional

pullout load due to plastic hinge formation in the hook is the same for all embedment lengths. With these assumptions, the peak pullout load of hooked fiber pullout at the end of Stage 2 can be expressed as Eq. 3.2. This equation represents a straight line when P_{peak} is plotted against L_e. τ_0 is deduced from the slope of the line and P_2 is the y-intercept. The peak loads of all the single fiber pullout curves are plotted against their respective embedment lengths in Figure 3.20, and τ_0 and P_2 are determined from the slope and y-intercept of the best-fit straight line.

$$P_{peak} = \pi d_f \tau_0 L_e + P_2 \tag{3.2}$$

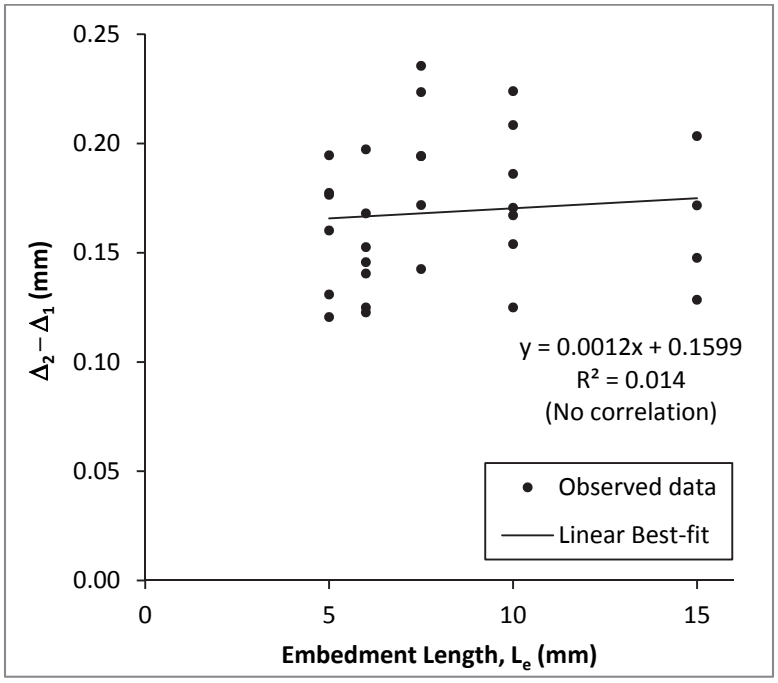

Figure 3.19: Observed Stage 2 displacements in SFP-H specimens

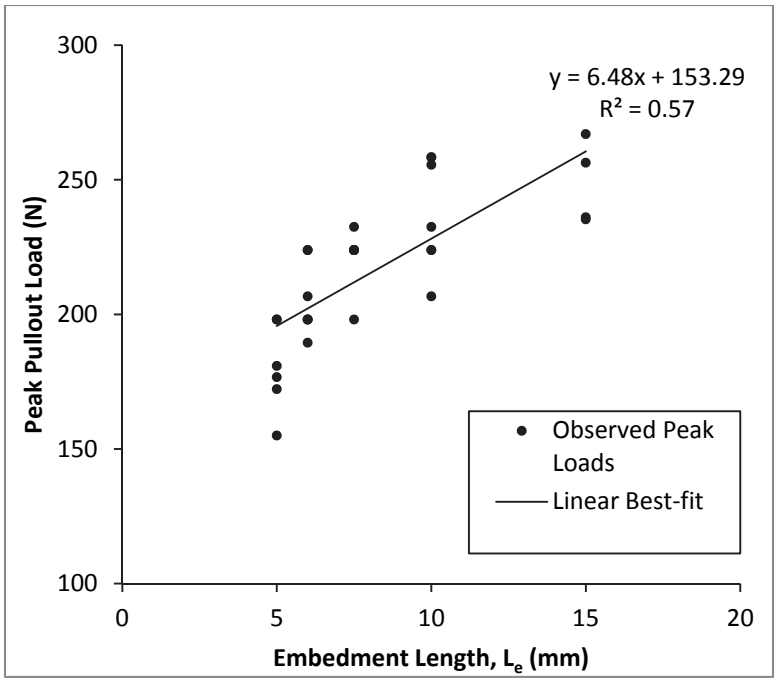

Figure 3.20: Plot of observed P_{peak} vs. L_e of SFP-H specimens for determining τ_0 and P_2

In Stage 3, pullout of the entire embedded segment of the fiber begins. Second order slip softening is assumed due to the concave up followed by convex up curvature of the observed pullout curves of both hooked and straight fibers. Two slip softening parameters β_1 and β_2 are used in the expressions for pullout load ($F_{p/d}$), which are determined by fitting third order polynomials to the observed pullout curves of straight fibers (Figure 3.18). The slip-softened frictional bond is modeled by the same expression in Stages 3, 4, and 5 until complete pullout of the embedded fiber. In addition to slip softening along the entire matrix tunnel, slip-dependent hinge softening is captured by two parameters, c_1 and c_2 computed by fitting third order polynomials to the observed pullout curves of hooked fibers.[18] In the expressions for F_{ph} in Stage 3, h_1 and h_2 are the hook dimensions shown in Figure 3.10.

The deactivation of plastic hinge PH2 at the start of Stage 4 is modeled as a linear decay of F_{ph} from F_3 (at $u = \Delta_3$) to F_4 (at $u = \Delta_4$), where F_3 and F_4 are the slip-softened hook pullout capacities P_2 and P_1, respectively (P_1 is the hook pullout capacity for one active hinge, PH1). After the complete deactivation of plastic hinge PH2 ($u > \Delta_3 + d_f$), only the slip-softened response of the plastic hinge PH1, P_1, remains active. The value of P_2 determined above in Figure 3.20 is verified here from the average of observed drops in loads of the hooked fiber pullout curves between Δ_3 and $\Delta_3 + d_f$.

Similar to Stage 4, Stage 5 is modeled as two sub-stages where the plastic hinge contribution, F_{ph}, is modeled to deactivate linearly from $F_4(\Delta_4)$ at $u = \Delta_4$ to 0 at $u = \Delta_4 + d_f$. The value of P_1 is determined from the average of observed drops in loads of the hooked fiber pullout curves between Δ_4 and $\Delta_4 + d_f$. After deactivation of both plastic hinges, the pullout load due to frictional bond gradually reduces to zero when $u = L_e + \Delta_2$.

A summary of all the micro-scale fiber/matrix interaction properties determined using this mathematical model and observed fiber pullout curves is presented in Table 3.6.

Table 3.6: Fiber/matrix interaction properties of hooked steel fibers in COR-TUF matrix

Property	Chemical Bond (G_d)	Frictional Bond (τ_0)	Slip softening parameters	Hook Pullout Capacities	Hinge softening parameters
Value	0 J/m^2	3.7 MPa	$\beta_1 = -0.08$ $\beta_2 = 0.005$	$P_2 = 153$ N $P_1 = 40$ N	$c_1 = -1.1$ $c_2 = 1$

3.5.2 Comparison with Experimental Results

Using the mathematical model presented in Table 3.5 and the micro-scale properties in Table 3.6, the modeled single fiber pullout behavior of hooked steel fibers is compared with a representative experimental curve for an SFP-H specimen with embedment length $L_f/2$ (the same curve as Figure 3.16) in Figure 3.21. Also plotted in this figure, are the individual contributions from debond/pullout mechanisms ($F_{d/p}$) and plastic hinges (F_{ph}). In addition, the experimental pullout curve of a straight fiber specimen (Specimen #1 in Figure 3.18a) with the same embedment length ($L_f/2$) as the hooked fiber is shown in Figure 3.21 to demonstrate that the hooked fiber pullout is similar to that of straight fiber pullout after deactivation of both plastic hinges. Overall, the modeled single fiber pullout curves satisfactorily capture the experimentally determined behavior.

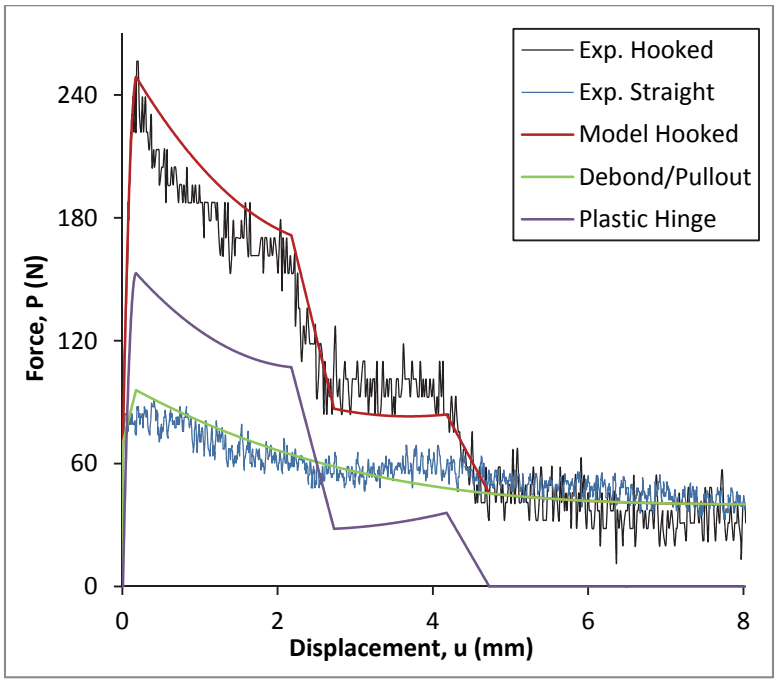

Figure 3.21: Comparison of experimental and analytical curves for the pullout of a hooked steel fiber embedded with length of 15 mm ($L_f/2$) in COR-TUF matrix

3.6 Single-crack Behavior of COR-TUF

The modeled single fiber pullout behavior (P-u) in the previous section is used as input in a scale-linking model[24] to compute the single-crack (σ-δ) behavior of COR-TUF, which is fundamental for determining the reason behind its lack of tensile ductility (Section 2.5). The scale-linking model is represented by Eq. 3.3. A single-crack in COR-TUF, with opening δ under tensile stress σ, is bridged by numerous fibers with varying embedment lengths (L_e) and inclination angles (ϕ) with respect to the principal tension direction (along which a matrix crack typically opens), as shown in Figure 3.22. In Section 3.5.1, the pullout force $P(u,L_e)$ on a single aligned fiber (ϕ = 0°) as a function of relative displacement, u, and embedment length, L_e (plus fiber/matrix interaction properties) is modeled. Therefore, in order to use the modeled $P(u,L_e)$ behavior to compute σ-δ relation, the following additional information is required: (1) a relation between u and δ (2) influence of inclination of non-aligned fibers (ϕ ≠ 0) on pullout force (3) number of fibers of all possible embedment lengths and inclination angles.

$$\sigma(\delta) = \frac{V_f}{A_f} \int_{\phi_1}^{\phi_2} \int_{0}^{(l_f/2)\cos\phi} P(\delta, L_e) e^{f\phi} p(L_e) p(\phi) dL_e d\phi \tag{3.3}$$

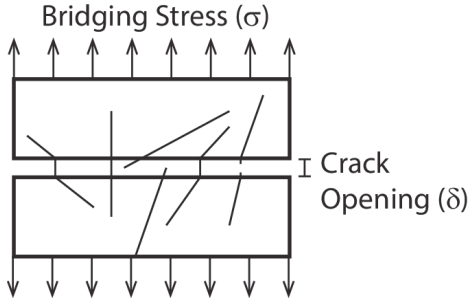

Figure 3.22: Schematic depiction of a crack opening

A fiber being stretched inside a crack has relative displacements, u_1 and u_2 (not necessarily equal due to differing embedment lengths on each side of the crack), corresponding to each face of the crack. By compatibility, $u_1 + u_2 + u_s = \delta$. u_s is the elastic stretching of the segment of the fiber within the crack, which is very small (due to high elastic modulus of the fiber) compared to slips u_1 and u_2 on either side of the crack, and is therefore neglected. In order to resolve δ into u_1 and u_2, equilibrium condition that the pullout forces, P_1 (computed using u_1 and L_{e1} – corresponding embedment length), and P_2 (computed using u_2 and L_{e2}) should be equal is used. This is true because both P_1 and P_2 represent the pullout force on the same fiber within a crack. Solving these equilibrium and compatibility conditions, $P(\delta,L_e)$ (L_e is the shorter of L_{e1} and L_{e2}) on a single fiber with $\phi = 0°$ is determined.[24]

The influence of non-zero fiber inclination (ϕ) with respect to the direction of σ is accounted by multiplying $P(\delta,L_e)$ by $e^{f\phi}$, where 'f' is the snubbing coefficient (or coefficient of friction).[25,26] This is based on the assumption that the fiber bending at the matrix face, where the fiber exits the matrix, can be simulated by a rope wrapped around a frictional drum.[25] The snubbing coefficient largely depends on frictional interaction between the fiber and matrix, which is further dependent on factors such as matrix strength, spall resistance, and roughness, and fiber strength and stiffness. A value of $f = 0.5$ is assumed in this study, similar to that used by Morton & Groves[25] in their study on steel wires embedded in epoxy matrix.

Out of the total number of fibers per unit cross section of the composite, computed as V_f/A_f (fiber volume fraction/cross-sectional area of one fiber), the number of fibers with a particular L_e and ϕ are statistically counted using probability distribution functions, $p(L_e)$ and

$p(\phi)$. $p(L_e)$ is typically assumed as a uniform distribution with a constant value of $2/L_f$ for all possible values of L_e from 0 to $L_f/2$. $p(\phi)$ can be determined either through observation (using conventional or fluorescence microscopy) or theoretical assumptions.[24] In this study, $p(\phi)$ is assumed equal to uniformly equal to $2/\pi$ corresponding to a 2D distribution of fibers, and $p(L_e)$ is taken as $2/L_f$.

With all the inputs described above, Eq. 3.3 is numerically computed to determine the σ-δ behavior of COR-TUF, as shown in Figure 3.23. As the hook dimensions (h_1 and h_2, both equal to 2 mm) are uniform in all fibers, distinct drops in bridging stress are visible in the post-peak s-d curve at about 2 mm and 4 mm. An inset showing the first 50 μm of the σ-δ curve is included in Figure 3.23 to show the bridging capacity (σ_0 = 13.2 MPa) and the corresponding crack opening (δ_0 = 28 μm).

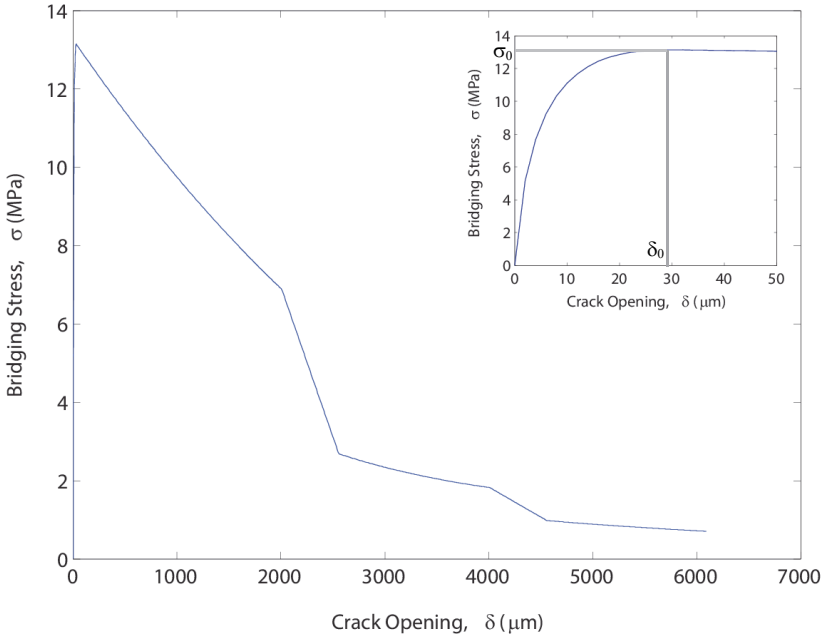

Figure 3.23: Computed single-crack (σ-δ) behavior of COR-TUF

From the inset in Figure 3.23, the complementary energy (J_b') can be computed as the complementary area of the σ-δ curve till δ_0, which is the product $\sigma_0\delta_0$ minus the area under the σ-δ curve till δ_0. J_b' thus computed for COR-TUF is 22.1 J/m^2.

The feasibility of multiple steady-state cracking (which results in tensile ductility) is determined by comparing σ_0 and J_b' with crack initiation strength (σ_{ci}) and crack tip toughness (J_{tip}), respectively, in accordance with the necessary conditions stated in Section 2.5. The strength criterion, which requires $\min(\sigma_0) > \sigma_{ci}$, is satisfied by COR-TUF, as σ_0 = 13.2 MPa (Figure 3.23 – assuming homogenous distribution of fibers so that $\min(\sigma_0) = \sigma_0$) and σ_{ci} = 8.0 MPa (Table 3.3 – average for coupons). However, the energy criterion, which requires $J_b' > J_{tip}$ (in fact $J_b' > 3.J_{tip}$ is required for robust multiple cracking[27]), is not satisfied by COR-TUF. J_{tip} can be approximated to G_m (fracture energy of the matrix) in the case of brittle matrix composites such as COR-TUF with low fiber volumes (3.6%). G_m can be estimated in terms of matrix fracture toughness (K_m) and matrix modulus (E_m) as K_m^2/E_m. K_m for the COR-TUF matrix is 1.17 MPa$\sqrt{m}$ (Section 3.3.4). E_m is assumed equal to the composite tensile modulus (E_c = 51 GPa measured in direct tension tests), as the fiber volume fraction is small. Using the above values of K_m and E_m, J_{tip} is computed equal to about 26.8 J/m^2, which is larger than J_b' (22.1 J/m^2). Therefore, while the strength criterion for multiple steady-state cracking is satisfied, the energy criterion is violated, which is the fundamental reason behind the lack of tensile ductility of COR-TUF.

3.7 Summary and Conclusions

The composite mechanical characterization of COR-TUF, primarily focusing on its uniaxial tensile response, was performed in this chapter. Two kinds of tensile specimens, rectangular coupons and large dogbones, were used for the direct uniaxial tension tests. Due to a more three-dimensional distribution of steel fibers in large dogbones compared to coupons, average ultimate strength of large dogbones (7.6 MPa) was about 10% lower than that of coupons (8.4 MPa). The average tensile strain capacity of coupons and large dogbones was 0.07% and 0.09%, respectively, with a large coefficient of variation of about 58% for coupons and about 50% for large dogbones. Severe matrix spalling was observed during these tensile tests. Thus, both types of COR-TUF specimens exhibited a lack of tensile ductility with a strain-softening behavior, along with large variability in tensile properties.

A detailed micro-scale investigation of COR-TUF was performed through single fiber pullout tests and micromechanics-based analytical modeling. The debond/pullout model typically used for modeling polymer fiber pullout from ECC matrixes was modified to include the influence of dual plastic hinge formation at the hooked end of the steel fiber in COR-TUF. The modified mathematical model was used to determine the micro-scale fiber/matrix interaction properties. A summary of these properties is given in Table 3.6. The fiber/matrix interaction properties were used as inputs in a scale-linking model to determine the single-crack (σ-δ) behavior of COR-TUF. The bridging capacity (σ_0 at $V_f = 3.6\%$) of steel fibers in COR-TUF thus computed is 13.2 MPa, and the complementary energy of fiber-bridging is 22 J/m^2. This micro-scale analysis revealed that in spite of satisfying the strength criterion for multiple cracking,

COR-TUF violates the energy criterion as the complementary energy of crack bridging is insufficient in overcoming the crack propagation resistance due to high fracture toughness of the matrix, which prevents COR-TUF from achieving tensile ductility.

References

1. O'Neil, E. F. (2008) "On Engineering the Microstructure of HPCs to Improve Strength, Rheology, and Frangibility" PhD Dissertation, Evanston, IL: Northwestern University, pp. 90.

2. Bekaert Corp. (2010) "Datasheet: Dramix ZP 305" Webpage: http://ncg-bg.com/assets/files/products/01_materials_for_industrial_floors/1_fibri_za_beton/Dramix%20ZP%20305_en.pdf. Accessed on June 19, 2013.

3. Rushing, T. S. (2009), private communication via email dated March 12, 2009 from Rushing to Michael Stults.

4. JSCE (2008) "Recommendations for Design and Construction of High Performance Fiber Reinforced Cement Composites with Multiple Fine Cracks." Tokyo, Japan: JSCE, pp. Testing Method 1-5.

5. O'Neil, E. F. (2008) "On Engineering the Microstructure of HPCs to Improve Strength, Rheology, and Frangibility" PhD Dissertation, Evanston, IL: Northwestern University, pp. 66.

6. Taylor, H. F. (1997). "Effects of high or low temperatures at atmospheric pressure" In *Cement Chemistry* (2nd ed.), London, UK: Thomas Telford, pp. 339-341.

7. ASTM (2011) "Standard Test Method for Compressive Strength of Hydraulic Cement Mortars (Using 2-in. or 50 mm Cube Specimens)" West Conshohocken, PA: ASTM.

8. ASTM (2003) "Test method for plane-strain fracture toughness of metallic materials" West Conshohocken, PA: ASTM.

9. Li, V. C., Mishra, D. K. & Wu, H. C. (1995) "Matrix design for pseudo strain-hardening fiber reinforced cementitious composites" *Journal of Materials and Structures*, 28(183), 586-595.

10. Bazant, Z. P. & Planas, J. (1998) "Brittleness Number" In *Fracture and Size Effect in Concrete and Other Quasibrittle Materials*, CRC Press: New York, NY, pp. 321.

11. Chanvillard, G. & Rigaud, S. (2003) "Complete Characterization of Tensile Properties of Ductal® UHPFRC According to French Recommendations," In *Proceedings of HPFRCC 4*, Naaman A. E. & Reinhardt, H. W. (Eds.), Ann Arbor, MI, pp. 21-34.

12. Lin, Z., Kanda, T. & Li, V. C. (1999) "On Interface Property Characterization and Performance of Fiber Reinforced Cementitious Composites" *Concrete Science and Engineering*, 1, 173-84.

13. Kanda, T. & Li, V.C. (1998) "Interface Property and Apparent Strength of a High Strength Hydrophilic Fiber in Cement Matrix" *Journal of Materials in Civil Engineering*, 10(1), 5-13.

14. FHWA (2006) "Material Property Characterization of Ultra-High Performance Concrete" *FHWA, US Department of Transportation*, McLean, VA, Pub No. FHWA-HRT-06-103, pp. 24-28.

15. O'Neil, E. F. (2008) "On Engineering the Microstructure of HPCs to Improve Strength, Rheology, and Frangibility" PhD Dissertation, Evanston, IL: Northwestern University, pp. 127.

16. Yang, E. H., Yang, Y. & Li, V. C. (2007) "Use of High Volumes of Fly Ash to Improve ECC Mechanical Properties and Material Greenness" *ACI Material Journal*, 104(6), 620-628.

17. Kim, D. J., El-Tawil, S., & Naaman, A. E. (2008) "Loading rate effect on pullout behavior of deformed steel Fibers" *ACI Material Journal*, 105(6), 576-584.

18. Alwan, J.M., Naaman, A.E. & Guerrero, P. (1999) "Effect of mechanical clamping on the pull-out response of hooked steel fibers embedded in cementitious matrix" *Concrete Science and Engineering*, 1, 15-25.

19. Alwan, J.M., Naaman, A.E. & Hansen, W. (1991) "Pull-out work of steel fibers from cementitious composites: analytical investigation" *Concrete Science and Engineering*, 13, 247-255.

20. Naaman, A.E., Namur, G.G., Alwan, J.M. & Husamuddin, N.S. (1991) "Fiber pullout and bond slip - I: analytical study" *ASCE Journal of Structural Engineering*, 117(9), 2769-2790.

21. Naaman, A.E., Namur, G.G., Alwan, J.M. & Husamuddin, N.S. (1991) "Fiber pullout and bond slip - II: experimental validation" *ASCE Journal of Structural Engineering*, 117(9), 2791-2800.

22. Husamuddin, N.S. & Naaman, A.E. (1995) "Prediction model for elastic modulus of high-performance fiber reinforced cement-based composites" *ACI Materials Journal*, 92(3), 304-314.

23. Robins, P., Austin, S. & Jones, P. (2002) "Pull-out behavior of hooked steel fibers" *Journal of Materials and Structures*, 35, 434-442.

24. Li, V. C., Wang, Y. & Backer, S. (1991). "A Micro Mechanical Model of Tension Softening and Bridging Toughening of Short Random Fiber Reinforced Brittle Matrix Composites," *Journal of Mechanics and Physics of Solids*, 39(5), 607-625.

25. Morton, J. & Groves, G. W. (1976) "The Effect of Metal Wires on the Fracture of a Brittle-Matrix Composite" *Journal of Material Science*, 11, 617-622.

26. Li, V. C., Wang, Y. & Backer S. (1990) "Effect of Inclining Angle, Bundling and Surface Treatment on Synthetic Fibre Pull-Out from a Cement Matrix," *Composites*, 21(2), 132-140.

27. Kanda, T. & Li, V. C. (1998) "Multiple Cracking Sequence and Saturation in Fiber Reinforced Cementitious Composites" *JCI Concrete Research and Technology*, 9(2), 19-33.

CHAPTER 4: DEVELOPMENT OF HIGH STRENGTH-HIGH DUCTILITY CONCRETE (HSHDC)

4.1 Introduction

This chapter describes the development of a new concrete, named High Strength-High Ductility Concrete (HSHDC), which combines very high compressive strength (similar to COR-TUF) and tensile ductility (similar to ECC) in a single material. The HSHDC development builds upon the conclusions of Chapter 2 about the contrasting design philosophies of HSC and ECC and of Chapter 3 about the fundamental reason behind lack of tensile ductility in COR-TUF. The general philosophy of design of HSHDC is to preserve the compressive strength of the COR-TUF matrix and simultaneously incorporate the principles of micromechanics in fiber selection and matrix modification in such a way that the fiber, matrix, and their interface act harmoniously to impart high tensile ductility, while maintaining high compressive strength.

In the following sections, the material design objectives along with the general design approach are presented. This is followed by specific details of the selection of materials and mix proportions, and their micromechanics basis. The experimental investigation for verifying tensile/compressive properties of these mixtures, leading towards the development of the HSHDC with target mechanical properties, is presented in Sections 4.4 and 4.5.

4.2 Design Objective and Approach

In this part of the research, the primary objective of the design of HSHDC is to achieve the following target mechanical properties in one material, while limiting their variability, under pseudo-static loading: (a) Direct uniaxial tensile strain capacity greater than 3% with coefficient of variation less than 15% of the average value, and (b) Uniaxial compressive strength greater than 150 MPa with coefficient of variation less than 10% of the average value. These property targets were selected considering the typical tensile strain capacity of ECC and compressive strength of COR-TUF.

The general approach towards achieving the target mechanical properties and reduce their variability is maximization of the pseudo-strain hardening (PSH) indices, while maintaining the conditions for high compressive strength of the matrix.

Kanda & Li[1] introduced two PSH indices for design purpose – PSH strength index, σ_0/σ_{fc}, and PSH energy index, J_b'/J_{tip}. The meaning of these symbols is presented in Section 2.5. The first ratio is a measure of the stress margin available to trigger multiple cracks accounting for flaw size variation. The second ratio is a measure of the energy margin accounting for variations in interfacial properties, fiber dispersion, and fracture toughness (due to matrix inhomogeneity). For robust multiple cracking in ECC, it was recommended to have $\sigma_0/\sigma_{fc} > 1.2$ and $J_b'/J_{tip} > 3$.[1]

In addition to the micromechanics principles, HSHDC development utilizes the COR-TUF matrix; however, certain modifications are required for synchronizing the behavior of the

matrix with the fibers to achieve tensile ductility. For maintaining high compressive strength, these modifications of the COR-TUF matrix must preserve the basic conditions for high strength (Section 2.3), which are dense particle packing, minimization of flaw size and number, low w/c ratio, matrix homogeneity, and high quality of microstructure (in terms of its density and CSH formation).

4.3 Materials and Mix Proportions

Following the aforementioned general approach for integrating high compressive strength and tensile ductility in one material, the selection methodology of materials and mix proportions is described in this section. The proportions by weight of all mixtures H1-H10 explored in this research to achieve the target mechanical properties of HSHDC are given in Table 4.1, and the ingredient proportions that are changed between successive mixtures are underlined in this table.

It was shown in Chapter 3 that the main limitation which prevents COR-TUF from achieving tensile ductility is the insufficient complementary energy of crack bridging. Therefore, as an initial development strategy for HSHDC, focus was placed on ensuring a high complementary energy thereby increasing PSH energy index. Matrix modification, that may potentially reduce the composite compressive strength, was avoided at first, and various alternative fibers were explored for enhancing the complementary energy of crack bridging. After a suitable fiber was selected, matrix proportions were altered to favorably modify matrix rheology and the composite mechanical properties.

Table 4.1: Mixture proportions

Mixture Name	Cement[a]	Silica Fume	Silica Flour	Silica Sand	Tap Water	HRW RA	Fiber[b]			
							Type	V_f	L_f (mm)	d_f (μm)
COR-TUF	1[c]	0.39	0.28	0.97	0.21	0.9%	SH	3.6%	30	550
H1	1	0.39	0.28	0.97	0.21	3.0%	AR	2%[d]	8	40
H2	1	0.39	0.28	0.97	0.21	1.5%	PE1	2%	12.7	38
H3	1	0.39	0.28	0.97	0.21	2.4%	PE2	2%	12.7	28
H4	1	0.39	0.28	0.83	0.21	2.1%	PE2	2%	12.7	28
H5[e]	1	0.39	0.28	0.70	0.21	1.8%	PE2	2%	12.7	28
H6	1	0.39	0.28	0.60	0.21	1.6%	PE2	2%	12.7	28
H7	1	0.39	0.28	0.70	0.21	2.0%	PE2	2.4%	12.7	28
H8	1	0.39	0.28	0.70	0.21	1.6%	PE2	1.6%	12.7	28
H9	1	0.46	0.21	0.70	0.21	2.2%	PE2	2%	12.7	28
H10	1	0.39	0.28	0.70 F110	0.21	2.0%	PE2	2%	12.7	28

[a] The class of each material ingredient is shown in Table 3.1. Description of all matrix ingredients is given in Section 3.2.

[b] Proportion of fiber in each mix is given in terms of volume fraction (V_f) of the total mix volume. L_f and d_f are fiber length and diameter, respectively. The naming of fiber type is abbreviated as follows: 'SH' = steel hooked (Dramix ZP 305); 'AR' = aramid fiber (Technora); 'PE1' = polyethylene 1 (Spectra 900); 'PE2' = polyethylene 2 (Spectra 1000).

[c] All mixture proportions are by weight of cement (except fiber, which is in terms of V_f).

[d] The ingredient proportions that are changed between successive mixtures are underlined.

[e] Mixtures H7-H10 use H5 as control, which is shown in bold.

Due to greater flexibility in the selection of properties in polymer fibers than steel fibers, the former were considered for the following investigations. Anticipating high interfacial bond due to the dense COR-TUF matrix, only very high strength polymer fibers were considered for HSHDC to ensure crack bridging without extensive fiber rupture.

The commercially available high strength polymer fibers can be classified into two broad categories based on their affinity to water as hydrophilic (e.g. Aromatic Polyesters and Polyamides) or hydrophobic (e.g. Polyethylene). In addition to frictional bond, hydrophilic fibers can form strong chemical bond with the cementitious matrix.[2] In contrast, hydrophobic fibers form almost no chemical bond with the cementitious matrix.

In this research, both types of fibers are explored in mixtures H1 and H2 – the mix proportions are presented in Table 4.1. In mixture H1, an aromatic polyamide (AR) fiber (Technora [hydrophilic]) is used, whereas in mixture H2, an ultra-high molecular weight polyethylene (PE1) fiber (Spectra 900 [hydrophobic]) is used. Anticipating stronger interfacial chemical bond with the hydrophilic fiber compared to the hydrophobic fiber of similar strength, shorter length (8 mm) of AR fiber is used as compared to the PE1 fiber (12.7 mm) to prevent excessive fiber rupture.[3] Smaller aspect ratio (L_f/d_f) of the AR fiber also assists fiber dispersion.[4] Both AR and PE1 fibers in mixtures H1 and H2 have almost similar diameters of 40 μm and 38 μm, respectively. Similar to PVA fibers in ECC, both AR and PE1 fibers were used at a fiber volume fraction of 2%.[4] Both mixtures H1 and H2 utilize unmodified COR-TUF matrix (Table 3.1) with the exception of HRWRA content, which is increased for the polymer fibers (more for AR fibers than PE fibers) compared to that used for steel fibers in COR-TUF to facilitate homogenous fiber dispersion.

In mixture H2 and other mixtures discussed below, significant increase in setting time was observed when HRWRA beyond 1.6% by cement weight is used. The set retardation is typical of high strength concretes utilizing high dosage of HRWRA.[5] It is recommended to allow

2 days of setting time at room temperature for mixtures with HRWRA content between 1.6% and 2.4% by cement weight, so that they achieve sufficient stiffness and strength for demolding. For mixtures with HRWRA content greater than 2.4% and up to 3%, 3 days of setting time is recommended. HRWRA dosage should not be increased beyond 3%, which may otherwise indefinitely prolong the setting time.

Due to its hydrophobic nature, PE1 fiber has significantly lower water demand and is easier to process than the AR fiber. As discussed in Section 4.5 below, H2 mixture with the PE1 fiber also exhibits significantly more desirable mechanical properties compared to H1, due mainly to homogenous fiber dispersion and favorable fiber/matrix interaction. Hence, only PE fiber is used in all subsequent mixtures.

Micromechanical analysis of the H2 mixture revealed the properties of interaction between the PE fiber and the COR-TUF matrix.[6] Using these interaction properties, it was predicted that another PE fiber, Spectra 1000 (abbreviated as PE2 in Table 4.1), with higher strength and higher aspect ratio will significantly enhance both the PSH indices, and therefore, the PE2 fiber was investigated in following mixtures.

The effects of increasing the fiber aspect ratio and strength on the mechanical properties of the composite were experimentally examined in the mixture H3 in comparison with H2. The PE2 fiber used in mixture H3 has the same length (L_f) as PE1, but PE2 has a finer diameter (d_f) of 28 μm compared to 38 μm of the PE1 fiber. A higher L_f/d_f ratio of PE2 (454) compared to PE1 (334) results in larger fiber/matrix interfacial area for the same fiber volume fraction,[7,8]

which is expected to increase the fiber bridging capacity and complementary energy, provided that excessive fiber breakage is avoided. Nominal tensile strength of the PE2 fiber (3000 MPa) is also higher than PE1 (2600 MPa), which allows PE2 to carry additional stress (due to higher aspect ratio) without breakage. Although using the PE2 fiber with higher aspect ratio is beneficial from micromechanics standpoint, it presents processing difficulties (in spite of increased HRWRA content) and negatively influences the composite mechanical properties (details in Section 4.5).

For addressing the processing difficulties and improving the fiber dispersion, the fresh matrix viscosity was reduced by lowering the sand/cement (s/c) weight ratio of the mix. The effects of viscosity on fiber dispersion in cementitious matrixes are well documented in the literature.[9,10,11] Due to very low water/cementitious material (w/cm) ratio of 0.15 used in the COR-TUF matrix, its plastic viscosity is too high (9.0 Pa.s) compared to other high ductility concretes with good fiber dispersion, such as ECC (mix viscosity of 2.2 Pa.s). The method adopted for determining the matrix viscosity is detailed below in Section 5.2.5. Reducing the s/c ratio increases the cement paste (and water) per unit volume of the mix, without changing the w/cm ratio (critical for strength), causing reduction in matrix viscosity. As a result, four s/c ratios were investigated in the mixtures H3-H6, as shown in Table 4.1.

The same objective of lowering the matrix viscosity (that was achieved by lowering s/c ratio above) was attempted by increasing HRWRA dosage (over 2.4% by cement weight); however, this caused lengthening of set times beyond two days, sometimes up to four days, making the use of the composite impractical. The cured compressive strength at 15 days (under

accelerated heat curing) was also reduced by HRWRA overdose. Such reduction in compressive strength is caused by the reduction in hydration rates of C_3S due to HRWRA overdose.[12] As discussed below in Section 4.5, mixture H5 showed the best mechanical properties among mixtures H3-H6, and for this reason, mixtures H7-H10 described below utilize H5 as the control mixture.

Mixtures H7 (V_f = 2.4%) and H8 (V_f = 1.6%) were prepared to determine the optimum fiber volume fraction (V_f). Micromechanical analysis[6] shows that increasing the fiber volume fraction enhances both PSH indices; however, it may be limited by practical limitations of mix processing. The dosage of HRWRA was varied almost in proportion to V_f in these mixtures to control the matrix rheology.

Matrix modifications aimed at enhancing the fiber/matrix interfacial density and reducing fracture toughness were attempted in mixtures H9 and H10, respectively. In mixture H9, 25% by weight of silica flour (particle size: 5-100 μm) is replaced by considerably finer sized silica fume (particle size: 0.1-1 μm), which is expected to increase the density of the interfacial transition zone between the PE2 fiber and cementitious matrix – thereby increasing the bridging capacity and PSH strength index. In mixture H10, the type of sand is changed from F55 (mean diameter of 210 μm) to F110 (mean diameter of 110 μm) to reduce the fracture toughness of the matrix, which is also expected to increase both PSH indices.

4.4 Specimens and Experimental Setup

All the mixtures H1-H10 were characterized by their responses under direct uniaxial tension and compression. For each mixture, four dogbone-shaped specimens (geometry in Figure 3.1) and three 2″ cubes were prepared for tension and compression tests, respectively. All the specimens were cured following the COR-TUF 7-4-2 curing procedure described in Section 3.3.2 and tested at 15 days after casting.

The experimental test setup for direct tension tests on dogbone specimens is shown in Figure 4.1. Aluminum plates were glued to the grip region of the dogbone specimens to achieve smooth gripping surfaces, thereby minimizing the stress concentrations. The dogbone specimens were gripped on these faces in a fixed-fixed type of end constraints. The tensile tests were conducted as per the recommendations of JSCE[13] for direct tension testing of dogbone specimens at 0.5 mm/min (0.02 in/min) using a displacement controlled closed loop test system with a maximum load capacity of 100 kN (22 kips). The strain in all the dogbone specimens was computed from the extension of the specimen measured by two LVDTs mounted parallel to the two side edges of the dogbone specimen (Figure 4.1). Thus, the dogbone specimens were tested under quasi-static uniaxial tension loading, and appropriate sensors were used to record uniaxial tensile load (to determine stress) and displacement (to determine strain).

The test setup used in this study for cube compression tests on COR-TUF is similar to that recommended in ASTM C109[14]. The compressive displacement rate applied on the cubes

was 30 μm/min, which translates into 1300 N/s for 2 inch cubes assuming an elastic modulus of 50 GPa for these mixtures.

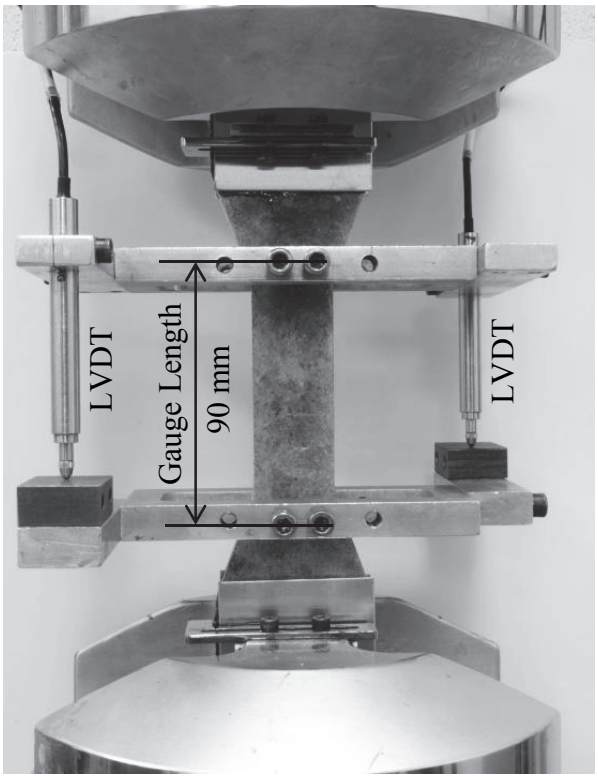

Figure 4.1: Direct tension test setup for dogbone specimens

4.5 Experimental Results and Discussion

The averages of the mechanical properties of all mixtures (H1-H10) investigated in this study, along with COR-TUF for comparison, are presented in Table 4.2. Representative tensile stress-strain curves of all mixtures are plotted in Figure 4.2. In this section, only a comparative discussion of the mechanical properties is presented. Detailed descriptions of the multiple

cracking process and the tensile stress-strain curves are presented in Section 5.3.2. A comparative chart plotting tensile ductility versus compressive strength of all mixtures H1-H10 (and COR-TUF) is shown in Figure 4.3.

Table 4.2: Average mechanical properties

Mixture Name	Brief Mixture Description[a]	f_c' (MPa)[b]	σ_{fc} (MPa)	σ_{ult} (MPa)	ε_{ult} (%)	COV in ε_{ult}
COR-TUF	Same as Chapter 3 (using coupons)	201	8.0	8.4	0.07	58%
H1	w/ Technora (AR) fiber	145	6.0	9.5	1.1	45%
H2	w/ Spectra 900 (PE1) fiber	160	5.7	11.8	3.5	40%
H3	w/ Spectra 1000 (PE2) fiber[c]; s/c = 0.97	149	6.5	13.0	2.1	28%
H4	s/c = 0.83	156	7.1	13.9	3.1	15%
H5	s/c = 0.70	163	8.3	14.3	3.4	13%
H6	s/c = 0.63	160	8.5	14.2	3.3	14%
H7	V_f = 2.4%[d]	174	8.2	14.9	3.6	21%
H8	V_f = 1.6%	161	8.3	12.0	2.0	12%
H9	25% silica flour replaced by silica fume	155	8.5	12.5	2.5	24%
H10	F55 sand replaced by F110	161	7.5	12.9	3.0	15%

[a] Only for quick reference – for complete description, refer Table 4.1.
[b] COV in f_c' was less than 10% for all mixtures.
[c] All mixtures following H3 utilize Spectra 1000 (PE2) fiber.
[d] Mixtures H7-H10 utilize s/c ratio of 0.70 – same as H5.

Both the fibers (AR and PE1) investigated in mixtures H1 and H2 perform better with the COR-TUF matrix than the steel fiber, and result in substantially higher tensile ductility of the composite, albeit with significant loss (20-25%) in compressive strength, compared to COR-TUF. The loss in compressive strength can be attributed to the use of significantly increased content of HRWRA (water-based) and entrapment of larger air voids (during mix processing) due to poorer fiber dispersion of the polymer fibers compared to steel fibers. Between the two

mixtures, the mixture H2 with the hydrophobic PE1 fiber exhibits better average mechanical properties (both compressive strength and tensile ductility) than H1. However, both mixtures H1 and H2 show high variability (COV $\geq$ 40%) in their tensile strain capacities among different specimens of the same material, which may be caused due to inhomogeneous fiber dispersion. Significantly greater degree of fiber clumping was experienced during the mix processing of H1 with AR fiber compared to H2 with PE1 fiber, which may be attributed to the greater absorption of water and negative impacts on mix rheology in mixture H1 compared to H2. Thus, the mixture H2 with PE1 fiber exhibits higher tensile ductility and compressive strength, and is easier to process compared to H1 with AR fiber.

The ultimate tensile strength of mix H3 (13.0 MPa) is greater than that of H2 (11.8 MPa) due to the increase in L_f/d_f ratio and strength of the PE fiber, as predicted by micromechanics.[6] However, higher aspect ratio of the fiber presented processing difficulties (in spite of increased HRWRA content) and caused reductions in average compressive strength and tensile ductility of mixture H3 compared to H2.

The reduction of sand-to-cement (s/c) ratio from 0.97 in mix H3 to 0.70 in the mix H5 led to improvements in mechanical properties. The tensile ductility increased from 2.1% of H3 to 3.4% of H5, while the compressive strength increased from 149 MPa of H3 to 163 MPa of H5. Along with improvements in average mechanical properties, a decrease in the variation of properties (COV) was observed which supports the hypothesis that controlled reduction in s/c ratio (limited to 0.70) improves the fiber dispersion homogeneity.

In order to test the aforementioned hypothesis, the degree of homogeneity of fiber dispersion in these composites was determined using fluorescence microscopy.[15] The fiber dispersion coefficient,[15] $\alpha \in [0,1]$, is used as a measure of fiber dispersion homogeneity at a specimen cross-section. $\alpha = 1$ implies a perfectly homogenous dispersion, whereas $\alpha = 0$ indicates no dispersion at all. Details about the use of fluorescence microscopy for observing PE fibers are given in Section 6.4.2. The value of α observed in H2 (with PE1 fiber) was 0.28 compared to 0.35-0.40 typically observed in ECC with good fiber dispersion.[15,16] In mixture H3 (with PE2 fiber), α is 0.25 which is smaller than H2 due to larger aspect ratio of the PE2 fiber compared to PE1. The value of α increases steadily with decreasing s/c ratio. α is equal to 0.30, 0.33, and 0.34 for mixes H4, H5, and H6, respectively. In spite of good fiber dispersion ($\alpha = 0.34$), the mix H6 shows a slight decline in the mechanical performance (Table 4.2), which points towards the dominance of negative effects on particle packing, workability, and compressive strength due to the over-reduction of sand. Thus, the improvement in mechanical properties from H3 to H5 is attributable to the observed increase in the degree of fiber dispersion homogeneity due to decrease in s/c ratio down to 0.70; however, further reduction of s/c ratio in mixture H6 negatively influences the mechanical performance.

The 20% increase in fiber volume fraction in mixture H7 (V_f = 2.4%) appears to marginally enhance both tensile ductility and compressive strength compared to mixture H5, although it is accompanied with an increase in variability. The slight increase in tensile ductility from 3.4% in H5 to 3.6% in H7 is likely due to the increase in the bridging capacity of the fibers enabling the initiation of a few more micro-cracks from smaller sized flaws. However, increasing the fiber volume hinders homogenous fiber dispersion, which is reflected by the increase in COV

of ε_{ult}. The compressive strength of mixture H7 is slightly greater than that of H5, which may be linked to the more effective stabilization of the wing cracks by increased fiber content. Although increasing the fiber content beyond 2% enhances the mechanical properties, but the gains are low compared to the increase in fiber volume, HRWRA content, and processing challenges.

Decreasing the fiber content by 20% in mixture H8 (V_f = 1.6%) causes a significant reduction in tensile ductility compared to H5, along with a borderline reduction in compressive strength. The decrease in the fiber volume fraction significantly reduces the crack bridging capacity, as the ultimate tensile stress reduces from 14.3 MPa in H5 to 12.0 MPa in H8. This increases the critical flaw size that can be initiated into a micro-crack causing a reduction in the number of micro-cracks and tensile ductility.

Replacement of 25% weight of silica flour in mixture H5 by silica fume in mixture H9 results in the reduction of both compressive strength and tensile ductility. Although the intent behind increasing the silica fume content was enhancement of the fiber/matrix interfacial bond by increasing the interfacial density, the detrimental effect on workability and viscosity of the mixture (further influencing fiber dispersion) appears to be more dominant causing overall reduction in mechanical performance. The ultimate tensile strength (a measure of bridging capacity) reduced to 12.5 MPa in H9 from 14.3 MPa in H5. Thus, sufficient content of silica flour, along with silica sand and silica fume, is required to maintain good matrix rheology and composite mechanical properties.

The use of finer F110 sand instead of F55 sand achieved its intended goal of reducing the matrix fracture toughness in mixture H10, as indicated by reduction in σ_{fc} (assuming constant maximum flaw size); however, it failed to enhance the composite mechanical performance compared to mixture H5. Similar to mixture H9 with increased silica fume content, the replacement of F55 sand by F110 sand caused significant reduction in σ_{ult} due to changes in mix rheology and fiber dispersion, which led to reduction in mechanical performance of mixture H10 compared to H5.

Considering the mechanical properties and their variability in all mixtures (H1-H10) together (shown in Figure 4.3), it can be observed that the mixture H5 has the best combination of compressive strength and tensile strain capacity, along with low COV that meets the material design objectives stated in Section 4.2. Additionally, there appears to be a trend of increasing tensile ductility with compressive strength (Figure 4.3), provided that good fiber dispersion is maintained. This is in contrast to the prevailing knowledge of other concretes, which exhibit loss of tensile ductility with increasing compressive strength. Such unique performance of these high-strength high-ductility mixtures is made possible by the micromechanically tailored interaction between the hydrophobic high strength PE fiber (of carefully chosen aspect ratio) and the densely packed matrix.

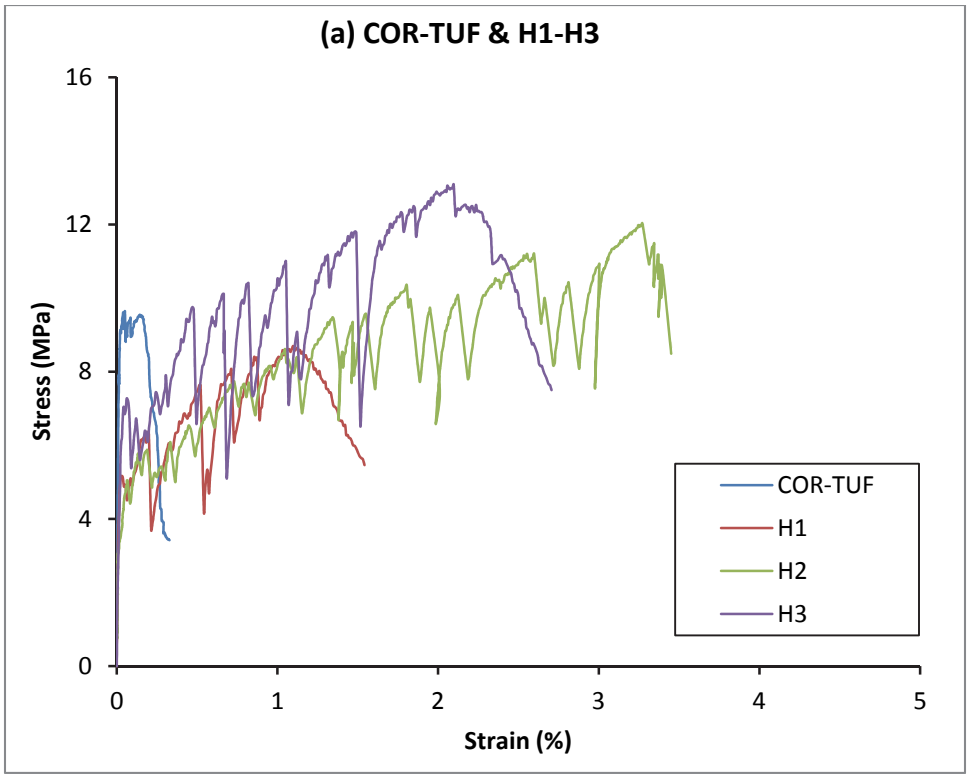

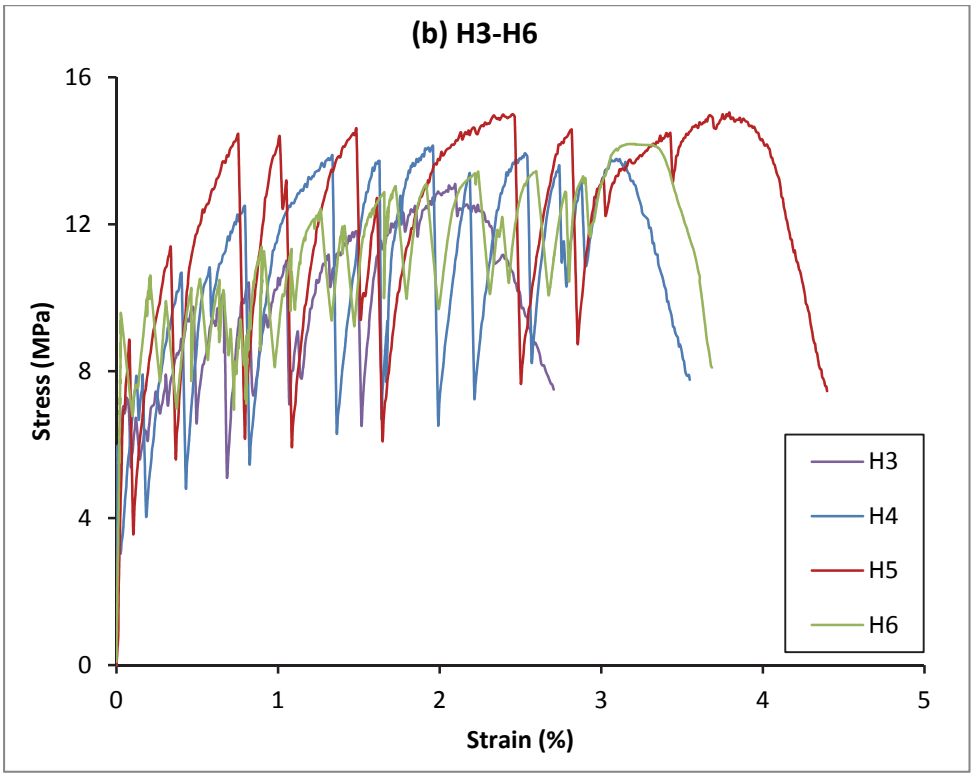

Figure 4.2: Representative tensile stress-strain curves

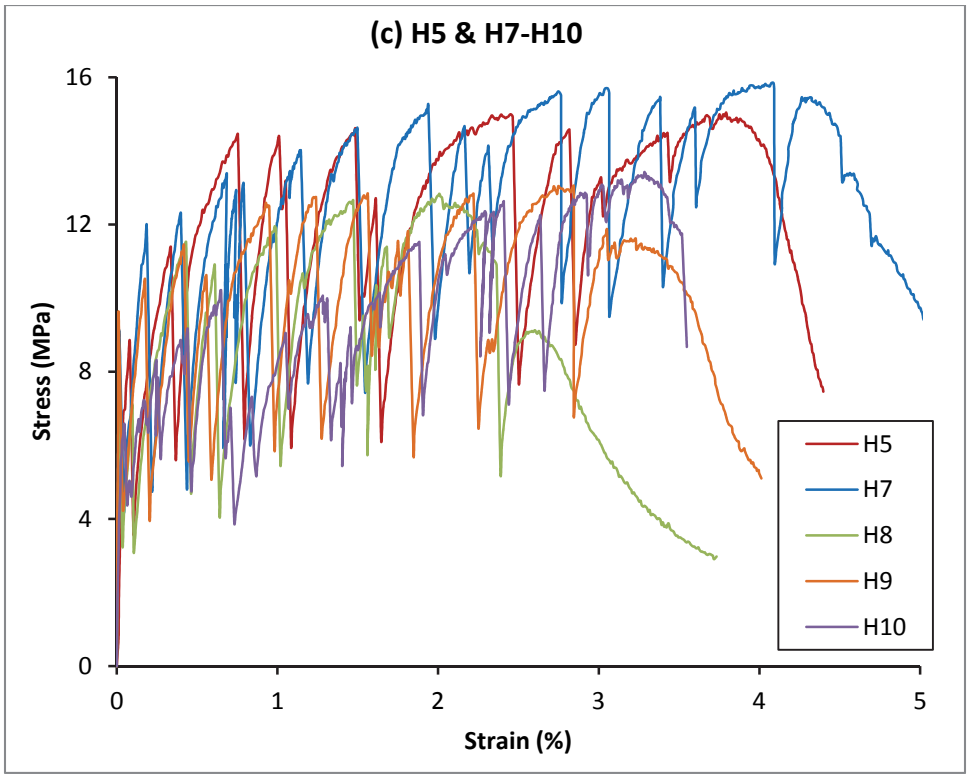

Figure 4.2: Representative tensile stress-strain curves

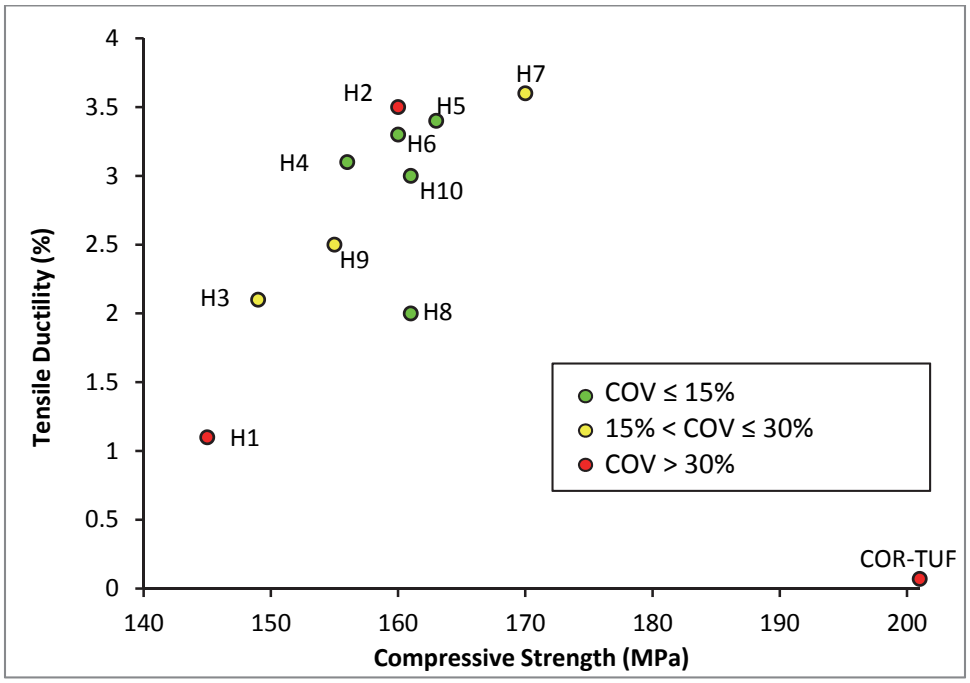

Figure 4.3: Comparison Chart

4.6 Summary and Conclusions

A set of fiber reinforced cementitious composites was investigated in this study that led to the development of a composite (H5) with unprecedented combination of compressive strength (163 MPa) and tensile ductility of (3.4% [COV of 13%]) in one material. The mixture H5 utilizes the micromechanically tailored interaction between high performance PE fibers and densely packed cementitious matrix to achieve such unique combination of properties. The principles behind the design of ECC and HSC were central in developing these composites, and experiments were used to verify and compare their mechanical properties.

The following conclusions can be drawn from this study:

- The hydrophobic PE fiber disperses more homogenously than the hydrophilic AR fiber in the high strength matrixes with very low w/c ratios. Due to better dispersion, the mechanical properties of the composite containing PE fibers outmatch those with AR fibers.
- Use of HRWRA beyond 1.6% by cement weight retards the setting time beyond 1 day. Setting times of 2 days and 3 days are recommended for HRWRA contents of 1.6% to 2.4% and 2.41% to 3%, respectively. A dosage higher than 3% is not recommended as it can indefinitely prolong the setting time and also significantly degrade the cured compressive strength.
- Larger aspect ratio of PE fiber, along with increased nominal strength, increases the crack bridging capacity of the fibers. However, the increase in aspect ratio is limited by processing difficulties.
- Decreasing the sand-to-cement (s/c) ratio from 0.97 used in COR-TUF matrix down to 0.70 leads to improvement in mechanical properties due to the observed increase in the degree of

fiber dispersion homogeneity; however, further reduction of s/c ratio below 0.70 negatively influences the mechanical performance.

- The PE2 fiber volume fraction of 2% is optimal for achieving the target mechanical properties. Although increasing the fiber content beyond 2% enhances the mechanical properties, the gains are low compared to the increase in fiber volume, HRWRA content, and processing challenges. Decreasing the fiber content under 2% (down to 1.6%) causes a significant reduction in tensile ductility, along with a borderline reduction in compressive strength.
- Increasing the silica fume content by replacing silica flour and replacing F55 sand by F110 sand caused significant reduction in σ_{ult} due to changes in mix rheology and fiber dispersion, which led to reduction in mechanical performance of the composite.

Overall, it was demonstrated that it is feasible to develop a concrete with high compressive strength and high tensile ductility by simultaneously incoporating the principles of micromechanics and high strength concrete design. The best mechanical performance was exhibited by mixture H5, along with low variability in properties. This mixture will be hereon referred as the High Strength-High Ductility Concrete (HSHDC). The composite mechanical properties and micro-scale fiber/matrix interactions of HSHDC are investigated in detail in the next two chapters.

References

1. Kanda, T. & Li, V. C. (1998) "Multiple Cracking Sequence and Saturation in Fiber Reinforced Cementitious Composites" *Journal of Concrete Research and Technology*, 9(2), 19-33.

2. Li, V. C., Wu, C., Wang, S., Ogawa, A. & Saito, T. (2002) "Interface Tailoring for Strain-Hardening PVA-ECC" *ACI Materials Journal*, 99(2), 463-472.

3. Maalej, M., Li, V.C. & Hashida, T. (1995) "Effect of Fiber Rupture on Tensile Properties of Short Fiber Composites" *ASCE Journal of Engineering Mechanics*, 121(8), 903-913.

4. Li, M. & Li, V. C. (2012) "Rheology, Fiber Dispersion, and Robust Properties of Engineered Cementitious Composites" *Materials and Structures*, 46(3), 405-20.

5. ACI Committee E-701 (2003) "Chemical Admixtures for Concrete" *ACI Education Bulletin E4-03*, Farmington Hills, MI: American Concrete Institute, pp. E4-6.

6. Li, V. C., Ranade, R. & Stults, M. D. (2010) "Development of High Strength-High Ductility Concrete: Micromechanics" *Briefing to ERDC (Sep 2010)*, slide 32.

7. Naaman, A. E. & Najm, H. (1991) "Bond-Slip Mechanisms of Steel Fibers in Concrete" *ACI Materials Journal*, 88(2), 135-145.

8. Lin, Z., Kanda, T., and Li, V. C. (1999) "On Interface Property Characterization and Performance of FRCC" *Concrete Science and Engineering*, 1, 173-184.

9. Chung, D. D. L. (2005) "Dispersion of Short Fibers in Cement" *ASCE Journal of Materials in Civil Engineering*, 17(4), 379-383.

10. Ozyurt, N., Mason, T. O. & Shah, S. P. (2007) "Correlation of fiber dispersion, rheology and mechanical performance of FRCs" *Cement and Concrete Composites*, 29(2), 70-79.

11. Yang, E.H., Sahmaran, M., Yang, Y. & Li, V. C. (2009) "Rheological Control in the Production of Engineered Cementitious Composites" *ACI Materials Journal*, 106(4), 357-366.

12. Gagne, R., Boisvert, A. & Pigeon, M. (1996) "Effects of Superplasticizer Dosage on Mechanical Properties, Permeability, and Freeze-Thaw Durability of High-Strength Concretes With and Without Silica Fume" *ACI Materials Journal*, 93(2), 111-20.

13. JSCE (2008) "Recommendations for Design and Construction of High Performance Fiber Reinforced Cement Composites with Multiple Fine Cracks." Tokyo, Japan: JSCE, pp. Testing Method 1-5.

14. ASTM (2011) "Standard Test Method for Compressive Strength of Hydraulic Cement Mortars (Using 2-in. or 50 mm Cube Specimens)" West Conshohocken, PA: ASTM.

15. Lee, B. Y., Kim, J. K., Kim, J. S. & Kim, Y. Y. (2009) "Quantitative evaluation technique of Polyvinyl Alcohol (PVA) fiber dispersion in engineered cementitious composites" *Cement and Concrete Composites*, 31(6), 408-417.

16. Ranade, R., Stults, M. D., Lee, B. Y. & Li, V. C. (2011) "Effects of Fiber Dispersion and Flaw Size Distribution on the Composite Properties of PVA-ECC" Parra-Montesinos et al. (Eds.) In *Proceedings of HPRCC-6*, 19-22 June, 2011, Ann Arbor, MI, pp. 106-113.

CHAPTER 5: COMPOSITE PROPERTIES OF HIGH STRENGTH-HIGH DUCTILITY CONCRETE

5.1 Introduction

This chapter reports the results of composite properties characterization tests conducted on High Strength-High Ductility Concrete (HSHDC) specimens under various loading conditions. While it is important to determine the composite properties of HSHDC for designing structural members using this material, the composite properties also serve as target for microstructural tailoring of the material as demonstrated in Chapter 4 which details the micromechanics-based development of HSHDC. This forms the central premise of the Integrated Structures and Materials Design (ISMD)[1] approach, where the composite properties of a material (in this case, HSHDC) serve as a crucial link between micro-scale material ingredient characteristics and structural performance. The macroscopic or composite-scale characterization experiments detailed in this chapter include direct tension, split-tension, flexure, and uniaxial compression tests, along with density and fresh properties of HSHDC and its matrix.

5.2 Experimental Investigation

5.2.1 Materials and Mix Proportions

The proportions for various constituent materials in HSHDC are the same as that used in Chapter 4 for mixture H5 in Table 4.1. These proportions are re-listed in Table 5.1 in form of weight per unit volume, along with typical particle size ranges of the constituent materials. The properties of the Spectra 1000 Polyethylene (henceforth, called PE) fiber are given in Table 5.2.

Table 5.1: Mix proportions of HSHDC

Constituent[a]	Particle size range	Mix Proportions (by weight)	Weight per unit volume	
	μm (1μm = 3.9×10^{-5} in)		(kg/m^3)	(lb/yd^3)
Cement (Class H)	5-80	1	907	1528
Silica Fume	0.1-1	0.389	353	595
Silica Flour	5-100	0.277	251	423
Silica Sand	100-600	0.700	635	1070
Tap Water	-	0.208	189	318
HRWRA	-	0.018	16	27
PE Fiber[b]	-	0.0214 (V_f = 2%)	19	33

[a] The specific brand name of each constituent is given in Table 3.1

[b] Properties of the PE fiber are given in Table 5.2

Table 5.2: Geometry and mechanical/physical properties of the PE Fiber

Diameter	Length	Volume Fraction	Nominal Strength	Young's Modulus	Elongation at break	Specific Gravity	Melting Temp.
28 μm	12.7 mm	2%	3000 MPa	100 GPa	3.1	0.97	150 °C

5.2.2 HSHDC Mixing Procedure

The steps involved in the mixing procedure of HSHDC are graphically represented along a timeline in Figure 5.1 and detailed below. The visual appearance of the mixture at all the time-points defining the start/end of various steps in Figure 5.1 is documented in Figure 5.2.

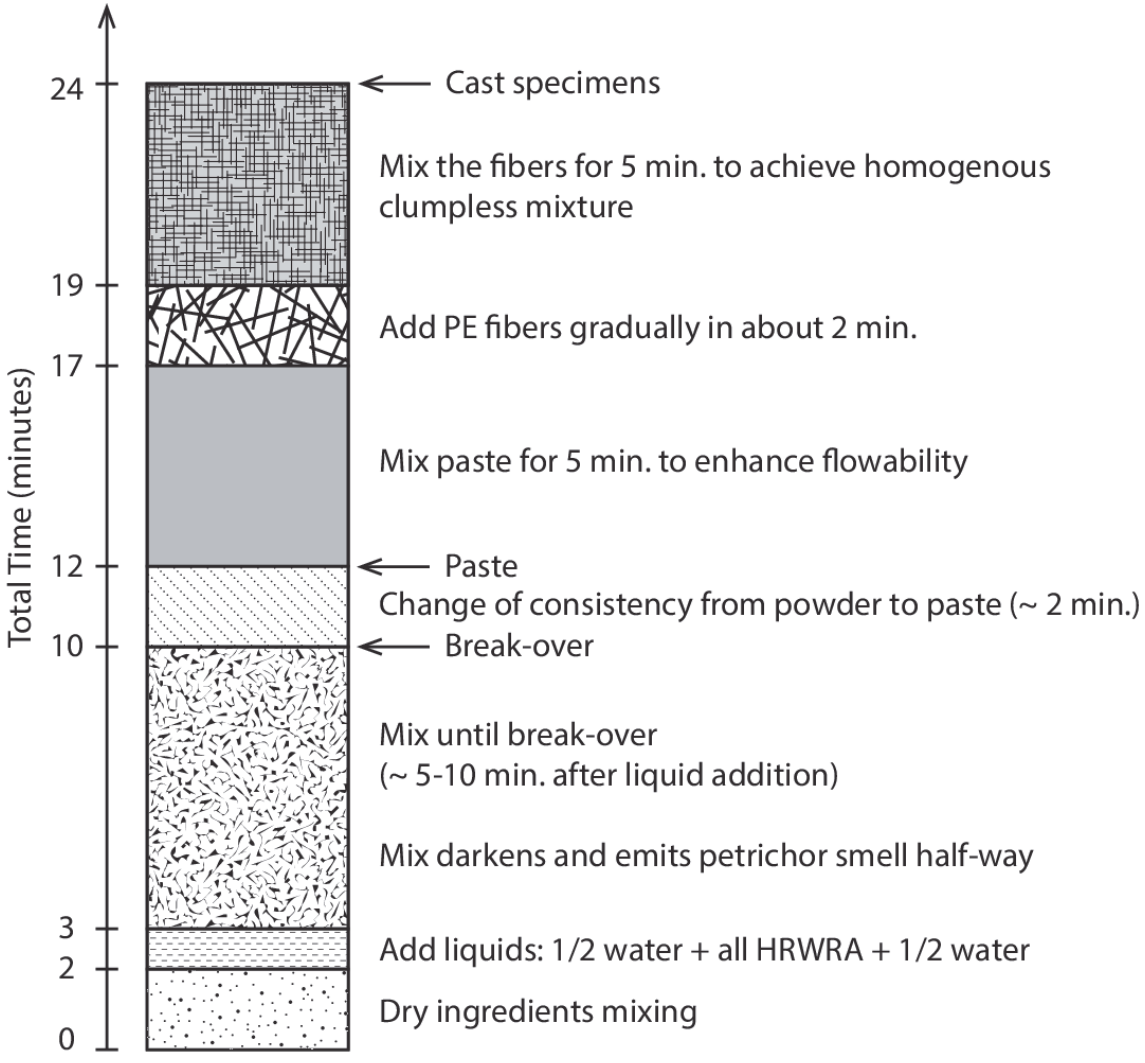

Figure 5.1: HSHDC Mixing Procedure

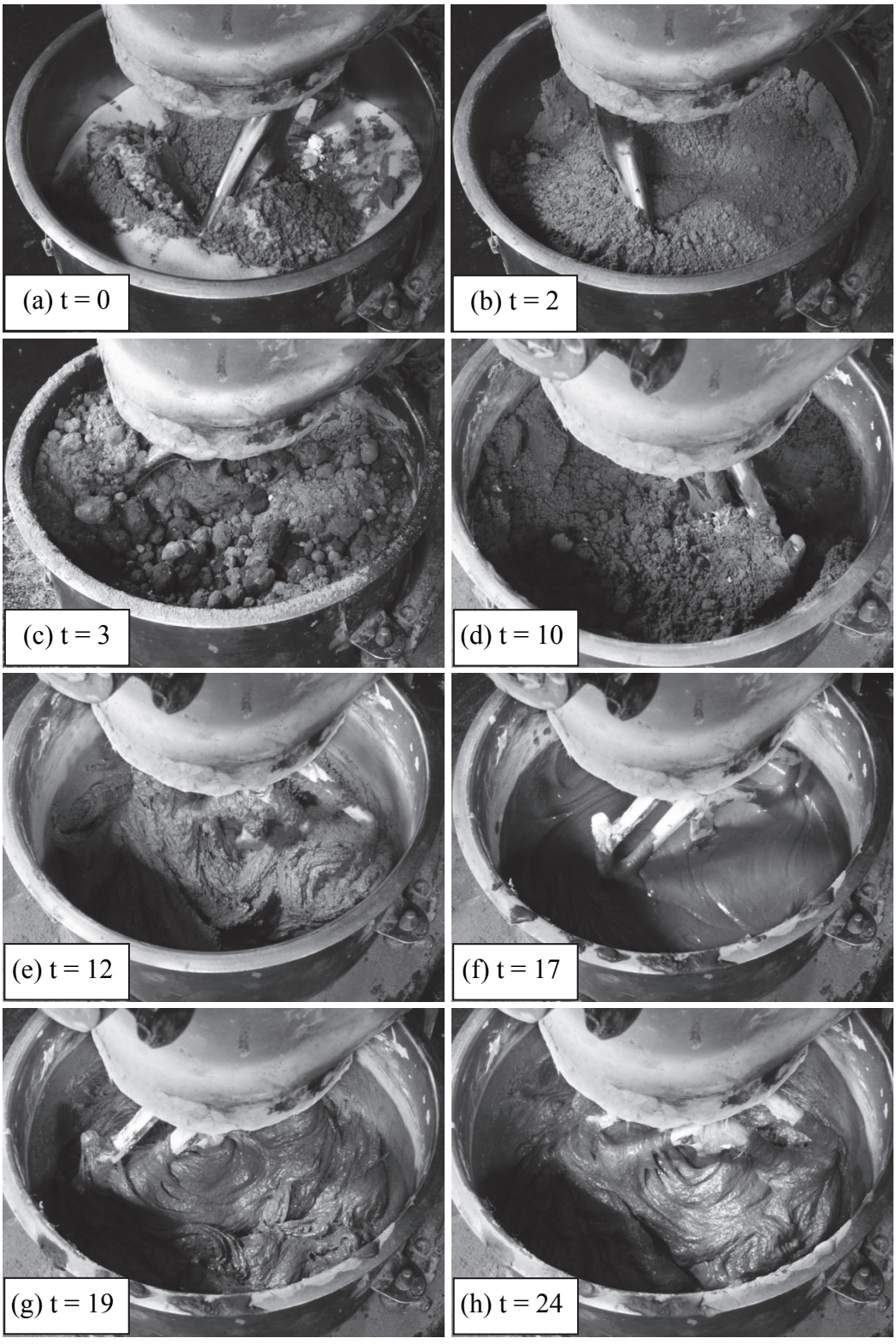

Figure 5.2: Various stages of HSHDC mixing
(Total time, t, is in minutes and the mixer shown is Hobart 5 qt. countertop mixer)

The steps for preparing the HSHDC mixture from raw material ingredients to moldable plastic state are given below. While the order of the steps is the same for all mix volumes and mixer types, the duration of each step may not be optimal in all cases. This timeline is appropriate for countertop and floor mixers (such as Hobart 5 qt. and 30 qt. mixers); although the durations of steps may still vary depending on the room environment (temperature and humidity), type and age of HRWRA, and quality of silica fume. The mixing speed should be preferably maintained at the slowest rate throughout the mixing procedure, unless explicitly stated otherwise.

1. All the dry matrix ingredients of HSHDC (silica fume, silica flour, cement, and sand) are added in the mixing bowl in the order of particle fineness with the smallest particle ingredient (silica fume) at the bottom of the bowl. This arrangement makes the dry mixing in the next step efficient as the larger (and heavier) particles on top naturally tend to sink towards the bottom.

2. Mixing of dry ingredients ensues for about 2 minutes. During this step, it may be required to cover the top of the mixing bowl to prevent silica fume from being airborne. This also limits the maximum batch size in a bowl of given volume as discussed below.

3. The liquids are added gradually over a minute duration in the order of ½ water, all HRWRA, and rest water. Some material may spew out during this step and, therefore, top-cover is recommended to be maintained in this step.

4. With all matrix ingredients in place, the mixing is continued for about 5-10 minutes until a stage called "break-over" is achieved. Due to extremely low w/c ratio, the mix looks dry (even with all liquids added) and has a powdery texture with almost no cohesion at the start of this step (Figure 5.2c). As the dry ingredients (particularly cement) are wetted by the water and HRWRA in about 3-5 minutes, the color of the mix darkens and a petrichor smell is emitted with a whisking sound. After about 5-10 minutes of mixing, the mixture becomes more cohesive and, as a result, starts to "break-over" (hence the name of the stage) and small chunks start to build. The mixture looks wet at this time and is about to transform into a plastic paste consistency (Figure 5.2d). An average duration of 7 minutes after liquid addition (10 minutes total) is assumed in the construction of timeline in Figure 5.1.

   The time to break-over after liquid addition serves as an indirect way to assess the mix viscosity. If the break-over happens less than 5 minutes after liquid addition (8 minutes total), the viscosity of the mix may be too low and HRWRA content should be reduced to correct this. On the other hand, if it takes longer than 10 minutes after liquid addition (13 minutes total) to achieve the break-over stage, the viscosity of the mix may be too high and HRWRA content should be increased to achieve break-over in the desired time interval of 5-10 minutes. The importance of matrix viscosity for the dispersion of fibers and consistent composite properties is well documented in Li et al.[2]

5. After break-over, the mix transforms to a stage called "3-parts" within 30-40 seconds, where the mixture, in addition to internal cohesion, starts to adhere to the bowl walls (reaching up to the brim of the bowl) and splits into roughly three equal parts. In another 30-40 seconds, the

3-parts collapse and combine at the bottom of the bowl. Finally, in about 2 minutes after break-over, the mix attains a paste-like consistency with good cohesion and small amount of paste begins to re-stick to the walls at this time (Figure 5.2e).

6. The paste mixing is continued for another 5 minutes at the slowest paddle speed to make its consistency more flowable and less viscous. This step duration can be reduced to 3 minutes by using the next higher mixing speed, which should be reduced back to the slowest speed before fiber addition in the next step. During this step, it is recommended to stop the mixing after about 2 minutes to clean any dry material sticking to the walls and, more importantly, the bottom of the bowl where the paddle does not reach. This can done by hand or using a small trowel. The dry material must not be removed from the paste which may otherwise change the mix composition. It can be simply mixed with paste by allowing additional mixing time of about 2 minutes. Figure 5.2f shows the paste consistency at the end of this step.

7. After about 17 minutes of total mixing time, the PE fibers are gradually added to the paste in steps. Addition of large chunks of PE fibers must be avoided and sufficient time should be given to the paste to disperse the added fibers. It normally takes about 2 minutes to add all the fibers. The motor of the mixer must be constantly checked to prevent overheating. If overheating occurs (or the mixing paddle stops), small amount of HRWRA (about 5% of total dosage) should be quickly introduced in the paste to reduce its viscosity. The visual appearance of the mixture just after the addition of all fibers is shown in Figure 5.2g.

8. The mixing process is continued for another 5 minutes to distribute the fibers homogenously in the matrix. The mixing is stopped at this point (Figure 5.2h) and the mix is tested for fiber clumps by hand. If there are negligible clumps and the mix feels homogenous, it can be cast into specimen molds at this time. This concludes the HSHDC mixing procedure.

Determination of the appropriate batch volume for a given mixing bowl: It is recommended to have the batch volume of HSHDC between 15-35% of the bowl volume (for countertop and floor mixers such as Hobart 5 qt. and 30 qt. mixers). The batch volume refers to the volume of the mixture at the end of the above mixing procedure, and is determined by the total volume of the specimens to be cast. The lower limit of 15% is based on the fact that a batch volume less than 15% of the bowl volume will not have sufficient volume to be mixed efficiently by the mixing paddle due to its geometry which provides maximum shear near the center of the bowl and tapers towards the bottom. The upper limit of 35% is dictated by the fact that the HSHDC matrix ingredients are about 2.5 times more voluminous in the dry unmixed state than the wet mixed state, which fills the bowl to about 90% of its height. As a result, a batch volume higher than 35% of the bowl volume will spill a lot of material out of the bowl during the dry mixing process, which must be avoided. In addition, larger batch volumes will make it more difficult for the mixer motor to function properly during fiber addition. Thus, the limits to the batch volume are mainly determined by the paddle and bowl geometries at the lower end and the total volume of the bowl relative to the volume of dry unmixed ingredients and the capacity of the mixer motor at the upper end.

5.2.3 Specimens

Uniaxial Tension and Compression Specimens: Eight dogbone-shaped specimens (Figure 3.1) were used in this study to measure the complete stress-strain behavior of HSHDC under direct uniaxial tension. The dogbone geometry forces most of the cracks to occur in the gauge region due to its smaller cross-sectional area thus allowing more reliable measurements of the tensile strains. In addition to the dogbone specimens for tensile tests, eight cubes of length 2″ and six cubes of length 3″ were cast to experimentally determine the uniaxial compression behavior of HSHDC.

Indirect Tension and Flexure Specimens: Three cylinders (henceforth called split-cylinders) with diameter of 4″ and length of 8″ were cast for split-tension (indirect tension) tests. Three beams with length of 14″ (span lengths of 12″), width of 4″, and depth of 4″ were cast for third-point flexure tests.

5.2.4 HSHDC Curing Procedure

Elevated temperature curing similar to COR-TUF (Section 3.3.2), but with slightly longer duration, was used for all HSHDC specimens. After casting the fresh HSHDC mix into specimen molds, they were sealed with plastic sheets and cured for two days at room temperature (23±3°C). Due to high dosage of HRWRA and the use of Class H cement that is slow setting, the specimens require more than 24 hours for attaining the stiffness necessary for demolding. Subsequently, the hardened specimens were removed from the molds and kept in a water tank for curing at room temperature for 7 days. This was followed by elevated temperature curing for 5

days in water at 90°C (instead of 4 days used for COR-TUF) and for 3 days in air at 90°C (instead of 2 days used for COR-TUF). The additional days of curing at elevated temperature under water and in air were found to be helpful in slightly improving the properties and reducing variability of performance from one batch to the other. Further increasing the curing time did not show any significant change in the mechanical properties. The HSHDC specimens were further kept in air at room temperature until 28 days after casting, at which time they were tested.

5.2.5 Experimental Setup

Fresh Properties Tests: Before curing HSHDC specimens, the fresh properties of matrix rheology (viscosity and yield stress) and composite flowability (slump) were measured, which are vital for quality material processing and field placement, respectively. The slump of HSHDC composite (with fibers) was measured according to the specifications of ASTM C143.[3] The viscosity of the HSHDC matrix (without fibers) was measured using a rotational rheometer (Bohlin CVO 100) with a cylindrical cup (C25) and vane arrangement.[4,5] A triangular shear rate-time protocol was used in which the shear rate was increased from 0 to 150 s^{-1} linearly with time in 80 seconds and then decreased linearly back to 0 in another 80 seconds. Two consecutive cycles (0-150-0-150-0 s^{-1}) were used for a sample and three such samples were used for the HSHDC matrix.

Density: The densities of cured HSHDC specimens were computed by dividing the observed weight of specimens in air (at room temperature and humidity) by the volume of water displaced, which is determined using a modified pycnometer.

Direct Tension Tests: The dogbone specimens were tested under quasi-static uniaxial tension loading using the procedure described in Section 4.4 (Figure 4.1) with the addition of strain gauges for accurate modulus measurements prior to first crack. In four out of the eight dogbone specimens prepared for the direct tension characterization of HSHDC, two strain gauges with gauge lengths of 20 mm were bonded to either side of the dogbone specimens parallel to the longitudinal loading direction as shown in Figure 5.3.

Uniaxial Compression Tests: The test setup used in this study for cube compression tests is shown in Figure 5.3. A closed loop displacement controlled compression testing machine with maximum load capacity of 2200 kN was used to load the cubes. The compressive displacement rate applied on the cubes was 30 μm/min, which translates into 1300 N/s for 2″ cubes assuming an elastic modulus of 51.2 GPa for HSHDC. This loading rates fall within the recommended range of 900-1800 N/s in ASTM C109.[6] A faster displacement rate of 45 μm/min was used for 3″ cubes to maintain the stress rate of about 0.5 MPa/s, same as that used for 2″ cubes. The compressive displacement in all the compression tests was measured using two high precision potentiometers with displacement range of ±5 mm placed parallel to two opposite faces of the cubes (Figure 5.3). In addition, for accurate elastic modulus measurement, the elastic compressive strain in four out of eight 2″ cubes was measured using two strain gauges (gauge length of 20 mm) bonded to two opposite faces of the cubes parallel to the loading axis. Thus, all compression tests were performed under quasi-static loading with appropriate sensors to accurately record load and displacement during the tests.

Indirect Tension Tests: For the split-tension (indirect tension) tests, a setup similar to that given in ASTM C496[7] was adopted. The compressive displacement rate applied on the split-cylinders was 100 μm/min. This displacement rate translates into split-tension stress increase rate of 1.2 MPa/min for HSHDC, which falls within the loading rate of 0.7-1.4 MPa/min recommended in ASTM C496.

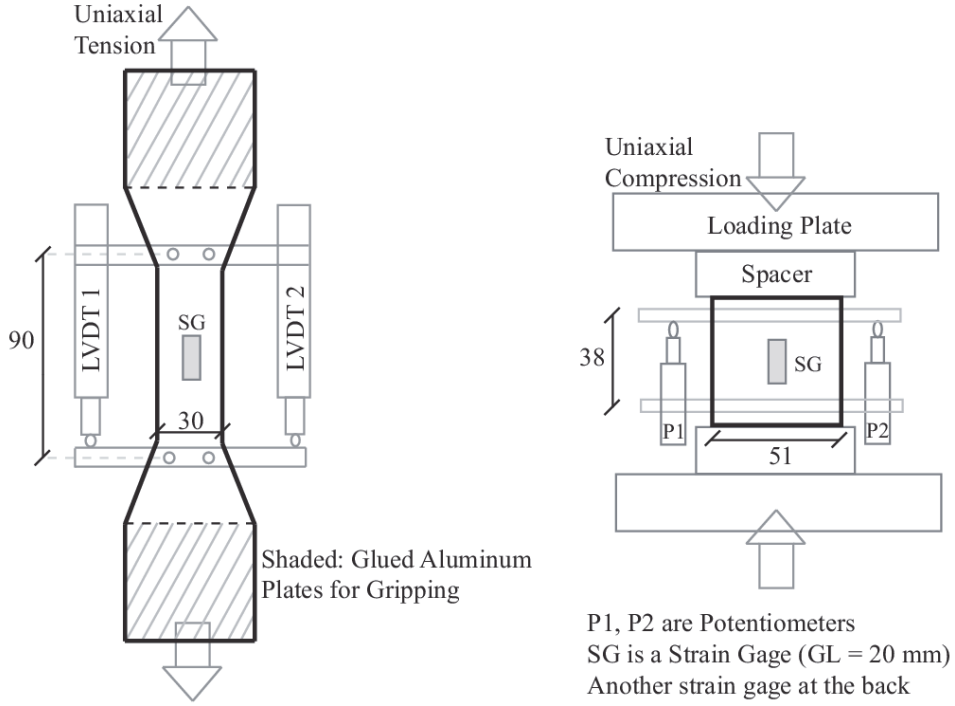

Figure 5.3: Uniaxial tension and compression test setups
All dimensions in mm

Flexure Tests: The third-point flexure tests on HSHDC beams were performed using the setup shown in Figure 5.4, which follows the ASTM C1609[8] standard test procedure. A constant mid-point net deflection rate of 50 μm/min was used in these flexure tests, as recommended in ASTM C1609. The mid-point net deflection was computed using two potentiometers mounted

on two sides of the beam (one of the two potentiometers is visible in Figure 5.4 – the other is on the back side).

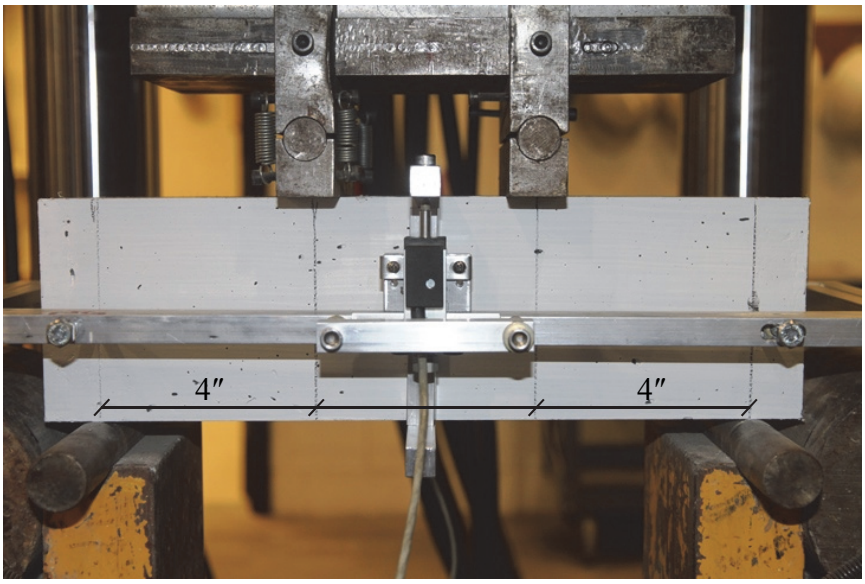

Figure 5.4: Flexure test setup for 4″x4″x14″ beams

5.3 Results and Discussion

5.3.1 Fresh Properties and Density

Flowability: HSHDC composite is moderately flowable with a slump of about 7.5″, measured using ASTM C143[3]. Moderate vibration is needed to place it properly in the molds or formwork. The slump of HSHDC can be increased by 1″ by increasing the HRWRA dosage by about 7%, without adversely affecting the fiber dispersion.

Matrix Rheology: The flow curves (shear stress versus shear strain rate) for three matrix samples (without fibers) of HSHDC were measured with a rotational rheometer. The flow curve of one out of three samples is shown in Figure 5.5. The flow curve of ECC matrix (mix proportions same as Mixture 5 in Yang et al[9]), that is self-consolidating, is also shown for comparison. The first cycle of the rheometry protocol can be relatively unstable and is typically not used in calculations. A straight line best-fitting the ascending branch of the flow curve during the second cycle (Figure 5.5) of rheometry protocol was used to compute the plastic viscosity and yield stress in accordance with the Bingham plastic fluid model.[10] The slope of the best-fit line is the plastic viscosity and the y-intercept of this line is the shear yield stress.

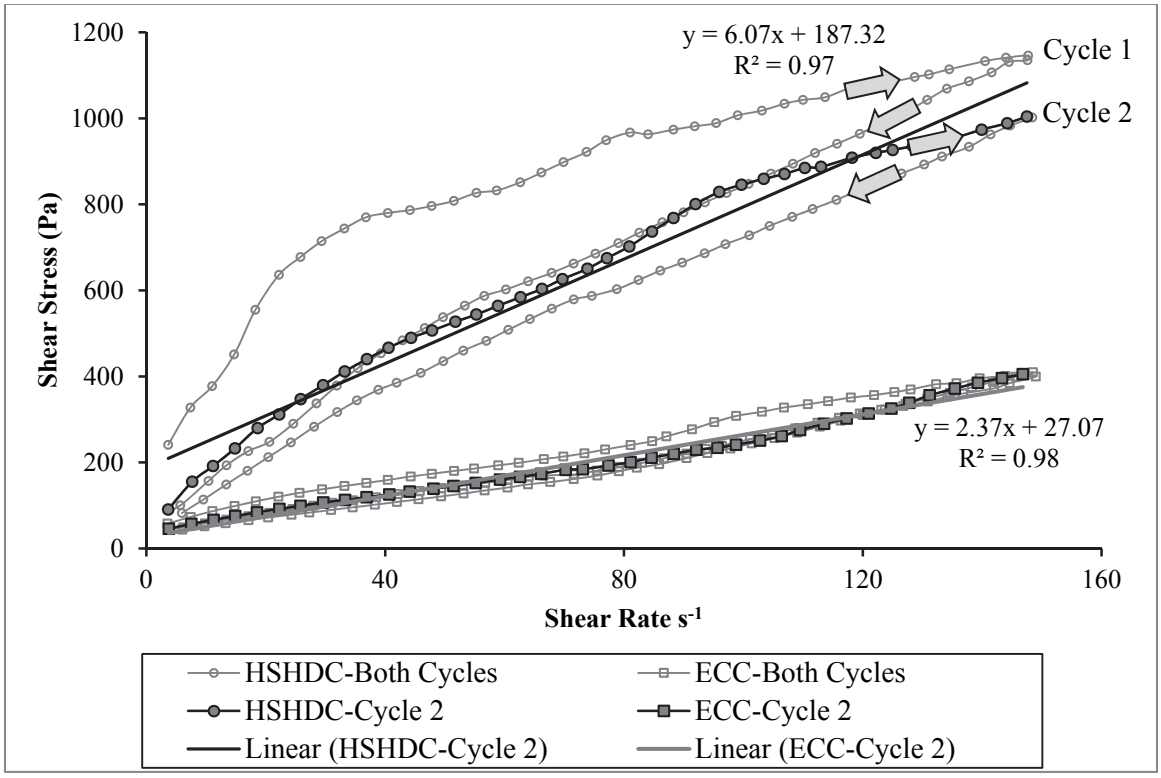

Figure 5.5: Flow curves of HSHDC and ECC matrixes

The average plastic viscosity of three matrix samples of HSHDC is equal to 6.0 Pa-s with COV of 5.1%, which is about 2.7 times the average plastic viscosity of ECC matrix (2.2 Pa-s) measured by the same method. The average shear yield stress of HSHDC matrix is equal to 186.2 Pa with COV of 7.3%, which is about 7 times the yield stress of ECC matrix (26.6 Pa). Thus, both the plastic viscosity and yield stress of HSHDC matrix are higher than that of ECC matrix, which is expected due to extremely low w/cm ratio of 0.15 in HSHDC compared to 0.26 in ECC.

Density: The bulk densities of all cured HSHDC specimens before mechanical testing were determined. The average densities of HSHDC dogbone specimens, split-cylinders, beams, 2″ cubes, and 3″ cubes were 2.34 g/cm^3, 2.31 g/cm^3, 2.32 g/cm^3, 2.32 g/cm^3, and 2.33 g/cm^3, respectively. The COV was less than 1.5% in all specimen types. In spite of the absence of coarse aggregates, the bulk density of HSHDC is similar to that of normal concrete (2.3-2.4 g/cm^3), which is attributable to the dense particle packing within the HSHDC matrix. Thus, the bulk density of HSHDC is uniform across various specimen types and is unaffected by the size and geometry of different specimen molds.

5.3.2 Direct Tension Behavior

The direct tension test results of all the eight dogbone specimens prepared for this study are shown in Figure 5.6. The x-axis in these figures shows the average tensile strain computed from the extensions of two LVDTs, and the y-axis represents the stress computed from the tensile load divided by the cross-sectional area of the dogbone specimens.

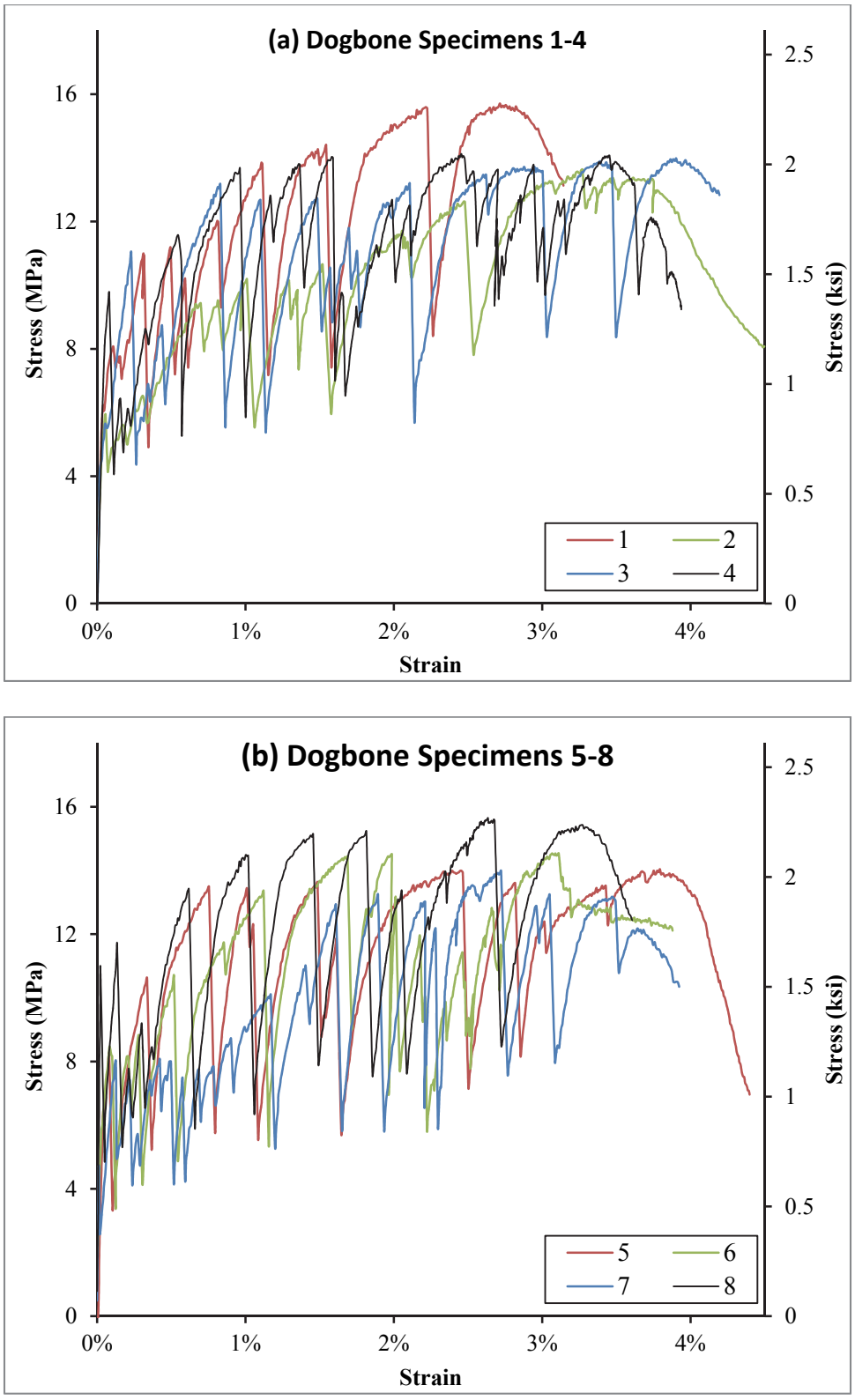

Figure 5.6: Direct tension behavior of HSHDC dogbone specimens

The tensile behavior of HSHDC dogbone specimens with multiple cracking is similar to that observed in ECC. As the load increases from zero, the tensile stress inside the composite increases linear-elastically. The matrix cracks for the first time when the stress intensity factor exceeds the fracture toughness of the matrix, typically at the largest internal flaw.[11] The crack propagates almost instantaneously throughout the section under steady-state (a direct result of satisfying the energy criterion for multiple cracking – Section 2.5) causing sudden drop in tensile stress as the load transfer capacity of the matrix at the section is lost. However, the fiber bridging capacity is not exceeded at the matrix cracking stress (due to satisfaction of the strength criterion – Section 2.5), and the tensile stress is gradually regained exceeding the first crack stress. The tensile stress increases until another crack is triggered at the next largest flaw and the process repeats until the fiber bridging capacity is exceeded by the applied tensile stress at one of these cracked sections. After this point, the tensile stress reduces monotonically following the bridging stress-crack opening (σ-δ) relation. Thus, the micromechanics-based design of HSHDC facilitates multiple micro-cracking of the matrix under tension which is the fundamental reason behind the extraordinary tensile ductility of the composite.

From Figure 5.6, the average of the ultimate (maximum) tensile strength of the dogbone specimens is 14.5 MPa with coefficient of variation (COV) of 6.2%. As mentioned above, the ultimate tensile strength is governed by the minimum of the bridging capacities at various cracks, which is further dependent on the interfacial bond, fiber volume, and fiber dispersion. The average of the corresponding tensile strain capacities is 3.4% with a COV of 11%. The average of the first crack strengths of these eight dogbone specimens is 8.3 MPa with COV of 12%. Due to such unique combination of strength and ductility in tension, the specific energy of HSHDC

under direct tension is greater than 300 kJ/m^3, which is almost twice that of ECC and an order of magnitude higher than Cor-tuf.[12]

The elastic modulus of HSHDC in tension was computed from the slope of best-fit straight line through the observed stress-strain data points (Figure 5.7) of four dogbone specimens, with strain computed using two strain gages. The average tensile elastic modulus of HSHDC thus computed is 48.4 GPa (7018 ksi) with COV of 1.1%.

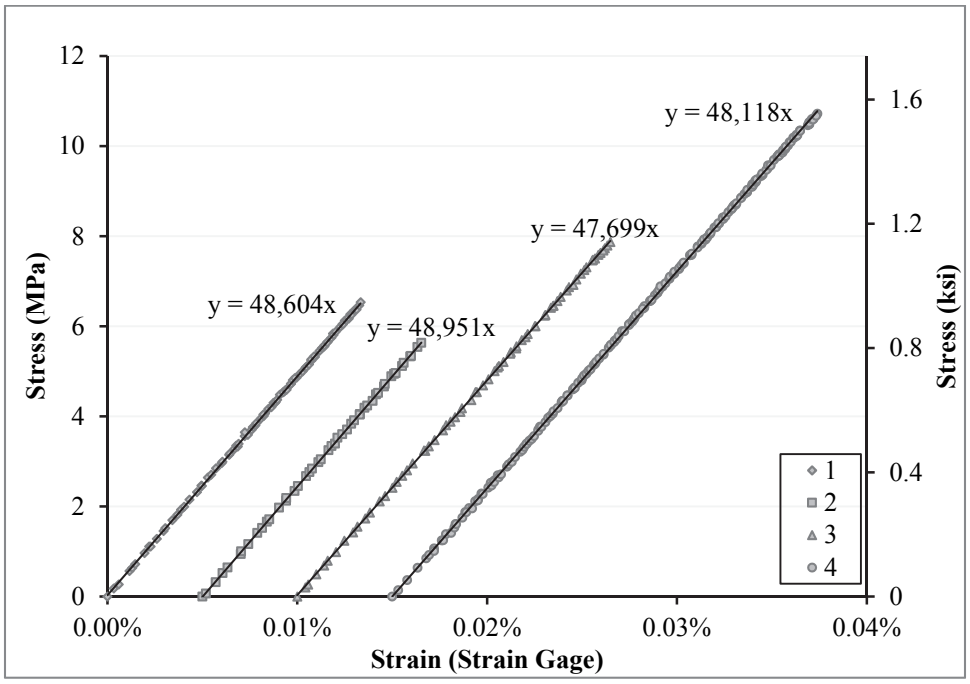

Figure 5.7: Pre-first crack direct tension test results of four dogbones (#1-4)
(Data points of different specimens are intentionally staggered by 0.005% strain along the x-axis for clarity)

5.3.3 Uniaxial Compression Behavior

Full compression test curves of all 2″ cubes tested in this study are presented in Figure 5.8. The pre-peak branch of these curves is extremely linear and elastic, which is typical of concretes with similar compressive strengths. Near the peak (within about 20% of the peak load), the stress-strain curve becomes non-linear and inelastic due to the nucleation of microcracks at grain boundaries, micro-defects, and other micro-scale heterogeneities. These cracks are stabilized through fiber-bridging in HSHDC resulting in a more ductile response and a flattened peak (in HSHDC) instead of a sharp peak typically observed in VHSC/UHPCs.[13,14,16] Furthermore, it can be seen in Figure 5.8 that the post-peak stress after the axial splitting[15] of an HSHDC cube does not suddenly drop to near zero but to a residual stress value of 60-80 MPa. Unlike VHSC/UHPCs that split into two parts in the post-peak stage, multiple vertical microcracks (parallel to the applied compression) appear on the faces of HSHDC cubes. Thereafter, the stress gradually decreases with increasing compressive displacement as the vertical microcracks open against the fiber-bridging, thus absorbing additional energy. Overall, HSHDC shows linear elastic behavior under uniaxial compression until 80% of its peak strength, followed by a relatively ductile near-peak and post-peak response.

The uniaxial compression strength results of all the cubes are summarized in Table 5.3. The average compressive strength of the 2″ cubes (166 MPa) is about 5% higher than that of the 3″ cubes (159 MPa). However, the strength variability (COV) of 3″ cubes (4.4%) is slightly lower than that of 2″ cubes (6.1%). This is expected as the local effect of a flaw or a weakness becomes less dominant as the specimen size increases.[16] Average elastic modulus of HSHDC

under uniaxial compression as measured for four 2″ cubes (#1-4) using strain gages is 51.2 GPa with COV of 1%. The compressive elastic modulus of HSHDC is approximately equal to that of Cor-tuf (51 GPa) as reported by O'Neil.[17] Thus, in addition to very high tensile ductility, HSHDC exhibits very high compressive strength with a slightly (5%) higher elastic modulus in compression than in tension.

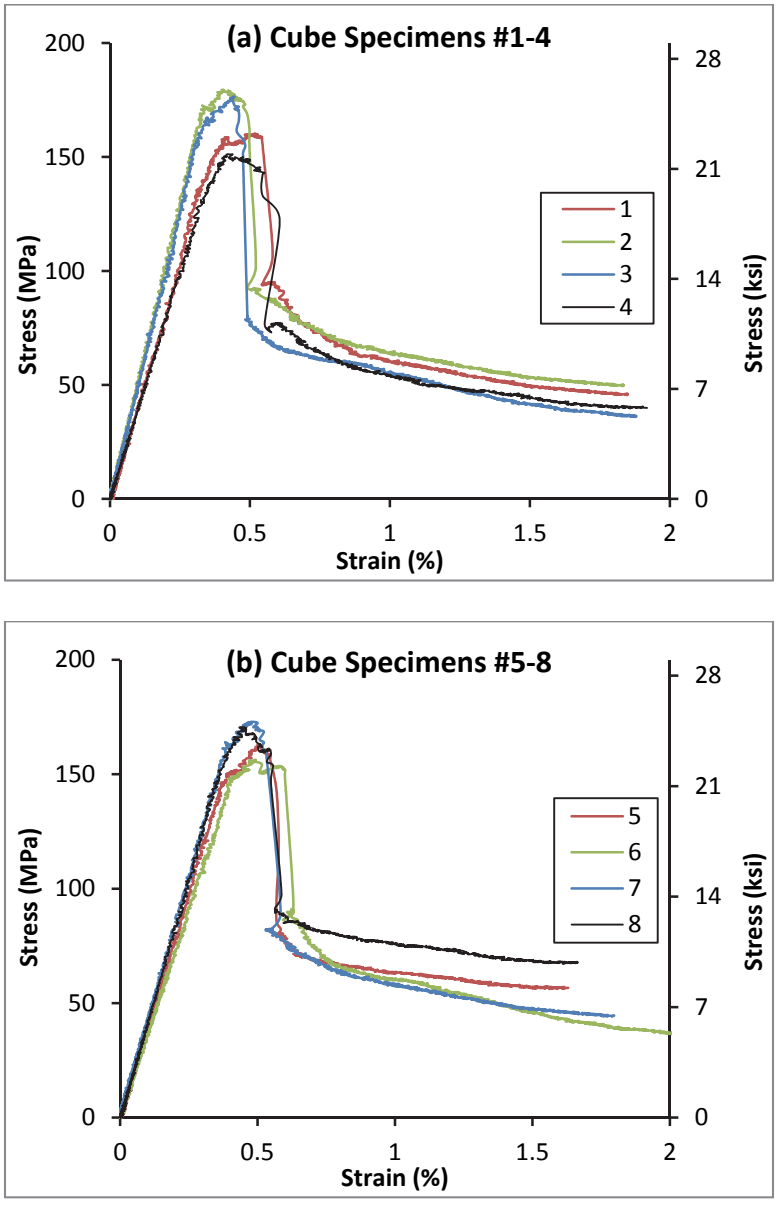

Figure 5.8: Uniaxial compression behavior of HSHDC 2″ cube specimens

Table 5.3: Uniaxial compressive strengths of HSHDC cubes

Specimen Number	**Uniaxial Compressive Strength** MPa (ksi)	
	2″ cubes	**3″ cubes**
1	160 (23.2)	168 (24.4)
2	179 (26.0)	153 (22.2)
3	176 (25.6)	160 (23.2)
4	151 (21.9)	157 (22.8)
5	163 (23.6)	167 (24.2)
6	156 (22.7)	151 (21.9)
7	173 (25.1)	-
8	171 (24.7)	-
Average	166 (24.1)	159 (23.1)
Standard Deviation	10 (1.5)	7 (1.0)
Coefficient of Variation (COV)	6.1%	4.4%

From the above results of tensile and compressive strengths of HSHDC, it can be observed that the tensile-to-compressive strength ratio of HSHDC (and other fiber-reinforced concretes such as ECC and COR-TUF) is larger than that of normal concrete. The ACI 318 building code[18] assumes the splitting tensile strength of concrete (which is almost equal to its uniaxial tensile strength due to the brittleness of concrete) to be $6.7\sqrt{f_c'}$ (psi), which makes the tensile-to-compressive strength ratio equal to $6.7/\sqrt{f_c'}$ (psi). This ratio is approximately equal to 1/10 for a concrete with compressive strength (f_c') of 31 MPa (4500 psi). The predicted tensile-to-compressive strength ratio decreases for higher strength concretes and evaluates to 1/23 for HSHDC with f_c' of 166 MPa (tensile strength of 7.2 MPa). Although this predicted tensile strength is close to the observed first crack strength of the HSHDC matrix (8.3 MPa), the tensile strength of the composite (14.5 MPa) is significantly greater than the predicted value. The observed and predicted tensile-to-compressive strength ratio of HSHDC, along with that of 4500 psi concrete, ECC, and COR-TUF, is plotted in Figure 5.9. The *suppression* of brittle fracture

failure mode in HSHDC and ECC and the *delay* of such failure mode in COR-TUF cause the tensile-to-compressive ratios of these concretes to be larger than normal concrete.

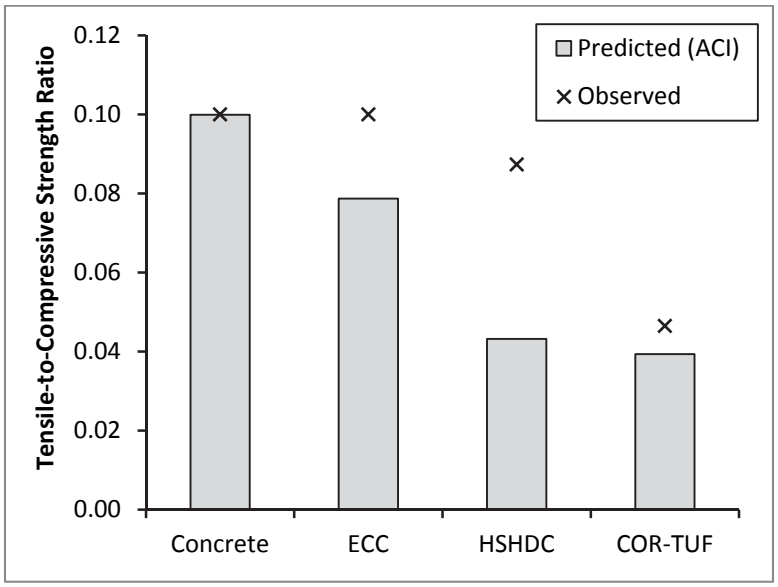

Figure 5.9: Comparison of tensile-to-compressive strength ratios of various concretes

5.3.4 Indirect Tension Behavior

The split-tension (indirect tension) test results of three HSHDC cylinders (Ø4″ x 8″) are shown in Figure 5.10. In this figure, the y-axis represents the split-tension stress computed from the applied compressive load and the dimensions of the cylinder using Equation 1 of ASTM C496.[7] The x-axis in Figure 5.10 represents the compressive displacement measured by the machine stroke. The average split-tension strength of HSHDC thus measured is 17.0 MPa with COV of 8.5%.

The results presented above show that the tensile strength of HSHDC is overestimated by the split-tension tests (17.0 MPa) as compared to the direct uniaxial tension tests (14.5 MPa). Split-tension tests[7] were originally designed to determine the tensile strength of normal concrete, which is a brittle material. However, unlike normal concrete, HSHDC shows an extremely ductile behavior which causes a change in the failure mode of the split-cylinders from almost pure tensile cracking to a combination of multiple tensile cracking and compressive crushing. This change in the failure mode of the split-cylinders causes a non-conservative estimation of the tensile strength of HSHDC and similar strain hardening materials.

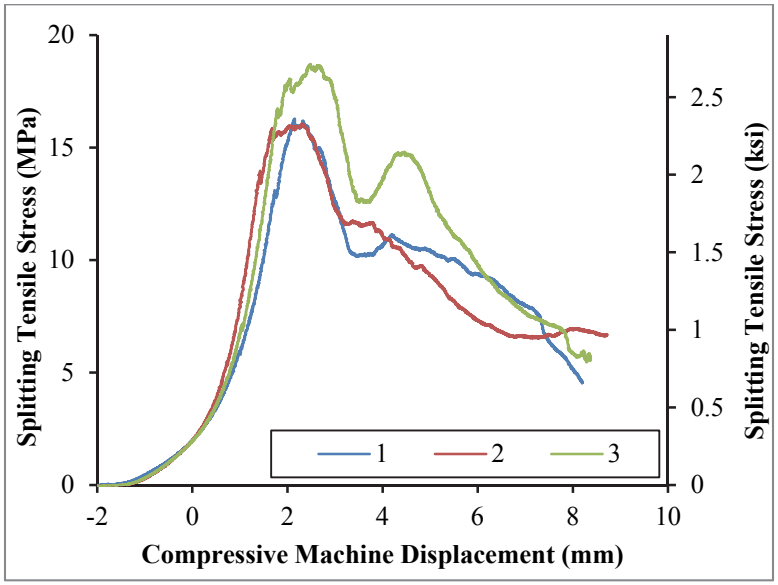

Figure 5.10: Indirect tension behavior of HSHDC (Ø4″ x 8″) split-cylinders

5.3.5 Flexural Behavior

The third-point flexure test results of three HSHDC beams (4″ x 4″ x 14″) are shown in Figure 5.11. In this figure, the flexural stress is plotted against the mid-point net deflection of the

beam. The flexural stress was computed from the applied compressive load and the dimensions of the beam using Equation 1 of ASTM C1609.[8] The mid-point net deflection was computed as an average of extensions of two potentiometers mounted at the longitudinal centerline of the beam. The average modulus of rupture (MOR) of the three beams thus computed is 31.8 MPa with COV of 14%. Along with such a high MOR, HSHDC beams exhibit extremely high ductility as the average of the mid-point net deflection at MOR is 7.7 mm (COV of 10%) which is 2.5% of the span length.

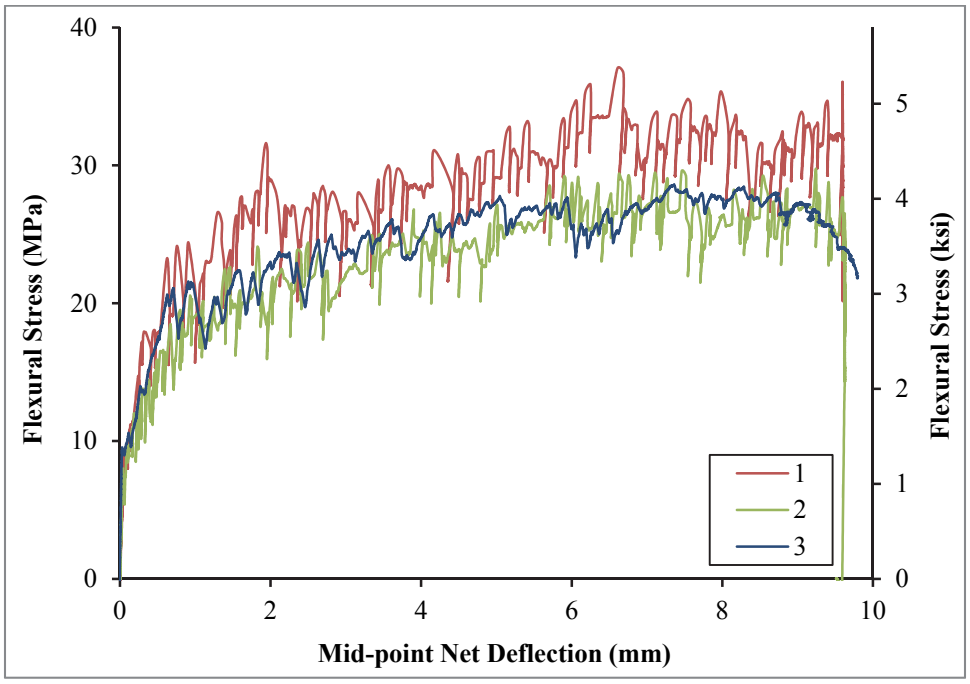

Figure 5.11: Flexural behavior of HSHDC 4″ x 4″ x 14″ beams

The high structural strength and ductility exhibited by the HSHDC beams are direct results of its high material strength and ductility. For instance, the MOR of HSHDC beams can be predicted from its properties under uniaxial tension and compression (detailed below) using the analytical model developed by Maalej and Li.[19] This analytical model was originally used to

predict the MOR of ECC beams based on the composite properties of ECC, but it can be applied, without loss of generality, to any strain hardening material. As reported above, the average tensile strain capacity (ε_{tu}) of HSHDC is 3.4%, its average first crack strength (σ_{tc}) is 8.3 MPa, and its ultimate tensile strength (σ_{tu}) is 14.5 MPa. According to Figures 12 and 13 in Maalej and Li,[19] the predicted MOR/σ_{tc} ratio is about 4 for a tensile strain capacity (ε_{tu}) of 3.4% and σ_{tu}/σ_{tc} ratio of 1.7 (14.5/8.3). In this study, the MOR/σ_{tc} ratio was found to be 3.8, which agrees well with the analytical prediction. This agreement demonstrates the plausibility of using third-point flexure test, which is easier to perform in the field than the direct tension test, as an alternative method for validating the performance of HSHDC, similar to the method for SHCC[20]; however, more exhaustive testing is required to quantify the reliability of such tests.

5.3.6 Multiple Cracking

Robust multiple micro-cracking is a distinct feature in all of the tension and compression specimens tested in this study. From the variety of specimens tested under different loading conditions, one representative tested specimen of each kind is shown in Figure 5.12, except the 3″ cube because its crack pattern is similar to that of the 2″ cube. Multiple cracking is clearly visible in all the tested specimens. Crack openings on the surfaces of dogbone specimens were measured using an optical microscope along the central longitudinal axis following the procedure detailed in the JSCE Report.[21] The average crack opening in HSHDC dogbone specimens is about 180 μm near the ultimate tensile stress (σ_{ult}), and the average residual crack opening (after load removal) is about 160 μm. The reduction in crack width after load removal is mainly due to the elastic recovery of the stretched PE fibers. The maximum crack width observed in HSHDC

dogbones specimens is up to 310 μm at σ_{ult}. In spite of higher fiber/matrix interfacial frictional bond in HSHDC (determined in Chapter 6) compared to ECC, the crack openings in HSHDC tensile specimens are 3-4 times larger than ECC due to absence of interfacial chemical bond and higher ultimate tensile stress. Similar to dogbones, HSHDC beams exhibit multiple flexural cracking perpendicular to the principal tensile stress field with the crack tips reaching up to about 85% of the total beam depth in the constant moment region of the beam. The HSHDC cubes remain intact with multiple vertical cracks and negligible spalling after sustaining the maximum compressive load. This controlled micro-cracking of micromechanically-tailored HSHDC results in an extremely ductile mechanical performance under tension, flexure, and compression loads.

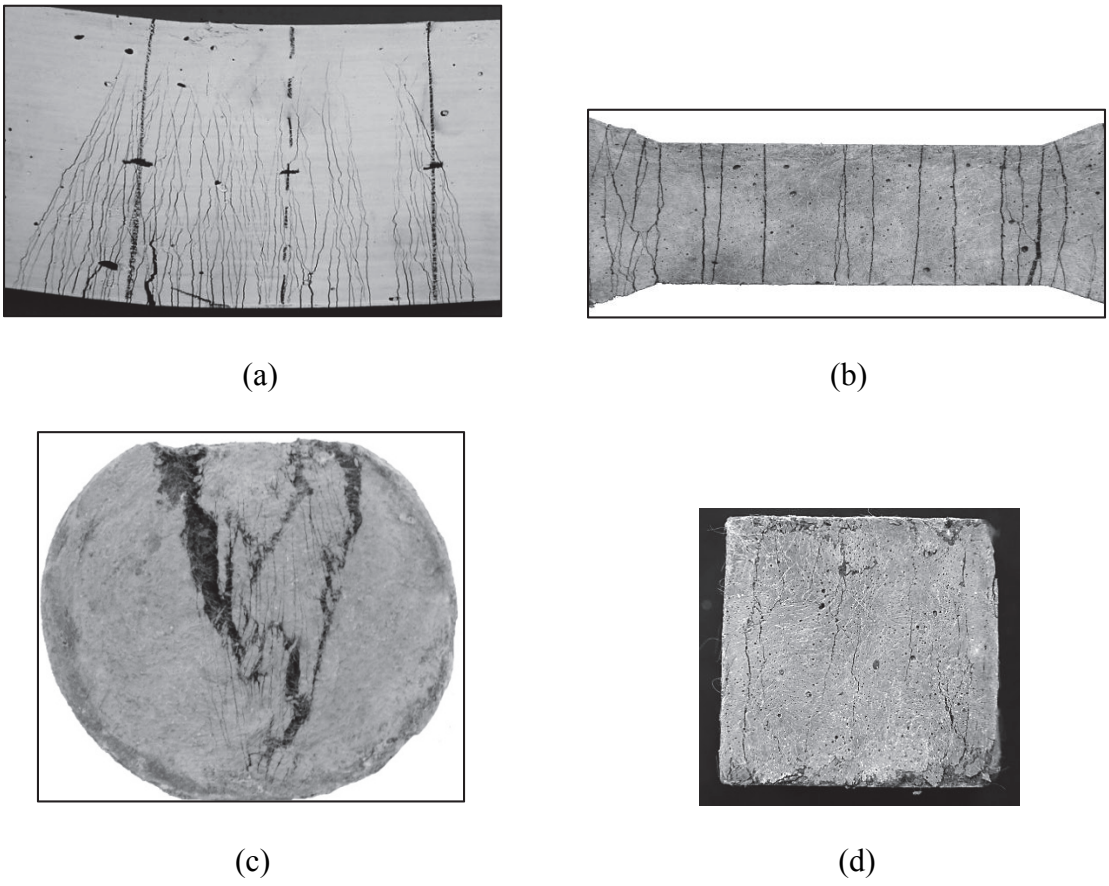

Figure 5.12: Crack patterns at failure in HSHDC specimens
(a) Beam (4 in x 4 in x 14 in) (b) Dogbone (c) Split-cylinder (Ø4″ x 8″) (d) 2″ cube

5.4 Summary and Conclusions

The properties of HSHDC determined in this chapter are summarized in Table 5.4. The following conclusions can be drawn from this experimental investigation.

- HSHDC exhibits a unique combination of compressive strength greater than 150 MPa and tensile ductility greater than 3% (with low COV), and therefore, meets the design objectives stated in Section 4.2. The specific energy of HSHDC under direct tension is greater than 300 kJ/m^3, which is almost twice that of ECC and an order of magnitude higher than COR-TUF.

- The observed ratio of flexural MOR to first crack strength of HSHDC matches the predictions of the analytical model developed for ECC, which points towards the similarity of multiple cracking behaviors of both materials. The inverse method developed for ECC can also be applied to HSHDC for quality control.

- Robust multiple micro-cracking is observed in all specimens tested in this study. However, the crack widths in HSHDC tensile specimens are 3-4 times larger than ECC due to absence of interfacial chemical bond and higher ultimate tensile stress. Reducing the crack opening under 100 μm is one of the objectives of investigation in Section 9.3.

- HSHDC is moderately flowable with a slump of about 7.5″, compared to nearly self-consolidating flowability of ECC. Both the fresh properties – plastic viscosity and yield stress – of HSHDC matrix are many times higher than that of ECC matrix due to extremely low w/cm

ratio of 0.15 in HSHDC compared to 0.26 in ECC. Due to tight particle packing, the bulk density of cured HSHDC is about the same as normal concrete with coarse aggregates and is 20% higher than that of typical (M45) ECC.

Table 5.4: Summary of properties of HSHDC

Property	**Specimens**	**Average Value**	**COV**
Slump	-	7.5″	-
Matrix plastic viscosity	-	6.0 Pa-s	5.1%
Matrix yield stress	-	186.2 Pa	7.3%
Density	All specimens	2.32 g/cm^3	1.5%
Compressive strength	2″ cubes	166 MPa	6.1%
Compressive strength	3″ cubes	159 MPa	4.4%
Compressive elastic modulus	2″ cubes	51.2 GPa	1.0%
Tensile ductility	JSCE dogbones	3.4%	11%
First crack strength	JSCE dogbones	8.3 MPa	12%
Direct tensile strength	JSCE dogbones	14.5 MPa	6.2%
Tensile elastic modulus	JSCE dogbones	48.4 GPa	1.1%
Average crack width (at tensile strength and residual)	JSCE dogbones	180 μm & 160 μm	-
Maximum crack width (at peak load)	JSCE dogbones	310 μm	-
Split-tensile strength	Ø4″ x 8″ cylinders	17.0 MPa	8.5%
Modulus of Rupture (MOR)	4″ x 4″ x 14″ beams	31.8 MPa	14%
Mid-point net deflection at MOR	4″ x 4″ x 14″ beams	2.5% of span length (12″)	10%

References

1. Li, V. C. (2007) “Integrated Structures and Materials Design” *Materials and Structures,* 40(4), 387-396.

2. Li, M. & Li, V. C. (2013) “Rheology, Fiber Dispersion, and Robust Properties of Engineered Cementitious Composites” *RILEM Journal of Materials and Structures*, 46(3), 405-420.

3. ASTM C143 (2010) “Standard Test Method for Slump of Hydraulic-Cement Concrete” American Society for Testing and Materials, West Conshohocken, PA, pp. 4.

4. Malvern Inst. Ltd. (2010) “Gemini/CVO Rheometer: User Manual” MAN0329, Is. 4, pp. 2:1-3:16.

5. Malvern Inst. Ltd. (2010) “Gemini/CVO Rheometer: Accessories” MAN0432, Is. 1.0, pp.2:12.

6. ASTM C109 (2011) “Standard Test Method for Compressive Strength of Hydraulic Cement Mortars (Using 2-in. or 50 mm Cube Specimens)” American Society for Testing and Materials, West Conshohocken, PA, pp. 10.

7. ASTM C496 (2004) “Standard Test Method for Splitting Tensile Strength of Cylindrical Concrete Specimens” American Society for Testing and Materials, West Conshohocken, PA, pp. 5.

8. ASTM C1609 (2010) “Standard Test Method for Flexural Performance of Fiber-Reinforced Concrete with Third-Point Loading” American Society for Testing and Materials, West Conshohocken, PA, pp. 9.

9. Yang, E. H., Yang, Y. & Li, V. C. (2007) “Use of High Volumes of Fly Ash to Improve ECC Mechanical Properties and Material Greenness” *ACI Materials Journal*, 104(6), 620-628.

10. Bingham, E. C. (1922) “Fluidity and Plasticity” New York: McGraw-Hill, pp. 448.

11. Ranade, R., Stults, M. D., Lee, B. Y. & Li, V. C. (2011) “Effects of Fiber Dispersion and Flaw Size Distribution on the Composite Properties of PVA-ECC” In Proc. of *HPRCC-6*, Parra-Montesinos et al. (Eds.), 19-22 June, 2011, Ann Arbor, MI, pp. 106-113.

12. Ranade, R., Stults, M. D., Li, V. C., Rushing, T. S., Roth, J. & Heard, W. F. (2011) “Development of High Strength-High Ductility Concrete” In Proc. of *SHCC-2*, Toledo Filho et al. (Eds.), 12-14 December, 2011, Rio de Janeiro, Brazil, pp. 1-8.

13. Wight, J. K. & MacGregor, J. G. (2009) “Stress-strain Curves for Concrete” In *Reinforced Concrete: Mechanics and Design* (5th ed.), Upper Saddle River, NJ: Prentice Hall, pp. 64-70.

14. Graybeal, B. A. (2007) “Compressive Behavior of Ultra-High-Performance Fiber-Reinforced Concrete” *ACI Materials Journal*, 104(2), 146-152.

15. Horii, H. & Nemat-Nasser, S. (1986) “Brittle Failure in Compression: Splitting, Faulting and Brittle-Ductile Transition” *Philosophical Transactions of the Royal Society of London, Series A, Mathematical and Physical Sciences*, 319(1549), 337-374.

16. FHWA (2006) “Compressive Testing” In *Material Property Characterization of Ultra-High Performance Concrete*, US Department of Transportation, McLean, VA, Pub No. FHWA-HRT-06-103, pp. 24-28.

17. O'Neil, E. F. (2008) "On Engineering the Microstructure of HPCs to Improve Strength, Rheology, and Frangibility" PhD Dissertation, Evanston, IL: Northwestern University, pp. 45.

18. ACI 318 (2008) "Building Code Requirements for Structural Concrete and Commentary" American Concrete Institute, Farmington Hills, MI, pp. 318-107.

19. Maalej, M. & Li, V. C. (1994) "Flexural/Tensile-Strength Ratio in Engineered Cementitious Composites" *ASCE Journal of Materials in Civil Engineering*, 6(4), 513-528.

20. Qian, S. & Li, V. C. (2007) "Simplified Inverse Method for Determining the Tensile Strain Capacity of Strain Hardening Cementitious Composites" *Journal of Advanced Concrete Technology*, 5(2), 235-246.

21. JSCE (2008) "Recommendations for Design and Construction of High Performance Fiber Reinforced Cement Composites with Multiple Fine Cracks." Tokyo, Japan: JSCE, pp. Testing Method 11-13.

CHAPTER 6: MICROSTRUCTURE AND MICROMECHANICS OF HIGH STRENGTH-HIGH DUCTILITY CONCRETE

6.1 Introduction

The microstructure and micro-scale mechanical behavior of the High Strength-High Ductility Concrete (HSHDC) are reported in this chapter. HSHDC, similar to other concretes, is a heterogeneous material at micro-, meso-length scales with multiple phases interacting with each other. The micromechanics-based design that is foundational for the development of HSHDC relies primarily on investigating and favorably tailoring the interaction between these phases (particularly fiber/matrix interactions) for achieving desirable composite properties. Thus, it is vital for composite property tailoring to investigate the microstructure and micro-scale behavior of HSHDC, and quantify the fiber-matrix interaction properties, which is the motivation behind this research.

The objectives of the research reported in this chapter are: first, to document the electron micrographs and elemental analysis of the major phases in HSHDC microstructure; second, to determine the fiber and flaw size distributions in HSHDC; third, to determine the fiber/matrix interaction properties of HSHDC; fourth, to ascertain whether the existing analytical fiber-pullout model for ECC completely explains the experimental fiber-pullout behavior of HSHDC (if not, investigate any new mechanisms); and fifth, to test whether the fundamental

micromechanics based conditions for strain hardening are satisfied by HSHDC. This study provides insights into the microstructure of HSHDC and establishes a micromechanics basis for the observed composite tensile strain-hardening behavior of HSHDC (reported in Chapter 5) by investigating micro-scale fiber/matrix interactions.

The micromechanical investigation procedure followed in this research for achieving the objectives #3-5 is shown schematically in Figure 6.1. Single fiber pullout tests were performed with varying embedment lengths and inclination angles with respect to the loading direction. While the existing debond and pullout models[1] (originally developed for ECC) were able to explain the observed aligned fiber (inclination angle = 0°) pullout satisfactorily, the increase in pullout load with inclination of fibers (observed in HSHDC in addition to the snubbing effect) could not be captured by these models. A new inclination-dependent hardening mechanism was proposed to explain the observed inclined fiber pullout in HSHDC, which was found to be unique to the high strength matrixes and beneficial for fiber bridging in HSHDC. The fiber-pullout mathematical model for ECC was modified accordingly to capture the new mechanism. The fiber/matrix interaction properties and mechanisms thus inferred from the single fiber pullout test results were used in a statistical scale-linking model[2] to analytically compute the bridging stress-crack opening (σ-δ) relation of HSHDC. This computed σ-δ relation was experimentally verified through single crack tests using notched rectangular coupon specimens. The σ-δ relation was finally used to check the two necessary conditions of multiple cracking[3] to achieve composite tensile ductility. Details of the micromechanical investigation of HSHDC following the above procedure are documented in this chapter.

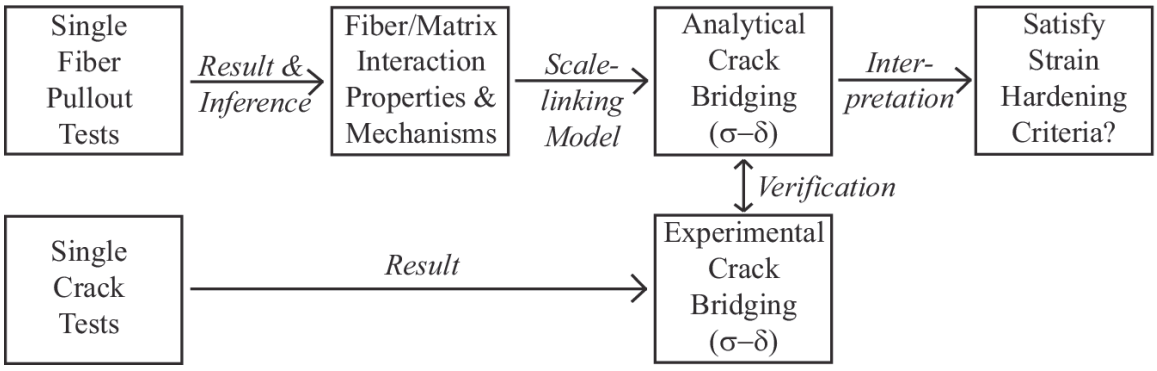

Figure 6.1: Micromechanical Investigation Procedure

6.2 Microstructure of HSHDC

In this section, the electron micrographs of the microstructure of HSHDC and its ingredients are documented, along with the identification of various phases – particularly, the interfacial transition zone (ITZ) between the PE fiber and the HSHDC matrix. A scanning electron microscope (SEM) is used to image small sections (about 1 cm x 1 cm – 0.5 cm deep) of HSHDC dogbones. All the HSHDC sections were ground and polished using the method described in Sakulich & Li.[4] A large field detector capturing the secondary electrons was used in a low vacuum (water) environment inside the SEM for these observations. Secondary electrons are more surface sensitive and provide a better (3D) view of the surface topography (particularly, the edges) than backscatter electrons. Backscatter electrons are useful for identifying elements as the intensity of backscatter electrons is proportional to the atomic mass of the element; however backscatter electron detection requires thinner and better-prepared specimen surfaces than secondary electron detection. Instead of backscatter, an energy-dispersive X-ray spectrum (EDS)

analyzer, attached to the SEM, is used in this study to identify the elements at specific locations of interest within the HSHDC sections. The observations are discussed below.

The micrographs of the ingredients of HSHDC (Table 5.1) are shown in Figure 6.2 and their energy-dispersive spectra are shown in Figure 6.3. These micrographs and energy spectra were obtained by analyzing the ingredients in their raw unmixed state. The coarsest ingredient in HSHDC is the sand. An average sand particle of F-60 foundry sand with diameter of about 250 μm is shown in Figure 6.2a. Class H cement and silica flour have similar size and flaky appearance under SEM but their energy spectra (Figure 6.3b and Figure 6.3c) are markedly distinct. While silica flour particles (mostly consisting of silicon and oxygen [SiO_2]) exhibit no calcium, the cement particles (mostly consisting of calcium silicates) exhibit significant amounts of calcium in their energy spectra, along with silicon, oxygen, and other elements. The aluminum peak in the cement spectrum is low, which is typical of Class H cements due to low calcium aluminate contents. The silica fume particles are the smallest (0.1-1 μm) in HSHDC, and are difficult to resolve under the SEM used in this research. In spite of this, the near-perfect round shape of silica fume particles is observable in Figure 6.2d. Two views of the PE fibers are shown in Figure 6.2e. While the 'Left' view focuses on the fiber cross-section, the 'Right' view captures the curved surface of the PE fiber. It can be observed in the 'Left' view that the cross-section of the PE fiber is slightly triangular, instead of being perfectly circular. This knowledge of the visual appearance and the elemental analysis of HSHDC ingredients in their raw state is utilized below in identifying various phases in the HSHDC sections.

Select micrographs of HSHDC sections are shown in Figure 6.4. A sand grain (S) and a fiber (F) are identified in Figure 6.4a, and a partially hydrated cement particle (C) and a silica flour (crushed quartz – Q) are identified in Figure 6.4b. In all micrographs, the sand particles are the biggest with the brightest appearance among matrix ingredients. The sharp surface features (Figure 6.4a) on the sand particles are 10-100 nm deep, which cause more intense emission of secondary electrons, and therefore, increase the local brightness in the HSHDC micrographs compared to the surrounding area. Similar increase in brightness is observed in silica flour particles, which is also useful in distinguishing them from the partially hydrated cement particles with similar size but darker color than the flour particles (Figure 6.4b). A few unreacted silica fume particles are visible at the fiber/matrix interface in Figure 6.4d. All the fiber/matrix interfaces are darker in color than both the fiber and the matrix, and appear as dark rings surrounding the bright fiber edges. Thus, the major phases of the HSHDC microstructure are identified.

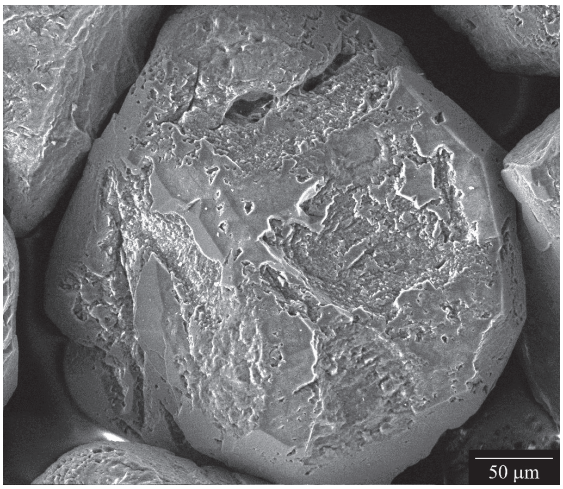

(a) Sand

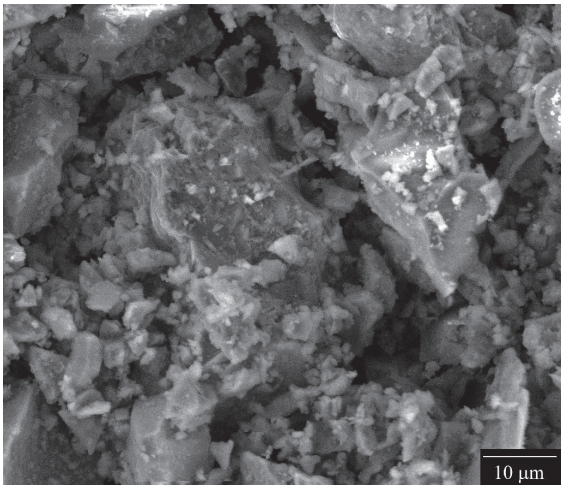

(b) Cement

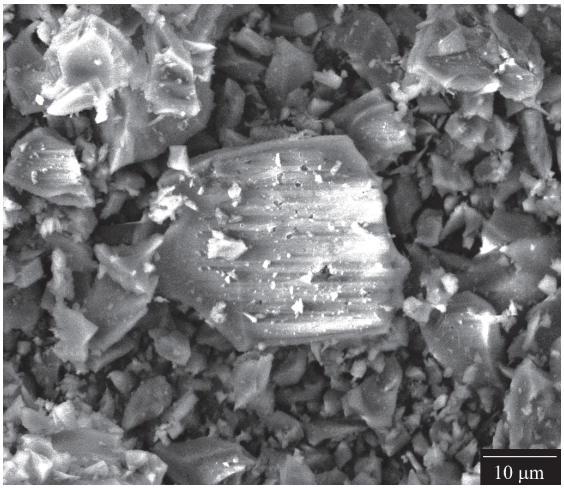

(c) Silica Flour

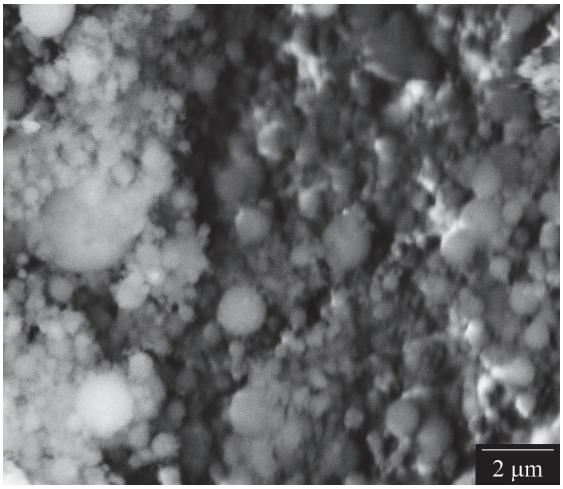

(d) Silica Fume

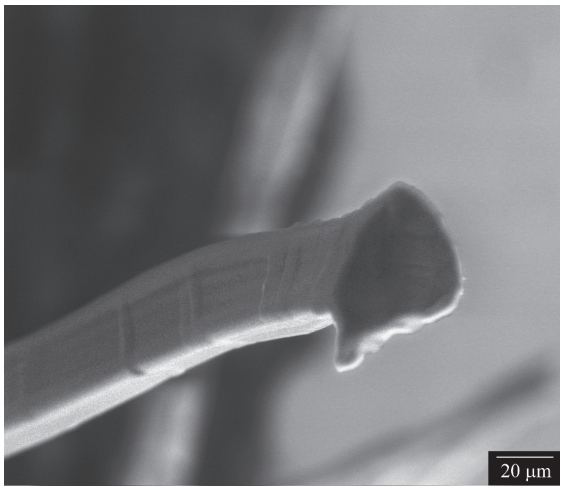

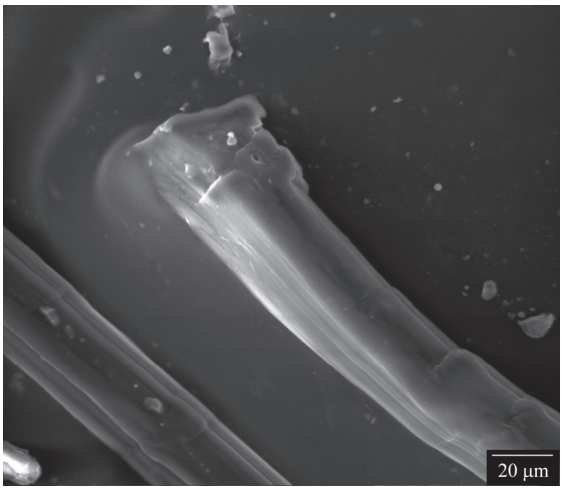

(e) Polyethylene fiber - Views ‘Left’ and ‘Right’

Figure 6.2: SEM micrographs of the HSHDC ingredients

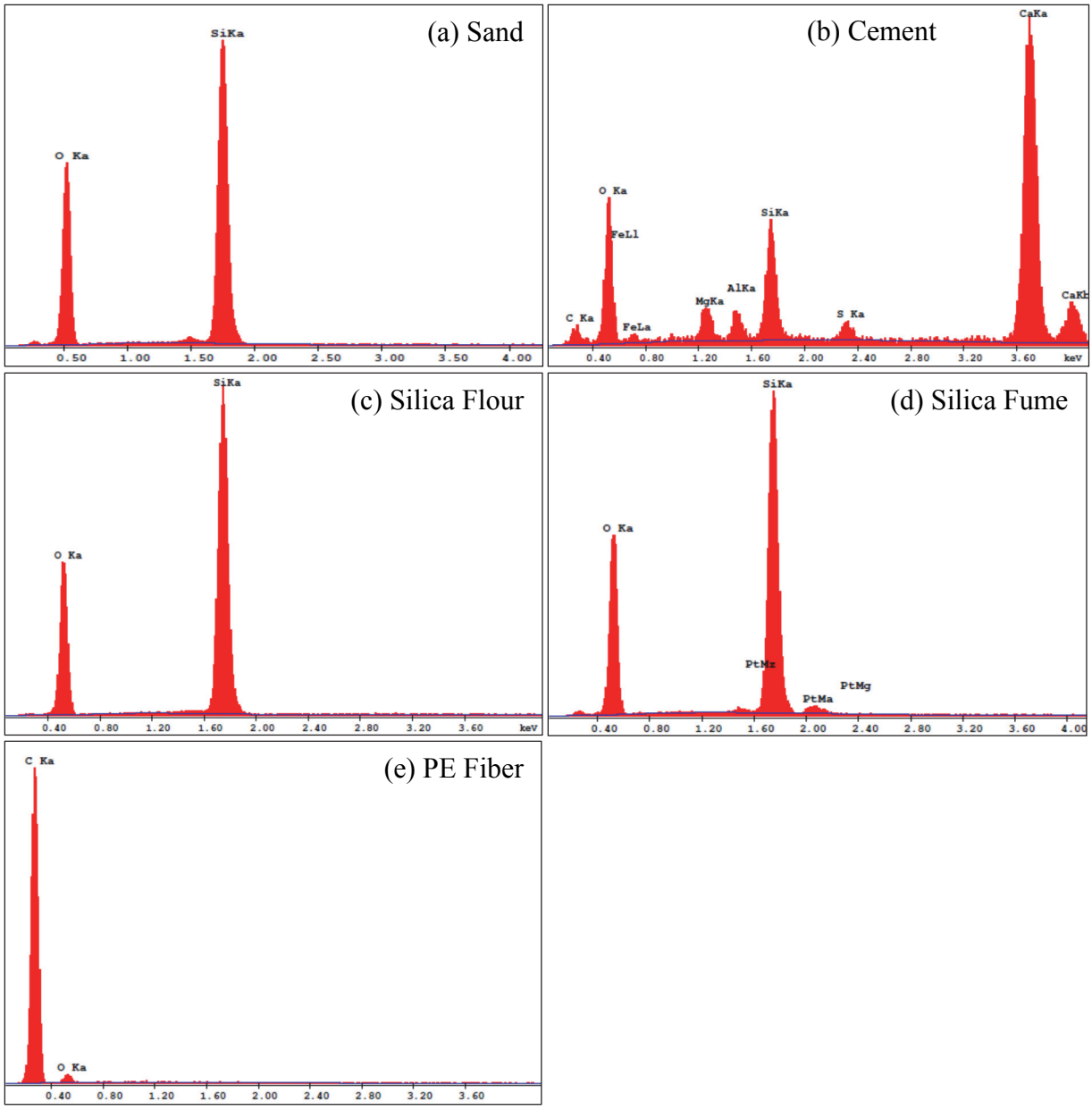

Figure 6.3: Energy-dispersive spectra of HSHDC ingredients
(y-axis in all the graphs is the relative number of counts during the scan time for each excitation energy (keV) level [x-axis])

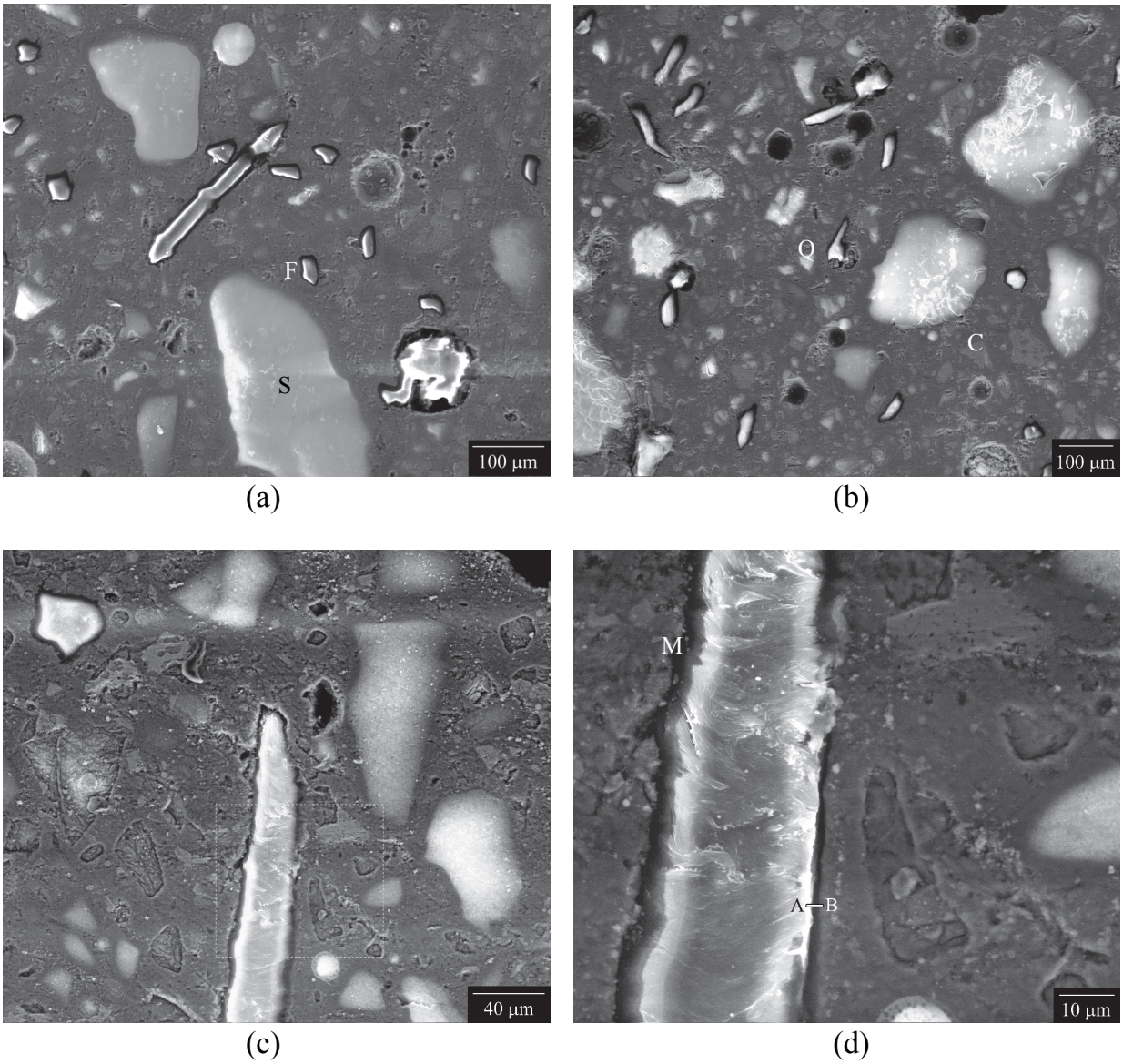

Figure 6.4: SEM micrographs of HSHDC sections

Notes: (1) S & F: Sand & Fiber in (a); Q & C: Silica Flour (Crushed Quartz) and Cement in (b);
M: Silica Fume (Microsilica) in (d)
(2) Zoomed view (dashed box) of (c) is shown in (d)
(3) Distance AB = 3 µm in (d)

The fiber/matrix interface is further investigated using EDS analysis. The EDS scan for element detection is performed at 11 equally spaced (at 300 nm) points along the line segment AB (3 μm) shown in Figure 6.4d. Closer spacing is not achievable with the EDS used in this research without significantly increasing the detection error. The energy spectra observed at A (inside fiber) and B (inside matrix) are shown in Figure 6.5, and the elemental compositions in terms of C/(Si+Ca) and Ca/Si ratios of atomic percentages are shown in Figure 6.6. Each data point in Figure 6.6 is an average of 3 observations at the same location. Two vertical grey lines in Figure 6.6 show the possible location of the ITZ, which is about 1.5 μm wide. The elemental composition changes significantly in this region and is relatively constant outside this zone. An ITZ of about 2-4 μm is observed between the steel fibers and the cementitious matrix in a UHPC with similar compressive strength as HSHDC.[5] The Ca/Si ratio increases in the ITZ, which is in contrast with the notion of ITZ densification by unreacted silica fume. The higher Ca/Si ratio at the ITZ may be due to higher concentration of calcium hydroxide there; however, higher resolution observations using techniques such as TEM are needed to confirm the elemental composition observation. Ca/Si ratio of less than 1 is consistently observed at all locations in this study, which indicates significant presence of silica fume particles in the bulk of the matrix.[6] For comparison, typical Ca/Si ratio for pure CSH is about 1.5-2. Overall, the EDS analysis provides vital insights into the width of the ITZ and its elemental composition, which can be used to favorably tailor the fiber/matrix bond.

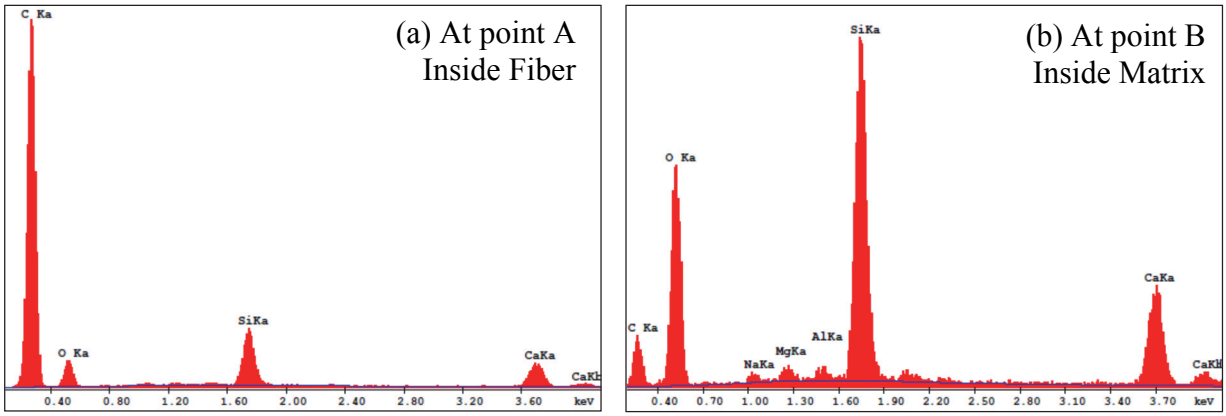

Figure 6.5: Energy-spectra at points A and B

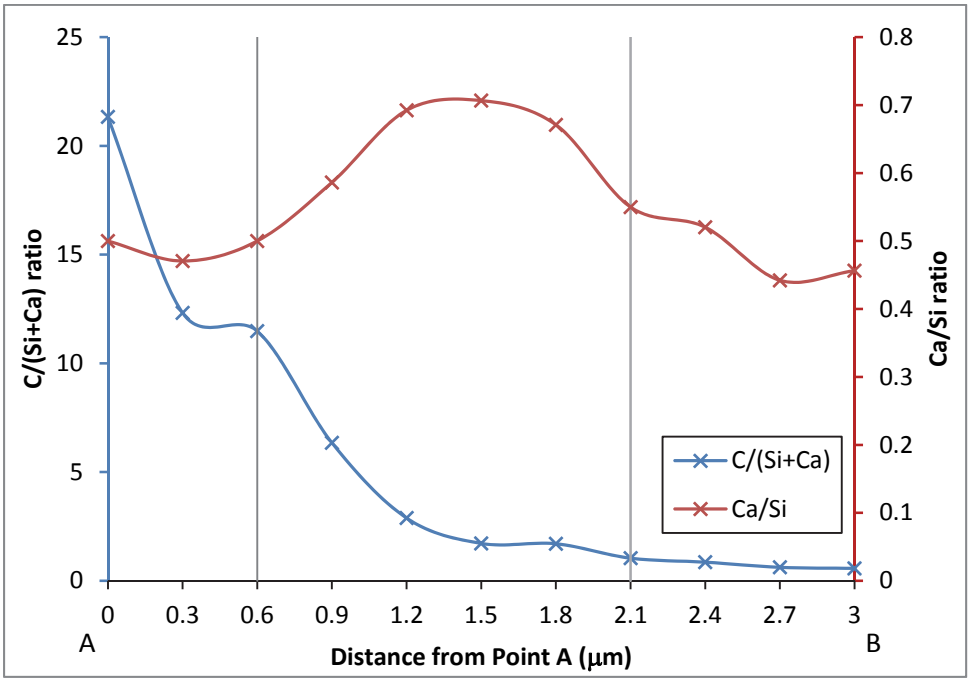

Figure 6.6: EDS analysis of segment AB

6.3 Largest Flaw Size Distribution

6.3.1 Relevance

The distribution of the largest flaw size across various cross-sections of HSHDC specimens has direct implications on tensile cracking strength and ductility as well as the compressive strength of HSHDC. As noted in Section 2.3, HSHDC, similar to all other cementitious materials, contains flaws (or weaknesses) in the form of entrapped air voids (during mix processing), weak aggregate-cement paste interface, capillary pores, etc. From fracture mechanics, it is known that the stress intensity increases with the flaw size, and as a result, the first crack in HSHDC matrix initiates from the largest flaw as ambient stress increases, also called the first crack strength of the matrix. While a small flaw size is desirable for high compressive strength, it also increases the matrix cracking strength under tension which reduces the stress margin needed for tensile ductility as explained in Sections 2.5 and 4.2. A flaw size distribution that has the majority of flaws small-sized, but also has a significant percentage of flaws with relatively large size, simultaneously, is desirable for achieving the right combination of compressive strength and tensile ductility.

6.3.2 Observation Method

An optical microscope is used to observe and measure the largest flaw sizes at the cross-sections of HSHDC specimens. The dogbone specimens described in Chapter 5 for direct tension testing of HSHDC are used in the largest flaw size observations. Each of the eight dogbone

specimens is sectioned at 10 places at about 9 mm interval along the gauge length of 80 mm. A typical cross-section of HSHDC is shown in Figure 6.7. Only the largest flaw size is recorded, and the collective observations at all the 80 sections are statistically analyzed below.

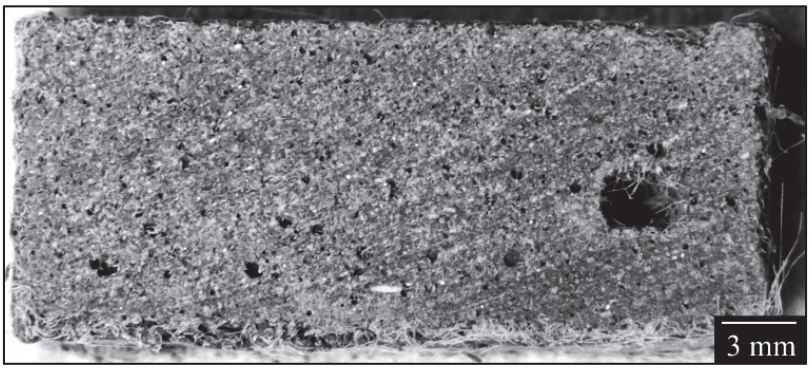

Figure 6.7: An HSHDC dogbone specimen cross-section
(Largest flaw size in this section = 2.6 mm)

6.3.3 Observations

The observed distribution of the largest flaw size across 80 HSHDC dogbone specimen cross-sections is shown in Figure 6.8 in form of a histogram. Continuous distributions best-fitting the observed data are also shown in this figure. While a lognormal distribution is the single best-fitting continuous distribution for the entire data, a weighted combination of this lognormal distribution with a Gaussian distribution fits the observed data more closely, particularly towards the upper end of the flaw sizes. The mean and standard deviations of log(flaw size) in the lognormal distribution are 0.231 and 0.868, respectively, and that of the flaw size in the Gaussian distribution are 4.2 mm and 0.7 mm, respectively. Linear weights of 0.9 and 0.1 are used for the lognormal and Gaussian distributions, respectively, to compute the combined distribution. While the lognormal trend is dominant for flaws smaller than 3 mm, the

Gaussian trend is dominant for the small fraction of flaws greater than 3 mm in the distribution of the largest flaw size in HSHDC.

The shapes of the flaw size distributions are similar in HSHDC and ECC; however, the largest flaw sizes are significantly smaller in HSHDC compared to ECC. While the average largest flaw size (expected value of the combined distribution) is about 1.3 mm in HSHDC, it is about 2.0 mm in ECC.[20] From Linear Elastic Fracture Mechanics (LEFM), the cracking strength is proportional to $K_{IC}/\sqrt{a}$, where K_{IC} is the fracture toughness of the material and a is the flaw size. The fracture toughness of the HSHDC matrix is 1.10 MPa$\sqrt{m}$ (Section 6.6.2), which is about two times that of the ECC-M45 matrix.[15] This increase in matrix fracture toughness coupled with decrease in average largest flaw size increases the matrix cracking strength of HSHDC by about 2.5 [$2/\sqrt{(1.3/2)}$] times compared to that of ECC, consistent with the measured first crack strength of HSHDC at 8.3 MPa and that of ECC-M45 at 3-4 MPa.

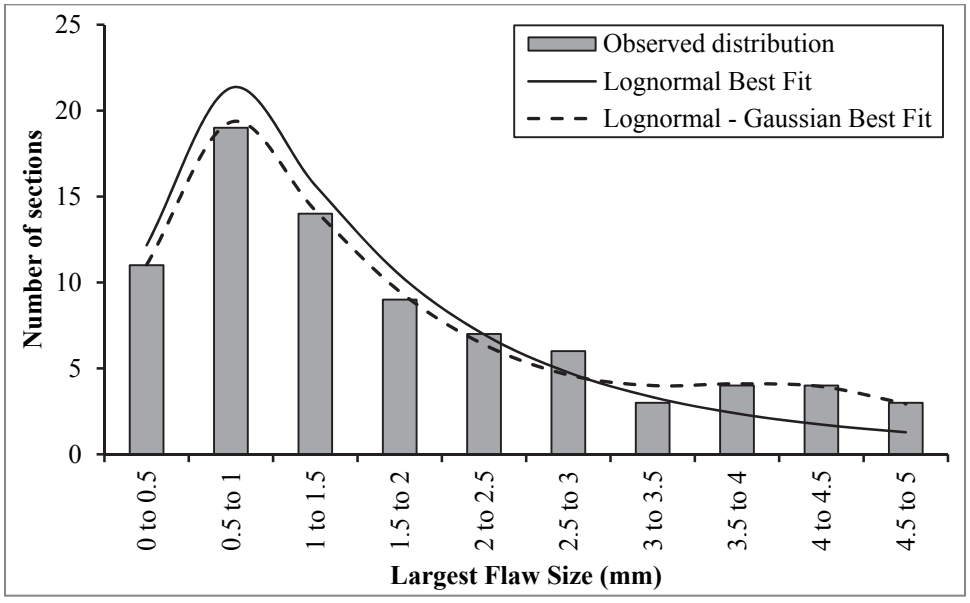

Figure 6.8: Distribution of largest flaw size across 80 HSHDC dogbone specimen cross-sections

6.4 Fiber Distribution

6.4.1 Relevance and Observation Quantities

The PE fibers are randomly distributed in the HSHDC matrix during mix preparation, and it results in a fibers distribution that can be described in terms of three types of variations (or inhomogeneity). The first type (*fiber scale*) of variation refers to the distribution of orientation (inclination angle, ϕ) of fibers with respect to the principal tensile direction. This is represented by a probability distribution function, $p(\phi)$. The second variation (*cross-section scale*) refers to inhomogeneity in the number of fibers at various locations within a single cross-section. This variation is captured by the fiber dispersion coefficient (α). The third variation (*specimen scale*) refers to the varying number of fibers at different cross-sections within one or more specimens. This variation is captured by a Gaussian probability distribution function of fiber volume fraction, $p(V_f)$. The experimental technique to determine these three fiber distribution parameters – $p(\phi)$, α, and $p(V_f)$ – is explained in Section 6.4.2.

In HSHDC, the short PE fibers bridge the multiple micro-cracks to maintain composite integrity resulting in the pseudo strain hardening behavior. All the three fiber distribution parameters [$p(\phi)$, α, and $p(V_f)$] directly influence the bridging capacity and efficiency of the fibers crossing a given crack plane as discussed below.

As discussed below in Section 6.4.3, the number of effective bridging fibers at an HSHDC cross-section is directly proportional to V_f and $p(\phi)$. A wider spread in $p(V_f)$ reduces the

minimum fiber volume fraction, min(V_f), and therefore, lowers the number of fibers and the bridging capacity of HSHDC, as discussed in Section 6.6.2. The bridging efficiency (η_f) in Eq. 6.4 below is particularly influenced by the change in $p(\phi)$. For instance, η_b is 1 (100% efficiency) for 1D distribution (all fibers aligned with the principal tensile stress direction), and it progressively decreases as the number of inclined fibers relative to aligned fibers increases. η_f is $2/\pi$ (0.64) for 2D and 0.5 for 3D distributions. The collective fiber bridging stress at an HSHDC cross-section typically decreases with decrease in bridging efficiency (η_f); however, an individual inclined fiber transfers greater force than an aligned fiber by taking advantage of snubbing and inclination hardening mechanisms discussed below. Hence, there is a trade-off between collective bridging efficiency of multiple fibers and the pullout force transferred by a single fiber. The influence of $p(\phi)$ and V_f on the crack bridging behavior (σ-δ relation) of HSHDC is quantified in Section 6.6.2.

The fiber distribution parameter, α, is not included in the bridging stress calculations, which assume a homogenous dispersion of fibers at a cross-section. However, the effect of α on the composite tensile ductility is indirectly accounted in the multiple cracking robustness criteria based on pseudo-strain hardening indices, described in Sections 2.5 and 4.2. Lower α is expected to reduce the average fiber/matrix frictional bond (τ_0). In the limit when all fibers are clumped together ($\alpha \rightarrow 0$), τ_0 approaches 0. On the other hand, when all fibers are perfectly dispersed ($\alpha=1$), τ_0 approaches the average τ_0 calculated for single fiber pullout. Thus, lower α is expected to reduce the fiber bridging capacity.

6.4.2 Observation Method

Fluorescence microscopy is used in this study to detect the fibers and determine the fiber distribution parameters. PE fibers are known to fluoresce and emit green light in the range of 440 to 460 nm wavelength when excited by ultra-violet incident light of 370 to 390 nm wavelength. An HSHDC specimen cross-section (Figure 6.9b) when viewed under a fluorescence microscope, therefore, appears as numerous green elliptical dots (fibers) on a black background (matrix), which can be utilized to determine the fiber distribution parameters as follows.

In this study, the cross-sections of both kinds of specimens – the single-crack coupon specimens and the dogbone specimens used for direct tension tests in Chapter 5 – are investigated. Two cross-sections were cut from un-cracked regions of each of the six coupons (used in single-crack tests – details in Section 6.5.1and 6.5.7) and two out of the ten sections cut for flaw size measurements (Section 6.3.2) from each of the eight dogbones (used in direct tension tests) were selected for fiber distribution observations. After polishing and surface preparation, each cross-section was observed under a fluorescence microscope. The field of view of the fluorescence microscope at the required resolution is only 2 mm x 2 mm. Therefore, about 90 pictures per dogbone and 230 pictures per coupon would be required to cover their entire cross sections. To achieve a reasonable processing time, the section was sampled at certain "observation squares" shown in Figure 6.9a by shaded rectangular squares inside the specimen cross-sections. Thus, 9 squares per dogbone section and 15 squares per coupon section were imaged and analyzed using the digital image processing method developed by Lee et al[7] to determine the fiber distribution parameters.

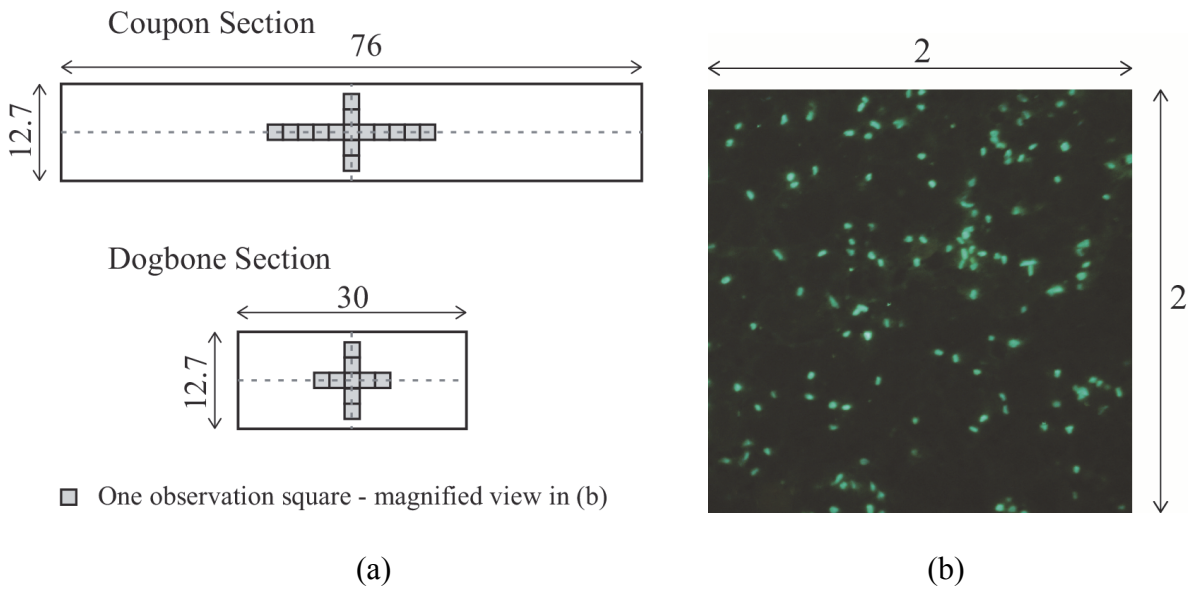

Figure 6.9: Fluorescence imaging of HSHDC specimen cross-sections
(a) Observation squares (15 for coupon and 9 for dogbone)
(b) Fluorescence image of one observation square
(All dimensions in mm)

The first fiber distribution parameter, p(ϕ) – fiber orientation distribution, is determined using the aspect ratio of the green elliptical sections of the PE fibers observed in the fluorescence image (Figure 6.9). The elliptical shape is due to the fact that the projection of cylindrical PE fibers on a plane inclined to their longitudinal axis is an ellipse. The minor axis of this ellipse is equal to the fiber diameter (d_f) and major axis (b) is equal to $d_f/\cos(\phi)$, where ϕ is the angle with respect to the outward normal of the specimen cross-section. Thus, the inclination angle or orientation (ϕ) of a fiber can be determined by Eq. 6.1.

$$\phi = \cos^{-1}\left(\frac{\text{Area of circular cross-section}}{\text{Area of elliptical projection}}\right) = \cos^{-1}\left(\frac{\pi d_f^2/4}{\pi d_f b/4}\right) \tag{6.1}$$

A digital image processing method developed by Lee et al[7] is employed to automatically detect the fibers using a segmentation algorithm, and compute their orientation using the above principle. Grouping the fibers with orientations in intervals of $\Delta\phi = 9°$ (therefore, 10 intervals from 0° to 90°), and plotting the number of such fibers against the ϕ-interval produces a histogram. A probability distribution best-fitting this histogram is $p(\phi)$.

The second fiber distribution parameter, α (fiber dispersion coefficient), is determined by the method used in Lee et al utilizing the fluorescence images. The fiber dispersion coefficient, α (Eq. 6.2), is inversely related to the exponent of the root mean square deviation of the number of fibers (x_i) in a unit area from the average value at that specimen cross-section ($\bar{x}$). Thus, if all the fibers are distributed homogeneously, the deviation ($x_i - \bar{x}$) from the average value is zero and $\alpha = 1$. Conversely, if all the fibers are grouped in one unit area (with no fibers in other unit areas), the deviation is very large and $\alpha \rightarrow 0$. Mathematically,

$$\alpha = \exp\left(-\frac{1}{\bar{x}} \sqrt{\frac{\sum_i \left(x_i - \bar{x} \right)^2}{n}} \right) \tag{6.2}$$

where, n is the number of unit areas in which a specimen cross-section is divided. In order to uniquely define n, Lee et al uses n equal to the total number of fibers in the specimen cross-section (in all unit areas) – this choice of n results in $\bar{x} = 1$.

The third fiber distribution parameter, $p(V_f)$, is obtained by counting the total number of fibers at multiple cross-sections. The average and standard deviation of this data are used to determine the best-fitting Gaussian probability distribution, $p(V_f)$. All the three fiber distribution

parameters are determined for HSHDC specimens below following the methods presented in this section.

6.4.3 Observations

A collective average fiber inclination histogram obtained by processing all the fluorescence images of HSHDC specimen cross-sections (dogbones and coupons) is shown in Figure 6.10. Best-fit continuous functions, p(ϕ), for the observed inclination distribution in dogbones and coupons are given by Eq. 6.3 and plotted (as solid lines of the same colors as the bars) in Figure 6.10 along with the typically assumed theoretical 2D [p(ϕ) = 2/π] and 3D [p(ϕ) = sin(ϕ)] distributions. These best-fit distributions are modeled as linear combinations of the 2D and 3D distributions (Eq. 6.3). The reason for restricting the 3D distribution at 54° is the observation of distinct drop in histogram after the class interval 45°-54° (with class mark of 49.5°), which may be caused by the limited thickness [12.7 mm (0.5 in)] of dogbones and coupons. The weights for 2D and 3D distributions are determined using least square estimation in one variable, *w* to best-fit the observed distribution. The best-fit value of *w* is 0.73 for coupons and 0.46 for dogbones of HSHDC.

$$\begin{aligned} p(\phi) &= w(2/\pi) + (1-w)\sin(\phi)/[\cos(0°) - \cos(54°)] \quad \forall \phi \in [0°, 54°] \\ p(\phi) &= w(2/\pi) \qquad\qquad\qquad\qquad\qquad\qquad\qquad\quad \forall \phi \in (54°, 90°] \end{aligned} \tag{6.3}$$

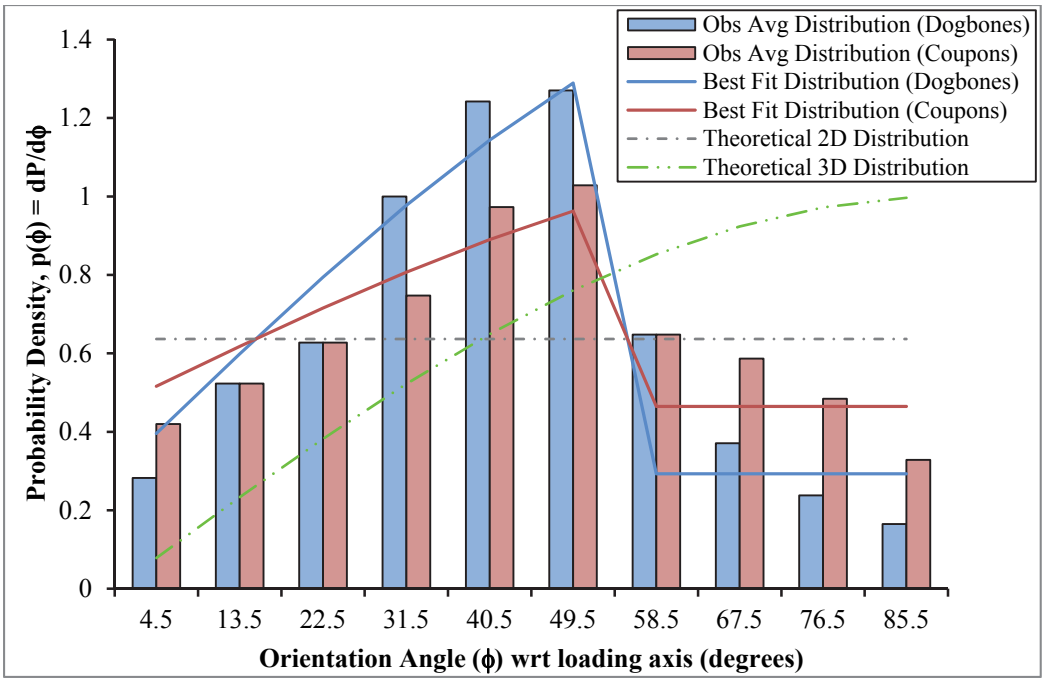

Figure 6.10: Observed and best-fit fiber orientation distributions

The average fiber dispersion coefficient, α_{avg}, is equal to 0.33 for the dogbone cross-sections and 0.34 for coupon cross-sections using the method in Lee et al.[7] α_{avg} for dogbone and coupon cross-sections was calculated by averaging the dispersion coefficients of 144 dogbone observation squares (9 observation squares for each of the 16 dogbone cross-sections) and 180 coupon observation squares (15 observation squares for each of the 12 coupon cross-sections), respectively. Slightly higher fiber dispersion homogeneity in coupons compared to dogbones is reasonable due to larger (almost 2.5 times) cross-sectional area of the coupons, which facilitates fiber dispersion.

The numbers of fibers observed per cm^2 of all the cross-sections are plotted in Figure 6.11 as data points (triangles and circles). D1-16 and C1-12 represent all the cross-sections investigated in this study. Average of the observed numbers of fibers in dogbone and coupon

cross-sections was 2275 fibers/cm^2 (with standard deviation of 179 fibers/cm^2) and 2156 fibers/cm^2 (with standard deviation of 130 fibers/cm^2), respectively. The average observed values are shown as solid red/blue lines in Figure 6.11. The numbers of effective fibers per unit cross-sectional area can also be determined theoretically by the formula $V_f\eta_f/A_f$ (shown by dashed lines in Figure 6.11), where V_f is the volume fraction (2% in the theoretical calculation), A_f is the cross-sectional area of the PE fiber, and η_f is the bridging efficiency. η_f is computed using Eq. 6.4, where p(z) is the distribution of embedded fiber's centroidal distance from the crack plane (assumed $2/L_f$).[3] η_f is 0.72 for dogbones, 0.68 for coupons, 0.64 for 2D, and 0.50 for 3D distributions. Due to the decreasing bridging efficiency (η_f), the numbers of fibers per cm^2 decreases from dogbones to coupons to 2D and 3D distributions.

$$\eta_f = \int_0^{\pi/2} \int_0^{(L_f/2)\cos(\phi)} p(z)\, p(\phi)\, dz\, d\phi \tag{6.4}$$

The observed average numbers of fibers in both dogbone and coupon sections are lesser than the theoretical values by 3.5% and 2.2%, respectively. This may be due to the variation in fiber distribution across sections and slight undercounting of lumped fibers by the image processing method.[7]

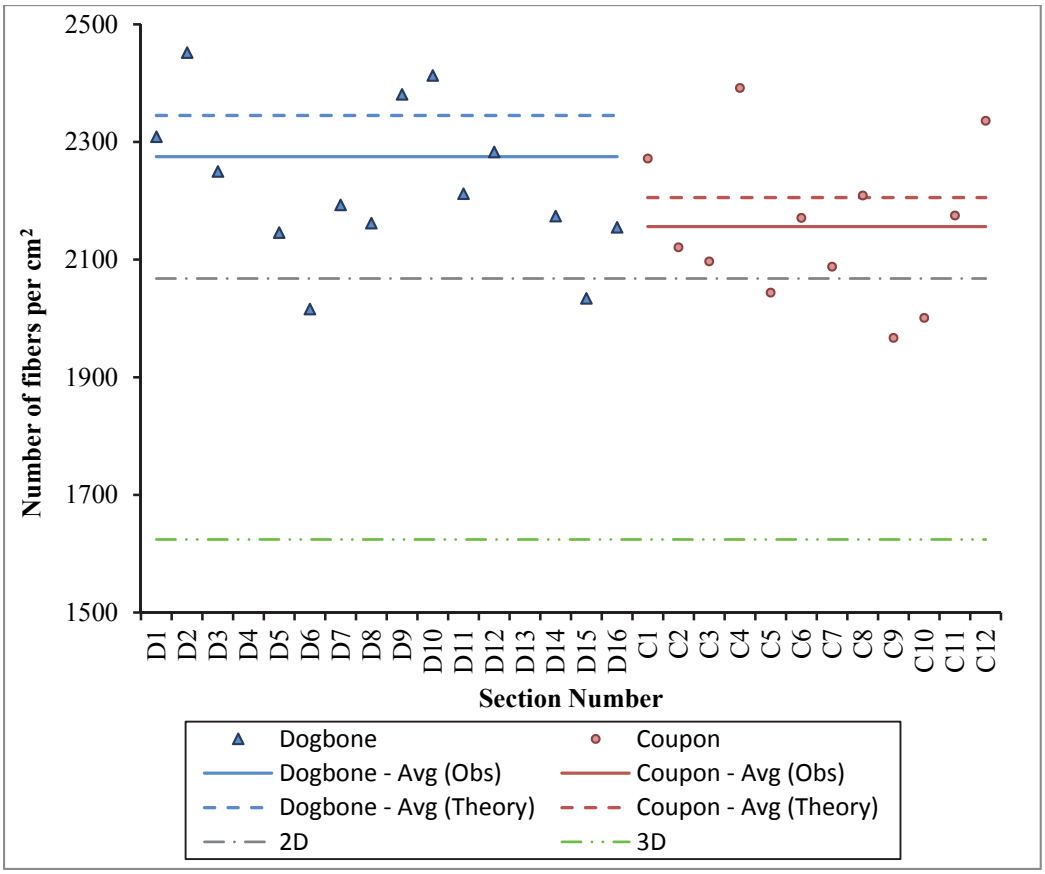

Figure 6.11: Observed and theoretical fiber numbers

The observed average and standard deviation of fiber numbers (discussed above) define the fiber number variation, $p(V_f)$ – which is assumed as a normal (Gaussian) distribution. The minimum bridging capacity, $\min(\sigma_0)$, in a multiple cracking composite specimen is most likely to occur at a cross-section with minimum number of fibers, $\min(V_f)$.

The $\min(V_f)$ for dogbone cross-sections is determined as follows. The standard deviation of fiber number in the 16 dogbone sections is 179/cm^2. Using ACI 318 method for statistical quality control of concrete strength (which also uses Gaussian distribution),[8,9] for 16 specimens, a multiplication factor of 1.16 is used to increase the standard deviation to 208/cm^2. Assuming

95% reliability and a normal distribution (multiplication factor of 1.96), the minimum number of fibers expected at a section of HSHDC dogbones is (1.96 times 208/cm^2) 407/cm^2 less than the observed average of 2275 fibers/cm^2, which is 1868 fibers/cm^2. This value (1868 fibers/cm^2) is about 80% of the theoretical average for dogbones (2345 fibers/cm^2). Therefore, min(V_f) for dogbones = 1.6% (80% of 2%), and by following a similar method as above, min(V_f) for coupons = 1.7% (as the standard deviation of p(V_f) is lesser for coupons than dogbones).

6.5 Experimental Investigation of the Micromechanical Behavior of HSHDC

The materials used in this investigation are HSHDC matrix (without fibers) for single-fiber pullout tests and HSHDC composite for single-crack tests. Mix proportions and fiber properties are presented in the last chapter in Tables 5.1 and 5.2, respectively.

6.5.1 Specimens

Two types of specimens were prepared for mechanical testing in this research: (a) single fiber pullout specimens, and (b) single-crack specimens. The details are given below.

Single-fiber pullout specimens: Fifty single-fiber pullout specimens were prepared in this research to determine the fiber/matrix interaction properties. Thirty out of the fifty specimens contained aligned fibers ($\phi = 0°$). The remaining twenty specimens contained inclined fibers with five specimens for each of the four different inclination angles, $\phi = 14°, 27°, 37°, 45°$, which are

equal to $\tan^{-1}(1/4)$, $\tan^{-1}(2/4)$, $\tan^{-1}(3/4)$, and $\tan^{-1}(4/4)$, respectively (Figure 6.12a). Specimens with higher inclination angles ($\phi > 45°$) were not studied because their preparation resulted in breakage or folding of fibers during casting. This led to a majority of non-usable specimens and wider scatter of results than the fibers with lower inclination (common observation in fiber reinforced composites[10]). Single fiber pullout test results typically exhibit a wide scatter (even for small inclination angles and aligned fibers) and the results of individual specimens are insufficient to infer the fiber/matrix interaction properties. To overcome this inherent variability of single fiber pullout tests, a large number (50) of specimens were tested in this research and the results from all the tests were collectively analyzed (details in Section 6.5.4) to compute average micromechanical properties.

The geometry of a single-fiber pullout specimen is shown in Figure 6.12b. PE and other polymer fibers are very flexible in transverse direction and cannot, therefore, be simply placed in the cementitious matrix. As a result, long uncut PE fibers were strung and tied across an opening, and the HSHDC matrix was cast around the fiber (Figure 6.12a). Further details of the single-fiber pullout specimen preparation are given in Katz and Li.[11] After curing (procedure is given in Section 5.3.4), the single-fiber pullout specimens were cut at varied depths (d in Figure 6.12) so as to vary the fiber embedment lengths (L_e in Figure 6.12b) and prepared for testing at 28 days (the single-fiber pullout test setup shown in Figure 6.12c is described in Section 6.5.2).

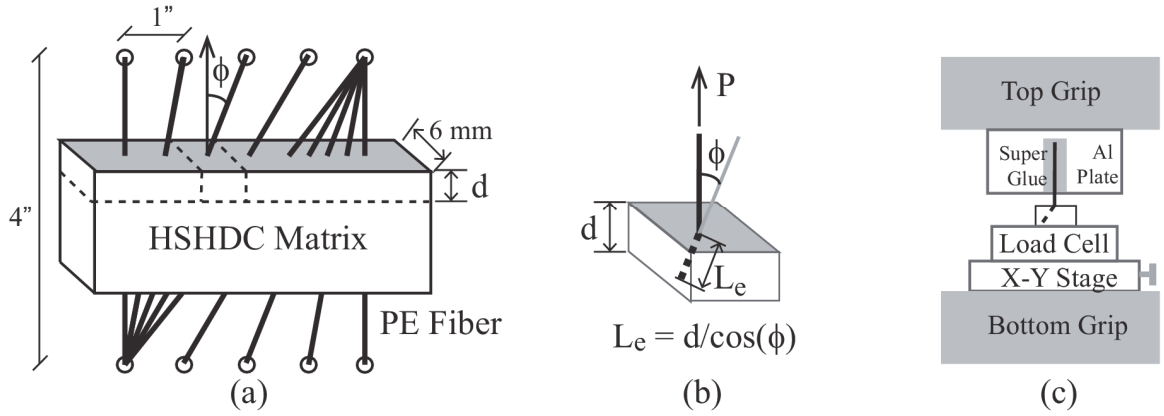

Figure 6.12: Single-fiber pullout test: (a) Casting of specimens (b) One specimen (c) Test setup

Single-crack specimens: One length scale higher, the collective bridging behavior of multiple fibers across a crack in HSHDC was empirically determined by single crack tests using notched rectangular coupon specimens. To deliberately enforce a single crack in a material that naturally tends to undergo multiple cracking, the specimen geometry and test set up schematically shown in Figure 6.13, and modeled after Paegle and Fischer,[12] are used. For preparing such specimens, six rectangular coupons of HSHDC with dimensions 12″ x 3″ x 0.5″ were cast and cured using the procedure described in Section 5.3.4. After curing, a continuous notch of width 600 μm was made all around the specimen with depths of 15 mm on the lateral sides and 2 mm on the other two sides (Figure 6.13 – Section A-A). The sharp notch forces the crack to occur at that section due to stress concentration and the substantially reduced cross sectional area ensures the exhaustion of the bridging capacity at stress levels lower than that required to trigger cracks in the rest of the specimen.

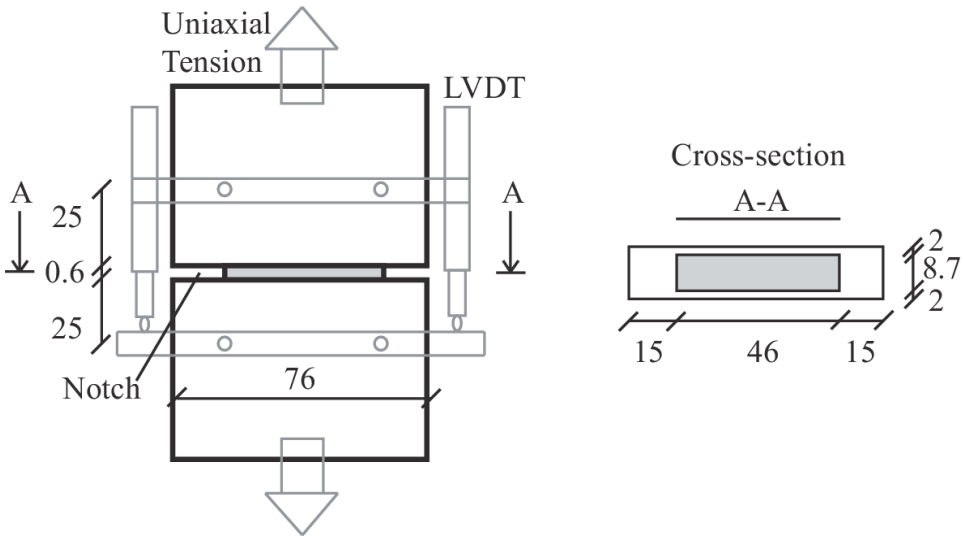

Figure 6.13: Single-crack specimen geometry and test setup
(All dimensions in mm)

6.5.2 Experimental Setup and Procedure

Single-fiber pullout experiments: The setup for single-fiber pullout tests is schematically shown in Figure 6.12c. The free end of the fiber was glued between two aluminum plates, which were held by the top grip of a tensile testing system. The bottom cross-section of the specimen was glued to a pedestal screwed into a high precision load cell with maximum capacity of 5 N and ±0.25% full scale accuracy. The load cell was attached in series to an x-y displacement stage that was held by the bottom grips of the test system. The free length of the fiber between the plates and the matrix face was kept constant at approximately 2 mm. The test was performed using an electrical test system with maximum load capacity of 10 kN under displacement control at the rate of 1 μm/s. In this test, the pullout load and the displacement of the bottom grip relative to the fixed top grip were recorded. The elastic stretching of the free fiber length was estimated based on the in-situ Young's modulus of the PE fiber (Table 5.2) and the pullout load. This

elastic stretching was subtracted from the relative displacement (u) of grips to compute the pullout displacement of the PE fiber relative to the matrix face. It was assumed that slippage and stretching in the glued portion of the fiber inside the aluminum plates were negligible. Hence, the single-fiber pullout tests were conducted under quasi-static loading, and pullout load and relative displacement were recorded using appropriate sensors.

Single-crack experiments: The notched rectangular coupon specimens were tested under direct tension using a displacement controlled closed loop test system at the rate of 0.5 mm/min. The crack opening was computed as average of extensions of two ultra-precision LVDTs with maximum non-linearity of ±0.25% full scale (full scale range is 10 mm) mounted parallel to the two side edges of the coupons (Figure 6.13), and the bridging stress was computed as tensile load divided by area of the ligament (46 mm x 8.7 mm).

6.5.3 Single-fiber Pullout Test Results

The single-fiber pullout test curves of five representative specimens with varying embedment lengths and inclination angles (ϕ) are shown in Figure 6.14. It should be noted that the abscissa units in Figure 6.14 (a) and (b) are deliberately kept distinct. The abscissa of Figure 6.14(a), intended to show the effect of varying embedment length in aligned fibers ($\phi = 0°$), is relative displacement u (mm), whereas the abscissa of Figure 6.14(b), intended to show the effect of varying inclination angle, is normalized relative displacement u/L_e (normalized by the respective embedment lengths). The complete set of all 50 test curves and summary of results is shown in Figure 6.15 and Figure 6.16 and Table 6.1.

Similar to a typical polymer fiber pullout of ECC,[1,13,14] two distinct phases can be observed in the test curves shown in Figure 6.14, which are debonding (pre-peak, monotonically increasing) and pullout (post-peak/kink). The debonding process, in general, results from breaking down of the interfacial chemical bond (G_d) plus the stretching of the fiber segment in the debonded zone against the fiber/matrix interfacial frictional bond (τ_0).[1] The load increases during this debonding process as additional energy is required to extend the debonding zone, until the whole embedded segment of the fiber is debonded. After complete debonding, the fiber enters the pullout phase in which the whole embedded segment of the fiber pulls out against interfacial friction only with continuously reduced embedment length. Due to linear reduction of embedded perimeter area of the fiber with relative displacement of the fiber (u), the pullout load should also decay linearly with u. However, it is observed in Figure 6.14, that the test curves in the pullout phase show slight curvatures (concave down) implying the presence of small amount of slip hardening (β),[13] which means increase in frictional bond with slippage. The load carried by the fiber for a given embedment length is also magnified in both debond and pullout phases at non-zero inclination angles due to snubbing effect[10] (characterized by snubbing coefficient, f) between inclined fibers and the matrix. Although this physical understanding of the debond-pullout mechanisms satisfactorily models the pullout behavior of ECC,[14] the pullout phase of inclined PE fibers embedded in the high strength HSHDC matrix cannot be completely captured by these mechanisms, and as a result, a new inclination-dependent hardening mechanism is proposed for HSHDC in Section 6.5.6.

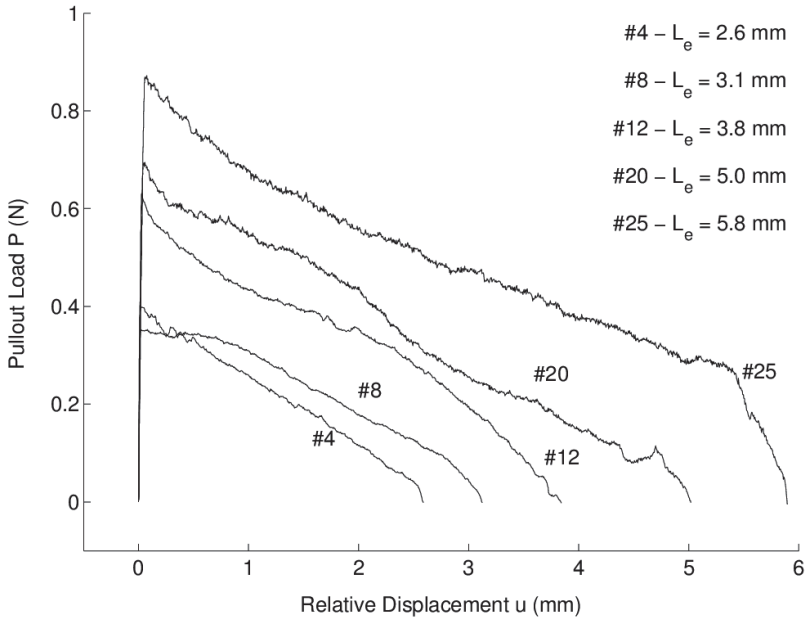

(a) Variable embedment length (L_e)

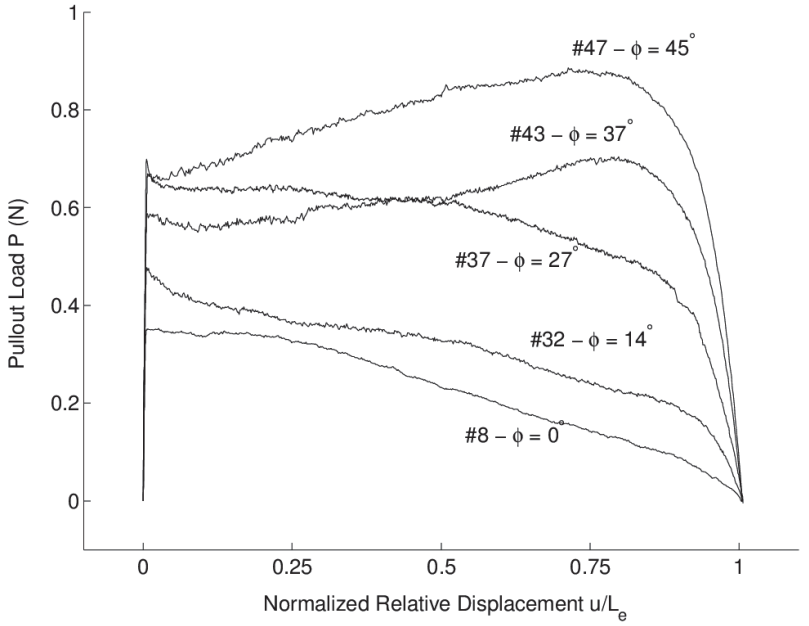

(b) Variable inclination length (ϕ)

Figure 6.14: Representative experimental single-fiber pullout curves

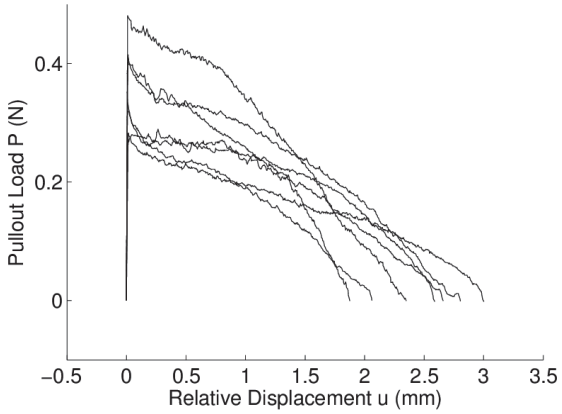

(a) $\phi = 0°$; L_e = 1.8 to 3 mm

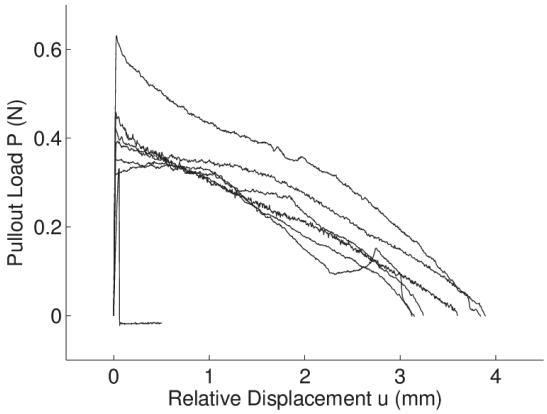

(b) $\phi = 0°$; L_e = 3 to 4 mm

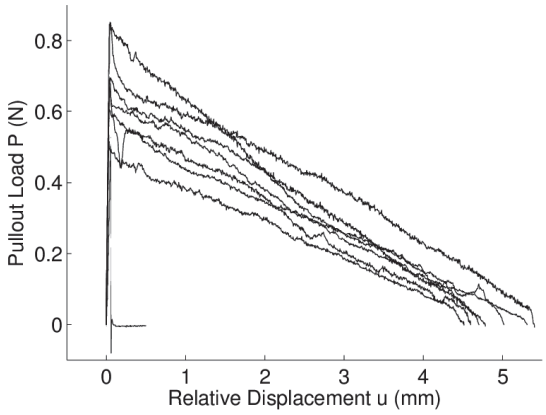

(c) $\phi = 0°$; L_e = 4 to 5.5 mm

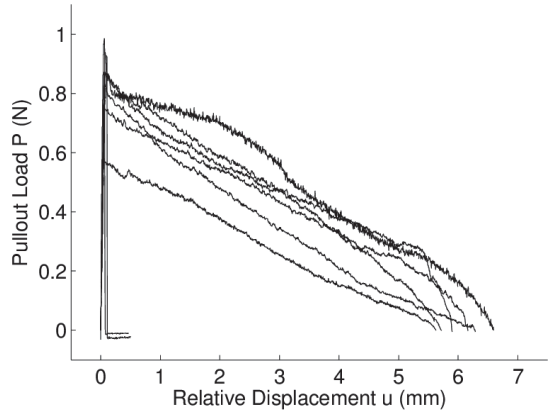

(d) $\phi = 0°$; L_e = 5.5 to 7 mm

Figure 6.15: Complete single fiber pullout test curves for aligned fibers ($\phi = 0°$) with varying embedment lengths (L_e)

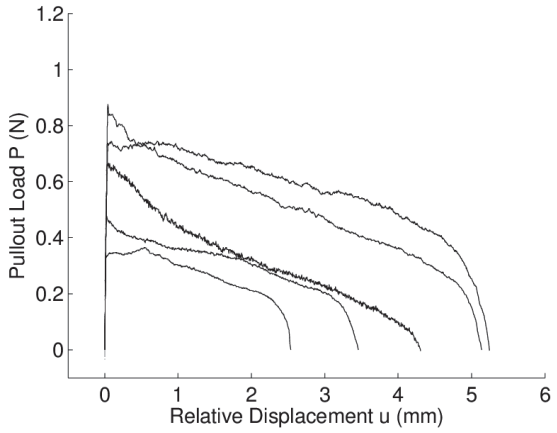

(e) $\phi = 14°$

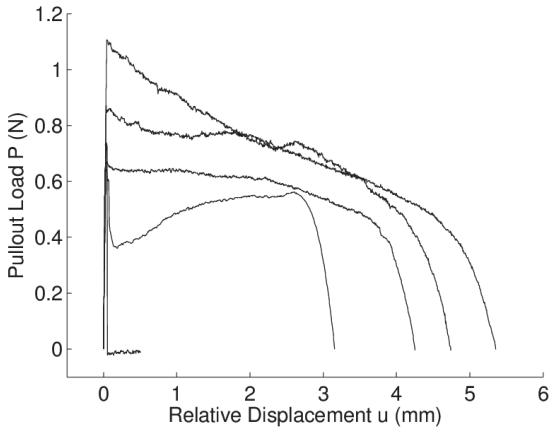

(f) $\phi = 27°$

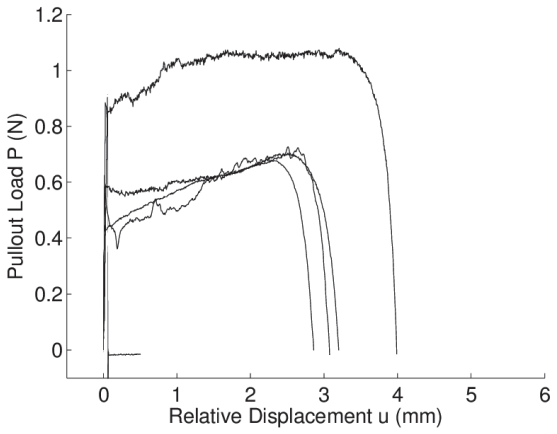

(g) $\phi = 37°$

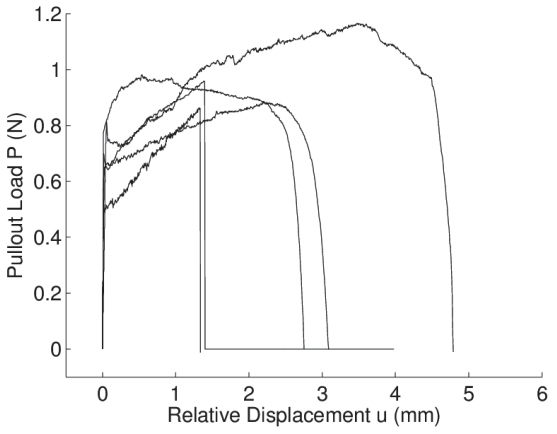

(h) $\phi = 45°$

Figure 6.16: Complete single fiber pullout test curves for various fiber inclination angles (ϕ) and embedment lengths (L_e)

Table 6.1: Summary of single-fiber pullout test results

Figure 6.16 No.	Specimen Number	Embedment Length (L_e) mm	Inclination Angle (ϕ) degree	Peak Debond Load (P_{peak}) N	Slip Hardening Parameter (β)	$\ln \frac{P_{peak}(\phi)}{P_{peak}(0)}$ [a]	$\mu.\phi$ [b] N/m
(a)	1	1.9	0	0.35	0.0305	Not applicable for $\phi = 0°$	Not applicable for $\phi = 0°$
	2	2.1	0	0.32	0.0087		
	3	2.3	0	0.48	0.0242		
	4	2.6	0	0.40	0.0063		
	5	2.6	0	0.28	0.0041		
	6	2.8	0	0.41	0.0059		
	7	3.0	0	0.28	-0.0049		
(b)	8	3.1	0	0.35	0.0023		
	9	3.1	0	0.32	0.0013		
	10	3.2	0	0.43	0.0035		
	11	3.6	0	0.46	-0.0016		
	12	3.8	0	0.63	0.0055		
	13	3.9	0	0.39	-0.0003		
	14	3.9	0	0.34	N/C[c]		
(c)	15	4.5	0	0.53	-0.0023		
	16	4.6	0	0.69	-0.0003		
	17	4.7	0	0.61	-0.0001		
	18	4.8	0	0.85	0.0029		
	19	4.8	0	0.54	N/C		
	20	5.0	0	0.69	0.0002		
	21	5.3	0	0.67	-0.0021		
	22	5.4	0	0.85	0.0012		
(d)	23	5.6	0	0.58	-0.0032		
	24	5.7	0	0.76	0.0018		
	25	5.8	0	0.87	0.0025		
	26	6.1	0	0.85	-0.0020		
	27	6.2	0	1.00	N/C		
	28	6.2	0	0.87	0.0007		
	29	6.5	0	0.89	0.0013		
	30	7.0	0	0.94	N/C		
(e)	31	2.5	14	0.33	Assumed same as the average value for aligned fibers	-0.02	76
	32	3.4	14	0.49		0.06	84
	33	4.3	14	0.66		0.14	17
	34	5.1	14	0.87		0.24	68
	35	5.2	14	0.73		0.04	114
(f)	36	3.1	27	0.64		0.42	225
	37	4.2	27	0.67		0.16	131
	38	4.7	27	0.87		0.31	109
	39	5.1	27	N/C		N/C	N/C
	40	5.3	27	1.11		0.44	84
(g)	41	2.8	37	0.44		0.14	262
	42	3.1	37	0.62		0.41	275
	43	3.2	37	0.59		0.32	239
	44	4.0	37	0.88		0.50	370
	45	4.4	37	N/C		N/C	N/C
(h)	46	2.7	45	0.77		0.74	334
	47	3.1	45	0.70		0.53	291
	48	2.8	45	0.80		0.75	380
	49	4.0	45	0.63		0.17	318
	50	5.5	45	0.90		0.19	219

[a] $P_{peak}(0)$ is the theoretical peak debond load of an aligned fiber ($\phi = 0°$) of the same embedment length as the inclined fiber assuming $\tau_0 = 1.53$ MPa.

[b] $\mu.\phi$ is the product of the inclination hardening parameter μ and inclination angle ϕ (radians).

[c] N/C means "Not Computable" because of premature fiber breakage before complete debonding.

6.5.4 Deduction of Fiber/Matrix Interfacial Bond Properties for Aligned Fibers

The fiber/matrix interfacial bond properties of chemical bond (G_d), frictional bond, (τ_0), and slip-hardening parameter (β) are determined in this section by analyzing the single-fiber pullout test results of the last section using the mathematical formulation of debond-pullout model described above. According to Lin et al,[1] the load carried by the fiber during the debonding (P_{debond}) stage can be modeled using Eq. 6.5 in terms of relative displacement (u) (assuming $V_f \approx 0$ for single fiber and, therefore, the volume weighted modulus ratio, $\eta = 0$).

$$P_{debond} = e^{f\phi}\sqrt{(\tau_0 u + G_d)\pi^2 E_f d_f^3 / 2} \qquad \forall u \le u_0 = \frac{2\tau_0 L_e^2}{E_f d_f} + \sqrt{\frac{8G_d L_e^2}{E_f d_f}} \tag{6.5}$$

where, E_f and d_f are in-situ Young's modulus and average diameter of the fiber (Table 5.2), f is the snubbing coefficient, u_0 is the critical relative displacement at complete debonding of the fiber and computed from fiber/matrix properties. Substituting $u = u_0$ in Eq. 6.5 yields the expression in Eq. 6.6 for peak load (P_{peak}) at complete debonding for aligned fibers ($\phi = 0°$).

$$P_{peak} = \pi d_f \tau_0 L_e + \sqrt{\pi^2 G_d E_f d_f^3 / 2} \tag{6.6}$$

Assuming constant G_d, Eq. 6.6 represents a linear relation between the variables P_{peak} and L_e. This linear relation assumes negligible slip-hardening during the debonding stage due to relatively small slippage compared with that during the pull-out stage. Out of the thirty aligned fiber specimens ($\phi = 0°$ - Figure 6.16a-d), four fibers ruptured before reaching the peak debond load, and are, therefore, excluded from the analysis (marked N/C in Table 6.1). The remaining twenty-six peak debond loads (P_{peak}) of aligned fiber pullout curves are summarized in Table 6.1 and plotted against their respective embedment lengths in Figure 6.17. Using the slope (equal to

0.134) of the best-fit straight line (shown in Figure 6.17) and the fiber diameter (d_f = 28 μm), the frictional bond (τ_0) is computed equal to 1.52 MPa from Eq. 6.6.

The chemical bond (G_d) is approximately equal to 0 J/m^2 due to negligibly small y-intercept (0.011). The absence of chemical bond is expected with PE due to its hydrophobic nature. This is further verified by the pullout curves (Figure 6.14) that show no sudden drop in load after the peak, which would otherwise correspond with the sudden release of energy accompanying the unstable propagation of the chemically debonding zone (modeled as a tunnel crack) as the embedded end of the fiber is approached.

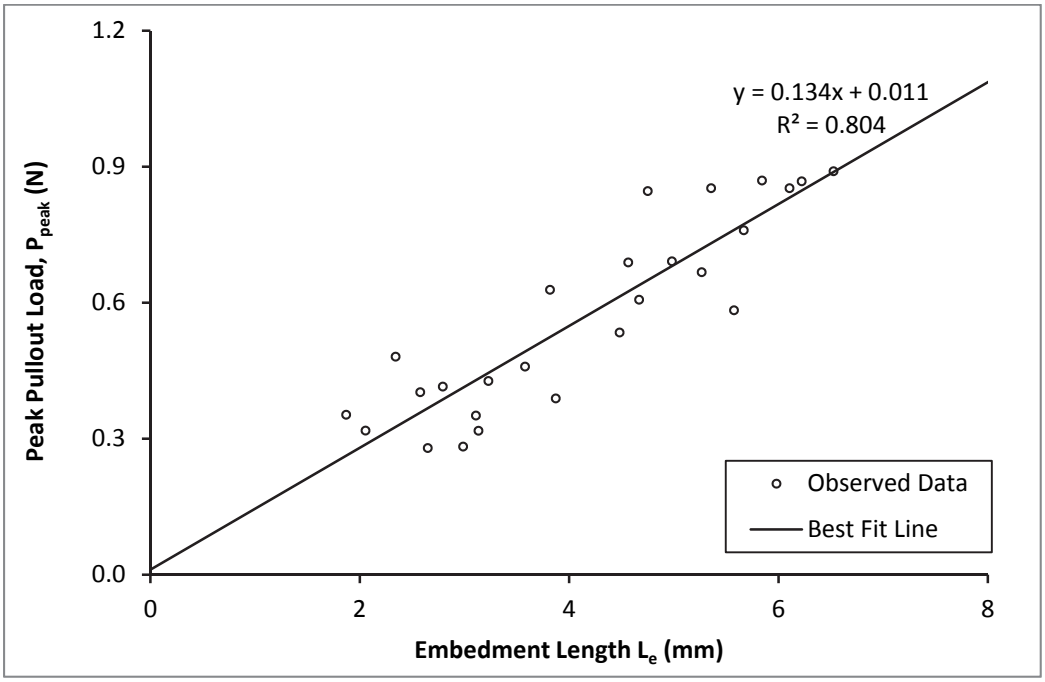

Figure 6.17: Deduction of interfacial bond (τ_0 and G_d)

Next, the slip hardening parameter (β) is determined from the post-peak curvatures of the aligned fiber pullout curves (Figure 6.16a-d). The slip hardening parameter is computed by best-

fitting the observed post-peak (pullout phase) inclined fiber pullout curves with the quadratic (in u) pullout load model in Eq. 6.7[1] using least square estimation with one unknown variable (β).

$$P_{pullout} = \pi d_f \tau_0 [1 + \beta(u - u_0)][L_e - (u - u_0)]e^{f\phi} \qquad \forall u > u_0 \tag{6.7}$$

where $P_{pullout}$ is the pullout load. The values of β thus computed for aligned fibers are summarized in Table 6.1. The average slip hardening parameter in HSHDC is 0.003, which is about two orders of magnitude smaller than that observed in ECC with PVA fibers.[15] The high performance PE fiber used in HSHDC is likely more abrasion resistant than the PVA fiber in ECC. In addition, the matrix "tunnel" surrounding the PE fiber in HSHDC is significantly smoother than ECC due to ultra-fine filler (microsilica) and dense particle packing. Both these factors result in small slip-hardening in HSHDC in spite of a high frictional bond.[16]

6.5.5 Deduction of the Snubbing Coefficient (f) for Inclined Fibers (ϕ > 0°)

The snubbing coefficient (f) is computed from the peak loads at complete debonding of the remaining twenty specimens with inclined fibers (ϕ > 0° - Figure 6.16e-h]. It was shown in a previous study[10] that the snubbing effect can be modeled as:

$$\ln[P_{peak}(\phi) / P_{peak}(0)] = f\phi \tag{6.8}$$

where, $P_{peak}(\phi)$ is the peak load for a specimen with fiber inclination angle of ϕ and embedment length L_e, and $P_{peak}(0)$ is the computed peak load, using Eq. 6.6, for an aligned fiber with the same L_e and the average τ_0 of 1.52 MPa (220 psi) determined above. The LHS of Eq. 6.8 is plotted for 18 out of 20 inclined fiber pullout specimens against ϕ in Figure 6.18 along with the

best-fit straight line (dashed line) – all values are also summarized in Table 6.1. The remaining two specimens ruptured prematurely before complete debonding and are, therefore, excluded from this analysis. The best-fit line (dashed line) does not pass through the origin because the average τ_0 (1.52 MPa) for the aligned fibers used to compute $P_{peak}(0)$ is different from the average interfacial frictional bond of the inclined fibers due to the inherent variability described above. To fit the model in Eq. 6.8, another best-fit line (solid line in Figure 6.18) with y-intercept forced to zero is computed. The change in slope of the two lines is only about 10%. It is assumed that the fibers with inclinations higher than 45° will follow similar trend. The snubbing coefficient is thus determined equal to 0.59.

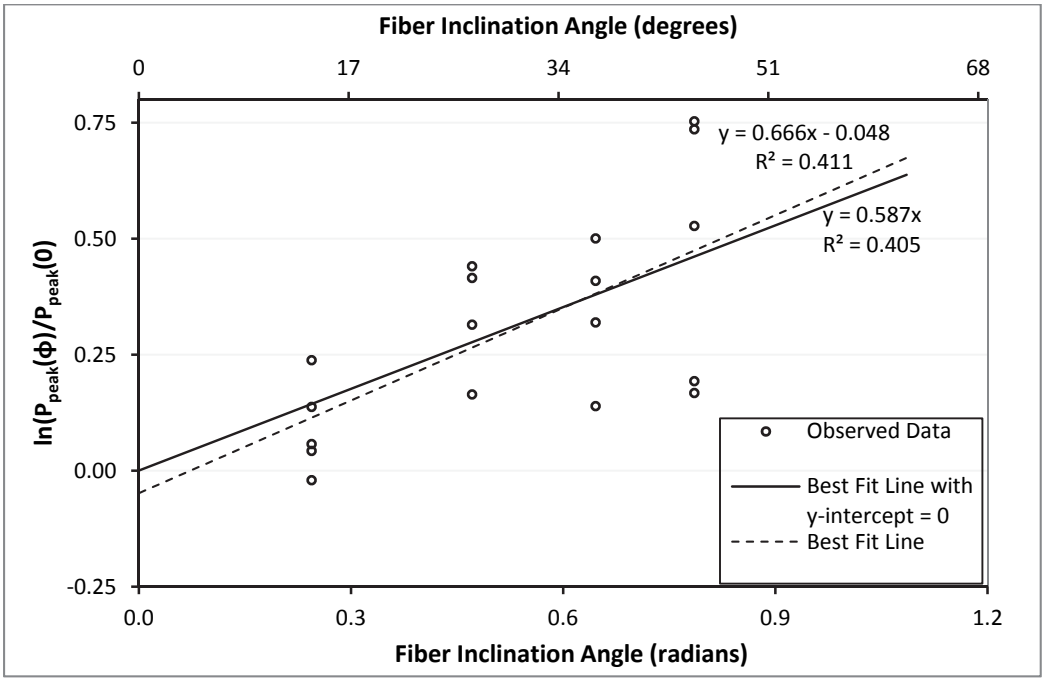

Figure 6.18: Deduction of snubbing coefficient (f)

6.5.6 Proposed Inclination-dependent Hardening Mechanism

The fiber/matrix interaction mechanisms described above and the micromechanical properties deduced therefrom, although largely descriptive of HSHDC, are incomplete in fully capturing the pullout behavior of the inclined PE fibers embedded in HSHDC matrix. Figure 6.19 shows the observed and modeled pullout behaviors of a randomly chosen, representative inclined fiber pullout specimen (number 43 in Table 6.1 with $\phi = 37°$). The computed curve (red dashed curve) using the ECC model (Eqs. 6.5 and 6.7) in Figure 6.19 does not correspond with the observed behavior (black solid curve) in the post-peak pullout phase, assuming the fiber/matrix interaction properties obtained for aligned fibers are the same for inclined fibers. Figure 6.20 shows the difference between the observed and the modeled load (using ECC model) plotted against the post-debonding (post-peak) relative displacement ($u - u_0$). As the difference in load seems to increase linearly with ($u - u_0$), a best-fit straight line closely fitting 90% of the curve is plotted in Figure 6.20 with a slope ($\mu.\phi$) equal to 0.239 N/mm or 239 N/m. Following the same procedure, such slopes ($\mu.\phi$) are obtained for all the inclined fiber pullout specimens and plotted in Figure 6.21 (all values are summarized in Table 6.1) against the fiber inclination angles. A straight line best-fitting these data points and passing through origin is further drawn to determine the inclination hardening parameter (constant for the composite), μ equal to 386 N/(m-rad), which is defined as the increase in pullout load per unit increase in inclination angle and slippage.

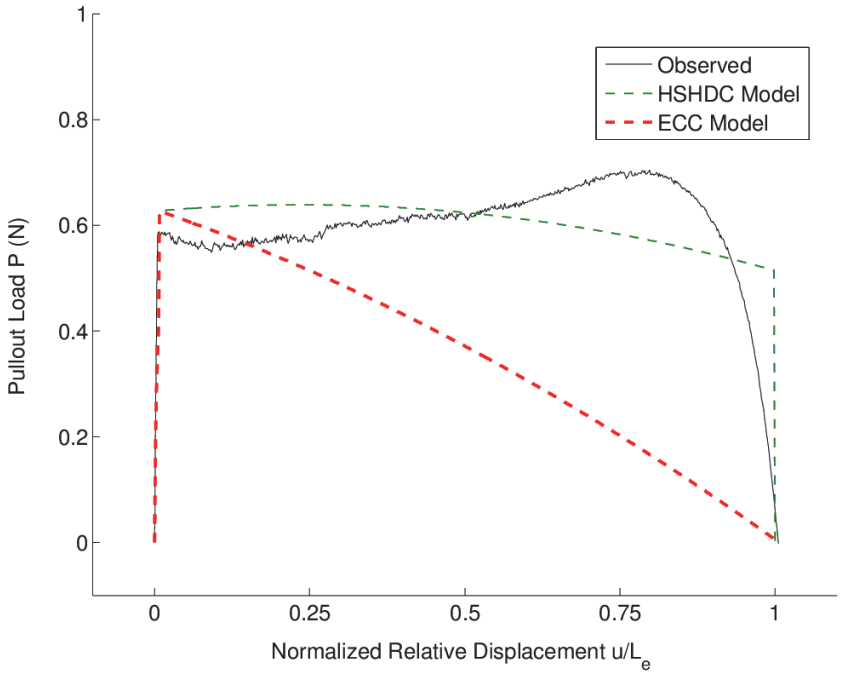

Figure 6.19: Observed and modeled single fiber pullout behavior of specimen number 43

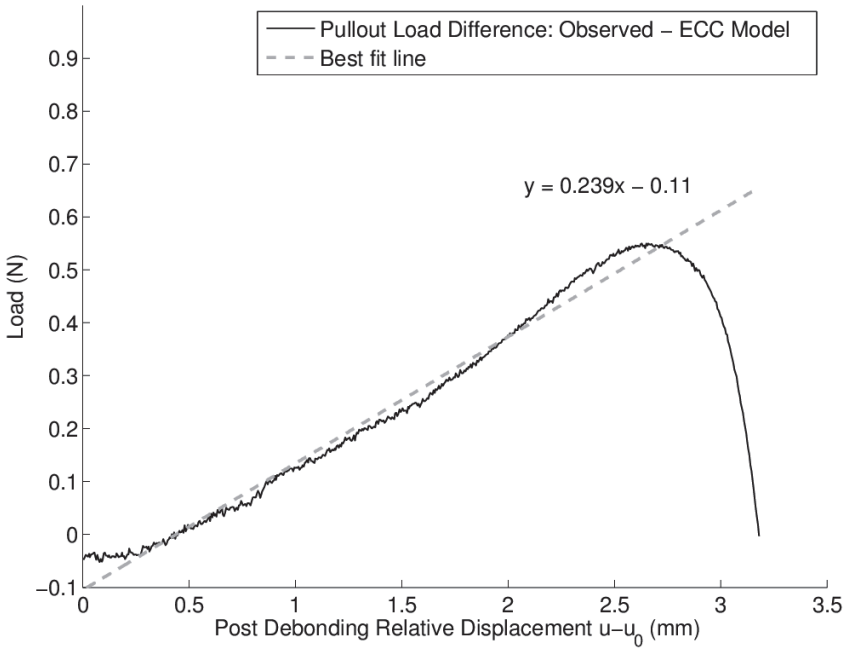

Figure 6.20: Deduction of μ.ϕ for specimen number 43

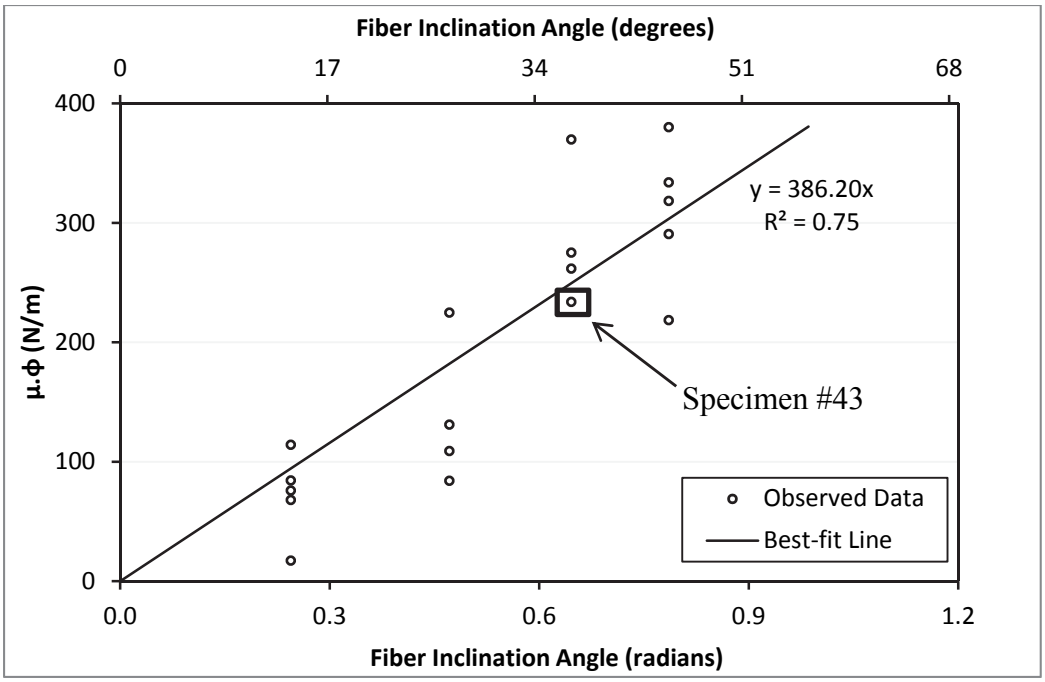

Figure 6.21: Deduction of inclination hardening parameter (μ)

It is assumed in the analytical investigation below that the trend of increasing pullout load with ϕ will continue for fiber inclinations greater than 45° (up to 90°) as the matrix wedge sharpness increases proportionally with ϕ. However, there may be a limiting ϕ beyond which the matrix micro-spalling (discussed below) occurs due to high stress concentration at a sharp matrix wedge, which may lead to a decrease in pullout load at very large ϕ. Further tests at higher inclination angles are required to investigate this possibility. Although for the planar HSHDC specimens used in this study, the number of fibers with very high inclination angles is low (discussed below) and, therefore, the assumption of increasing pullout load with ϕ is largely valid for this analysis.

The pullout phase load in ECC model (Eq. 6.7) can be modified to account for μ as shown in Eq. 6.9. The pullout behavior of specimen 43 computed using HSHDC model [with μ =

386 N/(m-rad)] is plotted as green dashed curve in Figure 6.19, which satisfactorily fits the observed curve.

$$P_{pullout} = \pi d_f \tau_0 [1 + \beta(u - u_0)][L_e - (u - u_0)]e^{f\phi} + \mu.\phi(u - u_0) \qquad \forall u > u_0 \tag{6.9}$$

A plausible physical explanation for the inclination-dependent hardening mechanism is the following. Due to the increase in tip sharpness of the matrix wedge (Figure 6.22a) with increase in fiber inclination angle, there is an increase in the clamping effect at the wedge tip as it digs into the fiber in the transverse direction (depicted exaggeratedly in Figure 6.22b). This clamping force also increases with increase in slip ($u-u_0$) because of the degradation of the fiber cross-section and resulting blockage of the fiber exit point. As a result the cross-section of the embedded fiber segment slowly reduces causing a pencil-tip shape along the length of the fiber (Figure 6.22c). This explanation is supported by the electron micrographs (Figure 6.23), displaying the pulled out ends of representative fibers which had been embedded in the matrix at each of the inclinations used in this study. These micrographs were obtained using a scanning electron microscope (SEM). The micrographs clearly show that the degradation of the fiber increases (in spite of similar embedment lengths) with inclination angle and slip, which supports the mathematical formulation (Eq. 6.9) and the above physical explanation.

This mechanism is in contrast with the micro-spalling phenomenon[17] (Figure 6.22d) observed in polymer fiber pullout in moderate strength ECC matrix. In ECC, the fiber is stronger than the matrix wedge tip and spalls the matrix causing a slight softening of the pullout load curve, whereas in HSHDC, the very high strength matrix (almost twice the K_m as ECC) resists the spalling and, instead, clamps the fiber causing hardening of the pullout load curve.

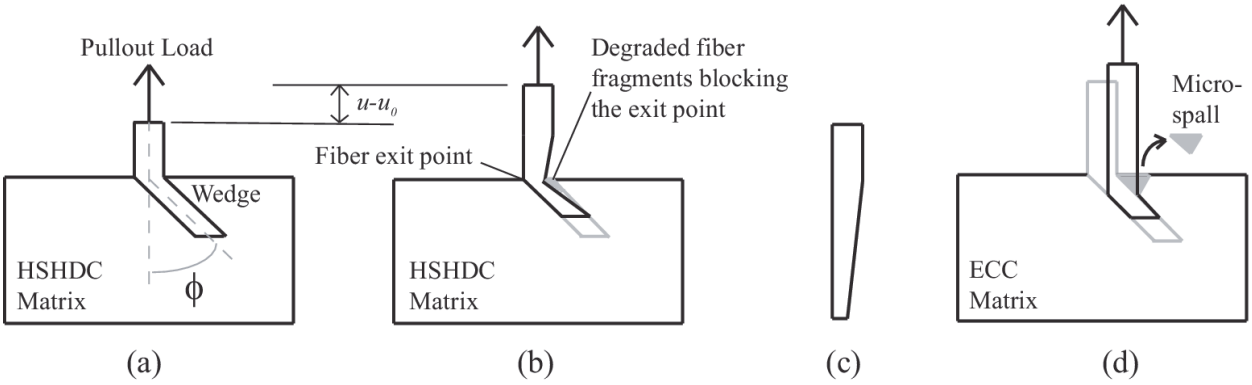

Figure 6.22: Schematic depiction of inclination-dependent hardening mechanism
(a) HSHDC matrix wedge at $u = u_0$ (b) fiber degradation at $u > u_0$ (c) pencil-tip shaped pulled out fiber end (d) micro-spall phenomenon observed in ECC

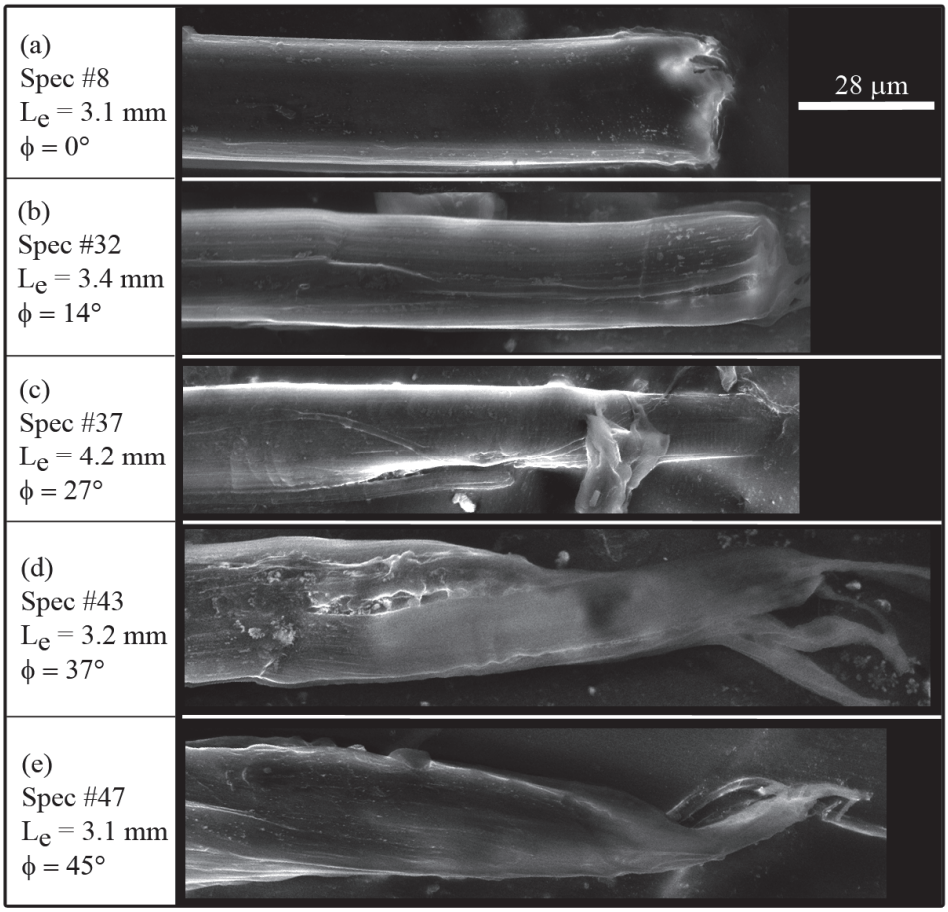

Figure 6.23: SEM generated micrographs of the embedded ends of the pulled out fibers

6.5.7 Single-crack Test Results

The bridging stress (σ)-crack opening (δ) relation (σ-δ curve) of HSHDC was empirically determined from six single crack tests with notched rectangular coupons (Figure 6.13) tested under direct tension. All the six measured curves (solid curves) are shown in Figure 6.24, along with two computed curves (shown by dashed curves) based on an analytical model detailed in Section 6.6. Two distinct phases are observed in the measured curves. Initially, when the ligament of a notched rectangular coupon is un-cracked, the tensile load rises elastically with applied displacement as the cementitious matrix carries majority of the load. This is accompanied by proportional increase in stress intensity factor at the notch tip. Once the stress intensity factor exceeds the fracture toughness of the matrix, sudden crack propagation occurs resulting in loss of tensile stress previously carried by the matrix (Figure 6.24). After this point, applied tensile load is in equilibrium with bridging stress σ transferred by the fibers across the crack. The tensile load increases again with increasing crack opening δ until the collective bridging capacity of the fibers is exhausted. The bridging stress gradually decreases after this point as increasing number of fibers are either pulled out or broken. For the multiple cracking criteria discussed below, only the portion of the σ-δ curve up to the bridging capacity is relevant. The average bridging capacity (peak of σ-δ curve) thus measured at the notched sections of the six specimens is 13.8 MPa.

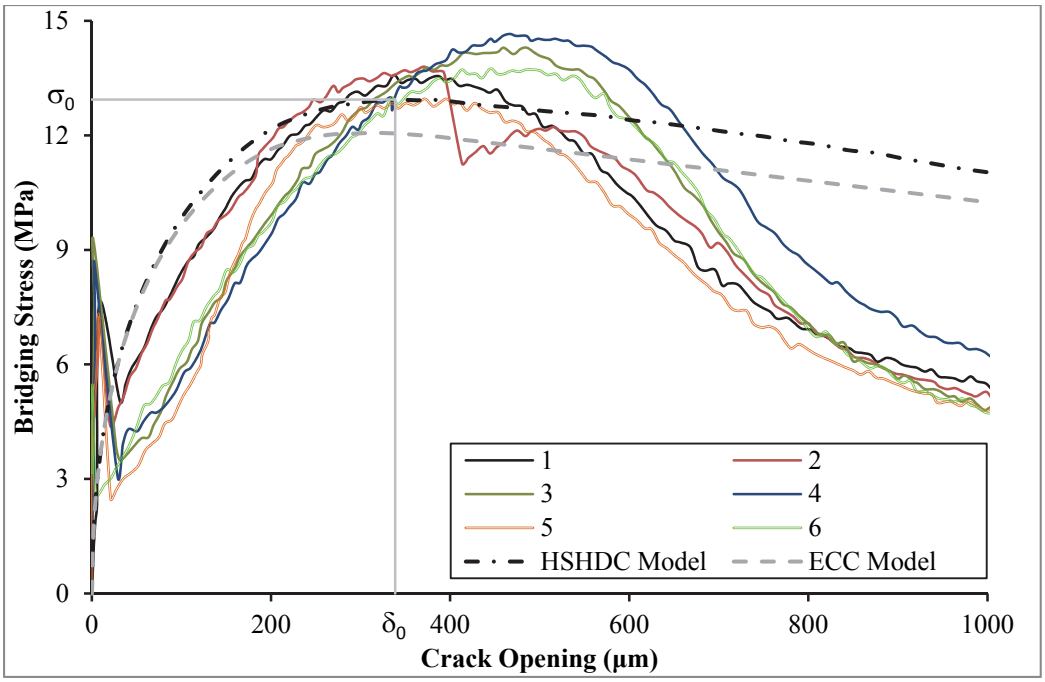

Figure 6.24: Measured and computed (using ECC and HSHDC models) crack bridging relations of HSHDC rectangular coupons

6.6 Analytical Investigation of the Micromechanical Behavior of HSHDC

The objective of this analytical investigation is to predict the single-crack bridging stress (σ) - crack opening (δ) relation of HSHDC using a statistical scale-linking model[2] and analyze its implications on the composite tensile behavior of HSHDC reported in Chapter 5. The deduced fiber/matrix interaction properties and fiber distribution parameters reported in previous sections are used as inputs in this model. Mathematically, the bridging stress, σ(δ) as a function of crack opening is given by:

$$\sigma(\delta) = \frac{V_f}{A_f} \int_0^{\pi/2} \int_0^{(L_f/2)\cos(\phi)} P(u)\, p(z)\, p(\phi)\, dz\, d\phi \tag{6.10}$$

where the crack opening (δ) is equal to the sum of the fiber pullout relative displacements (u_1 and u_2) on both sides of the crack (compatibility). P(u) is the single fiber pullout load modeled by Eqs. (6.5) and (6.9). By enforcing the equilibrium condition $P(u_1) = P(u_2)$, u_1 and u_2 are determined, as detailed in Yang et al.[17] L_e is the shorter of the two embedment lengths on either side of the crack. p(z) is the distribution of embedded fiber's centroidal distance from the crack plane (assumed $2/L_f$).[2] The probability density function for fiber inclination angles $p(\phi)$ for dogbones, coupons, and theoretical distributions (2D and 3D) is taken from Section 6.5.5.

6.6.1 Comparison with Observed Single-crack Behavior of Notched Coupons

Eq. 6.10 is numerically computed to yield the average σ-δ relation (for V_f = 2%) of HSHDC coupon specimens using both the HSHDC model (incorporating inclination-dependent hardening) and the ECC model. Both the modeled curves are plotted (dashed lines) in Figure 6.24 along with experimentally determined σ-δ relations using single-crack tests. The σ-δ curve computed using HSHDC model fits the observed curves more closely than the curve computed using ECC model, which further supports the inclination-dependent hardening mechanism propose in Section 6.5.6. The bridging capacity, σ_0 (at δ_0 = 338 μm), of the computed curve is 13.0 MPa for HSHDC model and 12.0 MPa for ECC model.

The computed curve using HSHDC model is initially steeper than the experimental curves. This behavior has been previously explained by Cook-Gordon effect,[17] in which premature fiber/matrix interface debonding results in wider crack opening. The Cook-Gordon effect is not included in the computed σ-δ curves. In spite of higher initial slope of the computed

σ-δ curve, it achieves a bridging capacity (13.0 MPa) similar to experimental curves as it is governed by the strength and geometry of the fibers, interfacial bond, and hardening properties. The higher slope of the computed σ-δ curve results in a conservative estimate of the complimentary energy (discussed below), which is desirable for checking the energy criterion of steady-state crack propagation. The softening branch (post-peak) of the computed curve overshoots the observed bridging stress. This may be caused by the frictional pullout load decay with additional slippage caused by the Cook-Gordon effect in the softening phase.[18] Overall, the computed σ-δ curve of HSHDC shows a good agreement with the experimental curves and is a useful tool for evaluating strain hardening criteria, as discussed below.

6.6.2 Implications for Multiple Cracking

The σ-δ curves are computed (using Eq. 6.10) for all orientation distributions – coupons, dogbones, 2D, and 3D (discussed in Section 6.4.3) – at average V_f (2%), and plotted in Figure 6.25. In order to account for the variation in V_f across sections, σ-δ curves are also computed for min(V_f) and max(V_f) for all orientation distributions. The min(V_f) for dogbones and coupons of HSHDC is determined as 1.6% and 1.7%, respectively, through statistical analysis in Section 6.4.3. Therefore, the max(V_f) for dogbones and coupons is taken as 2.4% and 2.3%, respectively. Although, the fiber distribution is expected to be more homogeneous for 2D and 3D (following similar trend from dogbone to coupon with larger cross-sectional area), the bounds of V_f are assumed conservatively to be the same as that for coupons. Using these bounds of V_f, the σ-δ curves are computed at min(V_f) and max(V_f), in addition to average V_f, and the results are discussed below.

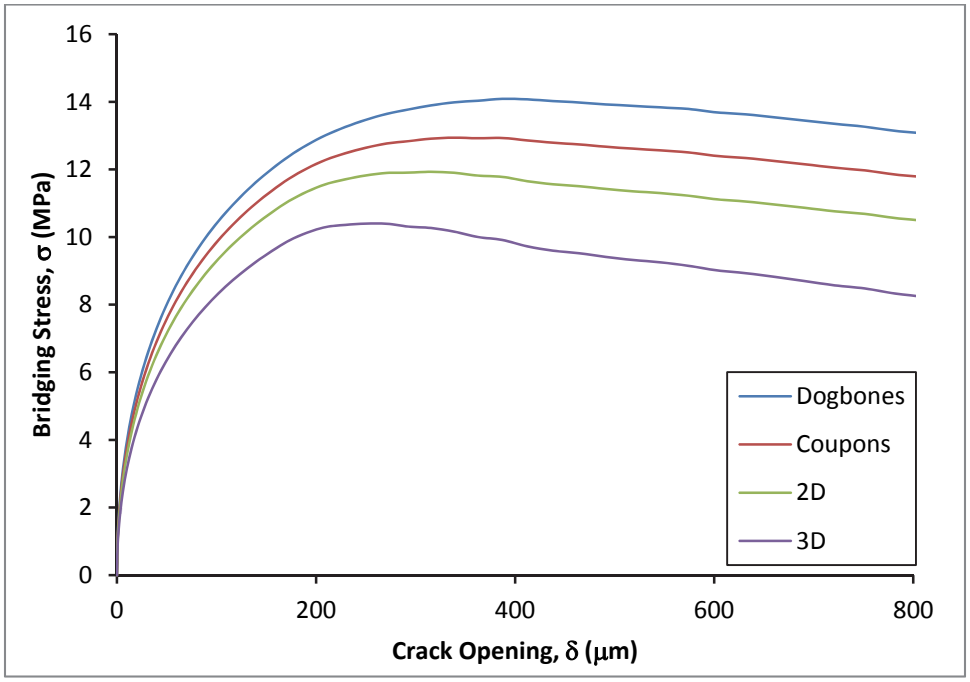

Figure 6.25: Computed σ-δ curves at V_f = 2% for various orientation distributions

The results of the σ-δ analysis for all orientation distributions, and the corresponding bridging capacity (σ_0) and complementary energy (J_b') (meaning of σ_0 and J_b' is explained in Section 2.5) are summarized in Table 6.2. It is observed that both σ_0 and J_b' are proportional to the volume fraction (V_f) of the fibers for all orientation distributions. Therefore, the min(σ_0) and min(J_b') are achieved with min(V_f).

Min(σ_0) and min(J_b') are divided respectively by the first crack strength [$\sigma_{ci(fc)}$] and crack tip toughness (J_{tip}) of HSHDC to compute the pseudo-strain hardening indices, $PSH_{strength}$ and PSH_{energy} (discussed in Section 4.2), which determine the feasibility of multiple cracking and tensile ductility. $\sigma_{ci(fc)}$ is 8.3 MPa as reported in Table 5.4, and J_{tip} can be approximately

computed as K_m^2/E_c (details in Section 3.6). The matrix fracture toughness K_m of HSHDC matrix is determined following the ASTM E399[19] procedure – same as that used to determine the K_m of COR-TUF matrix in Chapter 3. K_m of HSHDC matrix, determined from four notched beams, is 1.10 MPa√m with COV of 2.1%. Using E_c equal to 48.4 GPa reported in Table 5.4, along with K_m, J_{tip} for HSHDC is computed equal to 25.0 J/m^2. It can be observed in Table 6.2 that both the PSH indices for all orientation distributions are much greater than 1. Thus, the PSH indices of HSHDC not only satisfy the two necessary conditions for multiple cracking (Eqs. 2.1 and 2.2), but also stronger conditions of $PSH_{strength} > 1.2$ and $PSH_{energy} > 3$ (Section 4.2) which facilitate robust multiple cracking and tensile ductility for all orientation distributions, with the exception of $PSH_{strength}$ for 3D distribution (discussed below).

In spite of narrower margin between the $\sigma_{ci(fc)}$ and min(σ_0) estimated for 3D fiber distribution compared to other distributions, the 3D HSHDC specimens such as beams and split-tension cylinders exhibit saturated multiple cracking in their respective tension regions as reported in Chapter 5. A greater degree of homogeneity in dispersion of fibers in larger 3D specimens as compared to other distributions may be one of the reasons – it may be recalled that min(V_f) of 1.7% (same as that for coupons) is assumed for min(σ_0) calculation for 3D distribution. In addition, the computational analysis seems to underestimate the min(σ_0) compared to the observed tensile stress capacity of dogbone specimens as discussed below. These two reasons may explain the robust multiple cracking observed in the 3D HSHDC specimens despite low, yet greater than 1, $PSH_{strength}$ index.

Table 6.2: σ-δ analysis results

		Dogbones	Coupons	2D	3D
min(V_f)	σ_0 (MPa)	11.3	11.0	10.2	8.83
	J_b' (J/m^2)	776	682	581	468
avg(V_f)	σ_0 (MPa)	14.1	12.9	11.9	10.4
	J_b' (J/m^2)	969	802	682	550
max(V_f)	σ_0 (MPa)	16.9	14.9	13.7	12.0
	J_b' (J/m^2)	1161	922	785	633
min(σ_0) (MPa)		11.3	11.0	10.2	8.83
min(J_b') (J/m^2)		776	682	581	468
$PSH_{strength}$ [a]		1.36	1.32	1.23	1.06
PSH_{energy} [b]		31.0	27.3	23.2	18.7

[a] $PSH_{strength} = \min(\sigma_0)/\sigma_{ci(fc)}$; $\sigma_{ci(fc)}$ = 8.3 MPa from Table 5.4.
[b] $PSH_{energy} = J_b'/J_{tip}$; $J_{tip} \approx K_m^2/E_c$; K_m = 1.10 MPa$\sqrt{m}$ & E_c = 48.4 GPa from Table 5.4.

6.6.3 Comparison with Direct Tension Test Results of HSHDC Dogbones

The σ-δ analysis of dogbones is used in this section to gain insights into the tensile stress capacity and crack widths observed in HSHDC dogbone specimens (reported in Section 5.3.2). The computed σ-δ curves of HSHDC dogbones for min(V_f), avg(V_f), and max(V_f) are plotted in Figure 6.26. The cross-section with min(V_f) has the minimum bridging capacity which is expected to be the lower bound for the tensile stress capacity (σ_{ult}) of dogbone specimens as it is highly unlikely that the cross-section with min(V_f) will also have a large enough flaw to trigger a crack. It may be recalled that the probability of a cross-section to have min(V_f) is itself very low (5% - Section 6.4.3). This is supported by the fact that the σ_0 (peak) of min(V_f) curve in Figure 6.26 is 11.3 MPa, whereas the min(σ_{ult}) observed for HSHDC dogbones specimens is 13.6 MPa (for specimen #2 in Figure 5.6). Thus, the σ-δ analysis can be useful tool to provide a reasonable

conservative estimate of the ultimate tensile stress capacity of HSHDC dogbones, or other specimens with known fiber distribution.

Similar to the tensile stress capacity, the expected range of crack widths in HSHDC specimens can be estimated through the σ-δ analysis. For this purpose, a horizontal line is drawn parallel to the crack width axis in Figure 6.26. The crack widths corresponding to the points where the line intersects the σ-δ curves corresponding to min(V_f), avg(V_f), and max(V_f) are the estimates of minimum, average, and maximum crack widths in HSHDC dogbones near tensile stress capacity (σ_{ult}). The estimated crack widths determined in this way are: δ_{min} = 82 μm, δ_{avg} = 140 μm, and δ_{max} = 387 μm. The observed average crack width in HSHDC dogbone specimens at σ_{ult} is about 180 μm (Table 5.4), which is close to the estimated δ_{avg} from σ-δ analysis.

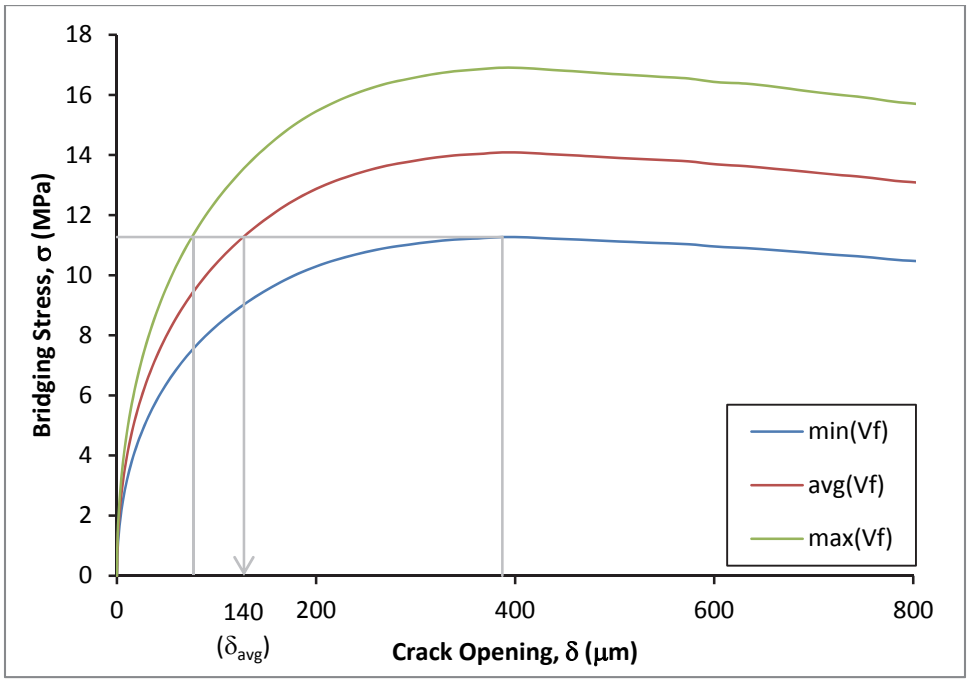

Figure 6.26: Computed σ-δ curves for HSHDC dogbones at various fiber volume fractions

6.7 Summary and Conclusions

The average micro-scale fiber/matrix interaction properties of HSHDC determined in this chapter are summarized in Table 6.3. The following conclusions can be drawn from the investigations in this chapter.

- The microstructure of HSHDC was observed using SEM and the elemental composition of various phases was determined using EDS analysis. The ITZ between the fiber/matrix was identified using the EDS analysis, but further observational evidence, e.g. in form of TEM images or nano-indentation, is needed to confirm the findings of this study.

- A weighted combination of lognormal distribution and a Gaussian distribution best-fits the observed distribution of largest flaw size across various HSHDC dogbone specimen cross-sections. The average largest flaw size (expected value of the combined distribution) is about 1.3 mm in HSHDC which is about 65% smaller than that observed in ECC.

- The fiber distribution in HSHDC dogbones and coupons was characterized by three parameters, namely, orientation distribution $p(\phi)$, dispersion coefficient (α), and number (or volume fraction) distribution $p(V_f)$. $p(\phi)$ in HSHDC dogbones and coupons is a combination of 2D and 3D distributions, limited by the specimen geometry. Majority of the fibers are oriented at inclination angles (ϕ) between 18° and 63°. Such moderately inclined fibers increase the bridging capacity of dogbones and coupons compared to theoretical 2D and 3D distributions. The average fiber dispersion coefficient (α_{avg}) determined using Lee et al[7] for HSHDC dogbones and coupons

is 0.33 and 0.34, respectively. These values are about 10-20% smaller than that observed in ECC with good fiber dispersion.[7,20] The min(V_f) estimated for HSHDC specimens with average volume fraction of 2% is 1.6% for dogbones and 1.7% for coupons, assuming Gaussian distribution [$p(V_f)$] of fiber volume fraction across various HSHDC cross-sections.

- The experimentally determined average interfacial frictional bond (τ_0) between the PE fiber and HSHDC matrix is 1.52 MPa. Such high interfacial frictional bond facilitated by dense particle packing of the very high strength matrix, accompanied by a negligible chemical bond (G_d), results in a high complementary energy (J_b') favorable for macroscopic strain-hardening response of HSHDC under direct tension. For comparison, the measured τ_0 for the same fiber in a moderate strength matrix has been reported to be 0.54-0.76 MPa.[21] Other fiber/matrix interaction properties of HSHDC determined in this research are snubbing coefficient ($f = 0.59$) and slip hardening parameter ($\beta = 0.003$). All micromechanical properties show wide scatter due to material inhomogeneity (similar to ECC) at micro-length scale.

- A new inclination-dependent hardening mechanism of fiber pullout in HSHDC is proposed, as the existing fiber/matrix interaction mechanisms developed for ECC are insufficient in completely describing the experimentally observed inclined fiber pullout behavior of PE fibers embedded in a very high strength HSHDC matrix. The ECC micromechanical model in the pullout phase is modified to incorporate this mechanism. The SEM micrographs provide evidence for this mechanism and its mathematical formulation. The closer match of the experimental curves to the computed σ-δ relation for coupons obtained using the modified HSHDC pullout model when compared with that from the ECC model provides further support

to this mechanism. The newly defined inclination hardening parameter, μ (constant property of the composite), is 386 N/(m-rad) for HSHDC.

- The σ-δ analysis provides a reasonable estimate of the ultimate tensile stress capacity and crack width range of HSHDC dogbones loaded under direct uniaxial tension. The $\min(\sigma_0)$ for predicted for HSHDC dogbones is 11.3 MPa, which provides a lower bound for the ultimate tensile stress capacity of HSHDC dogbones. Similarly, the observed average crack width in HSHDC dogbone specimens at σ_{ult} is about 180 μm, which is close to the estimated δ_{avg} of 140 μm from σ-δ analysis.

- The $\min(\sigma_0)$ and J_b' determined for HSHDC for all orientation distributions satisfy the necessary conditions for robust multiple cracking, thus providing a rational basis for the observed composite tensile ductility of HSHDC. It is further concluded that in spite of a higher matrix toughness compared with ECC, HSHDC maintains tensile ductility by enhanced fiber bridging with a strong interfacial frictional bond and fiber strength.

Table 6.3: Summary of micro-scale properties of HSHDC

Property	**Specimens**
Frictional bond (τ_0)	1.52 MPa
Chemical bond (G_d)	0 J/m^2
Slip hardening parameter (β)	0.003
Snubbing Coefficient (f)	0.59
Inclination hardening parameter (μ)	386 N/(m-rad)

References

1. Lin, Z., Kanda, T. & Li, V. C. (1999) "On Interface Property Characterization and Performance of Fiber Reinforced Cementitious Composites" *Concrete Science and Engineering*, 1, 173-84.

2. Li, V. C., Wang, Y. & Backer, S. (1991) "A Micromechanical Model of Tension-Softening and Bridging Toughening of Short Random Fiber Reinforced Brittle Matrix Composites" *Journal of Mechanics and Physics of Solids*, 39(5), 607-25.

3. Li, V.C. (1993) "From Micromechanics to Structural Engineering – The Design of Cementitious Composites for Civil Engineering" *JSCE Journal of Structural Mechanics and Earthquake Engineering*, 10(2), 37-48.

4. Sakulich, A. R. & Li, V. C. (2011) "Nanoscale characterization of engineered cementitious composites (ECC)" *Cement and Concrete Research*, 41, 169-75.

5. Scheydt, J. C. & Muller, H. S. (2012) "Microstructure of Ultra High Performance Concrete and its Impact on Durability" In Proceedings of *3rd International Symposium on UHPC and Nanotechnology for High Performance Construction Materials*, Kassel, Germany, March 7-9, 2012, pp. 349-56.

6. Lowke, D., Stengel, T., Schiebl, P. & Gehlen, C. (2012) "Control of Rheology, Strength and Fiber Bond of UHPC with Additions – Effect of Packing Density and Addition Type" In Proceedings of *3rd International Symposium on UHPC and Nanotechnology for High Performance Construction Materials*, Kassel, Germany, March 7-9, 2012, pp. 215-24.

7. Lee, B. Y., Kim, J. K., Kim, J. S. & Kim, Y. Y. (2009) "Quantitative Evaluation Technique of Polyvinyl Alcohol (PVA) Fiber Dispersion in Engineered Cementitious Composites" *Cement and Concrete Composites*, 31(6), 408-17.

8. ACI. (2008) "Sample Standard Deviation" In *Building Code Requirements for Structural Concrete and Commentary (ACI 318-08)*, Farmington Hills, MI: American Concrete Institute, pp. 66-67.

9. Mindess et al. (2003) "ACI Approach to Variability" In *Concrete* (2nd ed.), Upper Saddle River, NJ: Pearson Education Inc, pp. 405-409.

10. Li, V. C., Wang, Y. & Backer, S. (1990) "Effect of Inclining Angle, Bundling and Surface Treatment on Synthetic Fiber Pullout from Cement Matrix" *Composites Journal*, 20(2), 132-40.

11. Katz, A. & Li, V. C. (1996) "A Special Technique for Determining the Bond Strength of Carbon Fibers in Cement Matrix by Pullout Test" *J. of Materials Science Letters*, 15, 1821-23.

12. Paegle, I. & Fischer, G. (2011) "Evaluation of Standardized Test Methods to Characterize Fiber Reinforced Cement Composites." In Proceedings of *SHCC-2*, Filho et al. (Eds.), 12-14 December, 2011, Rio de Janeiro, Brazil, pp. 9-16.

13. Li, V. C., Wang, S. & Wu, C. (2001) "Tensile Strain-Hardening Behavior of PVA-ECC" *ACI Materials Journal*, 98(6), 483-492.

14. Li, V. C., Wu, C., Wang, S., Ogawa, A. & Saito, T. (2002) "Interface Tailoring for Strain-Hardening PVA-ECC" *ACI Materials Journal*, 99(2), 463-472.

15. Wang, S. & Li, V.C. (2007) "Engineered Cementitious Composites with High-Volume Fly Ash" *ACI Materials Journal*, 104(3), 233-241.

16. Wang, Y., Li, V. C. & Backer, S. (1988) "Modeling of Fiber Pull-out from a Cement Matrix" *Journal of Cement Composites and Lightweight Concrete*, 10(3), 143-149.

17. Yang, E. H., Wang, S., Yang, Y. & Li, V. C. (2008) "Fiber-bridging Constitutive Law of Engineered Cementitious Composites" *JCI J. of Advanced Concrete Technology*, 6(1), 1-13.

18. Li, V. C., Stang, H. & Krenchel, H. (1993) "Micromechanics of Crack Bridging in Fibre Reinforced Concrete" *Materials and Structures,* (26), 486-494.

19. ASTM (2003) "Test method for plane-strain fracture toughness of metallic materials" West Conshohocken, PA: ASTM.

20. Ranade, R., Stults, M. D., Lee, B. Y. & Li, V. C. (2011) "Effects of Fiber Dispersion and Flaw Size Distribution on the Composite Properties of PVA-ECC" Parra-Montesinos et al. (Eds.) In *Proceedings of HPRCC-6*, 19-22 June, 2011, Ann Arbor, MI, pp. 106-113.

21. Li, V. C. & Maalej, M. (1996) "Effect of Plasma Treatment of Polyethylene Fibers on Interface and Cementitious Composite Properties" *J. American Ceramics Society*, 79(1), 74-78.

PART III: MATERIAL AND STRUCTURAL RESILIENCE

CHAPTER 7: RATE EFFECTS IN HIGH STRENGTH-HIGH DUCTILITY CONCRETE

7.1 Introduction

As this doctoral research aims to develop a material for infrastructure resilience under extreme loads, it is imperative to not only investigate the performance of HSHDC under conventional pseudo-static rate (10^{-6} to $10^{-4}s^{-1}$ – simulating service load conditions) but also at high strain rates (> $0.1s^{-1}$) approaching extreme loading conditions such as impacts and blasts. While the behavior of the HSHDC under pseudo-static loading is extensively investigated in Part II of this thesis, this part (Part III comprising of Chapters 7 and 8) focuses on the behavior of HSHDC at strain rates several orders of magnitude higher than the pseudo-static rate. In this chapter, the effects of increasing strain rate on tensile performance of HSHDC at composite- and micro-scales are evaluated, which are used to investigate the behavior of HSHDC slabs under drop-weight impact and simulated blast loads in the next chapter.

The objectives of the research presented in this chapter are: (1) to investigate the influence of strain rate on the direct tension behavior of HSHDC, (2) to determine the influence

of strain rate on the fiber/matrix interaction properties and matrix fracture toughness of HSHDC, and (3) to investigate whether the micro-scale rate effects explain the composite-scale rate effects through σ-δ analysis (similar to that detailed in Section 6.6).

With the above objectives, this chapter is organized as follows. First, a literature review of the rate effects in normal concrete, ECC, and COR-TUF is presented. This is followed by the experimental details of the direct uniaxial tension tests on HSHDC dogbone specimens (for composite-scale investigation) and single fiber pullout specimens (for micro-scale investigation), along with fracture toughness tests on HSHDC matrix specimens. The observed behaviors in HSHDC at both scales are discussed and compared with the behavior of ECC. Following this, an analytical investigation linking the micro-scale behavior to the composite-scale behavior of HSHDC is presented. Finally, the key insights from this study are documented in the conclusions section.

7.2 Review of Rate effects in Concrete, ECC, and COR-TUF

7.2.1 Concrete

The high rate (dynamic) loading causes increase in apparent strength of concrete both in tension and compression. High rate loading implies that either the load or the displacement (or both) on a structure changes extremely fast with time in extreme events such as impacts, blasts, hurricanes, and earthquakes. A collection of results from past studies on high rate tests of

concrete tensile strength is shown in Figure 7.1. The figure also shows typical strain rates of various loading types. Similarly, the strain rate effects on concrete compressive strength are shown in Figure 7.2. The increase in dynamic strength of concrete seems to be almost twice in tension than in compression, especially at higher strain rates approaching impacts and blasts.

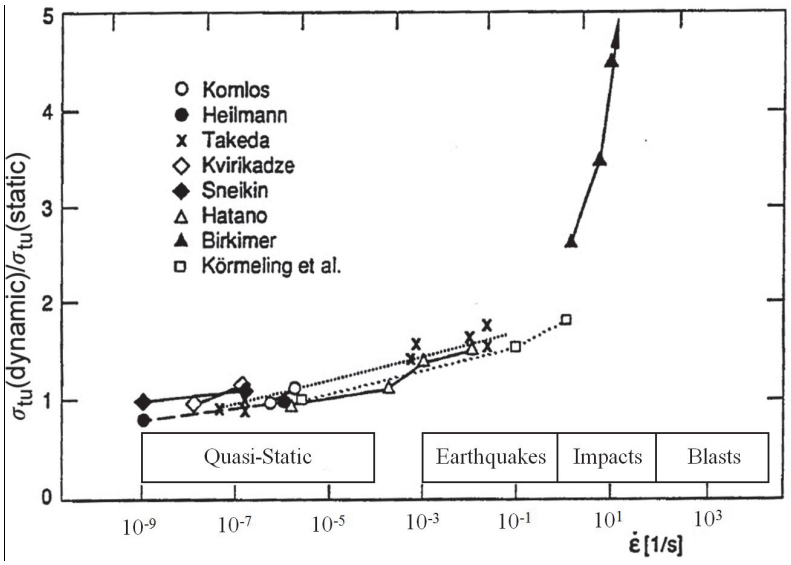

Figure 7.1: Effect of strain rate on tensile strength of concrete (Source: Chandra[1])

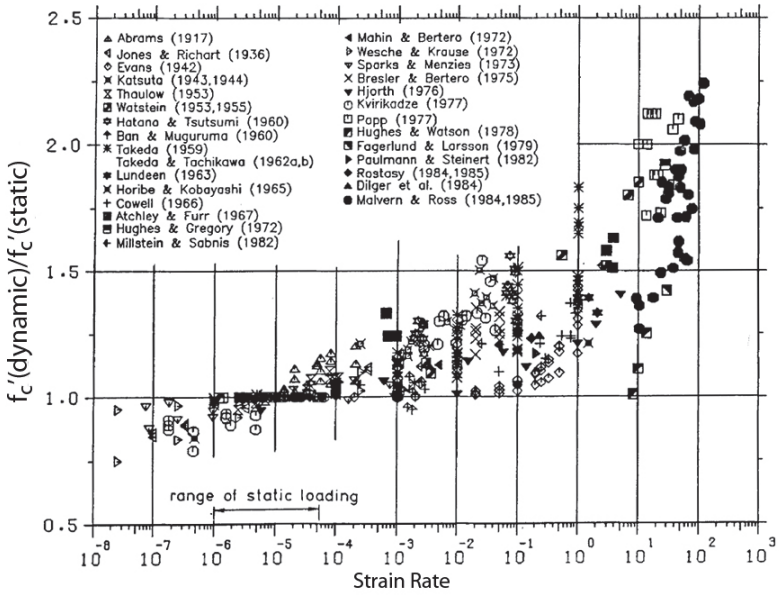

Figure 7.2: Effect of strain rates on compressive strength of concrete (Source: Bischoff & Perry[2])

Since 1950's, numerous researchers across the world have attempted to identify the reasons behind the rate sensitivity of concrete; however, there is still a lack of consensus among the research community due to extremely complex material behavior at various length scales and difficulty of testing at high load/strain rates. The plausible reasons for rate sensitivity of concrete discussed in the literature at various length scales are mentioned below.

Macro-scale: At macroscopic scale of structural elements, concrete can be idealized as homogenous and isotropic material with a single initial crack. The material near the crack tip experiences amplified stress. If the stress intensity factor near the crack tip reaches the critical value of fracture toughness (Irwin's fracture criterion), the crack propagates and the strain energy released is consumed in the microcracking, aggregate debonding and pulling out, as well as other inelastic processes in the damage zone surrounding the crack tip. The time rate of transfer of strain energy to crack tip inelastic zone is limited by a finite crack propagation velocity[3] that is further dependent on the applied strain rate on the structural element.[4]

The macroscopic explanation of the rate sensitivity of concrete is based on comparing the crack propagation velocity and the Rayleigh wave velocity. As the crack grows, the stresses and strains in front of the crack tip redistribute (increase), which also takes a finite amount of time as the new configuration communicates with the rest of the intact structure through Rayleigh waves. If the crack propagates at a velocity approaching the Rayleigh wave velocity, the stress intensity in front of the new location of crack tip does not change significantly by the time the crack tip reaches there. This leads to an apparent increase in strength due to weakening of crack driving forces (the energy release rate G) at the crack tip.[5] Many researchers have, however, observed

that the crack propagation velocities in concrete are significantly smaller than (≤ 15%) the Rayleigh wave velocity for strain rates up to $1s^{-1}$.[6,7] Inertia effects, which are directly proportional to acceleration, are also considered by some researchers to be significant at very high strain rates. Thus, the macroscopic analysis explains the increase in strength at high rates, but it does not satisfactorily explain its magnitude.

Meso-scale: The meso-scale (size of coarse aggregate) explanations of rate effects on concrete are based on the observations of crack paths and fracture process zone. At high strain rates, the cracks tend to cut through the aggregates instead of meandering around them along the weak aggregate-CSH interface.[5,8] Greater toughness of the aggregates than the interface leads to higher overall material toughness. At very high strain rates, however, an opposing phenomenon of reduction in fracture process zone is observed leading to a decrease in material toughness.[7,9] The fracture process zone in front of the crack tip is due to micro-cracking, which absorbs additional energy and enhances the toughness of the material. Very high strain rates do not allow enough time for micro-cracking to occur resulting in an under-developed fracture process zone and brittle behavior. This effect is, however, reduced in extremely brittle mortars, which do not possess large process zone even at slow strain rates. The strength of concrete is directly proportional to its toughness and, therefore, the aforementioned meso-scale effects on the toughness of concrete show similar effects on strength. The meso-scale explanation thus predicts an increase in material strength due to fracturing of coarse aggregates but a decrease in strength due to reduction of process zone size.

Nano-/Micro-scale: At nano-/micro-scales, the crack growth is considered as breakage of bonds between two particles (atoms or molecules) governed by thermodynamics.[8] Before fracture, particles are in permanent vibratory motions around their equilibrium positions that represent minimum potential energy states. There is an activation energy barrier which has to be overcome by the crack driving energy to break the bond between the two particles. Such energy transfer to the vibrating particles takes a finite time. At high strain rates, the material shows higher resistance to crack propagation as it fails to respond thermodynamically as fast as the strain change (thermal inertia).[10] This results in an increase in dynamic strength. Another effect at the microstructure level is that of creep or viscoelastic behavior of hardened cement paste. This especially affects extremely slow tests where stress relaxation occurs in front of the crack tip reducing the size of the process zone, thereby making the material response more brittle. Overall, the nano-/micro-scale explanations predict an increase in strength at high loading rates and a brittle response at very slow rates.

Thus, in the literature, there are several theories explaining the rate dependency of concrete strength; however, every theory is limited in its applicability. It is plausibly the combined effect of some or all of the above phenomena, which leads to the observed increase in compressive and tensile strengths of concrete with strain rate.

In both ECC and COR-TUF, fiber reinforcement is used, which improves both the static and dynamic performance of unreinforced concrete. The fibers transfer stress back and forth to the matrix through interfacial bond and, therefore, it is important to study the rate effects on the interfacial bond and viscoelastic nature of polymer fibers (especially in ECC).

7.2.2 ECC

A descending trend of tensile ductility with increasing strain rate was found by Yang[11] for unmodified M45-ECC (however, Yang also demonstrated that the material can be re-tailored using the principles of micromechanics to mitigate these detrimental rate effects). The rate dependence of unmodified M45-ECC under direct uniaxial tension at strain rates ranging from 10^{-5} to 10^{-1} s^{-1} is shown in Figure 7.3. Tensile ductility of unmodified M45-ECC reduces from 3% to 0.5% at the highest strain rate. Both first cracking strength and ultimate tensile strength were found to increase with increasing strain rate. Rate effects at smaller length scales were investigated to explain this composite behavior.

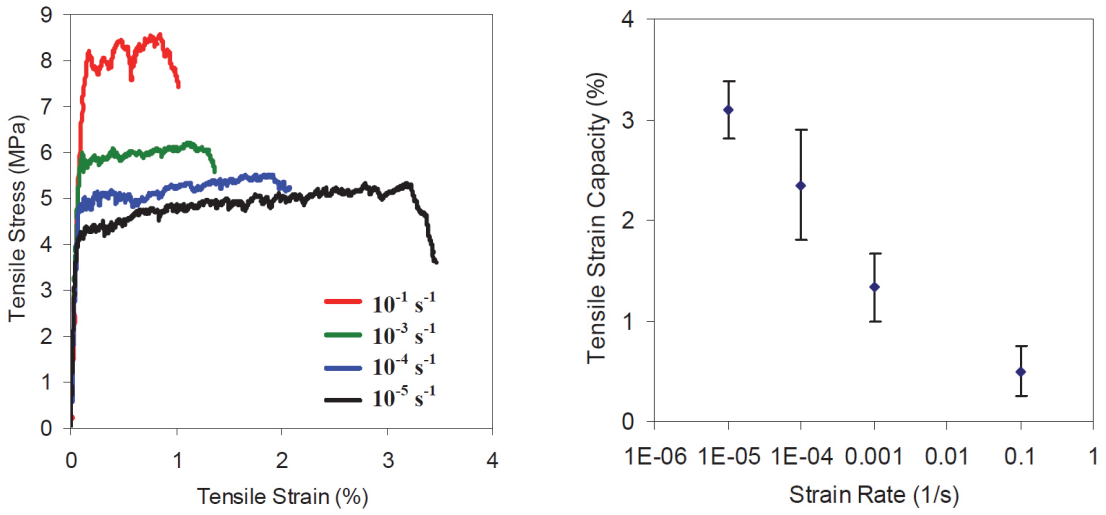

(a) (b)

Figure 7.3: Rate dependence of M45-ECC (a) uniaxial tensile stress-strain response (b) ultimate tensile strain capacity (Source: Yang[11])

The micromechanical rate effects on fiber, matrix, and interfacial properties were investigated by Yang[11,12] using single fiber pullout tests and matrix fracture toughness (notched

beam) tests. It was found that fiber modulus, fiber strength, matrix toughness, and interfacial chemical bond (G_d) increase with the loading rate. However, the frictional bond (τ_0) and the slip-hardening coefficient (β) of the fiber/matrix interface showed negligible rate dependencies over the range of loading speed tested (Figure 7.4). Increase in fiber modulus and interfacial chemical bond cause a reduction in the complimentary energy (J_b') (by increasing the slope and y-intercept of the σ-δ curve), which is detrimental to the steady-state cracking.

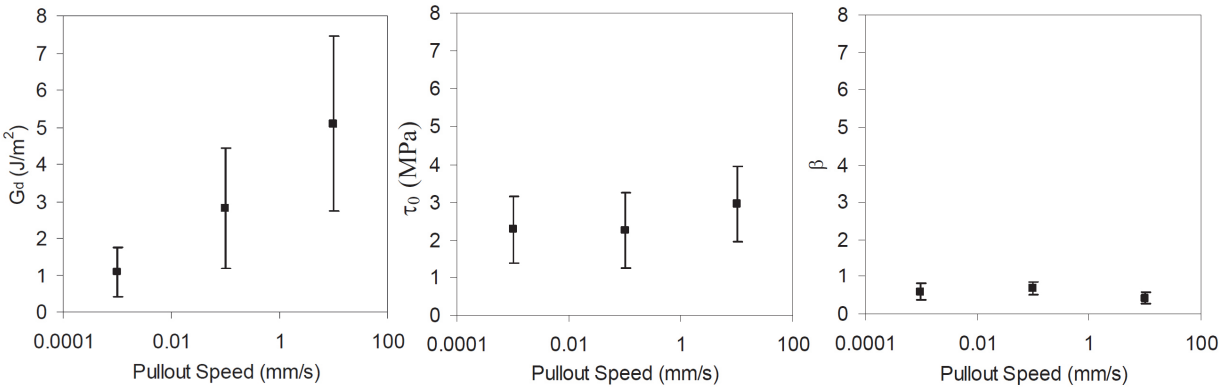

Figure 7.4: Rate dependence of interfacial parameters of ECC (Source: Yang[11])

Yang[11] showed that with the knowledge of the above rate effects on the micromechanical parameters, the material can be retailored to enhance the ductility at high rate loading. One of the target objectives was to reduce the chemical bond which was found sensitive to rate effects. This was achieved by using Poly-ethylene (PE) spectra fibers in lieu of PVA fibers as PE fibers are known to form almost no chemical bond with the cementitious matrix, unlike the PVA fibers. Also, corbitz sand, instead of silica sand, was used to lower the chemical bond because of the presence of carbon particles in corbitz sand. The fracture toughness of matrix was reduced through enhanced use of fly ash and introduction of lightweight aggregate (glass bubbles). This

was done in order to increase the PSH index J_b'/J_{tip} to promote pseudo strain hardening. Using these tailoring strategies aimed at reducing the chemical bond, the extreme tensile ductility of ECC (3 to 6%) at high strain rates up to 0.1 s^{-1} was restored.

Similar results were reported in Maalej et al[13] where the behavior of a hybrid-fiber ECC (1.5 vol% PE and 0.5 vol% steel fibers) subjected to dynamic tensile loading was investigated. Figure 7.5 shows the tensile stress-strain behavior of the hybrid-fiber ECC subjected to six different loading rates.

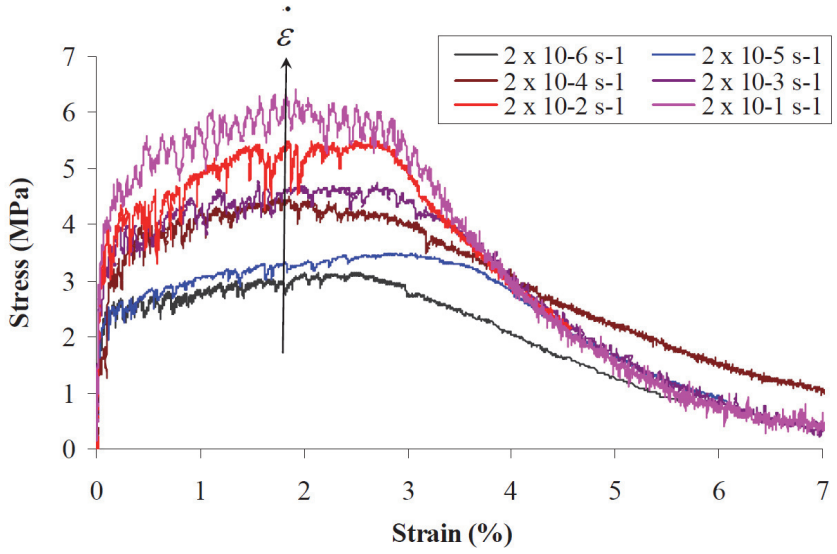

Figure 7.5: Uniaxial tensile stress-strain curves of rate tailored ECC using hybrid fibers (Maalej et al[13])

An opposite trend of increasing tensile ductility at very high strain rates (10 to 50 s^{-1}) was observed by Mechtcherine et al.[14] Microscopic analysis revealed that at such extremely high rates, the strength of the fiber increases and more fibers tend to pullout instead of rupturing. It was hypothesized in this study that the interfacial bond and fiber strength increase at different rates with applied strain rates. For strain rate lower than 0.01 s^{-1}, increase in interfacial bond is

more pronounced and the fiber strength becomes a limiting factor. On the other hand, for strain rates higher than 10 s^{-1}, the fiber strength increases sufficiently to bridge the increased stress transferred from the matrix through the interface. The difference in rate dependence of the interfacial bond and fiber strength causes the ECC tensile ductility to have concave-up dependence on loading rate with minima around 0.1-1 s^{-1}.

From the above discussion, it can be observed that the macroscopic properties of ECC such as strength and ductility are affected by high loading rates, which can be explained by the rate dependent changes in fiber, matrix, and interfacial properties at microscopic scales. Based on such insights into the micro-scale behavior, material retailoring is possible in order to achieve high tensile ductility at high strain rates.

7.2.3 COR-TUF

As described in Chapter 3, COR-TUF consists of very high compressive strength matrix and hooked steel fibers. Similar to ECC, the micro-scale fiber-matrix interaction at high velocities is important in determining the rate effects on the macroscopic properties of COR-TUF. In the literature, there is very limited published work on micromechanical analysis of COR-TUF even under pseudo static loading, let alone at higher strain rates. Kim[15] investigated the micromechanics of hooked steel fiber (same as in COR-TUF) pullout embedded in a high strength matrix ($f_c' \approx 90$ MPa). The magnitudes of effect might be different in COR-TUF but it is expected to show similar trends at high rates. The hooked ends of the steel fibers provide mechanical anchorage in addition to the frictional bond due to clamping action of the matrix

along the embedded fiber. The steel fibers, however, do not form any chemical bond with the cementitious matrix. As a result, no significant rate effect was found on the pullout of the hooked steel fibers in this study.[15]

In summary, the rate effects in cementitious materials have a significant impact on strength, ductility, and energy absorption of the material. Materials designed optimally for pseudo static loading may not perform as well under dynamic loading and vice-versa, but they can be retailored using micromechanics based design principles for achieving the desired macroscopic performance.

7.3 Experimental Investigation

Three types of specimens were cast in this study: (1) dogbones made of HSHDC composite, (2) single fiber pullout specimens with PE fibers embedded in HSHDC matrix, and (3) notched-beam specimens of HSHDC matrix (without fibers) for fracture toughness measurement. Details of the material ingredients and mix proportions of HSHDC are given in Section 5.2.1. The geometry, preparation, and testing procedure of the dogbone specimens of HSHDC are described in Section 4.4 and that of the single fiber pullout specimens are described in Section 6.5.2. The details of fracture toughness tests are given in Sections 3.3. In this study, six dogbone specimens, forty single fiber pullout specimens, and four notched beams were tested for each strain rate (detailed below) to reliably determine the average properties and their

variations at composite- and micro-scales. All specimens were cured following the HSHDC curing procedure described in Section 5.2.4.

The direct tension tests were performed at six different tensile strain rates: $10^{-4}s^{-1}$, $10^{-3}s^{-1}$, $10^{-2}s^{-1}$, $10^{-1}s^{-1}$, $1s^{-1}$, and $10s^{-1}$. The corresponding tensile displacement rates (gauge length of 90 mm – Figure 4.1) were 9 μm/s, 90 μm/s, 0.9 mm/s, 9 mm/s, 90 mm/s, and 0.9 m/s, respectively. The single fiber pullout tests were also performed at these six displacement rates. While the direct tension tests ranging from 9 μm/s to 9 mm/s were performed on the 100 kN load capacity hydraulic test system described in Section 4.4, the direct tension tests at 90 mm/s and 0.9 m/s were performed on a 10 kN load capacity electrical test system (described in Section 6.2.2), as the maximum possible displacement rate achievable with the 100 kN system is only 10 mm/s. Verification tests were performed at 9 mm/s on both test systems and no significant difference was observed in the composite tensile performance. The single fiber pullout tests at all the six tensile displacement rates were performed on the 10 kN system. The notched beams used for fracture toughness tests proved to be too bulky for the 10 kN system and, therefore, the fracture toughness tests were performed using the 100 kN system only at four different compressive displacement rates exponentially increasing from 9 μm/s to 9 mm/s. In this study, a lost motion assembly shown in Figure 7.6 for all tests conducted at displacement rates greater than 1 mm/s. The 'gap' shown in Figure 7.6 is set such that the actuator of the tensile test system achieves the desired displacement rate before engaging the specimen.

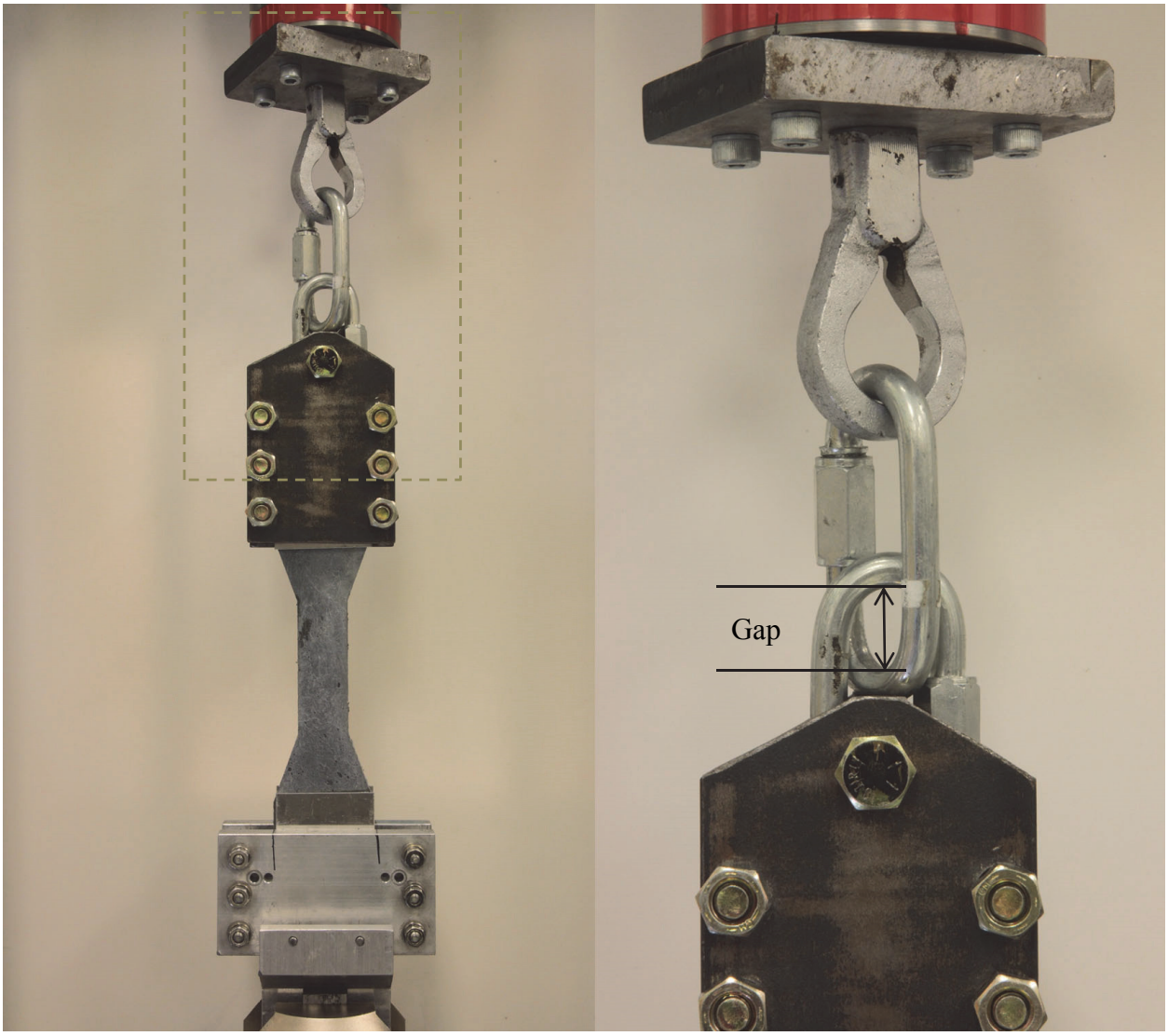

Figure 7.6: Direct tension test setup with lost motion assembly

7.4 Experimental Results and Discussion

7.4.1 Composite Response

One representative direct tension stress-strain curve for each of the six strain rates investigated in this study is shown in Figure 7.7. The multiple cracking process and the shape of the stress-strain curves is similar to the pseudo-static tensile response described in Section 5.3.2. A summary of the relevant tensile properties all 36 dogbone specimens (6 dogbones for each strain rate) is given in Table 7.1. These results in terms of average behaviors and variations are discussed below.

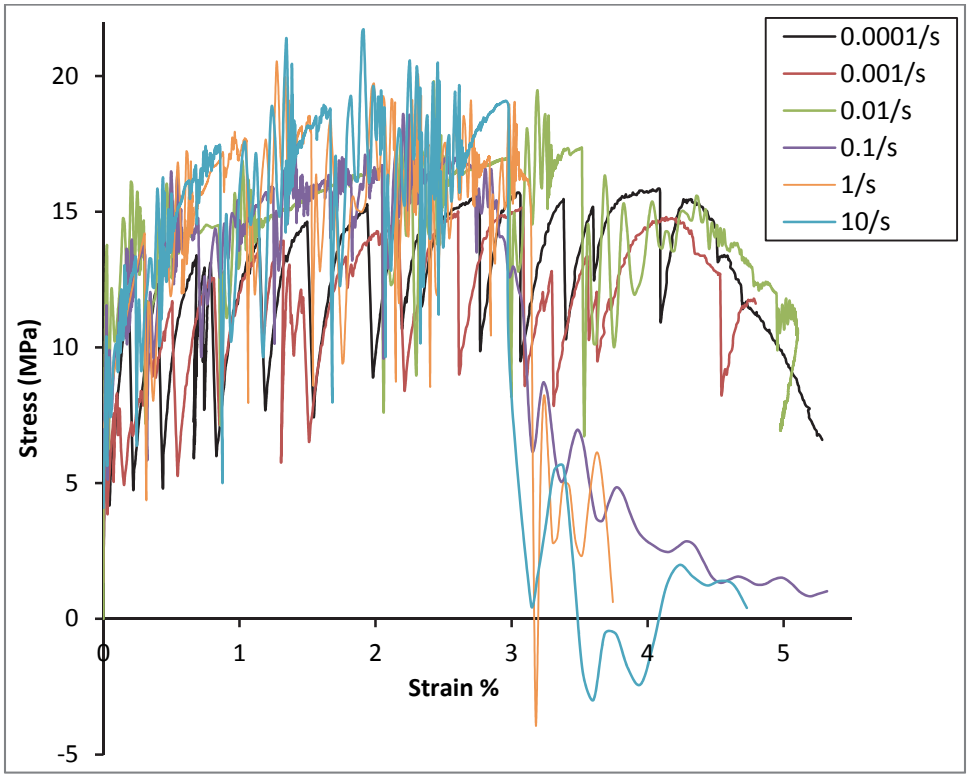

Figure 7.7: Direct tension response of HSHDC dogbones at various strain rates

Table 7.1*: Summary of properties of HSHDC dogbone specimens under direct tension

Strain Rate s^{-1}	Specimen No. #	First Crack Strength σ_{fc} (MPa)	Ultimate Tensile Strength σ_{ult} (MPa)	$PSH_{strength}$ σ_{ult}/σ_{fc}	Tensile Strain Capacity ε_{tu} (%)	Average Residual Crack Width δ_{avg} (μm)
0.0001	1	8.6	13.6	1.58	4.3	160
	2	9.1	15.0	1.64	3.7	
	3	6.6	15.6	2.36	4.8	
	4	8.7	13.3	1.53	4.0	
	5	7.5	15.8	2.09	4.7	
	6	8.2	13.5	1.64	3.9	
	Avg.	8.1	14.5	1.80	4.2	
	St. Dev.	0.9	1.1	0.3	0.4	
	COV	11%	8%	19%	10%	
0.001	7	7.2	14.3	1.99	3.3	150
	8	6.5	15.9	2.47	4.8	
	9	9.2	14.2	1.54	3.3	
	10	7.7	16.8	2.18	4.2	
	11	8.6	14.9	1.73	3.6	
	12	6.6	15.9	2.39	4.1	
	Avg.	7.6	15.3	2.05	3.9	
	St. Dev.	1.1	1.0	0.37	0.6	
	COV	14%	7%	18%	16%	
0.01	13	11.0	17.1	1.55	2.4	140
	14	7.6	17.6	2.32	3.1	
	15	7.2	15.4	2.14	2.8	
	16	9.2	15.2	1.65	3.7	
	17	8.7	17.4	2.01	3.5	
	18	9.8	15.1	1.55	4.5	
	Avg.	8.9	16.3	1.87	3.3	
	St. Dev.	1.4	1.2	0.33	0.8	
	COV	16%	7%	18%	23%	

* Continued on the next page.

Table 7.1: Summary of properties of HSHDC dogbone specimens under direct tension

Strain Rate s^{-1}	Specimen No. #	First Crack Strength σ_{fc} (MPa)	Ultimate Tensile Strength σ_{ult} (MPa)	$PSH_{strength}$ σ_{ult}/σ_{fc}	Tensile Strain Capacity ε_{tu} (%)	Average Residual Crack Width δ_{avg} (μm)
0.1	19	9.7	19.0	1.96	3.1	120
	20	8.2	18.7	2.27	3.7	
	21	10.1	16.9	1.67	3.2	
	22	10.9	18.6	1.70	2.2	
	23	12.7	15.4	1.22	1.9	
	24	6.8	16.1	2.38	3.1	
	Avg.	9.7	17.5	1.87	2.9	
	St. Dev.	2.1	1.5	0.43	0.7	
	COV	21%	9%	23%	23%	
1	25	7.4	16.5	2.23	3.9	110
	26	11.6	20.9	1.80	3.7	
	27	8.5	21.6	2.54	3.4	
	28	14.4	20.5	1.42	1.9	
	29	11.8	16.0	1.35	2.3	
	30	12.6	20.2	1.60	2.4	
	Avg.	11.1	19.3	1.82	2.9	
	St. Dev.	2.6	2.4	0.47	0.8	
	COV	24%	12%	26%	28%	
10	31	16.0	20.2	1.26	1.7	110
	32	10.6	22.5	2.12	3.6	
	33	11.7	21.5	1.85	2.6	
	34	8.4	16.2	1.93	3.3	
	35	14.6	22.8	1.56	2.2	
	36	13.1	20.5	1.56	2.9	
	Avg.	12.4	20.6	1.71	2.7	
	St. Dev.	2.8	2.4	0.31	0.7	
	COV	22%	12%	18%	26%	

In Figure 7.8, it can be observed that both average first crack strength (σ_{fc}) and average ultimate tensile strength (σ_{ult}) of dogbone specimens steadily increase with strain rate. From the lowest to the highest strain rate, while σ_{fc} increases by about 53% (8.1 MPa at 0.0001/s to 12.4 MPa to 10/s), σ_{ult} increases by about 42% (14.5 MPa at 0.0001/s to 20.6 MPa to 10/s). The plausible reasoning behind these increases based on the changes in fiber/matrix interaction properties and matrix fracture toughness are discussed in Section 7.5, respectively. As a result of the comparable increases in both σ_{fc} and σ_{ult}, the average strength index for pseudo-strain hardening ($PSH_{strength}$ – refer Section 4.2) remains almost constant around 1.8 (± 0.2) at all strain rates (Table 7.1).

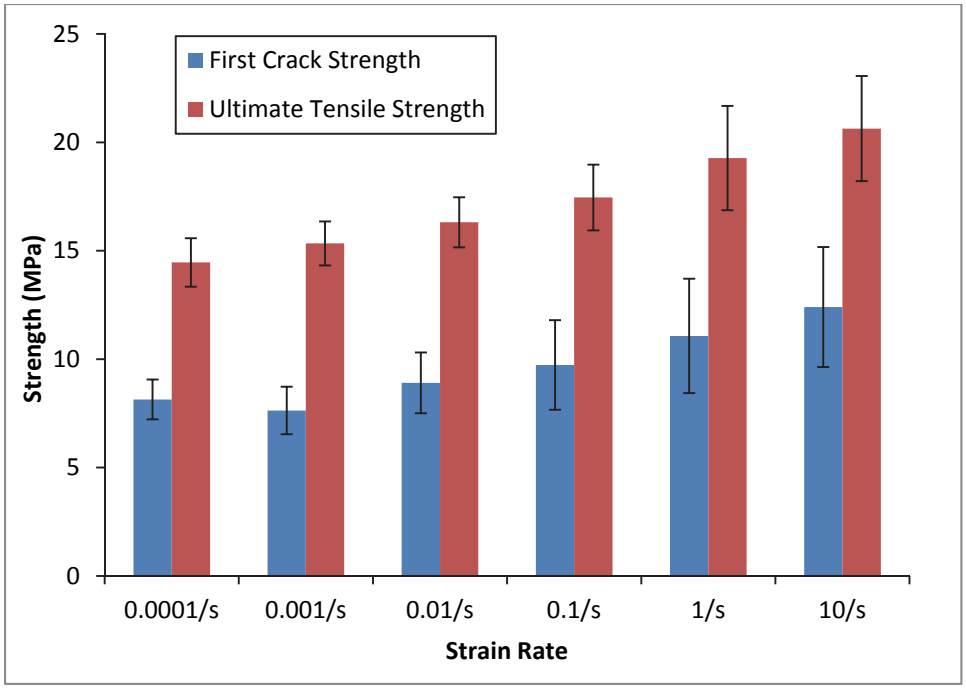

Figure 7.8: Rate effects on first crack strength and ultimate tensile strength of dogbone specimens

In spite of a relatively constant average $PSH_{strength}$ for various strain rates (which maintains the same number of cracks), the tensile strain capacity decreases with increasing strain rate up to 0.1/s and plateaus after that, as observed in Figure 7.9. The PSH_{energy} >> 1 at all rates and, therefore, does not limit steady-state cracking. Given these facts, the observed decrease in tensile strain capacity of about 31% (ε_{tu} is 4.2% at 0.0001/s and 2.9% at 0.1/s) can be attributed to corresponding reduction of about 25% in average residual crack width from 160 μm at 0.0001/s to 120 μm at 0.1/s. Similar to the trend in tensile strain capacity, the average residual crack width also plateaus after the strain rate of 0.1/s (Figure 7.9). Further insights into the micro-scale behavior that result in reducing crack widths and, therefore, tensile strain capacities at higher strain rates are presented below in Sections 7.4.2 and 7.5.

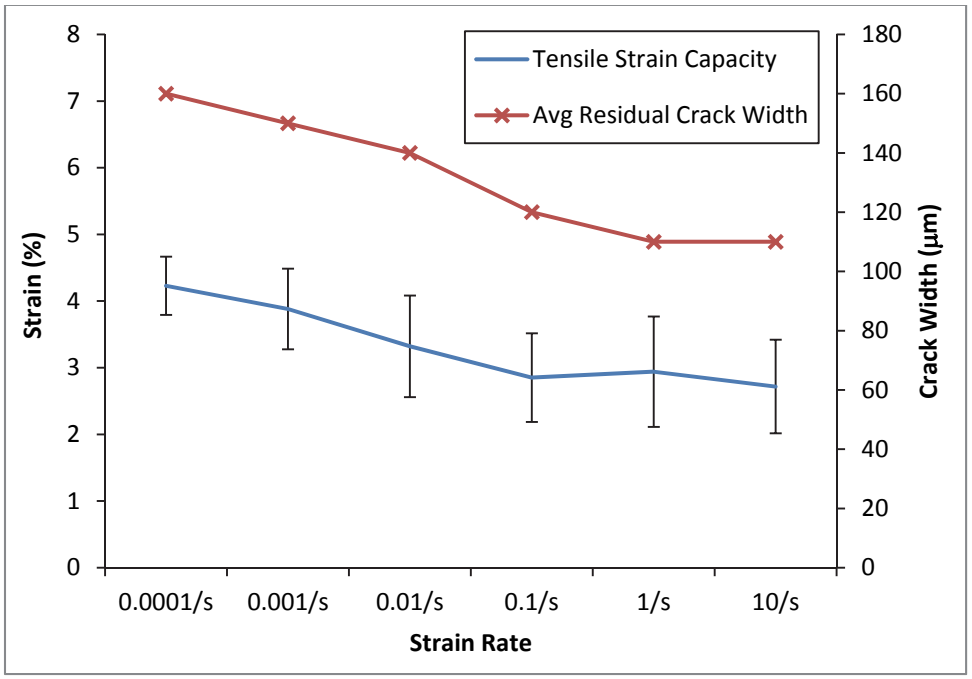

Figure 7.9: Rate effects on tensile strain capacity and average residual crack width of dogbone specimens

For individual dogbone specimens, a positive correlation between $PSH_{strength}$ and tensile strain capacity is observed, regardless of the strain rate. The $PSH_{strength}$ indices of all 36 dogbone specimens are plotted together in Figure 7.10. This observation supports the hypothesis that the fundamental principles of micromechanics for achieving or enhancing tensile ductility in HSHDC (and similar materials) are valid regardless of the strain rates.

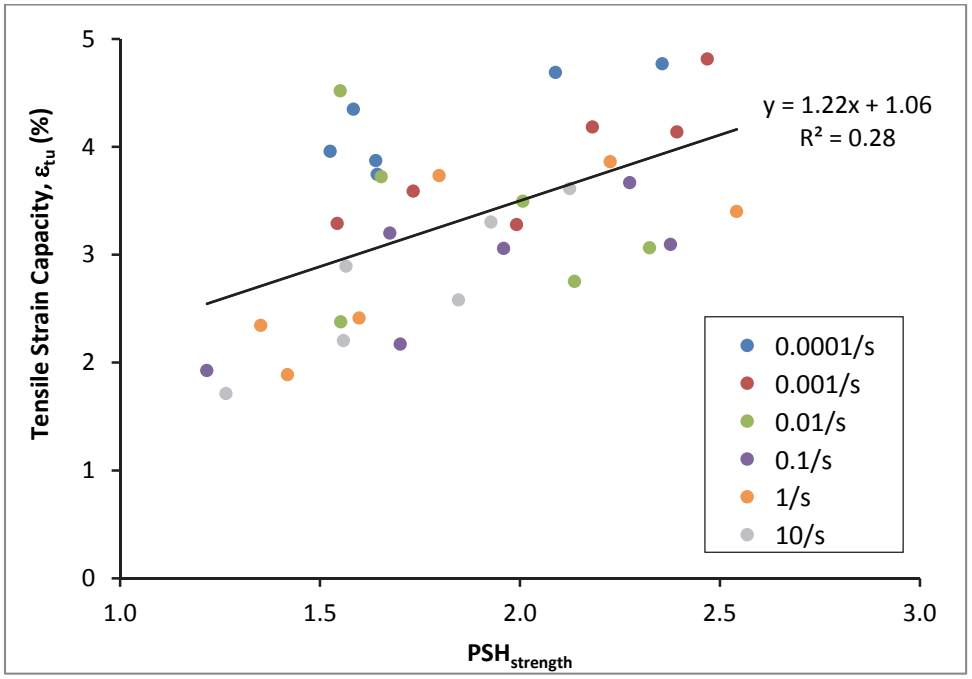

Figure 7.10: Correlation between tensile strain capacity and $PSH_{strength}$

All the mechanical properties of the dogbone specimens exhibit an increase in variation, shown by the standard deviation bars in Figure 7.8 and Figure 7.9, with strain rate. This behavior at the composite scale is caused by similar increase in variation of micro-scale fiber/matrix interaction properties and matrix fracture toughness with strain rate, as discussed in Section 7.5. In spite of the variation in properties, the minimum tensile ductility among all the 36 HSHDC dogbone specimens is 1.7% at 10/s exhibited by specimen #31.

7.4.2 Micro-scale Behavior

The displacement rate effects on the micro-scale fiber/matrix interaction properties and fiber properties are determined from single fiber pullout test results, whereas the rate effects on the matrix fracture toughness are determined from the notched-beam bending tests. Typical pullout curves of single PE fibers embedded in the HSHDC matrix are shown in Figure 6.15 and discussed in detail in Section 6.5.3. From the single fiber pullout test results, significant fiber/matrix interaction properties are determined using the analysis described in Sections 6.5.4-6.5.6. Details of the notched-beam test and matrix fracture toughness calculation are given in Section 3.3. In the following paragraphs of this section, rate effects on the average fiber/matrix interaction properties, fiber properties, and matrix fracture toughness, obtained using the same methodology as that used for pseudo-static tests in Chapters 3 and 6, are reported.

The observed variations of the fiber/matrix interfacial frictional bond (τ_0) and the slip hardening parameter (β) with displacement rate are shown in Figure 7.11. τ_0 increases only slightly (by 14%) over the six orders of displacement rates investigated in this study. This is consistent with the previous findings of Yang et al[12] and Maalej et al[13], who similarly reported weak dependence of τ_0 on displacement rate. As mentioned in Section 7.2.2, the main cause of rate dependency in ECC is the fiber/matrix chemical bond. The absence of chemical bond between PE fibers and HSHDC matrix makes overall interfacial bond less sensitive to rate effects. Although the slip hardening parameter (β) doubles from 0.003 at 0.009 mm/s to 0.006 at 900 mm/s (Figure 7.11), it causes insignificant increase in pullout force, particularly at low slip

(< 500 μm). For comparison, β for ECC is about 0.6.[16] These increases in τ_0 and β with displacement rate have minor influences on the bridging behavior of the PE fibers in HSHDC.

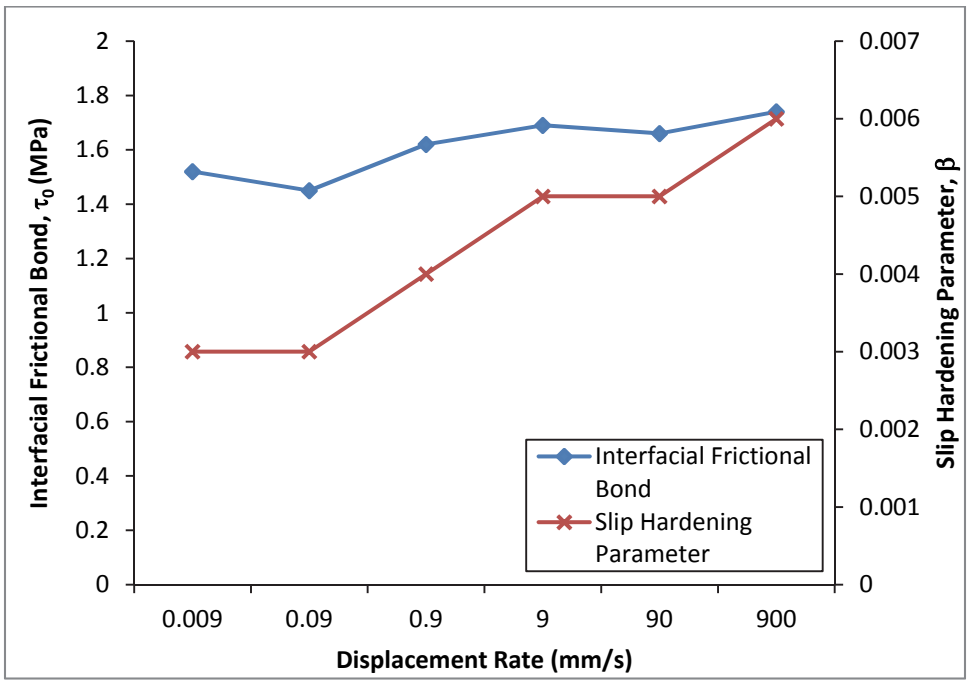

Figure 7.11: Rate effects on fiber/matrix interfacial bond properties

The fiber/matrix interaction properties: snubbing coefficient (f) and inclination hardening parameter (μ) (defined in Section 6.5.6), both, exhibit rate dependence as observed in Figure 7.12. The snubbing coefficient increases by about 27% from the slowest to the fastest displacement rate used in this study. The pullout load is, however, magnified by $e^{f\phi}$, which makes the effect on the pullout load less than 27%. For instance, for a fiber inclined at angle $\phi = 45°$ with respect to the loading axis, the ratio of the pullout load at high rate to that at pseudo-static rate is $e^{\phi(f_{hr}-f_{ps})} = e^{\pi/4(0.75-0.59)} = 1.13$, where f_{hr} and f_{ps} are the snubbing coefficients at displacement rates of 900 mm/s and 0.009 mm/s, respectively. This 13% increase in pullout load

due to increase in f is supplemented by the change in inclination hardening parameter (μ), which increases from 386 N/(m-rad) at 0.009 mm/s to 553 N/(m-rad) at 900 mm/s. This increase in μ causes about 43% increase in the inclination hardening contribution [$\mu\phi(u-u_0)$ in Eq. 6.5], which is at most 10% of the total pullout load. Therefore, this increase in μ due to displacement rate can cause maximum increase of about 4.3% (43% times 10%) in the fiber bridging stress. As both the snubbing and the inclination hardening mechanisms are based on the normal reaction from the matrix, these increases in f and μ may be caused by the increase in matrix fracture toughness, strength, and modulus at high strain rates. Thus, the rate dependencies of f and μ are moderately significant for the rate dependence of fiber-bridging (σ-δ curve) in HSHDC.

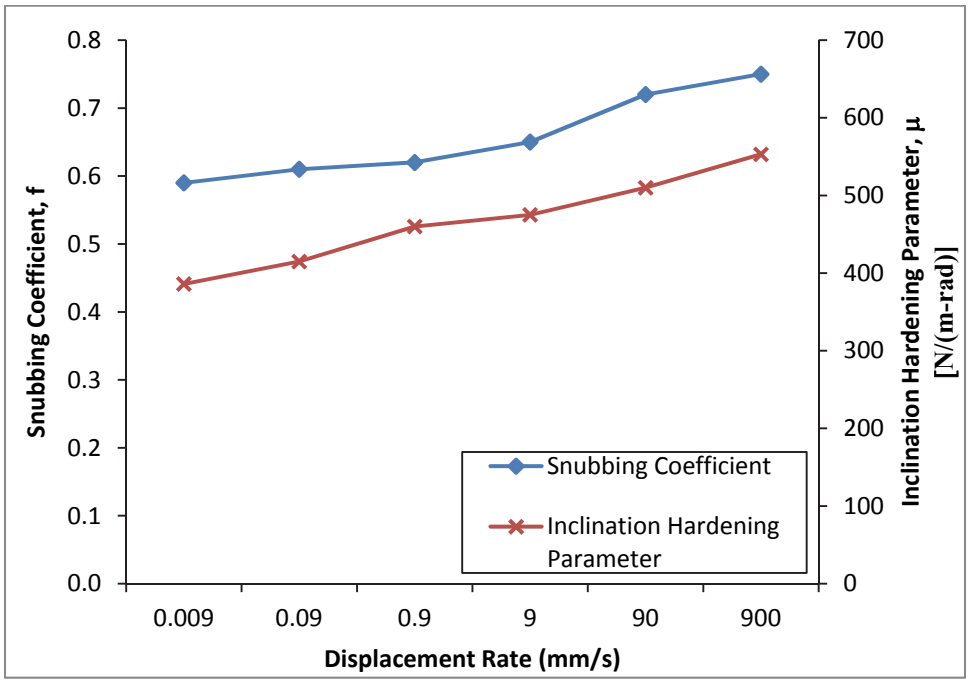

Figure 7.12: Rate effects on fiber/matrix interaction properties

The most consequential rate effects that directly influence the fiber-bridging in HSHDC are the increases in fiber strength and in-situ modulus. Polymers, in general, are known to have a viscoelastic behavior, which causes increase in fiber strength and in-situ modulus (and brittleness) with increase in strain rate.[17,18,19] In this study, single PE fibers of gauge lengths 20 mm were tested under displacement-controlled uniaxial tension using a high precision 5 N capacity load cell to measure pullout load. The variations in fiber strength and modulus with strain rate are plotted in Figure 7.13. While the PE fiber strength increases by about 21% of its pseudo-static value, the in-situ fiber modulus increases by approximately 85% of its pseudo-static value. These increases in fiber strength and modulus have significant impact on the fiber-bridging (σ-δ) curve of HSHDC as discussed in Section 7.5.

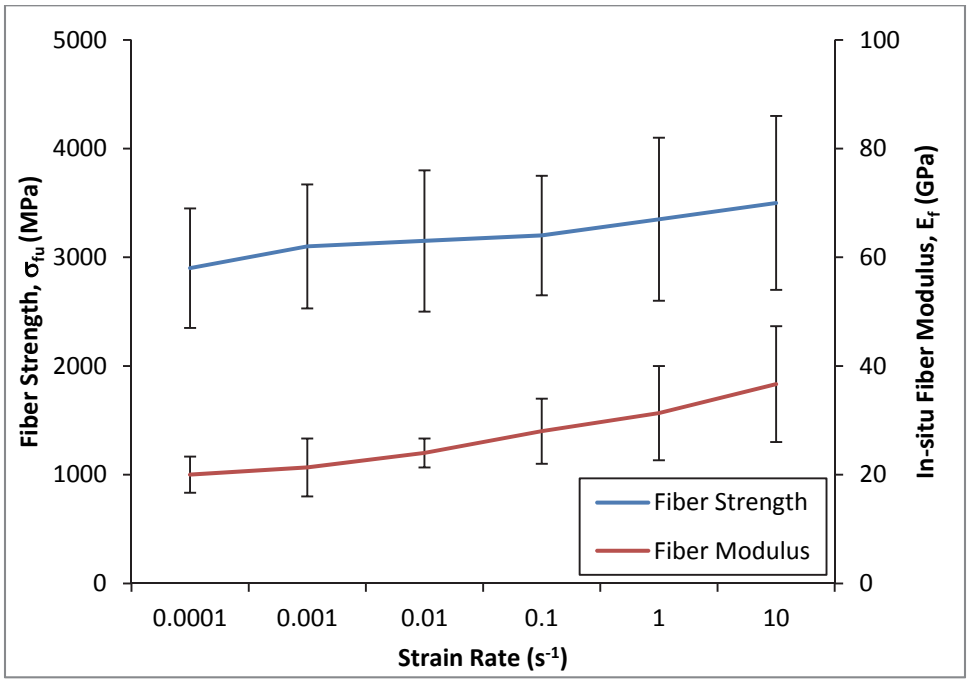

Figure 7.13: Rate effects on fiber properties

Both the necessary conditions of multiple cracking (Eqs. 2.1 and 2.2) depend as much on the matrix fracture toughness (K_m) as on the fiber-bridging (σ-δ) behavior, and therefore, the variation of K_m with displacement rate is investigated in this study along with the rate effects on the fiber/matrix interaction properties detailed above. The fracture toughness of HSHDC matrix increases from 1.10 MPa$\sqrt{m}$ at 0.009 mm/s to 1.31 MPa$\sqrt{m}$ at 9 mm/s. Unlike the fiber/matrix interaction properties which were measured at six different displacement rates, the matrix fracture toughness was measured only at four different displacement rates up to 9 mm/s due to the limits of the experimental setup as discussed above. This increase in fracture toughness causes proportional increase in σ_{ci} and quadratic increase in J_{tip}, which are both detrimental for the pseudo-strain hardening (PSH) indices (refer Section 4.2) and tensile ductility.

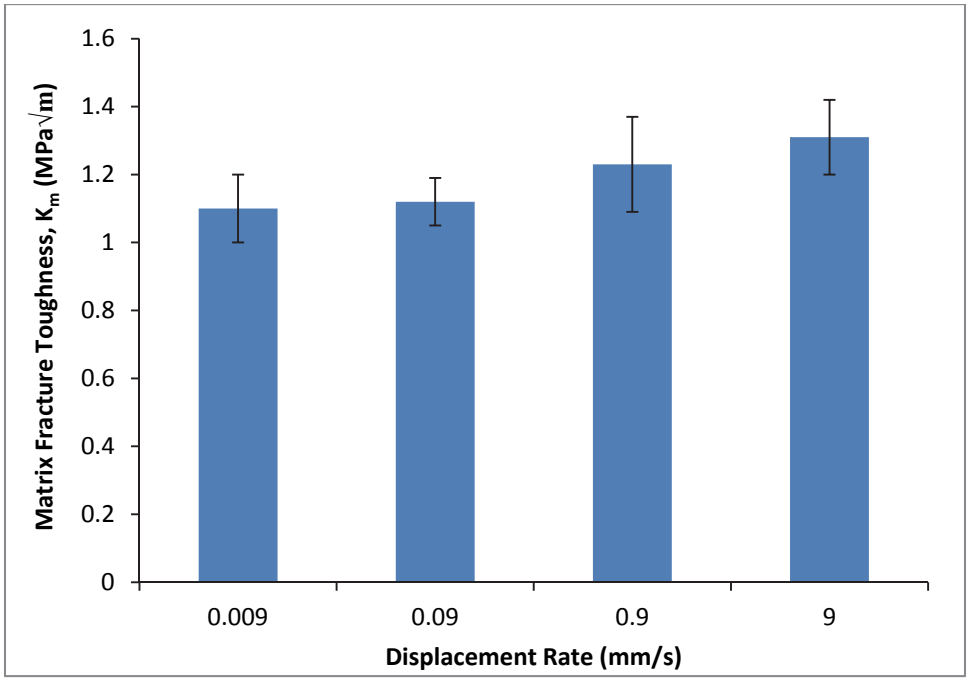

Figure 7.14: Rate effect on matrix fracture toughness

All the micro-scale properties discussed above exhibit an increase in variation with strain/displacement rates. While the variations in form of standard deviation bars are shown for fiber properties and matrix fracture toughness in Figure 7.13 and Figure 7.14, the variations in the fiber/matrix interaction properties are depicted as coefficient of determination (R^2) values in Figure 7.15 (due to the method used to determine these properties – refer Section 6.5). Lower R^2 values imply higher variation in properties, which is the case for all the fiber/matrix interaction properties examined in this study. This increase in the variation of fiber/matrix bond properties may be caused by corresponding increase in variation of fiber and matrix properties observed in Figures 7.13 and 7.14.

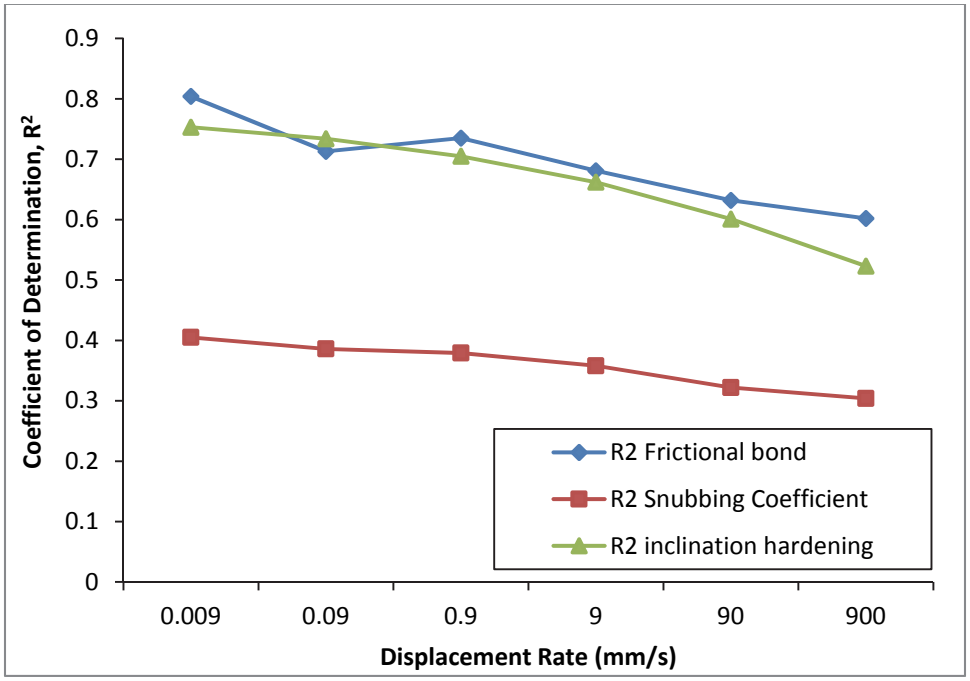

Figure 7.15: Measure of variation in fiber/matrix interaction properties determination

7.5 Scale-linking Analysis

In this section, it is determined whether the micro-scale rate effects can explain the response of HSHDC at the composite scale through scale-linking analysis similar to that described in Section 6.6. The Eq. 6.10 is numerically computed using the measured average values of fiber/matrix interaction properties (Section 7.4.2) at various displacement rates. The observed fiber orientation distribution [p(ϕ)] of dogbone specimens (Section 6.4) and volume fraction of 2% are used in these computations. The results of this analysis in form of computed fiber-bridging (σ-δ) curves are plotted in Figure 7.16 and discussed below.

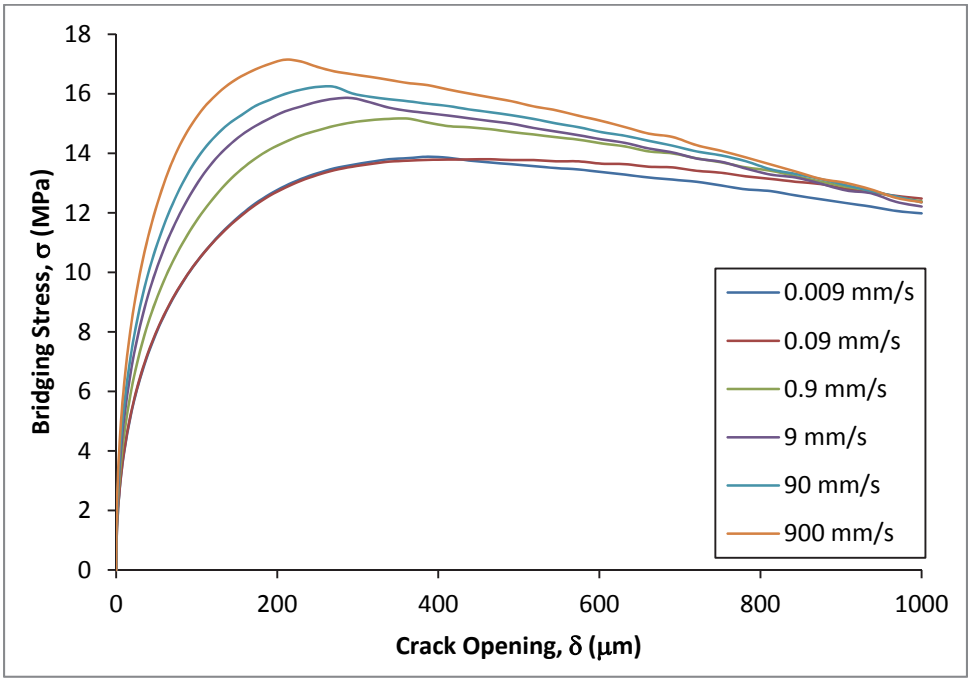

Figure 7.16: Rate effects on the computed fiber-bridging (σ-δ) behavior of HSHDC

It can be observed in Figure 7.16 that, with increasing displacement rate, both the rising slope and the peak of the computed σ-δ curve increase. While the fiber/matrix interaction properties of τ_0, β, f, and μ along with fiber modulus E_f determine the rising slope of the σ-δ curve, the fiber's strength (σ_{fu}) is the dominant factor in determining the peak of the σ-δ curve known as the fiber-bridging capacity (σ_0). Although the fiber/matrix interaction properties also significantly influence σ_0, it is most sensitive to changes in σ_{fu} in HSHDC. Thus, increasing fiber/matrix interaction properties and fiber modulus cause steeper σ-δ curves, and increasing fiber strength (supplemented by fiber/matrix interaction properties) causes increase in fiber-bridging capacity (σ_0) with increasing displacement rate.

As explained in the pseudo-static σ-δ analysis in Section 6.6, the slope of the σ-δ curve and σ_0 are closely related to the average crack width and ultimate tensile strength of the composite dogbone specimens. Min(σ_0) is the expected tensile stress capacity of the composite dogbone specimens and is taken as 80% of σ_0 due to inhomogeneity of fiber dispersion in HSHDC dogbones (refer Section 6.4). Additionally, the crack width corresponding to $0.80\sigma_0$ on the σ-δ curve for V_f = 2% is the expected value of average crack width in the HSHDC dogbone specimens. Steeper slope of σ-δ curve and greater σ_0 at higher displacement rate, therefore, imply smaller crack width and greater ultimate tensile strength.

By a similar analysis of σ-δ curves as that used for pseudo-static tests in Section 6.6, the ultimate tensile strength and average crack widths are predicted from Figure 7.16 for equivalent strain rates and are plotted in Figure 7.17 along with experimental results. In this figure, instead

of the absolute values of ultimate tensile strength and crack widths, percentages relative to the 'respective' pseudo-static values are plotted to show the rate effect. 'Respective' pseudo-static values at strain rate of 0.0001/s are: (1) Ultimate tensile strength (Experimental) = 14.5 MPa (Figure 7.8) (2) Ultimate tensile strength (Analytical) = 11.3 MPa (Figure 7.16 and Section 6.6.3 – the experimental pseudo-static strength is higher than analytically predicted strength) (3) Average (residual) crack width (Experimental) = 160 μm (Figure 7.9), and (4) Average crack width (Analytical) = 140 μm (Figure 7.16 and Section 6.5.3). A good match is observed in Figure 7.17 between analytical and experimental rate effects in ultimate tensile strength and crack widths, albeit with the exception of ultimate tensile strength predictions at 1/s and 10/s.

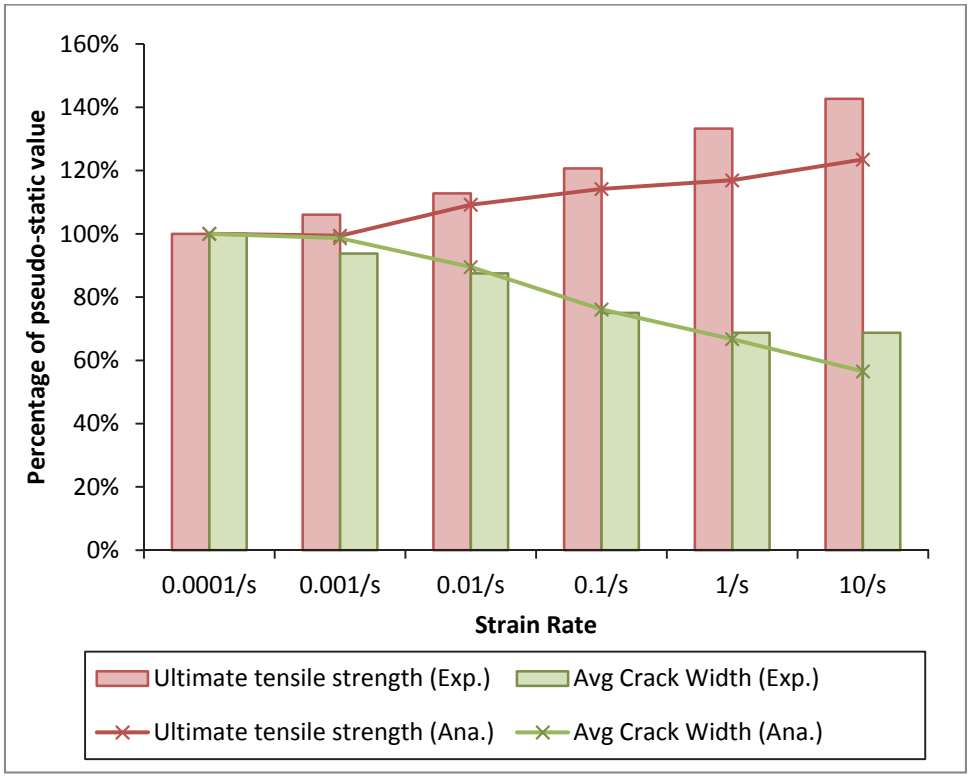

Figure 7.17: Comparison of experimentally determined rate effects on composite tensile properties with analytically predicted results

Although the overall observed trend of increasing ultimate tensile strength with strain rate is well predicted by the scale-linking model, there is a lack of agreement between the experimental and analytical values at the highest two strain rates investigated in this study. This may be due to (1) significant increase in variation of fiber/matrix interaction properties at these two strain rates (2) additional unknown hardening mechanisms at these two strain rates.

The changes in average matrix fracture toughness with strain rate are compared with that of average first crack strength of HSHDC dogbone specimens in Figure 7.18. As all the specimens belong to the same batch of material, the maximum flaw size is expected to be approximately similar in all specimens regardless of the strain rate. It is observed in Figure 7.18 that the first crack strength closely follows the trend in matrix fracture toughness, which is expected from Irwin's fracture criterion.

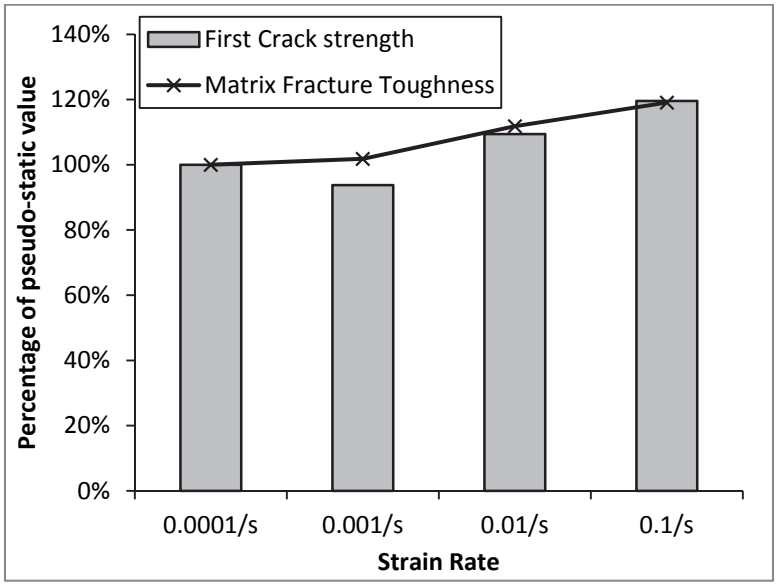

Figure 7.18: Comparison of observed rate effects in first crack strength of composite specimens and matrix fracture toughness

7.6 Conclusions

- *Composite-scale rate effects under direct tension*: As the strain rate is increased from 0.0001/s to 10/s, average first crack strength (σ_{fc}) and average ultimate tensile strength (σ_{ult}) of HSHDC dogbone specimens increase by about 53% and 42%, respectively. In spite of a relatively constant ratio of σ_{ult}/σ_{fc} with strain rate, the tensile strain capacity decreases with increasing strain rate from about 4.2% at 0.0001/s to 2.9% at 0.1/s and plateaus after that. Such variation in tensile strain capacity is attributable to a similar trend in average crack width which reduces from 160 μm at 0.0001/s to 120 μm at 0.1/s and plateaus for higher strain rates.

- *Micro-scale rate effects*: Almost all the fiber/matrix interaction properties, fiber properties, and matrix fracture toughness exhibit changes with displacement rate (equivalent to the strain rate in composite testing) to varying degrees. The interfacial frictional bond (τ_0) increases only slightly (by 14%) over the six orders of displacement rates investigated in this study (0.009 mm/s to 900 mm/s). Although the slip hardening parameter (β) doubles from 0.003 at 0.009 mm/s to 0.006 at 900 mm/s, it causes insignificant increase in pullout force, particularly at low slip (< 500 μm). The absence of chemical bond between the PE fiber and HSHDC matrix makes the overall fiber/matrix bond relatively insensitive to rate effects. Snubbing coefficient (f) and inclination hardening parameter (μ) increase by about 27% and 43%, respectively, which are determined to be moderately significant for the fiber-bridging in HSHDC. The changes that are the most consequential for fiber-bridging in HSHDC are the increases in PE fiber strength and modulus with strain rate. At the fastest rate, the PE fiber strength and modulus increase by about 21% and 85% of their respective pseudo-static values. This increase in fiber strength and

modulus coupled with the increase in fiber/matrix interaction properties result in the reduction of complementary energy (J_b') of the computed σ-δ curve of HSHDC from 969 J/m^2 at 0.009 mm/s to 663 J/m^2 at 9 mm/s.

The matrix fracture toughness increases from 1.10 MPa$\sqrt{m}$ at 0.009 mm/s to 1.31 MPa$\sqrt{m}$ at 9 mm/s, which increases the crack tip toughness ($J_{tip} \approx K_m^2/E_c$ – Sections 3.6 and 6.6) from 25 J/m^2 at 0.009 mm/s to 35 J/m^2 at 9 mm/s (conservatively assuming no increase in E_c in absence of data). Thus, in spite of the increase in the matrix fracture toughness, J_{tip} remains an order of magnitude smaller than J_b' even at high strain rates, which coupled with constant σ_{ult}/σ_{fc} ratio (1.8±0.2) facilitates multiple cracking at all strain rates investigated in this study.

- *Scale-linking*: The scale-linking analysis shows that the micro-scale rate effects satisfactorily explain the rate dependencies at the composite scale. The increase in matrix fracture toughness corresponds well with the increase in first crack strengths at composite-scale. The increases in fiber/matrix interaction properties and fiber strength and modulus justify the increase in ultimate tensile strength and decrease in average crack width, and therefore tensile strain capacity, with strain rate.

References

1. Chandra, D. (1993) "A fracture mechanics based constitutive model for concrete under high loading rates" PhD Dissertation, University Park, PA: Pennsylvania State University.

2. Bischoff, P.H. & Perry, S.H. (1991) "Compressive Behavior of Concrete at High Strain Rates" *RILEM Materials and Structures Journal*, 24(6), 425-450.

3. Stroh, A. N. (1957) "A theory of the fracture of metals" *Advances in Physics,* 6(24), 418-465.

4. Ross, C. A., Tedesco, J. W. & Kuennen, S. T. (1995) "Effects of Strain Rate on Concrete Strength" *ACI Materials Journal,* 92(1), 37-47.

5. ACI Committee 446 Subcommittee IV (2004) "Report on Dynamic Fracture of Concrete - ACI 446.4R-04" Farmington Hills, MI: American Concrete Institute.

6. Mindess, S., Banthia, N. & Yan, C. (1987) "The fracture toughness of concrete under impact loading" *Cement and Concrete Research,* 17(2), 231-241.

7. John, R. & Shah, S. P. (1986) "Fracture of concrete subjected to impact loading" *Cement, Concrete, and Aggregates: ASTM International,* 8(1), 24-32.

8. Bazant, Z. P. & Planas, J. (1998) "Effect of time, environment, and fatigue" In *Fracture and Size Effect in Concrete and Other Quasibrittle Materials*, Washington DC: CRC Press. pp. 388-398.

9. Du, J., Kobayashi, A. S. & Hawkins, N. M. (1989) "FEM dynamic fracture analysis of concrete beams" *ASCE Journal of Engineering Mechanics*, 115(10), 2136-49.

10. Mihashi, H. & Wittmann, F. H. (1980) "Stochastic Approach to Study the Influence of Rate of Loading on Strength of Concrete" *HERON*, 25(3).

11. Yang, E. H. (2008) "Designing Added Functions in Engineered Cementitious Composites" PhD Dissertation, Ann Arbor, MI: University of Michigan.

12. Yang, E. H. & Li, V. C. (2005) "Rate Dependence in Engineered Cementitious Composites" *Proceedings of RILEM Workshop on HPFRCC in Structural Applications*, Honululu, Hawaii: RILEM SARL, pp. 83-92.

13. Maalej, M., Quek, S. T. & Zhang, J. (2005) "Behavior of Hybrid-Fiber Engineered Cementitious Composites Subjected to Dynamic Tensile Loading and Projectile Impact" *Journal of Materials in Civil Engineering*, 17(2), 143-152.

14. Mechtcherine, V., Silva, F. D., Butler, M., Zhu, D. & Mobasher, B. (2010) "Fracture Behavior of HPFRCCs under dynamic tensile loads" In *Proceedings of European Conference on Fracture - ECF 18*, Mechtcherine, V. & Kaliske, M. (Eds.), Dresden, Germany: Aedificatio Publishers.

15. Kim, D. J., El-Tawil, S. & Naaman, A. E. (2008) "Loading Rate Effect on Pullout Behavior of Deformed Steel Fibers" *ACI Materials Journal*, 105(6), 576-584.

16. Wang, S. & Li, V.C. (2007) "Engineered Cementitious Composites with High-Volume Fly Ash" *ACI Materials Journal*, 104(3), 233-241.

17. Knauss, W. G., Emri, I. & Lu, H. (2008) “Mechanics of Polymers: Viscoelasticity” In *Springer Handbook of Experimental Solid Mechanics*, Sharpe, W. N. (Ed.), US: Springer, pp. 49-96.

18. Peijs, T., Smets, E. A. M. and Govaert, L. E. (1994) “Strain Rate and Temperature Effects on Energy Absorption of Polyethylene Fibers and Composites” *Applied Composite Materials*, 1, 35-54.

19. Jacob, G. C., Starbuck, J. M., Fellers, J. F., Simunovic, S. & Boeman, R. G. “Strain Rate Effects on the Mechanical Properties of Polymer Composite Materials” *Journal of Applied Polymer Science*, 94(1), 296-301.

CHAPTER 8: BEHAVIOR OF HSHDC SLABS UNDER IMPACT AND BLAST LOADS

8.1 Introduction

Impacts and blasts are grave hazards for our built environment with dangerous unintended consequences. Examples of damaging impact loads include trees, cars, and other objects hurled towards buildings during hurricanes,[1,2] and large vehicular impacts on bridge piers.[3] With the rise of terrorism in the 21st century, blasts have unfortunately become a more frequent threat to both civil and military infrastructure.[4] Mitigating the detrimental effects of impacts and blasts on the structural integrity of our infrastructure, thus making it more resilient, is a major challenge for modern engineers.

For overcoming this challenge, it is necessary to characterize the impact and blast loads and understand their interactions with the structure of interest. Both impacts and blasts are dynamic loads that impart significant amount of energy to a structure or a structural element in a very short time (typically, a few milliseconds). The interaction of these dynamic loads with a structure is a highly complex problem. Standards and guidelines such as AASHTO LRFD Bridge Design Specifications (2012),[5] ASCE-7 (2010),[6] US Army Technical Manual TM5-1300 (1990),[7] and Unified Facilities Criteria UFC 4-023-03 (2013),[8] along with numerous other archival journals and reports,[9] specify impact and blast loads along with reasonable

simplifications, safety factors, and methods for designing structures that can withstand impacts and blasts.

The majority of the existing damage mitigation methods in the aforementioned design guides focus on structural-scale solutions such as providing safety barriers for bridge piers, enforcing standoff distance using large walls, additional steel reinforcement, and structural fuse elements and redundancies to prevent progressive collapse, which may prove to be prohibitively expensive and not always implementable due to space constraints. The focus of this doctoral research is to seek material-scale solutions by enhancing the inherent damage tolerance and energy absorption capacity per unit volume of the material (through micromechanics-based material tailoring detailed in Chapters 4-6), and simultaneously modifying the structural configuration to optimally utilize the enhanced material properties.

The objectives of the research tasks presented in this chapter are: (1) to characterize and compare the behaviors of HSHDC and CORTUF slabs under impact loads both experimentally (through drop-weight tests) and analytically (using finite element [FE] analysis), and (2) to demonstrate the effectiveness of using HSHDC for blast protection through FE analysis. In this chapter, first, the experimental investigation through drop-weight impact tests on HSHDC and CORTUF slabs is detailed. This is followed by 3D non-linear rate-dependent FE modeling of the drop-weight experiments utilizing the material properties and rate effects reported in Chapters 3, 5, and 7. The results of the FE analysis are discussed and compared with the experimental results. The FE model is then used to determine the optimum configuration of layered slabs with CORTUF on the compression side and HSHDC on the tension side for simultaneously

optimizing material cost and mechanical performance. Furthermore, the performance of simply-supported HSHDC and CORTUF slabs under air-blast loads is compared using FE analysis. The details of these research tasks are given in the following sections.

8.2 Experimental Investigation through Drop-weight Tests

8.2.1 Specimens

Thin slabs of dimensions 12″x12″x1″ (thickness) as shown in Figure 8.1 were used in this experimental study. These slabs were made of either HSHDC or COR-TUF with no additional reinforcement. The mix ingredients, and mixing and curing procedures of COR-TUF and HSHDC are given in Chapter 3 and Chapter 6, respectively.

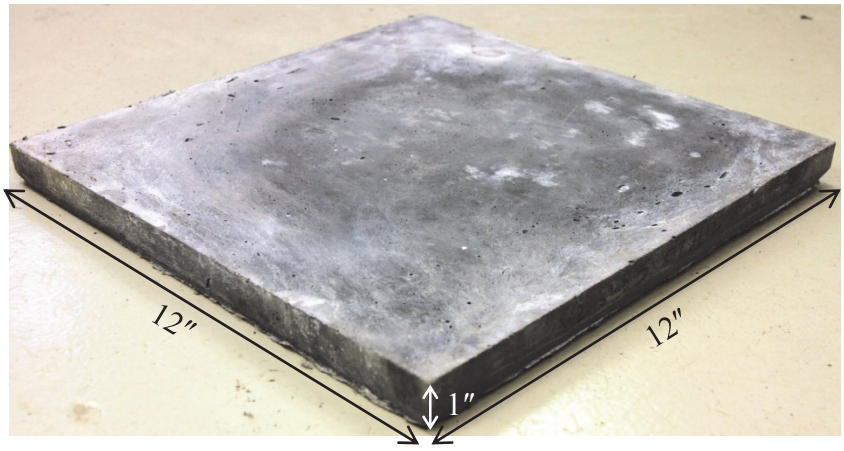

Figure 8.1: Geometry of the slabs used in drop-weight tests

8.2.2 Experimental Setup and Procedure

The drop-weight impact test setup used in this study is shown in Figure 8.2a. It consists of an impact head mounted under a loading tray, the total weight of which can be adjusted by adding or removing steel plates as required. The loading tray is connected to two pillow blocks. The pillow blocks slide smoothly on two vertical cylindrical precision ground (diameter tolerance less than 10 μm) hardened steel guide-shafts (1″ dia). These guide-shafts are mounted on the sturdy structural frame of the test setup which mainly consists of steel W6x12 beams. The drop-weight assembly, consisting of the impact head, the loading tray, and the pillow blocks, can be raised to a desired height by a hoisting rope. After hoisting to the desired height, the drop-weight assembly is connected to a series of adjustable links (Figure 8.2a) via an active electromagnet. At this point, the hoisting rope is disconnected. Switching off the electromagnet releases the drop-weight assembly for impact on the specimen kept on a steel specimen holder, which sits on an extremely heavy steel base.

The instrumentation used in the drop-weight tests is shown in Figure 8.2b. It consists of three parallel dynamic load cells (L1-3 in Figure 8.2b), each with a maximum capacity of 10,000 lbf, arranged such that their centers are equidistant from the center of the impact head. In order to ensure that all the load cells are engaged simultaneously at the moment of impact, the mounting screw that connects the impact head to the loading tray is pre-tensioned to apply pre-compression on all the load cells. In addition, the impact region on the specimen is sanded to ensure smooth and level contact with the impact head. The acceleration-time history of the drop-weight assembly is recorded by two accelerometers (A1 and A2) with maximum range of 1500g. These

accelerometers are mounted on the opposite sides of the loading tray and their readings are averaged, which eliminates any side-wobbling/vibration effects of the drop-weight assembly on the acceleration time-history. All the aforementioned sensors are connected to a high frequency data acquisition system with maximum sampling frequency of 1 MHz. As there are five sensors in all, each sensor can be sampled at a maximum frequency of 200 kHz. With this arrangement, the maximum recordable impact force and average acceleration of the impact head are 30,000 lbf and 1500g, respectively, at 200 kHz.

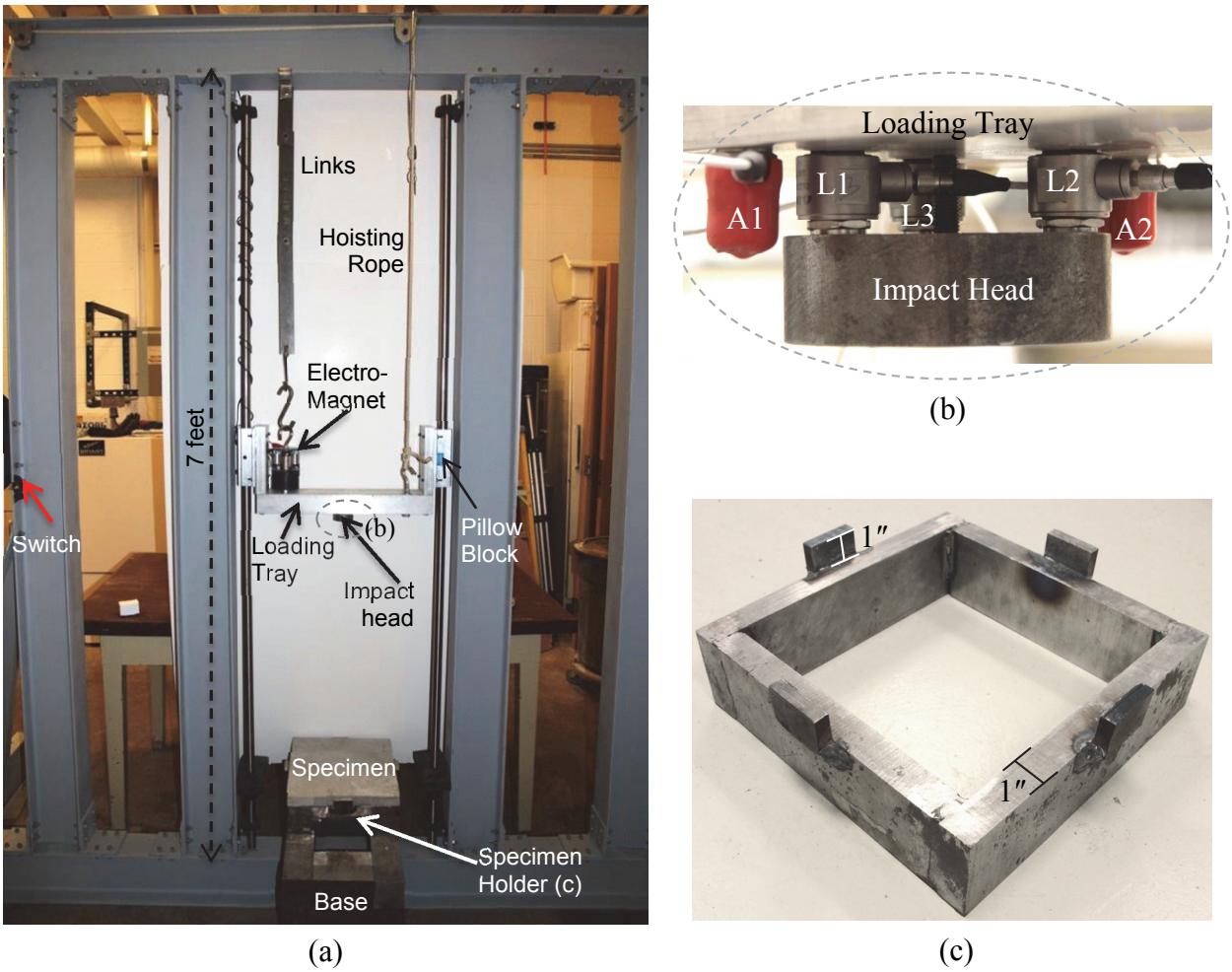

Figure 8.2: (a) Drop-weight impact test setup (b) Instrumentation [zoomed view of the dashed circle in (a)] (c) Specimen Holder

The experimental details of this drop-weight impact study, comparing the performance of HSHDC and COR-TUF slabs with varying kinetic energies of impact head and varying head diameter, are given in Table 8.1. A constant weight of 16.04 kg was dropped repeatedly on both HSHDC and COR-TUF slabs using a cylindrical steel head of diameter 3″ from three different heights of 0.35 m, 0.70 m, and 1.40 m. These drop-heights are chosen such that the kinetic energy of the impact head just before impact with the slab almost doubles for the next higher drop-height. The calculation of impact velocity (used to compute kinetic energy) is detailed in the next paragraph. The impacts are repeated for either 20 times or until slab failure, whichever occurs first. Almost zero rebound of the impact head either due to flexural failure of the slab or due to head penetration in the slab is deemed as 'slab failure'. In addition to the above set of impacts with the 3″ head, drop-weight impacts with a 2″ cylindrical head were used to qualitatively determine the influence of head size on the failure mode of HSHDC and COR-TUF slabs. The footprint of three required load cells is larger than the 2″ head's cap area, and therefore, no instrumentation was used for the impacts with the 2″ head. Two slabs each of HSHDC and COR-TUF were used in all the impact cases investigated in this study.

The impact velocity is indirectly calculated from the vertical position of the drop-weight assembly at different times. The principle of conservation of energy cannot be used in this case to determine the impact velocity because the energy expended to overcome the frictional force between the drop-weight assembly and the vertical guide-shafts is unknown. A 30 fps (frames per second) video of the drop, shot with a high-quality digital camera, provides the position of the drop weight assembly at time intervals of 1/30 seconds. If the frictional force between the drop-weight assembly and the guide-shafts is assumed constant, the impact velocity can be

determined using position-time observations as inputs in the Newtonian equations of motion. The computed impact velocities corresponding to various drop-heights are shown in Table 8.1.

Table 8.1: Experimental parameters of the drop-weight tests.

Specimens	Head Diameter	Drop Weight	Drop Height	Impact Velocity	Multiple Impacts
Instrumented Impacts					20 or head penetration without rebound – whichever occurs first
2 x (HSHDC & COR-TUF)*	3″	16.04 kg	0.35 m	2.30 m/s	
2 x (HSHDC & COR-TUF)			0.70 m	3.25 m/s	
2 x (HSHDC & COR-TUF)			1.40 m	4.60 m/s	
Non-instrumented Impacts					
2 x (HSHDC & COR-TUF)	2″	16.11 kg	0.70 m	3.25 m/s	

* Specimen naming example for the instrumented impacts: H4.60-1 => H for HSHDC; 4.60 for impact velocity (m/s); 1 for specimen number (out of 2 of this kind)

8.2.3 Results and Discussion

Single Impact: The contact force-time history of the drop-weight assembly's first impact on a representative HSHDC slab specimen H4.60-1 (naming scheme is given in the footnote of Table 8.1) are shown in Figure 8.3 and Figure 8.4, respectively. The total time taken for the impact head to come in contact with the HSHDC slab, depress it to maximum displacement, and rebound until the contact is lost at about 2.1 ms. These three stages of the drop-weight impact, S1-S3, are discussed below.

- Stage S1 comprises of the initial impulse (spike in contact force) reaching a maximum value of about 110 kN in 0.04 ms. During this stage, the impact head comes in contact with the

HSHDC slab. The peak contact force (PCF) is equal to the rate of change of momentum of the drop-weight assembly due to the impact. As a result, the PCF is not only dependent on the elastic stiffness and inertia of the slab, but also on the surface textures of the slab and the impact head. For instance, if the contact surfaces (particularly that of the slab) are rough, the transfer of momentum from the impact head to the slab will be slowed down by the crushing of the surface asperities, causing a decrease in the PCF. The observed PCF is also dependent on the sampling frequency of the data acquisition (DAQ) system, which in this case is limited to 200 kHz. Higher sampling frequency may result in higher observed PCF. Thus, the peak contact force, in a drop-weight test, is dependent on the mechanical and physical properties of the slab, its surface texture, and sampling frequency of the DAQ system.

- After this initial transfer of momentum in stage S1, the drop-weight assembly continues to depress the slab due to its remaining momentum; however, the slab and the impact head oscillate at different frequencies during the first half of stage S2. These oscillations are reflected in the contact force-time history in Figure 8.3 up to about 0.8 ms. After the slab is sufficiently deformed (with a small amount of plastic deformation), the slab and the drop-weight assembly move together to the bottommost position (maximum displacement), which marks the end of stage S2.

- During stage S3, the drop-weight assembly rebounds from the maximum displacement position until it completely loses contact with the slab. As a result, the contact force gradually reduces to zero during this stage.

The observed average acceleration-time history of the drop-weight assembly is shown in Figure 8.4, and the corresponding velocity and displacement-time histories, derived from the acceleration-time history, are shown in Figure 8.5 and Figure 8.6, respectively. In Figure 8.4, it is difficult to demarcate the three stages of impact as the intended signal of acceleration of the drop-weight assembly is contaminated by substantial noise in the form of flexural vibrations of the loading tray, where both the accelerometers are mounted. While the wobbling vibrations of the tray are nullified by taking the average of the two accelerometer readings, the flexural vibrations have the same sign and, therefore, remain in the average acceleration-time history.

Integrating the acceleration-time history to compute the velocity-time history (Figure 8.5) partially removes the effects of flexural vibrations of the loading tray as the area above and below the average acceleration is nullified to some extent. The rebound velocity of the drop-weight assembly (plateau toward the end of the velocity-time history) is about 1.0 m/s. Further integrating the velocity-time history produces the displacement-time history (Figure 8.6) of the drop-weight assembly. The maximum displacement position (end of stage 2) is clearly visible in the velocity and displacement-time histories at about 1.08 ms. While the velocity changes its sign (direction) at this time, the displacement reaches its maximum value. In this particular impact, the maximum displacement is about 2.8 mm. Thus, the acceleration-time history provides insights into the motion of the drop-weight assembly during the impact, which is also utilized in the next section to verify the results of the finite element analysis of HSHDC and COR-TUF slabs under impact loads in Section 8.3.6.1.

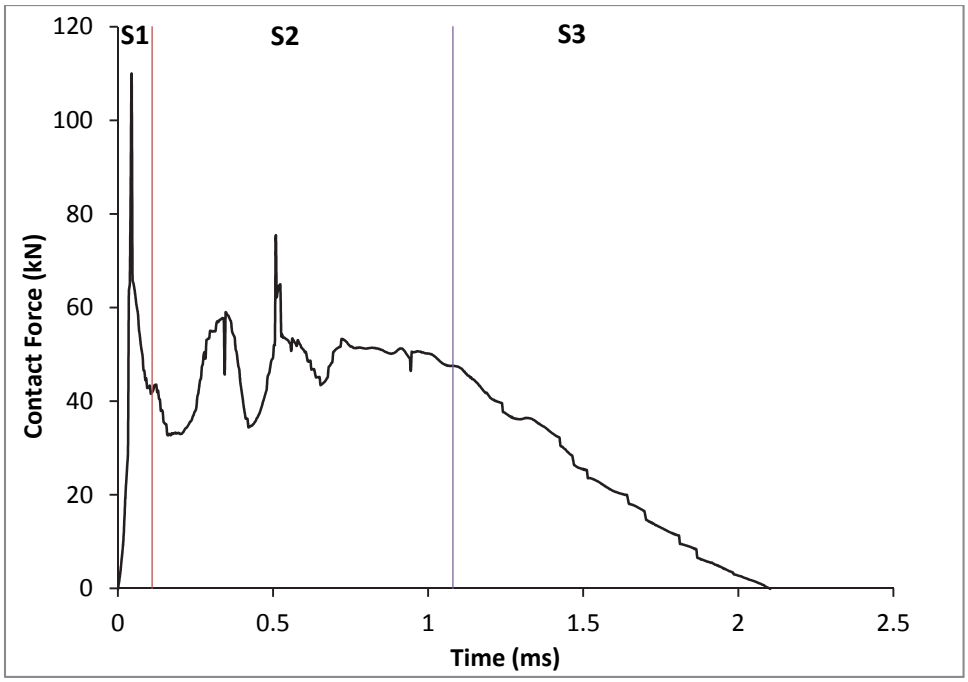

Figure 8.3: Observed contact force-time history of the first impact on HSHDC slab H4.60-1

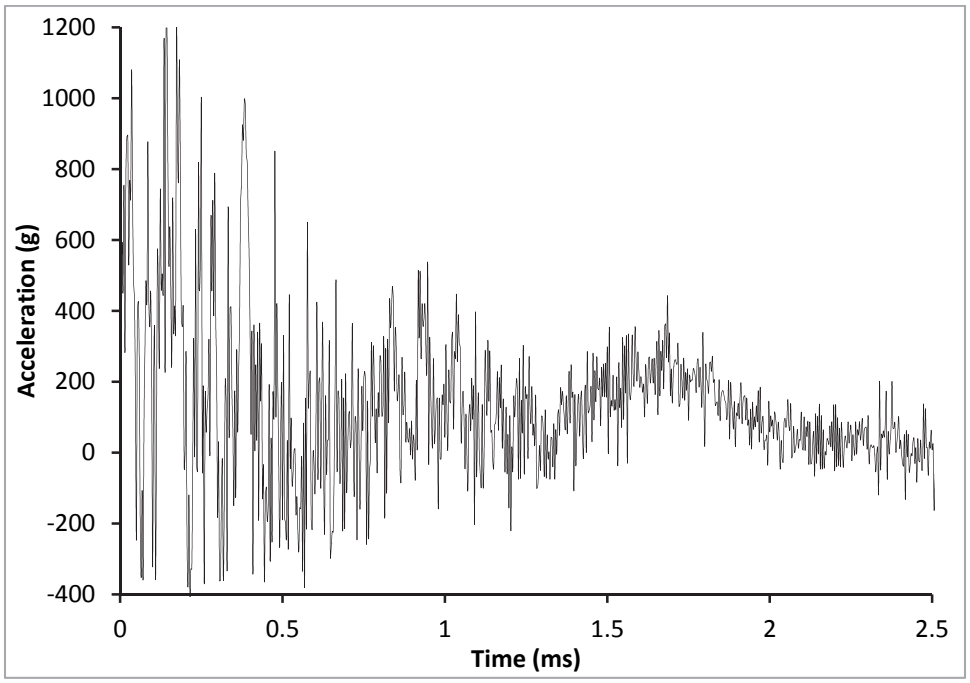

Figure 8.4: Observed average acceleration-time history of the drop-weight assembly during the first impact on HSHDC slab H4.60-1

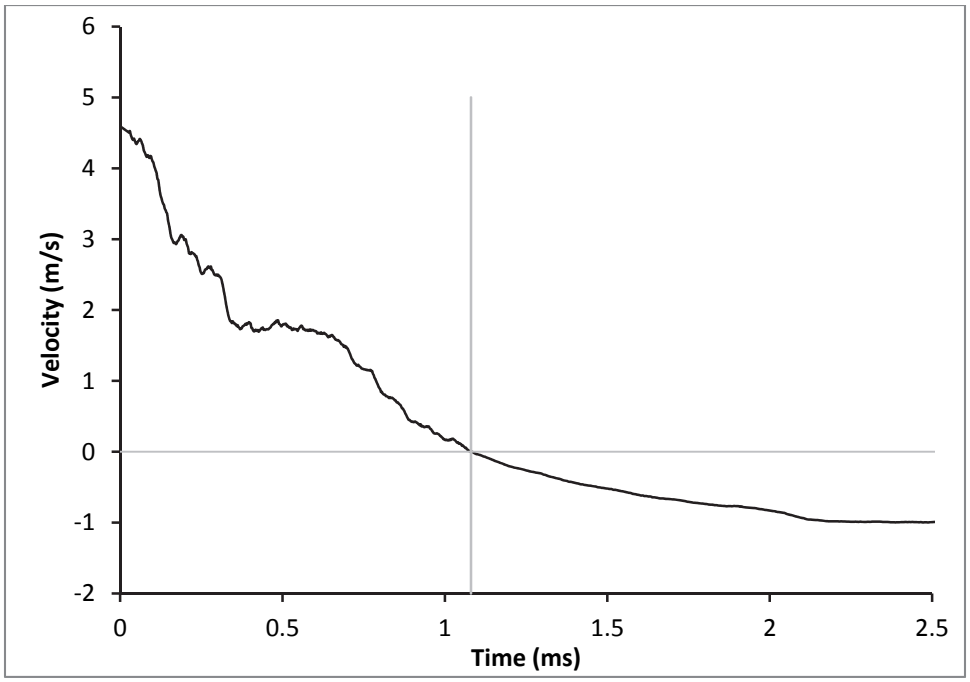

Figure 8.5: Derived velocity-time history of the drop-weight assembly during the first impact on HSHDC slab H4.60-1

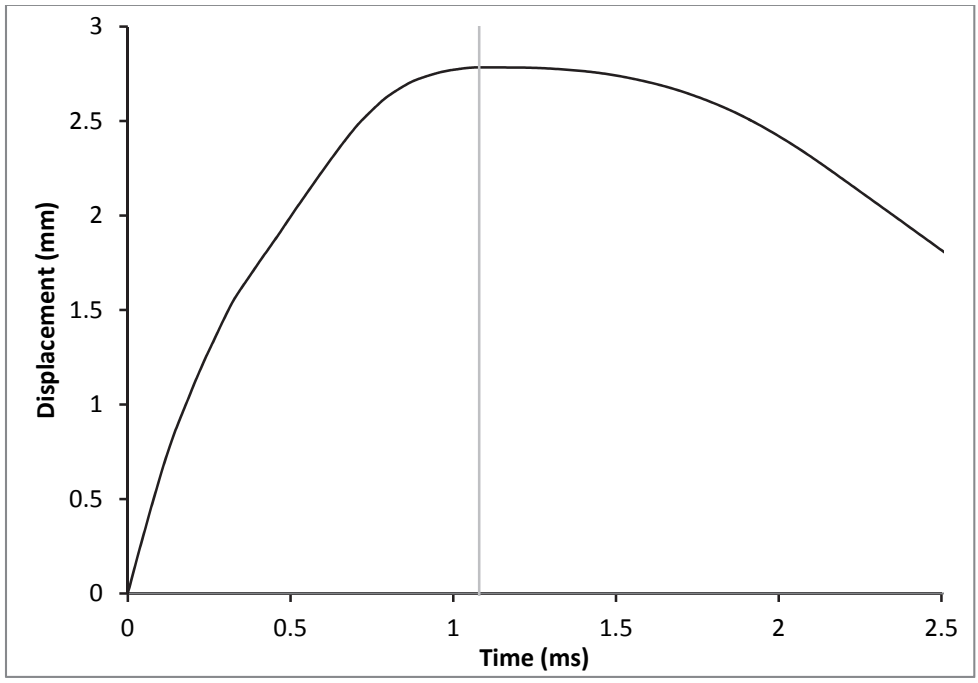

Figure 8.6: Derived displacement-time history of the drop-weight assembly during the first impact on HSHDC slab H4.60-1

Multiple Impacts: The impact load bearing capacities (measured using PCF) of HSHDC slabs are compared to that of COR-TUF slabs under multiple impacts in Figure 8.7. As shown in Table 8.1, these instrumented multiple impacts were performed with the 3″ impact head at three different impact velocities (2.30 m/s, 3.25 m/s, and 4.60 m/s). In all the graphs of Figure 8.7, the red and blue curves represent COR-TUF and HSHDC specimens, respectively (solid curve is specimen 1 and dashed curve is specimen 2).

It is observed in Figure 8.7a that, for the lowest velocity impacts at 2.30 m/s, the peak contact force (PCF) for the slabs of both materials remains almost constant. The energy imparted in these impacts is insufficient in deforming the slabs to produce any significant inelastic tensile strains at the bottom/back face. This is confirmed by the visual observations of the back faces of these slabs, which show only a few cracks at the end of 20 impacts in both materials. It should be noted that although the COR-TUF material is strain-softening under direct tension, the COR-TUF slab exhibits deflection-hardening under flexure to limited displacements. Thus, minor flexural damage caused by the lowest velocity impacts does not reduce the impact load bearing capacity of the slabs of either material.

Increasing the impact velocities to 3.25 m/s (Figure 8.7b) and 4.60 m/s (Figure 8.7c) increases the kinetic energy of the drop-weight assembly to 2 and 4 times, respectively, that of the impact at 2.30 m/s. Unlike the impacts at 2.30 m/s, these higher velocity impacts on HSHDC and COR-TUF slabs produce significant inelastic tensile strains, which accumulate with increasing number of impacts. As soon as the deflection-hardening capacity of the COR-TUF slab is exceeded, it starts to lose its impact load bearing capacity as observed by the drops in PCF

in Figure 8.7b and c. The drop in PCF of COR-TUF slabs occurs more rapidly at 4.60 m/s compared to 3.25 m/s. In contrast, PCF in HSHDC slabs remains almost constant for all the impact velocities investigated in this study. While the COR-TUF slabs fail (definition of 'failure' is given in Section 8.2.2) under flexure before 20 impacts at these higher velocities (except slab #C3.25-1, which, although did not fail, has significantly reduced PCF), HSHDC slabs maintain their integrity and continue to rebound the drop-weight assembly during all the 20 impacts. The damage tolerance of HSHDC, which is significantly higher than COR-TUF under tension, allows the HSHDC slabs to absorb more impact energy, while maintaining their structural integrity, compared to the COR-TUF slabs.

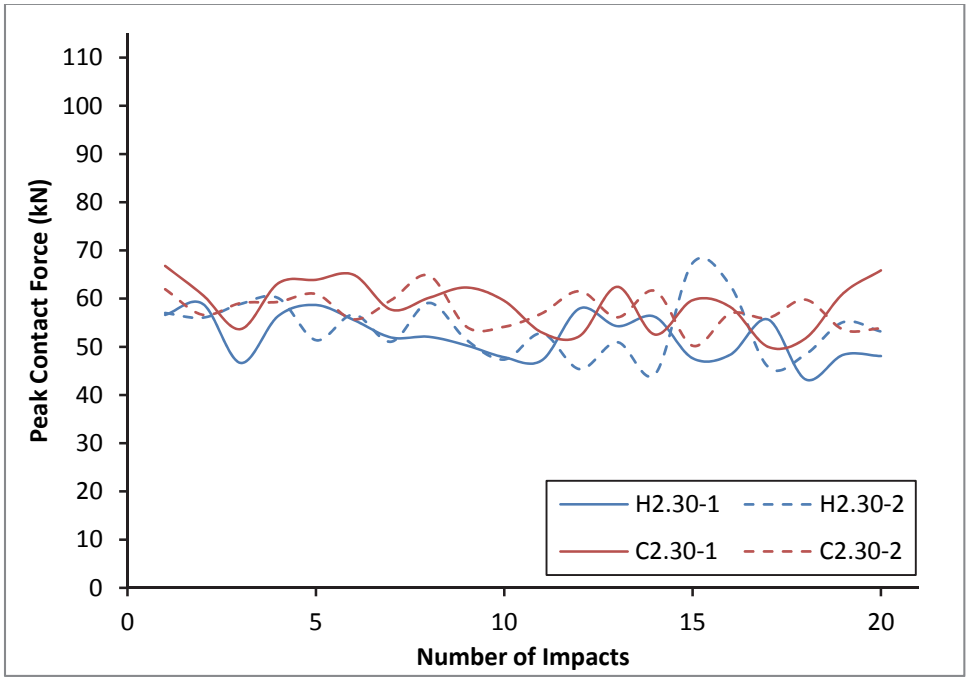

(a) Impact Velocity = 2.30 m/s

Figure 8.7: Comparison of HSHDC and COR-TUF slabs under multiple impacts

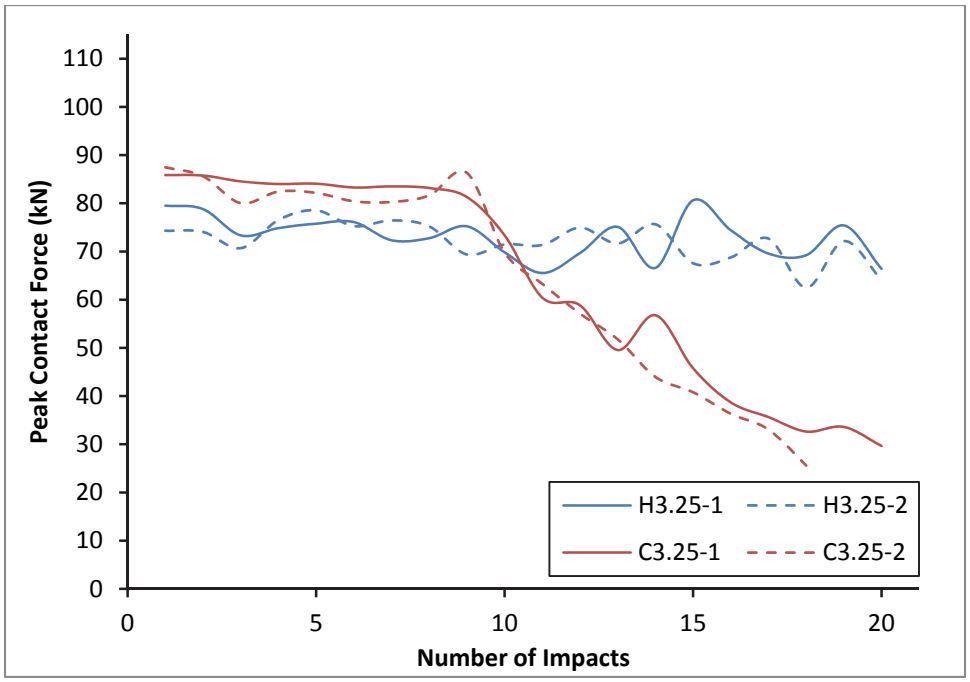

(b) Impact Velocity = 3.25 m/s

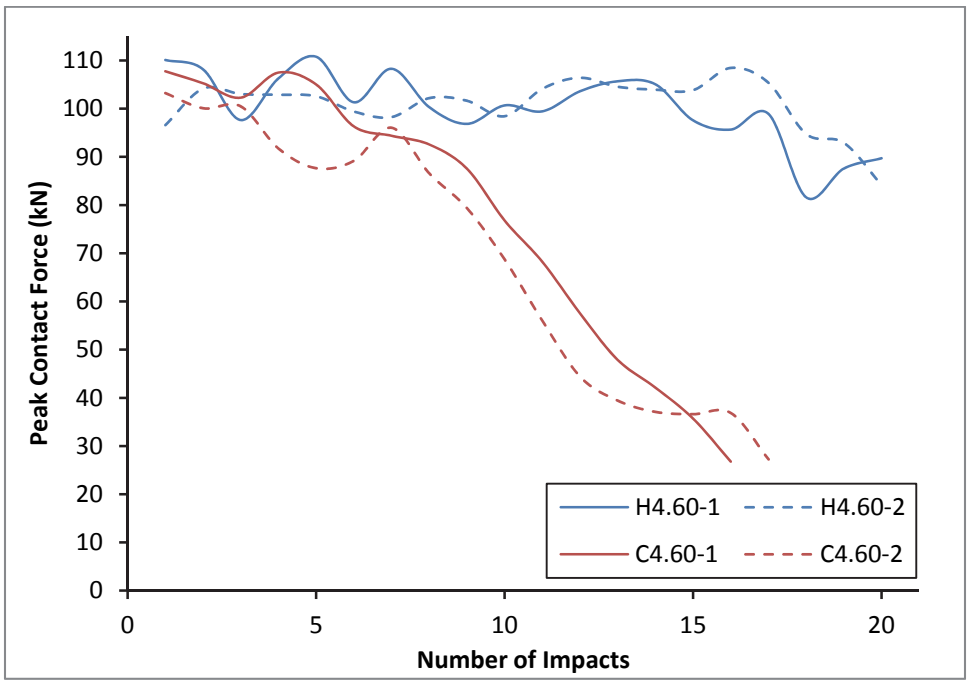

(c) Impact Velocity = 4.60 m/s

Figure 8.7: Comparison of HSHDC and COR-TUF slabs under multiple impacts

The visual appearance of the damage states of representative COR-TUF and HSHDC slabs after 20 impacts with 3″ head at 3.25 m/s is shown in Figure 8.8 and Figure 8.9. At its tensile face, the COR-TUF slab exhibits mainly four large flexural cracks emanating from the center of the slab. Due to the structural support conditions (Figure 8.2c), maximum principal tensile strain occurs normal to the sections joining the center to the third of the slab edges of these two-way symmetric slabs (shown through FE analysis below in Figure 8.25). The COR-TUF slab (Figure 8.8b) is unable to distribute the damage due to the material's tension-softening behavior, and therefore, the entire tensile strain localizes at these sections. The flexural damage concentration is so intensive that the flexural cracks reach the front (compression) face of the COR-TUF slabs and cause visible cracks (Figure 8.8a). Thus, the COR-TUF slabs exhibit quasi-brittle flexural failure with large localized flexural cracks and visible spalling.

In contrast with COR-TUF, the HSHDC slab (Figure 8.9b), due to its tension-hardening behavior, spreads the tensile strain into multiple fine cracks propagating radially outward in numerous directions from the center of the slab. A relatively large crack (relative to the other fine cracks in HSHDC) always occurs at the center of the HSHDC slab due to the presence of the maximum tensile stress at that location. Due to relatively uniform distribution of flexural damage in HSHDC slabs, there is no significant visible damage on the compression face. Additionally, almost no spalling is observed during the impacts on HSHDC slabs. Unlike COR-TUF, the HSHDC slabs exhibit ductile flexural behavior (without failure until 20 impacts) with well-distributed multiple fine radial cracks and almost no spalling.

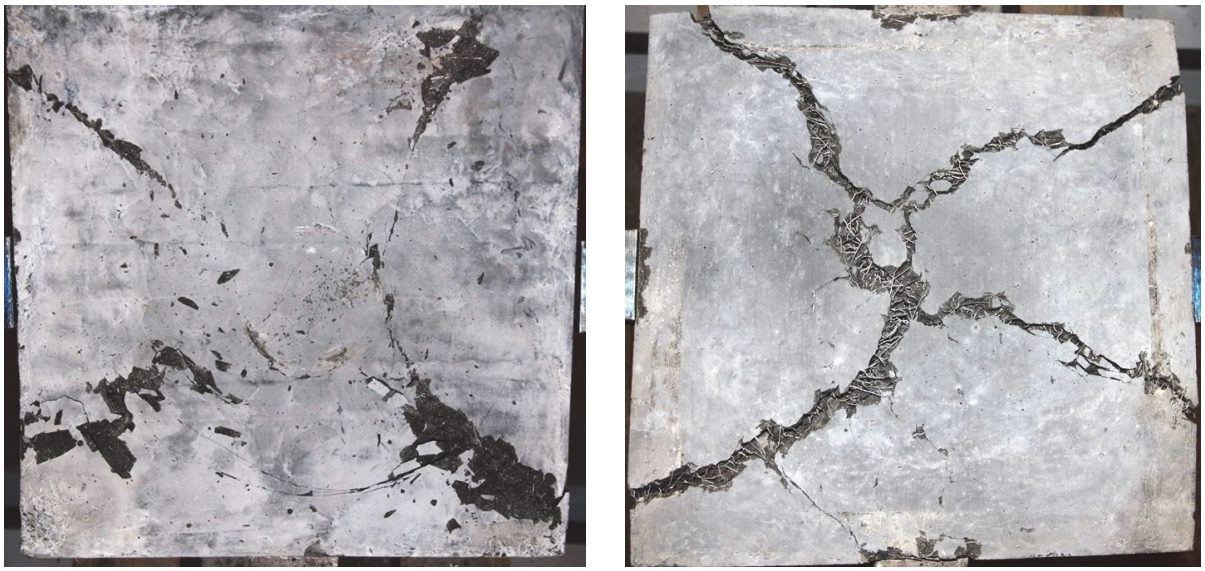

(a) Front (Compression) (b) Back (Tension)

Figure 8.8: Damage condition of the COR-TUF slab C3.25-1 after impact #19 with 3″ head (the slab disintegrates into 4 pieces after the next impact)

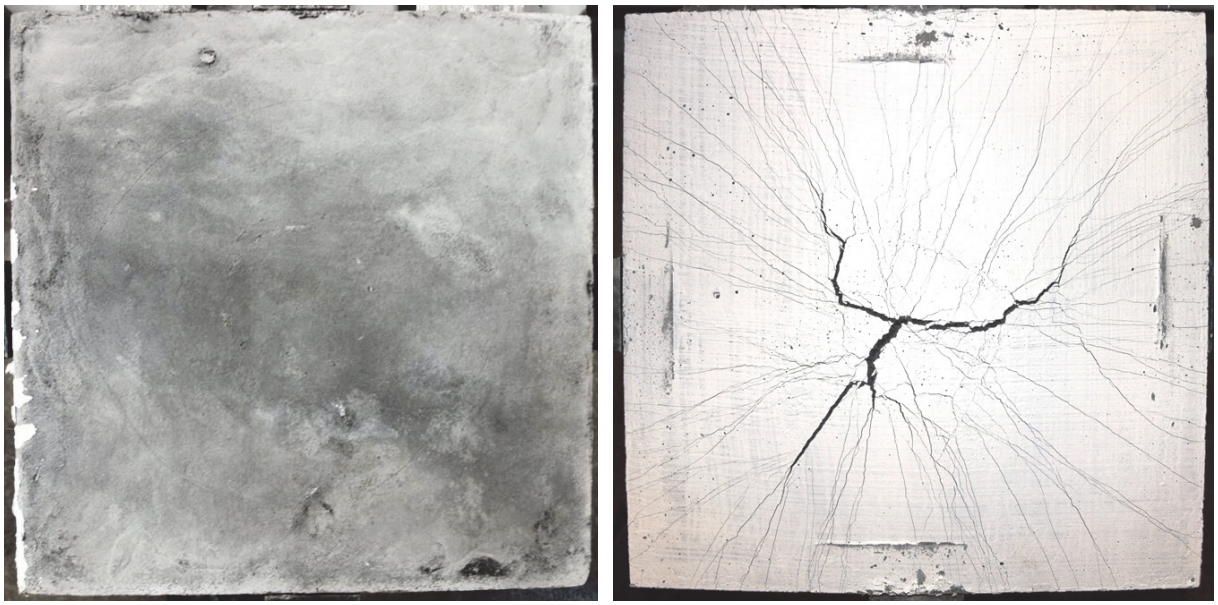

(a) Front (Compression) (b) Back (Tension)

Figure 8.9: Damage condition of the HSHDC slab H3.25-1 after impact #20 with 3″ head (back face of HSHDC is painted white to make the multiple fine cracks visible)

The visual observations of the damage patterns in HSHDC and COR-TUF slabs caused by the impacts with 3″ head (discussed above) at 3.25 m/s are compared to that caused by the impacts with 2″ head (non-instrumented) at the same velocity (the total weight of the drop-weight assembly is nearly constant). Comparing the front (compression) faces of the two COR-TUF slabs impacted by 2″ and 3″ heads, a punching-shear hole is visible in Figure 8.10a, which is absent in Figure 8.8a. The effect of the punching is also visible on the back (tension) face of the COR-TUF slab in Figure 8.10b. This brittle punching-shear failure of the COR-TUF slab by the 2″ head occurs at the 15th impact, which is 5 impacts less than that needed for the flexural failure of the COR-TUF slab by the 3″ head. In contrast, the punching-shear effect is not observed in the HSHDC slab on any face (Figure 8.11), and the ductile flexural behavior (without failure) is maintained even with the smaller 2″ head. The ductile behavior of HSHDC in tension also improves its shear behavior, similar to that observed in other strain hardening materials, such as ECC.[10] Thus, while the failure mode of the COR-TUF slabs changes from flexure to punching-shear on reducing the size of the impact head, no such effect is observed in HSHDC slabs due to the material's tensile ductility.

(a) Front (Compression) (b) Back (Tension)

Figure 8.10: Damage condition of the COR-TUF slab #1 after impact #15 with 2″ head at 3.25 m/s

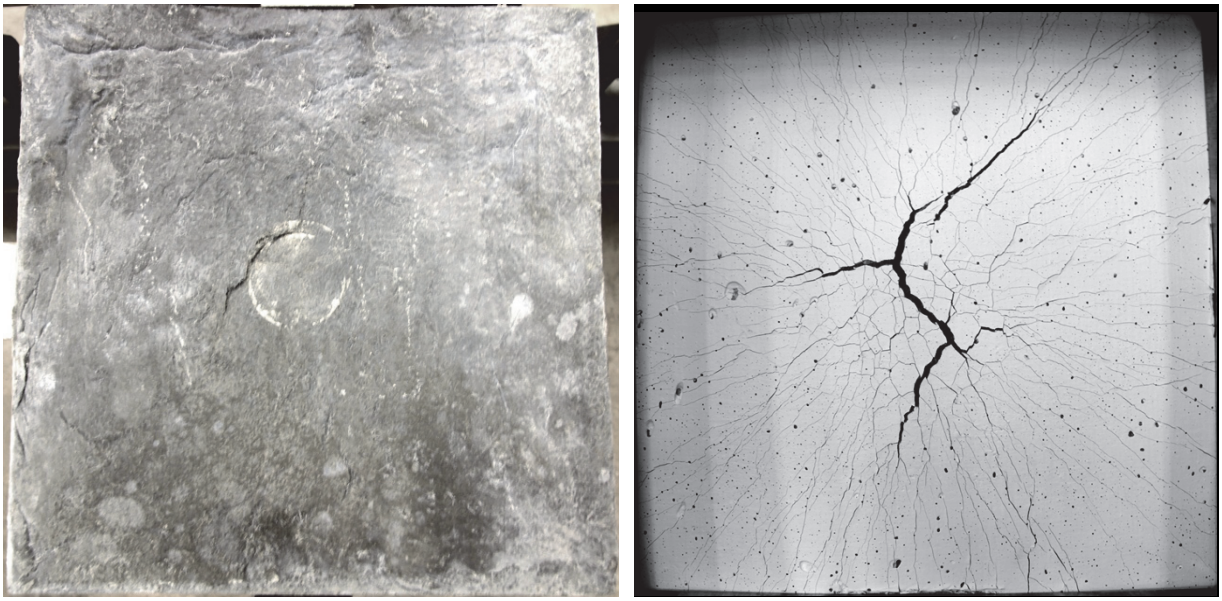

(a) Front (Compression) (b) Back (Tension)

Figure 8.11: Damage condition of the HSHDC slab #1 after impact #20 with 2″ head at 3.25 m/s

8.3 Finite Element Analysis of the Drop-Weight Tests

8.3.1 Introduction

The drop-weight experiments reported in Section 8.2 are simulated in this section using finite element (FE) analysis to achieve the following objectives: (1) to gain insights into the experimentally determined structural response of the slabs (2) to utilize the FE model as an optimization tool to efficiently design layered slabs (3) to utilize the FE model as a predictive tool for estimating the behavior of HSHDC and COR-TUF slabs under blast loads. The FE model developed in this study reduces the need for expensive experiments and can potentially serve as a powerful tool for the dynamic analysis of other structures utilizing HSHDC and similar strain-hardening materials – something that is lacking in the existing literature. The FE model developed for drop-weight tests is extended in the next section for simulating blast effects on HSHDC and COR-TUF slabs, which otherwise require a shock tube and extremely expensive experimental setups – achievable only at select laboratories in the country.

The FE analysis in this research was performed using the commercially available software LS-Dyna with Lagrangian mesh formulation and explicit time integration. These choices of the software, mesh formulation, and time integration method are discussed below.

Software: LS-Dyna, ABAQUS, and NASTRAN are the most widely used general-purpose FE softwares for dynamic analysis, along with numerous other special-purpose softwares. LS-Dyna was preferred to ABAQUS and NASTRAN in this research because LS-

Dyna is considered suitable in literature for modeling both impact and blast-related problems. On the other hand, ABAQUS and NASTRAN are commonly used in crash-related problems and are considered less efficient for blast-related problems. As both impacts and blasts are of interest in this research, LS-Dyna was chosen for the FE analysis.

Mesh Formulation: LS-Dyna has the capability of both Lagrangian and Eulerian mesh formulations (along with Arbitrary Lagrangian-Eulerian and mesh-free Smooth Particle Hydrodynamics formulations); however, only Lagrangian mesh formulation (with erosion) is used in this research. In the Lagrangian formulation, the element mesh stays attached with the material during deformation (almost all pseudo-static FE softwares employ this formulation for structural analysis). In other words, no material flow occurs between individual mesh elements. On the other hand, an Eulerian mesh remains fixed in space and does not deform with the material. Instead, it allows the material to flow from one element to another. The Lagrangian formulation is computationally faster than the Eulerian formulation for solving solid mechanics problems without severe element distortion, as additional time is expended in the Eulerian formulation for computing the transport of material between mesh elements.

The Eulerian formulation, typically used to model fluid mechanics problems involving material flow, is needed only for solving specific solid mechanics problems, such as projectile penetration problems, where severe element distortion occurs and local deformation of the target dominates the overall structural response. In both the problems investigated in this research – low velocity impacts with blunt objects and blasts, the element distortion is not severe and the

global deformation of the slabs dominates the overall structural response, and therefore, Lagrangian mesh formulation with erosion is deemed to be sufficient for this FE analysis.

Time integration method: Both implicit and explicit methods for direct time integration of variables (displacements [U], velocities [$\dot{U}$], and accelerations [$\ddot{U}$]) are available in LS-Dyna; however, as in most dynamic problems, only explicit method is used in this research. Similar to space, time is also divided into discrete intervals in a dynamic FE analysis, and the equilibrium of internal structural forces (stiffness, damping, and inertial forces) with the applied loads is sought at these discrete time intervals. Mathematically, this involves solving simultaneous differential equations (using matrix algebra) with the goal of determining the unknown variables (U, $\dot{U}$, and $\ddot{U}$) at the discrete time intervals. The distinctions between implicit and explicit integration methods used to solve these differential equations are discussed below.

In the explicit method, the equilibrium at time, t, is considered (using structural properties at time, t), and U, $\dot{U}$, and $\ddot{U}$ at time, t, are *explicitly* integrated using methods such as central difference to compute the U, $\dot{U}$, and $\ddot{U}$ at time, t + Δt. On the other hand, in implicit methods such as Houbolt, Wilson, and Newmark's methods, the equilibrium at time t + Δt is considered (by first determining the structural properties at time t + Δt) to directly calculate U, $\dot{U}$, and $\ddot{U}$ at time, t + Δt; hence, U, $\dot{U}$, and $\ddot{U}$ are *implicitly* integrated.

The explicit method is typically favored for dynamic problems with short duration (of the order of a few milliseconds) due to its computational speed. The determination of structural properties at t + Δt in implicit methods requires significant computational time, which makes

these methods computationally less efficient for dynamic problems. However, a significant limitation of the explicit method is that it is only conditionally stable, which means that the solution is convergent only if the time-steps Δt are small enough (T_n/π, where T_n is the smallest time period of the finite element assemblage with n degrees of freedom). LS-Dyna automatically ensures this stability condition during analysis by limiting the time-step size. The requirement of short time-step makes the use of explicit methods less attractive for pseudo-static analysis or dynamic problems lasting for long durations (of the order of seconds to minutes). The implicit method is typically used for such problems because it is unconditionally stable. The impact and blast-related problems investigated in this study meet the criteria of short-lasting dynamic problems, and therefore, only the explicit method of time integration is employed.

The FE analysis in this research consisted of the following steps: (1) modeling the geometry of various parts (slab, impact head, and support) of the drop-weight tests (2) meshing the parts with elements of appropriate type and size (3) material property assignment to various parts (requiring determination of a proper material model) (4) applying loads (impact velocity) and boundary conditions (5) solving the problem in LS-Dyna (6) post-processing and discussion of results. Each of these steps is discussed in detail below.

8.3.2 Geometry and Meshing

The FE model of the drop-weight test is shown in Figure 8.12. Due to the symmetry of the problem about two orthogonal axes, only a quarter of the square slab is modeled with appropriate boundary conditions. Meshing of the slab in LS-Dyna is performed using 8-node

constant stress solid (brick) elements with one-point integration. The stiffness form of the hourglass control method proposed by Flanagan & Belytschko[11] is activated in LS-Dyna to avoid zero-energy modes, which may form due to the reduced integration. Such hexahedral mesh elements have been widely used in impact and blast models of concrete structures with satisfactory performance.[12,13,14]

The size of the brick element for modeling the slab was determined from a mesh convergence study. In this study (Figure 8.13), the maximum displacement of the central node of the impact head's face in contact with the slab is determined for different levels of mesh refinement. As the size of a single element is reduced, the response of the slab becomes stiffer resulting in smaller displacement of the impact head. Decreasing the element size from 2 mm to 1 mm reduces the head displacement by only about 50 μm (< 2%); however, the computational time increases almost by 8 times due to as much increase in the number of elements. Thus, an element size of 2x2x2 mm^3 is used in this study for modeling the slab.

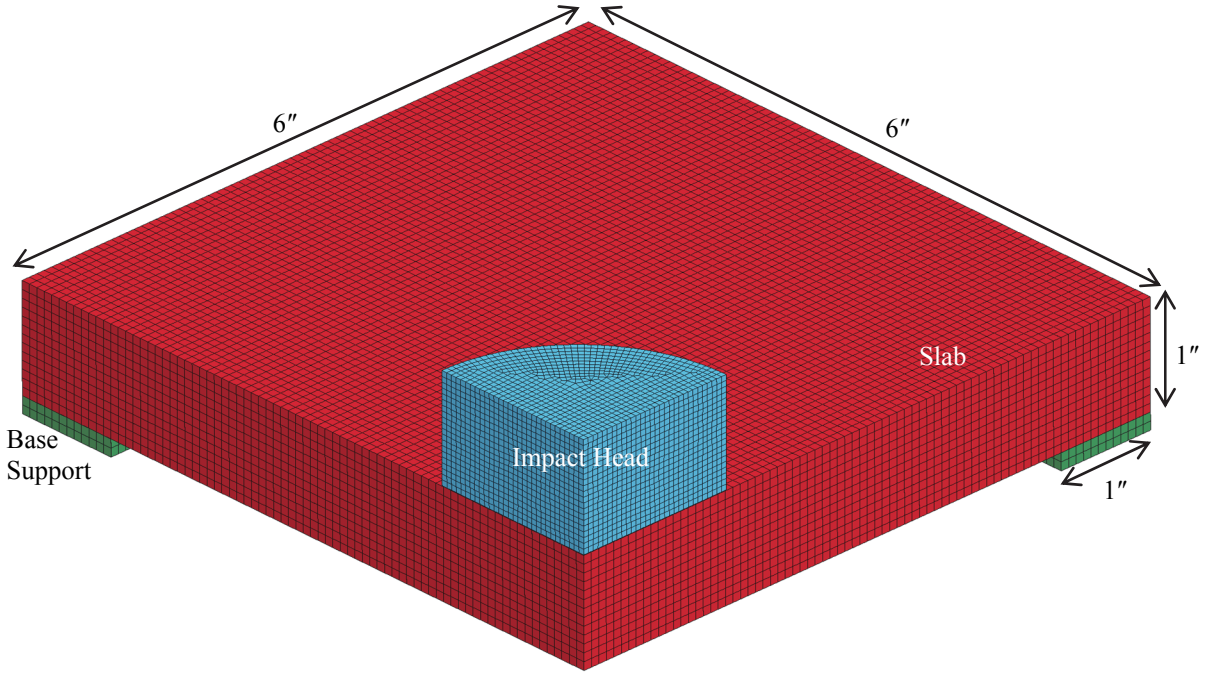

Figure 8.12: FE model of the drop-weight test

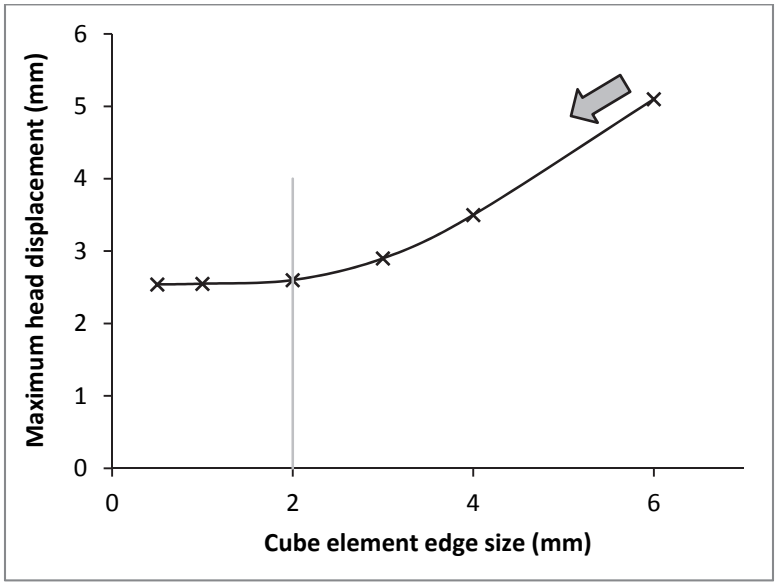

Figure 8.13: Mesh convergence study with impact velocity of 4.60 m/s

Similar to the slab, the impact head and the base support are also discretized using brick elements, although with different material (steel). For contact computations, it is advisable to

have the mesh density of contacting surfaces similar to each other. Hence, the element size determined optimal for the slab was also closely maintained for modeling the impact head and the base support.

8.3.3 Material Model for Slab Elements

8.3.3.1 *Introduction*

The FE modeling of concrete (and similar cement based materials, including FRC, HSHDC, COR-TUF, and ECC) poses unique challenges compared to other structural materials such as steel. Concrete is a highly complex and heterogeneous material with significant local variation of properties; therefore, modeling it as a homogenous material with average properties in FE analysis is a substantial assumption. To add to the complexity, concrete has a significantly different behavior in compression than in tension. Furthermore, the behavior of concrete, particularly its strength, under multi-axial loading is different than under uniaxial loading. These complexities of concrete behavior are dealt in concrete plasticity theory using three-dimensional failure surface (details in Section 8.3.4).

The concrete damage model MAT_072R3 of LS-Dyna material library, based on concrete plasticity theory, is used in this research for modeling HSHDC and COR-TUF materials in the slab elements. There are several other material models available in the LS-Dyna library for modeling concrete and tension-softening fiber-reinforced concretes (FRC), such as model numbers 16, 84/85, 96, 111, 159, 172, and 195. However, none of these models can be used to

model strain-hardening concretes such as HSHDC. Although MAT_072R3 model (also known as Karagozian and Case or K&C model) was also originally developed (by Malvar et al[12]) for concrete and tension-softening FRCs, it can be adopted for HSHDC because it has (1) three separate fixed 'loading surfaces' (yield, ultimate, and residual), and (2) two parameters for independently controlling the damage parameter in tension and in compression, as explained in detail below. While the mathematical details of the MAT_072R3 model are presented in Malvar et al and other texts on concrete plasticity, the objective of this sub-section (8.3.3) is to only outline the main features and setup of this model so that all the variables inputs required for modeling HSHDC and COR-TUF in LS-Dyna can be correctly determined.

8.3.3.2 *Stress-Invariants*

Before defining a 3D failure surface for concrete, it is imperative to identify a set of appropriate stress-invariants, which define the stress-state at a material point independent of the spatial coordinate system attached to the material. The 3D stress-state at any material point is typically represented by the Cauchy stress tensor (CST). However, the individual elements of this tensor are dependent on the coordinate system. The same stress-state can also be expressed in terms of three stress-invariants that are independent of the coordinate system, and are derivable from the elements of the CST. Example sets of stress-invariants are 3 principal stress: σ_1, σ_2 and σ_3; 3 invariants of the CST: I_1, I_2, and I_3; 3 invariants of the deviatoric stress tensor: J_1, J_2, and J_3. Although all these sets have clear mathematical definitions, none of them have a physical interpretation of the stress-state that is useful for understanding the failure criterion.

Therefore, in concrete plasticity, the three physically interpretable stress-invariants of ξ, r, and θ are often used to define the 3D stress-state.

The physical significance of ξ, r, and θ can be best understood in the Haigh-Westergaard (HW) stress-space (Figure 8.14), in which the three spatial axes are represented by the three principal stresses. Consider a stress-state P with coordinates (σ_1, σ_2, σ_3) in the HW space, as shown in Figure 8.14. Note that P is intentionally plotted in the octant: $-\sigma_1$, $-\sigma_2$, $-\sigma_3$, which contains the majority of possible stress-states for concrete (and also for HSHDC and COR-TUF). Instead of tracing the principal axes coordinates (σ_1, σ_2, σ_3) to reach P, it is also possible to first trace a distance $-\xi$ along the hydrostatic axis (where $\sigma_1 = \sigma_2 = \sigma_3$), and then, trace a distance r in the deviatoric plane (perpendicular to the hydrostatic axis) in the direction θ with respect to the projection of σ_1 axis (represented as σ_{1d} in Figure 8.14) in the deviatoric plane. Thus, ξ is a measure of the hydrostatic pressure ($\xi = -\sqrt{3}p$, where $p = I_1/3$), r is the measure of the effective deviatoric stress, and θ (Lode angle or angle of similarity) captures the relative closeness of the intermediate principal stress (σ_2) to the first principal stress compared to the third principal stress.

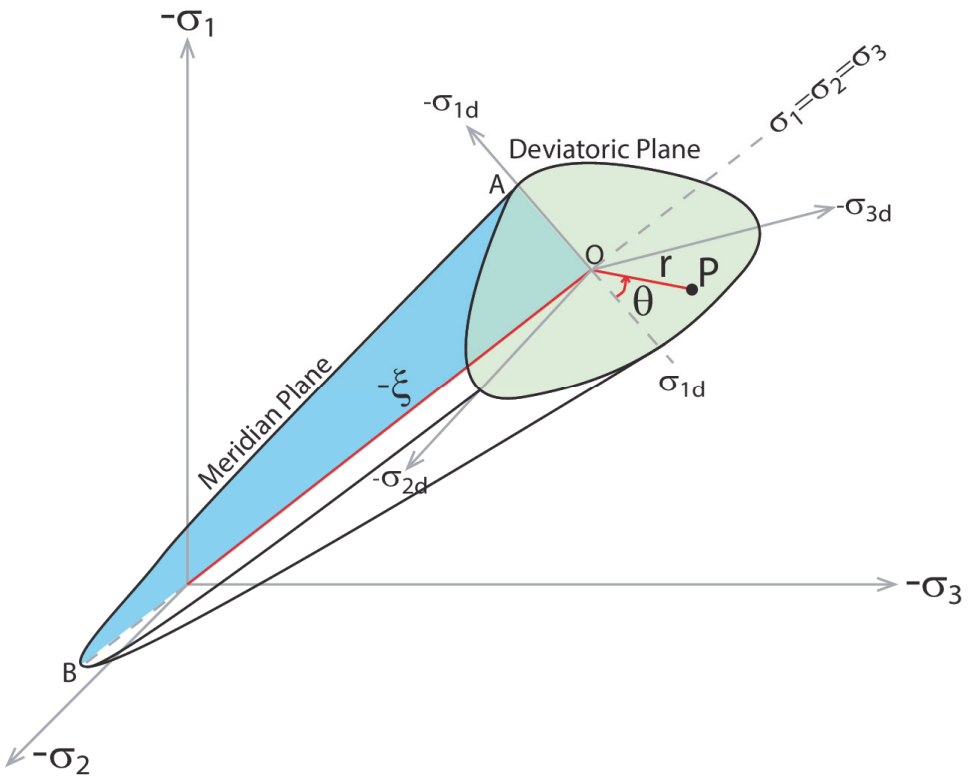

Figure 8.14: Stress-invariants ξ, r, θ and concrete's failure surface used in LS-Dyna material model MAT_072R3

The mathematical expressions for ξ, r, and θ in terms of I_1, J_2, and J_3 are given below. I_1, J_2, and J_3 are further relatable to the elements of CST.

$$\xi = \frac{I_1}{\sqrt{3}} = -\sqrt{3}p \tag{8.1}$$

$$r = \sqrt{2J_2} \tag{8.2}$$

$$\cos(3\theta) = \frac{3\sqrt{3}}{2}\frac{J_3}{J_2^{3/2}} \tag{8.3}$$

8.3.3.3 *Failure Surface*

A failure surface for a material is an envelope of critical stress-states such that (1) all stress-states falling inside (toward origin) this envelope represent elastic behavior, (2) all stress-states falling on the envelope represent inelastic behavior, and (3) stress-states outside this envelope are not achievable by the material; although, the failure surface itself can move and change shape and size depending on the plastic strain (or damage state) of the material. Unlike uniaxial criterion, where failure is defined by a single limiting value of stress, the three-dimensional (3D) failure criterion is defined by a critical combination of 3D stresses.

The shape of the 3D failure surface used in the LS-Dyna material model MAT_072R3 is depicted in Figure 8.14. This 3D surface is further explained below using its intersections with two types of planes orthogonal to each other – the meridian plane (ξ-r plane; θ constant) and the deviatoric plane (r-θ plane; ξ constant). The 3D failure 'surface' is a 2D 'curve' in these planes and is referred to as *failure curve* in the discussion below.

A meridian plane (e.g. AOB – shaded blue in Figure 8.14) is the locus of all stress-states with constant Lode angle (θ). All meridian planes are parallel to and contain the hydrostatic axis. The meridian planes which contain uniaxial tension and uniaxial compression as one of the possible stress-states are called the tensile and compressive meridian planes, and are located at θ = 0° and 60°, respectively. In Figure 8.14, the tensile meridian (θ = 0°) contains the first principal axis projection σ_{1d}, whereas the compressive meridian (θ = 60°) contains the third principal axis projection $-\sigma_{3d}$. In the meridian plane, the failure curve (p-$\Delta\sigma$ or ξ-r) is continuous

and its shape is convex, such that while the deviatoric stress capacity ($\Delta\sigma$, such that $r \le \sqrt{3/2}\Delta\sigma$) increases monotonically with the hydrostatic pressure ($p = -\xi/\sqrt{3}$), the slope dr/dp decreases monotonically with p (but always remains greater than 0).

A plane of stress-states perpendicular to the meridian planes (and also the hydrostatic axis), at a constant hydrostatic pressure (or constant ξ), is called a deviatoric plane (shaded green in Figure 8.14 – also known as octahedral plane). The failure curve (r-θ) in the deviatoric plane is determined by an elliptic interpolation (introduced by William & Wranke[15]) between the tensile and compressive meridians (i.e. between θ = 0° and 60°). It is assumed in the material model MAT_072R3 that concrete is an isotropic material, and as a result, the failure curve at any deviatoric plane has a three-fold symmetry about the principal stress axes projections ($-\sigma_{1d}$, $-\sigma_{2d}$, $-\sigma_{3d}$) on that deviatoric plane. The three-fold symmetry is used to completely determine the failure curve at a particular hydrostatic stress by mirroring the elliptical interpolation about the principal axes.

The failure curve in the tensile meridian plane (p-$\Delta\sigma$) is determined in the MAT_072R3 model by scaling the failure curve in the compressive meridian plane by a factor ψ(p) (a function of hydrostatic pressure p). It should be noted that ψ is not the ratio of tensile to compressive strengths, but it is the ratio of the deviatoric stress capacities in tensile and compressive meridian planes. In the model, ψ is assumed to vary from 0.5 at negative (tensile) pressures to 1 at high compressive pressures, based on experimental results. This change in ψ with pressure dictates the overall shape of the failure curve in a deviatoric plane, which is triangular (with vertices

along the positive principal axis projections) for small values of hydrostatic pressure and becomes increasingly circular (bulged) with growing hydrostatic pressure.

From the above discussion of the failure surface used in MAT_072R3 model, it can be concluded that the 3D failure surface can be completely defined at any damage state, if the following are known: (1) the failure curve p-$\Delta\sigma$ between hydrostatic pressure (p) and deviatoric stress capacity ($\Delta\sigma$) in the compressive meridian plane at a particular damage state, and (2) a scaling rule for $\Delta\sigma$ that is dependent on the damage state at the material point. In the next two sections, first, the damage dependent scaling rule [point (2) above] for $\Delta\sigma$ is discussed in terms of fixed 'loading surfaces' in the compressive meridian plane, followed by the determination of p-$\Delta\sigma$ relations in the meridian planes at these fixed loading surfaces for HSHDC and COR-TUF.

8.3.3.4 *Fixed Loading Surfaces*

The foregoing discussion of the 3D failure surface refers to the failure condition at a particular damage state (no dependence on damage state was discussed); in this section, the method employed in the MAT_072R3 model to determine the failure surface at varying damage states is discussed. For this purpose, three fixed 'loading surfaces' corresponding to the damage states of 'yield capacity', 'maximum capacity', and 'residual capacity' are defined, and the failure surface is assumed to travel between these fixed surfaces depending on the damage state of the material. For a uniaxial loading, these 'loading surfaces' are merely points on the stress-strain curve as schematically shown in Figure 8.15. The 3D failure surface is determined for any

damage state by interpolating between these fixed loading surfaces using a damage parameter, as explained below.

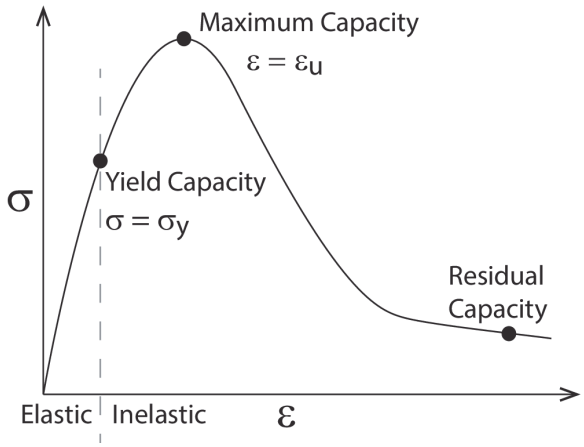

Figure 8.15: Schematic representation of the fixed loading surface locations

Similar to the 3D failure surface, the loading surfaces can also be completely determined from p-Δσ curves at the compressive meridian plane. In the MAT_072R3 model, the p-Δσ curves shown in Eqs. 8.4, 8.5, and 8.6 are used to define the loading surface at the compressive meridian plane. In these equations, the suffix of Δσ denotes the loading surface (y: yield; m: maximum; r: residual), and all parameters a's are input in the MAT_072R3 model by the user based on the experimental data (Section 8.3.3.6).

$$\Delta\sigma_y = a_{0y} + \frac{p}{a_{1y} + a_{2y}p} \tag{8.4}$$

$$\Delta\sigma_m = a_0 + \frac{p}{a_1 + a_2 p} \tag{8.5}$$

$$\Delta\sigma_r = \frac{p}{a_{1f} + a_{2f}p} \tag{8.6}$$

Similar to the failure surface mentioned above, the loading surfaces in the tensile meridian (p-$\Delta\sigma$ curves) are computed from their corresponding compressive meridian counterparts (Eqs. 8.4-8.6) using a multiplying factor ($\psi < 1$). However, the maximum loading surface in the tensile meridian, given by ψ times Eq. 8.5, is modified for pressures, $p < f_c'/3$, such that the maximum tensile stress is limited to f_t under uniaxial and triaxial loading. The p-$\Delta\sigma$ curve given by Eq. 8.7 is used for the maximum loading surface in the tensile meridian. It is easily verifiable that this curve (straight line) passes through both $(p,\Delta\sigma) = (-f_t/3, f_t$ – uniaxial tension point) and ($-f_t$,0 – triaxial tension point).

$$\Delta\sigma_m = \frac{3}{2}\left(p + f_t\right) \tag{8.7}$$

The deviatoric stress capacity ($\Delta\sigma$) in the compressive meridian of the failure surface at a particular damage state is determined by interpolating between these fixed loading surfaces using the damage parameter η, which is further dependent on a scalar quantity λ – the accumulative (monotonically increasing) effective plastic strain parameter. The interpolation expressions are given in Eqs. 8.8 and 8.9. In these equations, λ_m is the effective plastic strain parameter corresponding to the maximum value of η, when the failure surface coincides with the maximum loading surface (i.e. $\Delta\sigma = \Delta\sigma_m$).

$$\Delta\sigma = \eta\Delta\sigma_m + \left(1-\eta\right)\Delta\sigma_y \quad \text{for } 0 < \lambda \le \lambda_m \tag{8.8}$$

$$\Delta\sigma = \eta\Delta\sigma_m + \left(1-\eta\right)\Delta\sigma_r \quad \text{for } \lambda > \lambda_m \tag{8.9}$$

The migration of the failure surface between the fixed loading surfaces depends on the accumulated effective plastic strain parameter λ, which in turn governs the damage parameter η. When the material is elastic, $\lambda = 0$ (no plastic strain) and the failure surface coincides with the yield surface (i.e. $\Delta\sigma = \Delta\sigma_y$). As the material is loaded beyond the yield surface, plastic flow occurs in accordance with modified Prandtl-Reuss (fractionally associated) flow rule, and plastic strains develop in the material, which accumulate in the value of λ (discussed in the next section). For $0 < \lambda \leq \lambda_m$, the failure surface is interpolated between the maximum and the yield loading surfaces as η increases from 0 to 1; and for $\lambda > \lambda_m$, the failure surface is interpolated between the maximum and the residual loading surfaces as η decreases from 1 to 0. The η-λ relation is input by the user in the MAT_072R3 material model, and the relation used in this research is shown in Figure 8.16. The rising branch of the η-λ curve used in this research is the same as the default curve in the MAT_072R3 model. The falling branch of the η-λ curve is adjusted to match the softening behavior of HSHDC in uniaxial compression tests. In this manner, the deviatoric stress capacity, $\Delta\sigma$, is scaled between the fixed loading surfaces depending on the damage state.

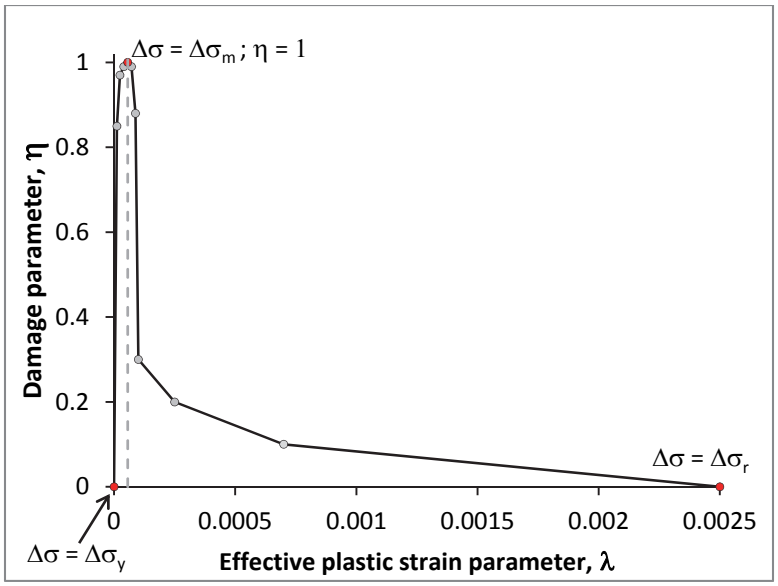

Figure 8.16: η-λ relation for HSHDC used in MAT_072R3 model

8.3.3.5 *Damage Accumulation*

The cumulative effective plastic strain parameter, λ, is computed in the MAT_072R3 model using Eq. 8.; where ε_{ij}^{p} is the tensorial plastic strain, f_t is the ultimate tensile strength, r_f is the rate factor (defined below), b_1 and b_2 are the damage scaling parameters, which control the rates ($d\lambda / d\overline{\varepsilon^{p}}$) of damage accumulation in λ for positive and negative pressures, respectively. The independent control of damage accumulation in tension ($p < 0$) and compression ($p \geq 0$) through separate parameters b_1 and b_2 is a unique feature of the MAT_072R3 model, which enables the adaptation of this model for strain-hardening materials such as HSHDC.

$$\lambda = \begin{cases} \int_0^{\overline{\varepsilon^p}} \dfrac{d\overline{\varepsilon^p}}{r_f\left(1+\left.p\right/ r_f f_t\right)^{b_1}} & \text{for } p \geq 0 \\ \int_0^{\overline{\varepsilon^p}} \dfrac{d\overline{\varepsilon^p}}{r_f\left(1+\left.p\right/ r_f f_t\right)^{b_2}} & \text{for } p < 0 \end{cases} \qquad \textit{where } \; d\overline{\varepsilon^p} = \sqrt{\frac{2}{3}\varepsilon_{ij}^p \varepsilon_{ij}^p} \tag{8.10}$$

Under compression ($p \geq 0$), increasing b_1 increases the denominator and slows down the damage accumulation in λ for a given effective plastic strain increment, $d\overline{\varepsilon^p}$, and makes the response more ductile, whereas under tension ($p < 0$), decreasing b_2 achieves the same objective of enhancing ductility. Note that the term $\left(1+\left.p\right/ r_f f_t\right)$ is less than 1 for $p < 0$, and therefore, increasing b_2 will decrease the denominator and make the response more brittle. The parameters b_1 and b_2 are determined by matching the uniaxial stress-strain curves, obtained by analyzing a single solid element in LS-Dyna under compression and tension, to the experimental material behavior.

In the MAT_072R3 model, another damage scaling parameter b_3, in addition to b_1 and b_2, is used for tackling spurious results for triaxial tensile loading. Such loading is not expected in the problem at hand, and therefore, in absence of experimental data, the default value of 1.1 (generated by the model for a concrete with equal compressive strength) is used.

8.3.3.6 *Input Parameters*

In the MAT_072R3 model, the input parameters a's, for defining the three loading surfaces in Eqs. 8.4-8.6, are determined using the available uniaxial experimental data (Chapter 5 and 6 for HSHDC and Chapter 3 for COR-TUF) and past studies on the behavior of confined high strength concrete. Specific data points in form of (p,Δσ) pairs listed in Table 8.2 are input in Eqs. 8.4-8.6 to solve for the parameters a's.

Table 8.2: Loading surfaces input parameter determination for HSHDC

Loading Surface	**Description/ Data point Reference**	**p**	**Δσ ($\sqrt{3J_2}$)**	**Parameter values for HSHDC**
$\Delta\sigma_m = a_0 + \frac{p}{a_1 + a_2 p}$	Uniaxial Compression/ Ref: Chapter 5	$f_c'/3$	f_c' (160 MPa)	a_0 = 24e6 a_1 = 0.366 a_2 = 4.91e-10
	Pure shear in plane stress $(\sigma_1,\sigma_2,\sigma_3) = (f_{tm},0,-f_{tm})$/ Ref: Matrix cracking strength, f_{tm}, from Chapter 5 ≈ 8 MPa	0	$3f_{tm}$ (24 MPa)	
	Highly confined compression/ Ref: Ottosen & Ristinmaa[16] (Tests by Balmer), similar values reported by others[17,18]	$4.62f_c'$	$6.49f_c'$	
$\Delta\sigma_y = a_{0y} + \frac{p}{a_{1y} + a_{2y} p}$	Yield surface assumed as locus of points at $\Delta\sigma_y = 0.45\Delta\sigma_m$ on triaxial compression paths/ Ref: Malvar et al[12] and Joy & Moxley[19]	0 MPa	29.2 MPa	a_{0y} = 22.6e6 a_{1y} = 0.397 a_{2y} = 1.17e-9
		10 MPa	47.8 MPa	
		100 MPa	176.2 MPa	
$\Delta\sigma_r = \frac{p}{a_{1f} + a_{2f} p}$	Brittle-ductile transition under triaxial compression assumed at $p = 4f_c'$; intermediate point assumed at $2f_c'$/ Ref: Chin[20] and Malvar et al[12]	$2f_c'$	$\Delta\sigma_m (p=2f_c') - f_{tm}$	a_{1f} = 0.356
		$4f_c'$	$\Delta\sigma_m (p=4f_c')$	a_{2f} = 4.80e-10

The values of the input parameters a's for defining the loading surfaces in the compressive meridian of COR-TUF, following the same procedure as for HSHDC used above, are listed in Table 8.3.

Table 8.3: Loading surfaces input parameters for COR-TUF

Maximum Surface	Yield Surface	Residual Surface
a_0 = 27e6 a_1 = 0.359 a_2 = 3.99e-10	a_{0y} = 24.6e6 a_{1y} = 0.410 a_{2y} = 1.52e-9	a_{1f} = 0.350 a_{2f} = 3.90e-10

Other input parameters in the MAT_072R3 material model listed in Table 8.4 include the following.

(i) Densities of COR-TUF and HSHDC based on experimental observations in Chapters 3 and 5, respectively.

(ii) Poisson ratio of both HSHDC and COR-TUF is assumed equal to 0.20, similar to concretes with comparable compressive strengths.

(iii) b_1, b_2, and b_3 are the damage scaling parameters detailed in the last section.

(iv) LOCWIDTH is the localization width of the crack assumed equal to the element size (determined in Section 8.3.2), which is 2 mm, to prevent localization instabilities and spurious mesh sensitivity. Decreasing LOCWIDTH increases the observed ductility in both tension and compression.

(v) f_t is the experimental uniaxial tensile strength

(vi) RSIZE and UCF are unit conversion factors given in LS-Dyna documentation.

Table 8.4: Other input parameters for HSHDC and COR-TUF

Input Parameter	**HSHDC**	**COR-TUF**
Density	2400 kg/m^3	2600 kg/m^3
Poisson Ratio	0.20	0.20
b_1, b_2, b_3	–0.55,–20,1.1	–0.55, –1,1.1
f_t	14.5 MPa	9.0 MPa
LOCWIDTH	0.002 m	
RSIZE, UCF	39.37, 1.45e-4	

8.3.3.7 *Equation of State, Rate Effects, and Material Erosion*

An 'equation of state' (EOS) describes the *hydrostatic behavior* of a material by relating the hydrostatic pressure to the volumetric strain. All the model parameters discussed thus far for defining the failure surface capture only the *deviatoric behavior* of the material. Therefore, an EOS is needed in order to complete the description of the material behavior. For this purpose, the EOS of type 8 (EOS 8) in LS-Dyna, which inputs tabulated pressure-volumetric strain data points (linear variation is assumed between the specified points) along with instantaneous bulk modulus at these points (for unloading), is used. The temperature dependent variation of hydrostatic pressure is neglected in this research. The equations of state used for HSHDC and COR-TUF are automatically generated by running LS-Dyna analysis for similar compressive strength concretes, which are assumed to have the same hydrostatic compressive behaviors as that of HSHDC and COR-TUF.

The rate effects on tensile and compressive strengths are incorporated by specifying a 'load curve' in LS-Dyna, which consists of tabulated data points of dimensionless dynamic increase factors (DIF) versus strain rate (linear variation is assumed between the specified

points). While the tensile DIFs are based on the experimental investigation in Chapter 7, the compressive DIFs are based on past studies on high strength concretes at high strain rates. The data points of the 'load curve' in LS-Dyna (plotted in Figure 8.17) are computed for tensile and compressive strain rates using mathematical expressions in Eqs. 8.11 and 8.12, respectively. The expressions for rate effects have a form similar to that recommended by the European Committee on Concrete[21] (Comité Euro-International du Béton or CEB) for normal strength concrete, but the coefficients and rate of increase are modified to fit the tensile test data in Chapter 7 and compressive strain rates for very-high strength concretes reported in literature.[22]

$$DIF_{Tens} = \begin{cases} c_1 \dot{\varepsilon}^{p_1} & \text{for } \dot{\varepsilon} \le 10 s^{-1} \\ c_2 \left(\dot{\varepsilon} / \dot{\varepsilon}_s \right)^{1/5} & \text{for } \dot{\varepsilon} > 10 s^{-1} \end{cases} \tag{8.11}$$

where, $c_1 = 1.331$, $c_2 = 0.064$, $p_1 = 0.022$, $\dot{\varepsilon}_s = 2 \times 10^{-6}$

$$DIF_{Comp} = \begin{cases} \left(\dot{\varepsilon} / \dot{\varepsilon}_s \right)^{p_2} & \text{for } \dot{\varepsilon} \le 30 s^{-1} \\ c_3 \left(\dot{\varepsilon} / \dot{\varepsilon}_s \right)^{1/5} & \text{for } \dot{\varepsilon} > 30 s^{-1} \end{cases} \tag{8.12}$$

where, $c_3 = 0.076$, $p_2 = 0.013$, $\dot{\varepsilon}_s = 3 \times 10^{-5}$

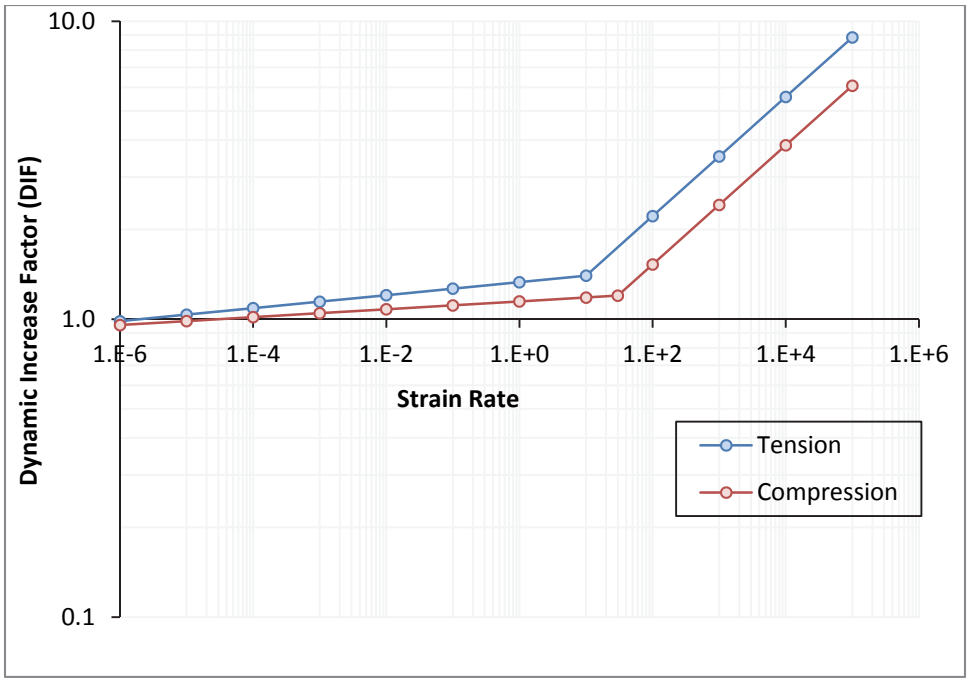

Figure 8.17: Rate effects model ('load curve' in LS-dyna) for material strength

Failure of the material is defined using tensile and compressive erosion criteria in this research. The tensile erosion criterion limits the maximum principal strain to 2.9% for HSHDC and 4.0% for COR-TUF. There is no mechanism in LS-Dyna to explicitly control the tensile ductility as a function of strain rate, and therefore, the erosion criteria is conservatively set to the minimum average tensile ductility of 2.9% observed in Chapter 7 for HSHDC under variable rate-direct tension tests. High rate direct tension test data for COR-TUF is unavailable. A rather high erosion strain limit of 4% is used for COR-TUF, which is based on the comparison between the FE analysis and the experimental observations of failure in COR-TUF slabs. Lower erosion strain limits cause excessive failure of elements in FE analysis, which is not observed in the drop-weight experiments. In addition, the tensile softening branch of the MAT_072R3 material model for COR-TUF touches zero stress at about 4.0% strain at $100s^{-1}$ strain rate (as shown in Section 8.3.3.8). The compressive erosion criteria used for the material models in this study limit

the maximum hydrostatic pressure to 400 MPa for HSHDC and 500 MPa for COR-TUF, accounting for the increase in strengths at high rates (10-1000 s^{-1}) under impact loads. In this manner, erosion criteria are used to limit the tensile strain capacity and compressive strength of HSHDC and COR-TUF in the LS-Dyna model.

8.3.3.8 *Single Element Uniaxial Tests*

As discussed above, there are a number of significant assumptions and variables involved in modeling the material behaviors of HSHDC and COR-TUF in LS-Dyna, and therefore, it is necessary to verify single element behavior with the available uniaxial experimental data, before using these material models for structural analysis of slabs. For this purpose, uniaxial tensile and compressive tests are simulated in LS-Dyna by assigning the material input parameters defined in Sections 8.3.3.6 and 8.3.3.7 to a single solid element of size 2 x 2 x 2 mm^3 (same as that used for slab modeling – Section 8.3.2), and the results are discussed below.

The results of the FE simulation of an HSHDC solid element under uniaxial tension loads at multiple strain rates are shown in Figure 8.18. As mentioned above, the uniaxial tensile stress-strain curves are terminated at 2.9% at all strain rates in the model using the tensile erosion criterion. The ultimate tensile strengths (Figure 8.18) closely match the experimental results at variable strain rates in Chapter 7. Although the first crack strengths of the modeled behavior are slightly higher than the corresponding values observed at low strain rates, they are more consistent with the observed first crack strengths at high strain rates (≥ 1 s^{-1}) in Chapter 7. The

strain rates in the slabs during impacts and blasts are typically greater than 1 s^{-1}, and therefore, the modeled uniaxial tensile behavior of HSHDC is acceptable.

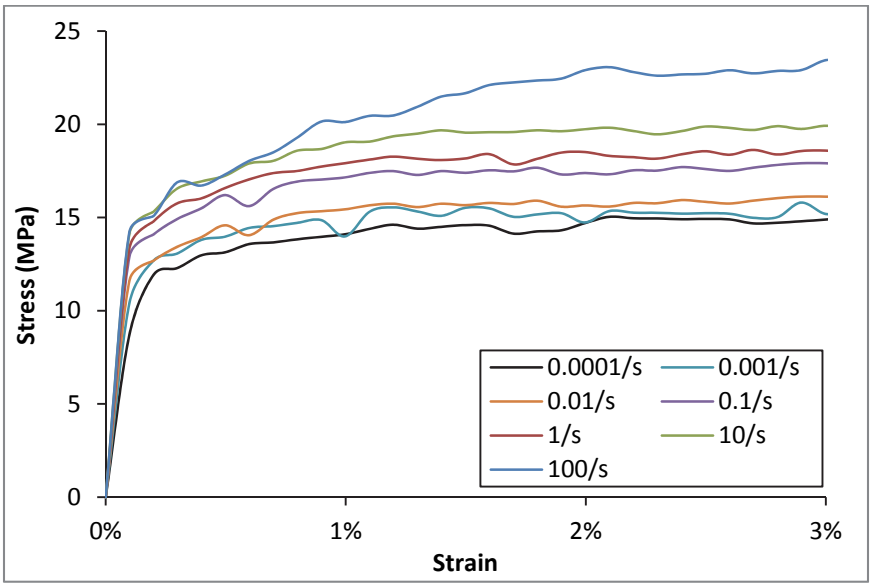

Figure 8.18: Uniaxial tensile behavior of a single HSHDC element in LS-Dyna

The results of the FE simulation of an HSHDC solid element under uniaxial compressive loads at multiple strain rates are shown in Figure 8.19. The compressive strengths of the HSHDC element at varying strain rates show a good agreement with that of concretes with similar compressive strengths in the literature. However, the compressive elastic modulus remains constant (at about 50 GPa) in the LS-Dyna model at all strain rates. This modeled behavior deviates from the experimental observations in high strength concretes (with coarse aggregates), which exhibit about 20% increase over the six orders of strain rates investigated in this study. Although, increasing the compressive elastic modulus is possible by changing the equation of state (EOS) from its default expression, such approach is not pursued in this research for the following reasons. First, there is no direct experimental data for either HSHDC or COR-TUF to

determine the appropriate changes in the EOS; second, changing the EOS also influences the tensile modulus, which matches well with the experimental behavior of HSHDC when default EOS is used; and third, the structural response (e.g. peak deflection) of the slab post-cracking is dominated by the tensile inelastic modulus of the material. Thus, the uniaxial response of single HSHDC element under compression is deemed suitable for modeling the slab behavior.

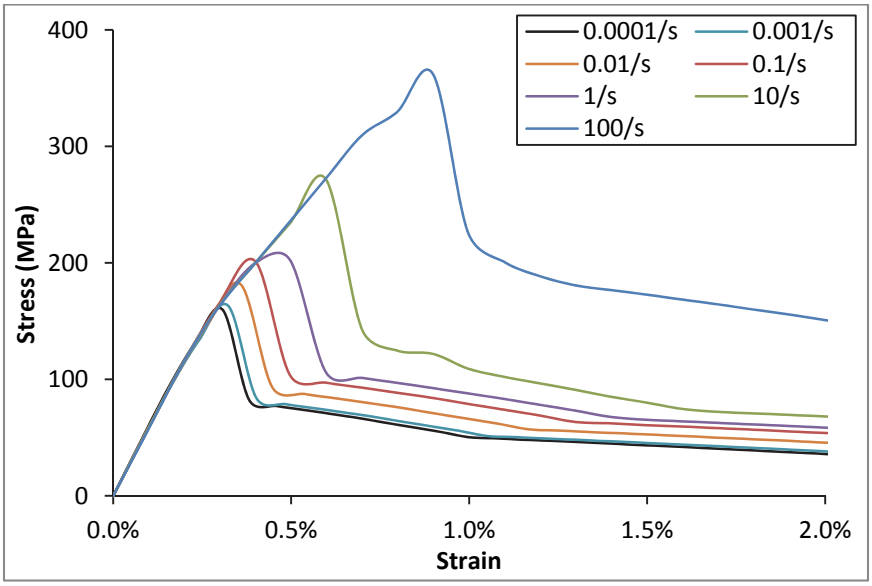

Figure 8.19: Uniaxial compressive behavior of a single HSHDC element in LS-Dyna

Similar single element analyses were conducted for a COR-TUF element, and the results at the strain rate of 100/s, which is the maximum order of strain rate computed during impact tests, are compared with that of HSHDC element in Figure 8.20. Evidently, the differences between the responses of HSHDC and COR-TUF are well captured in these analyses. Overall, the material behaviors of both HSHDC and COR-TUF are satisfactorily represented by the LS-Dyna MAT_072R3 model for the purpose of rate-dependent structural analysis of the slabs.

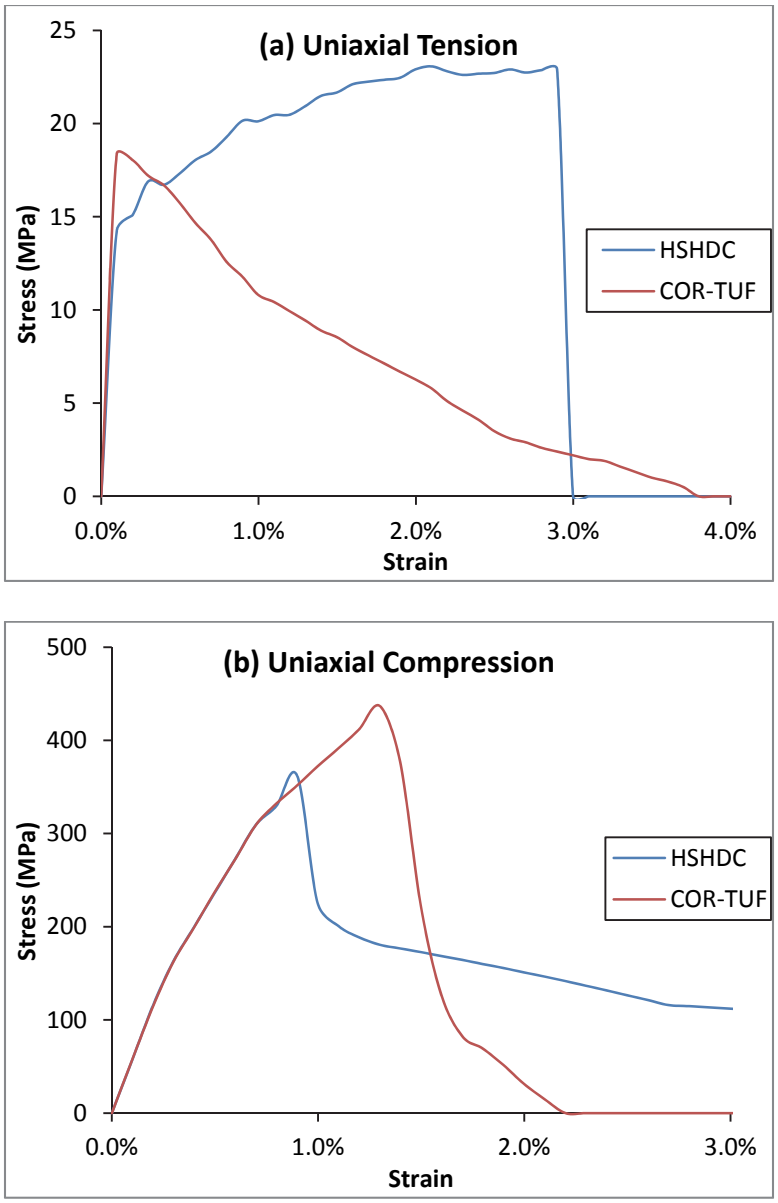

Figure 8.20: Comparison of HSHDC and COR-TUF single element behaviors

8.3.4 Material Model for Impact Head and Base Support

The impact head and the base support, physically made of 4140 steel, are modeled using the LS-Dyna material model MAT_003 that is typically used for modeling steel and other metals exhibiting isotropic behavior with plasticity and rate effects. The input properties for MAT_003 to model 4140 steel are summarized in Table 8.5.

Table 8.5: Input parameters for MAT_003 material model

Property	Value	Remarks
Density	139600 kg/m^3	Density of 4140 steel is only about 7800 kg/m^3; however, it is increased by 17.7 times, so that the weight of the entire drop-weight assembly (≈ 16 kg) is concentrated in the impact head. This also assists in matching the weight of the physical base support which is modeled as only 2 layers of 8 mm^3 elements (Figure 8.12).
Young's Modulus	200 GPa	Standard properties of 4140 steel
Poisson Ratio	0.30	
Yield Stress	415 MPa	
Tangent Modulus	0 GPa	Assumed elastic-perfectly plastic
SRC	255.4	Strain rate parameters in Cowper-Symonds model[23,24]
SRP	7.6	

8.3.5 Loading, Boundary Conditions, and Contacts

The loading in this FE analysis is applied in the form of uniform initial velocity equal to the impact velocity (V_i) at all nodes of the impact head (Figure 8.21). A constant downward acceleration due to gravity, g, is applied at all nodes to simulate gravity loads in LS-Dyna; however, their influence on the overall structural response is negligible as the accelerations due

to impact are of the order of 100g-1000g (as observed in the experimental investigation – Figure 8.4).

The external boundary conditions are applied at the base support, and the symmetry boundary conditions are applied at the x = 0 and y = 0 planes (P_x and P_y) of the slab, as shown in Figure 8.21. The base support is assumed to have no displacements (i.e. $u_x = u_y = u_z = 0$) at the bottom face. Due to symmetry about the x and y axes, the out of plane displacements and rotations are assumed zero (Figure 8.21) at both P_x and P_y planes.

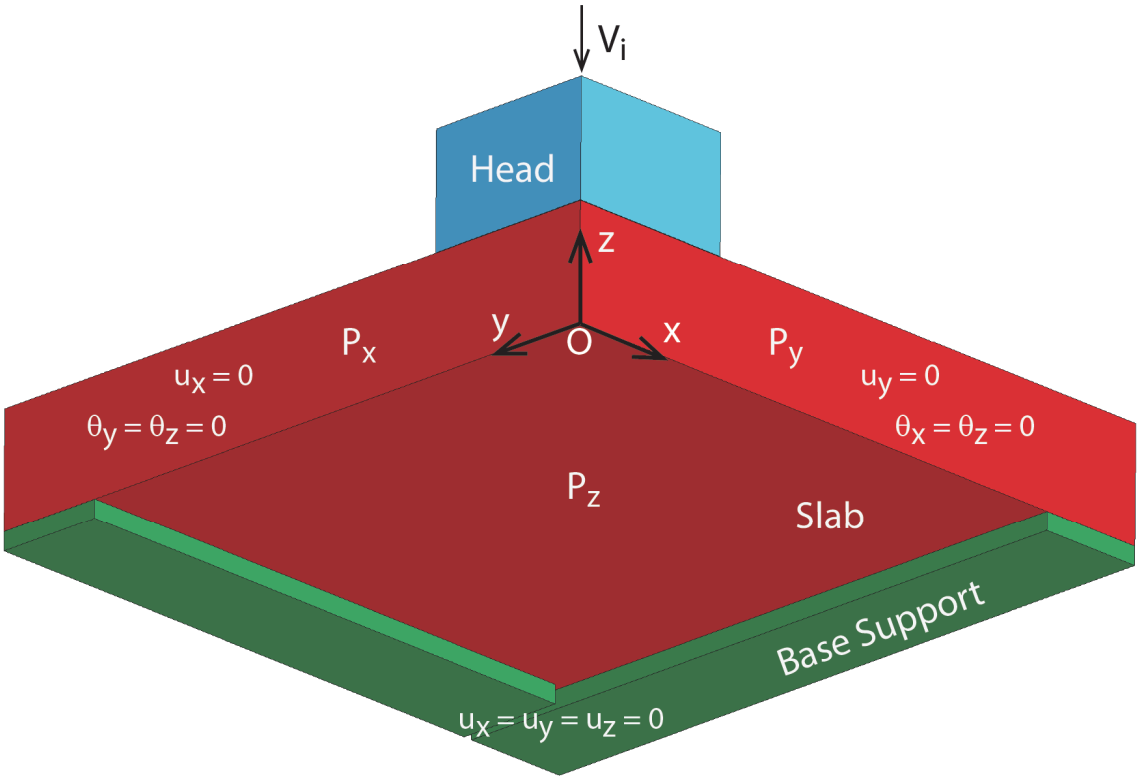

Figure 8.21: Boundary conditions of the slab-impact problem

The impact head is situated at 100 μm above the top face of the slab at time, t = 0. As the impact head falls and comes in contact with the slab, 'automatic surface-to-surface' contact in

LS-Dyna is applied for modeling the interaction between the impact head and the slab. The same contact model is also used for the contact between the slab and the base support. The significant input parameters, same for both contacts, are given in Table 8.6, and the slab is considered as the 'slave' in both contacts.

Table 8.6: Input parameters for contact definition in LS-Dyna

Property	Value	Remarks
Static coefficient of friction, FS	0.30	Refer: Chin[24]
Static coefficient of friction, FS	0.28	
Optional Input Card A is checked		
Soft constraint option	1	Soft constraint formulation is needed for contacts between materials with significantly different bulk moduli. In this case, HSHDC and COR-TUF in the inelastic stage have significantly lower modulus than steel, which justifies the use of this option.
All other parameters set to default values		

8.3.6 Results of the FE Analysis

This section is divided into two sub-sections. In the first sub-section (8.3.6.1), the structural response of the slabs determined from the FE analysis is verified with the experimental results (force time history, peak contact force, and maximum displacement) reported in Section 8.2.3. In the second sub-section (8.3.6.2), insights into the structural behavior are discussed, including dynamic stress and strain profiles and force-time history of the drop-weight impact.

8.3.6.1 *Quantitative Comparison with Experimental Results*

In Figure 8.22, the force-time history computed from the FE analysis, for the impact on an HSHDC slab with drop-weight of 16 kg and impact velocity of 4.6 m/s, is compared to the experimentally determined force-time history (as in Figure 8.3) of the corresponding drop-weight impact. The computed curve (FEA) in Figure 8.22 seems to have sharper contrast, with stronger peaks and valleys of the contact force with time, compared to the experimental curve. As mentioned in Section 8.2.2, the sampling frequency of the data acquisition system used in the drop-weight experiments is limited to 200 kHz per sensor, which limits the signal contrast. This particularly causes a large difference between the peak contact force (PCF) determined from experiment and that determined from FE analysis. In addition to sampling limitation, the influence of the surface texture of the slab (as discussed in Section 8.2.3) in slightly slowing down the drop-weight assembly, before the impact head starts compressing the bulk of the material, may also reduce the PCF. In spite of this discrepancy between the two curves in terms of signal contrast, the computationally determined response shows a good agreement, overall, with the experimental force-time history, as the area under the force-time curve (impulse or change of momentum) is approximately the same for both the curves.

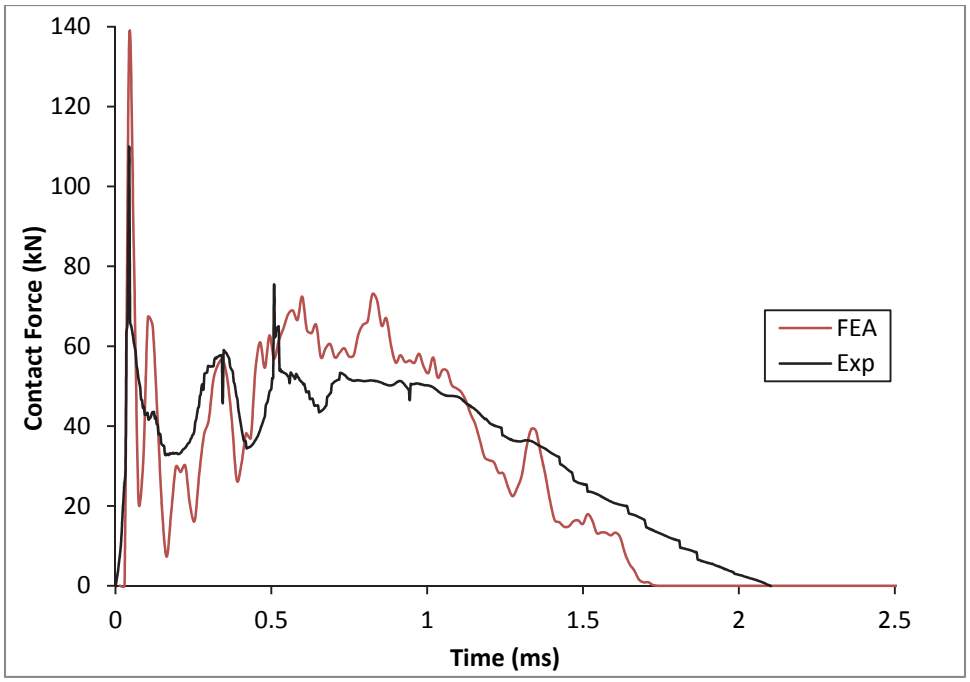

Figure 8.22: Comparison of FE analysis with experimentally determined force-time history of an HSHDC slab hit by 16 kg drop-weight at 4.6 m/s

Similar to the above analysis, the PCF, along with the maximum displacement, are determined for the first impacts of all the experimentally examined load cases, and the comparison of the results from FE analysis and drop-weight experiments is shown in Table 8.7. As discussed above, the computationally determined PCF's are significantly higher than the experimentally observed PCF's. In contrast, the maximum displacements computed from the FE analysis closely match the maximum displacements derived from the observed acceleration time histories. The error in displacement estimation is less than 13% for all the load cases investigated in this study. The limitation of the sampling frequency is overcome in displacement computation by the integration of acceleration-time history, resulting in a better agreement between the experimental observations and FE analysis.

Table 8.7: Comparison of FE analysis with experimental results of the first impact

Material	Impact Velocity (m/s)	Peak Contact Force (kN)			Maximum Displacement (mm)		
		FEA	Exp.	Error*	FEA	Exp.	Error*
HSHDC	2.30	100	57	75.4%	1.04	1.15	-9.6%
	3.25	121	77	57.1%	1.64	1.66	-1.2%
	4.60	146	103	41.7%	2.59	2.78	-6.8%
COR-TUF	2.30	107	64	67.2%	1.05	1.10	-4.5%
	3.25	134	87	54.0%	1.82	1.62	12.3%
	4.60	141	105	34.3%	3.31	3.49	-5.2%

* Error (%) = (FEA – Exp)/Exp x 100

An interesting observation in Table 8.7 is that almost all the experimentally determined maximum displacements are greater than those determined by the FE analysis (with the exception of 3.25 m/s velocity impact on COR-TUF slab). This may be caused due to the crushing of small asperities on the surface of the slabs, as discussed in Section 8.2.3. These asperities are of the order of 100 μm, which is consistent with the difference in maximum displacements determined by experiments and FE analysis.

From the above discussion, it can be concluded that the FE analysis, with MAT_072R3 material model for HSHDC and COR-TUF, can be used to reliably simulate the behavior of the slabs under drop-weight impact; particularly, the properties involving time-integration such as displacement, momentum/impulse, and total energy absorbed. In addition to the results discussed above, the FE analysis also provides insights into the slab behavior, such as dynamic stress and deformation profiles, which are discussed in the next sub-section.

8.3.6.2 *Insights into the Structural Behavior of Slabs under Drop-weight Impact*

The stress and strain profiles of HSHDC and COR-TUF slabs under impact with drop-weight of 16 kg at 4.6 m/s, obtained from FE analysis, are compared below at six selected displacements. The significance of these selected displacements is shown on the displacement-time histories (Figure 8.23) of the impact heads for the aforementioned impact load.

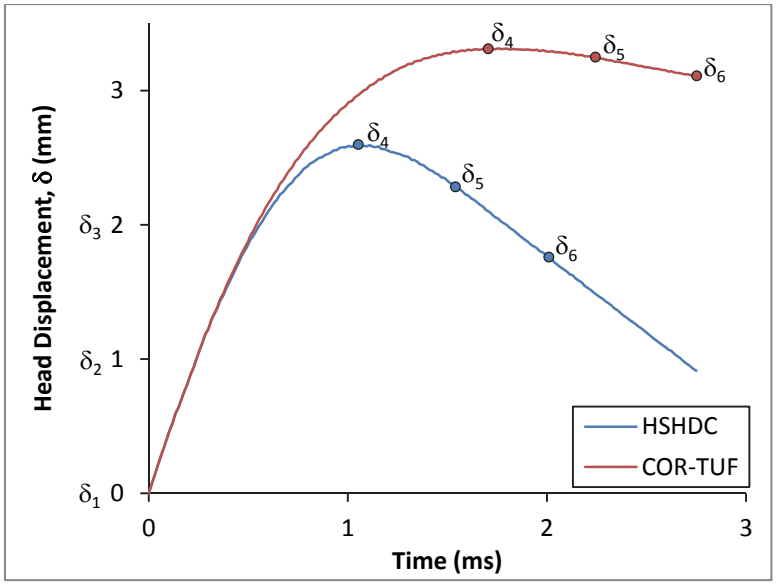

Figure 8.23: Locations of selected displacements for querying FE stress and strain profiles (Displacement-time histories for impacts with 16 kg drop-weight at 4.6 m/s)

As shown in Figure 8.23, the first three displacement levels (δ_1, δ_2, and δ_3) are the same for both HSHDC and COR-TUF. At $\delta_1 = 0$ mm, the head displacement comes in contact with the slab for the first time causing the peak contact force (PCF). δ_2 and δ_3 are chosen to be 1 mm and 2 mm, respectively, to compare the stress and strain profiles at the same head displacement levels. The last three displacement levels (δ_4, δ_5, and δ_6) are not the same for HSHDC and COR-

TUF. The fourth displacement level, δ_4, is equal to the maxima of the respective displacement-time histories. δ_6 is the residual displacement (d_r) at the time when the impact head loses contact with the slab. δ_5 is the average of δ_4 and δ_6 for the respective slabs in the middle of the rebound of the impact head. Hence, each of the six significant displacements corresponds to either a physically relevant displacement or contact force.

The stress and strain profiles of HSHDC and COR-TUF slabs are comparatively shown in Figures 8.24, 8.25, and 8.26 at the above six significant displacements of the impact head. Although the FE analysis is conducted only on a quarter of a slab utilizing symmetry, the stresses and strains are shown for the entire slab in these figures for better comprehension.

The hydrostatic pressure, $p = -(\sigma_1+\sigma_2+\sigma_3)/3$, at the centroidal sections (a section containing the centroid of the slab that is parallel to one of the four lateral sides of the slabs) of HSHDC and COR-TUF slabs is plotted in Figure 8.24 for all the six head displacements (δ_1 to δ_6). During the downward motion of the impact head (δ_1 to δ_4), the conical shape of the pressure contours at the slab section resemble that of a classical beam under flexure loads with compressive stresses (green, yellow, and red) at the top and tensile stresses (dark blue) at the bottom. As the slabs bend (displacements δ_2 to δ_4), higher compressive stresses are visible (as more intense red color on top) in the HSHDC slab section due to its greater tensile resistance than the COR-TUF slab. The neutral axis (light blue contour) is high, near the top, in both the slabs indicating inelastic deformation during the downward motion of the impact head. After achieving the maximum displacement (δ_4), low compressive stress (cyan and green) contours are visible at the bottom face of the slabs at δ_5 and δ_6, as the maximum tensile stress (dark blue)

contour moves upward in both HSHDC and COR-TUF slabs. Overall, the hydrostatic pressure profiles at the centroidal sections of the slabs are similar to that of a beam undergoing flexural vibrations, and the stresses generated in HSHDC slab are higher than that in COR-TUF slab due to superior tensile performance of the HSHDC material.

The maximum principal (tensile) strain distribution at the bottom face of the slabs is shown in Figure 8.25. At displacement δ_1, although no variation in strain contours is visible because of low principal strains [largely elastic with small inelastic strains (< 0.1%)], the strains and stresses do vary at the bottom face as observed in the pressure contours above. The tensile strains increase with increasing head displacement (δ_2 to δ_4). Due to the flexural mode of deformation and the boundary conditions, largest strains occur at the center of both HSHDC and COR-TUF slabs fanning out toward the thirds of the slab edges. However, the strain pattern is highly diffused in HSHDC slab as compared to COR-TUF slab. As pointed out in Section 8.2.3, the tensile ductility of HSHDC allows the material to spread the damage evenly, which is not possible in COR-TUF due to its tensile softening behavior. As a result, while the maximum principal strain remains under 1% in HSHDC slab at all displacements, they are as high as 3% in the COR-TUF slab. In the experimentally observed failure crack pattern in COR-TUF slabs (Figure 8.8) above, the major crack seems to follow one (weaker) of the two crack branches (seen in FE analysis) in each quadrant of the slab. The strain contours during the rebound stage (δ_5 and δ_6) appear almost similar to that at the maximum displacement (δ_4) due to negligible recovery of the tensile strain, which is largely inelastic in both HSHDC and COR-TUF slabs. The positive influence of the material's tensile ductility on the diffusion of the maximum principal strain at the bottom face of the slab is clearly noticeable in Figure 8.25.

The minimum principal (compressive) stress distribution at the top face of the slabs is shown in Figure 8.26. At displacement $\delta_1 = 0$, only the area directly under the impact head (and small surrounding area) exhibits non-zero compressive stress. It takes about 15 μs for the first stress wave to propagate from the center to the edges of the slab. With increasing displacements (δ_2 to δ_4), fan-shaped compressive stress contours appear at the top face of the slabs, similar to the tensile stress contours at the bottom face. As discussed above, the compressive stress is higher at the top face of the HSHDC slab than the COR-TUF slab due to the greater tensile resistance of the former material in the inelastic stage. The diffusion of tensile strain at the bottom face also assists in spreading the compressive stress more evenly at the top face of the HSHDC slab compared to the COR-TUF slab. This becomes particularly critical in the rebound stage (δ_5 and δ_6), as tensile stress (brown-dark red contours) appears over a larger area at the top face of the COR-TUF slab compared to HSHDC causing spalling of the material there, which is also visible in the experimental observations (Figure 8.8). Thus, in spite of its higher compressive strength than HSHDC, the COR-TUF slab under dynamic loads cracks significantly at the compressive face due to lack of tensile ductility.

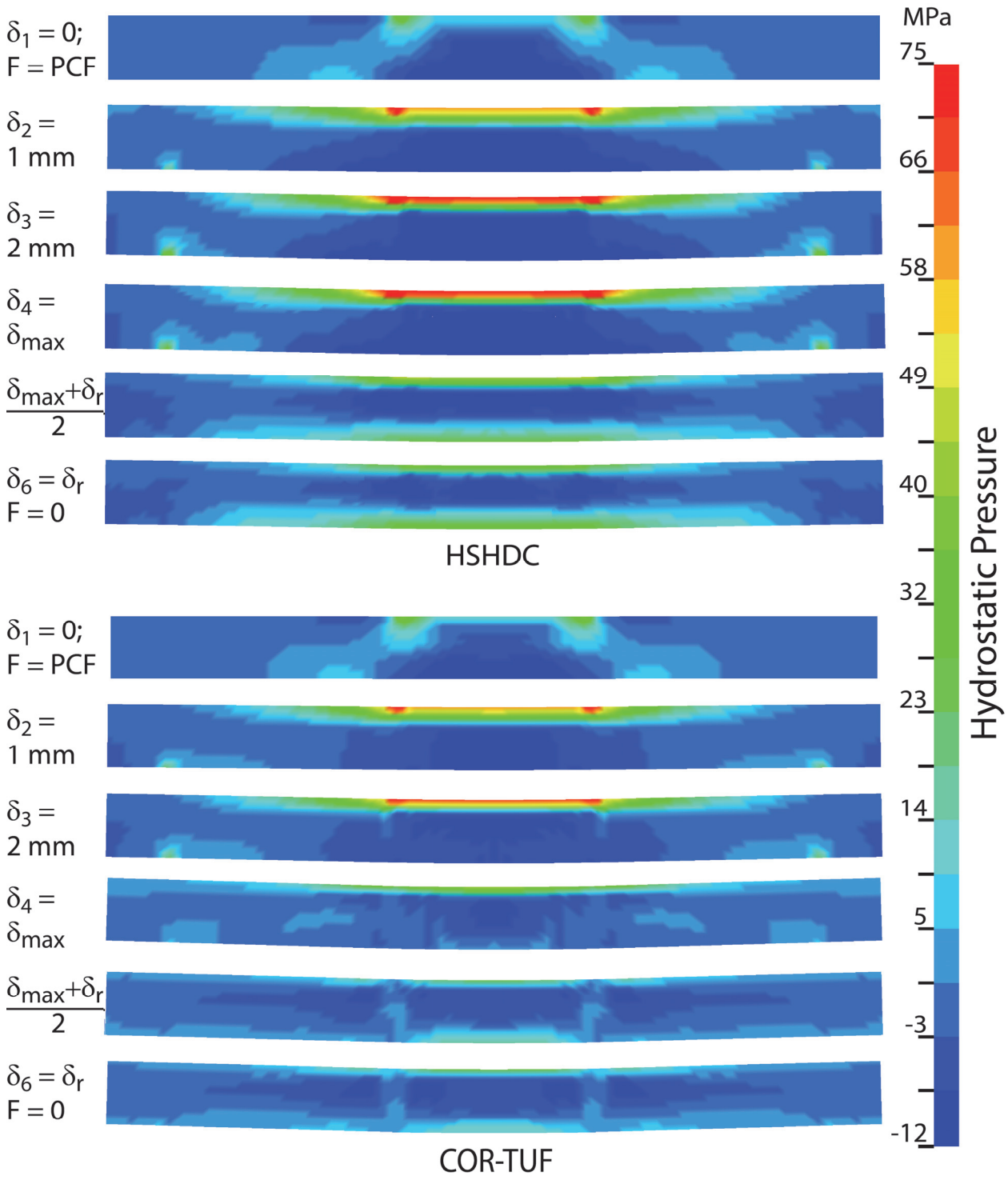

Figure 8.24: Hydrostatic pressure distribution at the centroidal section of the slab (compressive pressure is positive)

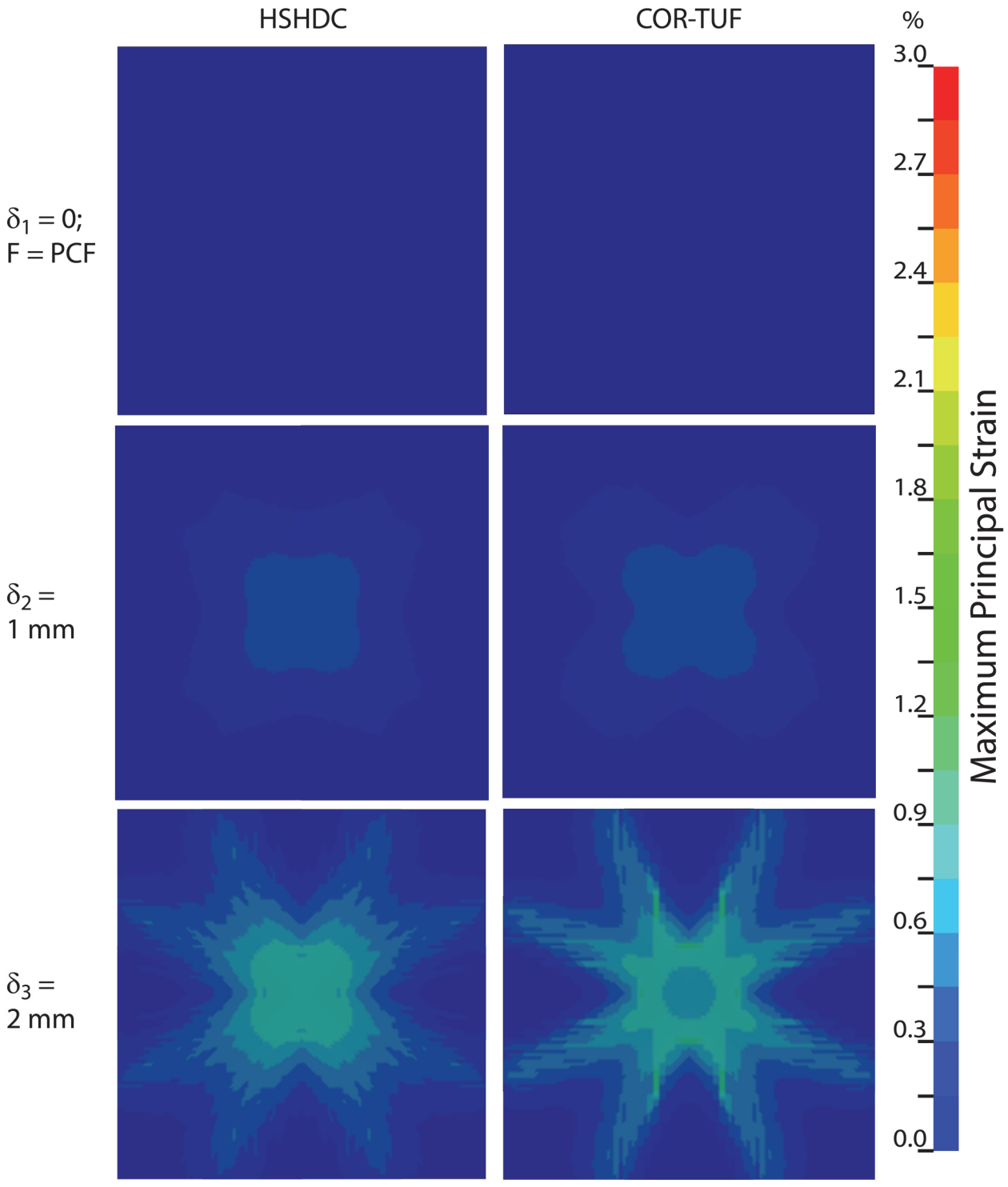

Figure 8.25(a): Maximum principal (tensile) strain distribution at the bottom face of the slab

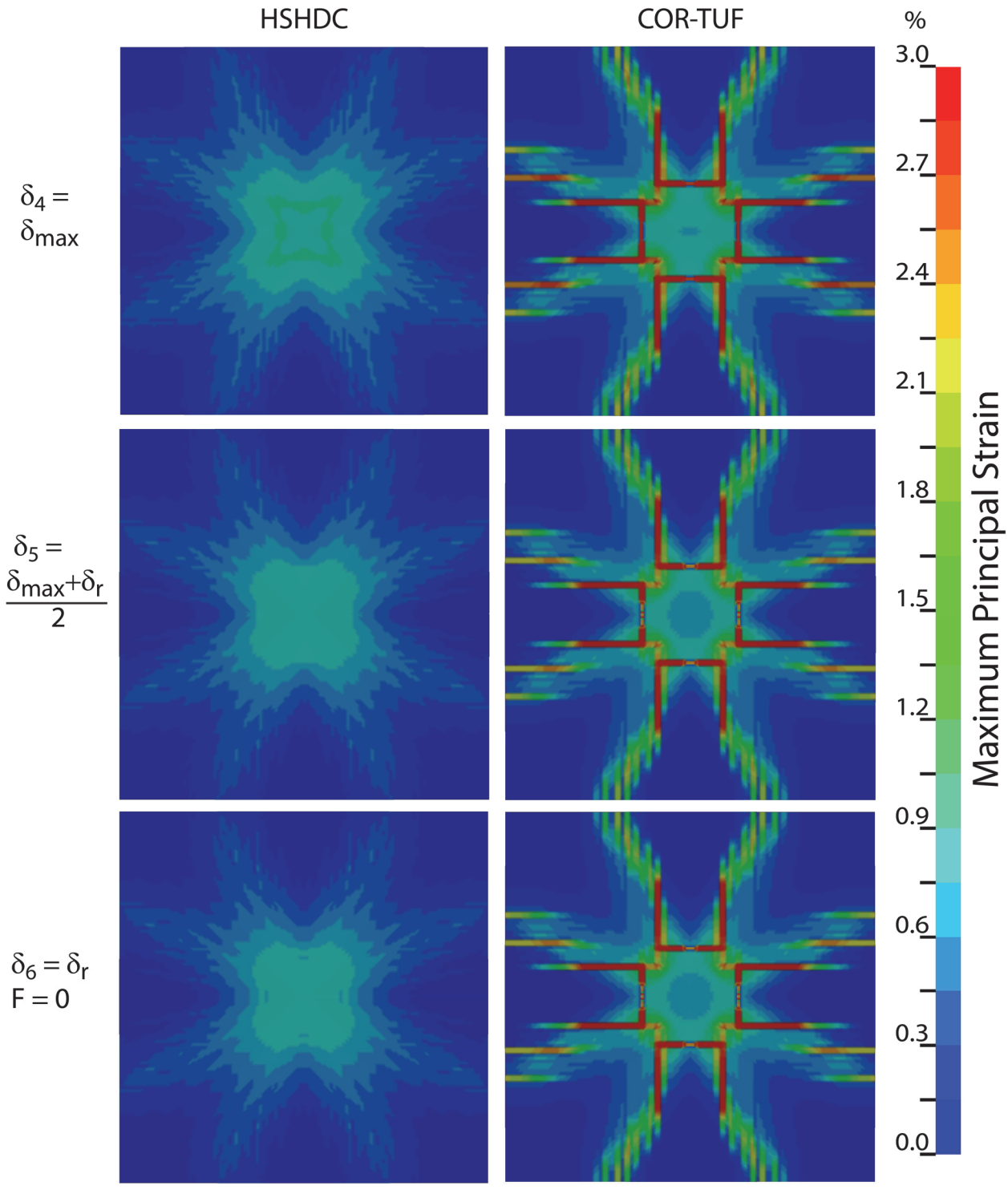

Figure 8.25(b): Maximum principal (tensile) strain distribution at the bottom face of the slab

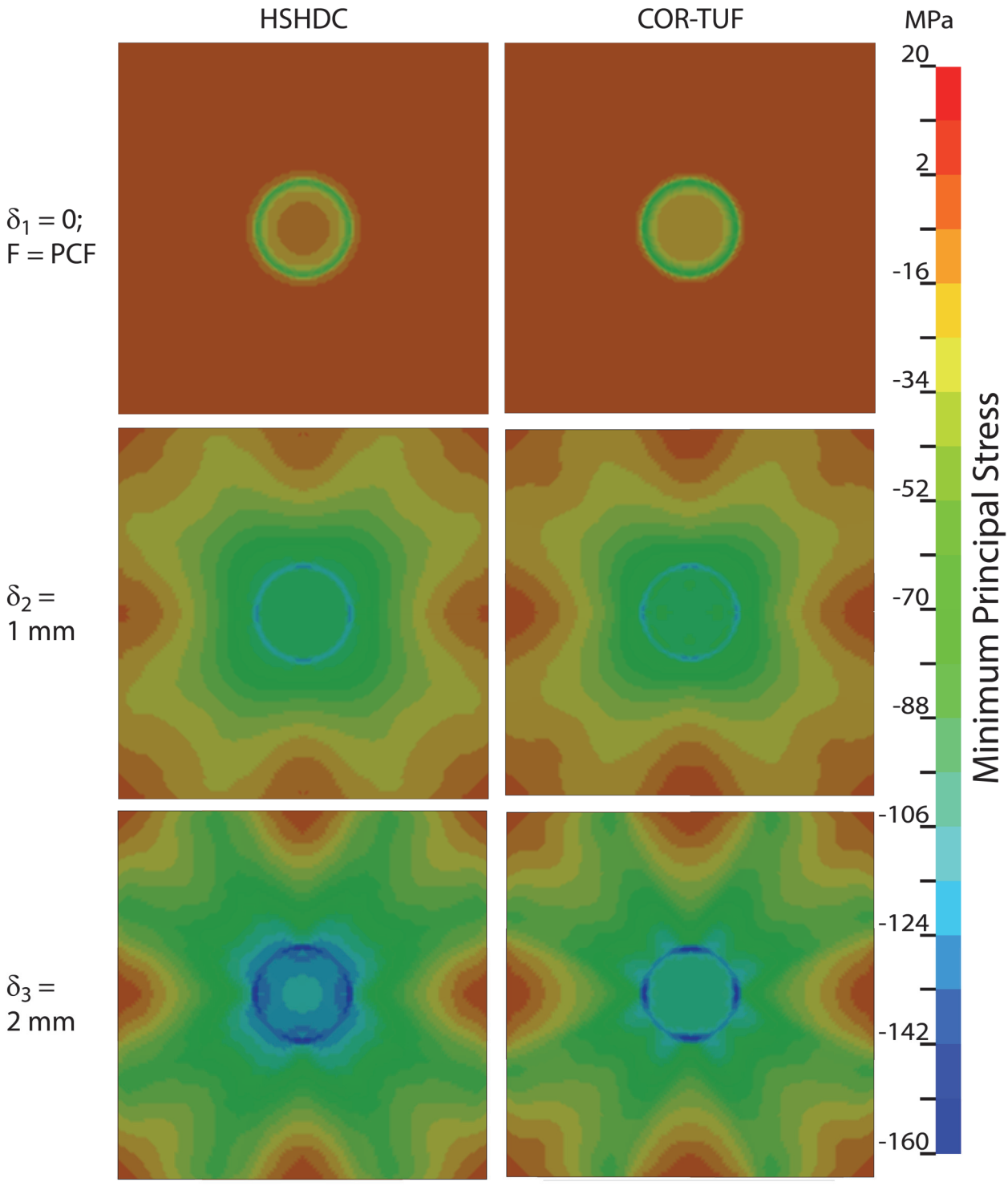

Figure 8.26(a): Minimum principal (compressive) stress distribution at the top face of the slab

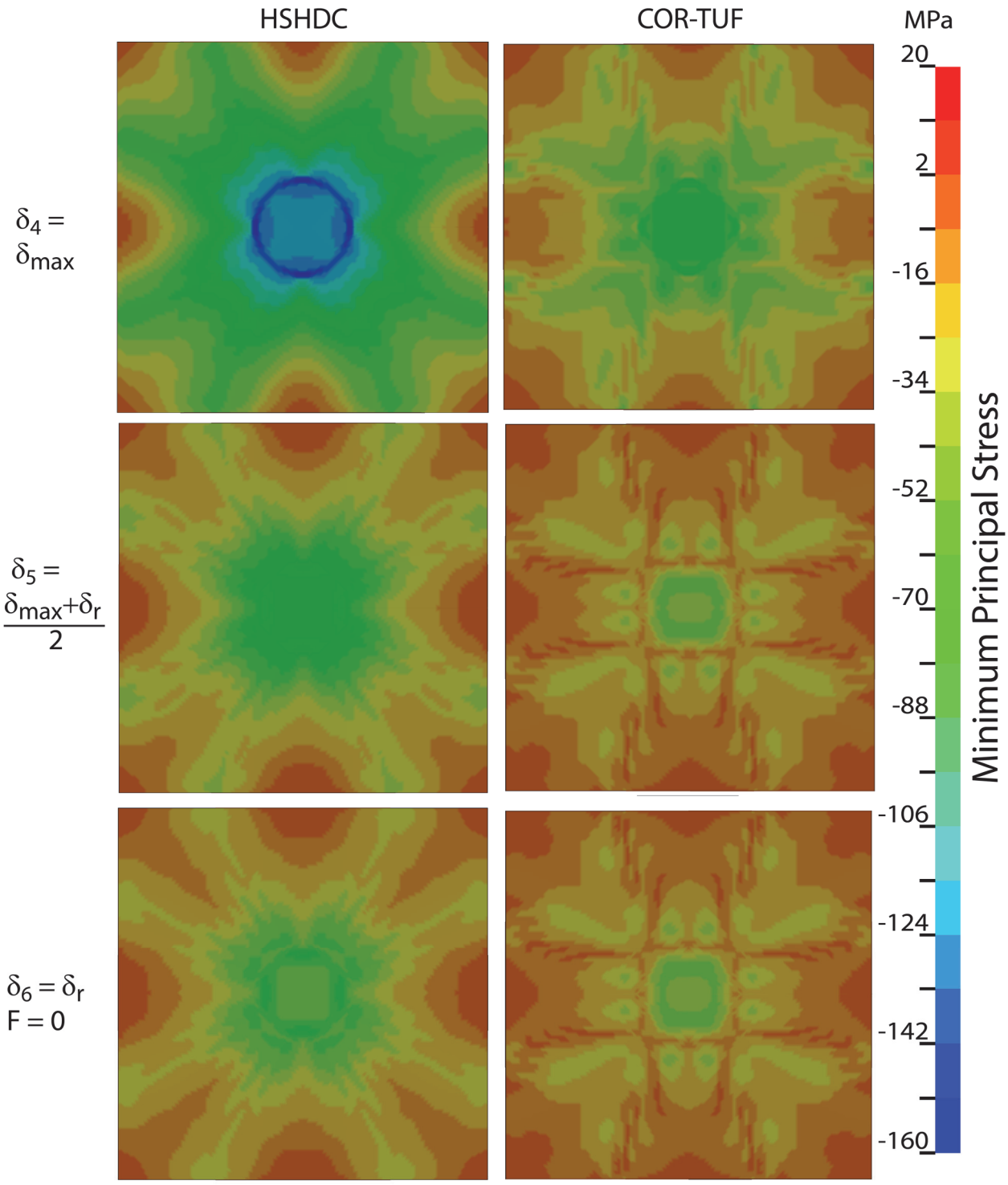

Figure 8.26(b): Minimum principal (compressive) stress distribution at the top face of the slab

The oscillations observed in the force-time history of the HSHDC slab (Figure 8.22) after the peak contact force, as the slab is depressed by the impact head to the maximum displacement, are attributable to the oscillations in the slab and the impact head at different frequencies (due to different stiffness). This is observable through FE analysis by tracking the relative distance between the centroidal nodes of the impact head and the slab, as shown in Figure 8.27. As mentioned above, the initial separation at time, t = 0 ms, between the impact head and the top face of the slab is 100 μm. The peak contact force is observed at time, $t = t_{PCF}$, when the relative between the centroidal nodes (in fact all nodes) of the slab and the impact head is zero. In spite of the oscillations, the relative distance between the slab and the impact head is always positive after t_{PCF} as the slab deforms under flexure with finite plastic deformation.

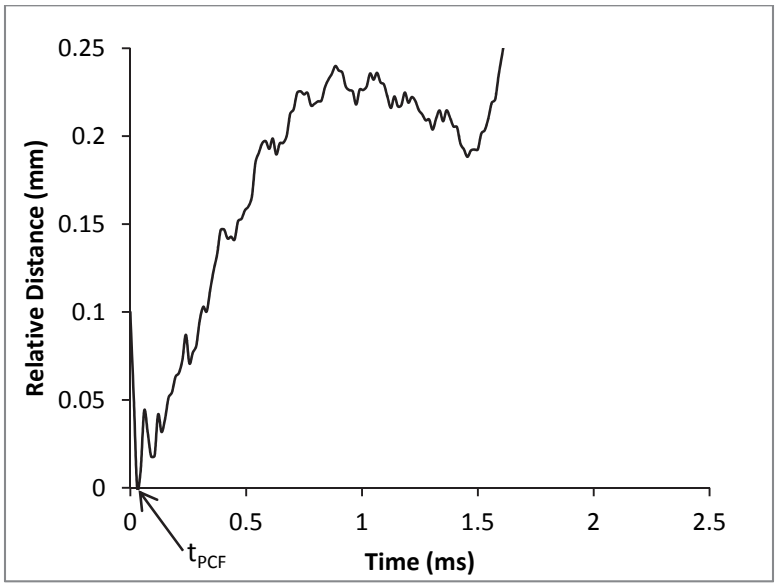

Figure 8.27: Relative distance between the centroidal nodes of the impact head and the slab

8.3.7 Layered Slabs

Cost and performance optimizations via functional layering of the slabs are demonstrated in this section using FE analysis as a tool to determine the structural behaviors of various slab configurations. Along with the significant difference in the tensile behaviors of HSHDC and COR-TUF, the costs of the two materials are also substantially dissimilar. While the tensile ductility of HSHDC is an order of magnitude greater than COR-TUF, cost per unit volume of HSHDC is about 2.7 times that of COR-TUF. This tradeoff between cost and mechanical performance is the motivation behind this optimization study.

As an example, the influence of a drop-weight impact of velocity 5.6 m/s on the slabs with varying material layer thicknesses (but the same total thickness of 1″) is investigated. The impact velocity of 5.6 m/s (greater than all the impact velocities investigated above) is chosen because it provides a good contrast between the performance of HSHDC and COR-TUF slabs. While the HSHDC slab remains intact after the impact, the COR-TUF slab fails under flexure. In the FE model, there are 13 element layers of equal height (about 2 mm each) along the slab thickness of 1″. Starting with all layers made of COR-TUF, increasing number of layers from the bottom of the slab is substituted by HSHDC, one at a time. Zero slippage is assumed in the FE analysis at the interface between HSHDC and COR-TUF layers. One of the layered slab configurations with the bottom 6 layers made of HSHDC and the top 7 made of COR-TUF, as an example, is shown in Figure 8.28.

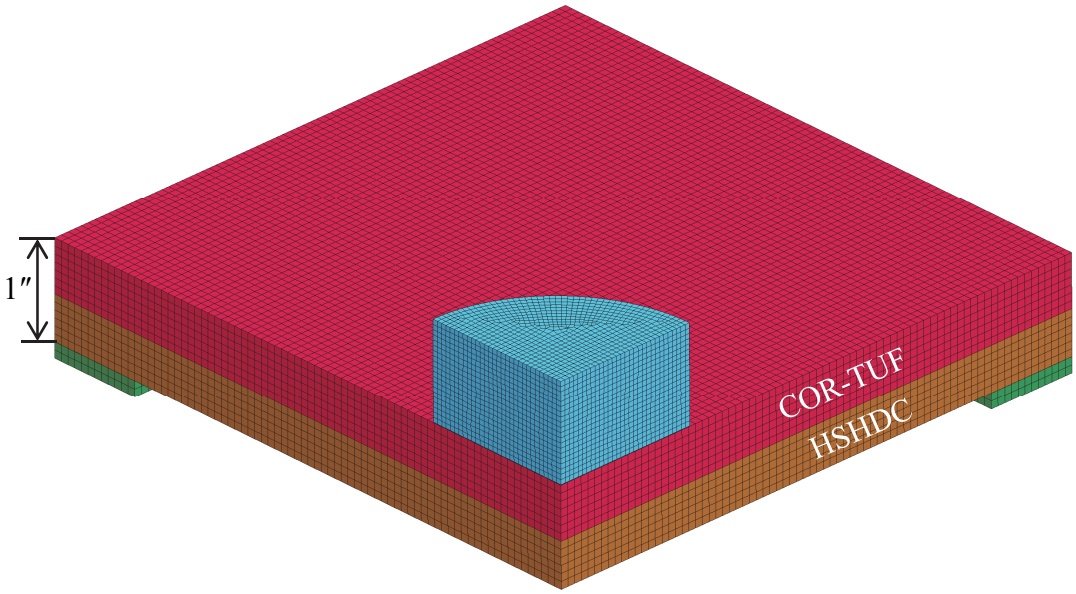

Figure 8.28: One of the layered configurations of the slab

The displacement-time histories of all the layered slab configurations are shown in Figure 8.29. The slab in which all layers are made of COR-TUF fails under the drop-weight impact of velocity 5.6 m/s, and shows no rebound. As the bottom COR-TUF layers are successively replaced with HSHDC, the impact resistance of the slab increases causing a decrease in head displacements. In spite of the reduced displacement, all the slab configurations with up to seven (out of 13) layers of HSHDC fail, and are, therefore, unacceptable (assuming positive rebound of the impact head is the safety criterion).

Slab configurations with 8 to 13 layers of HSHDC show positive rebound and are considered ‘safe’. The best mechanical performance (least head displacement) is obtained for the configuration with the bottom 11 layers of HSHDC and the top 2 layers of COR-TUF, and not for the configuration with all layers made of HSHDC. As shown above in the FE analysis, the neutral axis at maximum displacement is located approximately at 0.85″ from the bottom of the

slab. As a result, this configuration (with 11 layers of HSHDC or 84.6% of the total depth) optimally places HSHDC and COR-TUF in tension and compression regions of the slab, respectively, and therefore, results in the best mechanical performance (note that HSHDC is weaker in compression than COR-TUF). Although, all configurations with 8 to 13 layers of HSHDC are safe with positive rebound, only one of them represents the optimal configuration if certain weightage is given to both cost as well as mechanical performance, which is determined below using the penalty function approach.[25]

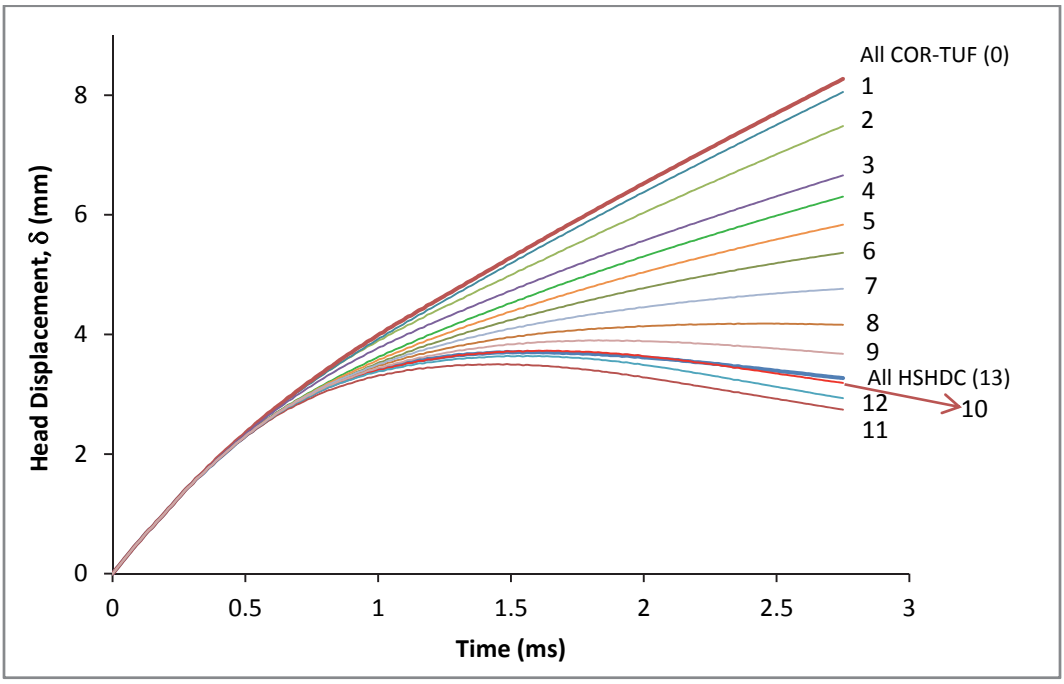

Figure 8.29: Displacement-time histories of layered slab
(Numbers 0-13 indicate the number of bottom layers of the slab made of HSHDC)

Both cost and mechanical performance are considered as the optimization functions in this study. In Figure 8.30, the maximum head displacements, δ_m, (peaks of the curves 8-13 in Figure 8.29) are plotted against the total material cost, c, of the respective slabs for all the 'safe'

configurations with 8 to 13 layers of HSHDC. As mentioned above, the best mechanical performance (least δ_m) is achieved for the slab with 11 layers of HSHDC; however, this may not be optimal if cost is also taken into consideration. A penalty function, Z, is defined as a linear combination $\delta_{mr} + \alpha c_r$, where δ_{mr} and c_r are the relative costs computed by dividing the δ_m and c by their respective maximum values, as shown in Table 8.8, and α is the exchange constant and its value depends on the relative importance given to δ_{mr} or c_r. For a particular value of α, the slab configuration which results in the minimum value of Z is the optimum configuration.

Three cases are analyzed in Table 8.8 with three different values of α. The Z values corresponding to the optimum configurations for each case are shown in bold-underlined font in Table 8.8. For the case when equal weightage is given to the mechanical performance and cost ($\alpha = 1$), the optimum configuration is the slab with 9 HSHDC layers. When the mechanical performance is given a higher weightage (by using $\alpha < 1$, thereby penalizing cost), the optimum configuration is the slab with 11 HSHDC layers, which is reasonable as it results in minimum δ_m (Figure 8.30). However, when the cost is given a higher weightage (by using $\alpha > 1$, thereby penalizing displacement) the optimum configuration is the slab with 8 HSHDC layers, which has the least cost. Thus, the penalty function approach provides a rational way to design the slabs for optimizing both impact resistance as well as cost.

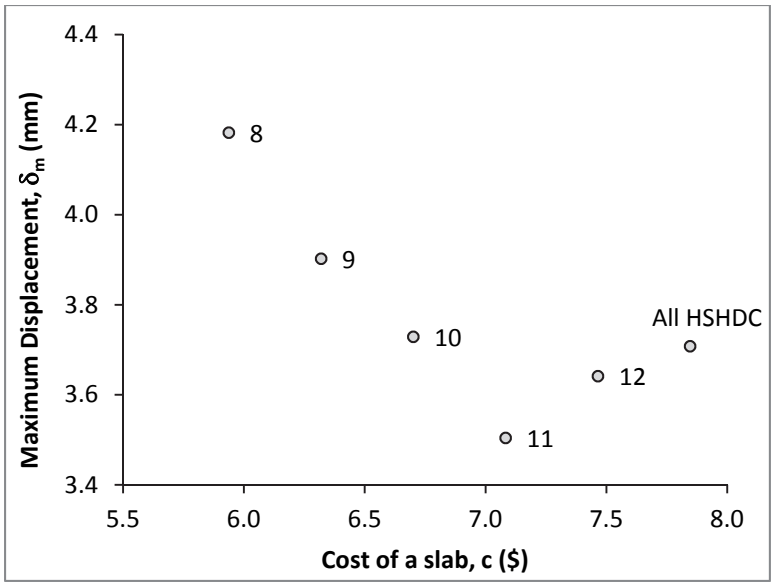

Figure 8.30: Performance-cost tradeoff of safe slab configurations

Table 8.8: Optimization analysis

No. of HSHDC Layers	Max Displacement, δ_m (mm)	Cost, c ($)	Relative disp., $\delta_{mr} = \delta/4.18$	Relative cost, $c_r = c/7.85$	$Z = \delta_{mr}+\alpha.c_r$		
					1	0.5	2
8	**4.18**	5.94	1.00	0.76	1.757	1.378	**2.513**
9	3.90	6.32	0.93	0.81	**1.738**	1.336	2.544
10	3.73	6.70	0.89	0.85	1.746	1.319	2.600
11	3.50	7.08	0.84	0.90	1.741	**1.289**	2.643
12	3.64	7.46	0.87	0.95	1.822	1.346	2.773
13	3.71	**7.85**	0.89	1.00	1.887	1.387	2.887

8.4 FE Simulation of HSHDC Slabs under Air-blasts

8.4.1 Introduction to Blast Loads

Blast loads on a structure are transient pressure waves created by sudden compression of air due to the release of tremendous amount of energy in a detonation near the structure. The amplitude and duration of a blast wave experienced by a structure depends, most importantly, on (1) energy released at the point of detonation, (2) distance from the point of detonation, and (3) amplification due to reflections from the ground. As a result, the blast loads are often characterized in terms of three main parameters – effective charge weight (W), standoff distance (R), and the location of detonation with respect to the ground.

The incident blast pressure on a structure at a particular point typically decays exponentially with time after attaining its peak positive value, and it is often expressed in the form of the Friedlander wave equation (Eq. 8.13).[26,27] This equation is graphically represented in Figure 8.31 by the green curve. Also shown in this figure is the reflected pressure (red curve) due to reflection of the incident wave by the structure itself. Various phases of the blast pressure-time curve are described below.

$$p(t) = P_0 + P_{so}\left(1 - \frac{t - t_a}{t_o}\right) e^{\frac{-b(t-t_a)}{t_o}} \quad \text{for} \quad t \geq t_a \tag{8.13}$$

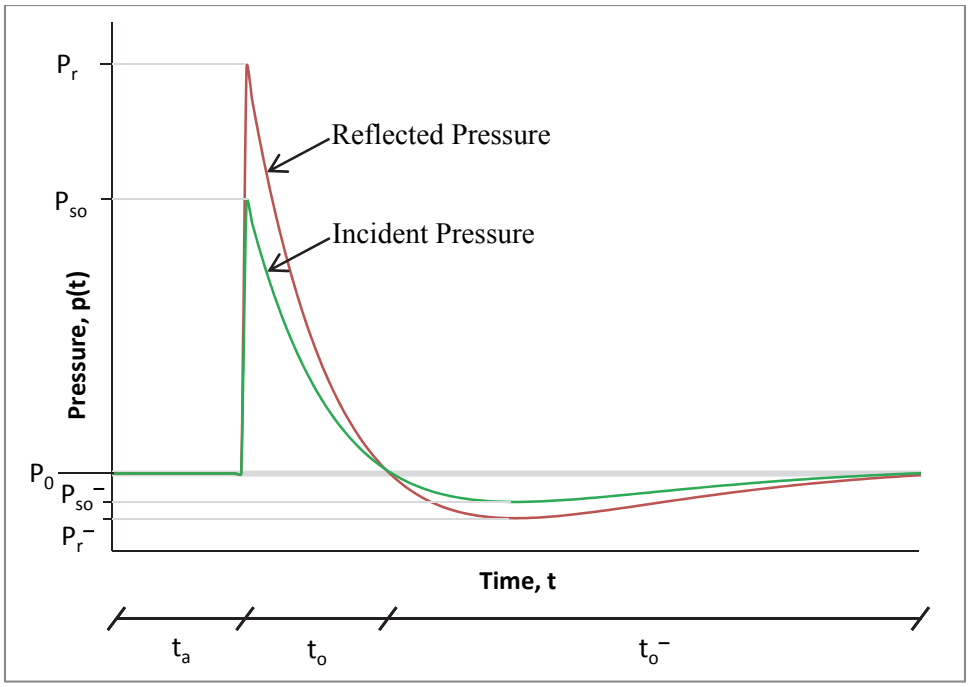

Figure 8.31: Typical blast pressure-time variation (after UFC[27])

- At the time of detonation (t = 0 ms), only the ambient atmospheric pressure (P_0 = 14.7 psi or 101 kPa at sea level) acts on the structure. The blast wave arrives at the structure at time, t = t_a. At this time, the peak pressure of the incident blast wave is P_{so}. As the blast wave interacts with the structure, the air molecules are further compressed as they are stopped by the structure in their path, and therefore, the peak reflected pressure, P_r (> P_{so}), is experienced by the structure almost at the same time (t = t_a).

- The incident and reflected pressures decay exponentially thereafter, at a rate controlled by the waveform parameter, b, to the ambient pressure, P_0, at time, t = t_a + t_o.

- Due to the expansion column of air, following the compression column, the incident and reflected pressures continue to drop below P_0 to minimum values of P_{so}^- and P_r^-, respectively. Subsequently, the pressure gradually returns to the ambient pressure in total time, t = t_a + t_o + t_o^- (Figure 8.31).

The areas under the 'positive' (above P_0) and 'negative' (below P_0) pressure phases are the positive and negative impulses, denoted by i_s and i_s^- for incident wave and i_r and i_r^- for the reflected wave. Another factor that influences the reflected pressure is the angle of incidence (α) of the pressure front at the point of interest in the structure, which causes a reduction in p(t) when α is increased from 0 to 90° in accordance with Figures 2-9 and 2-10 in the UFC.[28]

All the blast wave parameters discussed above (i.e. P_{so}, P_r, P_{so}^-, P_r^-, i_s, i_s^-, i_r, i_r^-, t_a, t_o, t_o^-) can be represented as functions of the scaled distance parameter $Z = R/W^{1/3}$ (refer Figures 2-7 and 2-8 in the UFC[28]). The concept of scaled distance is used to standardize all detonations (from a variety of explosives placed at different locations) in terms of the standard explosive, Trinitrotoluene (TNT), and its standoff distance to rationally compare and understand their influence on the structural behavior. For a given charge weight of any explosive, the effective charge weight, W, is the equivalent weight of TNT that is of the same shape and generates the same amount of heat energy as the actual explosive.[29] The standoff distance, R, is the perpendicular distance of the structure from the point of detonation. It is, therefore, possible for a structure to experience almost the same blast wave pressure due to multiple combinations of R and W, if Z remains the same in all the combinations.

In addition to R and W, the location of detonation point with respect to the ground also influences the blast wave, as the ground acts as a reflecting surface amplifying the original blast waves. For this reason, blasts are commonly classified into two broad categories: air-blasts and surface blasts (along with some combinations of these two limiting cases). The surface blast pressures are typically higher than the air blast pressures for the same R and W.

The structural response to blast loads is broadly classified into three categories: impulsive, dynamic, and quasi-static, depending on the ratio (t_o/T_n) of the positive blast pressure phase duration (t_o) to the natural time period of vibration (T_n) of the structure.[30] High pressure short duration blast waves with $t_o/T_n < 0.1$, generated by a charge placed very close to the structure, represent impulsive loading. In such loading, the maximum structural displacement/response occurs (relatively) long after the short impulse has passed. The impulse (area under the pressure-time curve), rather than the peak pressure, governs the structural response in this case. On the other hand, low pressure long lasting blast waves with $t_o/T_n > 10$, experienced by a structure perpendicular to the direction of propagation of the blast waves, represent quasi-static loading. In such loading, the maximum structural displacement/response may occur before the peak load is achieved, and therefore, the magnitude of the peak pressure (P_{so}) is important for determining the structural response. The range of t_o/T_n in between these two extremes (i.e. $0.1 \leq t_o/T_n \leq 10$) represents dynamic loading, where both peak pressure and impulse govern the structural response. Thus, the ratio t_o/T_n is central for determining the structural response, and as detailed below, the load cases investigated in this study belong to the dynamic loading category ($0.1 \leq t_o/T_n \leq 10$).

8.4.2 Blast Load Cases and Simulation in LS-Dyna

The following three investigations are performed in this study: (1) comparison of the responses of HSHDC and COR-TUF slabs for a TNT charge of 0.5 kg placed at 0.91 m (3 feet) from the center of the slab. (2) influence of varying TNT charge weights (0.1 kg, 0.3 kg, 0.5 kg, 0.6 kg, and 0.7 kg) on the structural response of HSHDC slab at a constant standoff distance of

0.91 m, and (3) influence of varying standoff distances (0.75 m, 0.80 m, 0.91 m, 1.10 m, and 1.75 m) on the structural response of HSHDC slab with a constant TNT charge of 0.5 kg.

In all the investigations above, the slabs with dimensions of 12″x12″x1″ (same as drop-weight experiments) are simply supported 0.5″ near the top and the bottom along the horizontal edges as shown in Figure 8.32. Similar support conditions are used in blast load simulator (shock tube), and therefore, the results of the FE analysis presented here will be comparable with experimental results in the future. All other inputs in LS-Dyna, including material models and mesh element size, are the same as that described for the simulation of drop-weight experiments in Section 8.3. In this study, the structural responses of the slabs are investigated based on the displacement of the mid-point (point 'P' in Figure 8.32) of the blast face (facing the point of detonation) of the slabs.

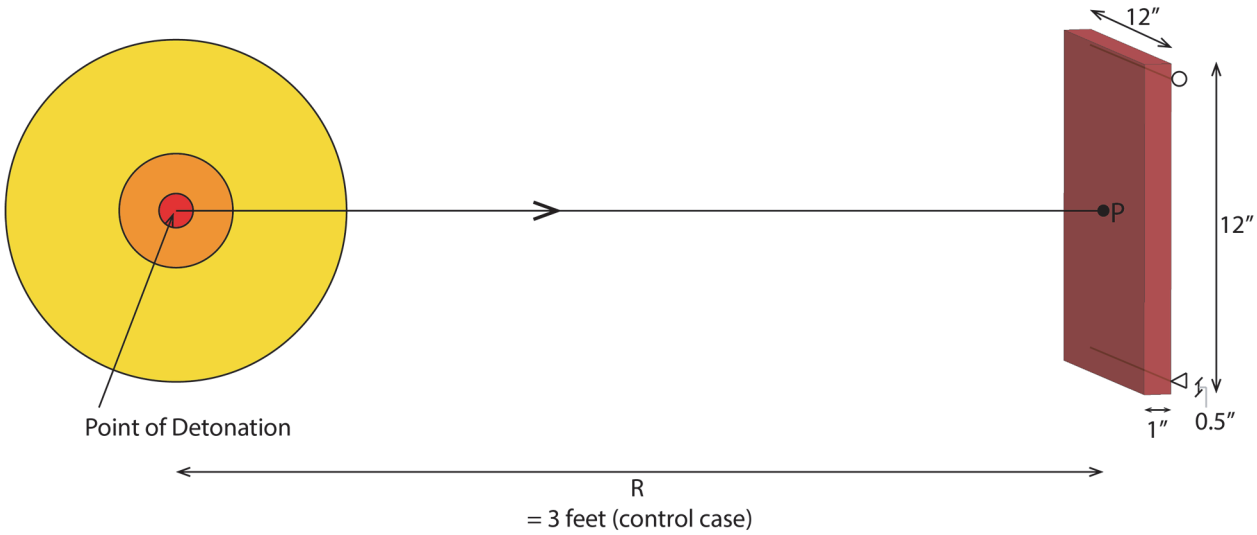

Figure 8.32: Geometry of the FE simulation of blast loads of HSHDC and COR-TUF slabs (R = 3 feet is shown to scale, relative to the slab dimensions, in this figure)

The aforementioned blast loads are applied in LS-Dyna using the LOAD_BLAST keyword. Sample inputs for the control load case (W = 0.5 kg and R = 0.91 m) are given in Table 8.9. There is no input in the LOAD_BLAST keyword that specifies the elements on which the blast load acts. Instead, a 'segment' of elements on which the blast force acts (front face of the slab facing the point of detonation) is first defined through entity creation. After the segment is created, LOAD_SEGMENT_SET keyword is used to link this segment set of elements to the LOAD_BLAST by pointing to the segment id and setting load curve id equal to –2. In addition, two virtual 'load curves,' with at least 2 data points in each load curve (e.g. 0,0 and 1,1), are defined with arbitrary ids for proper functioning of the model. The LOAD_BLAST keyword calls CONWEP subroutine in LS-Dyna, which is the programmed version of blast load charts in the Army technical manual and UFC. In this manner, the time varying pressure that should be applied on the selected elements due to the specified W and R of the detonation is determined in LS-Dyna.

Table 8.9: Input parameters for the LOAD-BLAST keyword

Property	Value	Remarks
Charge Weight	0.5 kg	
x,y,z location of the point of detonation	–0.91,0,0.1524 (unit = meters)	The slab's center is located at 0,0,0.1524 (0.1524 m is 6″)
Time zero of detonation	–0.55 ms	The FE computation in this case starts at 0.55 ms. The time zero of detonation is commonly set to a value slightly smaller in magnitude (with negative sign) than the time of arrival (t_a) , so that the computation time is not wasted until the blast wave arrives.
Unit system	2	SI unit system m, kg, s
Type of burst	2	For air blast (1 is for surface blast)
Input Card 2 (CFM to CFP) is not required.		

8.4.3 Results and Discussion

The mid-point displacement-time history of an HSHDC slab, along with the average pressure on the blast face of this slab, in response to the detonation of a TNT charge weighing 0.5 kg placed in air at a standoff distance of 0.91 m (3 feet) is shown in Figure 8.33. The peak average blast pressure (in excess of the atmospheric pressure) experienced by the slab is 2.6 MPa and the duration of the positive phase is about 0.6 ms. While the response (mid-point displacement) is dominated by the forcing function (blast pressure) until the end of the positive phase, the response thereafter is dominated by free vibrations with reducing amplitude and mean. The reduction in the amplitude is caused by damping (due to cracking and fiber/matrix inelastic interaction), whereas the reduction in the mean value (approximately shown by the dashed line in Figure 8.33) is caused by small negative blast pressure on the slab plus slight elastic recovery. Overall, the structural response of the slab is similar to that of a single degree of freedom spring-mass-damper system hit by a pulse load.

The normal stress profiles at the time points A to F (shown in Figure 8.33) on the slab plane facing the blast pressure are shown in Figure 8.34. It should be noted that negative normal stress indicates positive pressure in this figure. At state A, circular stress contours are visible, which indicate the spherical shape of the blast waves generated in the air-blast. The blast wave reaches the center point first (as it is the nearest location from the point of detonation), and within about 25 microseconds, it engulfs almost the entire slab at state B. As a result, the slab experiences maximum positive pressure (or negative normal stress) at state B. Average blast pressure drops to almost zero at state C. Thereafter, the average blast pressure is slightly positive

in states D, E, and F, as indicated by predominantly blue color of the normal stress contours throughout the slab.

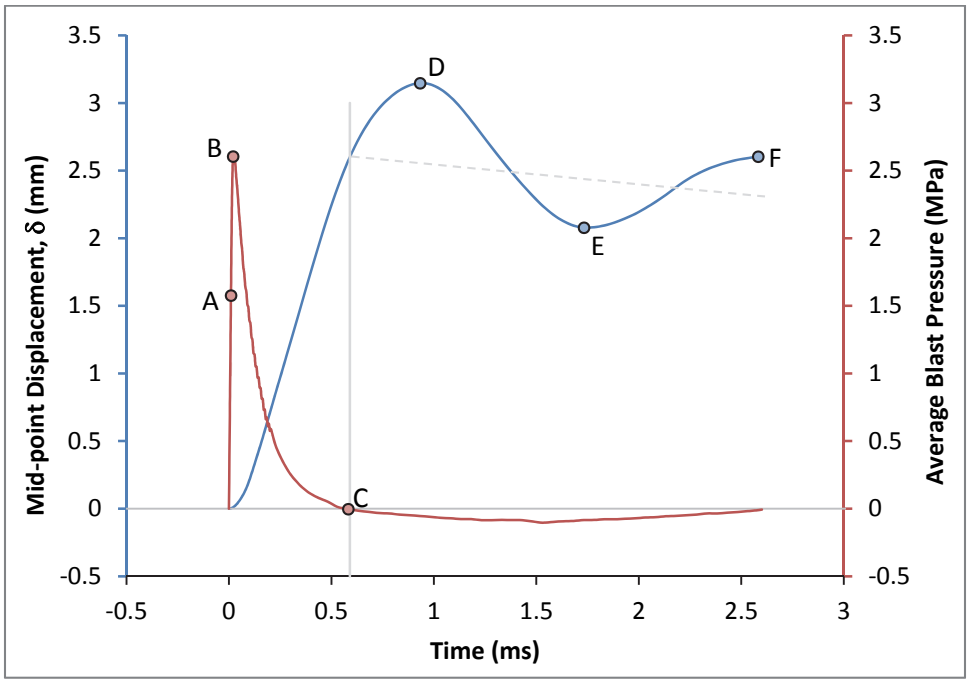

Figure 8.33: Average blast pressure and slab displacement in response to a 0.5 kg TNT charge placed at 0.91 m
(A to F are selected time points for querying FE results)

The maximum principal tensile strain at the time points A to F (shown in Figure 8.33) on the back face of the slab (facing away from the blast pressure) are shown in Figure 8.35. The colors used to denote various strain contours are changed among the states A to F in order to enhance the contrast of individual figures. In states A and B, elastic strains (< 0.01%) are visible on the back face of the slab in the regions directly underneath the blast pressure zone. Small inelastic tensile strains appear in state C with the maximum strain reaching up to 0.2% in the center fifth of the slab. Majority of the inelastic straining occurs in states D, E, and F, after the state C (i.e. after the positive blast pressure phase is over), due to free vibration (caused by the

blast energy imparted to the slab in the positive pressure phase) and small negative pressure. Maximum tensile strain reaches up to 2% at the central edges of the slab in states D, E, and F. Nevertheless, the HSHDC slab is able to safely distribute the flexural deformation in the mid-third section due to the material's tensile ductility.

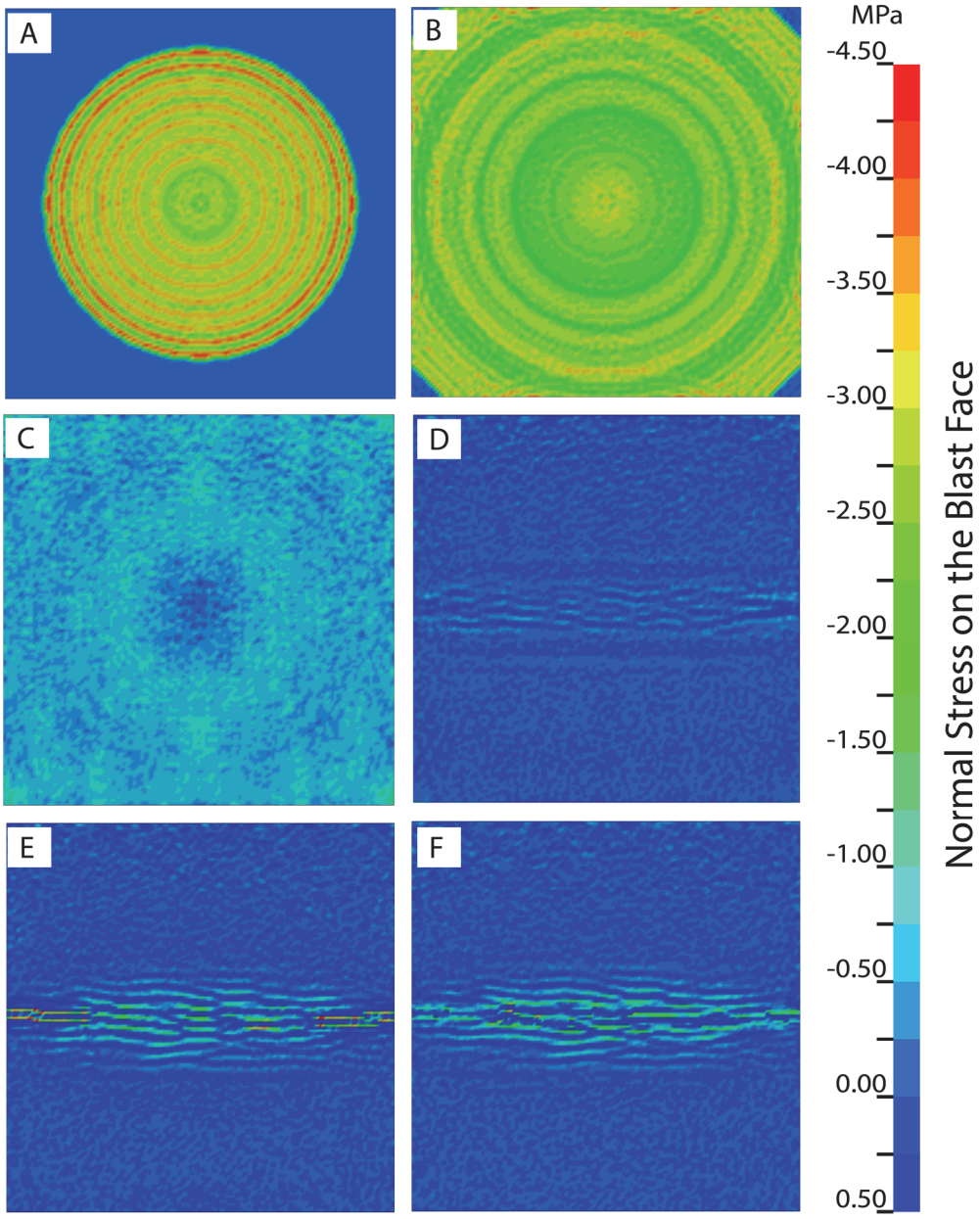

Figure 8.34: Normal stress at time points A to F (Figure 8.33) on the blast face of the slab

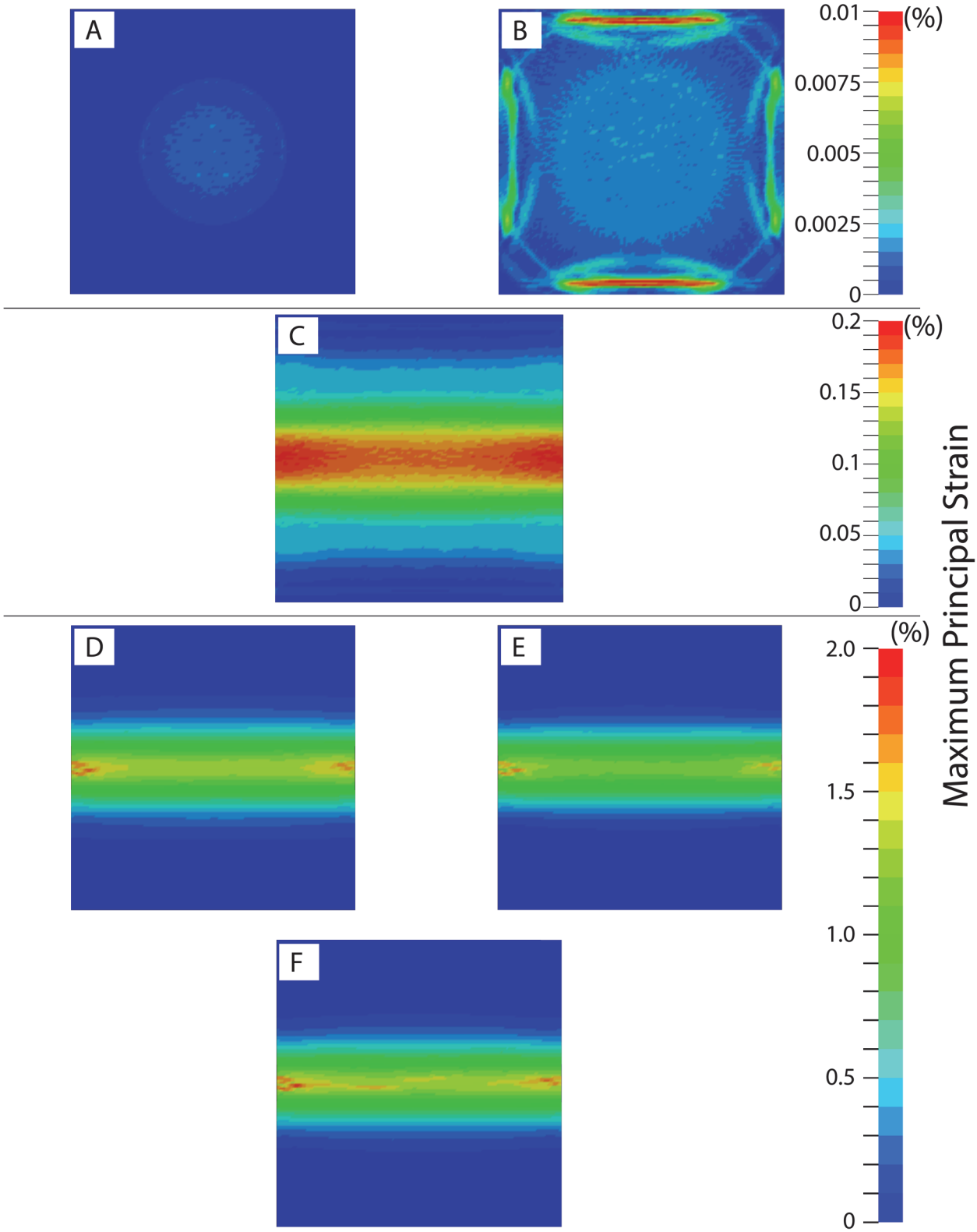

Figure 8.35: Maximum principal (tensile) strain on the back face of the slab

The mid-point displacements of HSHDC and COR-TUF slabs in response to the detonation of a TNT charge (W) of 0.5 kg placed at a distance (R) of 0.91 m (3 feet) are shown in Figure 8.36. Unlike the HSHDC slab, the COR-TUF slab is unable to distribute the tensile strain at the back face of the slab. As a result, the COR-TUF slab fails under this blast load as indicated by the monotonically increasing mid-point displacement of the slab, and the FE analysis stops at about 1.9 ms due to excessive erosion of elements.

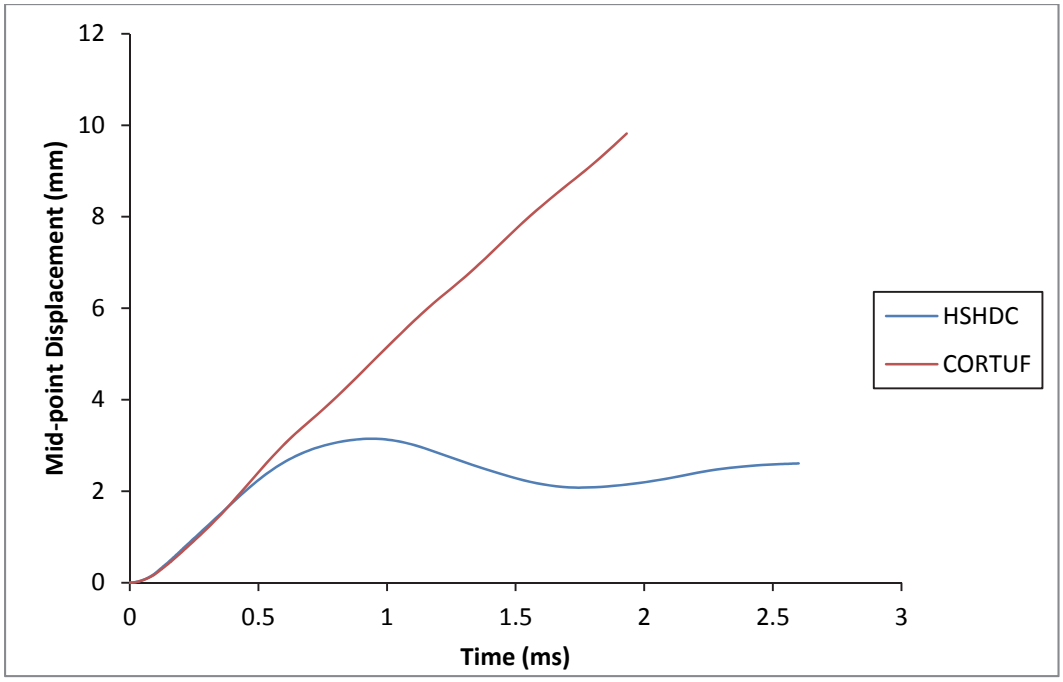

Figure 8.36: Comparison of HSHDC and COR-TUF slabs' responses to W=0.5 kg detonation at 0.91 m

The displacement-time histories of the HSHDC slab for varying weights placed at a constant distance of 0.91 m (3 feet) are shown in Figure 8.37. The maximum mid-point displacement of the slab, δ_{max}, for these load cases is plotted in Figure 8.38. In this figure, δ_{max} shows a quadratic increase quadratic with the charge weight (W) at a constant standoff distance.

The blue data point in Figure 8.38 represents the reference load case of W = 0.5 kg and R = 0.91 m. Further, in Figure 8.37, increasing the blast pressure on the slab first increases and then decreases the displacement amplitude during the free vibration. For small charge of 0.1 kg, majority of the slab remains elastic and, therefore, the amplitude is small. The amplitude is also small for large charge (0.7 kg) because the majority of the material undergoes significant inelastic deformation in this load case, and is unable to vibrate with large displacements. In spite of the reduction in displacement amplitude, the time period of oscillation, which is inversely proportional to the square root of the slab's flexural stiffness, appears to be constant (about 1 ms) in the first cycle for all the load cases, owing to the damage tolerance of the material.

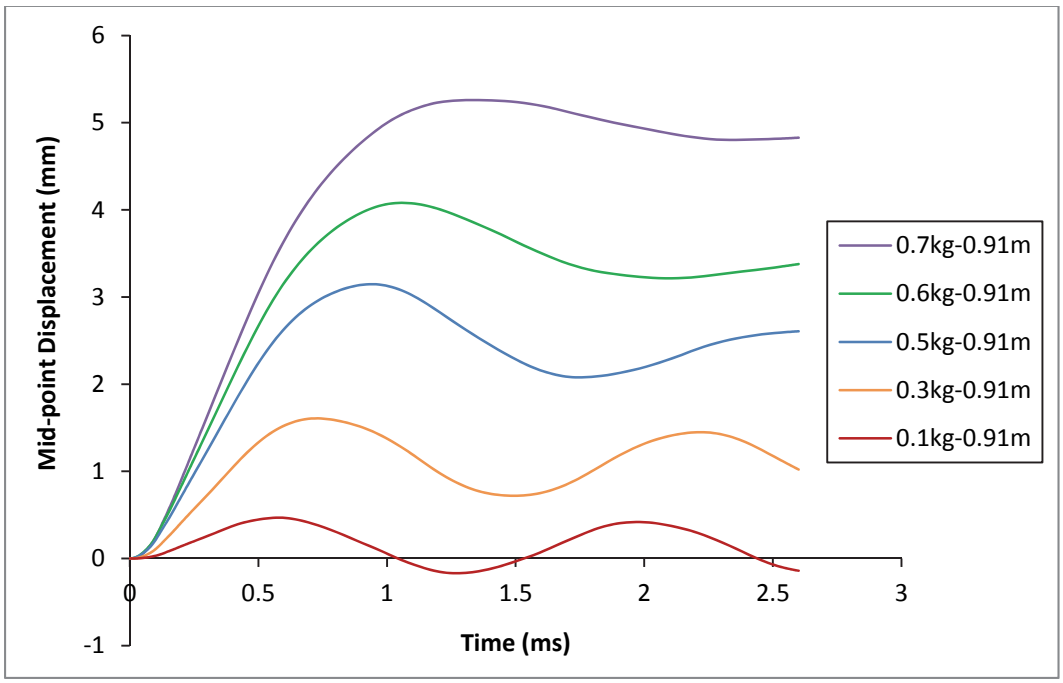

Figure 8.37: Response of HSHDC slab under varying charge weights placed at 0.91 m

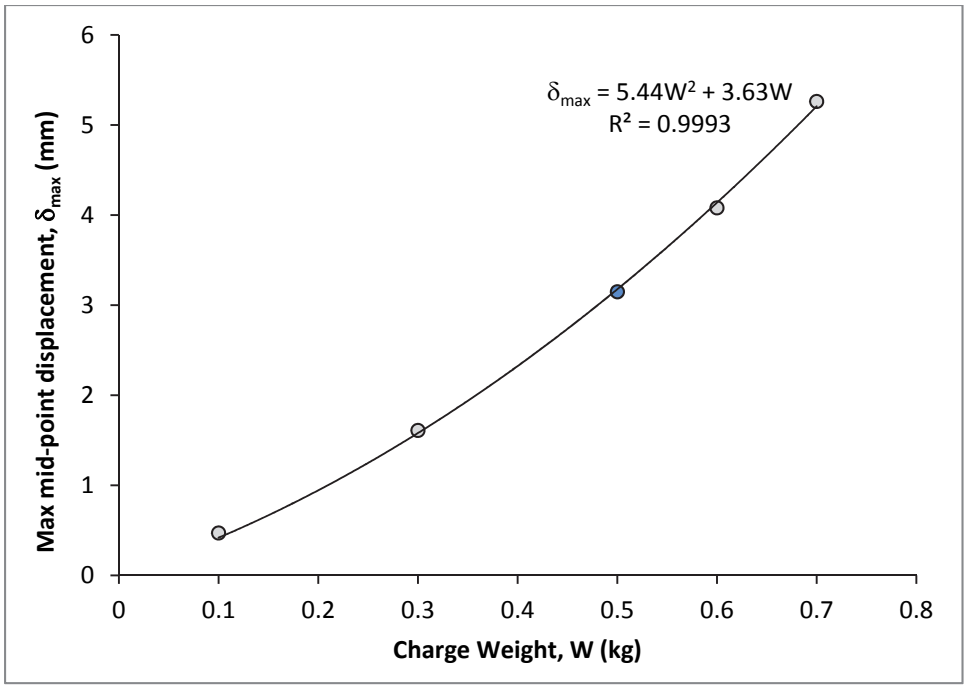

Figure 8.38: Influence of varying the charge weight on the maximum mid-point displacement of the HSHDC slab

The influence of varying the standoff distance (R) of a constant charge weight of 0.5 kg on the displacement-time histories of the HSHDC slab are shown in Figure 8.39. The maximum mid-point displacement of the slab, δ_{max}, for these load cases is plotted in Figure 8.40. In this figure, δ_{max} shows an exponential decline with increasing standoff distance. The blue data point in Figure 8.40 represents the reference load case of W = 0.5 kg and R = 0.91 m. The influence of reducing the standoff distance on the response of the HSHDC slab is qualitatively similar to that of increasing the charge weight on the amplitude and time period of vibration, as discussed above.

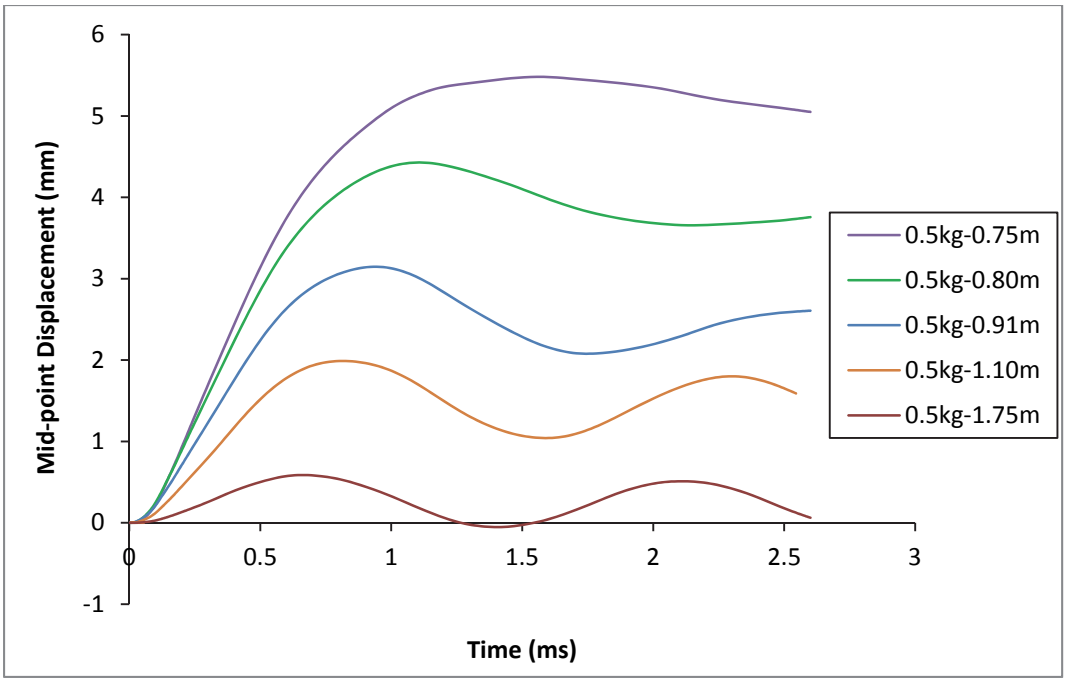

Figure 8.39: Response of HSHDC slab under varying standoff distance of 0.5 kg TNT charge

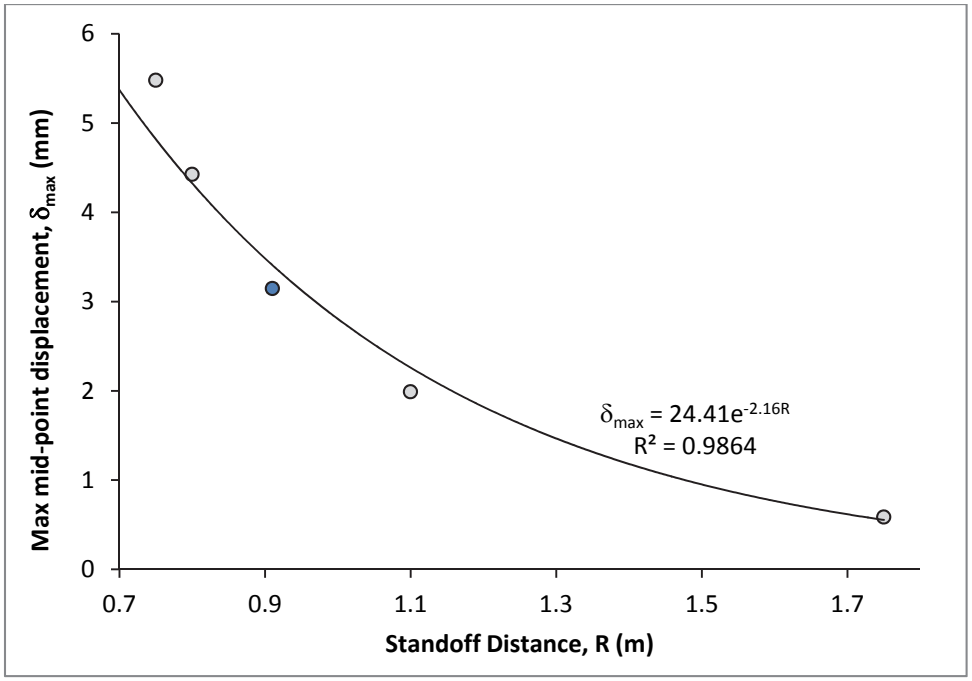

Figure 8.40: Influence of varying the standoff distance on the maximum mid-point displacement of the HSHDC slab

As majority of the blast wave parameters are expressed in terms of the scaled distance, $Z = R/W^{1/3}$, it is attempted in Figure 8.41 to find a correlation between the maximum displacement (δ_{max}) of the slab and Z for all the load combinations (varying W and varying R) investigated above. An exponentially reducing function seems to correlate well ($R^2 \approx 0.94$) with the computed δ_{max} for various load cases. Supported by experimental evidence, such insights into the peak structural behavior can be potentially used to establish the response and design spectra for HSHDC slabs.

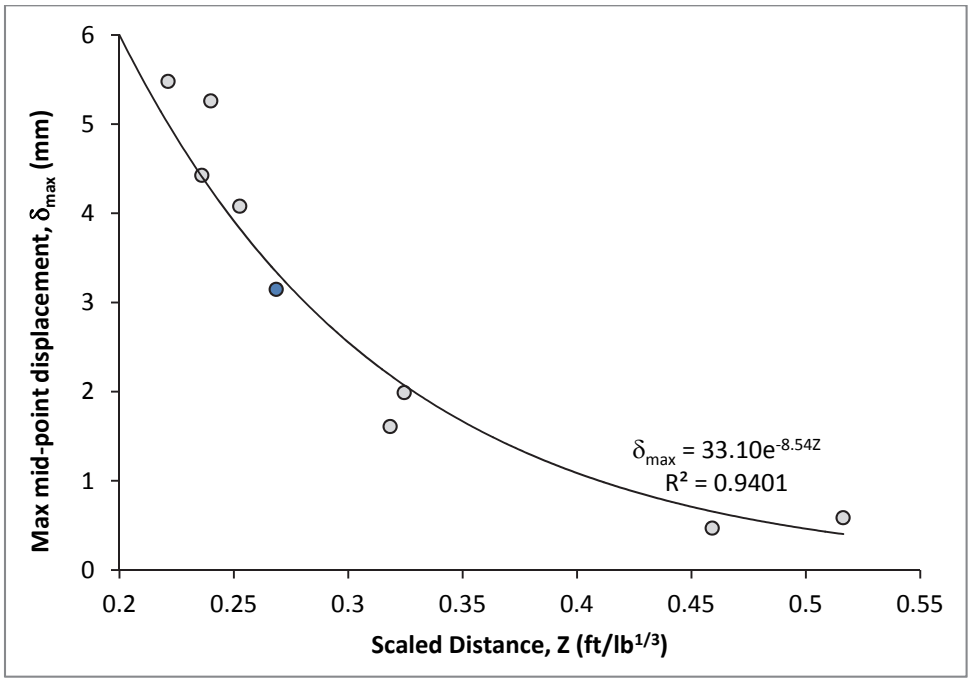

Figure 8.41: Variation of slab displacement with the scaled distance

8.5 Conclusions

The structural resilience of HSHDC slabs, in comparison with COR-TUF slabs, under drop-weight impact and blast loads is demonstrated in this chapter. The influence of impact loads on the slabs of both materials is investigated experimentally, using drop-weight tests, as well as analytically, using finite element (FE) method through the software LS-Dyna. The performance of HSHDC and COR-TUF slabs is also compared using FE analysis. Crucial insights into the behavior of HSHDC slabs, in terms of their response to varying charge weights and standoff distances are obtained for comparison with shock tube test results in the future. Overall, the following conclusions can be drawn from the investigations reported in this chapter.

- Under multiple drop-weight impacts (20 impacts or failure, whichever occurs first), while HSHDC slabs maintain their impact load bearing capacity (as measured by peak contact force [PCF]) and structural integrity, COR-TUF slabs gradually lose their capacity and fail before the 20^{th} impact. Increasing the impact velocity causes more rapid reduction of PCF of COR-TUF slabs with the number of impacts, whereas, it has negligible effect on the behavior of HSHDC slabs, which exhibit almost no reduction in PCF with the number of impacts at all velocities investigated in this study. Furthermore, the reduction in the size of the impact head causes premature punching shear failure in COR-TUF slabs. This catastrophic mode of failure is not observed in HSHDC slabs. While the COR-TUF slabs exhibit quasi-brittle flexural and shear failures accompanied by large localized cracks and excessive spalling, the HSHDC slabs exhibit ductile flexural behavior (without failure until 20 impacts) with well-distributed multiple fine radial cracks with almost no spalling, regardless of the impact head diameter.

- The drop-weight experiments were satisfactorily simulated in LS-Dyna, utilizing the MAT_072R3 material model to simulate the behavior of HSHDC and COR-TUF materials. In particular, the properties involving time-integration, such as displacement and area under the force-time curve (impulse), showed good agreement with the experimental results. Although there is a large discrepancy in the predicted PCFs as compared to experimentally determined PCFs of the slabs, it may be attributed to the experimental limitation of sampling frequency; additional experiments with higher sampling frequency are required to confirm this hypothesis.

- The FE analysis revealed that the tensile strain is evenly diffused at the back faces of the HSHDC slabs (due to flexural deformation) even under the most energetic impact investigated in this study, which supports the experimental observation of multiple fine cracks. In contrast, the FE analysis of the COR-TUF slab exhibits strain concentrations at the back face, which are consistent with the experimental observation of large (mm sized) cracks and early failure. The FE analysis shows that the ductile structural response of the HSHDC slab is a direct result of the material's tensile ductility, whereas a lack thereof causes a quasi-brittle behavior as observed in the COR-TUF slabs.

- The FE analysis of the layered slabs, along with the penalty function, is demonstrated as a useful tool for optimizing cost and impact resistance of the slabs, simultaneously. The relative importance given to cost and mechanical performance determine the optimum configuration of HSHDC and COR-TUF layers in the slabs.

- The FE analysis provided insights into the performance of HSHDC slabs under air-blast of varying charge weight and standoff distance. While the maximum mid-point displacement of the HSHDC slab exhibits an exponential decline with increasing standoff distance (R) and scaled distance (Z), it exhibits a quadratic increase with increasing charge weight (W). Overall, the structural response of the slab is similar to that of a single degree of freedom spring-mass-damper system hit by a pulse load.

References

1. Eamon, C. D., Fitzpatrick, P. & Truax, D. D. (2007) "Observations of Structural Damage Caused by Hurricane Katrina on the Mississippi Gulf Coast" *ASCE Journal of Performance of Constructed Facilities*, 21(2), 117-127.

2. Padgett, J., et al. (2008) "Bridge Damage and Repair Costs from Hurricane Katrina" *ASCE Journal of Bridge Engineering*, 13(1), 6-14.

3. El-Tawil, S. (2004) "Vehicle Collision with Bridge Piers" Report to Florida DOT, Ann Arbor, MI: University of Michigan, pp.3.

4. Stewart, M. G., Netherton, M. D. & Rosowsky, D. V. (2006) "Terrorism Risks and Blast Damage to Built Infrastructure" *Natural Hazards Review*, 7(3), 114-22.

5. AASHTO (2012) "AASHTO LRFD Bridge Design Specifications (6th Ed.)" Washington, DC.

6. ASCE-7 (2010) "Minimum Design Loads for Buildings and Other Structures" American Society of Civil Engineers, Reston, VA.

7. US Departments of the Army, the Navy and the Air Force (1990) "Structures to Resist the Effects of Accidental Explosions" Department of the Army Technical Manual TM 5-1300, Department of the Navy Publication NAVFAC P-397, Department of the Air Force Manual AFM 88-22, Washington, DC: US Department of Defense.

8. US DoD (2013) "Design of Buildings to Resist Progressive Collapse - UFC 4-023-03" Washington, DC: US Department of Defense.

9. National Research Council (2000) "Blast Mitigation for Structures" Washington, DC: National Academy Press.

10. Li, V.C., Mishra, D.K., Naaman, A.E., Wight, J.K., LaFave, J.M., Wu, H.C., & Inada, Y. (1994) "On the Shear Behavior of Engineered Cementitious Composites" *Advanced Cement Based Materials*, 1(3), 142-149.

11. Flanagan, D.P. & Belytschko, T. (1981) "A uniform strain hexahedron and quadrilateral with orthogonal hourglass control" *International Journal of Numerical Methods in Engineering*, 17(5), 679-706.

12. Malvar, L.J., Crawford, J.E., Wesevich, J.W. & Simons, D. (1997) "A plasticity concrete material model for DYNA3D" *International Journal of Impact Engineering*, 19(9–10), 847-873.

13. Schwer, L.E. (2004) "Preliminary Assessment of Non-Lagrangian Methods for Penetration Simulation" In Proceedings of *8th International LS-DYNA User Conference*, Dearborn, MI, May 2-3, 2004, pp.8.1-12.

14. Agardh, L. & Laine L. (1999) "3D FE-Simulation of High-Velocity Fragment Perforation of Reinforced Concrete Slabs" *International Journal of Impact Engineering*, 22, 911-922.

15. William, K.J. & Warnke, E.P. (1975) "Constitutive Model for the Triaxial Behavior of Concrete" In Proceedings of *International Association for Bridge and Structural Engineering: Seminar on Concrete Structures Subjected to Triaxial Stress*, Bergamo, Italy. v.19, pages 174-186.

16. Ottosen, N.S. & Ristinmaa, M. (2005) "The Mechanics of Constitutive Modeling" Elsevier Science Ltd, Oxford, UK.

17. Girgin, Z.C., Arioglu, N. & Arioglu, E. (2007) "Evaluation of Strength Criteria for Very-High-Strength Concretes under Triaxial Compression" *ACI Structural Journal*, 104(3), 277-283.

18. Attard, M.M., & Setunge, S. (1996) "Stress-Strain Relationship of Confined and Unconfined Concrete" *ACI Materials Journal*, 93(5), 432-442.

19. Joy, S. & Moxley, R. (1993) "Material Characterization, WSMR-5 ¾″ Concrete" Report to the Defense Special Weapons Agency, USAE Waterways Experiment Station, Vicksburg, MS.

20. Chin, L.S. (2006) "Finite Element Modeling of Hybrid-Fiber ECC Targets Subjected to Impact and Blast" PhD Dissertation, Singapore: National University of Singapore, pp. 54.

21. Comité Euro-International du Béton (1990) "Stress and Strain Rate Effects – Impact" In *CEB-FIP Model Code*, Trowbridge, UK: Redwood Books, pp. 48-50.

22. Wang, S., Zhang, M.H. & Quek, S.T. (2011) "Effect of high strain rate loading on compressive behavior of fiber-reinforced high-strength concrete" Magazine of Concrete Research, 63(11), 813-827.

23. LSTC (2012) "LS-Dyna Keyword User's Manual: Volume II Material Models" Livermore, California: Livermore Software Technology Corporation, pp. 1:52-53.

24. Chin, L.S. (2006) "Finite Element Modeling of Hybrid-Fiber ECC Targets Subjected to Impact and Blast" PhD Dissertation, Singapore: National University of Singapore, pp. 103-4.

25. Ashby, M.F. (2009) "Penalty Functions" In *Materials and the Environment: Eco-informed Material Choice*, Burlington, MA: Butterworth-Heinemann, pp. 176-8.

26. Larcher, M. (2008) "Air Blast Waves" In *Pressure-Time Functions for the Description of Air Blast Waves*, Ispra, Italy: Joint Research Center of the European Commission, pp. 6.

27. UFC 3-340-02 (2008) "Structures to Resist the Effects of Accidental Explosions" Washington, DC: US Department of Defense, pp.81. (UFC 3-340-02 is the same as the Army Technical Manual TM5-1300)

28. UFC 3-340-02 (2008) "Structures to Resist the Effects of Accidental Explosions" Washington, DC: US Department of Defense, pp.83-86.

29. UFC 3-340-02 (2008) "Structures to Resist the Effects of Accidental Explosions" Washington, DC: US Department of Defense, pp.40.

30. Smith, P. & Cormie, D. (2009) "Structural Response to Blast Loading" In *Blast Effects on Buildings (2nd Ed.)*, Thomas Telford, pp. 80-102.

PART IV: INFRASTRUCTURE SUSTAINABILITY AND INTEGRATION WITH RESILIENCE

CHAPTER 9: DEVELOPMENT OF GREEN, DURABLE HSHDC AND IMPACTS ON INFRASTRUCTURE SUSTAINABILITY

9.1 Introduction

In this chapter, the research focus shifts from resilience toward greenness of HSHDC and the environmental sustainability aspects of its potential infrastructure applications, while maintaining adequate resilience. The development of greener and more durable versions of HSHDC, compared to the version discussed thus far, is presented in this chapter. Here, greenness is measured in terms of the material sustainability index (MSI),[1] such as CO_2 emissions (carbon-MSI) and primary energy (energy-MSI) associated with unit volume of a material. Durability is indirectly measured in terms of average crack width under direct tension. It has been shown in literature that increasing crack width has a significant impact on the transport properties, (particularly, water permeability and chloride ion diffusion, whereas sorptivity decreases with increasing crack width), which in turn influence the durability of the structure in question. The development of these green and durable versions of HSHDC and their impacts on long-term infrastructure sustainability, using life cycle assessment (LCA), are presented in this chapter.

The carbon and energy MSIs of HSHDC and other concretes discussed in this research are shown in Figures 9.1 and 9.2, respectively. The computations of carbon dioxide (CO_2) emissions and primary energy of the composites are based on the inventory data of their ingredients in Table 9.1. HSHDC utilizes the largest cement content per unit volume among all four concretes, and therefore, has the largest cement related contribution to both MSIs as observed in these figures. In addition to cement, the polyethylene (PE) fibers also contribute significantly toward the MSI, particularly the energy-MSI, of HSHDC as explained below. Due to the large cement content and the use of polymer fibers in HSHDC, its carbon and energy MSIs are significantly higher compared to other concretes, and, therefore, the cement and polymer fiber content must be minimized to limit the detrimental impacts of the materials phase (of the HSHDC infrastructure life cycle) on the natural environment.

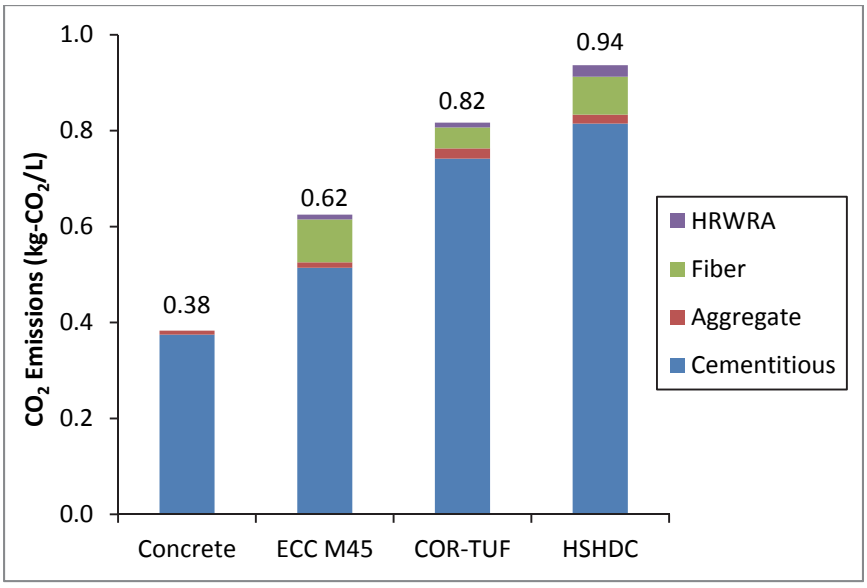

Figure 9.1: Carbon-MSI of various concretes
('Concrete' refers to normal concrete with 5000 psi compressive strength)

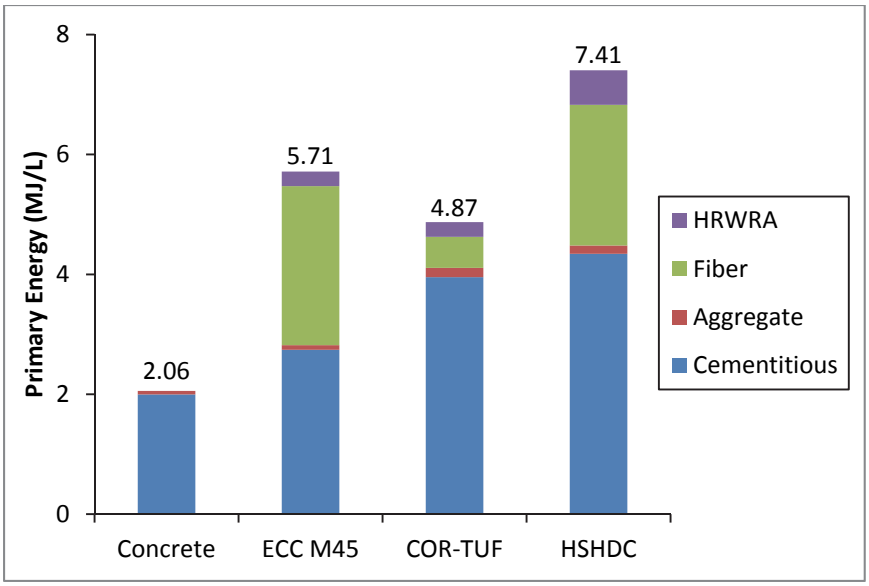

Figure 9.2: Energy-MSI of various concretes

Table 9.1: Carbon and energy intensities of ingredients of various concretes

Ingredient	Primary energy MJ/kg	CO_2 emissions kg-CO_2/kg
Cementitious Materials		
Type-I Cement = Oil Well Cement	4.8[2,3]	0.90[2,3]
Silica Fume	0[*R]	0[*R]
Slag	0.544[4]	0.021[4]
Fly Ash	0[*R]	0[*R]
Aggregates/Fillers		
F-55 Sand	0.136[2,5,6]	0.020[2,5,6]
Silica Flour	0.204[2,4,5,6]	0.030[2,4,5,6]
F-110 Sand	0.170[2,5,6]	0.025[2,5,6]
Natural Sand	0.023[7]	0.003[7]
Coarse Aggregate	0.035[7]	0.005[7]
Water and HRWRA		
Tap Water	0 (assumed negligible)	0 (assumed negligible)
Poly-carboxylate-based HRWRA	35.2[8]	1.46[8]
Fibers		
Polyethylene (PE)	121[9]	4.08[9]
Polyvinyl Alcohol (PVA)	101[10]	3.40[10]
Dramix Steel	2.02[11]	0.17[11]
Special Treatment and Chemicals		
Plasma Treatment of PE fiber	0.02 MJ/min[12]	0.008 kg-CO_2/min[12]
Silane Coupling Agent	34[13]	1.3[13]

[*R] Recycled material with negligible environmental impact

The contribution of the petroleum-based PE fibers on the primary energy of HSHDC (Figure 9.1) is relatively higher than that on CO_2 emissions of HSHDC (Figure 9.2). This is because, while the primary energy of the PE fiber includes the 'process energy' (consumed in manufacturing the fiber) plus the 'feedstock energy' (heat content of the petroleum-based inputs), the CO_2 inventory only accounts for the emissions during the manufacturing processes.

In addition to high carbon and energy intensities, another factor that limits the environmental sustainability of HSHDC's potential infrastructure application is its relatively large, although controlled, crack widths. The average residual crack width of HSHDC, reported in Chapter 6, is 160 μm, whereas, the maximum crack width observed in HSHDC (at peak load) is 310 μm. Although these crack widths fall below the recommendations of ACI[14] and AASHTO[15] codes (which provide reinforcement details with the intention of controlling the crack widths to about 400 μm), they are 3-5 times that of similarly strained ECC.

The influence of crack width on the transport properties of ECC and reinforced mortar are well documented in the literature. Both water permeability[16] and chloride ion diffusion[17] increase rapidly with crack widths. These transport properties, in turn, determine the frequency of repair and overall service life of the structure.[18] Reducing the crack widths in HSHDC is, therefore, an important objective for enhancing the long-term sustainability of HSHDC's potential infrastructure applications.

The objectives of the research reported in this chapter are: (1) to minimize the cement content in HSHDC, while maintaining the compressive strength greater than 150 MPa and tensile ductility greater than 3%, same as the original mechanical property targets of HSHDC in Section 4.2 – the HSHDC versions resulting from this work are referred as 'green' HSHDC; (2) to reduce the average residual crack width of HSHDC under 100 μm, with the same mechanical property targets as the first objective – the HSHDC versions resulting from this work are referred as 'durable' HSHDC; and (3) to investigate the life cycle impacts of the improvements in (1) and (2) using comparative life cycle analysis model[19] of an example infrastructure application (bridge deck link-slab). In this chapter, the adjectives 'green' and 'durable' for qualifying HSHDC are used only to distinguish the materials from each other and from the version of HSHDC discussed so far (which is referred as 'HSHDC' with no qualifying adjectives), and by no means imply that green HSHDC are not durable or durable HSHDC are not green.

The approach adopted for attaining green HSHDC involved partial substitution of the Class H (oil-well) cement by suitable recycled alternatives, while maintaining the mechanical properties above the set targets. In this research, class F[20] fly ash, grade 120[21] slag, and silica fume (all post-industrial recycled materials) were used to partially substitute Class H cement in HSHDC. Other recycled alternatives that have been used in concrete and ECC were screened out due to their significant detrimental impacts on the rheology and mechanical properties, particularly compressive strength, of HSHDC. Although the PE fiber, as discussed above, also contributes significantly toward the environmental impact of HSHDC (next to cement), its substitution was not investigated in this study. The details of green HSHDC development are given in Section 9.2.

The approach adopted for attaining durable HSHDC, with average residual crack width under 100 μm, entailed enhancing the fiber/matrix interfacial bond via two methods: (1) surface modification of the PE fibers through plasma treatment for enhancing their affinity to the matrix hydration products, and (2) addition of silane coupling agents in the matrix for enhancing its affinity to the PE fiber. The details of durable HSHDC development are given in Section 9.3.

9.2 Development of Green HSHDC

9.2.1 Experimental Investigation

The mix proportions of green HSHDCs investigated in this study, incorporating varying amounts of fly ash, slag, and silica fume, are given in Table 9.2. In this table, only the weight proportions of cement and its partial substitute (such that the total of the proportions is 1) are presented, along with HRWRA. The HRWRA content is adjusted in green HSHDC mix proportions to maintain the viscosity of their matrix near that of HSHDC matrix (6.0 Pa-s determined in Chapter 5). The weight proportions of the rest of the ingredients are the same as that shown in Table 5.1 (the HSHDC version investigated in Chapters 5 to 8), which are – (cement + substitute): silica fume : silica flour : sand : water : fiber = 1 : 0.389 : 0.277 : 0.700 : 0.208 : 0.0214 (V_f = 2%). The mixtures are named such that the first letter G indicates the series of 'Green' HSHDCs, the second letter indicates the cement substitute (F for fly ash, S for slag, and M for micro-silica or silica fume), and the number indicates the replacement percentage by weight of cement.

Table 9.2: Mix proportions of cement and its substitute in green HSHDCs (by weight)

Mix ID	Class H Cement	Class F Fly Ash (F)	Slag Cement (S)	Silica Fume (M)	HRWRA
G-F-15	0.85	0.15	0	0	0.017
G-F-25	0.75	0.25	0	0	0.018
G-F-35	0.65	0.35	0	0	0.018
G-S-15	0.85	0	0.15	0	0.018
G-S-25	0.75	0	0.25	0	0.019
G-S-35	0.65	0	0.35	0	0.021
G-M-15	0.85	0	0	0.15	0.020
G-M-25	0.75	0	0	0.25	0.022
G-M-35	0.65	0	0	0.35	0.026

The recycled pozzolanic materials used to partially substitute cement in this study, i.e. fly ash, slag, and silica fume, are industrial by-products (post-industrial recycled materials) sourced from various industries, as described below.

The class F fly ash is generated as a by-product in a coal fired power plant. The class F fly ash is typically obtained by burning anthracite and bituminous coal, whereas the class C fly ash is typically a by-product of burning lignite or subbituminous coal. The class F fly ash typically has lower levels of calcium oxide (CaO) compared to class C fly ash and, therefore, does not possess cementing properties (only pozzolanic properties). The class F fly ash used in this research is sourced from the Monroe plant of DTE Electric Company, and its chemical composition is given in Table 9.3.

Table 9.3: Chemical and physical analysis of the class F fly ash[22]

Chemical Analysis (% of total weight)		**Physical Analysis**	
Silicon Dioxide (SiO_2)	44.09%	Fineness, % retained on #325	16.85%
Aluminum Oxide (Al_2O_3)	23.21%	Strength Activity Index – 7 days	83%
Iron Oxide (Fe_2O_3)	8.39%	Strength Activity Index – 28 days	92%
Sulfur Trioxide (SO_3)	1.46%	Water Requirement, % control	97%
Calcium Oxide (CaO)	14.04%	Autoclave Soundness	0%
Moisture	0.05%	Density	2.45 g/cm^3
Loss on Ignition	0.56%		

Slag (also called Ground Granulated Blast Furnace Slag or GGBFS) is a by-product of iron separation from its ore in a blast furnace. Slag is the result of a high temperature reaction between limestone (flux) and the silicate-rich impurities of the iron ore. The slag from a blast furnace has pozzolanic as well as slightly cementing properties, and is further filtered and ground to varying levels of fineness. This step is associated with certain environmental impacts (Table 9.1), unlike fly ash and silica fume. The slag used in this research is grade 120, as specified in ASTM C989.[21]

Silica fume (also called Microsilica) is a by-product of producing silicon or ferrosilicon alloys. Silica fume is the smoke generated by burning a mixture of quartz, coal, and wood chips to produce silicon in an electric furnace. Silica fume consists primarily of amorphous silica and is extremely fine (0.1-1 μm), which makes it a very reactive pozzolanic material for high strength concrete applications.

For each of the green HSHDC mixtures in Table 9.2, four dogbones and three 2″ cubes, similar to that used in Chapter 5, were cast for the experimental determination of tensile and

compressive behaviors of these materials. All specimens were cured following the HSHDC curing procedure (Section 5.2.4). The test setups and procedures of experiments are same as that reported in Chapter 5, and the results are discussed below.

9.2.2 Results and Discussion

The average results of the tensile and compressive tests on green HSHDCs, along with their carbon and energy MSIs, are reported in Table 9.4. The composite properties of HSHDC determined in Chapter 5 are also included in this table for comparison. As cement contributes about 87% of the carbon-MSI (kg-CO_2/L) but only 59% of the energy-MSI (MJ/L) of HSHDC, substituting cement with recycled materials has relatively greater impact on the carbon-MSI compared to the energy-MSI. The densities of the three recycled substitutes are similar, and therefore, the reduction in MSI caused by these substitutes is almost the same at a given substitution level. The carbon-MSI is reduced by about 15%, 24%, and 33% at 15%, 25%, and 35% substitution, respectively, of cement by the recycled materials, whereas the energy-MSI is reduced by about 10%, 17%, and 23% at these substitution levels. In spite of the similar changes in MSIs, the effects of the three recycled substitutes on the mechanical performance of green HSHDC are quite dissimilar, as explained below.

Substitution with fly ash: The class F fly ash has an overall homogenizing effect on the composite properties of green HSHDC, particularly at the lower two levels of substitution (15% and 25%). The coefficient of variation (COV) drops down at these two substitution levels as compared to HSHDC. Due to its smooth spherical particles, fly ash acts as a lubricant during the mix processing of green HSHDC (similar effects are observed in ECC mixtures), which

enhances the mix rheology of the matrix and homogeneity of the composite through improved dispersion of fibers. However, this increase in homogeneity is also accompanied by decrease in compressive strength, particularly at 25% and 35% substitution levels, which may be caused by excessive use of pozzolanic material (HSHDC already contains large amount of silica fume – about 39% by weight of cement). The mixture G-F-35 does not meet the mechanical property targets (both strength and ductility) for green HSHDC, whereas the other two substitution levels meet the mechanical property targets while reducing the carbon and energy-MSIs.

Substitution with slag: Among the three recycled materials, slag's influence on the mechanical properties of green HSHDC is the most favorable at all replacement levels. While the tensile ductility is maintained at the level of HSHDC (within one standard deviation), the compressive strength is slightly increased by the use of slag, particularly at 25% replacement level. As mentioned above, slag particles not only act as pozzolanic materials and fillers, but also possess self-cementing properties due to the presence of calcium oxide. However, unlike fly ash, the mix processing with slag required increase in HRWRA dosage as the slag particles are more irregularly shaped than fly ash but have almost similar size as fly ash particles. Due to mix inhomogeneity, the compressive strength, tensile ductility, and COV of the mixture G-S-35, with 35% cement substituted by slag, are worse than that of HSHDC, whereas mixtures G-S-15 and G-S-25 have better mechanical performance than HSHDC and meet the mechanical property targets.

Substitution with silica fume: Although HSHDC already contains silica fume, its content was further increased to determine the influence on the mechanical performance, while reducing

environmental impacts. Unlike fly ash and slag, all the three substitution levels of silica fume resulted in poorer mechanical performance compared to HSHDC. The variability of properties was increased in these mixtures due to lack of mix homogeneity. In spite of larger dosage of HRWRA, the extremely fine particles of silica fume adsorb significant water during mixing and, therefore, negatively influence the mix rheology. Among the three substitution levels, only the mixture G-M-15 with 15% substitution of cement with silica fume met the average mechanical performance targets.

Table 9.4: Mechanical and environmental performance of Green HSHDCs

Mix ID	Compressive Strength, f_c' (MPa)	Tensile Strain Capacity, ε_{tu} (%) (COV)	Tensile Strength, σ_{tu} (MPa)	CO_2 Emissions (kg-CO_2/L)	Primary Energy (MJ/L)	Strength-ductility product, $f_c'.\varepsilon_{tu}$ (MPa)
HSHDC	166	3.4 (11.0%)	14.5	0.94	7.40	5.64
G-F-15	164	3.6 (8.9%)	14.6	0.80	6.64	5.90
G-F-25	155	3.1 (10.3%)	13.5	0.72	6.18	4.81
G-F-35	139	2.5 (14.5%)	13.2	0.63	5.70	3.48
G-S-15	170	3.1 (12.2%)	14.5	0.81	6.80	5.27
G-S-25	177	3.7 (15.5%)	14.8	0.73	6.43	6.55
G-S-35	161	2.4 (18.0%)	14.1	0.65	6.09	3.86
G-M-15	168	3.0 (17.0%)	13.9	0.80	6.69	5.04
G-M-25	151	2.3 (25.0%)	13.7	0.72	6.25	3.47
G-M-35	147	1.5 (19.0%)	13.1	0.63	5.87	2.21

The carbon and energy-MSIs of all the green HSHDCs that meet the target mechanical properties are plotted against the strength-ductility product (SDP) in Figure 9.3. SDP is defined as the product of the compressive strength and the tensile strain capacity of a material. This indicator of mechanical performance, proposed in this research, captures both the compressive strength and tensile ductility. It can be observed in Figure 9.3 that while the mixture G-F-25 is

the greenest HSHDC with the least carbon and energy-MSIs among all the mixtures investigated in this study, the mixture G-S-25 shows the best combination of mechanical and environmental performance, surpassing HSHDC in both performance criteria.

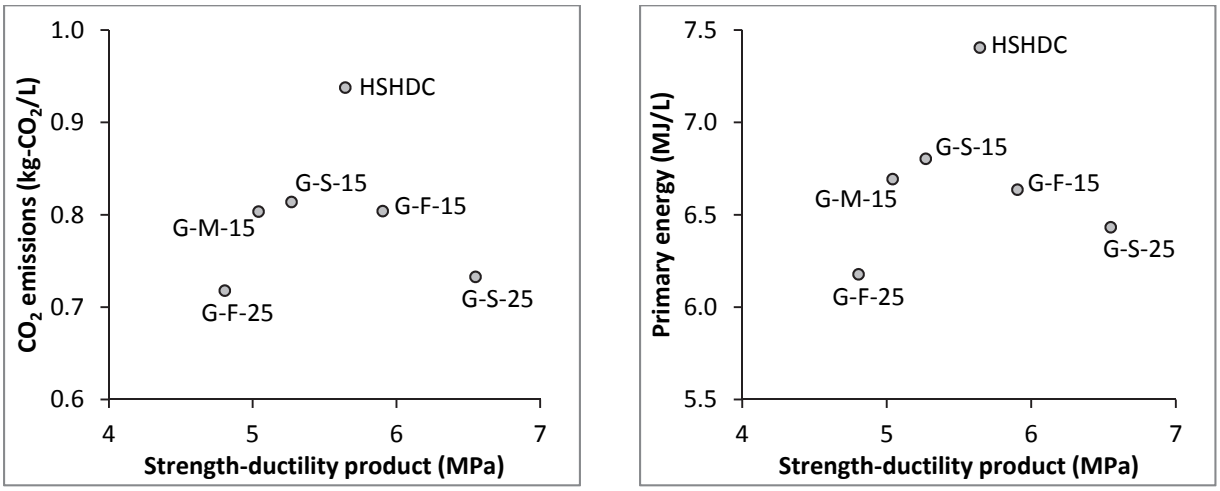

(a) Carbon-MSI (b) Energy-MSI

Figure 9.3: Environmental versus mechanical performance of green HSHDCs

9.3 Development of Durable HSHDC

Two approaches – plasma treatment of PE fibers and coupling agent addition in the HSHDC matrix – are explored for the development of durable HSHDC. As pointed out in Chapter 6, the fiber/matrix interfacial bond in HSHDC, similar to ECC, plays a central role in determining almost all the fiber-bridging properties. In particular, the fiber-bridging stiffness is directly controlled by the interfacial bond (Eqs. 6.5 and 6.9). The intended effect of both the approaches in this study is to enhance the interfacial bond between the PE fiber and the HSHDC matrix, so that the crack widths are limited under 100 μm.

9.3.1 Plasma Treatment Approach

9.3.1.1 *Working Principle and Treatment Process*

The PE fibers used in HSHDC are long chain carbon-based polymers [$-(CH_2\text{-}CH_2)_n-$ (n > 100,000)], which consist of a carbon backbone with each carbon atom covalently attached to two other carbon atoms (front and back) and two side hydrogen atoms. This extremely stable and non-polar structure is the reason behind the extraordinary mechanical properties and chemical inertness of the PE fibers. As a result, the interfacial bond of the PE fibers with the HSHDC matrix is largely frictional in nature (determined experimentally in Chapter 6), unlike PVA fibers in ECC which form chemical bond in addition to frictional bond. The plasma treatment of the PE fibers involves removal of the hydrogen atoms from the carbon chains, followed by their replacement with a desired polar or functional group to deliberately make the fiber surface chemically reactive and hydrophilic.

The plasma system used in this study is manufactured by AIRCO/Plasma Science (Model PS 300). It consists of a plasma chamber, in which the substrate (PE fibers) is placed before the start of the treatment. The chamber is depressurized using a vacuum pump to a desired initial pressure (of the order of 0.1 torr). Thereafter, a selected process gas is allowed to flow in the chamber at a controlled rate under an electromagnetic field applied using a radio-frequency power source, which breaks down the gas molecules into charged ions and free electrons. As these energetic species interact with the PE fibers, the hydrogen atoms are dislodged from the carbon-backbone of PE and the positive ions take their place creating a reactive fiber surface.

The energy involved in such plasma treatment is relatively low, and is insufficient to penetrate into the core of the fiber, which limits these modifications of the carbon chain to the surface of the fiber. The treatment time is typically only a few minutes, at the end of which the chamber is flushed with the same gas that is used for the plasma treatment to minimize any possible contamination as the chamber pressure is restored to the atmospheric pressure. The specimens, both composite and single-fiber, are cast as soon as possible after the treatment. Therefore, a number of parameters (type of gas, flow rate, power, and treatment time) can be controlled in a plasma treatment for achieving the desired surface modification of a given substrate.

Li and co-workers[23,24,25] performed a detailed investigation aimed at selecting the optimum parameters for plasma treatment of PE fibers to enhance the tensile behavior of ECC containing PE fibers (PEECC). That investigation was inspired by previous work[26,27,28,29,30] on enhancing the adhesion of PE fibers with polymer matrices using plasma treatment. Wu & Li[25] demonstrated that the plasma treatment of PE fibers not only enhanced the frictional bond (τ_0) but also the slip-hardening (β) behavior. In addition to increases in τ_0 and β, Wu & Li[25] observed, for the first time, the presence of chemical bond (G_d) in the PE fiber/cement interaction as a result of the plasma treatment.

Different gas plasmas uniquely influence the PE fiber/cementitious matrix interfacial bond. Wu & Li[25] observed that while the treatment of the PE fiber with Argon (Ar) plasma resulted in an increase in τ_0 and β, the treatment with oxygen (O_2) plasma predominantly caused an increase in G_d. The effects of ammonia (NH_3) plasma treatment were mixed, causing moderate increases in τ_0, β, and G_d. The influence of air plasma on the fiber/matrix interfacial

bond was similar to that of the O_2 plasma. A fixed flow rate of 58 mL/min and initial chamber pressure of 0.1 torr (for reference, atmospheric pressure at sea level is 760 torr) were used in all the investigations by Wu & Li.[25] Among the two power levels 100 W and 300 W investigated by Wu & Li,[25] superior interfacial properties were observed at 300 W as compared to 100 W. In addition, the high power plasma treatment caused the nature of the bond to be more chemical rather than frictional. Increase in chemical bond is more effective in reducing crack widths which is the objective of this study. Although these insights were obtained for the influence of plasma treatment on the interaction between the PE fibers and moderate strength cement paste (w/c = 0.30), they provide useful guidance for tailoring the interface between the PE fibers and HSHDC matrix (w/cm = 0.15) as well, as described below.

9.3.1.2 *Experimental Investigation*

The experimental investigation in this research involved single fiber pullout tests as well as composite tests under direct tension. The single fiber pullout tests (similar to that detailed in Chapter 6) were used to determine the optimum plasma treatment parameters for PE fibers embedded in the HSHDC matrix. The direct tension tests (similar to that detailed in Chapter 5) were performed on HSHDC dogbones to quantify the tensile performance advantages of the plasma treatment with optimum parameters at the composite scale.

In the first series of single fiber pullout tests of this study, three gases – Ar, NH_3, and O_2 were investigated at three treatment times. One of the three treatment times was taken to be the same as the optimum treatment time (OTT) determined by Wu & Li[25] for each gas, whereas the

other two times are chosen in the neighborhood of OTT to ascertain whether the OTT for maximizing the PE fiber/cement paste (w/c = 0.3) bond also maximizes the PE fiber/HSHDC matrix (w/cm = 0.15) bond. Thus, the treatment times explored in this study: for Ar gas were 2.5, 5 (OTT^{25}), and 7.5 minutes; for NH_3 gas were 0.5, 1 (OTT^{25}), and 1.5 minutes; and for O_2 gas were 7, 10 (OTT^{25}), and 13 minutes. In all the above plasma treatments, power level of 300 W was used with initial chamber pressure of 0.1 torr and gas flow rate of 58 mL/min (same as Wu & Li[25]).

Ten single fiber pullout specimens (straight fibers, $\phi = 0°$) with varying embedment lengths between 2 and 5 mm were prepared for each of the nine treatment procedures mentioned above (3 gases with 3 treatment times for each gas). The HSHDC curing procedure (Section 5.2.4) involving heat curing at 90°C for 8 days (5 days in water plus 3 days in air) was used for all the single fiber pullout specimens of the aforementioned first series.

As discussed in the results below, the relative increase in interfacial bond observed in this study was significantly lower than that observed by Wu & Li for the respective gas plasma treatments.[25] In order to ascertain whether the intense heat during HSHDC curing is the reason behind this observed discrepancy, a second series of single fiber pullout specimens (10 specimens per treatment procedure same as the first series) was prepared. In the second series, the PE fibers were treated with the three gases only for their respective optimum treatment times determined in the first series, thereby minimizing the experimental effort. Instead of the accelerated heat curing, these second series of single fiber pullout specimens were cured at room

temperature for 90 days (first 28 days under water and then in air) to achieve the same matrix compressive strength as the first series of specimens that underwent heat curing.

Four dogbone specimens and three 2″ cube specimens were prepared with the HSHDC matrix and PE fibers optimally treated (for respective OTT) by each gas, and cured under heat and at room temperature. The naming of the composite specimen sets is explained using an example: D-Ar-5-H, it implies that it is a Durable (D) HSHDC containing fibers treated by Argon (Ar) gas plasma for 5 minutes, and cured under accelerated heat (H) curing (R is used, instead of H, to denote room temperature curing).

9.3.1.3 *Results and Discussion*

The fiber/matrix interfacial bond properties deduced (using the analytical framework described in Chapter 6) from the results of the first series of single fiber pullout tests are summarized in Table 9.5. All gas plasmas enhance the PE fiber/HSHDC matrix interfacial bond to varying extents depending on the treatment time. The treatment time, t_2, is the OTT recommended by Wu & Li[25] for respective gas, whereas t_1 and t_3 are selected in the neighborhood of t_2 to further optimize the treatment time, if possible. The optimum combination of τ_0, β, and G_d for each gas is shown in bold in Table 9.5.

As observed by Wu & Li,[25] Ar gas plasma predominantly enhances τ_0 and β, O_2 gas plasma predominantly enhances G_d, and NH_3 gas plasma moderately enhances τ_0, β, and G_d. The maximum increases in τ_0 (from 1.52 MPa to 2.13 MPa) and β (from 0.003 to 0.089) are observed

when the PE fiber is treated with the Ar gas plasma for 5 minutes. The maximum increase in G_d (from 0 to 0.208 J/m^2) is observed with the treatment by O_2 gas plasma for 7.5 minutes. These increases in the fiber/matrix interfacial bond do not agree, in relative terms (treated/untreated), with that observed by Wu & Li[25]. For instance, the treatment with Ar gas plasma for 5 minutes results in an increase in τ_0 from 1.52 MPa to 2.13 MPa, which represents 40% increase ($\Delta\tau_0$ = 0.61 MPa) over the untreated value, whereas, Wu & Li observed τ_0 to increase from 0.51 MPa to 2.30 MPa (351% increase with $\Delta\tau_0$ = 1.79 MPa) with the same plasma treatment. Thus, while improvements in interfacial bond are observed in the first series of single fiber pullout specimens, their magnitudes are significantly lower than that observed in the prior research.[25]

Table 9.5: Interfacial bond properties observed in the first series of single fiber pullout specimens

	Frictional bond, τ_0 (MPa)			Slip-hardening, β			Chemical bond, G_d (J/m^2)		
Treatment times*	t_1	t_2	t_3	t_1	t_2	t_3	t_1	t_2	t_3
Untreated	1.52			0.003			0		
Ar	1.75	**2.13**	2.01	0.011	**0.089**	0.088	0.015	**0.021**	0.020
NH_3	1.66	1.75	**1.71**	0.005	0.004	**0.006**	0.069	0.080	**0.111**
O_2	**1.56**	1.60	1.50	**0.003**	0.002	0.003	**0.208**	0.200	0.182

* For Ar gas plasma, t_1 = 2.5 min; t_2 = 5 min; t_3 = 7.5 min
For NH_3 gas plasma, t_1 = 0.5 min; t_2 = 1 min; t_3 = 1.5 min
For O_2 gas plasma, t_1 = 7.5 min; t_2 = 10 min; t_3 = 12.5 min

In order to reconcile this discrepancy, the differences between the two experiments (this study and Wu & Li[25]) are scrutinized. The three major differences are: matrix (strength, density, and reactivity), PE fiber diameter, and curing procedure as discussed below.

The compressive strength of the matrix (cement paste with w/c = 0.3) used in Wu & Li is typically 30-50 MPa, whereas the HSHDC matrix has compressive strength greater than 150 MPa. As explained in Chapter 2, such high compressive strength is achieved, among other factors, through significantly denser microstructure and more reactive species within the HSHDC matrix compared to moderate strength matrices. However, these factors are not expected to reduce, if not improve, the effects of plasma treatment. The second difference is the PE fiber diameter, which is only 28 μm in HSHDC as compared to 38 μm used in Wu & Li.[25] Assuming that the plasma treatment only modifies the surface of the fiber (a few nanometers deep); this is also not expected to negatively influence the interfacial bond enhancements due to plasma treatment.

The third, and possibly the most significant, difference in this context is the curing procedure. While the HSHDC single fiber pullout specimens were cured under accelerated heat curing (including 8 days at 90°C), the specimens in Wu & Li[25] were cured at room temperature. Previous research[31] has shown deteriorating influence on the interfacial bond enhancements by the plasma treatment due to only one day of heat treatment at 80°C. According to Table III in Miller & Schwartz,[31] the interfacial shear strength of the PE fibers embedded in an epoxy resin post-heat treatment declines significantly, up to 50% for Ar gas plasma (the decrease is about 21% for O_2 gas plasma). Detachment and migration of the functional groups away from the fibers into the matrix under intense heat was concluded to be the underlying mechanism.[31] It is, therefore, hypothesized that the accelerated heat curing procedure adopted for the first series of HSHDC single fiber pullout specimens may have negatively influenced the interfacial bond enhancements.

In order to test this hypothesis, a second series of single fiber pullout specimens cured throughout at room temperature was prepared. These specimens of the second series were treated only for the optimum treatment times determined for each gas in the first series, which are 5 minutes for Ar, 1.5 minutes for NH_3, and 7.5 minutes for O_2 gas plasmas. The curing procedure consisted of 28 days water curing at room temperature, followed by air curing at room temperature until 90 days (after casting), at which time these specimens were tested.

The fiber/matrix interfacial bond properties deduced from the second series of single fiber pullout test results are summarized in Table 9.6. It is obvious from these results that all the second series of (no heat) specimens exhibit greater interfacial bond properties than the first series of (heat) specimens for the same plasma treatment. The interfacial bond enhancements also show better agreement with the increases observed in Wu & Li.[25] For instance, the treatment with Ar gas plasma for 5 minutes results in an increase in τ_0 from 1.52 MPa to 3.08 MPa (no heat), which represents $\Delta\tau_0$ of 1.56 MPa post-treatment, whereas, Wu & Li[25] observed τ_0 to increase from 0.51 MPa to 2.30 MPa ($\Delta\tau_0$ = 1.79 MPa) with the same plasma treatment. The results of the second series of the single fiber pullout tests, therefore, support the hypothesis that the accelerated heat curing is detrimental for interfacial bond enhancements achieved through plasma treatment; however, further research is needed to pinpoint the underlying mechanism behind such effect in HSHDC.

Table 9.6: Influence of heat curing on the interfacial bond properties

	Frictional bond, τ_0 (MPa)		Slip-hardening, β		Chemical bond, G_d (J/m^2)	
Untreated	1.52		0.003		0	
Curing	Heat	No Heat	Heat	No Heat	Heat	No Heat
Ar (5 min)	2.13	3.08	0.089	0.132	0.021	0.032
NH_3 (1.5 min)	1.71	2.54	0.006	0.009	0.111	0.166
O_2 (7.5 min)	1.56	2.25	0.003	0.004	0.208	0.273

The results of the composite uniaxial tensile and compressive tests on durable HSHDC specimens, along with the crack width observations, using the optimally treated fibers are summarized in Table 9.7. Only a slight increase in tensile strength of all the durable HSHDCs with plasma-treated fibers is observed. Considering the interfacial bond enhancements observed in the single fiber pullout tests and the fact that only a small fraction (about 10-15%) of PE fiber breakage is observed in HSHDC at the peak load (Chapter 6), a greater than observed increase in tensile strength (particularly for the room temperature-cured specimens) is expected.

Li et al[23] observed similar discrepancy between the expected and observed increase in the composite tensile strength due to the interfacial bond enhancement by plasma treatment. The most important reason behind this discrepancy, according to Li et al, may be the lack of uniformity and extent of plasma treatment of the bundled discontinuous fibers (used in composite specimens) compared to separated continuous fibers (used for single fiber pullout tests). The bundled discontinuous fibers may obstruct the treatment of the fibers within a bundle, even though only a small amount of fibers (10 g) was treated at one time. This possible inhomogeneity in plasma treatment of the discontinuous fibers is reflected by the high coefficients of variation of tensile strength of all durable HSHDCs investigated here.

The average crack widths (at peak load and residual) are reduced to some extent, particularly with NH_3 and O_2 gas plasmas that facilitate chemical bond formation of the PE fiber with the HSHDC matrix. Additionally, a greater elasticity in fiber bridging (difference between $\delta_{avg,u}$ and $\delta_{avg,r}$) is observed for D-NH_3 and D-O_2 specimens than D-Ar and HSHDC specimens. In spite of these changes in tensile strength and crack widths, the tensile ductility remains unaffected as the additional number of cracks formed due to larger tensile strength (while the first crack strength remains constant) compensate for the reduction in crack widths due to the plasma treatment of fibers.

Table 9.7: Mechanical performance of durable HSHDCs – plasma approach

Mix ID*	Compressive Strength, f_c' (MPa)	Tensile Strain Capacity, ε_{tu} (%) (COV)	Tensile Strength, σ_{tu} (MPa) (COV)	Avg. crack width at σ_{tu}, $\delta_{avg,u}$ (μm)	Avg. residual crack width $\delta_{avg,r}$ (μm)	Strength-ductility product, $f_c'.\varepsilon_{tu}$ (MPa)
HSHDC	166	3.4 (11%)	14.5 (6.2%)	180	160	5.64
D-Ar-5-H	162	3.2 (23%)	14.9 (7.7%)	190	165	5.18
D-Ar-5-R	152	3.6 (14%)	14.8 (9.5%)	180	160	5.47
D-NH_3-1.5-H	161	3.0 (27%)	13.7 (11%)	170	145	4.67
D-NH_3-1.5-R	155	3.2 (11%)	14.8 (8.4%)	175	155	4.96
D-O_2-7.5-H	169	3.9 (19%)	15.3 (10.1%)	175	140	6.59
D-O_2-7.5-R	156	3.4 (14%)	15.5 (6.9%)	165	135	5.30

* Naming scheme: 'D': durable HSHDC; gas molecular designation; treatment time (min); 'H' for heat curing and 'R' for room temperature curing – the heat cured specimens are tested at 17 days after casting, whereas the room temperature cured specimens are tested at 90 days after casting

The compressive strength of heat-cured durable HSHDC appears to be unaffected by the plasma treatment, as all the heat-cured specimens consistently exhibit compressive strengths between 160-170 MPa – same as that of HSHDC. However, the compressive strengths of room temperature-cured durable HSHDCs at 90 days are slightly smaller (by about 6% on average)

than that of the heat-cured durable HSHDCs, which may be caused by small changes in the nature of the cement-hydration products due to heat curing.

Overall, the plasma treatment of PE fibers partially achieves the objective of crack width reduction to some extent. However, heat curing and non-uniform plasma treatment of bundled fibers limit the effectiveness of plasma treatment in enhancing the mechanical performance of HSHDC.

9.3.2 Coupling Agent Approach

9.3.2.1 *Working Principle*

Addition of silane coupling agents[32] (henceforth, abbreviated as 'SCA') to the matrix for enhancing its bond with the PE fiber, thereby reducing crack widths, is explored as an alternative to the plasma treatment of fibers in this research. SCAs are typically used to form a durable bond between a siliceous inorganic material and an organic (typically polymer) material. For this purpose, an SCA has two functional groups to attach with both the materials. General structure of an SCA is shown in Figure 9.4. While the hydrolysable groups (X, typically alkoxy) attach to the siliceous material (e.g. calcium silicates in cement) after hydrolysis through siloxane linkages (Si–O–Si), the organofunctional group (R) attaches to the polymer (e.g. PE fiber). Thus, the SCAs can be used for bonding a variety of siliceous materials with various polymers by using appropriate functional groups R and X.

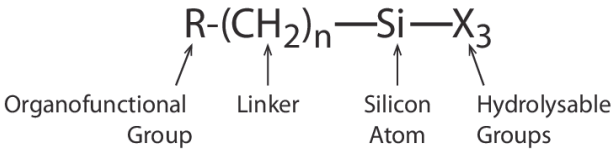

Figure 9.4: General structure of a silane coupling agent (SCA)[32]

9.3.2.2 *Experimental Investigation*

Two different SCAs are investigated in this study: amine-SCA and vinyl-SCA. Both SCAs are specifically recommended by the manufacturer (Gelest Inc.) for use with polyethylene.[32] The names 'amine' and 'vinyl' refer to the organofunctional group present in these two SCAs. The hydrolysable group (X) is a methoxy group in amine-SCA and an ethoxy group in vinyl-SCA.

Composite scale direct tensile and compressive tests were performed to determine the optimum dosages of the respective SCAs, and to select the more efficient SCA among the two (amine-SCA and vinyl-SCA) investigated in this study. Four dogbones and three 2″ cubes were cast for seven mixture compositions differing only by SCA type and dosage. The dosages of 0.5%, 1%, and 1.5% by cement weight were investigated for both SCAs in HSHDC. One additional mixture with amine-SCA dosage of 2% by cement weight was prepared to determine the best mechanical performance achievable with this SCA. During the fresh mix preparation, the SCAs are added at the very end (even after fibers) of the mixing procedure, as they tend to hydrolyze and withdraw water from the mixture, making it more difficult to continue the mixing process. All specimens were cured using the HSHDC curing procedure (with heat) and were tested at 17 days after casting. In addition to the composite specimens, two sets of 10 single fiber

pullout specimens were cast with the optimum dosages of each SCA to ascertain the corresponding interfacial bond enhancements for comparison with the plasma treatment.

9.3.2.3 *Results and Discussion*

The results of the composite tests are summarized in Table 9.8, in which the optimum mix proportion (with each SCA) and the corresponding mechanical performance and crack widths are highlighted in bold. Due to the enhanced fiber/matrix bond, the tensile strengths of the durable HSHDCs tend to increase with increasing dosage of both the SCAs, up to a maximum value followed by a plateau or a slight decline. The maximum tensile strength is achieved when the amine and vinyl-SCAs are used at dosages of 1.5% and 1.0%, respectively. Simultaneously, the crack widths almost monotonically reduce with increasing dosage of the SCAs. The least residual crack width observed in this study with vinyl-SCA dosage of 1.5% by cement weight is 105 μm, which is close to the objective of 100 μm. In spite of the reduction in crack width with increasing SCA dosage, the tensile strain capacity follows the trend of the tensile strength, as it reaches a maximum value of 3.9% for amine-SCA dosage of 1.5% and 4.6% for vinyl-SCA dosage of 1.0% by cement weight. The enhanced tensile strength of the composites with SCA, with the same first crack strength as HSHDC, increases the $PSH_{strength}$ (Sections 2.5 and 4.2), which improves multiple cracking and tensile ductility.

In addition to the enhancements in the tensile performance, the increasing dosage of SCAs causes significant increase in the compressive strength of durable HSHDCs as well. Maximum compressive strengths of 205 MPa (same as COR-TUF) and 174 MPa are achieved

with 1.0% dosage of vinyl-SCA and 1.5% dosage of amine-SCA. There may be two possible reasons behind this observation. First, as mentioned above, the SCAs undergo hydrolysis (and polymerization) as soon as they come in contact with the mix water during the mixing process (for this reason, SCAs are introduced at the very end of the mixing procedure). As no additional water is added, this effectively reduces the water content (w/c ratio) available for the cement hydration, which has a positive influence on the compressive strength. Second, the multiple wing cracks formed during the compressive loading may undergo greater stabilization due to enhanced fiber-bridging, which may delay the joining of the wing cracks and, therefore, enhance the compressive strength. Thus, withdrawal of mix water due to the hydrolysis of SCA, and wing crack stabilization due to better fiber-bridging are identified as the possible reasons behind the increase in compressive strength with the addition of SCAs.

The best performance overall is exhibited by the mix D-V-1.0%. With 205 MPa compressive strength, 4.6% tensile ductility, and only 110 μm residual crack width, this HSHDC shows the best mechanical and durability performance in this entire doctoral research. The tensile stress-strain curves of all four dogbones of this durable HSHDC are given in Figure 9.5.

Table 9.8: Mechanical performance of durable HSHDCs – coupling agent approach

Mix ID*	Compressive Strength, f_c' (MPa)	Tensile Strain Capacity, ε_{tu} (%) (COV)	Tensile Strength, σ_{tu} (MPa) (COV)	Avg. crack width at σ_{tu}, $\delta_{avg,u}$ (μm)	Avg. residual crack width $\delta_{avg,r}$ (μm)	Strength-ductility product, $f_c'.\varepsilon_{tu}$ (MPa)
HSHDC	166	3.4 (11%)	14.5 (6.2%)	180	160	5.64
D-A-0.5%	168	3.7 (10%)	14.3 (7.1%)	165	140	6.22
D-A-1.0%	165	3.7 (12%)	14.9 (6.5%)	170	150	6.11
D-A-1.5%	**174**	**3.9 (14%)**	**15.3 (4.8%)**	**150**	**125**	**6.79**
D-A-2.0%	172	3.2 (15%)	15.2 (9.1%)	155	125	5.50
D-V-0.5%	185	4.1 (8.9%)	15.3 (5.5%)	160	135	7.59
D-V-1.0%	**205**	**4.6 (19%)**	**16.1 (6.3%)**	**135**	**110**	**9.43**
D-V-1.5%	198	3.9 (18%)	15.8 (6.9%)	130	105	7.72

* Naming scheme: 'D': durable HSHDC; 'A' or 'V' for amine-SCA or vinyl-SCA; dosage by cement weight

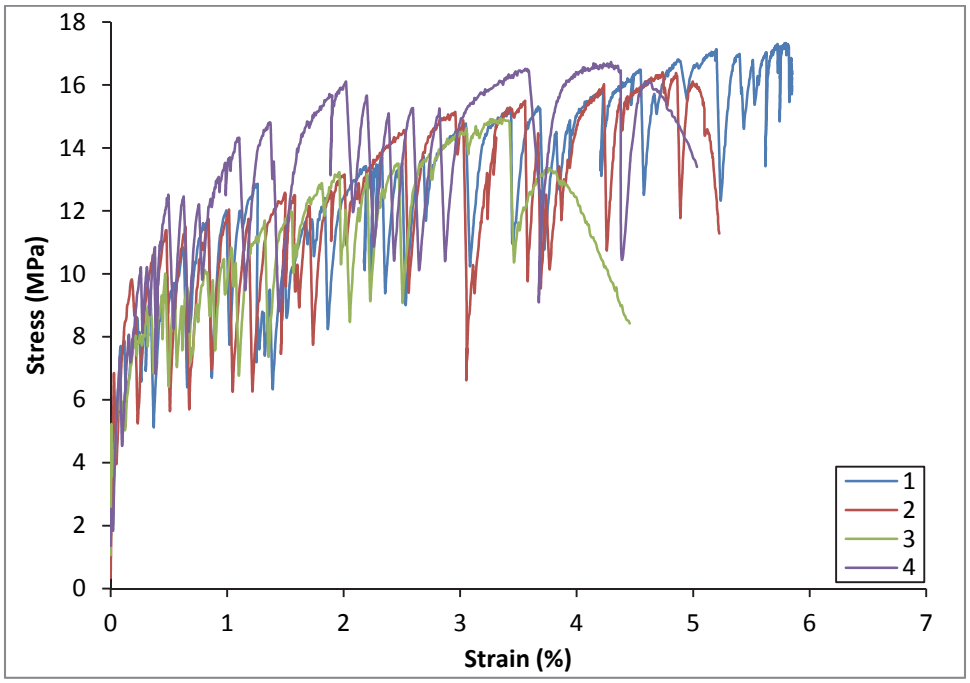

Figure 9.5: Tensile performance of durable HSHDC: D-V-1.0%

The results of the single fiber pullout tests on specimens with optimum dosages of the two SCAs are summarized in Table 9.9. The maximum increase in all the interfacial bond properties is obtained with vinyl-SCA at the dosage of 1.0% by cement weight. τ_0 increases by about 13%, and the G_d increases to 0.124 J/m^2 for the mixture D-V-1.0%. Among the two SCAs, the vinyl-SCA is more efficient causing greater increases in τ_0 and G_d with smaller dosage than amine-SCA. These increases in the interfacial bond properties with SCAs, although significant, are smaller than those observed with the plasma treatment of PE fibers (Table 9.6) and room temperature curing.

Table 9.9: Influence of silane coupling agents on the interfacial bond properties

	Frictional bond, τ_0 (MPa)	Slip-hardening, β	Chemical bond, G_d (J/m^2)
HSHDC	1.52	0.003	0
D-A-1.5%	1.65	0.011	0.085
D-V-1.0%	1.72	0.013	0.124

In order to compare the composite-scale performance gains from plasma treatment and coupling agents, the strength-ductility product (defined in Section 9.2.2) is plotted against the average residual crack width in Figure 9.6 for all the durable HSHDC mixtures investigated in this study (Tables 9.7 and 9.8). With respect to HSHDC, all the mixtures containing plasma treated fibers, except D-O_2-7.5-H (note that the first letter 'D' is dropped in Figure 9.6 to minimize clutter), exhibit a tradeoff between mechanical performance enhancements versus crack width reductions. On the other hand, all the mixtures containing the SCAs, except D-A-2.0%, exhibit agreement between the two objectives. This is in spite of the fact that the plasma treatment enhances the interfacial bond of an individual continuous fiber more effectively than

the SCAs. It is obvious from Figure 9.6 that the mixtures containing the SCAs not only exhibit smaller crack widths but also better mechanical performance as compared to the mixtures containing the plasma treated fibers, which may be caused due to the fact that the dispersion of the SCAs in the HSHDC matrix is more homogenous than the gas plasma on the bundled discontinuous PE fibers.

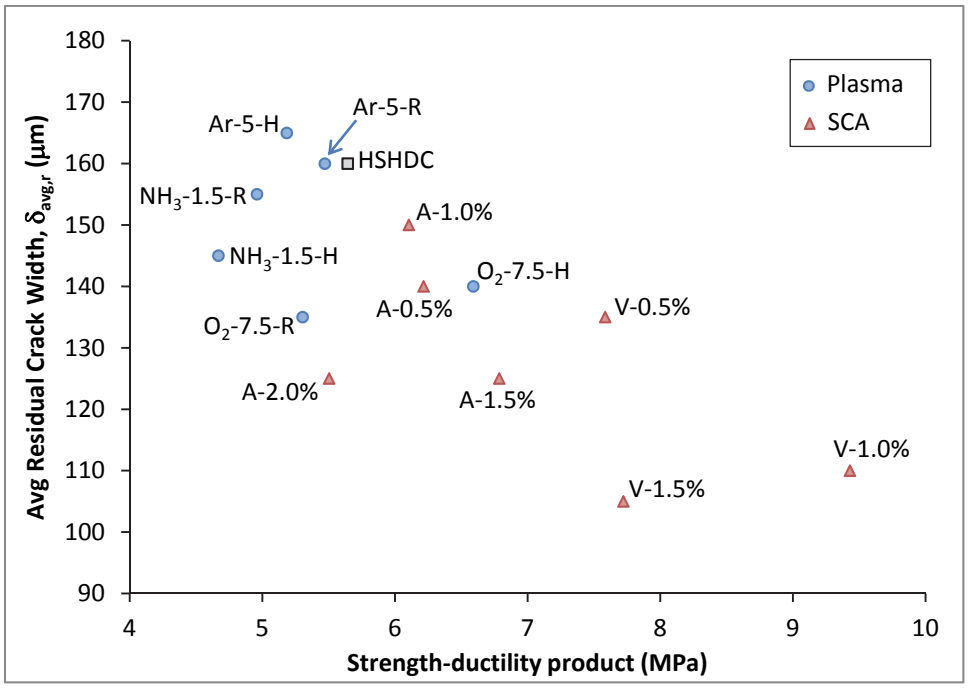

Figure 9.6: Crack width versus mechanical performance of durable HSHDCs
(The first letter 'D' is intentionally dropped from the names of all mixtures the shown in the figure to minimize clutter)

9.4 Environmental Life Cycle Assessment of an HSHDC Infrastructure Application

In Figures 9.1 and 9.2 above, it is observed that the material carbon and energy-MSIs of HSHDC are significantly greater than concrete and ECC; however, such materials perspective alone does not capture the durability, and resulting long-term environmental performance advantages, of HSHDC. The brittle fracture failure mode is eliminated in HSHDC, similar to ECC, and the crack widths are inherently constrained. Due to such behavior, the transport properties, and therefore long-term durability, of HSHDC are expected to be significantly superior to normal concrete. Additionally, the reductions in MSIs and crack widths achieved in green and durable versions of HSHDC above are further expected to enhance its life cycle performance. This section presents a life-cycle perspective of using HSHDC in an infrastructure application, comparing its performance with conventional infrastructure materials and ECC.

A bridge deck, which strategically utilizes a link-slab made of ductile materials such as HSHDC or ECC instead of conventional expansion joints, is chosen as an example infrastructure application in this research. A process-based comparative life cycle model for a bridge deck with link-slab and with a conventional expansion joint, developed by Keoleian et al,[33] is used for the life cycle assessment. The objective of this research is to comparatively investigate the environmental life cycle performances of bridge decks containing link-slabs made of HSHDC, ECC, and other green and durable HSHDCs developed above, and a bridge deck with conventional expansion joint.

9.4.1 Introduction to Life Cycle Assessment (LCA) and Bridge Deck Model

Life Cycle Assessment (LCA) is a framework designed to evaluate the environmental performance of a product or a process throughout its life cycle. In general, life cycle assessment consists of four phases, viz. raw material acquisition, production, use, and end-of-life, along with the transportation involved between every phase (ISO 14040: 2006[34]). LCA of a product entails four basic steps:

1. *Definition of the goal and scope of the assessment*: This step involves defining the functional unit, system boundaries, and relevant data required.
2. *Inventory analysis*: A cumulative audit of inputs (materials and energy) and outputs (wastes and emissions) at every phase of the product's life cycle is performed in this step.
3. *Impact assessment*: This step translates the results of inventory analysis into environmental impact in terms of its magnitude and significance.
4. *Interpretation*: The results of the inventory analysis and/or impact assessment are analyzed in this step and are used to draw conclusions and recommendations for sustainability. For example, comparison of multiple products or processes (with the same function) in terms of their environmental impacts, identification of the most significant phase with maximum impact among various phases of a product's life cycle, etc.

Bridge decks are chosen as an example infrastructure application for investigating the life cycle performance of HSHDC using the above framework, as it effectively utilizes HSHDC's durability. A majority of highway bridges within the United States are composed of multiple

span steel or prestressed concrete girders which are simply supported at piers or bents. These girders support cast-in-place concrete decks to form a composite bridge deck system. Mechanical expansion joints are typically installed at the end of these simple span decks to allow for deck deformations imposed by deflection, concrete shrinkage, and temperature variations. The mechanical expansion joints in bridge decks are expensive to install and maintain, while deterioration of joint performance leads to severe damage of the bridge deck, beam end, and substructure.[35] The durability of beam ends, girder bearings, and supporting structures can be compromised by water leaking and the flow of deicing chemicals through the joints.

A possible approach to alleviate this durability problem is to replace the mechanical deck joints in multi-span bridges by link-slabs made of ductile concretes such as HSHDC.[36] A link-slab is the section of the deck connecting the two adjacent simple-span girders, instead of the mechanical joint. Due to their extremely ductile tensile behavior with controlled crack widths, ductile concretes are ideal for link-slabs.

Keoleian et al[33] developed a life cycle model for comparing the environmental sustainability of bridge decks containing either a link-slab made of ECC or a conventional expansion joint. The unique features of this process-based life cycle model are: (1) ability to capture the influence of material durability on the structure's environmental performance, and (2) explicit inclusion of the use-phase (traffic) environmental impact. Both these features of Keoleian et al's model are necessary to comprehensively evaluate the impact of material choices on the environmental life cycle performance of the bridge deck.

Keoleian et al[33] modeled the deck of the Grove Street Bridge in Ypsilanti, MI, constructed (in 1972) and maintained by the Michigan Department of Transportation (MDoT). An ECC link-slab replaced the corroded steel expansion joint in this bridge deck in 2005. Although this model by Keoleian et al[33] only accounted for the remainder of the bridge's service life (another 60 years), Kendall[38] expanded the model for the entire 90 year service life of the bridge. This 90 year life cycle model is used in this study. The Grove street bridge deck (functional unit for this LCA) is 0.1 mile (160 m) long, four lanes wide, and 9″ deep resting on steel girders supported by a steel reinforced substructure. The bridge is estimated to have a constant traffic flow rate of 35,000 cars/day in each direction. A schematic sketch of the bridge deck showing the location of the link slab/expansion joint is given in Figure 9.7. The details of the structural design of the bridge deck and, particularly, the link slab are presented in Li et al.[37]

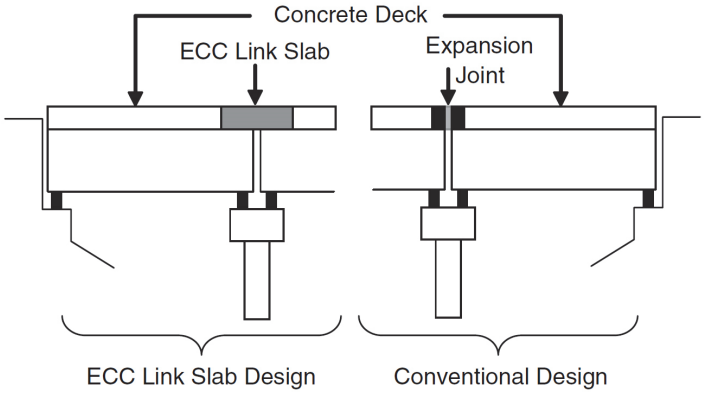

Figure 9.7: Bridge deck system definition (after Kendall[38])

According to Keoleian et al,[33] for the purpose of inventory analysis (accounting total inputs and outputs of materials and energy), the life cycle of the bridge deck can be divided into four main phases, plus distribution, which are shown in Figure 9.8, and explained below.

Materials: The materials phase includes the production and processing of all the construction materials (concrete, ECC/HSHDC, steel). A variety of material data sets, detailed in Table 1 of Keoleian et al,[33] are used for inventory accounting of this phase. Many of these data sets are referred for determining the carbon and energy intensities of the material ingredients of HSHDC, as shown in Table 9.1.

Construction: All the construction-related inputs and outputs, including equipment use and construction-related traffic congestion, are grouped together in the construction phase. This phase includes the initial construction as well as maintenance and repair. US EPA's NONROAD[39] model is used for accounting the emissions from construction equipment. An integrated structures-materials deterioration model, which is discussed below, is used to determine the maintenance schedule. Although, the traffic congestion due to the construction activities comes under the construction phase in Figure 9.8, it is represented separately as 'traffic' in the LCA results and discussion below due to its significance. The 'traffic' phase only accounts for the difference between the traffic flow during construction and that during normal highway conditions. Traffic delay estimates are modeled using the KyUCP model,[40] and the vehicular emissions are modeled using the US EPA's MOBILE6.2[41] software.

Use: The use phase inventory includes the fuel consumption and emissions for the vehicles using this bridge over the entire service life of 90 years, excluding the time when the bridge is under maintenance (as that is included in the construction phase). According to Keoleian et al,[33] the impacts of the use phase are so large that they obscure the energy use and emissions from other phases. Additionally, the model predicts no difference between the use

phases of the bridge deck whether it uses a link-slab or a conventional expansion joint. Therefore, the use phase is not considered in this comparative life cycle analysis.

End-of-life: The LCA model assumes all cementitious materials are landfilled with zero recycling. However, 20% of steel is assumed to have been recycled.[33]

Distribution: This phase mainly includes the transportation of materials and equipment back and forth from the bridge site.[33]

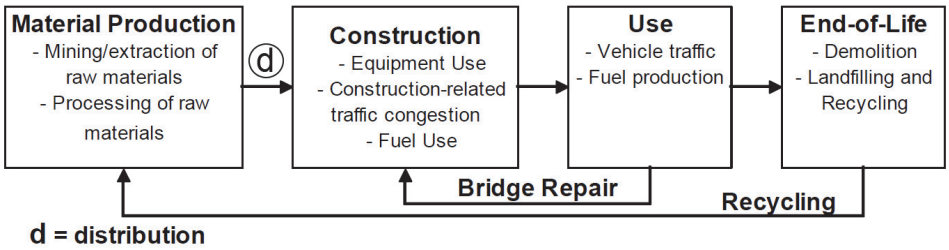

Figure 9.8: Life cycle of a bridge deck[33]

The bridge deck LCA model uses a maintenance schedule to estimate the inputs and outputs of energy and emissions during maintenance of the bridge. While the MDoT's regular maintenance schedule is used for modeling the bridge deck with the conventional expansion joint, the maintenance schedule based on an integrated structures-materials deterioration model developed by Lepech[42] is used for modeling bridge deck with link-slabs.

Lepech's deterioration model[42] couples the component/material deterioration of the link-slab with the structural deterioration (for the rest of the structure) model for jointless bridges.

According to Lepech,[42] the link-slab service life is governed by the serviceability limit state (rather than ultimate limit state), which in turn is reached mainly due to chloride ion diffusion (particularly, in Michigan bridge decks) and resulting corrosion of the rebars. Lepech[42] extended the work of Liu & Weyers[43] and Thoft-Christensen,[44] on estimating the corrosion time of reinforced concrete, for predicting the corrosion time, and service life, of ECC link-slab. This link-slab deterioration model is combined with the structural deterioration model of jointless bridge decks[45] to determine the complete maintenance schedule of the bridge deck with link-slabs, which is calculated for HSHDC along with other model parameters in the next section.

9.4.2 Model Parameters

Kendall[38] developed a software (in spreadsheet) that implements the LCA methodology developed in Keoleian et al[33] for comparing various material choices, and it is used in this study for comparing the life cycle performances of hypothetical bridge decks containing link-slabs made of various HSHDC versions developed above. The material-dependent inputs required for this software are: (1) material and energy intensities of various ingredients of HSHDC, and (2) maintenance schedule for each material based on the service life of the link-slab made with each HSHDC. While the material and energy intensities of HSHDC ingredients are given in Table 9.1, the maintenance schedule for each HSHDC is determined below.

The corrosion of rebars in reinforced cementitious materials is commonly classified into two broad phases: initiation (or pre-depassivation) phase and propagation (post-depassivation) phase. Due to high alkalinity of the hydrated cementitious matrix, a passive oxide layer is formed

around the steel rebars within a few days after placement, which prevents the rebar corrosion. However, as the chloride ions penetrate and build up around the rebar over time, this passive oxide layer is destroyed (or depassivated) and the corrosion of the rebar initiates. This time that marks the initiation of rebar corrosion demarcates the initiation and propagation phases. As the rust begins to build up around the rebar, a tensile pressure is exerted on the surrounding cementitious 'matrix' because of the larger volume of the products of the chemical reaction as compared to the reactants. While such tensile stress causes cracking in concrete, which soon leads to spalling and loss of concrete cover, ductile materials such as HSHDC and ECC diffuse the expansive displacement demand into multiple micro-cracking and maintain the integrity of the cover, thereby substantially extending the propagation time and service life of the reinforced link-slab.

The initiation time is computed from the Fick's law of diffusion in Eq. 9.1. Here C is the chloride ion concentration (as % weight of the cement/concrete), which is a function of distance, x, from the exposed concrete cover surface, and time, t. D_c is the diffusion coefficient. D_c for uncracked UHPC with compressive strength of about 150 MPa is 1.3 x 10^{-13} m^2/s at 28 days,[46] which is an order of magnitude smaller than uncracked ECC. This is because of the significantly denser microstructure of UHPC compared to ECC. D_c for uncracked HSHDC is assumed to be equal to uncracked UHPC. However, cracks are expected to occur at early age due to restrained shrinkage and high cement content in HSHDC. Therefore, D_c in the cracked state is computed for HSHDC, as explained below, for computing the initiation (depassivation) time.

$$\frac{dC(x,t)}{dt} = D_c \frac{d^2C(x,t)}{dx^2} \tag{9.1}$$

The chloride ion diffusion coefficient, D_c, of HSHDC in the cracked state is estimated using the methodology described in Li et al.[47] A tensile strain due to shrinkage is assumed equal to 0.3%, which is significantly higher than that expected in the field.[48] At this strain, the average tensile stress in HSHDC is about 10 MPa (Figure 5.6). Using the σ-δ relation of HSHDC (Figure 6.25), the corresponding crack width at 10 MPa is almost half that at 14.5 MPa (ultimate tensile strength). Hence, due to shrinkage, average crack width of HSHDC is estimated to be about 90 μm (180/2 μm – as the average crack width in HSHDC at ultimate tensile strength is 180 μm). The diffusion coefficient is estimated for this crack width, assuming quadratic variation of D_c with the crack width (δ) observed by Sahmaran et al.[17] Eq. 9.2 is used to estimate D_c (m^2/s) for various HSHDCs depending on their estimated crack widths (δ in meters). This expression assumes the same rate of increase in D_c with crack width as experimentally determined by Sahmaran et al;[17] however, the D_c for zero crack width (δ = 0) is set equal to the uncracked D_c for UHPC mentioned above.

$$D_c = 1.3\times10^{-13} + 0.0012\left(\delta^2\right) \tag{9.2}$$

The computed value of D_c for each material is used in the Fick's law (Eq. 9.1) to compute the initiation time. This computation is performed using the Life-365 software,[49] which numerically solves the differential equation (9.1) to determine the initiation time for each material, which is given in Table 9.10.

Lepech's deterioration model[42] for predicting the service life of ECC link-slabs post-depassivation (after initiation time) is used to predict the propagation time of HSHDC link-slabs,

which, along with the initiation time, estimates the total service life of the link-slab. In Lepech's model (Figure 9.9), the post-depassivation service life of the link-slab is only a function of ECC's strain capacity. Lepech's model is applicable for any ductile material, and it is used in this study to determine the post-depassivation service life of the HSHDC link-slab based on its strain capacity – the results are shown in Table 9.10.

Table 9.10: Service life estimation of HSHDC link-slabs

Material	Crack Width at σ_{ult} (μm)	Crack Width at 0.3% strain (μm)	D_c (10^{-12} m^2/s)	Initiation Time (years)	Tensile Strain Capacity (%)	Propagation Time (years)	Total Service Life (years)
ECC-M45	60	40	2.05	25.3	4.0	96.3	121.6
HSHDC	180	90	9.85	6.6	3.4	70.4	77.0
G-F-15	190	95	10.96	6.1	3.6	78.6	84.7
G-F-25	185	93	10.40	6.0	3.1	58.9	64.9
G-S-15	170	85	8.80	7.2	3.1	58.9	66.1
G-S-25	170	85	8.80	7.2	3.7	82.8	90.0
G-M-15	160	80	7.81	7.8	3.0	55.4	63.2
D-Ar-5-H	190	95	10.96	6.1	3.2	62.6	68.7
D-Ar-5-R	180	90	9.85	6.6	3.6	78.6	85.2
D-NH_3-1.5-H	170	85	8.80	7.2	3.0	55.4	62.6
D-NH_3-1.5-R	175	88	9.32	6.8	3.2	62.6	69.4
D-O_2-7.5-H	175	88	9.32	6.8	3.9	91.7	98.5
D-O_2-7.5-R	165	83	8.30	7.5	3.4	70.4	77.9
D-A-0.5%	165	83	8.30	7.5	3.7	82.8	90.3
D-A-1.0%	170	85	8.80	7.2	3.7	82.8	90.0
D-A-1.5%	150	75	6.88	8.6	3.9	91.7	100.3
D-A-2.0%	155	78	7.34	8.2	3.2	62.6	70.8
D-V-0.5%	160	80	7.81	7.8	4.1	101.0	108.8
D-V-1.0%	135	68	5.60	10.1	4.6	126.3	136.4
D-V-1.5%	130	65	5.20	10.7	3.9	91.7	102.4

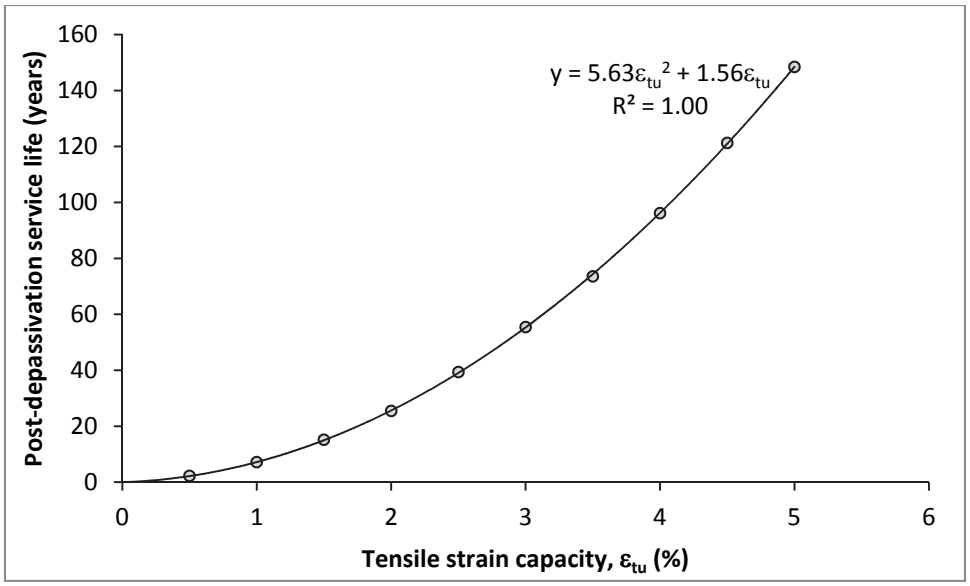

Figure 9.9: Lepech's post-depassivation service life estimation model[42]

As shown by Lepech,[42] the jointless bridge deck maintenance schedule is updated with the additional construction event of link-slab replacement at the end of the service life of the link-slab. For instance, HSHDC link-slab has a total estimated life of 77 years; at which time, it is replaced as shown in the maintenance timeline (Figure 9.10). In order to save construction costs, the agency may opt to replace the link-slab at the 70-year patch repair event (Figure 9.10). Such consolidation of maintenance events can reduce the environmental impacts of link-slab replacement; however, in this study, link-slab replacement is considered as a separate maintenance event.

Overall, while the influence of crack width of strain hardening concretes is captured in the corrosion initiation phase, the influence of their tensile ductility is captured in the propagation phase – both of which are included in the total service life and maintenance schedule of the link-slab. Using the carbon and energy intensities of individual materials, along with their

maintenance timelines, as inputs into Kendall's numerical model,[38] the life cycle assessment is performed for the bridge deck over its 90 year service life, and the results are discussed in the next section.

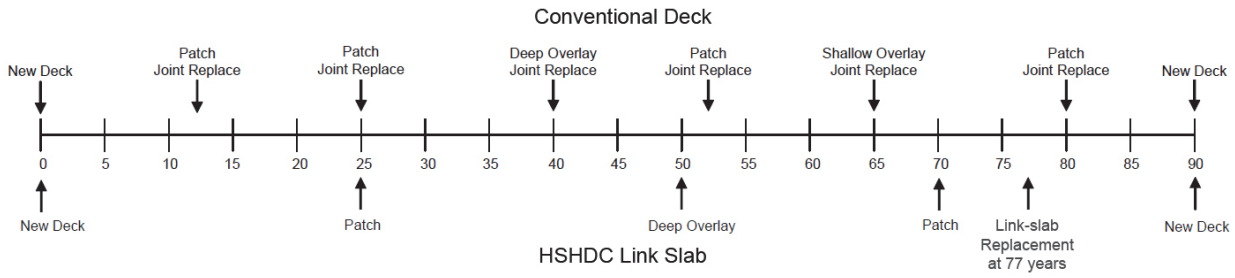

Figure 9.10: Maintenance schedules of bridge decks with conventional expansion joints and HSHDC link-slabs

9.4.3 Results of LCA and Discussion

The results of the LCA (inventory) are shown in Figure 9.11 (CO_2 emissions) and Figure 9.12 (primary energy). Although the LCA model by Kendall[38] generates a number of other environmental performance indicators, this discussion is limited to the two most commonly reported indicators: CO_2 emissions and primary energy. The results of the bridge decks LCA with conventional expansion joint and ECC link-slab resemble the results presented in Kendall,[38] and form the upper and lower bounds for both indicators in this discussion. Both the indicators for the ECC link-slab deck are about 40% less than the deck with the conventional expansion joint. This is mainly due to significantly reduced frequency (almost half) of maintenance events for durable ECC link-slabs compared to the steel expansion joints, causing less frequent construction-related traffic congestion, which is the phase with the most dominant influence on the life cycle performance of the bridge deck (Figures 9.11 and 9.12).

The life cycle CO_2 emissions and primary energy of the HSHDC link-slab deck are estimated to be about 16% greater than ECC. Unlike ECC link-slab with an estimated service life greater than 90 years, the HSHDC link-slab has a predicted service life of 77 years (< 90 years), and therefore, needs a replacement before the end of the bridge deck's service life. The 16% difference between the environmental performance of decks with HSHDC and ECC link-slabs is mainly due to the traffic congestion during this additional maintenance event. In spite of significantly higher MSIs of HSHDC compared to ECC and additional link-slab construction, the materials phase contribution (to the life cycle performance indicators) of HSHDC is only slightly (1.4%) greater than ECC as the link-slab only constitutes a small volume of the entire bridge deck. As a result, the HSHDC link-slab deck is about 30% superior to the conventional system over the service life of 90 years in terms of both total CO_2 emissions and primary energy.

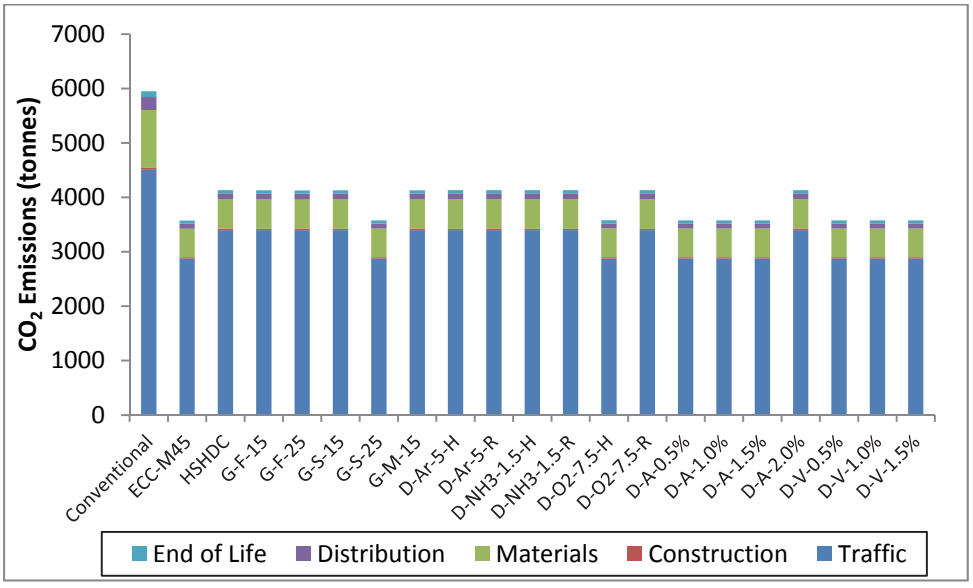

Figure 9.11: CO_2 emissions over 90 years' service life of the bridge deck

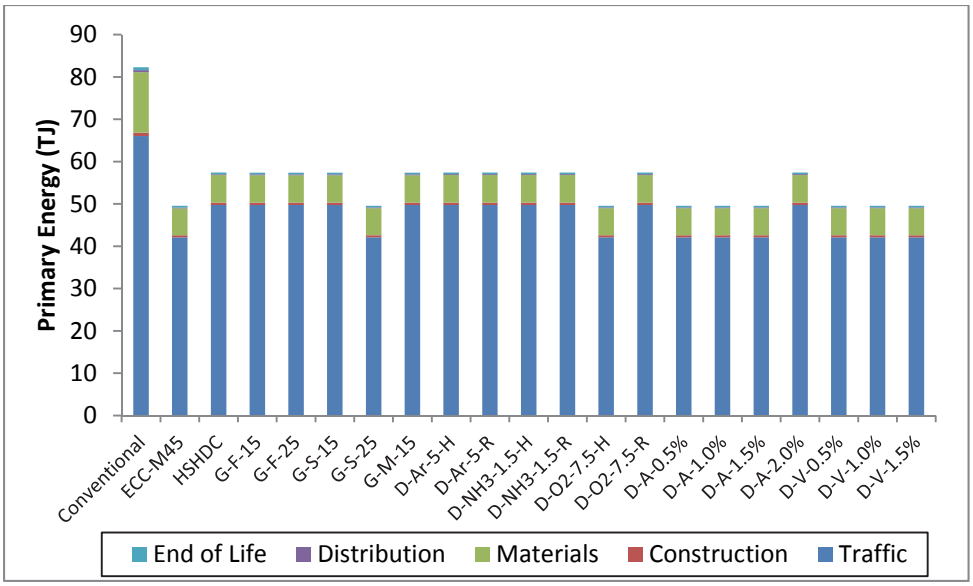

Figure 9.12: Primary energy consumption over 90 years' service life of the bridge deck

In spite of lower MSIs of green HSHDCs compared to HSHDC, the bridge deck link-slabs made with all the green HSHDCs, except G-S-25, are estimated to have approximately the same life cycle performance as the deck with HSHDC link-slab. This observation is due to relatively low significance of the materials phase in the life cycle of the bridge deck, and the fact that all these green HSHDCs are highly ductile and durable (as minimum tensile ductility was set at 3% for developing green HSHDCs), which results in the same number of maintenance events as HSHDC.

The exception is the deck with G-S-25 link-slab, which has lower life cycle environmental impacts than the deck with HSHDC link-slab (G-S-25 has almost the same life cycle performance as the deck with ECC link-slab). This is because the average tensile ductility of G-S-25 (3.7%) is greater than HSHDC (3.4%), which results in a longer post-depassivation service life (propagation time), extending the total service life of the link-slab beyond 90 years.

The longer service life of the G-S-25 link-slab (greater than the bridge deck's service life) makes the link-slab replacement event unnecessary, thereby saving the associated environment impacts (mainly traffic congestion-related).

Almost half of the durable HSHDCs, particularly the mixtures containing plasma treated fibers, performed environmentally at almost the same level as HSHDC, whereas the remaining half (mixtures containing coupling agents) are estimated to exhibit lower environmental impact indicators (almost same as ECC) in the link-slab application. The durable HSHDCs that exhibit lower environmental impacts achieve such performance mainly due to enhanced tensile ductility. These durable HSHDCs have significantly reduced crack widths as well. However, the increase in the initiation time caused by crack width reduction is relatively marginal compared to the gains in post-depassivation service life achieved by enhancing tensile ductility. For instance, consider the mixtures HSHDC and D-V-1.5% in Table 9.10. While the 27% reduction in crack width from 90 μm in HSHDC to 65 μm in D-V-1.5% causes the initiation time to increase by about 4 years (from 6.6 to 10.7 years), only a 14% increase in tensile ductility (from 3.4% to 3.9%) causes the propagation time to increase by about 20 years. Thus, reduction in crack width of HSHDC (or similar strain hardening concretes) should be pursued as an objective for environmental material design (for link-slab application) only if it also enhances (or at least maintains) tensile ductility.

For material design, the tensile ductility targets, for a particular material crack width and structural service life, can be determined from this analysis. For instance, assuming the crack width in HSHDC of 90 μm, which provides an initiation time of 6.6 years, the minimum tensile

ductility (from Figure 9.9) for ensuring full 90 year service life of the link-slab requiring no replacement in-between is 3.7% (by solving $5.63\varepsilon_{tu}^2 + 1.56\varepsilon_{tu} = 90 - 6.6$).

9.5 Conclusions

The feasibility of developing greener and more durable HSHDCs, while preserving and even improving the mechanical performance (both compressive strength and tensile ductility), is demonstrated in this chapter. While the research on green HSHDC development adds to the very limited knowledge on greening concretes with similar compressive strengths (UHPCs), the systematic interfacial tailoring of the fiber/matrix bond proves the effectiveness of the micromechanics-based approach for developing durable HSHDCs with significantly reduced crack widths. The life cycle assessment of an example HSHDC infrastructure application (bridge deck link-slabs) provides mechanical property targets and framework for continued material development aimed at enhancing infrastructure sustainability. Specific conclusions are given below.

- Among the three recycled material substitutes for cement investigated in this study: fly ash, slag, and silica fume, slag's influence on the mechanical properties of green HSHDC is the most favorable at all replacement levels. Although cement substitution with fly ash enhances mix homogeneity, thereby reducing the variability in mechanical properties, it causes reduction in compressive strength. Cement substitution with silica fume negatively influences all the mechanical properties due to high water demand and poor mix rheology. The optimum

combination of mechanical performance and reduction in MSI is achieved with grade 120 slag replacing 25% by weight of class H cement in HSHDC. This cement substitution by slag caused 23% decrease in CO_2 emissions and 15% decrease in primary energy associated with unit volume of HSHDC, while simultaneously causing a slight increase in both tensile ductility (3.7%, as compared to 3.4% of HSHDC) and compressive strength (177 MPa, as compared to 166 MPa of HSHDC).

- Plasma treatment of continuous (uncut) PE fibers can significantly increase the PE fiber/matrix interfacial bond; however, uneven distribution of plasma treatment in discontinuous fibers and heat curing of composite specimens limit the effectiveness of plasma treatment for reducing crack widths in HSHDC, while enhancing (or maintaining) the mechanical properties. While the O_2 gas plasma most effectively enhances the chemical bond, Ar gar plasma is the most effective for enhancing the frictional bond and slip-hardening behavior. The largest reduction in residual crack width (from 160 μm of HSHDC to 135 μm) is observed in the HSHDC cured at room temperature for 90 days containing PE fibers treated with the O_2 gas plasma for 7.5 minutes.

- Small dosages (< 2% by cement weight) of silane coupling agents can effectively enhance the PE fiber/matrix bond (although less than plasma treatment for a continuous fiber) and cause reduction of the composite crack width under tension. In addition to crack width reduction, the silane coupling agents also improve the ultimate tensile strength, tensile ductility, and compressive strength of HSHDC. These improvements in mechanical performance are likely caused by more effective fiber bridging due to enhanced fiber/matrix bond (and high fiber

strength, which prevents fiber breakage). Another factor increasing compressive strength may be the reduction in w/c ratio caused by the hydrolysis of the coupling agents upon mixing with the rest of the ingredients.

- Among the two silane coupling agents (amine and vinyl-silanes) investigated in this study, vinyl-silane seems to be more effective for enhancing fiber/matrix bond, reducing crack width, and improving mechanical properties. The best composite performance is exhibited by the HSHDC containing vinyl-silane dosage of 1% by cement weight achieving compressive strength of 205 MPa, tensile ductility of 4.6%, and residual crack width of 110 μm.

- From the comparative life cycle assessment of bridge decks over their service life of 90 years, it is estimated that the bridge deck containing HSHDC link-slab application will have about 30% lower environmental impacts (CO_2 emissions and primary energy) than the deck containing conventional expansion joint. This is mainly due to considerably less frequent repairs needed for bridge deck with durable HSHDC link-slab (with controlled crack width and strain capacity) than the bridge deck with the conventional expansion joint. The dominant phase in the life cycle of the bridge decks is the construction-related traffic congestion, which accounts for about 75-85% of the total life cycle impacts.

- In spite of lower life cycle environmental impact than the conventional system, the bridge deck with the HSHDC link-slab has greater environmental impact than the bridge deck with ECC link-slab. This is mainly due to an additional link-slab replacement event needed for HSHDC link-slab due to its lower service life (of 77 years, which is less than the bridge deck's service life of 90 years) than the ECC link-slab (which has service life greater than 90 years).

- From the LCA comparison of HSHDC link-slab with its greener and more durable versions developed in this study, it is concluded that reduction in crack width of HSHDC (or similar strain hardening concretes) should be pursued as an objective for environmental material design (for link-slab application) only if it also enhances (or at least maintains) tensile ductility. This is because increase in the corrosion initiation time caused by crack width reduction is relatively marginal compared to the gains in propagation time achieved by enhancing tensile ductility.

References

1. Li, V. C., Lepech, M., Wang, S., Weimann, M. & Keoleian, G. (2004) "Development of Green ECC for Sustainable Infrastructure System" In Proceedings of *International Workshop on Sustainable Development and Concrete Technology*, Iowa State University, Ames, IA, pp. 181-92.

2. Marceau, M. L., Nisbet, M. A. & VanGeem, M. G. (2006) "Life Cycle Inventory of Portland Cement Manufacture" Portland Cement Association, Skokie, IL, pp. 10,16.

3. WBSCD (2011) "Cement Industry Energy and CO2 Performance" World Business Council for Sustainable Development - Cement Sustainability Initiative, pp. 14-16.

4. Marceau, M. L. & VanGeem, M. G. (2003) "Life cycle inventory of slag manufacturing process" Construction Technology Laboratories (CTL) Project No. 312012, Slag Association, Skokie, IL.

5. Ecobilan-PricewaterhouseCoopers (2001) "TEAM/DEAM databases" Ecobilan, Rockville, MD.

6. US EPA (2008) "National Mobile Inventory Model" United States Environmental Protection Agency, Washington, DC.

7. Marceau, M. L., Nisbet, M. A. & VanGeem, M. G. (2007) "Life cycle inventory of Portland cement concrete" Report No. 3011, Portland Cement Association, Skokie, IL.

8. Bousted, I. (2005) "Acrylonitrile" In *Eco-Profiles for the European Plastics Industry*, Association of European Plastic Manufacturers, Brussels, Belgium.

9. Keoleian, G., Miller, S., De-Kleine, R, Fang, A. & Mosley, J. (2012) "Life Cycle Material Data Update for GREET Model" Center for Sustainable Systems, Report #CSS-12-12, University of Michigan, Ann Arbor.

10. Frazão, R. & Fernandes R. (2004) "Comparative Analysis of the Life Cycle of AT Fibre-cement and NT Fibre-cement" Report by Central University of Venezuela prepared for Cimianto, Sociedade Técnica de Hidráulica, S.A., pp. 8.

11. Stengel, T. & Schiebl, P. (2009) "Life Cycle Assessment of UHPC Bridge Construction" Journal of Architecture, Civil Engineering, and Environment (ACEE), 1, 109-18.

12. EIA (2011) "Annual Energy Review 2010" Washington, DC: Energy Information Administration, US Department of Energy.

13. Bousted, I. (2005) "Polyurethane Flexible Foam" In *Eco-Profiles for the European Plastics Industry*, Association of European Plastic Manufacturers, Brussels, Belgium.

14. ACI Committee 318 (1999) "Building Code Requirements for Structural Concrete and Commentary" Farmington Hills, MI: American Concrete Institute, pp. 114.

15. AASHTO (2012) "LRFD Bridge Design Specifications" Washington, DC: American Association of State Highway Officials, pp. 5-45.

16. Lepech, M.D. & Li, V.C. (2009) "Water Permeability of Engineered Cementitious Composites" *Cement and Concrete Composites*, 31(10), 744-53.

17. Sahmaran, M., Li, M. & Li, V.C. (2007) "Transport Properties of Engineered Cementitious Composites under Chloride Exposure" *ACI Materials Journal*, 104(6), 604-11.

18. Kendall, A., Keoleian, G.A. & Lepech, M.D. (2008) "Materials Design for Sustainability through Life Cycle Modeling of Engineered Cementitious Composites" *Materials and Structures*, 41(6), 1117-1131.

19. Kendall, A., Keoleian, G.A. & Helfand, G.E. (2008) "Integrated Life-Cycle Assessment and Life-Cycle Cost Analysis Model for Concrete Bridge Deck Applications" *Journal of Infrastructure Systems*, 14(3), 214-22.

20. ASTM C618 (2012) "Standard Specification for Coal Fly Ash and Raw or Calcined Natural Pozzolan for Use in Concrete" West Conshohocken, PA: American Society for Testing and Materials.

21. ASTM C989 (2012) "Standard Specification for Slag for Use in Concrete and Mortars" West Conshohocken, PA: American Society for Testing and Materials.

22. Bergman, B. (2012) "ASTM C618 / AASHTO M295 Testing of DTE Monroe Fly Ash" Taylorsville, Georgia: Materials Testing and Research Facility.

23. Li, V.C., Wu, H.C. & Chan, Y.W. (1996) "Effect of Plasma Treatment of Polyethylene Fibers on Interface and Cementitious Composite Properties" Journal of American Ceramic Society, 79(3), 700-04.

24. Wu, H.C. & Li, V.C. (1997) "Basic Interfacial Characteristic of Polyethylene Fiber/Cement Composites and its Modification by Plasma" In Proceedings of *5th International Symposium on Brittle Matrix Composites*, Warsaw, Poland, Oct 13-15, 1997, pp.14-23.

25. Wu, H.C. & Li, V.C. (1999) "Fiber/cement interface tailoring with plasma treatment" *Cement and Concrete Composites*, 21(3), 205-12.

26. Kaplan, S.L., Rose, P.W., Nguyen, H.X. & Chang, H.W. (1988) "Gas Plasma Treatment of Spectra Fiber" *SAMPE Quarterly*, 19(4), 55-59.

27. Hild, D.N. & Schwartz, P. (1992) "Plasma Treated Ultra-High Strength Polyethylene Fibers Part 1: Characterization by Electron Spectroscopy for Chemical Analysis" *Journal of Adhesion Science and Technology*, 6, 879-96.

28. Brown, J.R., Chappell, P.J.C. & Mathys, Z. (1992) "Plasma Surface Modification of Advanced Organic Fibers" *Journal of Material Science*, 27, 3167-72.

29. Li, Z.F., Natravali, A.N. & Sachse, W. (1992) "Ammonia Plasma Treatment of Ultra-High Strength Polyethylene Fibers for Improved Adhesion to Epoxy Resin" *Journal of Material Science*, 27, 4625-32.

30. Hild, D.N. & Schwartz, P. (1992) "Plasma Treated Ultra-High Strength Polyethylene Fibers Part II: Mechanical Properties of PMMA Composites" *Journal of Adhesion Science and Technology*, 6, 897-921.

31. Miller, A. & Schwartz, P. (1997) "Effects of Oven Aging on Plasma Treated Ultra High Strength Polyethylene" *Plasmas and Polymers*, 2(2), 115-32.

32. Arkles, B. (2006) “Silane Coupling Agents: Connecting Across Boundaries” Morrisville, PA: Gelest Inc.

33. Keoleian, G.A. et al (2005) “Life Cycle Modeling of Concrete Bridge Design: Comparison of Engineered Cementitious Composite Link Slabs and Conventional Steel Expansion Joints” *Journal of Infrastructure Systems*, 11(1), 51-60.

34. ISO 14040 (2006) “Environmental management -- Life cycle assessment -- Principles and framework” Geneva, Switzerland: International Organization for Standardization.

35. Wolde-Tinsae, A. M. & Klinger, J. E. (1987) “Integral Bridge Design and Construction” Maryland Department of Transportation - Report No.FHWA/MD-87/04.

36. Alampalli, S. & Yannotti, A. P. (1998) “In-Service Performance of Integral Bridges and Jointless Decks” *Transportation Research Record 1624*, pp. 1-7.

37. Li, V.C., Lepech, M.D. & Li, M. (2005) “Field Demonstration of Durable Link Slabs for Jointless Bridge Decks Cased on Strain-Hardening Cementitious Composites” *Research Report RC-1471*, Lansing, MI: Michigan Department of Transportation.

38. Kendall, A. (2007) “Concrete Infrastructure Sustainability: Life Cycle Metrics, Materials Design, and Optimized Distribution of Cement Production” PhD Dissertation, Ann Arbor, MI: University of Michigan.

39. US EPA (2000) “NONROAD Software” Ann Arbor, MI: United States Environmental Protection Agency.

40. Kentucky Transportation Center (2002) “The cost of construction delays and traffic control for life-cycle cost analysis of pavements” Lexington, KY: Kentucky Transportation Center, University of Kentucky.

41. US EPA (2002) “MOBILE 6.2” Ann Arbor, MI: United States Environmental Protection Agency.

42. Lepech, M.D. (2006) “A Paradigm for Integrated Structures and Materials Design For Sustainable Transportation Infrastructure” PhD Dissertation, Ann Arbor, MI: University of Michigan, pp. 184-236.

43. Liu, Y. & Weyers, R. (1998) “Modeling the Time-to-Corrosion Cracking in Chloride Contaminated Reinforced Concrete Structures” *ACI Materials Journal*, 95(6), 675-681.

44. Thoft-Christensen, P. (2000) “Modeling of the Deterioration of Reinforced Concrete Structures” In *Proceedings of IFIP Conference on Optimization and Reliability of Structural Systems*, Ann Arbor, MI, September 25-27, pp. 15-26.

45. Yanev, B. & Chen, X. (1993) “Life-cycle Performance of New York City Bridges” *Transportation Research Record No. 1389*, Washington, D.C.: Transportation Research Board.

46. FHWA (2013) “Ultra-High Performance Concrete: A State-of-the-Art Report for the Bridge Community” *Publication No. FHWA-HRT-13-060*, McLean, VA: US DoT Federal Highway Administration, pp. 45.

47. Li, M., Ranade, R., Kan, L. & Li V.C. (2010) "On Improving the Infrastructure Service Life Using ECC to Mitigate Rebar Corrosion" In *Proceedings of RILEM 2nd International Symposium on Service Life Design for Infrastructure*, 4-6 October, 2010, Delft, Netherlands. pp. 773-781.

48. Li, M. & Li, V.C. (2006) "Behavior of ECC/Concrete Layered Repair System under Drying Shrinkage Conditions" *Journal of Restoration of Buildings and Monuments*, 12(2), 143-60.

49. Bentz, E.C. & Thomas, M.D.A. (2013) "Life-365™ Service Life Prediction Model™" Lovettsville, VA: Silica Fume Association.

CHAPTER 10: NEW FRAMEWORK FOR ASSESSING THE IMPACT OF MATERIALS ON INFRASTRUCTURE RESILIENCE AND SUSTAINABILITY SIMULTANEOUSLY

10.1 Introduction

In the last decade, with growing threats of climate change and terrorism on our built environment coupled with ever-increasing demand for infrastructure and tightening budgets, resilience and sustainability of infrastructure have both become the primary concerns of researchers, engineers, planners, and other stakeholders of civil infrastructure worldwide. As a result, significant advances have been made recently to improve infrastructure resilience and sustainability, a few of which have been mentioned in the previous chapters of this dissertation.[1,2,3,4] However, these efforts have been largely decoupled from each other, perhaps due to seemingly non-concurrent objectives.[5] This chapter considers the resilience and sustainability of infrastructure together to develop a novel framework for assessing the impact of advanced materials such as HSHDC on both these performance metrics of infrastructure.

Indeed, the infrastructure resilience and sustainability have developed as separate areas of investigation. Sustainability is often not a concern for structural engineers in the design process of resilient structures to withstand extreme natural and manmade hazards, as life safety trumps other issues in such cases. Vice versa, resilience is not considered by industrial ecologists while

assessing the sustainability of infrastructure under service loads, as the structures are presumed to be safe. With interdisciplinary research and practice in recent years, which has created more awareness among both the disciplines, the need for integrated assessments of resilience and sustainability of infrastructures is being gradually realized. An integrated assessment of infrastructure resilience and sustainability is of interest in this dissertation, as the materials such as HSHDC are tailored to enhance both the resilience and sustainability of civil infrastructure, simultaneously.

Several researchers have attempted to define and quantify resilience not only for structures or infrastructure but also for ecosystems, societies, and economies. Some of the first definitions were given by Holling (1973),[6] Gordon (1978),[7] Timmerman (1981),[8] and many more, but the definition of resilience continues to evolve to the present day [e.g. Bocchini (2013)[5]]. For the purpose of this dissertation, resilience of a structure is defined as the combination of (1) the structure's ability to withstand abnormally severe loads/displacements with recoverable damage, and (2) the ability of the society and economy (that utilize the structure) to restore the structure back to the level of functionality prior to the disrupting event in short time at low environmental and economic cost. In this regard, "robustness" of the structure to withstand unexpected loads and "rapidity" of recovery are often identified in literature as the *goals* of resilience, whereas structural (also socio-economic) "redundancy" and socio-economic "resourcefulness" are the *means* to achieve resilience (the resilience metrics are discussed in the next section).

Similar to resilience, the definition of sustainability has also evolved over the years. Yet, the classic definition in the UN report by Brundtland (1987)[9] has appeared in the majority of literature, which states that "sustainable development is the development that meets the needs of the present without compromising the ability of future generations to meet their own needs." The widely accepted practical interpretation of this definition in the context of sustainable infrastructure is: an infrastructure that meets the needs of the present while minimizing its harmful impacts on the environment, economy, and society. Although this interpretation does not guarantee that the future generations will be able to meet their needs, it maximizes their opportunity to do so. Among the three dimensions of sustainability (environment, economy, and society), the environmental dimension often gets the most attention (e.g. Chapter 9 of this dissertation), perhaps due to historical reasons as the interest in sustainability has been mostly motivated by the concern for the natural environment.

In spite of the differences between resilience and sustainability, there are some similarities among the two which must be recognized. Most importantly, both concepts take a holistic view of infrastructure and its interactions with the environment, economy, and society. Both resilience and sustainability assessments consider the entire life-cycle of a structure; however, they focus on different events in the life-cycle. While the sustainability assessment focuses on the predictable low-consequence maintenance events, resilience assessment focuses on the rare but high-consequence events during the structure's service life. Due to these similarities, an integrated life cycle assessment of infrastructure considering the probabilities of low and high-frequency events (risk analysis-based[10]) can be performed, as proposed by Bocchini et al.[5]

In the following section, the metrics typically used for quantifying resilience and sustainability of infrastructure are reviewed, with emphasis on the metrics chosen for this research. Subsequently, the proposed framework for assessing the influence of materials on infrastructure resilience and sustainability, simultaneously, is outlined in Section 10.3. Finally, a numerical application of this framework to an example structure is demonstrated in Section 10.4.

10.2 Resilience and Sustainability Metrics

One of the most comprehensive frameworks to quantify (seismic) resilience is presented in Bruneau et al.[11] The resilience metric presented in Bruneau et al[11] and elsewhere are well represented graphically in form of a "resilience triangle" in Bocchini et al[5], as shown in Figure 10.1. In this figure, an extreme event (e.g. blast/impact/earthquake/hurricane) occurs at time, t_0, which severely reduces the structural functionality, Q(t) (a function of time), depicted as an instantaneous vertical drop. "Robustness" is defined as the residual functionality of the structure remaining immediately after the extreme event. The recovery of the structure to 100% functionality, that takes place along the actual curved path Q(t), is approximated by a dashed straight line with slope equal to the average rate of recovery (dQ/dt), defined as "rapidity". The rate of recovery (rapidity) determines the time taken, $t_r - t_0$, for the complete recovery. The shaded area of the resilience triangle in Figure 10.1 is a metric for computing the loss of resilience (R_L). Extending this concept, a resilience index, $R \in [0,1]$, can be defined as the area complementary to R_L normalized by the observation time horizon, t_h, as shown in Figure 10.2. Therefore, increasing robustness and rapidity increase the resilience index, R.

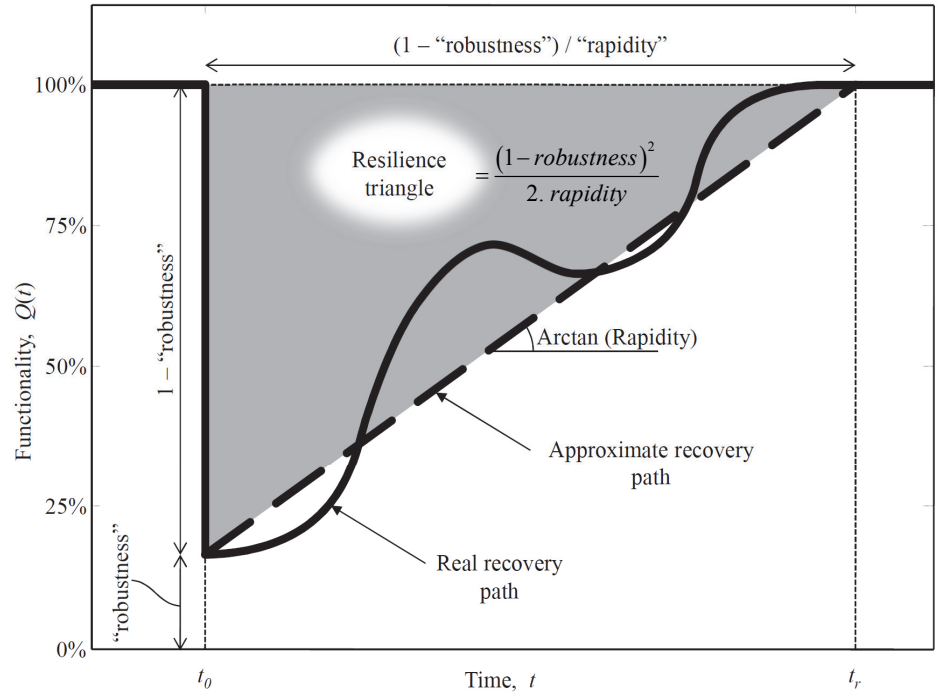

Figure 10.1: Resilience Triangle (Source: Bocchini et al[5])

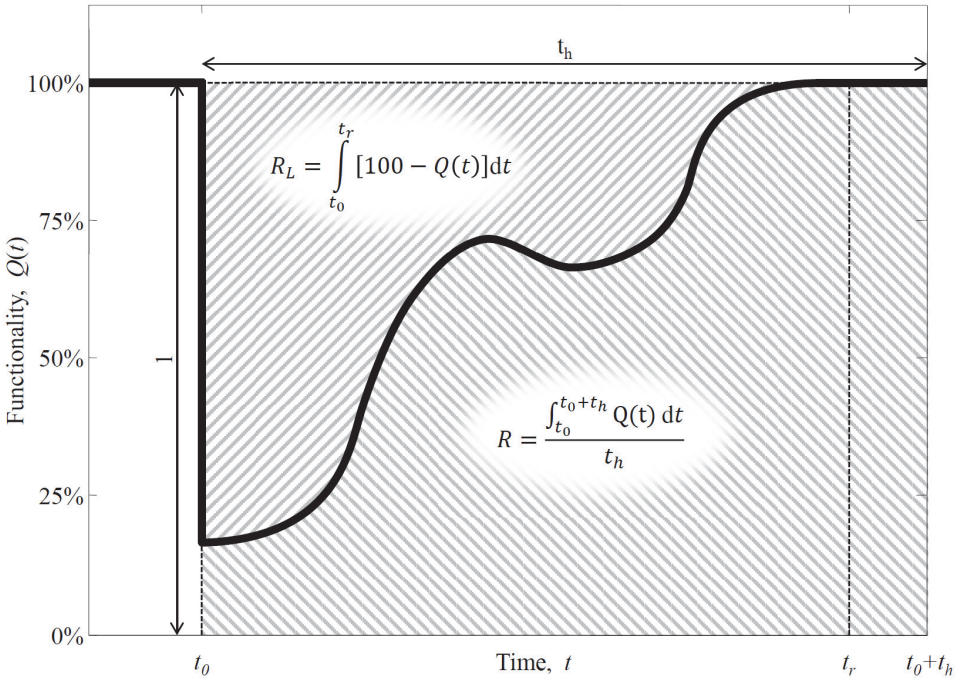

Figure 10.2: Resilience Loss (R_L) and Resilience Index (R) (Source: Bocchini et al[5])

Another metric for resilience is the recovery cost (C_r), which is dependent, among other factors, on the structural robustness and rapidity of recovery discussed above. C_r is one of the system-level performance measures defined in the Performance-Based Earthquake Engineering methodology developed by the Pacific Earthquake Engineering Research (PEER) Center.[12] There are four stages of analyses involved in computing C_r: hazard analysis, structural analysis, damage analysis, and loss analysis. These analyses stages are shown in Figure 10.3. Although this methodology was developed for seismic hazard analysis, the analyses stages are applicable for any hazard in general as explained below.

The first stage of the PEER methodology is the probabilistic hazard analysis. The inputs of this analysis are the hazard identification parameters depending on the type of hazard. For instance, location, distance from the structure, ground attenuation, and magnitude and recurrence intervals for earthquakes; TNT charge weight, standoff distance, and threat assessment for blast loads (Chapter 8); wind speeds and recurrence rates for hurricanes; etc. The output of the hazard analysis is the aggregated probability of forces (or peak ground accelerations) exceeding certain critical values. In the second stage, a structural analysis (using finite element or other methods) is performed for these external forces that may be experienced by the structure due to various hazards. The structural analysis yields vital parameters regarding structural response parameters such as inter-story drift or beam deflections, which depends on the material, sectional, and geometrical properties of the structural members. The third stage is the damage analysis, which takes the structural response parameters as inputs and determines damage states using fragility or damage functions. Finally, a loss analysis is performed to estimate the recovery cost based on the damage state. Depending on the scope of the investigation, the recovery cost may include not

only the direct economic costs of repair, but also indirect costs such as loss of life and other social/environmental costs.

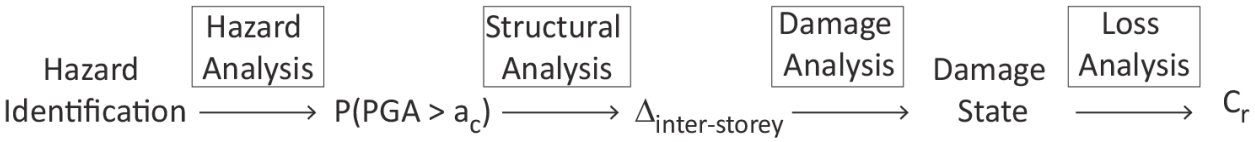

Figure 10.3: PEER methodology for performance-based earthquake engineering

The framework used to compute C_r in this research is mathematically represented by Eq. 10.1. The first term P_i is the output of the hazard analysis for the i^{th} hazard. P_i is the probability that the i^{th} hazard generates an overload F_i that is above a critical value of the structure's capacity F_u, which is a function of material strength (e.g. compressive strength, f_c'), sectional properties, S, and geometrical properties, G, and calculated using structural analysis. The second term in Eq. 10.1 is a damage function ($f_{d,i}$) for the i^{th} hazard, which is dependent on a structural response parameter, Δ (such as inter-story drift). Δ, in turn may further depend, among other parameters, on the applied force (F_i), material's tensile ductility (ε_{tu}), tensile and compressive strengths (σ_{tu} and f_c'). Other factors affecting Δ can be external support bracings, reinforcement detailing, etc. $f_{d,i}$ is determined, deterministically or probabilistically, through fragility curves or other damage analysis methods in combination with the structural analysis. For instance, fragility functions determine the probability of damage exceeding a certain value for a given structural response parameter (e.g. inter-story drift), which would yield probabilistic $f_{d,i}$. The third term in Eq. 10.1 is a combination of the damage costs ($C_{d,i}$) (direct economic damage plus indirect costs due to loss of life and environmental damage) and time value of recovery ($C_{t,i}$, which depends on rapidity of recovery) for the i^{th} hazard.

$$C_r = \sum_{i=1}^{n} \underbrace{P_i\left(F_i > F_u\left(f_c', S, G\right)\right)}_{\text{Hazard/Structural Analysis}} . \underbrace{f_{d,i}\left(\Delta\left(F_i, \varepsilon_{tu}, \sigma_{tu}, f_c' \ldots\right)\right)}_{\text{Structural/Damage Analysis}} . \underbrace{\left(C_{d,i} + C_{t,i}\right)}_{\text{Loss Analysis}} \tag{10.1}$$

A closer examination of Eq. 10.1 provides further insights into the factors affecting each of the three terms and the overall recovery cost, C_r. The following three observations are made:

1. Increasing the strength of materials (f_c') and sectional size of structural members (S) increases the structural load capacity (F_u), which reduces the probability (P_i) of the force generated by the hazard to exceed the structural capacity. Reduction in P_i, in turn, reduces C_r and, therefore, enhances resilience.

2. The damage function, $f_{d,i}$, is expected to vary with a structural response parameter Δ, which further depends on ε_{tu}, and other parameters (F_i, σ_{tu}, f_c',), as shown qualitatively in Figure 10.4 using hypothetical functions. The properties of the damage function are: (a) damage level at zero ductility regardless of load is 100%, (b) damage level reduces with increasing ductility (or other material property); however, it plateaus and becomes asymptotic to certain damage level. This implies that increasing material tensile ductility (or other material property) beyond a certain value has reducing marginal return. (c) For a given material ductility, the damage level increases with increase in overload F_i. Obviously, reducing $f_{d,i}$ by enhancing material properties reduces C_r and, therefore, enhances resilience.

3. The loss associated with the i^{th} hazard can be reduced by minimizing the consequences of structural damage. The methods to achieve this are (a) by incorporating sufficient structural redundancy, which reduces the cost of damage ($C_{d,i}$), and (b) by enhancing the socio-economic resourcefulness to enhance the rapidity of recovery, which reduces the time value of recovery

($C_{t,i}$) . Both these measures, which are rather independent of the material properties, can significantly reduce the recovery cost, C_r.

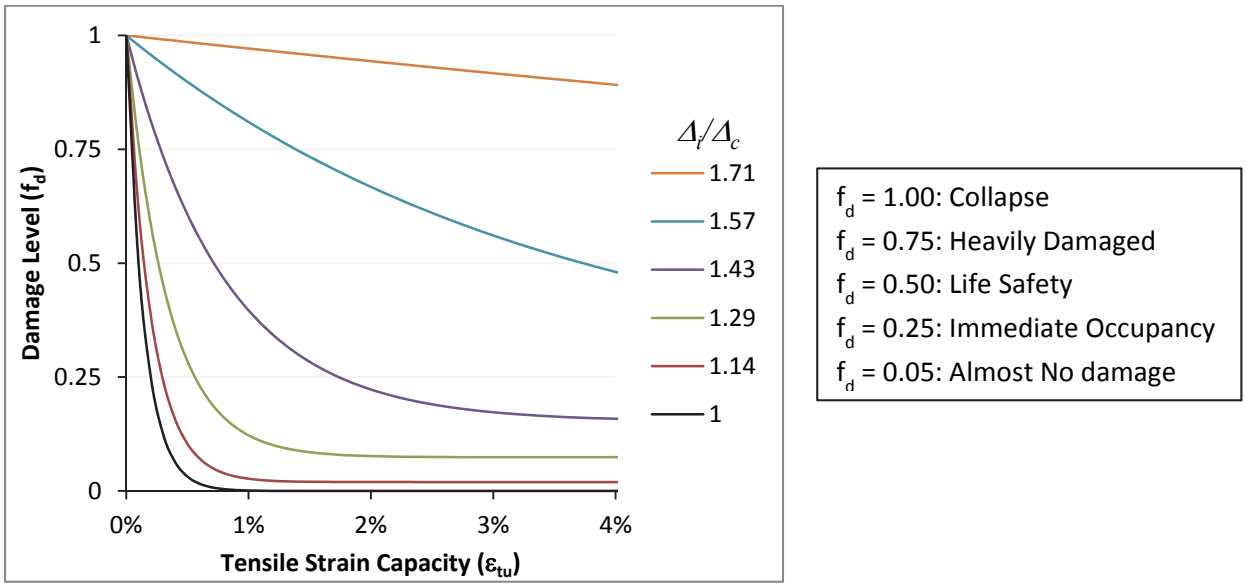

Figure 10.4: Qualitative variation of damage with overload and tensile strain capacity of concrete

The environmental and economic dimensions of sustainability have been quantified systematically in literature using life cycle assessment and life cycle cost analysis. As discussed in Chapter 9, the outputs of such analyses such as total CO_2 emissions and life cycle cost are well defined metrics of environmental and economic sustainability, and the same are used in this research. In contrast, the social sustainability metrics such as human development index, human health and safety, etc. are less tangible and there is a lack of consensus about the methodology used to determine these metrics. An even bigger challenge is to link a single structure's resilience and sustainability to these larger scale social sustainability metrics. Due to the preliminary nature of this research where the emphasis is more on the framework rather than the computations, its

scope with regard to sustainability is limited to only the environmental and economic metrics of total CO_2 emissions and life cycle cost, respectively.

The computations of life cycle CO_2 emissions (E_L) and cost (C_L) in this research include the emissions (E_r) and costs (C_r) (weighted by the probability of the corresponding hazard, P_i) associated with the post-disaster structural recovery, in addition to the impacts associated with the materials, construction and maintenance, use, and end-of-life phases of structural life-cycle under service loads. Hence, E_L and C_L are given by Eqs. 10.2 and 10.3. In these equations, 'E' represents CO_2 emissions (tonnes) and 'C' represents cost ($). The suffixes 'm', 's', 'r', and 'L' represent initial materials and construction phases, rest of the service life (maintenance + use + end-of-life), post-disaster recovery (weighted by probability of occurrence during the structure's service life of the i^{th} hazard), and total life-cycle.

$$E_L = E_m + E_s + E_r \tag{10.2}$$

$$C_L = C_m + C_s + C_r \tag{10.3}$$

10.3 Proposed Framework

The framework for comparing the performance of various materials, thereby selecting the best material option, in a structural application considering its life-cycle resilience and sustainability is presented here. The starting point in this framework is a structure or a structural member designed according to the applicable building code with the conventional material (e.g.

reinforced concrete), which ensures that the structure performs its intended *function* (in other words, the structure is safe and serviceable under normal service conditions). The building code for the structure may include the design specifications for ensuring structural safety in the face of known hazards. For instance, a building code in California typically accounts for certain ground motions by specifying rules for increasing the capacity of the structural members (by using larger sections) and for more ductile reinforcement detailing compared to non-seismically active regions. This ensures desired (ductile) behavior of the structure during an earthquake, if the corresponding ground motion is less severe than that anticipated in design. Using this design of the structure with the conventional material, the next step of this framework is to compute the expected recovery cost (C_r) using Eq. 10.1, and life cycle environmental impact (E_L) and economic cost (C_L) using Eqs. 10.2 and 10.3 (where the inputs come from a life-cycle inventory analysis, similar to that discussed in Chapter 9).

For choosing the optimal material for a structural application considering both resilience and sustainability, the objective of this framework is to maximize sustainability, while ensuring adequate resilience. This is achieved by minimizing the *objective functions*, i.e. life-cycle environmental impact (E_L) and economic cost (C_L), under the *constraint* that the recovery cost (C_r) must not exceed a critical value (C_{ru}). Independent of the material, C_{ru} can be set at a particular value depending on a number of factors such as the risk-tolerance (in case the actual C_r after a disaster exceeds C_{ru}), economic considerations, regulation (building codes), and importance factors of structures (e.g. C_{ru} for hospitals, fire stations, and police stations may be set lower than other structures). For a given material, sectional and geometrical properties of the

structural members are the *free variables* (that can be changed to meet the objectives while satisfying the function and constraint defined above) in this optimization problem.

With this optimization methodology, the value of C_r with the conventional material is first checked to determine if it is lower than C_{ru}. If $C_r \leq C_{ru}$, then, the corresponding E_L and C_L are considered in the optimization process. However, if $C_r > C_{ru}$, then, an iterative redesign of the structure is undertaken by changing the free variables (section and geometry of the structure), until the condition $C_r \leq C_{ru}$ is satisfied.

The same steps, as above, are repeated for all the materials under consideration. From this process, a set of viable *solutions* (structural designs – one for each material) emerges, all of which satisfy the resilience constraint. For each structural design, there is an associated pair of E_L and C_L. The goal is to find an optimal solution, which minimizes the combination of E_L and C_L, defined by a penalty function, Z,[13] in Eq. 10.4. Here, α is the exchange constant with units \$/MJ, which assigns a dollar value to each tonne of CO_2 emissions saved. A tradeoff plot, similar to Figure 8.10 in Ashby[13], can be created to graphically represent all the viable solutions, one of which with the lowest Z is the optimal material solution. An example structural application is used to numerically demonstrate this framework in the following Section.

$$Z = C_L + \alpha E_L \tag{10.4}$$

10.4 Example Structural Application

In this section a moment-resisting structural column subjected to severe horizontal pushover load is used as an example to demonstrate the application of the new framework for analyzing various materials, and determining the most resilient and sustainable option. This example is taken from a standard text on Reinforced Concrete Design.[14] This column is designed for ultimate axial load demand (P_u) of 450 kips, ultimate uniaxial moment demand of (M_u) of 120 kip-ft, and ultimate shear demand (V_u) of 14 kips. This column is part of a braced frame and has an unsupported length of 10 ft. The designed column is 16″x16″ with 1.5″ clear concrete cover, and it contains longitudinal steel reinforcement in form of 6 - 1″ (No.8) rebars arranged as shown in Figure 10.5. In addition, No. 3 ties are placed at 16″ center-to-center distance for adequate shear resistance. The yield strength of steel is 60 ksi and the compressive strength of concrete is 4 ksi. This column is designed according to the ACI 318 (2008)[15] building code.

The resilience of this column under a severe horizontal force, F (exceeding V_u), as shown in Figure 10.5(a) is determined through analytical investigation of its force-displacement (F-Δ) relation. The assumption here is that the structural/functional damage (in the rest of the structure), and therefore the recovery cost (C_r), is proportional to the drift or displacement (Δ) of this column. In this analysis, the column is assumed to be a cantilever under a constant uniaxial service load P, equal to 270 kips which is 60% of the ultimate demand (450 kips). Δ is the displacement of the "free end" in the direction of F (horizontal). For determining the F-Δ relation, the moment-curvature (M-ϕ) relation of a column section is first determined using equilibrium, compatibility, and constitutive relations of steel and concrete. Details of the analysis

method are given in Wight & MacGregor.[16] As the problem is statically determinate, the moment variation (for an applied force, F) at various sections of the column is independent of the material properties. The M-ϕ relation can be, therefore, inverted (up to peak M) to determine the curvature variation along the column for the applied force, F, and using the second moment-area theorem, tip displacement (Δ) of the column is determined from the curvature variation.

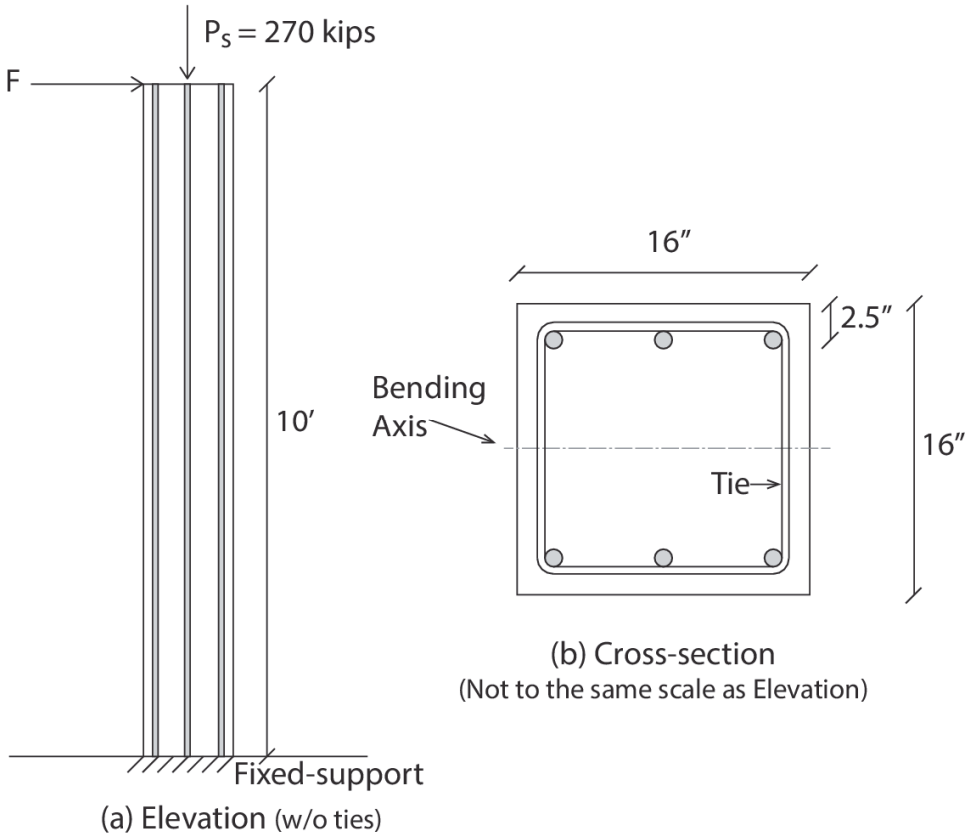

Figure 10.5: Column example (a) Elevation: support conditions and loading (b) Cross-section: reinforcement detailing

Figure 10.6 shows the computed M-ϕ and F-Δ relations (solid curves) for the above-designed column with specified concrete, named here as "Concrete 1" (with f_c' = 4000 psi), under constant uniaxial service load (P_s in Figure 10.5a). Also shown in this figure are the

dashed curves for the above column in absence of P_s for understanding the structural response, which is detailed in Section 10.5 (to avoid distraction from the flow of the example).

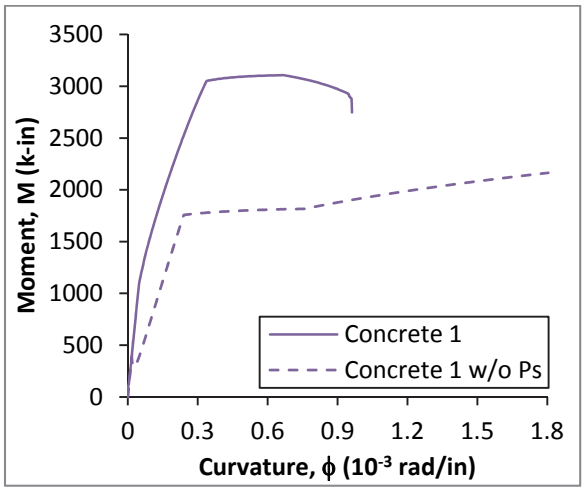

(a) M-ϕ relation of a column section

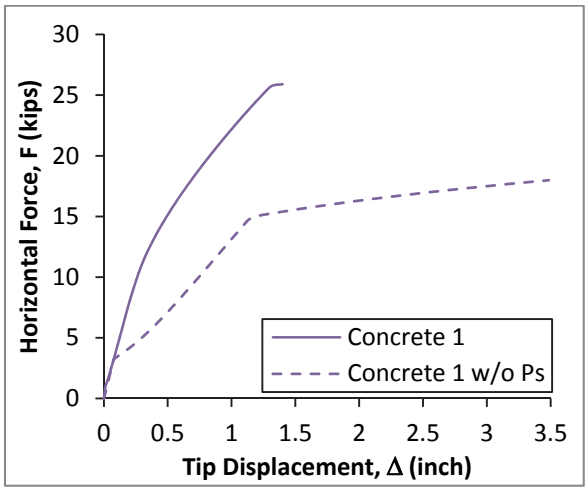

(b) F-Δ behavior of the column

Figure 10.6: M-ϕ and F-Δ relations for the column designed with Concrete 1

The hazard assumed for this analysis is expected to impart a horizontal force of 20 kips on the column with the probability of occurrence of 1% during its service life. From the F-Δ curve of the axially loaded column, the Δ corresponding to F = 20 kips is 0.83″. According to the proposed framework, the next steps in computing the recovery cost (C_r) would be to translate this Δ into damage state (f_d), which when multiplied by the damage costs for complete failure and the probability of occurrence (1%) gives expected C_r. However, both f_d and damage costs are unknown in this example (they can be estimated if the details about the structure that this column supports are known). As an alternative, instead of limiting the recovery cost (C_r), the displacement (Δ) can be equivalently constrained to achieve adequate resilience, provided (1) the damage costs for complete failure ($C_{d,i}$ and $C_{t,i}$ in Eq. 10.1) are assumed constant, and (2) f_d is a

monotonically increasing function of Δ. Thus, mathematically, the resilient constraint $C_r \leq C_{ru}$ is equivalent to $\Delta \leq \Delta_u$. As this is a comparative investigation of various materials, Δ_u can be set equal to the displacement of a reinforced-HSHDC column with the same dimensions and reinforcement detailing as the concrete column but with concrete replaced by HSHDC.

The M-ϕ and F-Δ behaviors corresponding to the reinforced columns of Concrete 1, Concrete 2 (with $f_c' = 7000$ psi – same as that of ECC-M45), ECC-M45, COR-TUF, and HSHDC (vinyl silane-HSHDC) are shown in Figure 10.7 and Figure 10.8, respectively. In this study, COR-TUF and HSHDC are assumed to have different tensile behaviors as determined experimentally in this dissertation, but they are assumed to have the same compressive behavior (even though HSHDC is more ductile in compression as well) for isolating the effects of tensile ductility on the column behavior. These curves are discussed in Section 10.5.

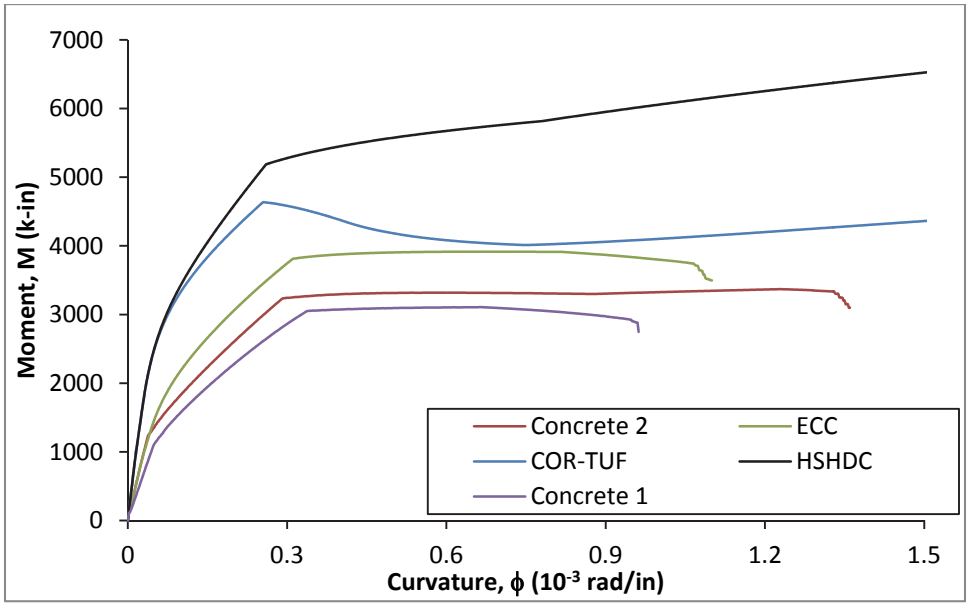

Figure 10.7: M-ϕ relations for the columns designed with various concrete materials (Note: all columns have the same steel reinforcement)

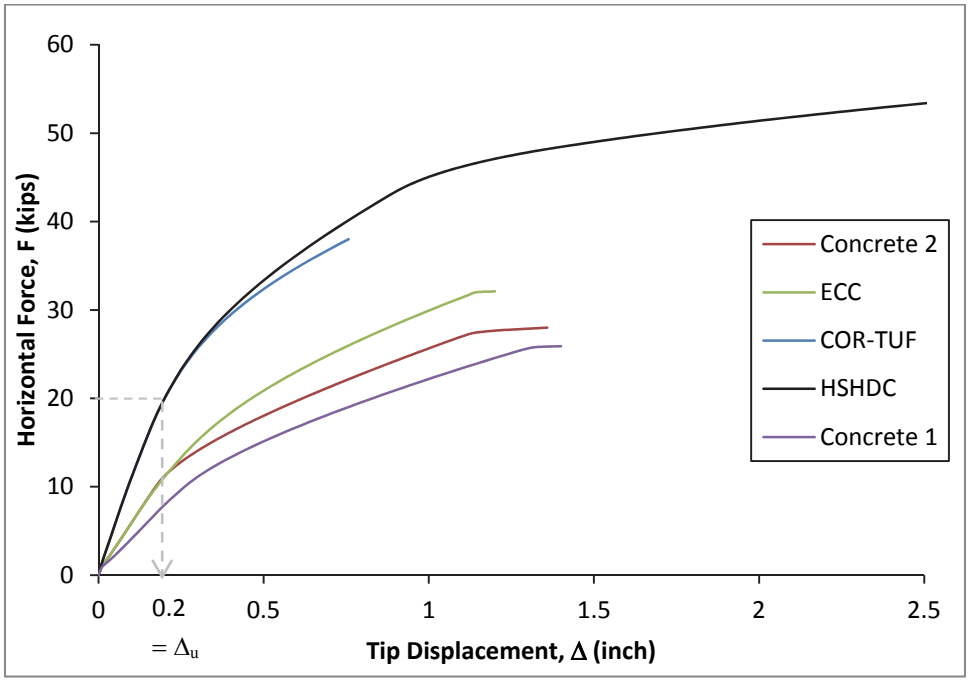

Figure 10.8: F-Δ relations for the columns designed with various concrete materials

From the F-Δ behavior of HSHDC column (Figure 10.8), the tip displacement (Δ) corresponding the horizontal force of 20 kips is 0.20″, which is set equal to Δ_u (the maximum allowable Δ) for all other concretes to satisfy the resilience constraint, as discussed above. While the section dimensions of Concrete 2 and ECC are increased (keeping the same reinforcement), reinforcement area of COR-TUF is increased by 225% (keeping the same overall sectional dimensions) to achieve the same Δ and sufficient M-ϕ ductility.

It should be noted that although it is not necessary to increase the COR-TUF column's reinforcement from the resilience standpoint (as $\Delta \leq 0.2''$ is satisfied by the unchanged COR-TUF column); such under-reinforced column will not be acceptable in the code-prescribed limit state design as it has a catastrophic mode of failure with significant softening. Furthermore, these

designs are achieved with minimum changes to the original configuration, and are by no means unique as a number of, potentially better, combinations of column dimensions and reinforcement are possible, which can adequately support the specified loads and meet the resilience criterion.

The M-ϕ and F-Δ behaviors of the column configurations that satisfy the resilience constraint are shown in Figure 10.9 and Figure 10.10, respectively. The letters 'D' and 'R' are added to the names of the columns to signify larger section dimensions and increased reinforcement, respectively.

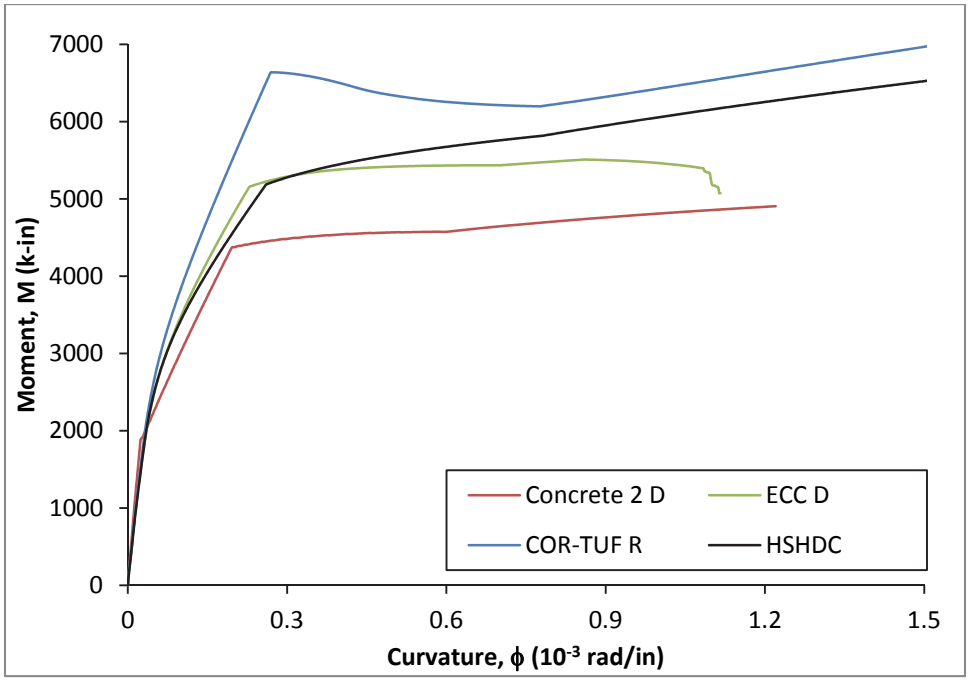

Figure 10.9: M-ϕ relations for the columns designed to meet the resilience criterion

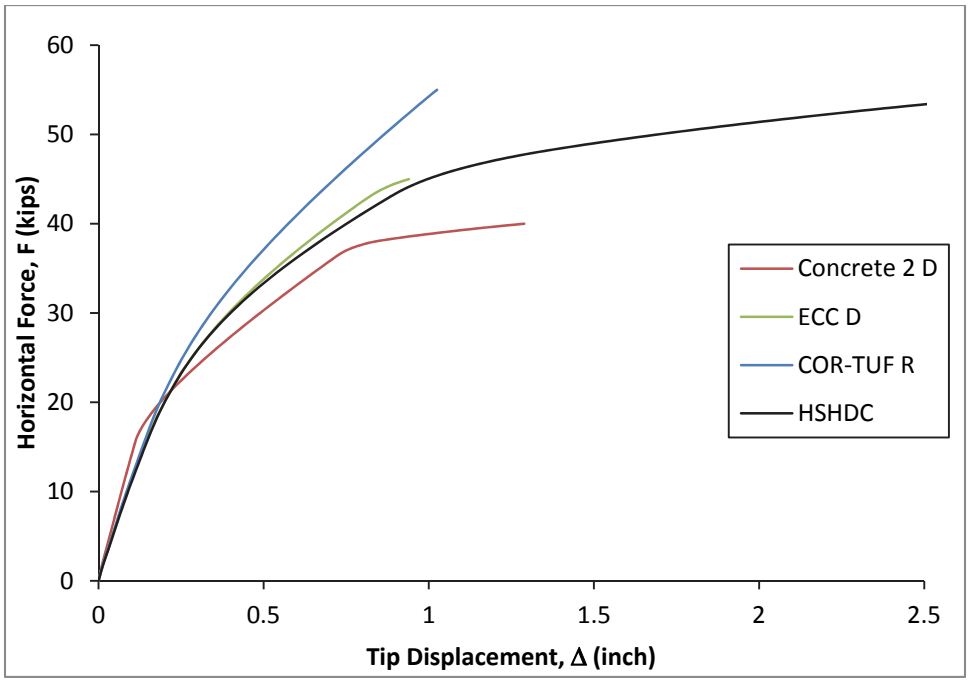

Figure 10.10: F-Δ relations for the columns designed to meet the resilience criterion (Note that HSHDC is unmodified, whereas other columns either have larger dimensions ['D'] or increased reinforcement ['R'])

The life-cycle CO_2 emissions (E_L) and economic cost (C_L) calculations of these viable solutions are performed using Eqs. 10.2 and 10.3, respectively, and the results are summarized in Table 10.1. The material cost and carbon emissions per unit volume are computed using the ingredient cost and energy intensities (Table 9.1 and external cost data). The cost and carbon emissions of the column are then calculated using the volumes of concrete and steel in the column. The column constitutes only a small part of the rest of the structure (like the link-slab in the bridge deck in Chapter 9).

In order to determine all the initial material costs associated with the column without the knowledge of the actual structure, an estimate of the material weight that is supported by this column is obtained based on its design load, P_u (equal to 450 kips as stated above). One of the

most typical load combinations to determine this load is $1.2D + 1.6L$[17], where D and L are the dead and live loads, respectively. Assuming L/D ratio of 1, D is computed equal to 161 kips. Further assuming that all this weight is associated with reinforced concrete in the rest of the structure, its corresponding volume and, therefore, cost (C_m) and carbon emissions (E_m) can be computed by adding the cost and CO_2 emissions of the column to that of this dead weight of reinforced concrete. The parameters used in this calculation are: density of reinforced concrete (2450 kg/m^3), unit cost (\$300/m^3)[18], and environmental impacts of concrete (Table 10.1) and steel[19] with reinforcement ratio of 1%.

The cost and CO_2 emissions associated with the rest of the service life phases (C_s and E_s) are assumed to be twice that of C_m and E_m, respectively, for the brittle materials (Concrete and COR-TUF), and equal to C_m and E_m, respectively, for the ductile materials (ECC and HSHDC). The contributions from the post-disaster recovery (the third terms in Eqs. 10.2 and 10.3) to the total life-cycle costs and emissions are neglected in this comparative study. This is because under the assumptions made above and the fact that the re-design of columns meets the resilience constraint closely (i.e. Δ at 20 kips $\approx 0.20''$ for all materials), the contribution from the post-disaster recovery will be almost the same for all materials. Hence, the total cost and CO_2 emissions are computed by adding the initial materials/construction stage contributions (C_m and E_m) and the contributions from the rest of the service-life phases (aggregated in C_s and E_s).

For combining the cost and CO_2 emissions into the penalty function, Z, the exchange constant, α, (\$/tonne-CO_2 emissions) is set equal to the suggested carbon tax for the US in literature (by policy researchers), which is \$30/tonne-CO_2.[20] However, this value is considered

too low by climate scientists, which propose a tax of up to \$100/tonne-CO_2. Both these values of exchange constants are used in this analysis to determine the corresponding Z values for all materials. As the minimum value of Z is achieved with ECC for both values of α, this analysis estimates that the ECC column will be the most sustainable with adequate resilience for the hazard considered in this study.

HSHDC column is a close second and performs significantly better than COR-TUF and concrete columns. It should be noted that the real-estate costs lost due to larger cross-section of the ECC column are not included in the above calculation, which may be more important to the owner and the architect for a number of structures. Additionally, HSHDC has significantly greater deflection capacity than the ECC column, which may make it more attractive for hazards more severe than that considered in this example.

Table 10.1: Life-cycle environmental and economic cost calculations

	Concrete 2 L	ECC L	COR-TUF R	HSHDC
Material cost (\$/m^3)	85	322	1222	3325
Column cost (\$) (incl. steel)	155	321	804	1738
C_m (\$)	9082	9248	9731	10665
C_s (\$)	18164	9248	19462	10665
C_L (\$)	27245	18496	29193	21330
Carbon-MSI (tonne-CO_2/m^3)	0.43	0.62	0.82	0.94
Column CO_2 emissions	0.43	0.56	0.68	0.59
E_m (tonne-CO_2)	17.16	17.29	17.41	17.32
E_s (tonne-CO2)	34.31	17.29	34.82	17.32
E_L (tonne-CO2)	51.47	34.58	52.23	34.64
Z (α = \$30/tonne-CO_2)	28789	19533	30760	22370
Z (α = \$100/tonne-CO_2)	32392	21954	34416	24794

10.5 Discussion of M-ϕ and F-Δ curves

For concrete 1, the dashed M-ϕ curve (Figure 10.6a) corresponding to the column without P_s shows three kinks typically observed in reinforced concrete beam-column members. These kinks at about M = 300 k-in, $\phi = 0.24 \times 10^{-3}$ rad/in, and $\phi = 0.72 \times 10^{-3}$ rad/in represent tensile cracking of concrete, tensile yielding of steel rebar, and the start of the tensile strain hardening of the rebar, respectively. Finally, the maximum moment capacity is reached when the concrete is deemed to have crushed under compression (when maximum compressive strain in concrete reaches 0.6%) at section curvature (ϕ) of about 1.8 rad/in. These key changes in M-ϕ behavior are clearly reflected in the corresponding F-Δ response (dashed curve of Figure 10.6b), except the kink corresponding to the start of strain hardening in steel, which, although present, is not obvious in the dashed curve of Figure 10.6b. This is because the change in the slope of M-ϕ curve is small and it is further diffused in the overall F-Δ curve, which is an integration of M-ϕ behaviors at multiple sections. Thus, the M-ϕ and F-Δ dashed curves for the column made with concrete 1 without the axial load correspond well with each other.

Similar kinks are visible in the M-ϕ and F-Δ behaviors of the axially loaded concrete columns (solid curves in Figure 10.6); however, the constant uniaxial compressive load acts as a prestressing force on the column which causes a shift and a change in the order of occurrence of the kinks that are observed in the column without the axial load. Due to the axial compressive load, the concrete cracking is delayed as the associated kink (also less drastic slope reduction) in the solid curve of Figure 10.6a occurs at moment of about 1100 k-in. The second kink, corresponding to tensile steel yielding, is also delayed for the same reason. Unlike the dashed

curve in which the third kink corresponds to the start of strain hardening in tension steel, the third kink in the solid curve (peak of the solid curve) corresponds to the yielding of compression steel. This premature yielding of compression steel also occurs due to the axial load. As a result the moment resistance of the axially loaded column section starts to reduce because of simultaneously reducing concrete compressive stress (concrete compressive stress reduces in the axially free column section too at this stage; however, this loss in stress is picked up by the elastic compression steel). Finally, the section fails when concrete crushes at the curvature of about 0.9×10^{-3} rad/in. The F-Δ curve is computed only till the fixed end section of the column reaches its maximum moment capacity (the stability is lost after that), and it, therefore, reflects two out of the three kinks of the M-ϕ curve up to the peak as explained above (the end of the solid F-Δ curve corresponds to the third kink, i.e. peak, of the solid M-ϕ curve).

In Figure 10.7, although the first two kinks in the M-ϕ curves of all concretes, corresponding to concrete cracking and yielding of the tension steel, are the same as that for Concrete 1 explained above, the third kink is different. While the compression steel yields first (producing a peak M followed by negative M-ϕ slope) in concrete 1 (explained above) and ECC columns, the strain hardening of tension steel occurs first (producing a kink followed by positive M-ϕ slope) in concrete 2 and HSHDC columns. COR-TUF column section seems to soften after the yielding of tensile steel. These observations are further discussed below.

Concrete 2 has the same compressive strength as ECC; however, due to its brittleness under tension, Concrete 2, unlike ECC, is unable to produce sufficient tensile force in the section to cause yielding of the compression steel before the strain hardening of the tension steel.

Therefore, the tensile ductility of ECC material (assumed 4%, with first crack strength of 3.5 MPa and ultimate tensile strength of 5 MPa) negatively influences the sectional (M-ϕ) ductility, if the reinforcement is kept constant. It must be emphasized that with appropriate reinforcement detailing which efficiently utilizes post-cracking tensile strength of ECC, the sectional ductility of ECC column can be enhanced far beyond that of the concrete 2 column.

The influence of the material ductility on the sectional ductility reverses, as compared to concrete 2 and ECC, when the M-ϕ curves of HSHDC and COR-TUF in Figure 10.7 are compared. COR-TUF column seems be greatly under-reinforced in tension as the tensile reinforcement, post-yielding, is not able to compensate for the compressive force developed in COR-TUF column section due to COR-TUF's compressive strength, which causes sectional softening. On the other hand, HSHDC has substantial post-cracking tensile strength, in addition to same compressive strength as COR-TUF, to generate sufficient tensile force to compensate similar increase in compressive force. As a result, while the COR-TUF column section softens (decreasing M), HSHDC column section continues to harden (with increasing M) post-yielding of tensile steel.

The F-Δ curves, as explained above for concrete 1, reflect the changes in M-ϕ curves. Overall, for the same dimensions of the concrete column and steel reinforcement, HSHDC section outperforms all other concretes both in terms of horizontal force capacity and ductility (particularly ductility, as HSHDC column has almost twice the drift capacity as the columns of all other concretes).

10.6 Conclusions

A new framework for evaluating the influence of different materials on infrastructure resilience and sustainability, simultaneously, is developed in this Chapter. This framework is posed in form of an optimization problem that treats infrastructure resilience as a constraint and environmental and economic costs (sustainability) as objective functions. Evaluation of various materials in a simple structural application demonstrates the effectiveness of this framework for making informed material choices that are optimal for both infrastructure resilience and sustainability.

A moment-resisting structural column subjected to severe horizontal pushover force is used as an example in this chapter to demonstrate the application of the new framework for analyzing various materials. From the analysis, ECC and HSHDC emerged as the most sustainable materials, while satisfying adequate resilience. Although the ECC column was evaluated slightly better than the HSHDC column for the considered hazard, the HSHDC column with smaller column dimensions has greater deflection capacity than the ECC column. This is made possible by efficiently utilizing HSHDC's significantly higher compressive strength than ECC, along with post-cracking tensile strength and ductility.

References

1. UFC 3-340-02 (2008) "Structures to Resist the Effects of Accidental Explosions" Washington, DC: US Department of Defense.

2. Smith, P. & Cormie, D. (2009) *Blast Effects on Buildings (2nd Ed.)*, Thomas Telford.

3. Kendall, A. (2007) "Concrete Infrastructure Sustainability: Life Cycle Metrics, Materials Design, and Optimized Distribution of Cement Production" PhD Dissertation, Ann Arbor, MI: University of Michigan.

4. Lepech, M.D. (2006) "A Paradigm for Integrated Structures and Materials Design For Sustainable Transportation Infrastructure" PhD Dissertation, Ann Arbor, MI: University of Michigan.

5. Bocchini, P., Frangopol, D., Ummenhofer, T. & Zinke, T. (2013) "Resilience and Sustainability of the Civil Infrastructure: Towards a Unified Approach" *Journal of Infrastructure Systems*, DOI: 10.1061/(ASCE)IS.1943-555X.0000177.

6. Holling, C.S. (1973) "Resilience and Stability of Ecological Systems" *Annual Review of Ecology and Systematics*, 4(1), 1–23.

7. Gordon, J.E. (1978) *Structures*, London, UK: Penguin Books, pp. 89-91.

8. Timmerman, P. (1981) "Vulnerability, Resilience and the Collapse of Society: A review of Models and Possible Climatic Applications" *Environmental Monograph, Institute for Environmental Studies, University of Toronto, Canada*, 1, pp. 19.

9. Brundtland, G. H. (1987) *Our Common Future*, Report of the United Nations World Commission on Environment and Development, Oxford, UK: Oxford University Press.

10. Puppe, C. (1991) *Distorted Probabilities and Choice under Risk*, Lecture notes in economics and mathematical systems, V.363, Springer, Germany.

11. Bruneau, M., Chang, S.E., Eguchi, R.T., Lee, G.C., O'Rourke, T.D., Reinhorn, A.M., Shinozuka, M., Tierney, K., Wallace, W.A. & Winterfeldt, D.V. (2003) "A Framework to Quantitatively Assess and Enhance the Seismic Resilience of Communities" *Earthquake Spectra*, 19(4), 733–752.

12. Porter, K., Kennedy, R. & Bachman, R. (2007) "Creating Fragility Functions for Performance-Based Earthquake Engineering" *Earthquake Spectra*, 23(2), 471-89.

13. Ashby, M.F. (2009) "Penalty Functions" In *Materials and the Environment: Eco-informed Material Choice*, Butterworth-Heinemann: New York, NY, pp.176-8.

14. Wight, J.K. & MacGregor, J.G. (2009) "Example 11-2: Design of a Tied Column for a Given Pu and Mu" In *Reinforced Concrete: Mechanics and Design (5th Edition)*, Upper Saddle River, NJ: Pearson Education Inc., pp.521-4.

15. ACI 318 (2008) "Building Code Requirements for Structural Concrete and Commentary" Farmington Hills, MI: American Concrete Institute.

16. Wight, J.K. & MacGregor, J.G. (2009) "Flexure: Behavior and Nominal Strength of Beam Sections" In *Reinforced Concrete: Mechanics and Design (5th Edition)*, Upper Saddle River, NJ: Pearson Education Inc., pp.103-17.

17. Wight, J.K. & MacGregor, J.G. (2009) “Load Combinations” In *Reinforced Concrete: Mechanics and Design (5th Edition)*, Upper Saddle River, NJ: Pearson Education Inc., pp.23-24.

18. Huynh, P. (2012) “Price Index for Selected Highway Construction Items” California Department of Transportation, Sacramento, CA.

19. Johnson, T.W. “Comparison of Environmental Impacts of Steel and Concrete as Building Materials Using the Life Cycle Assessment Method” MS Dissertation, Cambridge, MA: Massachusetts Institute of Technology.

20. Mori, K. (2012) “Modeling the impact of a carbon tax: A trial analysis for Washington State” *Energy Policy*, 48, 627-39.

PART V: SYNTHESIS

CHAPTER 11: CONCLUDING REMARKS

11.1 Research Overview

This doctoral research focused on the multi-scale development and investigation of a new class of concrete, with unprecedented combination of mechanical properties, and its influence on infrastructure resilience and sustainability. The research tasks, as summarized below, are divided into three parts in this dissertation – Part II: Material Development, Part III: Material and Structural Resilience, and Part IV: Infrastructure Sustainability and Integration with Resilience (Part I is Introduction and Part V is Synthesis).

The material development, detailed in Part II of this dissertation, commenced in Chapter 2 with a thorough literature review of existing concretes with ultra-high compressive strength (e.g. COR-TUF) and tensile ductility (e.g. ECC) to gain insights into each material's development, and to identify the challenges for integrating high compressive strength and tensile ductility in a single concrete. Fundamental differences in the material design philosophies of these two concretes emerged from this study. The high strength concrete design focuses on enhancing matrix strength to *prevent* or delay the mechanical damage (cracking) through

methods such as dense particle packing, flaw size and number minimization, and microstructure and toughness enhancements. On the other hand, the high ductility concrete design focuses, among other factors, on the fiber/matrix interaction to efficiently *manage* the damage by facilitating controlled micro-cracking through the micromechanics-based tailoring and selection of mixture ingredients. It is concluded in Chapter 2 that for achieving a concrete with ultra-high compressive strength and tensile ductility, it is necessary to maintain the matrix attributes for high compressive strength (e.g. dense particle packing), while tailoring the fiber/matrix interaction, simultaneously, to satisfy the micromechanics-based conditions for multiple cracking.

Using COR-TUF as a starting point for the material development in this doctoral research, the characterization of its composite tensile behavior and micro-scale fiber/matrix interactions was performed, which is detailed in Chapter 3. COR-TUF is a UHPC developed at US Army ERDC, whose matrix is specifically tailored to achieve ultra-high compressive strength in excess of 200 MPa. However, COR-TUF specimens exhibited a lack of tensile ductility (< 0.1% under direct tension) in this study with a strain-softening behavior, along with large variability in tensile properties and severe matrix spalling. A detailed micro-scale investigation of COR-TUF was performed through single fiber pullout tests and micromechanics-based analytical modeling. This micro-scale analysis, in Chapter 3, revealed that in spite of satisfying the strength criterion for multiple cracking, COR-TUF violates the energy criterion as the complementary energy of crack bridging is insufficient in overcoming the crack propagation resistance due to high fracture toughness of the matrix, which prevents COR-TUF from achieving tensile ductility.

Building upon the insights of Chapters 2 and 3, the micromechanics-based mixture ingredient (both fiber and matrix) selection and the experimental determination of the composite mechanical properties of various mixtures, leading up to the development of a new concrete named High Strength High Ductility Concrete (HSHDC), is detailed in Chapter 4. Selection of the fiber type and geometry, based on the micromechanical analysis, and matrix modifications for improving mix rheology were significant for achieving HSHDC. The practical insights into the influence of material ingredients on the mixtures' fresh properties and the influence of the fresh properties on fiber dispersion and composite properties are also discussed in this chapter. HSHDC developed in Chapter 4 possesses a unique combination of compressive strength (163 MPa) and tensile ductility (3.4%), unparalleled by any other concrete with short discontinuous fibers. The harmonious interaction between the ultra-high molecular weight polyethylene (PE) fibers and modified COR-TUF matrix with ultra-high compressive strength, enabled by the micromechanics-based design, is the reason behind HSHDC's unmatched mechanical performance.

The composite-scale experimental characterization of HSHDC through direct tension, split-tension, flexure, and uniaxial compression tests are detailed in Chapter 5. The curing procedure of HSHDC was slightly modified in Chapter 5, compared to Chapter 4, to further enhance its mechanical properties and reduce variability. The average compressive strength and tensile ductility of this HSHDC are 166 MPa and 3.4% (with COV of 11%), respectively. The average first crack strength, uniaxial, split-tension, and flexural strengths (MOR) of HSHDC are experimentally determined equal to 8.3 MPa, 14.5 MPa, 17.0 MPa, and 31.8 MPa (with peak

deflection of 2.5% of the span length), respectively. Robust multiple micro-cracking is observed in all HSHDC specimens. However, the crack widths in HSHDC tensile specimens are 3-4 times larger than ECC due to absence of interfacial chemical bond and higher ultimate tensile stress. Reducing the crack widths was one of the objectives of investigation detailed in Chapter 9. In addition to the mechanical properties and crack widths, experimental determination of fresh properties and density of HSHDC and its matrix is also reported in Chapter 5.

The microstructure and micro-scale mechanical behavior of HSHDC are reported in Chapter 6. A number of logically organized research tasks were performed in this investigation. First, the electron micrographs and elemental analysis of the major phases in HSHDC microstructure were documented. The ITZ between the fiber/matrix was identified using EDS analysis. Second, the fiber and flaw size distributions in HSHDC were determined through fluorescence and optical microscopy, respectively. Fiber and flaw size distributions of HSHDC provide measures of heterogeneities in the material that are caused by the mix processing, specimen geometry, and casting methods. Third, the fiber/matrix interaction properties of HSHDC were experimentally determined using single fiber pullout tests with aligned and inclined fibers (for determining snubbing coefficient and inclination-hardening, along with fiber/matrix bond properties). While the frictional bond between the PE fiber and HSHDC matrix was found to be greater (however, with negligible slip-hardening) than that between the PVA fiber and ECC matrix, chemical bond was almost negligible in HSHDC. In the course of this investigation, a new mechanism of inclination-hardening was discovered, which was found to be unique in HSHDC due to its high strength matrix. The tunnel crack mathematical model for computing single fiber pullout behavior was appropriately modified to capture the observed

mechanism. Finally, a scale-linking analysis was performed to verify that the fundamental conditions of micromechanics for strain hardening are satisfied by HSHDC for various fiber distributions, which provides a rational basis behind its robust tensile ductility.

In Part III of this dissertation (Chapter 7 and 8), the resilience of HSHDC at various length scales is examined. While the multi-scale mechanical property characterization of HSHDC detailed in Chapters 5 and 6 used experiments performed at pseudo-static strain rate, Chapters 7 and 8 focused on high rate behavior of HSHDC under direct tension, impact, and blast loads, which are typically experienced during extreme events.

The details of the direct tension tests at high strain rates (from 10^{-4}/s to 10/s) performed on the composite single fiber pullout specimens of HSHDC are given in Chapter 7. Comparable increases of about 40-50% (over the strain rate range 10^{-4}/s to 10/s) were observed in both first crack strength and the ultimate tensile strength of HSHDC. The tensile strain capacity of HSHDC was found to decrease with increasing strain rate from about 4.2% at 10^{-4}/s to 2.9% at 0.1/s but remain constant thereafter (mainly caused due to reduction in crack widths, which show similar trend). The micro-scale investigation revealed slight increases in all the fiber/matrix interaction properties; however, the absence of chemical bond between the PE fiber and HSHDC matrix makes the overall fiber/matrix bond relatively insensitive to rate effects in comparison to ECC. Increases in PE fiber strength and modulus with strain rate were found to be the most consequential for fiber-bridging in HSHDC. At the fastest rate, the PE fiber strength and modulus increase by about 21% and 85% of their respective pseudo-static values. The increases in micro-scale fiber strength and modulus justify the increase in the ultimate tensile strength and

decrease in average crack width with strain rate. In spite of the increase in the matrix fracture toughness and decrease in complementary energy (due to increase in fiber-bridging stiffness), J_{tip} remains an order of magnitude smaller than J_b' even at high strain rates, which coupled with constant σ_{ult}/σ_{fc} ratio (1.8±0.2) facilitates multiple cracking at all strain rates investigated in this study.

The behavior of HSHDC slabs under impact and blast loads, and its comparison with that of COR-TUF slabs, is detailed in Chapter 8. First, an experimental investigation of HSHDC and CORTUF slabs under drop-weight impact tests (with varying impact energies) was performed. Under multiple drop-weight impacts (20 impacts or failure, whichever occurs first), the COR-TUF slabs exhibit quasi-brittle flexural and shear failures accompanied by large localized cracks and excessive spalling. On the other hand, the HSHDC slabs exhibit ductile flexural behavior (without failure until 20 impacts) with well-distributed multiple fine radial cracks with almost no spalling, regardless of the impact head diameter. These drop-weight experiments were satisfactorily simulated using Finite Element (FE) Analysis in LS-Dyna, utilizing the MAT_072R3 material model to simulate the behavior of HSHDC and COR-TUF materials. This FE analysis, which was further expanded to blast loads, achieved the following: (1) provided insights, in terms of stress and strain contours, into the experimentally determined structural response of the slabs, (2) optimized the layered slab configuration for simultaneously maximizing impact resistance and minimizing cost, and (3) predicted the behavior of HSHDC and COR-TUF slabs under blast loads, which can be verified with shock-tube tests in the future.

Part IV of this thesis (Chapters 9 and 10) focused on the sustainability aspects of HSHDC and its infrastructure applications, while maintaining adequate resilience. The development of greener and more durable versions of HSHDC (with smaller crack widths), compared to the version discussed thus far, is presented in Chapter 9. The development of green HSHDC involved partial substitution of the Class H (oil-well) cement by suitable recycled alternatives, while maintaining the mechanical properties above the set targets (compressive strength > 150 MPa and tensile ductility > 3%). It is concluded that the optimum combination of mechanical performance and reduction in MSI is achieved with grade 120 slag replacing 25% by weight of class H cement in HSHDC. The approach adopted for attaining durable HSHDC, with reduced average residual crack width, entailed enhancing the fiber/matrix interfacial bond via two methods: (1) plasma treatment of PE fibers, and (2) addition of silane coupling agents in the matrix. While the plasma treatment was effective in enhancing the bond of an individual continuous fiber with the HSHDC matrix (provided no heat is applied during curing), the silane coupling agents proved to be more effective in achieving the desired reduction in crack widths, along with simultaneous improvement in the mechanical properties due to better dispersion in the composite.

In addition to the above material development, the life cycle environmental performances of all the green and durable versions of HSHDC were compared in Chapter 9 using process-based life cycle assessment (LCA) of bridge deck, which strategically employs HSHDC in the link-slabs instead of conventional steel expansion joints. This LCA estimates that the bridge deck containing HSHDC link-slab application will have about 30% lower environmental impacts (CO_2 emissions and primary energy) than the deck containing conventional expansion joint over

the 90 years-service life of the bridge deck, mainly due to HSHDC's ductility and durability. From the life cycle comparison of various green and durable HSHDCs, it is concluded that reduction in MSI and/or crack width of HSHDC (or similar strain hardening concretes) should be pursued as an objective for environmental material design only if it also enhances (or at least maintains) tensile ductility, which plays the paramount role in determining the service life of the link-slabs assuming rebar corrosion-dominated deterioration model.

A new framework for evaluating the influence of different materials on infrastructure resilience and sustainability, simultaneously, is developed in the penultimate chapter (Chapter 10) of this dissertation. This framework is posed in form of an optimization problem that treats infrastructure resilience as a constraint and environmental and economic costs (sustainability) as objective functions. Evaluation of various materials in a simple structural application demonstrates the effectiveness of this framework for making informed material choices that are optimal for both infrastructure resilience and sustainability.

Overall, the research activities reported in this dissertation describe the systematic development of a novel concrete specifically aimed at simultaneously enhancing the resilience and sustainability of our infrastructure.

11.2 Scientific Contributions and Research Impact

The major scientific contributions and the broader impacts of the associated research are highlighted below in order of their appearance in this dissertation:

Fundamental cause of the lack of tensile ductility of COR-TUF: COR-TUF and similar high-strength fiber-reinforced concretes (e.g. Ductal®, RPC, etc.), whose design philosophy focuses on achieving high compressive strength and toughness (but not tensile ductility – the distinction between toughness and tensile ductility is presented in Section 2.3), lack tensile ductility, in spite of the use of large volume of fibers (e.g. V_f = 3.6% in COR-TUF). Through micromechanics-based investigation of the fiber/matrix interaction and σ-δ analysis, the violation of the energy criterion for multiple cracking was identified as the underlying cause of such behavior. This insight is central for not only achieving HSHDC, but also for guiding the future of design of ductile high-strength concretes as well.

Invention of HSHDC and database of its multi-scale properties: The invention of high-strength high-ductility concrete (HSHDC) in this research demonstrated, for the first time, that it is feasible to achieve a concrete (reinforced with discontinuous fibers at low volume fractions) with ultra-high compressive strength (> 150 MPa) and tensile ductility (> 3%), simultaneously. It has opened a new avenue of material development, which, instead of trading-off strength for ductility (and vice-versa), achieves both the objectives at the same time, which is essential for infrastructure resilience and sustainability. The database of the unique properties of HSHDC determined in this study at multiple length scales from 10^{-6} m (fiber/matrix interaction

properties) to 10^0 m (HSHDC beams and slabs) will act as benchmarks for designing and comparing future concretes of this class of materials.

Discovery of new micro-scale fiber/matrix interaction mechanism and mathematical model improvement: The micromechanics-based investigation of HSHDC led to the discovery of a new inclination-dependent hardening mechanism of fiber pullout in HSHDC. The existing fiber/matrix interaction mechanisms developed for ECC were found to be incomplete in describing the experimentally observed inclined fiber pullout behavior of PE fibers embedded in a very high strength HSHDC matrix. The inclination-hardening mechanism contrasts with the micro-spalling phenomenon observed in polymer fiber pullout in moderate strength ECC matrix. The SEM micrographs provide evidence for this mechanism and its mathematical formulation. The closer match of the experimental curves to the computed σ-δ relation for coupons obtained using the modified HSHDC pullout model when compared with that from the ECC model provides further support to this mechanism.

Systematic framework for micromechanics-based analysis: A number of logically organized research tasks, utilizing a variety of investigation techniques, were conducted for the micromechanical analysis of HSHDC, as detailed in Chapter 6. Although almost all of these tasks have been employed in the past for analyzing ECC and other fiber reinforced concretes at separate instances, a systematic framework integrating these tasks in a logical manner was absent in the literature. Chapter 6 of this dissertation provides such systematic framework for the micromechanics-based investigation that is applicable to not only HSHDC but to any fiber reinforced concrete in general.

Rate effects in HSHDC at multiple length scales: High rate direct tension tests on the composite and single fiber pullout specimens revealed unique effects of strain rate in HSHDC. At micro-scale, the fiber/matrix bond is found to be relatively insensitive to rate effects (compared to ECC), as the nature of the bond is largely frictional in HSHDC which does not vary significantly with strain rate. Although the matrix fracture toughness increases, it is compensated by almost similar relative increase in ultimate tensile strength caused by increases in fiber strength and modulus (which increase fiber-bridging capacity) at high strain rates. As a result, the HSHDC composite specimens, compared to ECC, show smaller drop in tensile ductility from 4.2% at 10^{-4}/s to a plateau at 2.9% in the strain-rate range of 10^{-1}/s-10/s. These insights into HSHDC's behavior at high strain rates are useful for modeling and understanding the behavior of the structural elements (made of HSHDC) under extreme loading conditions.

Mechanisms of damage tolerance in HSHDC slabs under impact and blast loads: The experimental and numerical investigations (using finite element analysis) of HSHDC slabs demonstrated that the concentrated impact and blast energy is efficiently absorbed by the HSHDC slabs through diffused flexural micro-cracking, which is a direct result of HSHDC's tensile ductility. The material-scale damage tolerance of HSHDC translates into structural-scale damage tolerance in this manner. Such behavior was demonstrated, both experimentally and numerically, to be in sharp contrast with COR-TUF slabs, which showed damage localization and premature catastrophic failure. ECC slabs in previous studies have been shown to exhibit a response similar to HSHDC slabs; however, as the fracture toughness and fiber-bridging capacity of the HSHDC matrix are more than two-three times that of ECC (and both composites have the

same tensile ductility), the flexural micro-cracking in HSHDC slab overall absorbs significantly higher energy compared to a same-sized ECC slab. In addition to tensile ductility, the high compressive strength and modulus of HSHDC also limits slab deflections, which is crucial for achieving structural resilience (lower recovery cost).

Finite element material model for HSHDC: The MAT_072R3 material model in LS-Dyna is utilized for simulating the rate-dependent strain-hardening behavior of HSHDC (under multi-axial stress states) in this doctoral research. There are very few studies in literature, which have modeled strain-hardening concretes in rate-dependent finite element analysis. To the best of the author's knowledge, there is no model at present in the material library of any commercial rate-dependent finite element software for simulating the unique behavior of strain-hardening concretes such as HSHDC and ECC. Even the MAT_072R3 model, used in this research, was originally designed to simulate the behavior of concrete or strain-softening fiber reinforced concretes.

Taking advantage of two separate damage evolution parameters in tension and compression (in spite of having only one damage function [η-λ]) in the MAT_072R3 model and raising the built-in tensile pressure cutoff, the strain-hardening behavior of HSHDC was successfully modeled in this dissertation. An understanding of this material model (its relevant input parameters) from the perspective of a user (with basic solid mechanics background) wanting to simulate the strain-hardening behavior of ductile concretes is presented in this dissertation. Thus, the FE model presented here will serve as a useful guide for researchers in the

future to simulate ductile concretes with MAT_072R3 model, or to develop an improved model that explicitly considers the tensile strain-hardening behavior of ductile concretes.

Novel use of silane coupling agents for tailoring the fiber/matrix interfacial bond in HSHDC: Silane coupling agents are typically used to form a durable bond between siliceous inorganic material inclusions in an organic (typically polymer) resin. Although silane coupling agents have been used in the past to enhance hydrophobicity of concrete for durability applications, this research for the first-time demonstrates the use of silane coupling agents to systematically tailor the fiber/matrix interfacial bond in a fiber-reinforced concrete. It is experimentally shown in this research that small dosages (< 2% by cement weight) of silane coupling agents can effectively enhance the PE fiber/matrix bond and cause reduction of the composite crack width under tension. In addition to crack width reduction, the silane coupling agents also improve the ultimate tensile strength, tensile ductility, and compressive strength of HSHDC. Using vinyl-silane coupling agent, a version of HSHDC has been developed which has compressive strength of 205 MPa, tensile ductility of 4.6%, tensile strength of 16.1 MPa, and residual crack width of 110 μm; this combination of properties is a record for discontinuous-fiber reinforced cementitious composites.

New framework for evaluating the influence of materials on infrastructure resilience and sustainability simultaneously: The majority of the existing design frameworks treats infrastructure resilience and sustainability separately. However, such decoupled approach may result in the improvement of either resilience or sustainability at the cost of the other. For instance, using larger-sized structural members for enhancing resilience may reduce

sustainability due to greater materials usage. In Chapter 10 of this dissertation, a preliminary framework of material design is proposed as an optimization problem, which considers resilience as a constraint, and environmental and economic cost as objectives functions for minimization. As this framework is further developed in the future, it can potentially assist structural engineers in making the right material choice depending on their design objectives, which need not be limited to service-level structural performance (the current practice) but also include structural performance under extreme loads (resilience) and environmental sustainability indicators.

11.3 Recommendations for Future Research

For continued development of HSHDC, leading to its utilization in infrastructure applications, the following investigations are recommended.

Multi-axial behavior of HSHDC and rate effects under compressive loads: The finite element model in this dissertation requires inputs regarding multi-axial behavior of HSHDC and rate effects in HSHDC under compression. As the experimental investigation in this research focused only on the uniaxial behavior of HSHDC and rate effects under tensile loads, a number of the required inputs were taken from the literature on high strength concrete assuming similar behavior in compression. In order to improve the accuracy of the predictions of the finite element model, it is important to experimentally determine the multi-axial behavior of HSHDC and rate effects under compressive loads, and use that data as input in the finite element model.

Long term durability property measurements: The transport properties of HSHDC, such as permeability, chloride ion diffusivity, and sorptivity under varying pre-tensioning should be measured to characterize the long term durability of HSHDC. Insights into the influence of crack patterns of HSHDC on these transport properties will be further useful for re-tailoring the material for maximizing durability, while maintaining its mechanical properties. In addition, self-healing of micro-cracks under laboratory and natural environment is of interest. Accelerated corrosion tests using applied current can be used to study the corrosion of rebars in R/HSHDC.

Cost minimization: Currently, the cost of HSHDC per unit volume is about 2.7 times that of a UHPC with comparable compressive strength (e.g. COR-TUF). Since the PE fiber accounts for about 84% of the cost of HSHDC, hybridizing spectra with steel or other polymer fibers is expected to significantly reduce the cost. Such hybridization must be guided by the micromechanical design approach, which will ensure the satisfaction of the necessary strain hardening criteria for maintaining tensile ductility. Building upon the knowledge generated in this dissertation, the fiber/matrix interfacial bond enhancement through plasma treatment and coupling agents may be further investigated for minimizing cost.

Large-scale manufacture of HSHDC: For scaling up the mixing procedure for large batches of HSHDC, investigations aimed at correlating the fresh properties of the HSHDC matrix (plastic viscosity and yield stress) with fiber dispersion, as shown in this thesis for small batch size, should be undertaken for large batches as well. Determination of complete flow curves (shear stress-strain rate) in combination with these correlations will provide information about the optimum viscosity needed to achieve good fiber dispersion at a certain mixing shear

rate (function of the mixer). The desired viscosity can be achieved either by regulating the HRWRA dosage or slight modifications in the matrix proportions. Mechanical tests must be performed to verify the consistency of the mechanical properties among various batch sizes.

Shrinkage and creep: Due to high cement content and absence of coarse aggregates, HSHDC is prone to micro-cracking under restrained shrinkage. Such micro-cracking may not be critical for safety as it is inherently controlled by fiber reinforcement; however, it may create serviceability problems, and therefore, needs to be experimentally quantified. Creep, under sustained loads, within the matrix and the PE fibers may also influence the long term behavior of HSHDC. As a result, studies determining shrinkage and creep behaviors of HSHDC should be undertaken for potential structural applications.

Interactions between steel reinforcement and HSHDC: Due to its extreme tensile ductility of the same order of magnitude as steel, HSHDC is expected to be more compatible when deforming with steel reinforcing bars than other concretes. For instance, the influence of tensile ductility of HSHDC on strain distribution in the reinforcement and interfacial bond stress (between steel rebar and HSHDC) is of interest. As the majority of the tensile strength of real structures comes from the steel reinforcement, it is imperative to investigate this interaction between HSHDC and steel rebar for infrastructure applications.

Life cycle analysis of HSHDC's potential infrastructure applications: While the LCA model of bridge deck with link-slabs was used in this research as a tool to compare the influence of enhancements in material greenness (through cement substitution) and durability (through

crack width reduction and increase in tensile strain capacity) on infrastructure sustainability, this application does not utilize the extreme compressive strength of HSHDC (it only utilizes its tensile ductility). This model, therefore, undervalues HSHDC's influence on infrastructure sustainability when compared with ECC. LCA of applications such as seismically designed moment frames or even the extension of the bridge deck model which includes the central bridge column designed for resilience under vehicle impacts can be used in the future to effectively demonstrate the influence of HSHDC on infrastructure sustainability.